Somnath Ghosh
Christopher Woodward
Craig Przybyla *Editors*

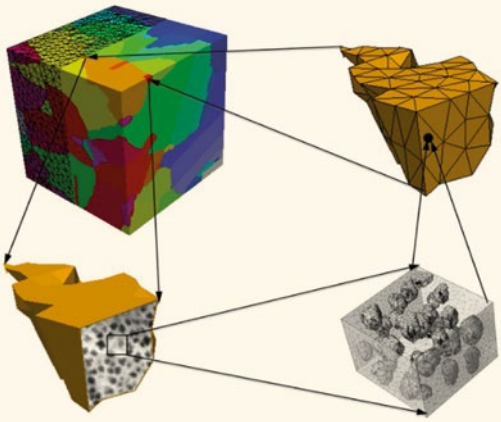

Integrated Computational Materials Engineering (ICME)

Advancing Computational and Experimental Methods

Springer

Integrated Computational Materials Engineering (ICME)

Somnath Ghosh • Christopher Woodward
Craig Przybyla
Editors

Integrated Computational Materials Engineering (ICME)

Advancing Computational and Experimental Methods

Springer

Editors
Somnath Ghosh
Departments of Civil, Mechanical Engineering and Materials Science & Engineering
Johns Hopkins University
Baltimore, MD, USA

Craig Przybyla
Air Force Research Laboratory/RX
Wright-Patterson Air Force Base
Dayton, OH, USA

Christopher Woodward
Air Force Research Laboratory/RX
Wright-Patterson Air Force Base
Dayton, OH, USA

ISBN 978-3-030-40561-8 ISBN 978-3-030-40562-5 (eBook)
https://doi.org/10.1007/978-3-030-40562-5

This book is dedicated to all researchers in the Center of Excellence on Integrated Materials Modeling (CEIMM) and Air Force Research Laboratories, whose dedication made this possible.

Preface

The Integrated Computational Materials Engineering (ICME) thrust is an integral part of the Materials Genome Initiative (MGI) that has been launched to advance multi-scale materials modeling for addressing complex materials structure-property-performance-processing relationships. It is viewed as the integration of computational tools for materials discovery, design, and sustained development, with information technologies, component design systems, and manufacturing process simulations, to foster improved product performance, manufacturability, and sustainability. The ICME thrust is aimed at novel innovations in fundamental science and engineering of materials for providing significant tools that can bridge the gap between materials engineering and component design. Robust theoretical, computational, and experimental methods pertaining to materials, performances, and process models are emerging as a consequence of this thrust. High-performance structural applications that have been hitherto restricted to available structural materials with limited ability to integrate new materials into the design process are now opening up to new possibilities with the advances made in this thrust.

While structural engineering has greatly benefited from the introduction of effective computational tools, such as finite element, finite difference, and boundary element methods, advances in computational and experimental methods have been more piecemeal for the materials community. This is due to the underlying complexities in processing-structure-property relationships for different classes of materials like metals, polymer matrix composites, and ceramics. The materials science paradigm for structural materials relates the internal structure, produced through processing, to the desired properties and response. The ICME approach has helped create synergistic advances in materials research, blending advanced computational mechanics with materials characterization, multi-scale modeling, and experimental property acquisition, providing a strong computational backbone for integrating computational tools and data handling methods with high pedigree experimental methods for accelerating materials transition into component design to achieve improved product manufacturability, performance, and sustainability.

In the spirit of fostering foundational advances in computational and experimental methodologies supporting the ICME theme, the Materials and Manufacturing Directorate of the Air Force Research Laboratory at Wright Patterson Air Force Base and the Air Force Office of Scientific Research jointly initiated the *Center of Excellence on Integrated Materials Modeling (CEIMM)* in 2012, with Johns Hopkins University as the lead institution. Other major partners were the University of California at Santa Barbara and the University of Illinois at Urbana-Champaign. CEIMM was focused on the development of fundamental science and common threads of computational and experimental methods pertaining to structural materials. The central philosophy was to overcome limitations of empiricism-based phenomenological models through physics-based 4-D spatiotemporal multi-scaling approaches, transcending materials classes and boundaries between computational materials science and computational mechanics. Research in CEIMM has developed novel theoretical, computational, and experimental methods for advancing the state of the art in science and engineering of ICME-related fields without being material-specific. This includes mechanical modeling of high-temperature metals and composite materials including predicting spatial and temporal response and properties like strength, crystal plasticity, fracture, and fatigue. Significant advances have been made in computational multi-scale modeling, materials characterization, and experiments to efficiently describe the evolution of heterogeneities and outlier structures and their effect on the balance of structural properties. A suite of methods and models have been developed for two classes of structural materials, namely, nickel-based superalloys and epoxy-matrix carbon fiber composites. The unifying platform is accomplished through the incorporation of fundamental physics-based multi-spatial and temporal scale modeling, in lieu of conventional empiricism.

This book discusses significant research advancements in ICME that have taken place under the aegis of CEIMM. It includes contributions from other thought leaders in the field, who are leading researchers in ICME from prominent academic institutions and government laboratories. It also introduces theoretical, computational, and experimental methods, advancing the state of the art in science and engineering of the ICME fields for structural materials. A special focus is on two structural materials listed below:

1. *Ni-based superalloys*, e.g., René 88DT, characterized by polycrystalline microstructures with sub-grain heterogeneities in the form of secondary $\gamma - \gamma'$ phases;
2. *Polymer matrix composites* with carbon fibers in epoxy matrix.

Four themes are broadly addressed in this book. They are:

- *Multi-scale Data Acquisition, Characterization, and Image-Based Virtual Models:* This introduces methods of acquiring high-fidelity materials microstructural data and methods of advanced microstructural characterization and addresses the generation of three-dimensional statistically equivalent virtual models.

- *Physics-Based Multi-scale Model Development:* The development of image-based micromechanical computational models with morphological and crystallographic details is discussed. The models represent dominant deformation and failure mechanisms at each scale. Comprehensive methods of identifying representative volume elements (RVEs) based on microstructure and materials response or properties are detailed. Associated boundary conditions for RVEs with non-uniform microstructures are derived. Hierarchical multi-scale models for connecting mechanisms at different scales are discussed. Spatial scales encompass atomistic scales, mesoscales of coarse-grained models and discrete dislocations, and microscales of polyphase and polycrystalline microstructures.
- *Experimental Methods for Constitutive Models and Failure Processes:* Novel experiments for aiding the development of computational models, with information on mechanisms and data for calibration and validation are addressed. Experiments characterize relevant properties and microstructural responses over a range of operating conditions.
- *Probabilistic Modeling and Uncertainty Quantification:* This discusses probabilistic models accounting for stochastic distributions of materials microstructure and properties.

The relations between microstructural morphology, crystallography, and mechanisms to the materials response at different scales are investigated.

This book is a collection of 14 chapters that discuss aspects of ICME developments, ranging from physics-based multi-scale computational methods to experimental data acquisition and uncertainty quantification. The first eight chapters deal with experiments and modeling of polycrystalline alloys, with a focus on Ni-based superalloys. Chapter 1 details methods of 3D microstructural data acquisition for predicting monotonic and cyclic properties of superalloys. It provides information on the distribution of important structural features, namely, precipitates, annealing twins and grains. Data structures and workflow tools for generating and analyzing materials data in an ICME context are discussed in Chap. 2. Chapter 3 details fundamental aspects of statistically equivalent virtual microstructures and microstructure and property-based statistically equivalent representative volume elements (M-SERVE and P-SERVE) of Ni-based superalloys at multiple scales. The two specific scales considered are the sub-grain scale of intragranular $\gamma - \gamma'$ microstructures and the polycrystalline scale of grain ensembles with annealing twins. Chapter 4 provides an overview of micro-tensile experiments and characterizations for the superalloy René 88DT. A computational micromechanics model of the polycrystalline superalloys application to Inconel 718 is presented in Chap. 5. A combination of simulations and tests, together with computational homogenization strategies, is used to predict the mechanical behavior of these superalloys. A comparison of deterministic and non-deterministic calibration methods for crystal plasticity model parameters is made in Chap. 6. Chapter 7 reports on the soft-coupled linkage between a macroscale damage model and mesoscale calculations of a suite of polycrystal instantiations of tantalum. A macroscale model is used to represent a

tantalum on tantalum plate impact experiment and predict the point in time in the loading profile when porosity is likely to initiate. Chapter 8, the last chapter in the category, projects a framework for quantifying effects of characterization error on the predicted local elastic response in polycrystalline materials.

Chapter 9 presents a unique materials agnostic data-driven framework to develop structure-property linkages and addresses curation of materials' knowledge from the available data sets in computationally efficient manner to extract and use the processing-structure-property relationships. Chapters 10 through 13 focus on the development of ICME-related techniques for polymer matrix composites. Chapter 10 provides a review of multi-scale modeling efforts involving molecular dynamics modeling of epoxy and epoxy-based composites for structural, thermal, mechanical, and interfacial properties. In Chap. 11, a novel microstructural statistics-informed boundary condition has been developed for statistically equivalent representative volume elements (serve) of polydispersed elastic composites. Chapters 12 and 13 relate to transverse failure of unidirectional composites, including sensitivity to interfacial properties and geometric modeling. Chapter 14, the final chapter, deals with the challenges in modeling dynamic behavior of granular media, reactive powder mixtures, energetic and composite materials, and multiphase materials. It discusses possible ways of exploring topology, property contrasts, and microstructural morphology to link dynamic response to micro- and mesoscale behavior.

It is our expectation that this book will address many of the current gaps in the ICME theme and will be a leading resource for practitioners of ICME. The materials presented in this book will enable researchers in academia, government laboratories, and industries to comprehend and approach ICME-related issues involved in predicting materials performance and failure with a focus on the structure-materials interaction. The book is expected to be an important scientific compilation of high value to the ICME community, especially in mechanical engineering, materials science and engineering, aerospace engineering, civil engineering, and other disciplines. We gratefully acknowledge the research support from the Air Force Office of Scientific Research (Program Managers Drs. Fariba Fahroo and Ali Sayir) and the Air Force Research Laboratories (Chief Scientists Dr. Barry Farmer and Timothy J. Bunning). This work would not have been possible without the financial and technical support of Johns Hopkins University and the Air Force Research Laboratory's Materials and Manufacturing Directorate. Chris Woodward recognizes the insightful discussions with Dr. Jeff Bauer during the conceptual phases of the center and the significant contributions and guidance of Dr. Tim Breitzman during the first 2 years of the project.

We, the editors, would like to extend our sincere thanks and appreciation to all the contributing authors of this volume for embracing our vision and providing excellent state-of-the-art articles on different topics in the general field. We are also thankful to the Springer editorial staff for their support with the production of this book. Somnath Ghosh expresses his love and deep appreciation to his wife, Chandreyee, for her constant encouragement and support throughout this project.

Craig Przybyla expresses his love and appreciation to his wife, Laura, and children, Elizabeth, Dallin, William, Christian, Emma, and Jane, for their unfailing support and encouragement in all his professional endeavors. Chris Woodward recognizes the love and support of his wife, Leslie, over the course of this project.

Baltimore, MD, USA — Somnath Ghosh
Dayton, OH, USA — Craig Przybyla
Dayton, OH, USA — Christopher Woodward
September 2019

Acknowledgment

This work has been supported through Grant No. FA9550-12-1-445 to the Center of Excellence on Integrated Materials Modeling (CEIMM) at Johns Hopkins University awarded by the AFOSR/RSL Computational Mathematics Program (Program Managers Dr. Fariba Fahroo and Dr. Ali Sayir). This support is gratefully acknowledged.

Contents

Contributors

Angel Agrawal Department of Aerospace Engineering, University of Illinois, Urbana, IL, USA

Akbar Bagri Departments of Mechanical and Civil Engineering, Johns Hopkins University, Baltimore, MD, USA

Geoffrey Bomarito Durability, Damage Tolerance and Reliability Branch, NASA Langley Research Center, Hampton, VA, USA

David Brandyberry Department of Aerospace Engineering, University of Illinois, Urbana, IL, USA

C. A. Bronkhorst Theoretical Division, Los Alamos National Laboratory, Los Alamos, NM, USA
Department of Engineering Physics, University of Wisconsin, Madison, WI, USA

H. Cho School of Mechanical and Aerospace Engineering, Korea Advanced Institute of Science and Technology, Daejeon, Republic of Korea

Amanda Criner Materials and Manufacturing Directorate, Air Force Research Laboratory, Dayton, OH, USA

Aitor Cruzado Department of Aerospace Engineering, Texas A&M University, College Station, TX, USA
Center for Intelligent Multifunctional Materials and Structures, TEES, Texas A& M University, College Station, TX, USA

Sean P. Donegan Air Force Research Laboratory, Materials and Manufacturing Directorate, Wright-Patterson Air Force Base, Dayton, OH, USA

David W. Eastman Department of Mechanical Engineering, Johns Hopkins University, Baltimore, MD, USA

Mclean P. Echlin The Materials Department, University of California Santa Barbara, Santa Barbara, CA, USA

Jaafar A. El-Awady Department of Mechanical Engineering, Whiting School of Engineering, The Johns Hopkins University, Baltimore, MD, USA

Philippe Geubelle Department of Aerospace Engineering, University of Illinois, Urbana, IL, USA

Somnath Ghosh Departments of Civil, Mechanical Engineering and Materials Science & Engineering, Johns Hopkins University, Baltimore, MD, USA

Manny Gonzales Materials and Manufacturing Directorate, Air Force Research Laboratory, WPAFB, Dayton, OH, USA

Lori Graham-Brady Department of Civil Engineering, Johns Hopkins University, Baltimore, MD, USA

G. T. Gray III Materials Science and Technology Division, Los Alamos National Laboratory, Los Alamos, NM, USA

Michael A. Groeber Air Force Research Laboratory, Materials and Manufacturing Directorate, Wright-Patterson Air Force Base, Dayton, OH, USA
The Ohio State University, Department of Integrated Systems Engineering, Columbus, OH, USA

Kevin J. Hemker Department of Mechanical Engineering, Johns Hopkins University, Baltimore, MD, USA

Jacob Hochhalter Department of Mechanical Engineering, University of Utah, Salt Lake City, UT, USA

George Jefferson Air Force Research Laboratory/RX, Wright-Patterson Air Force Base, Dayton, OH, USA

Anthony Klepacki Department of Aerospace Engineering, University of Illinois, Urbana, IL, USA

Dhirendra V. Kubair Department of Civil Engineering, Johns Hopkins University, Baltimore, MD, USA

William C. Lenthe The Materials Department, University of California Santa Barbara, Santa Barbara, CA, USA

Patrick Leser Durability, Damage Tolerance and Reliability Branch, NASA Langley Research Center, Hampton, VA, USA

William Leser Durability, Damage Tolerance and Reliability Branch, NASA Langley Research Center, Hampton, VA, USA

V. Livescu Materials Science and Technology Division, Los Alamos National Laboratory, Los Alamos, NM, USA

Javier Llorca IMDEA Materials Institute, Getafe, Madrid, Spain
Department of Materials Science, Polytechnic University of Madrid, Madrid, Spain

P. W. Marcy Computer, Computational, and Statistical Sciences Division, Los Alamos National Laboratory, Los Alamos, NM, USA

Christopher Montgomery Department of Materials Science and Engineering, University of Illinois, Urbana, IL, USA

Ahmad Najafi Department of Mechanical Engineering and Mechanics, Drexel University, Philadelphia, PA, USA

Kyle Nixon Department of Aerospace Engineering, University of Illinois, Urbana, IL, USA

Triplicane Parthasarathy UES, Inc, Dayton, OH, USA

Dipen Patel UES, Inc, Dayton, OH, USA

Maxwell Pinz Departments of Mechanical and Civil Engineering, Johns Hopkins University, Baltimore, MD, USA

Tresa M. Pollock The Materials Department, University of California Santa Barbara, Santa Barbara, CA, USA

Craig Przybyla Air Force Research Laboratory/RX, Wright-Patterson Air Force Base, Dayton, OH, USA

Michael Rossol Department of Materials Science and Engineering, University of Illinois, Urbana, IL, USA

Tim Ruggles Durability, Damage Tolerance and Reliability Branch, National Institute of Aerospace, Hampton, VA, USA

Javier Segurado IMDEA Materials Institute, Getafe, Madrid, Spain
Department of Materials Science, Polytechnic University of Madrid, Madrid, Spain

Paul A. Shade Materials and Manufacturing Directorate, Air Force Research Laboratory, Wright-Patterson AFB, Dayton, OH, USA

Maryam Shakiba Department of Civil and Environmental Engineering, Virginia Tech., Blacksburg, VA, USA

Nancy Sottos Department of Materials Science and Engineering, University of Illinois, Urbana, IL, USA

Jean-Charles Stinville The Materials Department, University of California Santa Barbara, Santa Barbara, CA, USA

Naresh N. Thadhani School of Materials Science and Engineering, Georgia Institute of Technology, Atlanta, GA, USA

Michael D. Uchic Materials and Manufacturing Directorate, Air Force Research Laboratory, Wright-Patterson AFB, Dayton, OH, USA

S. A. Vander Wiel Computer, Computational, and Statistical Sciences Division, Los Alamos National Laboratory, Los Alamos, NM, USA

Noah Wade Department of Civil Engineering, Johns Hopkins University, Baltimore, MD, USA

James Warner Durability, Damage Tolerance and Reliability Branch, NASA Langley Research Center, Hampton, VA, USA

George Weber Departments of Mechanical and Civil Engineering, Johns Hopkins University, Baltimore, MD, USA

Christopher Woodward Air Force Research Laboratory/RX, Wright-Patterson Air Force Base, Dayton, OH, USA

Xiawa Wu Department of Mechanical Engineering, Whiting School of Engineering, The Johns Hopkins University, Baltimore, MD, USA
Mechanical Engineering, The Pennsylvania State University, The Behrend College, Erie, PA, USA

Saikumar Yeratapally Durability, Damage Tolerance and Reliability Branch, National Institute of Aerospace, Hampton, VA, USA

Scott Zacek Department of Aerospace Engineering, University of Illinois, Urbana, IL, USA

Xiang Zhang Department of Mechanical Engineering, University of Wyoming, Laramie, WY, USA

The original version of this book was revised: A new co-author has been added in Chapter 12. The correction to this book is available at https://doi.org/10.1007/978-3-030-40562-5_15

Acquisition of 3D Data for Prediction of Monotonic and Cyclic Properties of Superalloys

McLean P. Echlin, William C. Lenthe, Jean-Charles Stinville, and Tresa M. Pollock

1 Superalloys and Fatigue

Turbine engines have continuously improved in performance and efficiency due to advances in materials and coatings, combined with the application of advanced thermomechanical, heat transfer, and aerodynamic design methodologies. Turbine disks are among the most safety-critical components in an aircraft engine and have therefore been the subject of extensive development and characterization studies [1–3]. Polycrystalline nickel-base superalloys are the typical material of choice for turbine disks due to their high fatigue resistance and ultimate tensile strength and good thermomechanical and thermochemical stability at elevated temperatures [4, 5]. Powder metallurgy processing is used to produce disk components with highly controlled grain size distributions, controlled inclusion (carbide and nitride) content via powder stock filtering, and near net shape part geometries [1–5]. Inclusion content and grain structure have both been shown to be influential in the fatigue life of disk alloys [6, 7]. An improved predictive capability of the mechanical performance of these alloys is required to enhance life prediction and reliability as well as guide the development of new alloys and processing paths.

Predicting fatigue properties of superalloys is particularly challenging, due to the localized character of the plasticity during cycling and its strong dependence on material structure. The schematic in Fig. 1 shows the microstructure of a polycrystalline superalloy, containing annealing twins as well as the $L1_2$ γ' precipitate strengthening phase, and the approximate length scales at which they

M. P. Echlin (✉) · W. C. Lenthe · J.-C. Stinville · T. M. Pollock
The Materials Department, University of California Santa Barbara, Santa Barbara, CA, USA
e-mail: mechlin@ucsb.edu; jeancharles_stinville@ucsb.edu; tresap@ucsb.edu

S. Ghosh et al. (eds.), *Integrated Computational Materials Engineering (ICME)*,
https://doi.org/10.1007/978-3-030-40562-5_1

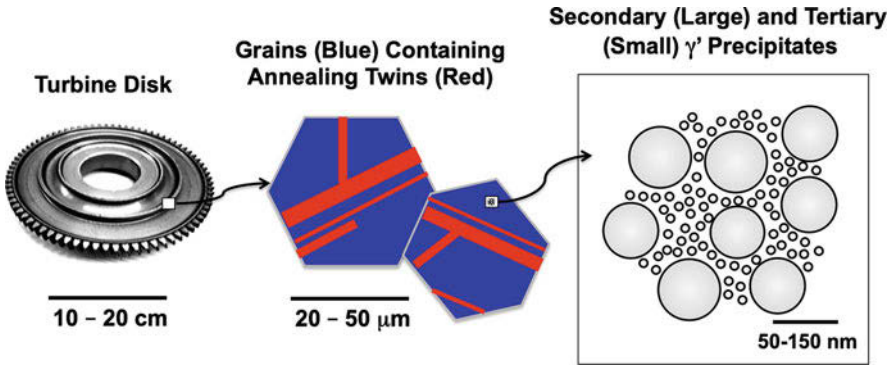

Fig. 1 Turbine disks (left) are often made from supersolvus nickel superalloys, such as René 88DT. This class of polycrystalline superalloys used for disks have microstructure at various length scales from precipitate structure (10's–100's nm as shown on the right) to twin related domain structure (10's–100 μm as shown in the center) with grains containing multiple, fine twinned structures of varying sizes that are crystallographically related to the parent material. They are strengthened by $L1_2$ γ' precipitates, which can exist over a range of length scales, depending on the processing conditions. Populations of secondary and tertiary γ' particles exist within the γ matrix phase (right), with the secondary particles typically being around 100 nm in diameter in René 88DT

exist. The fraction of $\Sigma 3$ annealing twin boundaries, a product of the processing path, can approach 46% by 2D measurement [8] or 70% by 3D measurement of the total boundary length fraction [9]. There is relatively limited crystallographic texture in these materials as a result of powder metallurgy processing or forging under nominally superplastic conditions. Depending on the alloy composition and processing route, populations of secondary and tertiary γ' particles exist within the γ matrix phase. The γ' precipitates inhibit the passage of dislocations through the γ matrix [5, 10], by requiring them to either shear through or bow around the ordered precipitates or cross-slip to continue to glide, effectively strengthening the material up to the solvus temperature of the precipitates. Typically, powder metallurgy consolidated components are oil quenched from near 1150 °C and then aged at 760 °C to produce a volume fraction near 40% of secondary and tertiary γ' precipitates [3].

In powder metallurgy superalloys such as René 88DT [1–3] cracks initiate in large grains that are in the tail of the size distribution and contain favorably oriented annealing twin boundaries [8, 11, 12] or at nonmetallic inclusions [7, 13, 14]. Though the annealing twin boundaries form during thermomechanical processing, the mechanisms by which they form are still not understood well enough to fully control their size and distribution. The relatively small grain size combined with moderate levels of $L1_2$ ordered precipitates imparts yield strengths above 1 GPa [4]. The relatively small grain size also limits the maximum length over which strain localization and slip events can occur over [6, 15, 16], before impinging on the adjacent high angle grain boundary, causing dislocation pileups.

Fatigue cracks typically initiate at the "weakest link" of the material structure. Rigorous models for fatigue thus require knowledge of the volume of the material that must be interrogated to capture the "rare" combinations of material structure that result in early strain localization and subsequent crack initiation [6, 7]. This, in turn, requires three-dimensional information on the distribution of important structural features: precipitates, annealing twins, grains, and in some cases carbides, nitrides, and oxides.

Nickel-base superalloys used for disks have microstructure at various length scales from precipitate structure (10's–100's nm) to twin related domain structure (10's–100 μm) with grains containing multiple, fine twinned structures of varying sizes that are crystallographically related to the parent material.

2 Importance of 3D Data

Many materials can be characterized using targeted 2D sections to analyze the microstructure, especially when the microstructure is isotropic and its features can be captured with well-known distributions [17, 18]. However, 2D inferences about structure and crystallography will be incomplete when investigating materials with rare features or heterogeneously distributed microstructure [17, 19, 20].

Nickel-base superalloys used for disks have microstructure at various length scales from precipitate structure (10's–100's nm) to twin related domain structure (10's–100 μm) with grains containing multiple, fine twinned structures of varying sizes that are crystallographically related to the parent material. Full 3D characterization is required to quantify the geometrical characteristics of the twins as well as to capture the five grain boundary parameters (three orientation parameters and two boundary normal parameters) [21–23]. The twin structures, which have been shown to be critical for the localization of strain [15, 16] and eventually the initiation of fatigue cracks [8, 11, 12], can be thin compared to the grain structure (μm thick) and may or may not extend across the entire grain.

A range of 3D tomography techniques have emerged in recent years that utilize femtosecond pulsed lasers [24, 25], mechanical polishing [26–29], broad ion beams [30], focused ion beams (FIB) [31–33], plasma FIBs [21, 34], and microtomes or serial block face SEM imaging [35, 36] to remove material in a serial sectioning approach. If only grain information is needed, then a combination of near-field [37–39] and far-field X-ray imaging allows for direct, nondestructive 3D characterization [40–44]. With current data collection and reconstruction methods, the X-ray diffraction methods have difficulty reconstructing crystallographic features that are below 5–10 μm in size, including fine twin structure, and also with crystals with preexisting strain gradients such as in samples that have been plastically deformed. Here we focus on serial sectioning approaches, due to the presence of thin micron-scaled annealing twins which are challenging to characterize with X-ray techniques.

Manual serial sectioning polishing techniques are effective for relatively coarse sectioning resolutions, especially if fiducial depth markers are incorporated; how-

ever much more advanced robotic polishing systems have been developed for optical imaging [45] and electron microscopy [26–29]. Currently, cm^3 volumes have been captured using the AFRL/RoboMet LEROY sectioning systems, as well as entire turbine blade components [46] using manual polishing approaches. For SEM imaging combined with robotic serial sectioning, the vacuum cycling and sample transfer time sets a limit on the minimum cycle time, which makes experiments with limited SEM imaging more time-consuming compared to other electron-optics-based serial sectioning systems.

FIB and Xe-plasma FIBs (PFIB) are rather limited with respect to the total accessible volume that can be analyzed as well as the types of material and speed at which materials can be sectioned. Microtomes have been shown to be useful, but primarily for biological samples and soft structural materials such as aluminum and polymers, and microanalytical analysis is challenging due to the extreme mechanical deformation imparted at the cut face.

X-rays have proven difficult to access large volumes of material with μm-scale microstructural features, although the techniques for software reconstruction are rapidly improving allowing access to deformed metallic samples [47, 48] and in situ dislocation imaging [49]. The advantages of X-ray diffraction contrast tomography (DCT) and the TriBeam femtosecond laser-based technique can be found elsewhere [50]. The resolution of synchrotron DCT and the high energy diffraction microscopy (HEDM) have dramatically improved [47], especially due to new reconstruction algorithms that identify grains and diffraction spots. These codes are actively being improved by the growing community of DCT users and scientists, facilitated by the open repositories at the beamlines and the open-sourced nature of the code. Routine access to synchrotron facilities can be challenging and requires careful preparation, motivating efforts for the development of a range of lab-based X-ray techniques that can be made available more broadly and with short notice. The available lab-scaled DCT systems [51, 52] are most effective for in situ experiments on materials with coarser grains than those accessible by synchrotron X-ray diffraction experiments and mostly for undeformed samples; however the reconstruction codes and scanning speeds are improving rapidly.

3 The TriBeam

The TriBeam microscope, shown in Fig. 2, is a modified FEI/Thermo Fisher Scientific Versa 3D focused ion beam scanning electron microscope (FIB-SEM) designed for high-speed, low-damage, bulk (mm^3-scaled) serial sectioning [24, 25]. A femtosecond laser beam has been incorporated into the FIB-SEM chamber with scanning lens, optics, and an alignment system. Multimodal data may be collected between material removal steps using a range of detectors for grain orientation information (electron backscatter diffraction – EBSD), chemical information (energy dispersive X-ray spectroscopy – EDS), atomic density (backscatter electron detector), and topographical and morphological information (secondary electron

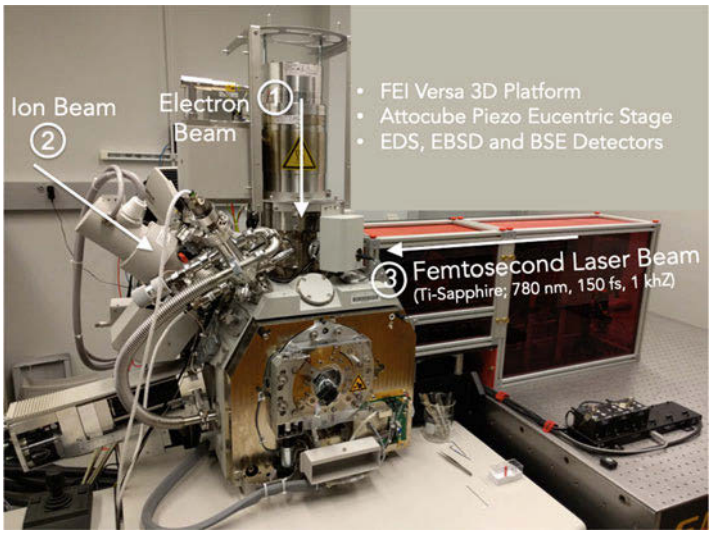

Fig. 2 The TriBeam microscope. The optics and beamline is contained within the red box on the right. The electron and focused ion beam are indicated. The femtosecond laser and beamline are directly aligned into the FIB-SEM via a coupled floating optics table

detector). Previous studies have shown that the damage resulting from femtosecond laser ablation is limited to dislocation injection in structural materials [53, 54]. To date, a wide range of materials including metals [55–57], ceramics [50], composites [58], and semiconductors [59] have been imaged in 3D using the TriBeam. The stock mechanically driven microscope stages are used to position the sample into the scanned laser beam (down to 0.5–1 μm slice thickness), or custom attocube piezoelectric stages can be utilized for slice thicknesses below 1 μm. However, the reliability and stiffness of the stock microscope stages are superior.

A typical 3D nickel dataset contains several hundred slices, with each slice requiring 1–100 min for acquisition, depending on the imaging modalities, imaging resolution, and whether FIB cleanup is required. The femtosecond laser ablation material removal step (1–3 min) is a very small fraction of the total slice time, which is typically dominated by the resolution at which EBSD data is gathered and whether FIB cleanup is performed.

The data in Table 1 shows the slice times that would be required for a hypothetical collection of a 1 mm^3 volume TriBeam dataset, with and without FIB cleanup and with 1 μm cubic voxels. Ga+ FIB cleaning requires approximately 1 min per every 20,000 μm^2 at glancing angles between 3 and 10°. The time required for cleanup does not change with glancing angle because the FIB dosage per area is held constant, resulting in increased dwell times at more glancing FIB beam angles. Experiments that do not require a FIB cleanup step reduce the total cycle time significantly, as shown in the last column in Table 1. Materials that do not require FIB cleanup in order to obtain acceptable quality EBSD patterns generally

Table 1 Times and percent of total cycle time required for imaging steps, material removal, stage moves, and surface cleanup that would be required during a 1 mm^3 experiment with 1 μm cubic voxel resolution

Operation	Slice time (min)	% of total cycle time	% of total cycle time (no FIB)
EBSD	30	33.7	76.9
Glancing FIB	50	56.1	-
SEM imaging	3	3.4	7.7
Fs laser Abl.	3	3.4	7.7
Stage moves	3	3.4	7.7

have good thermo-mechanical properties [53, 54]. Furthermore, new TriBeam instruments [60] that are based on a Xe-plasma FIB (PFIB) platform can perform focused ion beam cleanup with 30 kV and μA's of current, reducing the cleanup time by at least a factor of 20×. However, PFIB ion columns are still 3–4 orders of magnitude slower in terms of material removal speeds than a femtosecond laser, affirming the need for a multibeam system. The EBSD collection times described can easily scale to be much longer if the mapping resolution in x and y is finer than 1μm over a 1 mm^2 mapping area.

The latest CMOS-based EBSD cameras can collect patterns at rates up to 3000–5000 points per second. These cameras attain high pattern collection speeds through binning modes, whereby the full resolution of the camera is reduced by averaging the intensity from square regions of pixels. Binning increases the electron collection per binned pixel area and therefore allows for the reduction in exposure times, increasing pattern collection speed. Furthermore, the binned pattern resolutions are reduced, expediting the transfer rates between the hardware and decreasing computational times for indexing. These very high speeds are useful for gathering information suitable for grain mapping of single phase materials that diffract well, using Hough-based EBSD pattern indexing [61, 62]. In practice, larger EBSD pattern sizes are required for gathering more detailed information than grain maps while using Hough indexing, such as subgrain misorientation gradients, multiple phase indexing, and overlapping pattern information near grain boundaries. In this case, a longer exposure time and lower binning modes are necessary (slower collection speeds) for enhanced EBSD band contrast, typically yielding speeds of 500–800 EBSD patterns collected per second (50–80% of maximum). For instance, in order to collect a 3D EBSD dataset with well-defined subgrain orientation gradients, then the EBSD collection rate would likely need to be under 1500 pps. New methods such as dictionary indexing (DI) [63–67] and EMSphInx [68] are able to index EBSD patterns with relatively small resolutions (72 × 72 pixels), high noise, and low band contrast while maintaining angular orientation indexing resolution of 0.2–0.8° [69]. DI is substantially slower than Hough indexing however, currently limiting it to be an offline post-processing indexing mode, although the emerging EMSphInx method promises to increase the indexing speeds substantially [68].

The following actions may be incorporated into the workflow for a 3D experiment, depending on the data necessitated: femtosecond laser ablation and pole piece shutter insert/retract, glancing angle FIB milling (cleanup), stage movements, precision stage positioning by fiducial alignments with image processing scripts, detector insert/retracts (EBSD, EDS, BSE), EBSD data collection, EDS mapping, SE/BSE image collection, image processing for on-the-fly feature identification and FIB cleanup, automated electron beam tilt alignment and current measurements, and laser beam stability and power measurements. The example data collection times in Table 1 have been simplified to the primary detector imaging modes, laser ablation, FIB cleaning, and stage movements. More details about the TriBeam tomography setup can be found here [24].

3D datasets of nickel disk material were collected at different resolutions, as shown in Fig. 3, in order to characterize the γ' precipitates, high-resolution twin structure regions, and large volumes for grain and twin scale information. The resolution and sizes of the TriBeam datasets are summarized in Table 2.

A γ' precipitate dataset was collected from René 88DT using a FEI Quanta 3D DualBeam FIB-SEM with a ion beam sectioning resolution of 20 nm. A total volume of $5 \times 4.25 \times 4.5\,\mu m$ was reconstructed from 221 slices. BSE images from this dataset were segmented in the ImageJ/FIJI software package [70] and reconstructed to measure precipitate characteristics in this René 88DT polycrystalline superalloy.

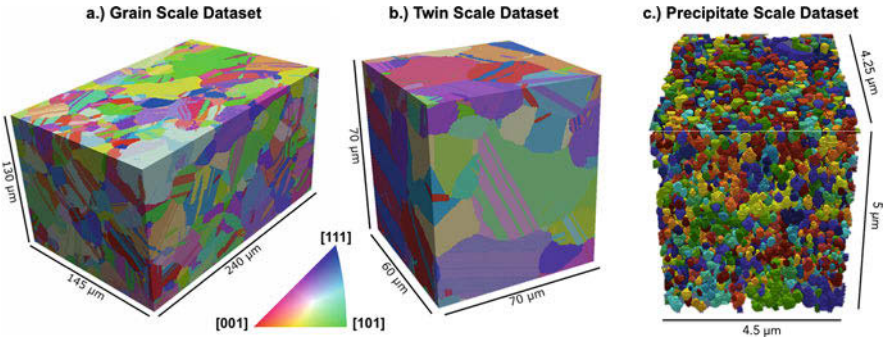

Fig. 3 TriBeam and FIB serial section datasets were collected from Ni-base disk material at resolutions to capture (left) large volumes of grain and twin data, (center) a high-resolution dataset containing detailed twin boundary regions, and (right) the γ' precipitates. The precipitate dataset coloring is showing individual precipitates as different random colors, whereas the grain and twin scale datasets are colored by IPF coloring

Table 2 Resolution, size, and dimensions of René 88DT 3D EBSD serial section datasets collected using the TriBeam microscope

Name	Resolution (µm)	Size (voxels)	Dimensions (µm)
Twin scale	$0.10 \times 0.10 \times 0.50$	$742 \times 993 \times 140$	$60 \times 70 \times 70$
Grain scale	$0.30 \times 0.30 \times 0.75$	$802 \times 482 \times 199$	$240 \times 145 \times 130$
Crack	$0.30 \times 0.30 \times 0.75$	$429 \times 757 \times 127$	$120 \times 200 \times 90$
Inclusion	$0.55 \times 0.55 \times 0.75$	$534 \times 802 \times 143$	$400 \times 600 \times 105$

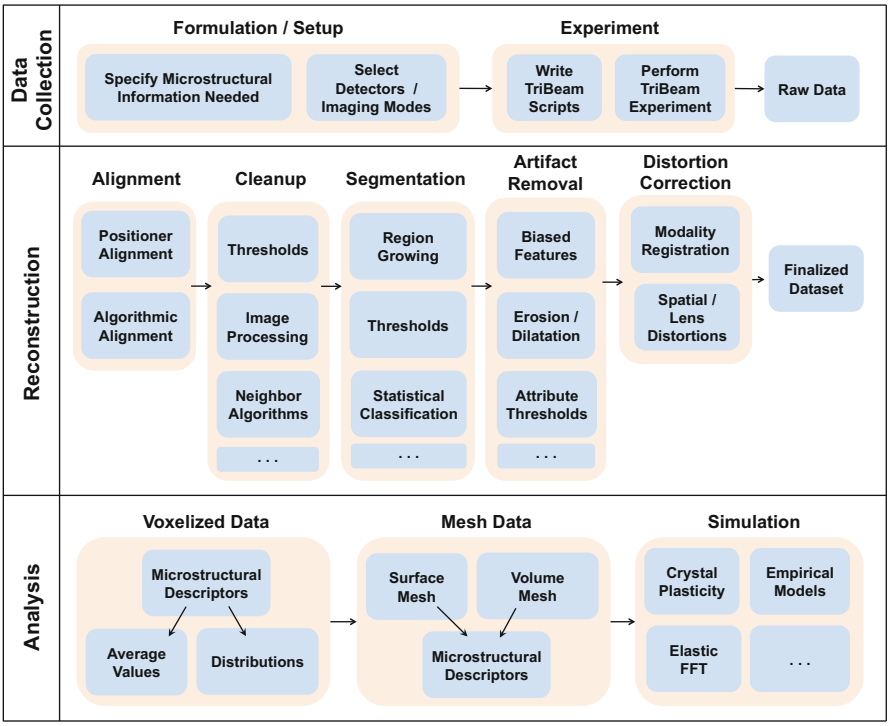

Fig. 4 The 3D EBSD data that is produced by the TriBeam requires a number of post-processing steps, which are described schematically here. Each dataset requires somewhat different parameters; however the core structure of that processing is relatively constant

A series of 3D EBSD TriBeam datasets were collected at various resolutions and at targeted features, including a fatigue crack initiation site and from a region where high-resolution digital image correlation (DIC) strain information had been collected [15, 71]. The characteristics of these René 88DT datasets are listed in Table 2, as well as an identifying name.

The workflow for acquiring, reconstructing, and analyzing 3D datasets is shown in Fig. 4. Briefly, this workflow includes defining data collection parameters that are closely tied to an understanding of the problem to be solved. These parameters include the 3D resolution necessary to capture the relevant microstructural features, which imaging modalities are required, or very specific parameters such as EBSD dwell time for pattern diffraction quality or potential pseudosymmetry complications [72–74]. Reconstruction of the 3D data happens next in the workflow, where a finalized dataset will be defined for analysis. Slice alignment, data cleanup, image segmentation, artifact removal, and distortion correction may be performed during this step. Data cleanup and artifact removal are always rooted in an understanding of the material via detailed 2D characterization. For instance, a minimum grain size filter may be applied if it is well-known that grains of a very small size do

not exist. Analysis of the data may be either based on voxelized or meshed data formats, depending on whether access to microstructural descriptors is desired, or direct property simulation. However, some microstructural descriptors may require meshed data formats as well, such as grain boundary inclinations.

For TriBeam EBSD datasets, DREAM.3D [75] is used to perform all reconstruction steps except for distortion corrections, which are performed using the methods described for strontium titanate [50] and a nickel superalloy [76]. The reconstruction steps can be clustered into four major groups: slice alignment, data cleanup, grain or feature segmentation, and artifact removal.

Although generating a preliminary dataset reconstruction is trivial with modern software tools, creating a high-quality reconstruction is still a significant challenge and often requires more time than dataset collection. Procedures that reduce noise or improve data quality greatly enhance the ability to extract high fidelity information from the dataset for modeling. Alignment and segmentation are by far the most difficult tasks. Alignment can be particularly challenging for small datasets where the morphology of a few dominant features dictates shifts computed during registration. Creating sample pedestals like the one fabricated using wire EDM shown in Fig. 5 that are small enough to collect data from the entire sample surface makes alignment significantly easier, and recovering the original sample shape provides a simple validation of alignment quality [20]. The pedestal fabrication procedure is a coarser scaled equivalency to the FIB procedures pioneered by Uchic. In many instances the pedestals used to collect data shown here were of the order of 1×1 mm in cross section by several mm in height. Orientation gradients and systemic misindexing due to pseudosymmetry are the most serious challenge for segmentation, when present.

Dataset volumes can become many terabytes in size, mostly due to the collection of raw EBSD patterns (EBSPs) or full spectrum EDS maps. The approximate scale

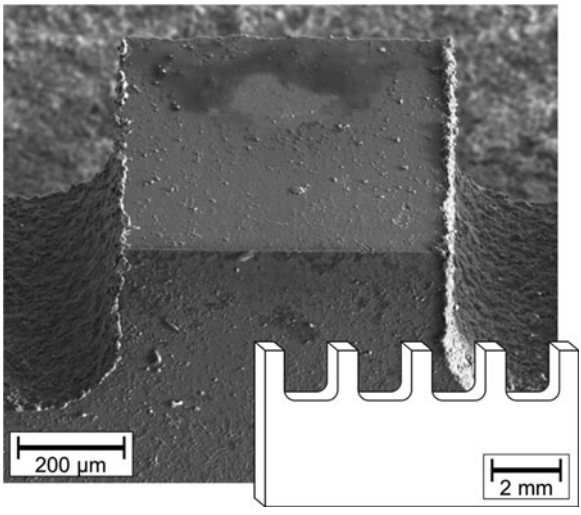

Fig. 5 Wire EDM is often used to create custom mm-scaled sample pedestals for targeted and untargeted TriBeam sectioning. The roughly 10 µm EDM heat-affected zone is mechanically polished away before TriBeam experiments or is located adjacent to a region where data will not be collected. The pedestal geometry is used in order to reduce material redeposition during laser ablation and to prevent shadowing of the EBSD signal at high sample tilt angles

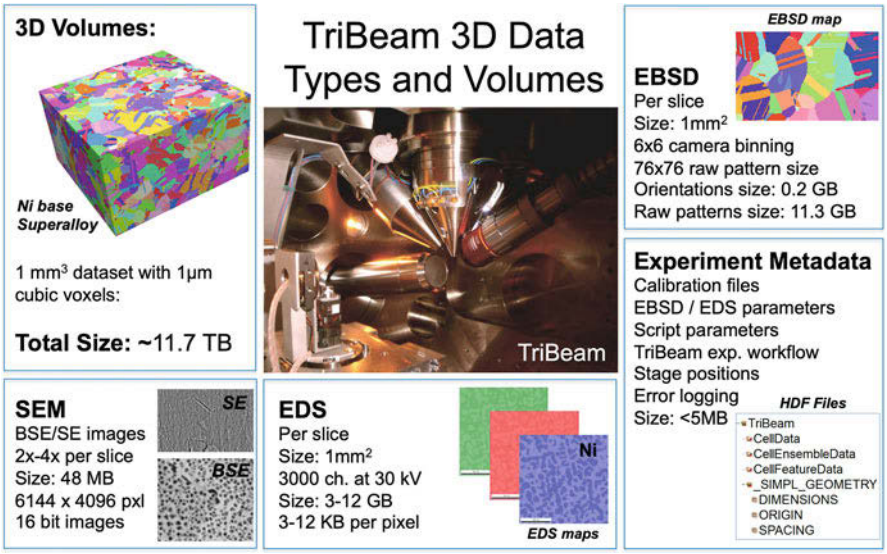

Fig. 6 Data usage is shown for the imaging modalities available during a hypothetical TriBeam experiment all scaled up for collection of 1 mm^3 of material at 1 µm cubic voxel size. Raw EBSPs, indexed EBSD maps, and EDS data take up the majority of the total data stored, with the rest being attributed to SEM images and metadata

of data usage is described in Fig. 6, where imaging data takes up much less than 1%, and the balance being EBSD indexed data, raw EBSPs, and full spectrum EDS data. EBSPs are stored so that re-indexing of the grain orientations can be performed with EMsoft dictionary indexing [63–66, 77], EMSphInx [68], or with higher-resolution Hough indexing parameters in the EDAX software OIM Analysis [78, 79]. EBSPs can scale to much larger sizes, depending on the EBSD detector resolution and whether a binning mode is used. For instance, using a EDAX Hikari camera to capture EBSPs at each mapping location can generate patterns of size 76×76 pixels for $6\times$ binning (as shown in the example in Fig. 6) up to full resolution patterns of roughly 480×480 pixels. Full spectrum EDS mapping also can require massive amounts of data storage, with 1000 channels typically recorded per 10 kV electron beam energy. Depending on the data type chosen to store the arrays and assuming 30 kV electron accelerating voltage, 3–12 KB is consumed for each spectrum, resulting in 3–12 GB per mm^2 mapping area at 1 µm resolution. The challenges with gathering such large full spectrum EDS data and detailed analysis are described in more detail elsewhere [80]. During an experiment, metadata such as the detector configurations and calibrations, stage position logs, hardware error logging (microscope, femtosecond laser and output, optics beamline, EBSD, EDS), and script parameters are all stored in HDF5 data containers similar to those formulated by Jackson and De Graef [81].

4 Targeted 3D Data

The microstructural configuration (neighborhood) is demonstrated to be influential to the initiation of fatigue cracks [6, 7, 9, 82]. A postmortem analysis of fatigue samples is a good way to identify systematic microstructural characteristics that result in fatigue cracks. Samples of René 88DT were cycled with fully reversed loading and then interrupted at 80% lifetime (R = −1, 1 Hz, peak load 758 MPa) such that the regions surrounding the initiated fatigue cracks could be investigated. Previous work has shown that this polycrystalline superalloy spends much of its life (80%) initiating cracks [82], before they propagate into the next few grains and then begin short crack-type growth.

A dataset was gathered in the TriBeam system from a region where a typical fatigue crack had initiated. The FIB was used to clean a 250-μm-wide region after femtosecond laser ablation using a 15 nA, 30 kV Ga^+ beam at an angle of 3° to the surface. Although EBSD maps containing high-quality diffraction patterns are obtainable from the laser-ablated surface in René 88DT, FIB cleaning was still performed in order to guarantee that small and thin twin features (<1 μm) were well resolved. The total collection time per slice was 53 min, with 28 min EBSD collection, 20 min FIB, and the balance stage movements and SEM imaging. The dataset is comprised of 127 slices collected at a 0.75 μm slice thickness and 0.3 μm EBSD resolution.

Both the 3D fatigue crack location and the microstructural neighborhood at the surface and subsurface were reconstructed. Twin boundaries are visible adjacent to the crack initiation location in Fig. 7, as expected based on the room temperature

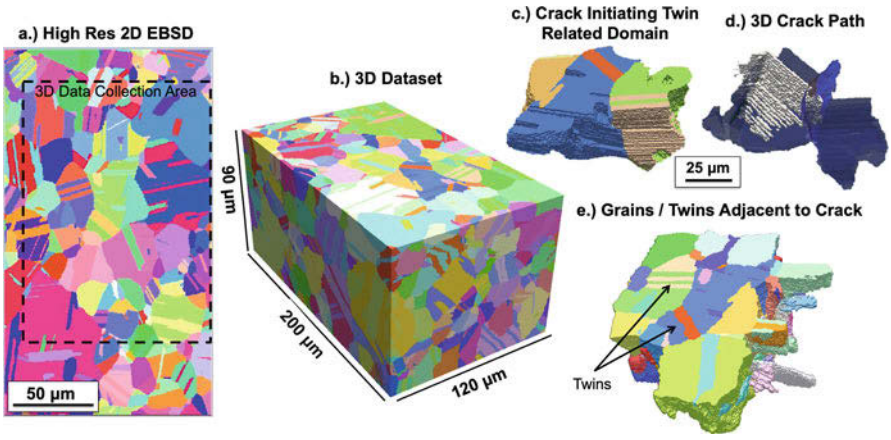

Fig. 7 A region containing a crack (**a**) was identified and a targeted 3D dataset collected beneath (**b**) in order to investigate the microstructure and local loading conditions leading to failure. The 3D dataset is 200 × 120 × 90 μm with a 0.75 μm slice thickness and 0.3 μm EBSD resolution. The crack initiating twin related domain (**c**) and the crack path (**d**) are shown along with the microstructure surrounding the crack path (**e**)

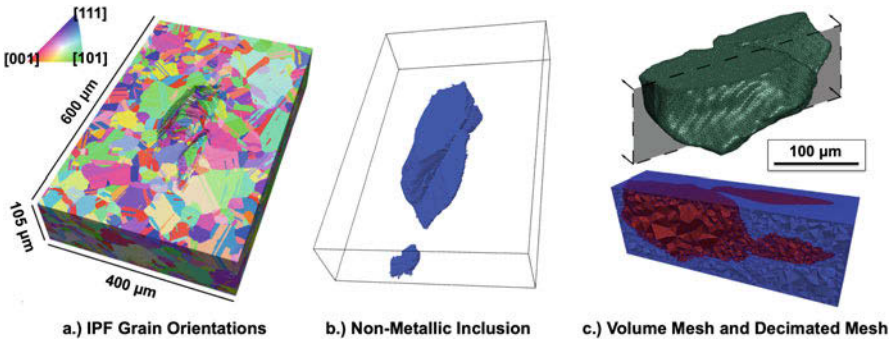

Fig. 8 (Left) reconstruction of a targeted TriBeam dataset containing the grain structure surrounding a nonmetallic inclusion (center) and a volume mesh of the inclusion for use in finite element modeling (right)

fatigue crack initiation criterion developed previously for polycrystalline superalloys [9, 82]. Briefly, this criterion predicts crack initiation in highly loaded grains (large Schmid factor) where the slip trace is parallel to a large twin boundary, and the elastic mismatch between the twin and parent grain are large.

Nonmetallic inclusions have been shown to initiate cracks in polycrystalline nickel superalloys, particularly at elevated temperatures (400–650 °C) during high cycle fatigue at stresses near 768–965 MPa [6, 7]. The crystallographic configuration surrounding an inclusion, particularly in the vicinity of peak stress concentrations, is of particular importance to the localization of strain and eventually the initiation of cracks [6, 7, 13, 14, 83]. A targeted 3D dataset was collected for a volume containing a crack initiating nonmetallic inclusion, shown in Fig. 8. The inclusion was volume meshed according to the details in [84], and mechanical loading was simulated using Abaqus. Direct comparisons between the simulation and DIC strain measurements showed good qualitative agreement, particularly when the interface between the matrix and inclusion is considered to be debonded [83]. The DIC measurements capture the localization of strain into bands along twin boundaries, whereas the elastic regime Abaqus simulations show a continuum representation. The exact details of this comparison can be found elsewhere [83, 84].

While not discussed here, the third phase of the workflow is analysis of the 3D dataset. This often requires development of algorithms and specialized routines to extract information from the dataset. Given the size of these datasets, it should be emphasized that manual analysis of features is rarely feasible. In addition to traditional stereological measurements, 3D data enables calculations not possible in 2D. Some unique 3D measurements are well established but nontrivial, e.g., degree of coherence of the twins in these René 88DT datasets requiring careful surface meshing to measure boundary normals [9, 84]. Significant capacity for novel analyses also exists, e.g., characterizing twin related domains via connectivity networks.

5 Future Needs

The most obvious limitation of the TriBeam approach, like most other 3D techniques, is the cost and time required for acquisition and reconstruction of the dataset. Crystallographic orientation mapping in SEM is usually performed via EBSD, which has seen recent speed improvements with the replacement of CCDs with CMOS cameras into standard phosphor-optics-type setups. It is likely that rates will continue somewhat with direct electron (DE) detectors, which may also have the advantage of enhanced electron sensitivity. We expect these CMOS and DE systems combined with emerging indexing algorithms [63–66, 68, 77] will decrease collection times and increase data mapping quality. The other significant time restriction is (if necessary) the glancing angle surface cleaning of the femtosecond laser-ablated surfaces. Currently the TriBeam uses a Ga^+ FIB with 65 nA beam current. Xenon plasma FIBs are available and have been integrated into a new prototype TriBeam [60] to produce currents up to 20 times higher than a Ga^+ FIB [85], which can scale to a similar 20× surface cleanup rate increase, depending on the material.

Data sharing, provenance, and portability have become a key issue for the large-scale and collaborative efforts required to tackle scientific problems with 3D data. A new software and data infrastructure, BisQue [86–88], has been useful for addressing the data challenges and providing a platform on which data versions can be synchronized between collaborative institutions and parallelized, parameterized processing of data workflows is possible.

Data merging from various modalities including HR-DIC, synchrotron X-ray DCT, and TriBeam tomography is challenging due to the complex distortions associated with each experimental method. For instance, SEMs can have spatial distortions and drift distortions from the electron optics and sample charging effects [71, 89]. New algorithms are being developed to perform and address data merging including those used for combining synchrotron diffraction contrast tomography and TriBeam tomography [50] and a generalized multimodal data merging approach using an evolutionary optimization machine learning algorithm [76].

Furthermore, developments in digital image correlation (DIC) via high-resolution DIC and Heaviside-DIC [90] and coupling with EBSD data are being used to predict strain localization, slip transmission across boundaries, and how strain can create “microvolumes” [91], where non-Schmid-type loading conditions are imposed on adjacent grains across a grain boundary. Opportunities for the targeted investigation of the influence of the subsurface 3D grain structure on strain localization and transmission phenomenon are also emerging.

At the precipitate scale, the glide of dislocations that locally shear precipitates results in strain localization along twin boundaries [15, 16, 71, 92, 93]. These are ultimately sites for crack initiation, and their intersection with grain boundaries dominates the early stages of crack growth [6, 12, 94–98]. The new 3D characterization capabilities described here, in combination with multiscale plasticity models, ultimately enable much higher fidelity prediction of properties such as yield strength

and fatigue crack initiation life. New capabilities for the in situ monitoring of dislocation activity in thin samples during loading in the SEM, using a stem detector (tSEM), are likely to reveal additional details about the early stages of localization [99, 100].

Advances in microscopes, techniques, and analysis software for 3D data have enabled the process of assessing targeted volumes for direct input to modeling. New access to large and targeted volumes of multimodal data, such as the René 88DT datasets shown, enables integration of tools for measuring and predicting strain and the simulation capabilities that are demonstrated in the companion chapters. Ultimately integration of all of these experimental techniques with advanced computational approaches promises significant advances in our capability to predict the life of critical components such as the turbine disk.

Acknowledgements This research was conducted with the support of AFOSR Grant FA9550-12-1-0445. We acknowledge Mike Uchic for useful discussions about focused ion beams and General Electric for the René 88DT material. We also acknowledge Stuart Wright for useful discussions about microanalytical data.

References

1. D. Krueger, R. Kissinger, R. Menzies, in *Superalloys*, ed. by S. Antolovich (TMS-AIME, Warrendale, 1992), pp. 277–286
2. D. Chang, D. Krueger, R. Sprague, in *Superalloys 1984, Proceedings of the Fifth International Symposium on Superalloys* (1984), pp. 245–273
3. S. Wlodek, M. Kelly, D. Alden, Superalloys **1996**, 129 (1996)
4. T.M. Pollock, S. Tin, J. Propuls. Power **22**(2), 361 (2006). https://doi.org/10.2514/1.18239
5. R. Reed, *The Superalloys: Fundamentals and Applications* (Cambridge University Press, 2006). http://books.google.com/books?id=SIUGcd4a-EkC
6. J.C. Stinville, E. Martin, M. Karadge, S. Ismonov, M. Soare, T. Hanlon, S. Sundaram, M.P. Echlin, P.G. Callahan, W.C. Lenthe, V. Miller, J. Miao, A.E. Wessman, R. Finlay, A. Loghin, J. Marte, T.M. Pollock, Acta Mater. **152**, 16 (2018). https://doi.org/10.1016/j.actamat.2018.03.035
7. J.C. Stinville, E. Martin, M. Karadge, S. Ismonov, M. Soare, T. Hanlon, S. Sundaram, M.P. Echlin, P.G. Callahan, W.C. Lenthe, J. Miao, A.E. Wessman, R. Finlay, A. Loghin, J. Marte, T.M. Pollock, Metall. Mater. Trans. A **49**(9), 3865 (2018). https://doi.org/10.1007/s11661-018-4780-3
8. J.C. Stinville, W.C. Lenthe, M.P. Echlin, P.G. Callahan, D. Texier, T.M. Pollock, Int. J. Fract. (2017). https://doi.org/10.1007/s10704-017-0241-z
9. W.C. Lenthe, J.C. Stinville, M.P. Echlin, T.M. Pollock, in *Superalloys 2016* (John Wiley & Sons, Inc., 2016), pp. 569–577. https://doi.org/10.1002/9781119075646.ch61
10. J. Stinville, E.R. Yao, P.G. Callahan, J. Shin, F. Wang, M.P. Echlin, T.M. Pollock, D.S. Gianola, Acta Mater. **168**, 152 (2019). https://doi.org/10.1016/j.actamat.2018.12.061
11. J. Miao, T. Pollock, J. Jones, in *Superalloys*, ed. by R. Reed, K.A. Green, P. Caron, T. Gabb, M. Fahrmann, E. Huron, S. Woodard (TMS, Warrendale, 2008), pp. 589–597
12. J. Miao, T.M. Pollock, J.W. Jones, Acta Mater. **57**(20), 5964 (2009). https://doi.org/10.1016/j.actamat.2009.08.022. http://www.sciencedirect.com/science/article/pii/S1359645409005357

13. D. Texier, J.C. Stinville, M.P. Echlin, S. Pierret, P. Villechaise, T.M. Pollock, J. Cormier, Acta Mater. **165**, 241 (2019). https://doi.org/10.1016/j.actamat.2018.11.051
14. D. Texier, A.C. Gómez, S. Pierret, J.M. Franchet, T.M. Pollock, P. Villechaise, J. Cormier, Metall. Mater. Trans. A **47**(3), 1096 (2016). https://doi.org/10.1007/s11661-015-3291-8
15. J. Stinville, N. Vanderesse, F. Bridier, P. Bocher, T. Pollock, Acta Mater. **98**, 29 (2015). https://doi.org/10.1016/j.actamat.2015.07.016
16. C.A. Stein, A. Cerrone, T. Ozturk, S. Lee, P. Kenesei, H. Tucker, R. Pokharel, J. Lind, C. Hefferan, R.M. Suter, A.R. Ingraffea, A.D. Rollett, Curr. Opin. Solid State Mater. Sci. **18**(4), 244 (2014). https://doi.org/10.1016/j.cossms.2014.06.001
17. S. Torquato, *Random Heterogeneous Materials* (Springer New York, 2002). https://doi.org/10.1007/978-1-4757-6355-3
18. E.E. Underwood, in *Microstructural Analysis* (Springer US, 1973), pp. 35–66. https://doi.org/10.1007/978-1-4615-8693-7_3
19. R.T. DeHoff, J. Microsc. **131**(3), 259 (1983). https://doi.org/10.1111/j.1365-2818.1983.tb04254.x
20. M.D. Uchic, M.A. Groeber, D.M. Dimiduk, J. Simmons, Scr. Mater. **55**(1), 23 (2006). https://doi.org/10.1016/j.scriptamat.2006.02.039
21. M.N. Kelly, K. Glowinski, N.T. Nuhfer, G.S. Rohrer, Acta Mater. **111**, 22 (2016). https://doi.org/10.1016/j.actamat.2016.03.029
22. K. Glowinski, A. Morawiec, Metall. Mater. Trans. A **45**(8), 3189 (2014). https://doi.org/10.1007/s11661-014-2325-y
23. G.S. Rohrer, V. Randle, in *Electron Backscatter Diffraction in Materials Science* (Springer US, 2009), pp. 215–229. https://doi.org/10.1007/978-0-387-88136-2_16
24. M.P. Echlin, M. Straw, S. Randolph, J. Filevich, T.M. Pollock, Mater. Charact. **100**, 1 (2015). https://doi.org/10.1016/j.matchar.2014.10.023
25. M.P. Echlin, A. Mottura, C.J. Torbet, T.M. Pollock, Rev. Sci. Instrum. **83**(2), 023701 (2012). https://doi.org/10.1063/1.3680111
26. B.L. Boyce, M.D. Uchic, MRS Bull. **44**(4), 273 (2019). https://doi.org/10.1557/mrs.2019.75
27. M. Uchic, M. Groeber, J. Spowart, M. Shah, M. Scott, P. Callahan, A. Shiveley, M. Chapman, An automated multi-modal serial sectioning system for characterization of grain-scale microstructures in engineering materials. Report # afrl-rx-wp-tp-2012-0254, Air Force Research Labs (2012)
28. J. Rowenhorst, L. Nguyen, R.W. Fonda, Microsc. Microanal. **24**(S1), 552 (2018). https://doi.org/10.1017/s1431927618003252
29. L. Nguyen, D. Rowenhorst, Microsc. Microanal. **23**(S1), 354 (2017). https://doi.org/10.1017/s1431927617002458
30. B. Winiarski, A. Gholinia, K. Mingard, M. Gee, G. Thompson, P. Withers, Ultramicroscopy **172**, 52 (2017). https://doi.org/10.1016/j.ultramic.2016.10.014
31. G. West, R. Thomson, J. Microsc. **233**(3), 442 (2009). https://doi.org/10.1111/j.1365-2818.2009.03138.x
32. S.J. Dillon, G.S. Rohrer, J. Am. Ceram. Soc. **92**(7), 1580 (2009). https://doi.org/10.1111/j.1551-2916.2009.03064.x
33. L. Holzer, M. Cantoni, *Nanofabrication Using Focused Ion and Electron beams: Principles and Applications*, 559201222, pp. 410–435. Oxford University Press. edited by Ivo Utke, Stanislav Moshkalev, Phillip Russell. (2012) ISBN: 0199920990
34. T. Burnett, R. Kelley, B. Winiarski, L. Contreras, M. Daly, A. Gholinia, M. Burke, P. Withers, Ultramicroscopy **161**, 119 (2016). https://doi.org/10.1016/j.ultramic.2015.11.001
35. A. Zankel, J. Wagner, P. Poelt, Micron **62**, 66 (2014). https://doi.org/10.1016/j.micron.2014.03.002
36. T. Hashimoto, G.E. Thompson, X. Zhou, P.J. Withers, Ultramicroscopy **163**, 6 (2016). https://doi.org/10.1016/j.ultramic.2016.01.005
37. J. Baruchel, G. Peix, J. Buffiere, E. Maire, P. Merle, *X-Ray Tomography in Material Science* (Hermes Science, 2000). https://books.google.com/books?id=keAe_sdyBlQC

38. H. Proudhon, in *From Microstructure Investigations to Multiscale Modeling* (John Wiley & Sons, Inc., 2017), pp. 1–39. https://doi.org/10.1002/9781119476757.ch1
39. H.F. Poulsen, S. Schmidt, D.J. Jensen, H.O. Sørensen, E.M. Lauridsen, U.L. Olsen, W. Ludwig, A. King, J.P. Wright, G.B. Vaughan, in *Strain and Dislocation Gradients from Diffraction* (Imperial College Press, 2014), pp. 205–253. https://doi.org/10.1142/9781908979636_0006
40. M.P. Miller, M. Obstalecki, E. Fontes, D.C. Pagan, J.P.C. Ruff, A.J. Beaudoin, Synchrotron Radiat. News **30**(3), 4 (2017). https://doi.org/10.1080/08940886.2017.1316124
41. J.C. Schuren, P.A. Shade, J.V. Bernier, S.F. Li, B. Blank, J. Lind, P. Kenesei, U. Lienert, R.M. Suter, T.J. Turner, D.M. Dimiduk, J. Almer, Curr. Opin. Solid State Mater. Sci. **19**(4), 235 (2015). https://doi.org/10.1016/j.cossms.2014.11.003
42. T.J. Turner, P.A. Shade, J.V. Bernier, S.F. Li, J.C. Schuren, J. Lind, U. Lienert, P. Kenesei, R.M. Suter, B. Blank, J. Almer, Integr. Mater. Manuf. Innov. **5**(1) (2016). https://doi.org/10.1186/s40192-016-0048-1
43. L. Wang, J. Lind, H. Phukan, P. Kenesei, J.S. Park, R. Suter, A. Beaudoin, T. Bieler, Scr. Mater. **92**, 35 (2014). https://doi.org/10.1016/j.scriptamat.2014.08.008
44. W.A. Tayon, K.E. Nygren, R.E. Crooks, D.C. Pagan, Acta Mater. (2019). https://doi.org/10.1016/j.actamat.2019.04.030
45. J. Madison, J.E. Spowart, D.J. Rowenhorst, T.M. Pollock, JOM **60**(7), 26 (2008). https://doi.org/10.1007/s11837-008-0085-0
46. M. Tschopp, M. Groeber, R. Fahringer, J. Simmons, A. Rosenberger, C. Woodward, Scr. Mater. **62**(6), 357 (2010). https://doi.org/10.1016/j.scriptamat.2009.10.038
47. L. Renversade, R. Quey, W. Ludwig, D. Menasche, S. Maddali, R.M. Suter, A. Borbély, IUCrJ **3**(1), 32 (2016). https://doi.org/10.1107/s2052252515019995
48. N. Viganò, A. Tanguy, S. Hallais, A. Dimanov, M. Bornert, K.J. Batenburg, W. Ludwig, Sci. Rep. **6**(1) (2016). https://doi.org/10.1038/srep20618
49. H. Simons, A. King, W. Ludwig, C. Detlefs, W. Pantleon, S. Schmidt, F. Stöhr, I. Snigireva, A. Snigirev, H.F. Poulsen, Nat. Commun. **6**(1) (2015). https://doi.org/10.1038/ncomms7098
50. W.C. Lenthe, M.P. Echlin, A. Trenkle, M. Syha, P. Gumbsch, T.M. Pollock, J. Appl. Crystallogr. **48**(4), 1034 (2015). https://doi.org/10.1107/s1600576715009231
51. J. Sun, Y. Zhang, A. Lyckegaard, F. Bachmann, E. Lauridsen, D.J. Jensen, Scr. Mater. **163**, 77 (2019). https://doi.org/10.1016/j.scriptamat.2019.01.007
52. R. Keinan, H. Bale, N. Gueninchault, E. Lauridsen, A. Shahani, Acta Mater. **148**, 225 (2018). https://doi.org/10.1016/j.actamat.2018.01.045
53. M.P. Echlin, M.S. Titus, M. Straw, P. Gumbsch, T.M. Pollock, Acta Mater. **124**, 37 (2017). https://doi.org/10.1016/j.actamat.2016.10.055
54. M.S. Titus, M.P. Echlin, P. Gumbsch, T.M. Pollock, J. Appl. Phys. **118**(7), 075901 (2015). https://doi.org/10.1063/1.4928772
55. M.P. Echlin, W.C. Lenthe, T.M. Pollock, Integr. Mater. Manuf. Innov. **3**(1) (2014). https://doi.org/10.1186/s40192-014-0021-9
56. A.T. Polonsky, M.P. Echlin, W.C. Lenthe, R.R. Dehoff, M.M. Kirka, T.M. Pollock, Mater. Charact. **143**, 171 (2018). https://doi.org/10.1016/j.matchar.2018.02.020
57. K. Chatterjee, M.P. Echlin, M. Kasemer, P.G. Callahan, T.M. Pollock, P. Dawson, Acta Mater. **157**, 21 (2018). https://doi.org/10.1016/j.actamat.2018.07.011
58. M.P. Echlin, A. Mottura, M. Wang, P.J. Mignone, D.P. Riley, G.V. Franks, T.M. Pollock, Acta Mater. **64**, 307 (2014). https://doi.org/10.1016/j.actamat.2013.10.043
59. J.E. Douglas, M.P. Echlin, W.C. Lenthe, R. Seshadri, T.M. Pollock, APL Mater **3**(9), 096107 (2015). https://doi.org/10.1063/1.4931764
60. S.J. Randolph, J. Filevich, A. Botman, R. Gannon, C. Rue, M. Straw, J. Vac. Sci. Technol. B **36**(6), 06JB01 (2018). https://doi.org/10.1116/1.5047806
61. K. Lassen, J. Microsc. **190**(3), 375 (1998). https://doi.org/10.1046/j.1365-2818.1998.00330.x
62. S.I. Wright, in *Electron Backscatter Diffraction in Materials Science* (Springer US, 2000), pp. 51–64. https://doi.org/10.1007/978-1-4757-3205-4_5

63. M.D. Graef, M. Jackson, Saransh13, Wlenthe, J. Kleingers, S. Wright, Josephtessmer. Emsoft-org/emsoft: release 4.2 to synchronize with di tutorial paper (2019). https://doi.org/10.5281/zenodo.2581285. https://zenodo.org/record/2581285
64. M.A. Jackson, E. Pascal, M.D. Graef, Integr. Mater. Manuf. Innov. (2019). https://doi.org/10.1007/s40192-019-00137-4
65. F. Ram, S. Wright, S. Singh, M.D. Graef, Ultramicroscopy **181**, 17 (2017). https://doi.org/10.1016/j.ultramic.2017.04.016
66. S. Singh, M.D. Graef, Model. Simul. Mater. Sci. Eng. **24**(8), 085013 (2016). https://doi.org/10.1088/0965-0393/24/8/085013
67. S. Singh, Y. Guo, B. Winiarski, T.L. Burnett, P.J. Withers, M.D. Graef, Sci. Rep. **8**(1) (2018). https://doi.org/10.1038/s41598-018-29315-8
68. W. Lenthe, S. Singh, M.D. Graef, Ultramicroscopy **207**, 112841 (2019). https://doi.org/10.1016/j.ultramic.2019.112841
69. F. Ram, S. Wright, S. Singh, M.D. Graef, Ultramicroscopy **181**, 17 (2017). https://doi.org/10.1016/j.ultramic.2017.04.016
70. J. Schindelin, I. Arganda-Carreras, E. Frise, V. Kaynig, M. Longair, T. Pietzsch, S. Preibisch, C. Rueden, S. Saalfeld, B. Schmid, J.Y. Tinevez, D.J. White, V. Hartenstein, K. Eliceiri, P. Tomancak, A. Cardona, Nat. Methods **9**(7), 676 (2012). https://doi.org/10.1038/nmeth.2019
71. J. Stinville, M. Echlin, D. Texier, F. Bridier, P. Bocher, T. Pollock, Exp. Mech. 1–20 (2015). https://doi.org/10.1007/s11340-015-0083-4
72. K. Marquardt, M.D. Graef, S. Singh, H. Marquardt, A. Rosenthal, S. Koizuimi, Am. Mineral. **102**(9), 1843 (2017). https://doi.org/10.2138/am-2017-6062
73. G. Nolze, A. Winkelmann, A.P. Boyle, Ultramicroscopy **160**, 146 (2016). https://doi.org/10.1016/j.ultramic.2015.10.010
74. G. Nolze, M. Jürgens, J. Olbricht, A. Winkelmann, Acta Mater. **159**, 408 (2018). https://doi.org/10.1016/j.actamat.2018.08.028
75. M.A. Groeber, M.A. Jackson, Integr. Mater. Manuf. Innov. **3**(1) (2014). https://doi.org/10.1186/2193-9772-3-5
76. M.A. Charpagne, F. Strub, T.M. Pollock, Mater. Charact. **150**, 184 (2019). https://doi.org/10.1016/j.matchar.2019.01.033
77. S. Singh, Y. Guo, B. Winiarski, T.L. Burnett, P.J. Withers, M.D. Graef, Sci. Rep. **8**(1) (2018). https://doi.org/10.1038/s41598-018-29315-8
78. P.T. Brewick, S.I. Wright, D.J. Rowenhorst, Ultramicroscopy **200**, 50 (2019). https://doi.org/10.1016/j.ultramic.2019.02.013
79. S.I. Wright, M.M. Nowell, S.P. Lindeman, P.P. Camus, M.D. Graef, M.A. Jackson, Ultramicroscopy **159**, 81 (2015). https://doi.org/10.1016/j.ultramic.2015.08.001
80. P.G. Kotula, M.R. Keenan, J.R. Michael, Microsc. Microanal. **12**(01), 36 (2006). https://doi.org/10.1017/s1431927606060193
81. M. Jackson, J.P. Simmons, M.D. Graef, Model. Simul. Mater. Sci. Eng. **18**(6), 065008 (2010). https://doi.org/10.1088/0965-0393/18/6/065008
82. J.C. Stinville, W.C. Lenthe, M.P. Echlin, P.G. Callahan, D. Texier, T.M. Pollock, Int. J. Fract. **208**(1–2), 221 (2017). https://doi.org/10.1007/s10704-017-0241-z
83. J.C. Stinville, V.M. Miller, T.M. Pollock, in *Superalloys 2016* (John Wiley & Sons, Inc., 2016), pp. 897–905. https://doi.org/10.1002/9781119075646.ch96
84. W.C. Lenthe, Twin related domains in polycrystalline nickel-base superalloys: 3D structure and fatigue. Ph.D. thesis, University of California, Santa Barbara (2017)
85. L. Kwakman, M. Straw, G. Coustillier, M. Sentis, J. Beyersdorfer, J. Schischka, F. Naumann, F. Altmann, in *Proceedings of the 39th International Symposium for Testing and Failure Analysis (ISTFA)* (2013), pp. 17–25
86. K. Kvilekval, D. Fedorov, B. Obara, A. Singh, B.S. Manjunath, Bioinformatics **26**(4), 544 (2009). https://doi.org/10.1093/bioinformatics/btp699
87. A.T. Polonsky, C.A. Lang, K.G. Kvilekval, M.I. Latypov, M.P. Echlin, B.S. Manjunath, T.M. Pollock, Integr. Mater. Manuf. Innov. **8**(1), 37 (2019). https://doi.org/10.1007/s40192-019-00126-7

88. M.I. Latypov, A. Khan, C.A. Lang, K. Kvilekval, A.T. Polonsky, M.P. Echlin, I.J. Beyerlein, B.S. Manjunath, T.M. Pollock, Integr. Mater. Manuf. Innov. **8**(1), 52 (2019). https://doi.org/10.1007/s40192-019-00128-5
89. A. Kammers, S. Daly, Exp. Mech. **53**(9), 1743 (2013). https://doi.org/10.1007/s11340-013-9782-x
90. F. Bourdin, J. Stinville, M. Echlin, P. Callahan, W. Lenthe, C. Torbet, D. Texier, F. Bridier, J. Cormier, P. Villechaise, T. Pollock, V. Valle, Acta Mater. **157**, 307 (2018). https://doi.org/10.1016/j.actamat.2018.07.013
91. J. Genée, L. Signor, P. Villechaise, Mater. Sci. Eng. A **701**, 24 (2017). https://doi.org/10.1016/j.msea.2017.06.072
92. A. Heinz, P. Neumann, Acta Metall. Mater. **38**(10), 1933 (1990). https://doi.org/10.1016/0956-7151(90)90305-Z. http://www.sciencedirect.com/science/article/pii/095671519090305Z
93. A. Cerrone, A. Spear, J. Tucker, C.A. Stein, A.D. Rollett, A.R. Ingraffea, Mater. Sci. Technol. (MS&T) **2013**, 1649 (2013)
94. J. Stinville, W. Lenthe, J. Miao, T. Pollock, Acta Mater. **103**, 461 (2016). https://doi.org/10.1016/j.actamat.2015.09.050
95. A. Shyam, W. Milligan, Acta Mater. **53**(3), 835 (2005). https://doi.org/10.1016/j.actamat.2004.10.036. http://www.sciencedirect.com/science/article/pii/S1359645404006548
96. M. Mineur, P. Villechaise, J. Mendez, Mater. Sci. Eng. A **286**(2), 257 (2000). https://doi.org/10.1016/S0921-5093(00)00804-2
97. J. Polák, in *Comprehensive Structural Integrity* (Elsevier, 2003), pp. 1–39. https://doi.org/10.1016/b0-08-043749-4/04060-x
98. H. Mughrabi, Metall. Mater. Trans. A **40**(6), 1257 (2009). https://doi.org/10.1007/s11661-009-9839-8
99. J. Stinville, E.R. Yao, P.G. Callahan, J. Shin, F. Wang, M.P. Echlin, T.M. Pollock, D.S. Gianola, Acta Mater. **168**, 152 (2019). https://doi.org/10.1016/j.actamat.2018.12.061
100. P.G. Callahan, J.C. Stinville, E.R. Yao, M.P. Echlin, M.S. Titus, M.D. Graef, D.S. Gianola, T.M. Pollock, Ultramicroscopy **186**, 49 (2018). https://doi.org/10.1016/j.ultramic.2017.11.004

Data Structures and Workflows for ICME

Sean P. Donegan and Michael A. Groeber

1 Introduction

Integrated computational materials engineering (ICME) represents a grand challenge within materials research and development. Effective ICME involves coupling materials characterization and experimentation with simulation tools to produce a holistic understanding of the materials system, promising to accelerate the materials development enterprise. Under the Center of Excellence on Integrated Materials Modeling (CEIMM), significant strides were made in developing state-of-the-art experimental methods and simulation techniques for interrogating material structure and behavior across multiple scales. In parallel to these method developments, several advances were made in designing data structures and workflow tools that possess the required flexibility and extensibility to operate on the data produced by such advanced methods. Such software tools are a critical enabling component for effective ICME; the National Academy of Sciences noted cyberinfrastructure as a crucial factor for ICME, to include databases, software, and computational hardware [1]. Additionally, these tools enable workflows that properly integrate models and experimentation at each stage of the materials development lifecycle. Figure 1 schematically shows such a workflow for optimization of microstructure and properties in a titanium forging.

S. P. Donegan (✉)
Air Force Research Laboratory, Materials and Manufacturing Directorate, Wright-Patterson Air Force Base, Dayton, OH, USA
e-mail: sean.donegan@us.af.mil

M. A. Groeber
Air Force Research Laboratory, Materials and Manufacturing Directorate, Wright-Patterson Air Force Base, Dayton, OH, USA

The Ohio State University, Department of Integrated Systems Engineering, Columbus, OH, USA

S. Ghosh et al. (eds.), *Integrated Computational Materials Engineering (ICME)*,
https://doi.org/10.1007/978-3-030-40562-5_2

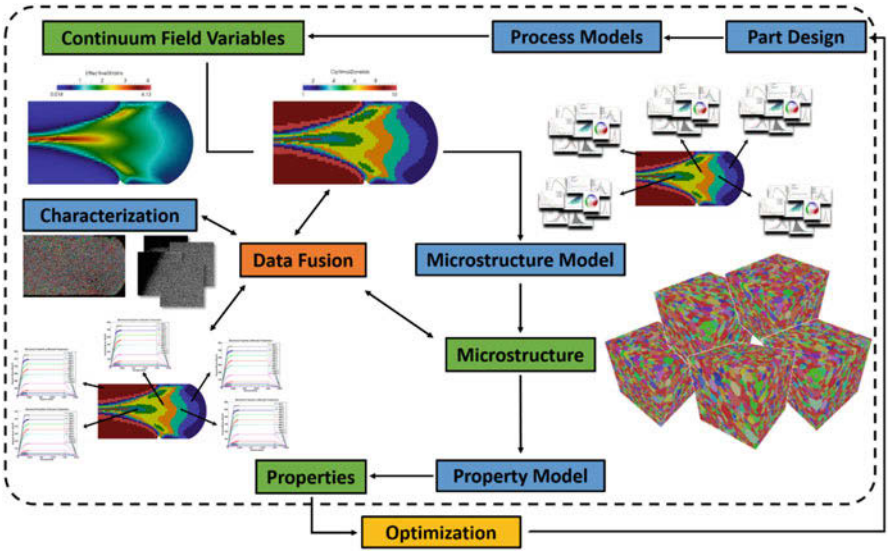

Fig. 1 Schematic of an ICME workflow for optimizing the microstructure and properties in a titanium forging. Blue boxes represent data generation tools, while green boxes represent output information from said tools

In the workflow shown in Fig. 1, an initial part design serves as an envelope for a forging process simulation, which yields *continuum field variables*: materials information, such as temperature or strain, which vary as a function of space and time. These variables feed a data-driven model that *zones* the component geometry, identifying those regions that have undergone a similar process history. Features of the process zones, defined by their constituent continuum field variables, serve as input to a microstructural evolution model. This process yields mean field microstructural measures, such as grain-size distribution and texture, at each zone. In turn, this microstructural information feeds a property model, predicting mechanical behavior for each zone. This mechanical information is finally looped back to the designer, informing modifications of the overall component geometry. Additionally, the model outputs are continuously validated by fusion with characterization measurements. Note the interplay between model and experimental data at each stage of the workflow and the transition of information across length and time scales. The cornerstone of an effective ICME workflow tool is the ability to seamlessly integrate these information streams, allowing an investigator freedom to explore the complex materials design space.

Designing and implementing ICME software tools is complicated by the variety of data streams available for modern materials research. Key features that define the breadth of ICME data include:

- *Geometry*: Simulation and characterization methods are capable of producing spatial data organized on varying topologies. These include unstructured point clouds, surface and volumetric meshes, and image/grid-like geometries.

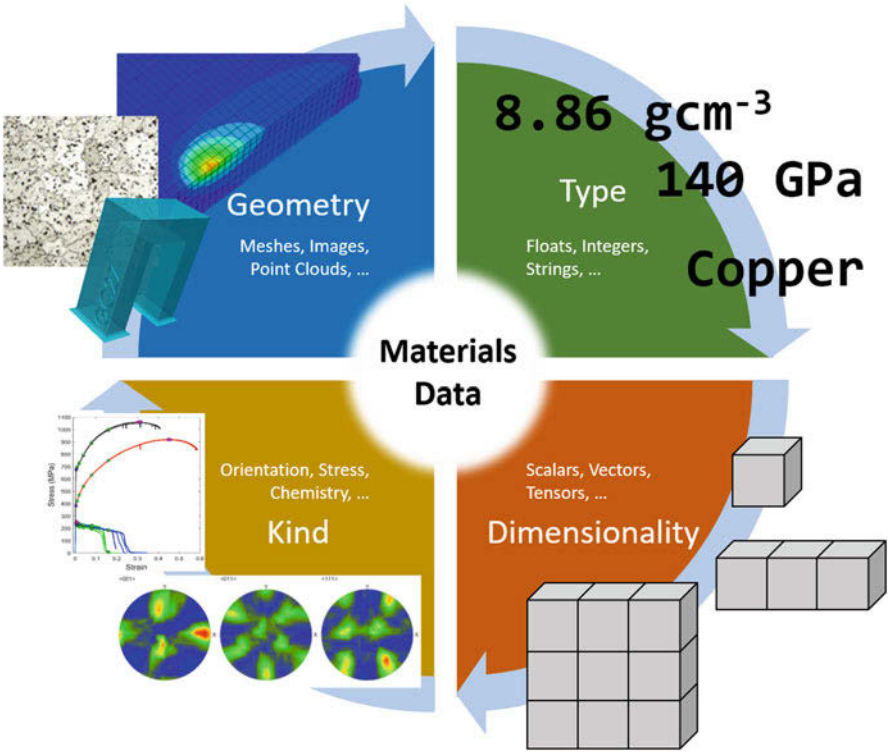

Fig. 2 Schematic of the four key features that define ICME data. Note that a single dataset will often exhibit variation in all four quadrants

- *Type*: Data streams may be of any fundamental data type, such as floating point numbers, integers, or strings, each with various precisions or encodings.
- *Kind*: The data may be representative of various materials phenomena. For example, spectroscopy measurements represent chemical composition, whereas crystal plasticity simulations output localized stress and strain tensors.
- *Dimensionality*: Materials data are inherently multidimensional, both in space, time, and kind. Second-rank tensorial data contains up to nine unique elements, whereas image intensity values are scalar.

Figure 2 graphically shows these four key features with schematic examples.

The challenge of ICME software development is properly generalizing to capture such disparate data streams in a cohesive manner. Once catalogued together, the data can be used to develop analyses that extend beyond the limits of single modalities. For example, validating ICME models requires coupling the model outputs to experimental measurements. Enacting this process robustly is a complex workflow challenge that requires a core structure capable of handling the different data streams. This chapter seeks to elaborate on such challenges in ICME software development. It is organized as follows:

- A select overview of various ICME software tools currently in use, including both commercial and open-source solutions
- A description of the requirements that a successful ICME workflow manager must meet
- An example implementation of such a workflow manager
- Presentation of a case study that highlights the utility of an ICME software infrastructure for solving modern materials problems

This chapter does not discuss details regarding data storage or infrastructure systems, such as Materials Commons [2], The Materials Data Facility (MDF) [3], or the Materials Project [4], or visualization tools, such as ParaView [5]. Instead, the focus is on tools used to generate and analyze materials data in an ICME context.

2 ICME Software Tools

We consider the following general categories for ICME tools: *simulation*, in which a physics-based model is used to generate information about a material process, evolution, or behavior, and *analytics*, where simulation and characterization data are postprocessed to produce additional information streams. A key distinguishing feature in this definition of simulation tools is the use of physics-informed models. Analytics tools may also be used to model materials, but we distinguish these from simulation tools as being *data-driven*. Such data-driven approaches typically use characterization or simulation data to fit surrogate models that approximate the underlying material physics without the need for explicit parameterization.

3 Simulation Tools

Materials modeling and simulation has a rich history that extends beyond the genesis of ICME. Within metals processing, DEFORM® has been commercially used since the early 1990s to simulate hot forging processes in both 2D and 3D [6]. Further capabilities include simulation of cold forming, machining, heat treatments, and microstructure evolution [6]. Similarly, ProCAST is a commercially available simulation package for casting processes, with support for die casting, investment casting, and continuous casting [7].

Behavior modeling of structural materials typically consists of solving a set of constitutive equations with supplied boundary conditions using a numerical method. The most commonly used numerical approach is the finite element method (FEM), in which a material volume is discretized into distinct elements on which local solutions are computed. Commercially available FEM packages include Abaqus [8] and ANSYS [9], both of which are used extensively within the aerospace supply chain to simulate material response. Several open-source FEM solutions also exist. Albany is a modular, general FEM solver for partial differential equations built

using reusable libraries [10, 11]. The Multiphysics Object Oriented Simulation Environment (MOOSE) is a similar package that relies on a generic software architecture, utilizing Jacobian-free Newton-Krylov methods [12, 13]. Other approaches besides FEM exist for solving systems of partial differential equations. For example, problems may be recast into convolutional forms, allowing for solutions using spectral (Fourier-based) solvers. Examples include simulating the elastic response of composite materials [14, 15], eigenstrains in thermal barrier coatings [16], and the viscoplastic response of polycrystals [17, 18]. The Düsseldorf Advanced Materials Simulation Kit (DAMASK) implements the spectral approach for solving the polycrystalline elasto-viscoplastic problem in an open-source format [19].

First principle and small-scale simulation tools also have a wide use within research and development. The Vienna Ab initio Simulation Package (VASP) is a broad toolset for electronic structure calculations, with capabilities for computing energy functionals, optical properties, and many-body problems [20]. The Large-scale Atomic/Molecular Massively Parallel Simulator (LAMMPS) is an open-source tool developed by Sandia National Laboratories for molecular dynamics problems [21]. For investigating dislocation dynamics, the open-source ParaDiS tool is available from Lawrence Livermore National Laboratory [22].

While the above software packages are only a small sampling of the toolsets available to a materials researcher, their outputs produce highly disparate data streams. For example, data from an FEM simulation are topologically organized onto a mesh, which may consist of a variety of unit element types (triangles, quadrilaterals, tetrahedra, hexahedra, etc.). However, a spectral solver requires data on a regular grid. Data may even exist on line segments, as in dislocation dynamics, or points, as in molecular dynamics. Additionally, data may be scalar (e.g., temperature fields from a DEFORM® forging simulation), vector (e.g., atomic displacement vectors from LAMMPS), or tensorial (e.g., strain tensors from polycrystalline viscoplasticity evaluated using DAMASK). Simulation data are also typically time dependent; this results in an additional dimension, which, in certain models, may also result in a change in geometry. The same variety of data is observed for characterization information. For example, atom probe tomography yields information about points in space (i.e., atoms), while computed tomography produces volumetric images. Electron backscatter diffraction (EBSD) scans yield orientation data on regular grids, which can be represented in only three numbers. However, the original Kikuchi patterns, which are of significant interest in applications such as high-resolution strain imaging, may be images that are upwards of 1024×1024 in dimension. If storage of these original patterns is desired, then the EBSD scan would store a pattern image at each grid location. The diversity of data forms generated by simulation packages and characterization techniques presents a unique integration challenge for downstream analytic tools.

3.1 Analytic Tools

Unlike the wealth of tools available for materials simulation, software specifically for materials analytics is a relatively nascent field. Historically, processing data

from materials characterization or simulation was typically accomplished using bespoke solutions tailored to a particular problem type. However, with the advent of relatively inexpensive computational infrastructure, availability of modern statistical and machine learning algorithms, and the popularity of open-source development, several tools for materials data analytics have gained traction within the industrial and research communities.

Since much of the characterization data collected in materials research take the form of n-D images, many analytics tools have been developed specifically tailored for image processing. Avizo™ is a commercial software package that provides image processing and analytics capabilities for materials images, including segmentation, computation of feature statistics such as size and shape, and meshing [23]. Similarly, the commercial GeoDict® software provides solutions for computed tomography processing, fiber analysis, and synthetic composite simulation [24]. For 3D EBSD data, ESPRIT QUBE commercially provides solutions for reconstruction and alignment, misorientation segmentation, and texture analysis [25].

Several open-source tools provide more general capabilities than the commercial products described above. The Materials Knowledge System in Python (PyMKS) is an open-source Python framework intended to provide data science approaches for solving various materials problems [26]. PyMKS has support for a variety of analytics tailored to materials, such as microstructure quantification using 2-point statistics [27] and fitting surrogate convolutional kernels to FEM data, producing highly accelerated elastic models [28]. A similar toolset is the Materials-Agnostic Platform for Informatics and Exploration (Magpie), an open-source Java-based library for fitting various machine learning models to materials data [29]. Specifically for texture analysis, the MATLAB toolbox MTEX provides capabilities for plotting pole figures, segmenting grains, and computing orientation distribution functions [30, 31]. Also leveraging MATLAB, the Materials Image Processing and Automated Reconstruction (MIPAR™) software provides proprietary routines customized for 2D and 3D materials image analysis [32].

3.2 Example Tools from Other Fields

Materials is not the only field that must contend with multiscale, multimodal, hierarchical information. Specifically, the medical and biomedical communities often handle multimodal information streams, however with a focus on n-D images. One of the most widely used tools for scientific biomedical image analysis is ImageJ [34, 35]. Publically funded by the National Institutes of Health, ImageJ is a Java-based library and application that contains a wide variety of common and advanced image processing methods. Fiji is a popular open-source distribution of ImageJ that contains several additional plugins for advanced image analysis and segmentation [36, 37]. Another popular library for medical image analysis is the open-source Insight Segmentation and Registration Toolkit (ITK) [38, 39]. ITK, by taking advantage of generic template programming techniques in C++, provides highly

flexible image processing techniques applicable to n-D images, including robust approaches for multimodal image registration. ITK utilizes a pipeline construct to build workflows for image processing problems and is particularly suited to processing 3D medical imaging modalities, such as computed tomography and magnetic resonance imaging. ITK on its own is a pure library; the open-source 3D Slicer application provides a graphical front end to many ITK functionalities, including registration, with capabilities for 3D visualization and volume rendering [40, 41]. 3D Slicer leverages the Visualization Toolkit (VTK), which provides a platform-agnostic rendering engine along with a wide variety of geometric processing tools, such as connectivity, smoothing, and mesh fairing [42, 43].

Another open-source software tool for analyzing biomedical information is SCIRun, supported by the Center for Integrative Biomedical Computing [44, 45]. SCIRun provides a graphical programming interface for building simulation and analysis workflows tailored to biomedical data, with a focus on bioelectric fields. This visual programming approach is similar to the interface paradigm adopted by DREAM.3D. For application-agnostic data mining and machine learning tasks, the open-source Orange application provides a visual programming front end built on top of Python's rich set of available analytics libraries [46, 47]. A tool with similar capabilities to Orange is the open-source Java-based Waikato Environment for Knowledge Analysis (Weka) [48, 49]. Weka provides several machine learning functionalities, and it also provides plugin support for data-driven image segmentation in Fiji.

The above examples motivate a more generic need for extensible data processing and handling in scientific analysis. As the materials community begins to broadly adopt the ICME paradigm, it is prudent to take advantage of the strides made in other fields in implementing workflow tools, particularly in medical and biomedical image analysis. Leveraging the lessons learned from these previous tools can accelerate the development of materials applications, allowing for the allocation of development resources toward addressing fundamental materials data problems that are not shared in other fields.

4 Building an Extensible ICME Data Schema and Workflow Tool

We now consider the critical aspects that define a successful ICME workflow tool: a scalable, efficient data structure; modularity and plug-and-play capability for building workflows; and standardized data access and metadata labeling. The primary interest is for processing data that is accessible via a spatiotemporal index. We refer to this sort of data in general as *field data*. These kind of data are naturally generated by many types of materials characterization and simulation approaches. Note that we do not directly consider scalar material properties, such as thermophysical constants. While these constants are integrally important

for automated materials discovery workflows, the present focus is placed on the processing and analysis of materials field data.

4.1 Data Handling Requirements

Given the wide variety of data types produced by characterization and software tools, a successful implementation of an ICME workflow manager must utilize a flexible data structure to properly ingest and handle the different materials information streams. The previously introduced critical aspects that help define the diversity of materials data are: *geometry*, *type*, *kind*, and *dimensionality*. An ICME data schema must implement a structure capable of handling variety in each of these categories. Practically, this translates to a requirement to represent data on different topology types, including point clouds, 2D and 3D meshes, and regular and irregular rectilinear grids. A crucial component of representing these geometries is a capability to store them together within a consistent spatial reference frame, which enables direct correlation between different datasets. Such correlative workflows are a cornerstone of effective ICME, allowing for direct validation of simulation results using experimental measurements or simultaneous analysis of multimodal information.

A result of this capability is an additional requirement to store data on any *unit element* that composes a geometry. More generally, an effective data structure should be flexible enough to store information on any component of a set of simplicial complexes. Figure 2 showcases a simplified example of this need for output from a crystal viscoplasticity simulation. Output from such a simulation may be geometrically represented as a set of connected tetrahedra that tile the 3D volume. Resulting stress and strain tensors could be stored on the vertices of the tetrahedra, while crystal orientations might be stored on the tetrahedra themselves. Additionally, further connectivity analysis may require information storage on the faces or edges that compose the tetrahedra. For example, it may be advantageous to store information about misorientations across grain boundaries, which would naturally be stored on tetrahedral faces. Similarly, identification of triple lines would be stored on tetrahedral edges where three grains meet. Importantly, what kind of information, and where it should be stored, may not be known a priori for any given problem; thus, the data structure should be extensible enough to handle changing user requirements.

While cursory, the example in Fig. 3 demonstrates the requirement for flexibility in geometric data storage. It also communicates a need for efficient storage of multidimensional information. Triple line identifiers are scalar, while orientations and full misorientations are at least three components. Stress and strain tensors, as symmetric second-rank tensors, require storage of at least six components. In principle, the number and shape of components is arbitrary, tailorable to the specific application or analysis workflow. A common example of this specificity is the number of time steps for a given simulation, which imposes an additional dimension

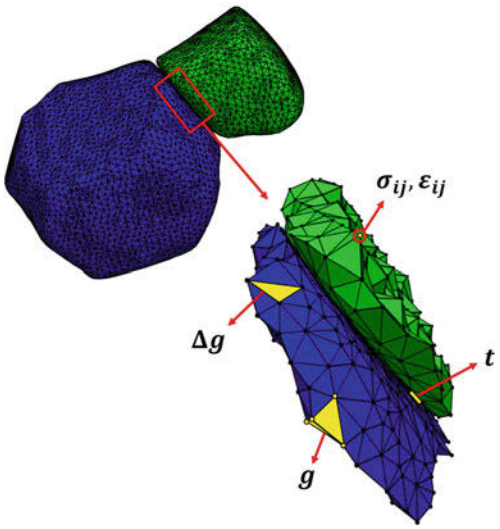

Fig. 3 A schematic example of two grains from a crystal plasticity simulation, each meshed by a set of tetrahedra. The data structure should be capable of storing information on all unit elements of the mesh: points, edges, faces, and tetrahedra, with support for various component dimensions. The data in this example are stress and strain tensors (σ_{ij} and ε_{ij}), triple line identifiers (t), misorientation (Δg), and grain orientation (g)

on the data. Thus, a scalable approach to storing multicomponent data is necessary. Another practical requirement is the fundamental type used to represent the data. Identifiers may be stored as integers, while orientations may be stored as floating point numbers. Precision may also vary (e.g., 32-bit or 64-bit floating point), while integers must consider being signed or unsigned. Data type handling is partly tied to the implementation: certain languages, such as C and C++, utilize strong typing, whereas Python utilizes the weaker duck typing. Regardless, a successful data schema must be capable of representing data of various types, with adjustments as needed for the given language.

A final data handling requirement stems from the natural structure of materials. Materials are inherently hierarchical: physical phenomena couple across multiple length scales to yield observed behavior and performance at the macroscale. Representing this natural hierarchy is critical to fully capturing the space of materials information. Figure 4 shows an example of this hierarchy for a cast Ni-base superalloy blade. Note the inherent coupling and reciprocity across the scale continuum. An ICME data structure must be capable of allowing users to efficiently move across these scales; thus, a mapping scheme is required that shifts reference up and down the hierarchy. For field data, this translates to an ability for arbitrarily grouping the various simplicial complexes that comprise the data geometry, which can then be continuously grouped further until all data are members of a unifying set.

4.2 Modular Workflow Requirements

Beyond efficient storage of materials field data, a user should be capable of interacting with that data through a standardized interface. Ideally, this interface

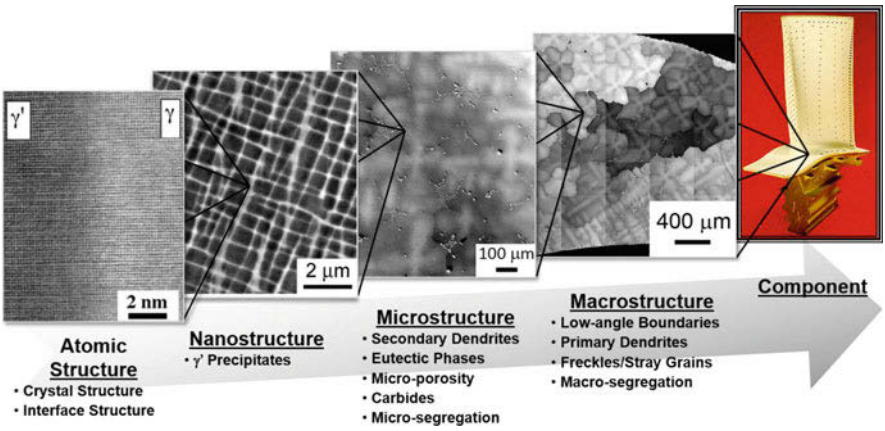

Fig. 4 An example of the hierarchy of materials structure in a cast Ni-base superalloy blade. Note that the physics of one scale are tightly coupled to the phenomena at another scale. Properly compositing this multiscale and hierarchical information together requires a flexible and extensible data structure. (Figure reproduced courtesy Dennis Dimiduk and Michael Uchic)

defines the parameters through which the data structure may be accessed, to include: creating new data structure objects, interrogating the properties of existing objects, and modifying existing objects as needed for the present context. To facilitate this interaction, it is desirable to not only standardize the application interface for the data structure itself but also the functional interface by which such interactions are implemented. This functional interface should enable the storage and retrieval of each parameter setting, which is needed for workflow archival and reproducibility. Thus, a workflow for analyzing a collection of materials field data can be conveniently represented as a sequence of these standardized functions.

Representing a workflow in this manner also immediately satisfies an additional requirement for flexibility: since materials problems and the data informing them are constantly evolving, users should not be restricted in building ICME workflows. By composing a workflow from self-contained functions, a user is free to add, delete, swap, and move these functions as appropriate for the given application. This flexibility imposes a complication for testing internal consistency for a constructed workflow. Confirming a workflow is valid for a given set of parameters is trivial if the workflow is constructed a priori. But for on-the-fly development, explicit validation is subject to combinatorial explosion as the number of available functions increases. To solve this issue, the functions within an ICME workflow manager must be capable of performing self-consistency checks, pursuant to the overall application interface of the global data structure. Thus, the overall workflow can be validated by examining the consistency of each individual function.

After construction of a workflow, it is desirable to serialize the workflow. This addresses two needs: the ability to archive workflows for future use and the ability to share workflows with collaborators. An important aspect of this serialization process

is the storage of the parameter settings used in each function of the workflow. Since the constructed workflow may be complex, and itself hierarchical, a sufficiently flexible format must be used for serialization. Ideally, this format would also be human-readable and should be standardized for broad access outside of materials-specific tools.

4.3 Data Access and Metadata Labeling Requirements

After a successful execution of a workflow, the computed data should be serializable into an accessible data format. Since the implemented data structure is highly generic and flexible, the chosen data format must also be equally flexible. Similar to the format for workflow serialization, the data format must also belong to an open standard, allowing access outside of materials toolsets. Ideally, this format should also be size and speed efficient, allowing for fast reading and writing, an enabler for the large datasets inherent in many ICME workflows. Stored information may be either *heavy*, the dense data comprising the bulk of the content in terms of size, or *light*, consisting of metadata such as material name, component dimensions, data type, time step, etc. The format must therefore be capable of storing either heavy or light data. It is desirable to store the processing history of a set of data along with the data itself; thus, the history remains innately coupled with the data, which allows for reproducibility and transparency. Therefore, the data format must enable the workflow to be stored alongside the data and additionally allow for further functions and their parameter settings to be appended to the workflow should future processing be necessary.

5 SIMPL and DREAM.3D: Enabling ICME Workflows

To satisfy the above requirements for an ICME workflow tool, the Air Force Research Laboratory in partnership with BlueQuartz Software developed a software framework known as the Digital Representation Environment for the Analysis of Microstructure in 3D (DREAM.3D). DREAM.3D is an open-source software tool explicitly designed to enable the creation of generic materials analytics workflows that are adaptable to any kind of input, regardless of geometric topology or data type [33]. Specific capabilities include 2D and 3D EBSD reconstruction and analysis, n-D image processing, feature identification and quantification, surface meshing, texture analysis, and synthetic microstructure generation. DREAM.3D's unique capabilities stem from an underlying data structure and management library: The Spatial Information Management Protocol Library (SIMPL). SIMPL is an open-source C++ library that implements an abstract data structure, including a well-defined application programming interface [50]. Additionally, SIMPL defines a functional interface for interacting with the data structure. This interface is

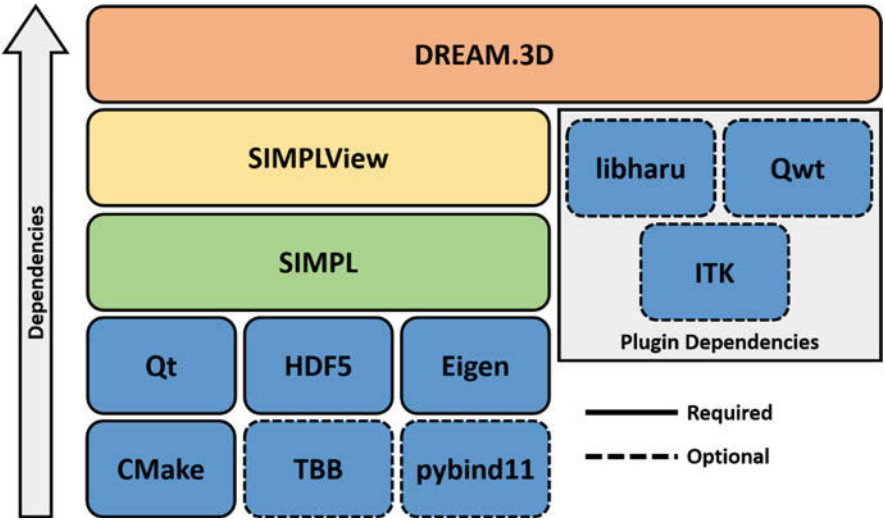

Fig. 5 The dependency tree for DREAM.3D. Items in blue are open-source dependent libraries. Note that this modular design allows for libraries to be added or swapped where necessary, granting flexibility to the overall software architecture

characterized by *filters*, self-contained functions that perform a unit operation on the data structure state. Filters may be sequenced to form a *pipeline*, the fundamental execution unit of a SIMPL workflow. SIMPL also allows for extensions via a *plugin* interface. Users may add their own functionalities to SIMPL by adhering to the plugin architecture. DREAM.3D constitutes an open-source collection of SIMPL plugins tailored for analysis of materials data, along with facilities for processing materials-specific information [33, 51]. Additionally, DREAM.3D utilizes a graphical front end called SIMPLView [52]. All the various projects associated with DREAM.3D are distributed under the permissive 3-clause BSD license. This open-source development has enabled collaborations and contributions across academia, government, and industry.

Figure 5 shows the overall software architecture of DREAM.3D, including dependent libraries. Dependencies generally progress up from the bottom of Fig. 5. SIMPL makes heavy use of the Qt library for various functionalities, such as container objects, string representations, and platform-agnostic file system access [53]. Additionally, Qt provides the facilities for producing the front-end graphical interface in SIMPLView. SIMPL utilizes the HDF5 file format and library for data serialization [54]. Eigen is leveraged for highly efficient linear algebra and matrix manipulations [55]. Optionally, Intel's Threading Building Blocks provides thread-based parallelism [56], while pybind11 automatically creates Python bindings for SIMPL classes and filters [57]. For all projects, CMake is used to enable easy cross-platform building [58].

A key component of the DREAM.3D software architecture is its modular nature; this allows for dependencies to be added or swapped as needed for a given application. Most commonly, this approach is taken for adding new plugin dependencies. For example, an image processing plugin in DREAM.3D leverages ITK as an underlying dependency, bringing the power and flexibility of a tool originally designed for medical image analysis into the materials domain.

The following sections overview the structure of both SIMPL and DREAM.3D, including: data structure; filter, pipeline, and plugin infrastructure; graphical interface; and analysis capabilities.

5.1 SIMPL Data Structure

The SIMPL data structure is inspired by approaches in other well-known libraries, such as VTK, along with methods in combinatorics and topology. The data structure was designed to directly address those requirements stated in the Data Handling Requirements section above. Principally, the data structure takes the form of a tree; since trees are hierarchical, the data structure is able to naturally conform to the grouping requirements needed for materials data. Items within the data structure are generally termed *objects*, with four primary types of objects available:

- *Data Container Array*: The root node of the data structure. The data container array has access to create and retrieve all descended children objects and check the structure for validity.
- *Data Container*: The direct descendant of data container array, data containers store attribute matrix objects that correspond to a *unique* geometry. Data containers are therefore distinguished by what geometry they represent.
- *Attribute Matrix*: Stored within data containers, attribute matrices contain the objects that store the dense data on each geometry. Attribute matrices are distinguished by a type identifier which signifies at what specific grouping hierarchy the data should be associated. Additionally, attribute matrices define the shape of the underlying dense data.
- *Attribute Array*: Attribute arrays are the leaves of the data structure tree and store the heavy field data for a given dataset.

Objects within the data structure have an associated name; similar to a standard file system, no two objects at the same level of the tree are allowed to have the same name. Additionally, objects deeper within the tree have a unique *path*, the concatenation of all parent object names with the child. An example data structure is shown in Fig. 6. In this example, two data containers are stored in the data container array, one that represents an image and one that represents a surface mesh.

Geometries are a special kind of data structure object, represented by the red boxes in Fig. 6. A data container may only store one geometry, and usually this geometry is unique within the overall data structure. The child attribute matrices

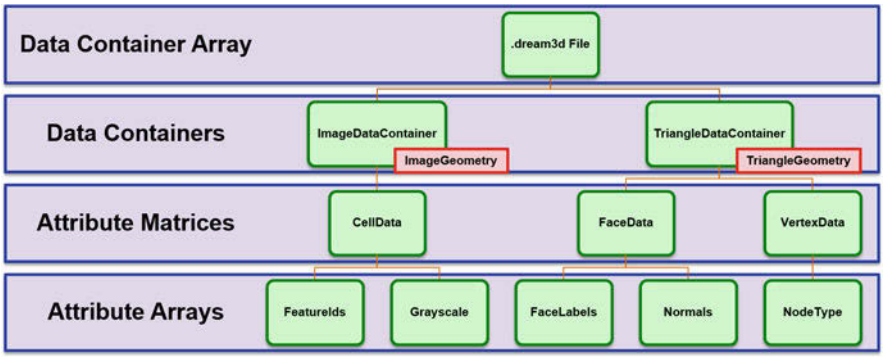

Fig. 6 An example SIMPL data structure, representing storage of an image and a surface mesh. (Figure reproduced from the DREAM.3D user manual)

and attribute arrays for a given data container store information that corresponds to the data container's geometry object. Geometries are distinguished by the dimensionality of the fundamental unit element that serves as that geometry's primary building block. There are four primary unit element types: vertices (0-dim), edges (1-dim), faces (2-dim), and cells (3-dim). In principle, the data structure allows storage of higher dimensional simplices; however, for materials data analysis, it is rare for such higher dimensional elements to be needed. For a given geometry, data may be stored on any of the unit elements that comprise the geometry, as shown in Fig. 7.

Data may be stored on any of the unit elements that form a given geometric object. For example, if the fundamental geometric object is a quadrilateral, data may be stored on the vertices, edges, or faces of the polygons, but not cells, since no object within the geometry is volumetric.

SIMPL defines an interface to which implemented geometries must adhere. This abstract interface class enforces that geometries store their connectivity, understand how to compute derivatives, import and export themselves, etc. Filters are able to leverage this generalization, which enables algorithms to operate across different geometries. Currently, SIMPL implements eight geometric classes, along with a special null geometry. These geometries are shown in Table 1.

Similar to the overall data structure, geometries in SIMPL adhere to a hierarchy, as shown in Fig. 8. Geometries may be generally categorized as either *structured*, where explicit definition of point coordinates is not needed, or *unstructured*, where point coordinates must be explicitly stored. The structured geometries are the image and rectilinear geometries, commonly referred to as *grids*. An n-D image is defined implicitly by just three values: its position in space, defined by the origin; the resolution along each dimension; and the number of elements in each dimension. Thus, an n-D image needs only 3n numbers to be fully defined. A rectilinear grid, however, may admit variable resolution along each orthogonal direction. For an

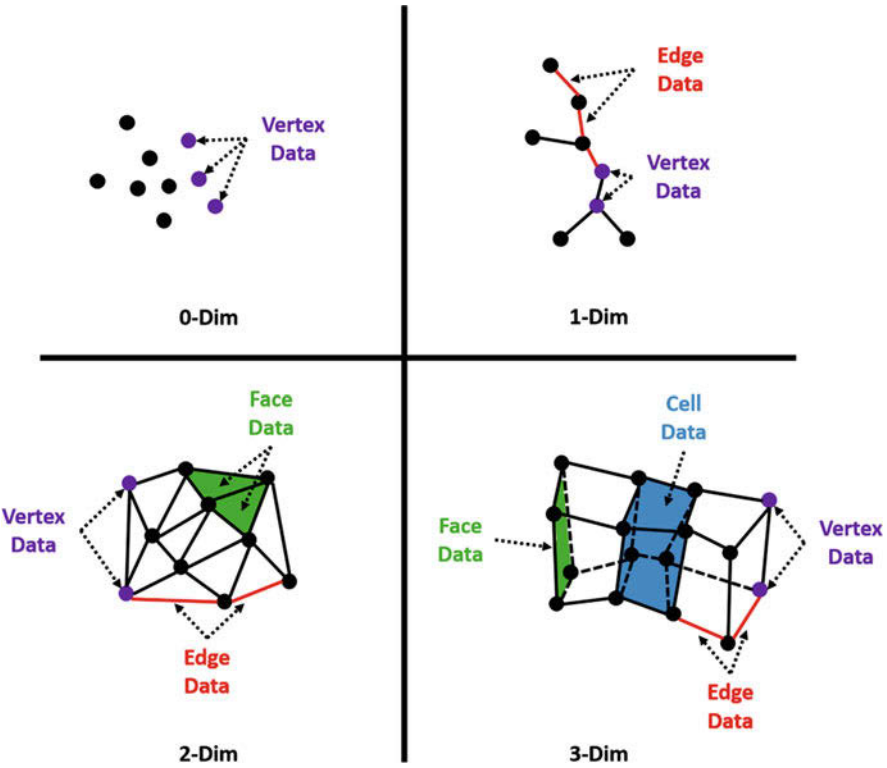

Fig. 7 Schematic showing building-block unit elements for SIMPL geometries. Note how data may be stored on any unit element that comprises a given simplex. (Figure reproduced courtesy Groeber and Jackson [33])

n-D rectilinear grid, the total number of values, v, needed for complete definition is given by the following equation:

$$v = \sum_{i=0}^{n} N_i + 1$$

where N_i is the number of elements along the ith dimension.

The unstructured geometries require explicit definition of point coordinates. Additionally, for any geometry other than vertex, the connectivity between points must be stored. SIMPL represents unstructured geometries using *shared element lists*. In the shared element list schema, only unique unit elements are stored; for example, if two triangles share an edge, then the two vertices that comprise that edge are shared, and need not be stored twice. Despite their simplicity, shared element lists offer a number of benefits: highly efficient storage of the geometric

Table 1 Currently implemented SIMPL geometries, along with their topology and associated data types

NAME	Topology	Associated data	Description
Unknown	N/A	Any	The null geometry, used when the underlying data have no spatial indices
Vertex	0	Vertex	A set of points, or point cloud
Edge	1	Edge/vertex	A set of edges, forming lines
Triangle	2	Face/edge/vertex	A set of triangles, forming a surface mesh
Quadrilateral	2	Face/edge/vertex	A set of quadrilaterals, forming a surface mesh
Image	3	Cell	A structured rectilinear grid composed of pixels/voxels of constant resolution
Rectgrid	3	Cell	An unstructured rectilinear grid, composed of pixels/voxels of variable resolution
Tetrahedral	3	Cell/face/edge/vertex	A set of tetrahedra, forming a volume mesh
Hexahedral	3	Cell/face/edge/vertex	A set of hexahedra, forming a volume mesh

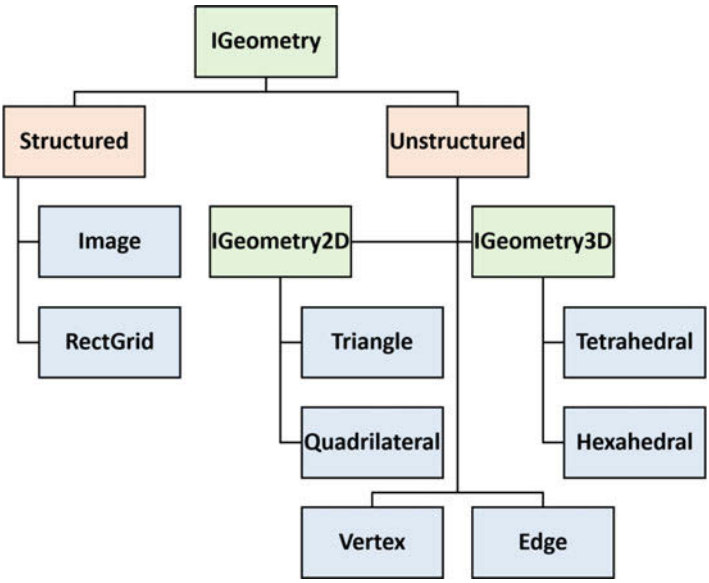

Fig. 8 The inheritance hierarchy of SIMPL geometries. By providing abstract interfaces, represented in green, SIMPL allows for generic algorithm programming, reducing code replication

information, fast static access of the geometry, and the ability to store nonmanifold simplices. However, shared element lists suffer from inefficient manipulations of the geometry. For example, a shared element architecture is not suited toward mesh refinement or decimation.

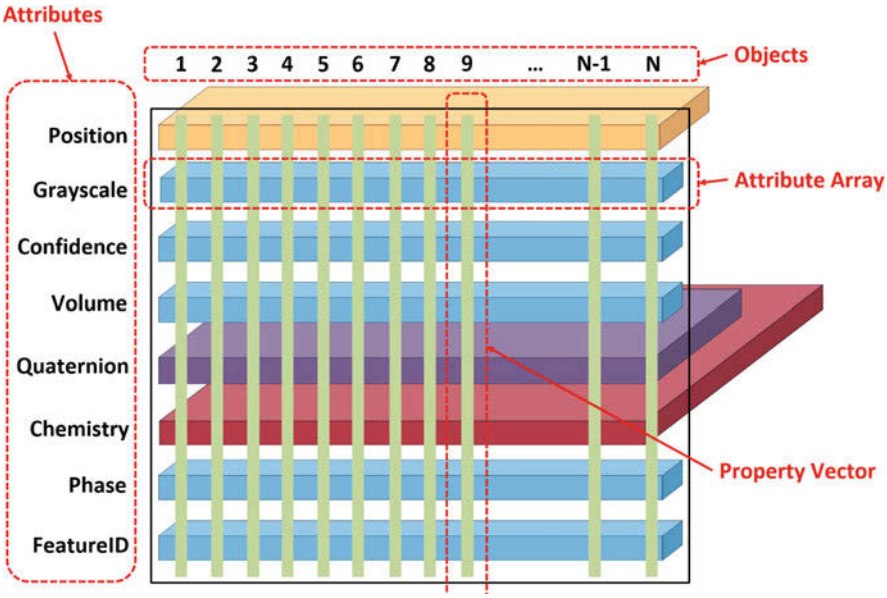

Fig. 9 Schematic of an Nx1 attribute matrix. Objects may be elements, features, or ensembles. (Figure reproduced from the DREAM.3D user manual)

SIMPL represents hierarchy within a given geometric dataset through the concepts of *features* and *ensembles*. Features are groups of geometric elements. For example, an EBSD scan may have its pixels grouped into grains under some threshold for misorientation. Data may then be associated with these features, such as size, shape, and average orientation. Features may also be grouped into ensembles. In the EBSD example, grains may be grouped together based on their crystal structure. Note that ensembles may also be grouped together recursively; all subsequent groupings are also referred to as ensembles. Data are mapped between levels of the scale hierarchy using an identifier array; this array denotes to which feature or ensemble an object lower in the hierarchy belongs.

Associating data with geometries, features, and ensembles is organized through attribute matrices. Attribute matrices themselves do not store heavy data; instead, they serve to define the type of data being stored and its shape. Dense data are stored in attribute array objects, which are contained within attribute matrices. There are three general types of attribute matrices: *element*, which store data associated to the unit elements of a geometry; *feature*, which store data for groups of elements; and *ensemble*, which store data for groups of features. There are four types of element attribute matrices, corresponding to the four basic unit elements: vertex, edge, face, and cell. Other than a type, an attribute matrix also has a shape; in the SIMPL ontology, this shape is referred to as the *tuple dimensions*. Figure 9 shows an example attribute matrix of N objects, where the tuple dimensions are Nx1.

For a raveled attribute matrix with scalar dimensions, the rows are comprised of specific attribute arrays, while the columns represent particular objects. This storage scheme generalizes to higher dimensions, where attribute arrays are stored in hyper-rows and objects are denoted by the hyper-columns. Note that an attribute matrix is extensible: new attribute arrays may simply be appended to the matrix without the need for resizing. Attribute matrices may be interrogated in either direction: obtaining arrays along (hyper)-rows, which return information about a given attribute for each object, or property vectors along each (hyper)-column, yielding a list of attributes for a specific objet.

Attribute arrays, the (hyper-)rows of attribute matrices, are the final leaves of the overall data tree. These arrays store dense, heavy data. Arrays may be *multicomponent*, defining a depth dimension at each tuple. The overall array shape, tuple dimensions, is inherited from the dimensions of its parent attribute matrix. SIMPL allows for any fundamental data type to be stored within an attribute array, including various precision integers and floating point numbers. Attribute arrays are stored compactly within attribute matrices, even if the arrays do not share the same component dimensions: therefore, an attribute matrix is sparse in its depth dimension, as shown in Fig. 9.

The SIMPL data structure is highly flexible and customizable. In order to serialize it to storage, a data format must be used that is similarly flexible. SIMPL utilizes the Hierarchical Data Format, or HDF5, as its data format [54]. HDF5 is a binary file format whose data model allows for explicit hierarchy by organizing information into *groups*, similar to folders on a file system, while dense data are stored in *datasets*. SIMPL takes advantage of this model by mapping its data container arrays, data containers, and attribute matrices to groups in an HDF5 file, with attribute arrays being stored in datasets. An example mapping for a SIMPL data file is shown in Fig. 10. HDF5 is an open standard which enables easy cross-platform data sharing and data transfer to toolsets other than SIMPL or DREAM.3D.

Similar to SIMPL, HDF5 allows for dense data to have arbitrary shape and component dimensions and store any fundamental data type. Critically, the analysis workflow used to generate the SIMPL data structure is stored along with the data within the SIMPL file, enabling reproducibility and archival.

5.2 Filters, Pipelines, and Plugins

SIMPL defines a standard interface for interacting with the data structure through the concept of *filters*. A filter is simply a self-contained function that performs some operational interaction with the data structure, such as creating a new object (i.e., computing some new information) or modifying an existing object. Filters adhere to a standardized interface defined in an abstract base class. A critical feature of filters is their ability to request parameters from a user and translate these requests into queries of the data structure. For example, a user may select an attribute array by supplying a filter with a path; the filter interface will then utilize this path to

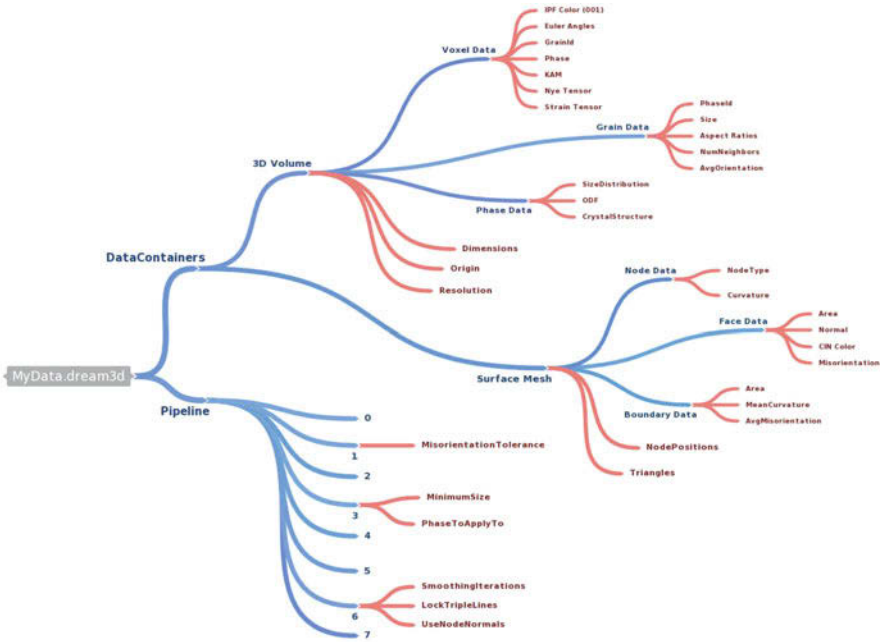

Fig. 10 Schematic of a SIMPL data structure storage scheme in an HDF5 file

access the array in the data structure and make it available for computation when the filter runs. Importantly, filters are also capable of performing validity checks when processing their parameters. This validation procedure is referred to as a *preflight* state. During preflight, a filter performs the necessary validation checks, modifying the data structure as needed *by proxy*: memory is not allocated and computations are not run during preflight, but any object creation or removal is represented in the data structure.

By creating a sequence of filters, a user instantiates a workflow that creates, modifies, and saves a SIMPL data structure. This sequence of filters is referred to as a *pipeline*. Pipelines orchestrate the task of requesting filters to preflight themselves, ensuring that the overall pipeline is in a valid state before allowing execution. Additionally, pipelines may be serialized using the JSON file format. JSON enables a human-readable transfer format for saving user-defined pipelines; the constituents of a JSON pipeline file are simply the sequence of filters with their explicit parameter settings. Note that a JSON file can be encoded as a string; this capability is leveraged to store the pipeline within the HDF5 SIMPL file schema as a string dataset.

SIMPL provides an interface for defining self-contained groups of filters called *plugins*. Programmatically, plugins are dynamically loaded libraries that comprise a collection of SIMPL filters, along with any additional support code necessary for the filters' operation. DREAM.3D itself is simply a collection of SIMPL plugins

with capabilities customized for materials data analysis. Since all interaction with the SIMPL data structure is governed by a standardized interface, filters are able to leverage functionalities across plugins, which results in less code duplication. A canonical example is computing the size of features: this problem essentially reduces to summing the volumes of each constituent element that belong to a set of features. This computation is the same, regardless if the features define a set of grains or a collection of pores. Thus, when adding new filters via plugins, a developer can avoid re-implementing such a generic algorithm as size computation and instead focus on designing those functions that are specific to the problem space.

5.3 SIMPLView: The Standard SIMPL Graphical Interface

SIMPL on its own does not require a user interface. SIMPL may be used as a library, in which the data structure, filters, and pipelines would be accessible via code; or using a command-line interface. SIMPL does contain a set of pre-defined graphical widgets that allow developers to rapidly generate user interfaces. The most widely used implementation of this feature is SIMPLView [52]. SIMPLView is a basic interface to the functionalities of SIMPL, allowing users to construct pipelines using a visual programming style. SIMPLView is most widely recognized as the interface of DREAM.3D. Note, however, that SIMPLView may be swapped with any other graphical interface implementation as needed; therefore, the user experience is highly customizable to the particular application. SIMPLView is under active development; the current incarnation of the interface is shown in Fig. 11.

The major components of SIMPLView are comprised of *panes*: the toolbox pane, pipeline view, filter parameters, data structure, and pipeline issues and output. The toolbox lists all available filters, both alphabetically and categorized by functionality. Additionally, the toolbox stores *bookmarks*, which are the locations of saved JSON pipeline files. The pipeline view is the main focus window of the interface: here the user constructs a pipeline by building a sequence of filters. The filter parameters pane shows the user what variables may be set for a selected filter in the pipeline view. By using the data structure pane, the user may view the status of the current SIMPL data structure, inspecting attributes such as geometry types and array dimensions. Finally, any pipeline issues or output are shown in their corresponding panes. When constructing a pipeline, SIMPLView communicates the current pipeline state to SIMPL, which orchestrates the preflight procedure to validate the settings provided by the user. If issues arise, the user is presented with an error message in the pipeline issues pane. Recall that during preflight, no actual computations are undertaken; the user must finish constructing a valid pipeline that completes preflight without errors before execution is allowed. While SIMPLView exposes only the basic operations of SIMPL, it does offer customization features: all panes can be hidden or moved, and support is available for skinning the interface.

SIMPLView does not have present capabilities for visualization. Instead, SIMPL leverages the open-source ParaView application to provide visualization

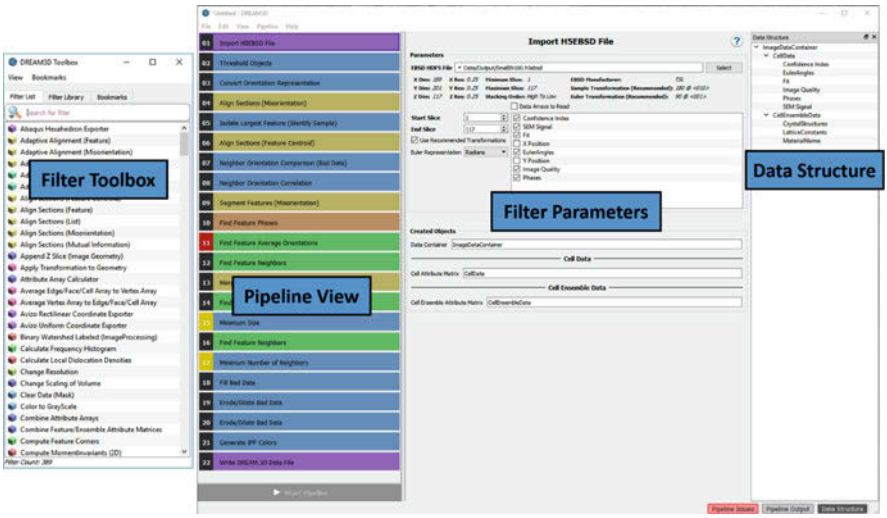

Fig. 11 The current version of SIMPLView, as implemented in the DREAM.3D distribution, with major components of the interface labeled. In this rendering, the pipeline issues and output are hidden

capabilities. When exporting a SIMPL data file, the user may elect to write a companion XDMF file, which is essentially an XML document that explains how the data are organized in the HDF5 file [59]. ParaView has facilities to import this XDMF file, allowing for efficient volumetric visualization of the data processed by SIMPL.

5.4 DREAM.3D: An ICME Workflow Tool

DREAM.3D is essentially a set of SIMPL plugins customized to process materials data. As such, it inherits all the benefits of the SIMPL data structure described above. DREAM.3D contains a number of capabilities, including:

- Import and export of a variety of file formats, including many image formats, FEM file formats, generic ASCII and binary files, HDF5 files, and the SIMPL file format
- Feature identification approaches, such as expectation maximization, connected components segmentation including metrics such as misorientation, and clustering approaches
- Texture analysis, including pole figure plotting, orientation distribution function sampling, disorientation and average orientation computations, and fundamental zone reductions
- Reconstruction of 3D data from 2D slices, for both images and crystallographic EBSD measurements

- Data processing and cleanup functionalities, including robust image processing courtesy ITK
- Statistical computations such as feature size and shape distributions, histograms, and distribution fitting
- Surface and volumetric meshing
- Instantiation of synthetic microstructures from morphological and crystallographic statistics, provided either from generative statistical models or experimental measurements

Leveraging the above functionalities in concert with the flexibility of SIMPL, a user can construct arbitrarily complex workflows for difficult ICME problems. In the following section, such a problem is introduced as a case study to demonstrate the utility of DREAM.3D.

6 Case Study: Ti-6242Si Pancake Forging

This section presents a case study for an ICME workflow concerned with quantitatively relating processing parameters in a titanium disk forging to measured microstructure characteristics. Unless otherwise noted, all processing and analysis steps presented were performed using DREAM.3D. This problem is a subset of the workflow shown in Fig. 1. Specifically, we are interested in those procedures shown in Fig. 12. A cylinder of Ti-6Al-2Sn-4Zr-2Mo-0.1Si (Ti-6242Si) with diameter 25.4 mm and height 38.1 mm was forged into a pancake with an average true height strain of 1.07. After forging, the pancake was cross-sectioned radially and characterized using both backscatter electron (BSE) imaging and EBSD. Concurrently, the forging process was simulated using DEFORM®. This forging was part of a larger study in which additional cylinders were excised from the same parent billet and isothermally compressed. Specific experimental and simulation details may be found in Pilchak et al. [60].

This work was motivated to develop quantitative relationships between process history and resulting microstructure. Specifically, microstructure features of interest are microtexture regions (MTRs). MTRs are relatively large (i.e., millimeters, to centimeters) regions of similar crystallographic orientation that form in near-alpha titanium alloys [61]. These regions have been identified as prime factors implicated in dwell fatigue debits of titanium forgings [62, 63]. In order to understand the impact the process state has on MTRs, the model output from DEFORM® was fused with the characterization data. Then, the model data was zoned using an approach from unsupervised machine learning, partitioning the forging geometry into discrete regions of self-similar processing history. With the characterization information colocated with these zones, an assessment can be made concerning the types of microstructure expected for a given process. This zoning procedure has the additional benefit of signifying to a designer which regions of a component

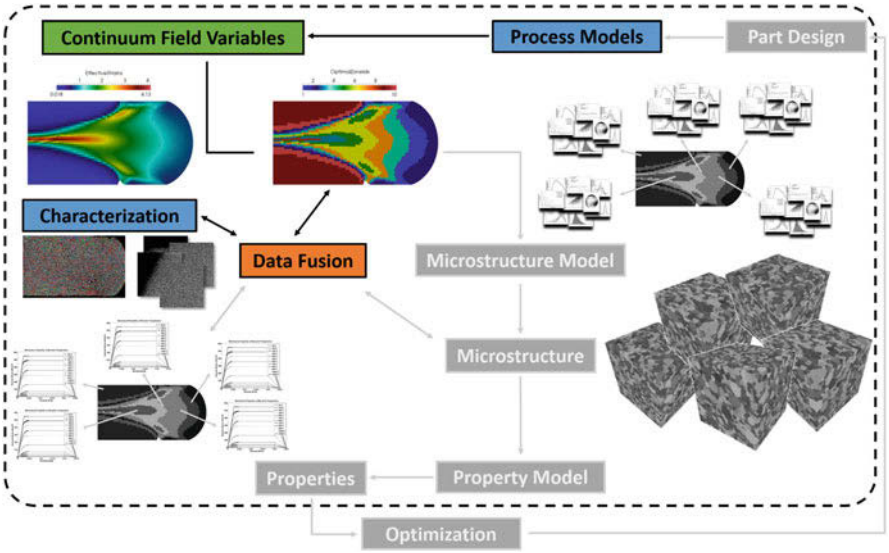

Fig. 12 The specific workflow items for the titanium disk case study. Model data from a process simulation produce continuum field variables, which are then reduced to zones. These data are fused to characterization measurements, allowing for microstructure to be assessed per zone

are most distinct, serving as an indication for where additional measurements may be prudent. For example, a zoning scheme may indicate where samples should be excised for further mechanical testing. Here, we focus on the problem of relating the zoned geometry to microstructure, instead of determining an optimal component cutup.

6.1 Zoning Process Histories

The pancake forging process was simulated using DEFORM®. Since the geometry is radially and axially symmetric, a single half cross-section was simulated in 2D. The underlying quadrilateral FEM mesh was dynamically remeshed as appropriate as the component was strained. DEFORM® optionally allows for tracking the initial material points until the final time step. The total evolution of an example pancake forging model is shown in Fig. 13.

For the present analysis, several field values were computed, including effective strains, full stress and strain tensors, and damage accumulation. Together, these fields yield a high-dimensional description of the forging process history. We wish to develop a scheme that effectively zones this process history into discrete categories. In the parlance of machine learning, this procedure can be considered an application

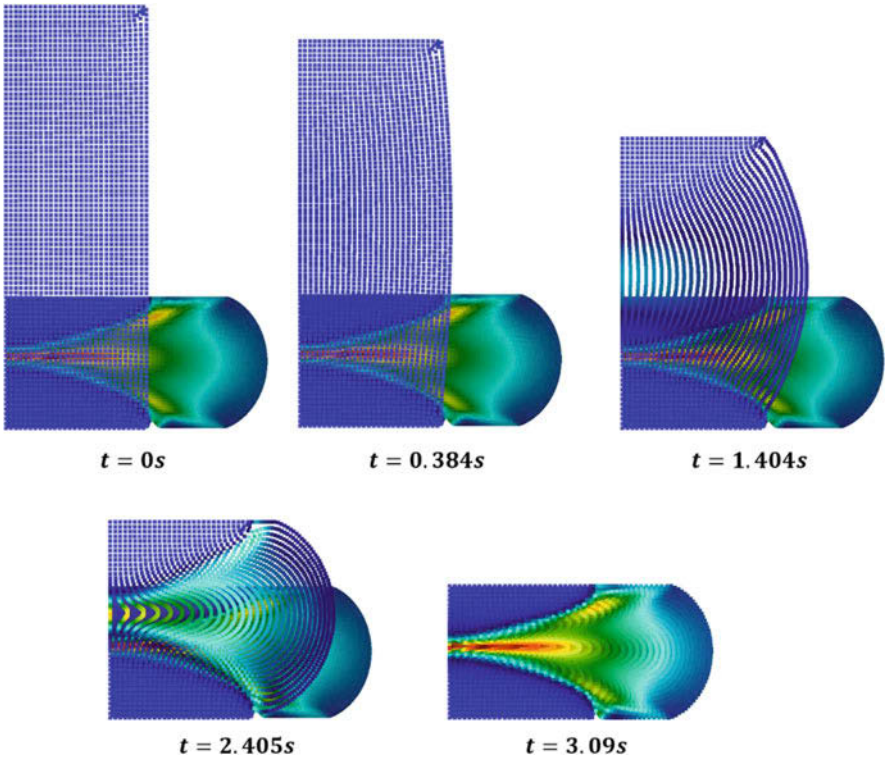

Fig. 13 Evolution of an example 2D DEFORM® pancake forging model. The points represent the tracked material points across all time steps, while the underlying mesh is for the final time step. Elements are colored by their effective strain

of cluster analysis. Cluster analysis seeks to classify an input space such that points that are most similar, according to some metric, are categorized in the same cluster [64]. In the context of zoning, the clustering procedure would ideally be performed on a latent space that best captures the process history relevant for the given response. For this example, that response is the representation of microstructure obtained from the EBSD and BSE measurements. While the relevant process history may be some linear combination of the various time-dependent fields produced from the DEFORM® simulation, we demonstrate a zoning procedure using only the strain tensors from the final time step for simplicity. For the relevant simulation, these strains are shown in Fig. 14. While the overall sample volume is conserved, individual element volumes may not be preserved; hence, the 2D strain tensor at a given element may not be uniquely symmetric. Thus, for this example, all four components of the 2D strain tensor are used.

To produce a zoning of the strain tensors, we utilize the *k*-medoids algorithm from cluster analysis [65]. *k*-medoids labels a set of points into *k* classes such that each datum is placed into the cluster with the closest medoid value, where the

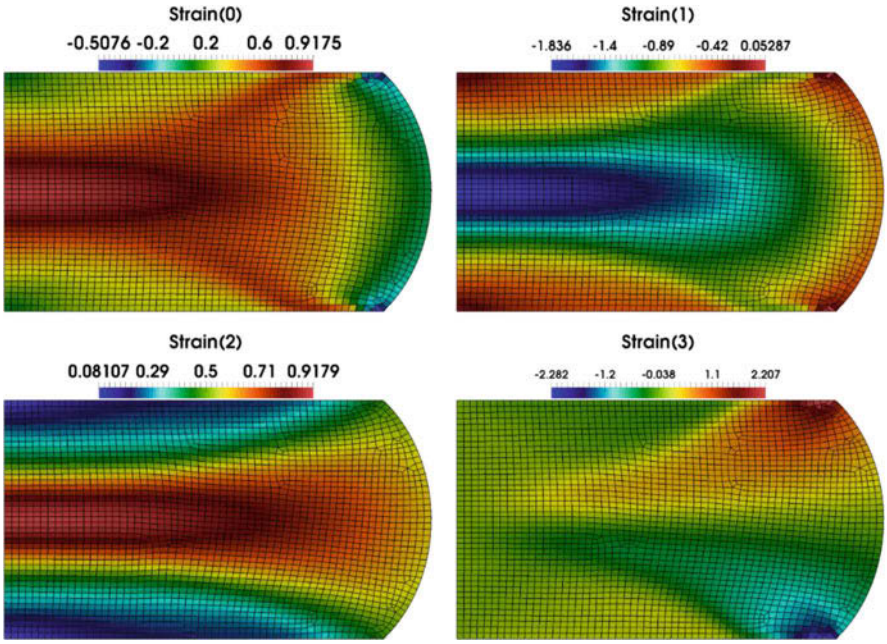

Fig. 14 The strain components from the final time step of the DEFORM® simulation. The underlying mesh has been emphasized to better show the quadrilateral geometry

medoid is a representative datum for that cluster. This approach is reminiscent of the classic k-means algorithm, in which data are placed in clusters with the closets cluster mean [66]. For a set of d-dimensional data points $\mathbf{X} = \{x_i\}$ and k clusters $\mathbf{C} = \{c_k\}$, k-medoids attempts to solve the following minimization:

$$\min_{\mathbf{C}} \sum_{i=1}^{k} \sum_{x_i \in c_k} d\left(x_i, m_k\right)$$

where m_k is the medoid of cluster c_k and $d(a, b)$ is some distance metric between points a and b. A benefit of k-medoids is the ability to customize the choice of metric, which is useful for problems where the standard l_2 norm may be inappropriate. This optimization is computationally intensive; however, several heuristic algorithms exist that perform well in practice. We utilize the partition around medoids algorithm, which iteratively minimizes the total distances within each cluster by recursively checking medoid candidates for a given partition, reassigning points to new clusters as medoids are moved [65]. k-medoids has the advantage of being *unsupervised*: the clustering model does not require training data other than the input. However, the choice of k is problem dependent, and imprudent choices of k may lead to spurious results. Various quality metrics exist

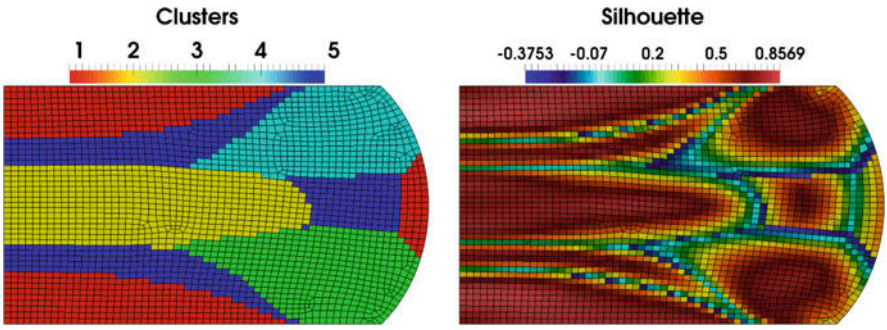

Fig. 15 The clustering of the 4-dimensional strain space with $k = 5$ (left) and the corresponding silhouette (right)

for determining the fitness of a particular choice for k. For a given set of clusters $\mathbf{C} = \{c_k\}$ and points $\mathbf{X} = \{x_i\}$, we define the following quantities:

$$a_i = \frac{\sum_{x_j \in c_{k,i}} d\left(x_i, x_j\right)}{n_{k,i}}$$

where $n_{k,i}$ is the number of points in cluster k to which x_i belongs and

$$b_i = \min_{\mathbf{C}} \frac{\sum_{x_j \notin c_{,i}} d\left(x_i, x_j\right)}{n_{k,j}}$$

Thus, a_i represents the average distance of datum x_i to all other points in their parent cluster, and b_i is the minimum average distance of x_i to all other points in any other cluster. The silhouette metric is then defined as follows [67]:

$$s_i = \frac{b_i - a_i}{\max\left\{a_i, b_i\right\}}$$

The range of possible silhouette is thus $-1 \leq s_i \leq 1$. For a well-clustered datum, $a_i \ll b_i$ and $s_i \approx 1$, whereas a datum that has been placed in an incorrect cluster will have $s_i \approx -1$. Using k-medoids with a squared l_2 norm, we cluster the 4-dimensional strain space with $k = 5$ and compute the corresponding silhouette, as shown in Fig. 15.

From the silhouette map in Fig. 15, we see that most data are effectively grouped in their parent cluster. The data that are poorly clustered tend to lie along the boundaries of zones, which is reasonable given the continuous nature of the strain field.

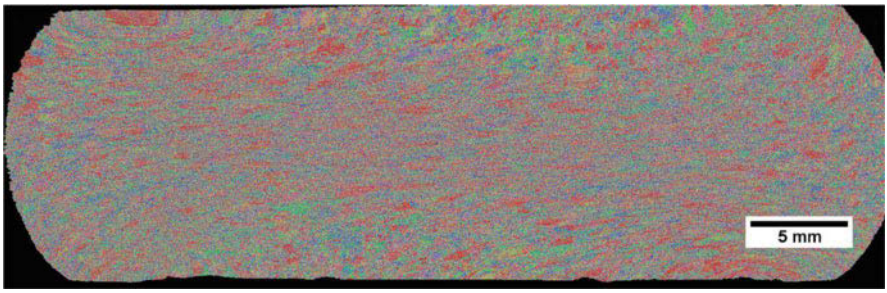

Fig. 16 The stitched cross-sectional EBSD montage of the pancake forging, colored using 001 IPF colors

6.2 Processing Characterization Data

In order to relate the zoned process history to microstructure, the collected characterization data must be processed and relevant statistics extracted. The physical pancake forging corresponding to the DEFORM® simulation in the above section was cross-sectioned and imaged using both EBSD and BSE. Due to the size of the specimen, both modalities required montage collections. Individual EBSD tiles were collected with a step size of 15 μm and stitched together using the AnyStitch software [68]. The stitched EBSD montage is shown in Fig. 16. After stitching, alpha particles within the EBSD data were identified by segmenting using a 5° misorientation. These alpha particle orientations were then clustered into five zones using *k*-medoids, and the resulting partition was spatially segmented to identify individual MTRs. Additionally, several statistics about the MTR features were computed, including areas, axis lengths, and morphological orientations.

The BSE imaging produced 979 2048×2048 image tiles with a pixel resolution of 0.5 μm, collected with roughly 20% tile overlap. The total BSE montage was constructed using the image stitching plugin in Fiji [69]. After stitching, the two-phase structure was segmented by applying a simple threshold. An example BSE tile and its segmented counterpart are shown in Fig. 17.

6.3 Registration and Fusion

In order to quantitatively assess the relationship between the process zones and the resulting microstructure, the DEFORM® simulation must be registered and fused with the EBSD and BSE characterizations. First, the EBSD and BSE montages are cropped to only the right half of the images, since the DEFORM® simulation was only run for one symmetric half of the forging. The DEFORM® and BSE montages were then resampled onto image grids with 15 μm pixel spacing, the same as the EBSD. The DEFORM mesh was resampled using nearest neighbor interpolation.

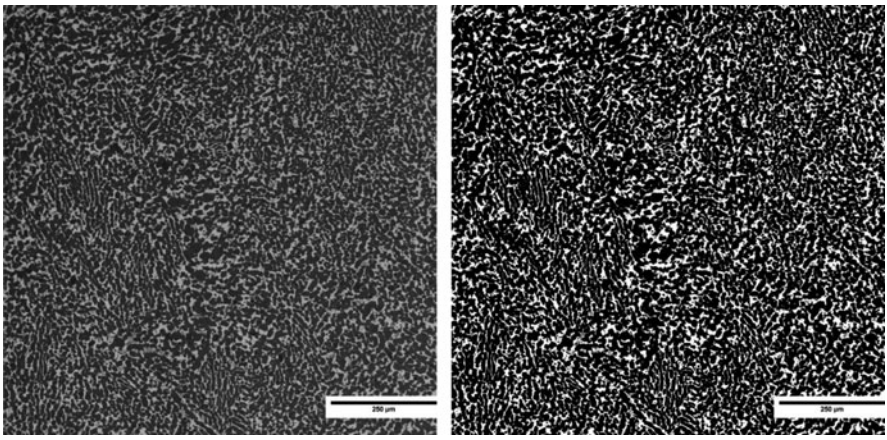

Fig. 17 Original BSE tile (left) and corresponding binary segmented image (right)

Fig. 18 The mask of the identified component in each of the resampled datasets: EBSD (right), BSE (middle), and DEFORM® (right)

For the BSE montage, a 15 μm window was passed over the segmented high-resolution montage and the average value of the binary segmentation was computed within this window. This procedure yields an alpha area fraction at each 15 μm pixel.

The resampling procedure conveniently brings all datasets onto the same geometric topology; however, they are still misaligned relative to one another. To register the datasets together, the component was first identified in each of the modalities. Figure 18 shows these component masks.

Since the goal is to determine correspondence between process zones and microstructure, we do not wish to a priori assume any relationships that would bias the registration. Instead, we identify the component geometry in each modality since we expect it to be relatively invariant between each dataset. Thus, the component geometry itself can be used as a registration datum. To obtain points for registration, the exterior of the masks shown in Fig. 18 are regularly sampled. These sampled points are shown in Fig. 19.

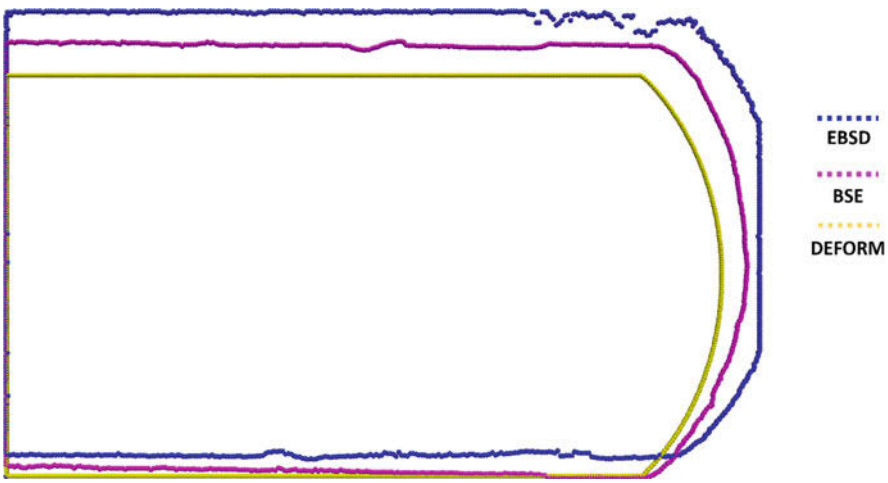

Fig. 19 Sampled exterior points, used for registration, from each of the modalities

We compute the transform that best brings sampled points into alignment using a least-squares approach that is robust to noise [70]. The goal is to estimate the rotation R, translation t, and scaling s that best minimize the squared error between two sets of points, $\mathbf{X} \in \mathbb{R}^d$ and $\mathbf{Y} \in \mathbb{R}^d$:

$$\varepsilon^2(R, t, s) = \frac{1}{2}\sum_{i=1}^{n} \|y_i - (sRx_i + t)\|^2$$

The above minimization is possible for solutions in R, t, s from the following equations:

$$R = USV^{\mathrm{T}}$$

$$t = \mu_y - sR\mu_x$$

$$s = \frac{1}{\sigma_x^2} tr(DS)$$

where UDV^{T} is the singular value decomposition of $\mathbf{X}\mathbf{Y}^{\mathrm{T}}$ and

$$S = \begin{cases} I, & \det\left(\boldsymbol{X}\boldsymbol{Y}^{\mathrm{T}}\right) \geq 0 \\ \mathrm{diag}\,(1, 1, \ldots, 1, -1), & \det\left(\boldsymbol{X}\boldsymbol{Y}^{\mathrm{T}}\right) < 0 \end{cases}$$

μ_x and μ_y are the average positions of $\mathbf{X}$ and $\mathbf{Y}$, and σ_x^2 is the variance of $\mathbf{X}$. Using the above approach, the EBSD registration points were first transformed to

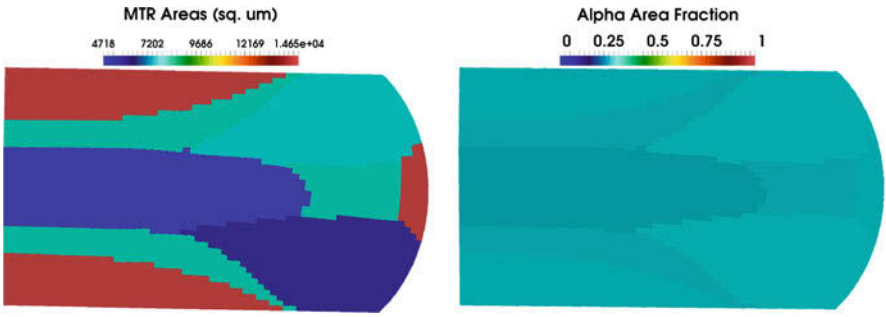

Fig. 20 Zoned regions of process history colored by MTR areas (left) and alpha area fraction (right)

the DEFORM® reference frame, with both datasets followed by being transformed to the BSE reference frame. After applying the transformations on the resampled image geometries, the resulting aligned images were fused on the same grid using nearest neighbor interpolation. On this new resampled geometry, the strain tensors from the DEFORM® simulation were rezoned using $k = 5$. After performing this fusion, it is possible to assess microstructure characteristics per zone. Figure 19 shows the process zones colored by different aspects of the microstructure. In Fig. 20, the average MTR area, as measured from the EBSD, and alpha area fraction, determined from the segmentation of the BSE image montage, are shown for each zone. Note that since the data have been fused onto the same geometry, this approach presents a direct comparison between the zoned process variables and the resulting microstructure. The average MTRs are much larger in the zones that correspond to regions of large strain, as compared to the zones central to the forging. The alpha area fraction, however, does not vary substantially with the strain zones.

This visualization demonstrates the power of a flexible ICME tool: the ability to simultaneously represent various geometries (i.e., images, meshes, and points), data shapes (i.e., tensorial strains, vector orientations, and scalar image intensities), and complex hierarchy (i.e., zoned process variables, identified MTRs, and segmented BSE images) allows for novel analyses to be conducted. DREAM.3D, by leveraging SIMPL, is able to effectively manage these disparate data streams and orchestrate their fusion to produce actionable information. Thanks to the reusability of filters via plugins, characterization steps such as computing sizes of features or finding average values within features did not require reimplementation, freeing the development time to be spent on devising a robust zoning and registration procedure. Additionally, since SIMPL archives pipeline information along with the raw data, researchers are able to confidently store data and reproduce workflows as needed. Indeed, the authors greatly benefited from this functionality in constructing figures for this use case.

7 Summary

We have presented an overview of the ICME software applications available to a modern materials researcher, with a focus on simulation and analytics tools that generate and process field data. In order to properly handle the myriad kinds of information these tools produce, we have sketched an outline of the requirements that an ICME workflow manager should aspire to address. We define requirements on such a tool's data structure, modularity, data access, and workflow capabilities. As an example of one tool that satisfies these requirements, we showcased SIMPL, the Spatial Information Management Protocol Library, along with its most prominent user, the Digital Representation Environment for the Analysis of Microstructure in 3D, or DREAM.3D. To demonstrate how DREAM.3D can leverage SIMPL's features, a case study was outlined that shows how to address a common problem in ICME workflows: quantitatively relating process simulation to measure microstructure. This worked example showed how process variables from a forging simulation of a Ti-6242Si cylinder could be directly coupled with resulting microstructure characterized using EBSD and BSE imaging.

As a community, materials research and development must still make progress on developing easily shareable toolsets for analysis, driven by the continuing adoption of ICME techniques and data-driven methods. Other fields, such as bioinformatics, have made this transition successfully; the materials community should heed the lessons learned from these other sister fields and seek to grow tools that foster development on those problem spaces unique to materials. Additionally, teaching the next generation of materials researchers how to reason through materials problems with an ICME lens is paramount. Developing robust, standardized, and open tools for the growing community ensures that the goals of ICME are achievable.

Acknowledgments The authors would like to acknowledge Mike Jackson, for his vision and programming expertise in enabling the implementation of the SIMPL architecture; Dennis Dimiduk, for his consistent support and fruitful discussions; Adam Pilchak, for motivating the demonstrated ICME use case and providing the data and material; Mike Uchic, for providing characterization support and contribution to the vision of SIMPL; and Chris Woodward, for his unyielding support in the early stages of designing DREAM.3D.

References

1. National Research Council, *Integrated Computational Materials Engineering: A Transformational Discipline for Improved Competitiveness and National Security* (The National Academies Press, Washington, DC, 2008). https://doi.org/10.17226/12199.
2. B. Puchala, G. Tarcea, E.A. Marquis, M. Hedstrom, H.V. Jagadish, J.E. Allison, The materials commons: a collaborative platform and information repository for the global materials community. JOM **68**(8), 2035–2044 (2016). https://doi.org/10.1007/s11837-016-1998-7
3. B. Blaiszik, K. Chard, J. Pruyne, R. Ananthakrishnan, S. Tuecke, I. Foster, The materials data facility: data services to advance materials science research. JOM **68**(8), 2045–2052 (2016). https://doi.org/10.1007/s11837-016-2001-3

4. A. Jain, S.P. Ong, G. Hautier, W. Chen, W.D. Richards, S. Dacek, S. Cholia, D. Gunter, D. Skinner, G. Ceder, K.A. Persson, Commentary: the materials project: a materials genome approach to accelerating materials innovation. APL Mater **1**(1) (2013). https://doi.org/10.1063/1.4812323
5. J. Ahrens, B. Gevecki, C. Law, ParaView: an end-user tool for large data visualization, in *Visualization Handbook*, (Elsevier, Amsterdam, 2005)
6. Applications. (Scientific Forming Technologies Corporation) [Online]. Available: https://www.deform.com/applications/. Accessed Mar 2019
7. Casting Applications. (ESI Group) [Online]. Available: https://www.esi-group.com/software-solutions/virtual-manufacturing/casting/applications. Accessed Mar 2019
8. Abaqus Unified FEA. (Dassault Systemes) [Online]. Available: https://www.3ds.com/products-services/simulia/products/abaqus/. Accessed Mar 2019
9. ANSYS. (ANSYS) [Online]. Available: https://www.ansys.com/. Accessed Mar 2019
10. Albany. (Sandia National Laboratories, Center for Computing Research) [Online]. Available: https://cfwebprod.sandia.gov/cfdocs/CompResearch/templates/insert/project.cfm?proj=28. Accessed Mar 2019
11. A.G. Salinger, R.A. Bartlett, A.M. Bradley, Q. Chen, I.P. Demeshko, X. Gao, G.A. Hansen, A. Mota, R.P. Muller, E. Nielsen, J.T. Ostien, R.P. Pawlowski, M. Perego, E.T. Phipps, W. Sun, I.K. Tezaur, Albany: using component-based design to develop a flexible, generic multiphysics analysis code. Int J Multiscale Comput Eng **14**(4), 415–438 (2016). https://doi.org/10.1615/IntJMultCompEng.2016017040
12. MOOSE: Multiphysics Object Oriented Simulation Environment. (Idaho National Laboratory) [Online]. Available: https://mooseframework.org/. Accessed Mar 2019
13. D. Gaston, C. Newman, G. Hansen, D. Lebrun-Grandie, MOOSE: A parallel computational framework for coupled systems of nonlinear equations. Nucl. Eng. Des. **239**(10), 1768–1778 (2009)
14. H. Moulinec, P. Suquet, A numerical method for computing the overall response of nonlinear composites with complex microstructure. Comput. Methods Appl. Mech. Eng. **157**(1–2), 69–94 (1998). https://doi.org/10.1016/S0045-7825(97)00218-1
15. J.C. Michel, H. Moulinec, P. Suquet, A computational scheme for linear and non-linear composites with arbitrary phase contrast. Numer Methods Eng **52**(1–2), 139–160 (2001). https://doi.org/10.1002/nme.275
16. S.P. Donegan, A.D. Rollett, Simulation of residual stress and elastic energy density in thermal barrier coatings using fast Fourier transforms. Acta Mater. **96**, 212–228 (2015). https://doi.org/10.1016/j.actamat.2015.06.019
17. R. A. Lebensohn, N-site modeling of a 3D viscoplastic polycrystal using Fast Fourier Transform. Acta Mater. **49**(14), 2723–2737 (2001). https://doi.org/10.1016/S1359-6454(01)00172-0
18. P. Eisenlohr, M. Diehl, R.A. Lebensohn, F. Roters, A spectral method solution to crystal elasto-viscoplasticity at finite strains. Int. J. Plast. **46**, 37–53 (2013). https://doi.org/10.1016/j.ijplas.2012.09.012
19. F. Roters, M. Diehl, P. Shanthraj, P. Eisenlohr, C. Reuber, S.L. Wong, T. Maiti, A. Ebrahimi, T. Hochrainer, H.-O. Fabritius, S. Nikolov, M. Friak, N. Fujita, N. Grilli, K.G.F. Janssens, N. Jia, P.J.J. Kok, D. Ma, F. Meiner, E. Werner, M. Stricker, D. Weygand, D. Raabe, DAMASK – The Dusseldorf advanced material simulation kit for modeling multi-physics crystal plasticity, thermal, and damage phenomena from the single crystal up to the component scale. Comput. Mater. Sci. **158**, 420–478 (2019)
20. What is VASP? (VASP Software GmbH) [Online]. Available: https://www.vasp.at/index.php/about-vasp/59-about-vasp. Accessed Mar 2019
21. LAMMPS Molecular Dynamics Simulator. (Sandia National Laboratories) [Online]. Available: https://lammps.sandia.gov/. Accessed Mar 2019
22. ParaDiS. (Lawrence Livermore National Laboratory) [Online]. Available: http://paradis.stanford.edu/site/home. Accessed Mar 2019

23. Avizo for Materials Science. (ThermoFisher Scientific) [Online]. Available: https://www.thermofisher.com/us/en/home/industrial/electron-microscopy/electron-microscopy-instruments-workflow-solutions/3d-visualization-analysis-software/avizo-materials-science.html. Accessed Mar 2019
24. GeoDict – The Digital Material Laboratory. (Math2Market GmbH) [Online]. Available: https://www.math2market.com/Solutions/aboutGD.php. Accessed Mar 2019
25. ESPRIT QUBE – Advanced 3D analysis of EBSD/EDS Data. (Bruker Corporation) [Online]. Available: https://www.bruker.com/products/x-ray-diffraction-and-elemental-analysis/eds-wds-ebsd-sem-micro-xrf-and-sem-micro-ct/quantax-ebsd/esprit-qube.html. Accessed Mar 2019
26. D. Wheeler, D. Brough, T. Fast, S. Kalidindi, A. Reid, *PyMKS: Materials Knowledge System in Python* (2014). https://doi.org/10.6084/m9.figshare.1015761
27. S.R. Niezgoda, D.T. Fullwood, S.R. Kalidindi, Delineation of the space of 2-point correlations in a composite material system. Acta Mater. **56**(18), 5285–5292 (2008). https://doi.org/10.1016/j.actamat.2008.07.005
28. T. Fast, S.R. Kalidindi, Formulation and calibration of higher-order elastic localization relationships using the MKS approach. Acta Mater. **59**(11), 4595–4605 (2011)
29. Magpie. (Wolverton Research Group) [Online]. Available: https://bitbucket.org/wolverton/magpie. Accessed Mar 2019
30. MTEX Toolbox [Online]. Available: http://mtex-toolbox.github.io/. Accessed Mar 2019
31. F. Bachmann, R. Hielscher, H. Schaeben, Texture analysis with MTEX – Free and open source software toolbox. Solid State Phenom. **160**, 63–68 (2010)
32. J.M. Sosa, D.E. Huber, B. Welk, H.L. Fraser, Development and application of MIPAR: A novel software package for two- and three-dimensional microstructural characterization. Integr Mater Manuf Innov **3**(10), 123 (2014). https://doi.org/10.1186/2193-9772-3-10
33. M.A. Groeber, M.A. Jackson, DREAM.3D: A digital representation environment for the analysis of microstructure in 3D. Integr Mater Manuf Innov **3**(5), 56 (2014). https://doi.org/10.1186/2193-9772-3-5
34. ImageJ: Image Processing and Analysis in Java. (National Institutes of Health) [Online]. Available: https://imagej.nih.gov/ij/index.html. Accessed Mar 2019
35. C.A. Schneider, W.S. Rasband, K.W. Eliceri, NIH image to ImageJ: 25 years of image analysis. Nat. Methods **9**, 671–675 (2012). https://doi.org/10.1038/nmeth.2089
36. Fiji [Online]. Available: https://fiji.sc/. Accessed Mar 2019
37. J. Schindelin, I. Arganda-Carreras, E. Frise, V. Kaynig, M. Longair, T. Pietzsch, S. Preibisch, C. Rueden, S. Saalfeld, B. Schmid, J.-Y. Tinevez, D.J. White, V. Hartenstein, K. Eliceiri, P. Tomancak, A. Cardona, Fiji: An open-source platform for biological image analysis. Nat. Methods **9**, 676–682 (2012). https://doi.org/10.1038/nmeth.2019
38. ITK. (Kitware, Inc.) [Online]. Available: https://itk.org/. Accessed Mar 2019
39. T.S. Yoo, M.J. Ackerman, W.E. Lorensen, W. Schroeder, V. Chalana, S. Aylward, D. Metaxas, R. Whitaker, Engineering and algorithm design for an image processing Api: A technical report on ITK – The insight toolkit. Stud. Health Technol. Inform., 586–592 (2002). https://doi.org/10.3233/978-1-60750-929-5-586.
40. 3D Slicer [Online]. Available: https://www.slicer.org/. Accessed Mar 2019
41. R. Kikinis, S.D. Pieper, K.G. Vosburgh, 3D slicer: A platform for subjet-specific image analysis, visualization, and clinical support, in *Intraoperative Imaging and Image-Guided Therapy*, (2014), pp. 277–289. https://doi.org/10.1007/978-1-4614-7657-3_19
42. VTK (Kitware, Inc.) [Online]. Available: https://vtk.org/. Accessed Mar 2019
43. W. Schroeder, K. Martin, B. Lorensen, *The Visualization Toolkit*, 4th edn. (Kitware, 2006)
44. SCIRun. (The NIH/NIGMS Center for Integrative Biomedical Computing) [Online]. Available: http://www.sci.utah.edu/cibc-software/scirun.html. Accessed Mar 2019
45. S.G. Parker, C.R. Johnson, SCIRun: a scientific programming environment for computational steering, in *Proceedings of the 1995 ACM/IEEE Conference on Supercomputing*, San Diego, 1995. https://doi.org/10.1109/SUPERC.1995.241689

46. Orange – Data Mining Fruitful & Fun. (University of Ljubljana) [Online]. Available: https://orange.biolab.si/. Accessed Mar 2019
47. J. Demsar, T. Curk, A. Erjavec, C. Gorup, T. Hocevar, M. Milutinovic, M. Mozina, M. Polajnar, M. Toplak, A. Staric, M. Stajdohar, L. Umek, L. Zagar, J. Zbontar, M. Zitnik, B. Zupan, Orange: data mining toolbox in Python. J. Mach. Learn. Res. **14**, 2349–2353 (2013)
48. Weka 3: Data Mining Software in Java. (University of Waikato) [Online]. Available: https://www.cs.waikato.ac.nz/ml/weka/index.html. Accessed Mar 2019
49. E. Frank, M.A. Hall, I.H. Witten, The WEKA workbench, in *Data Mining: Practical Machine Learning Tools and Techniques*, (Morgan Kaufmann, 2016)
50. SIMPL. (BlueQuartz Software, LLC) [Online]. Available: https://github.com/BlueQuartzSoftware/SIMPL. Accessed Mar 2019
51. DREAM3D. (BlueQuartz Software, LLC) [Online]. Available: https://github.com/BlueQuartzSoftware/DREAM3D. Accessed March 2019
52. SIMPLView. (BlueQuartz Software, LLC) [Online]. Available: https://github.com/BlueQuartzSoftware/SIMPLView. Accessed Mar 2019
53. QT | Cross-platform software development for embedded & desktop [Online]. Available: https://www.qt.io/. Accessed Mar 2019
54. Hierarchical Data Format, version 5. (The HDF Group, 1997–2019) [Online]. Available: http://www.hdfgroup.org/HDF5/
55. G. Guennebaud, B. Jacob, Eigen v3. (2010) [Online]. Available: http://eigen.tuxfamily.org. Accessed March 2019
56. Intel Threading Building Blocks. (Intel Corporation) [Online]. Available: https://www.threadingbuildingblocks.org/. Accessed Mar 2019
57. W. Jakob, J. Rhinelander, D. Moldovan, pybind11 – Seamless operability between C++11 and Python. (2019). [Online]. Available: https://github.com/pybind/pybind11. Accessed Mar 2019
58. CMake. (Kitware, Inc.) [Online]. Available: https://cmake.org/. Accessed Mar 2019
59. Xdmf [Online]. Available: http://xdmf.org/index.php/Main_Page. Accessed Mar 2019
60. A.L. Pilchak, J. Shank, J.C. Tucker, S. Srivatsa, P.N. Fagin, S.L. Semiatin, A dataset for the development, verification, and validation of microstructure-sensitive process models for near-alpha titanium alloys. Integr Mater Manuf Innov **5**(14), 259 (2016). https://doi.org/10.1186/s40192-016-0056-1
61. A.P. Woodfield, M.D. Gorman, R.R. Corderman, J.A. Sutliff, B. Yamrom, Effect of Microstructure on Dwell Fatigue Behavior of Ti-6242, in *Titanium '95: Science and Technology*, (Birmingham, 1996)
62. A.L. Pilchak, A. Huston, W.J. Porter, D.J. Buchanan, R. John, Growth of small and long fatigue cracks in Ti-6Al-4V subjected to cyclic and dwell fatigue, in *Proceedings of the 13th World Conference on Titanium*, Warrendale, 2016.
63. A.L. Pilchak, A simple model to account for the rolw of microtexture on fatigue and dwell fatigue lifetimes of titanium alloys. Scr. Mater. **74**, 68–71 (2014). https://doi.org/10.1016/j.scriptamat.2013.10.024
64. A.K. Jain, M.N. Murty, P.J. Flynn, Data clustering: A review. ACM Comput. Surv. **31**(3), 265–323 (1999). https://doi.org/10.1145/331499.331504
65. L. Kaufman, P.J. Rousseeuw, Clustering by means of medoids, in *Proceedings of Statistical Data Analysis Based on the L1 Norm*, Neuchatel, 1987
66. A.K. Jain, Data clustering: 50 years beyond K-means. Pattern Recogn. Lett. **31**(8), 651–666 (2010). https://doi.org/10.1016/j.patrec.2009.09.011
67. P.J. Rousseeuw, Silhouettes: A graphical aid to the interpretation and validation of cluster analysis. J. Comput. Appl. Math. **20**, 53–65 (1987). https://doi.org/10.1016/0377-0427(87)90125-7
68. A.L. Pilchak, A.R. Shiveley, J.S. Tiley, D.L. Ballard, AnyStitch: A tool for combining electron backscatter diffraction data sets. J. Microsc. **244**(1), 38–44 (2011). https://doi.org/10.1111/j.1365-2818.2011.03496.x

69. S. Preibisch, S. Saalfeld, P. Tomancak, Globally optimzal stitching of tiled 3D microscopic image acquisitions. Bioinformatics **25**(11), 1463–1465 (2009). https://doi.org/10.1093/bioinformatics/btp184
70. S. Umeyama, Least-squares estimation of transformation parameters between two point patterns. IEEE Trans Pattern Anal Mach Intell **13**, 376–380 (1991). https://doi.org/10.1109/34.88573

Multi-scale Microstructure and Property-Based Statistically Equivalent RVEs for Modeling Nickel-Based Superalloys

Somnath Ghosh, George Weber, Maxwell Pinz, Akbar Bagri, Tresa M. Pollock, Will Lenthe, Jean-Charles Stinville, Michael D. Uchic, and Christopher Woodward

1 Introduction

Nickel-based superalloys are widely used in propulsion components of the aerospace industry such as turbine engine blades, disks, casings, and liners. These superalloys are able to maintain their strength at a range of low to high temperatures, which allow engines to operate at high efficiency without mechanical failure [1, 2]. Large economic gains can be achieved by improving reliability and life of their aerospace applications through better predictability of relevant properties. These alloys possess a desirable combination of high-temperature strength and toughness, oxidation, creep resistance, and high-temperature stability that is attributed to the existence of a two-phase $\gamma - \gamma'$ matrix-precipitate microstructure as shown in Fig. 1.

S. Ghosh (✉)
Departments of Civil, Mechanical Engineering and Materials Science & Engineering, Johns Hopkins University, Baltimore, MD, USA
e-mail: sghosh20@jhu.edu

G. Weber · M. Pinz · A. Bagri
Departments of Mechanical and Civil Engineering, Johns Hopkins University, Baltimore, MD, USA
e-mail: gweber5@jhu.edu; mpinz1@jhu.edu; abagri1@jhu.edu

T. M. Pollock · W. Lenthe · J.-C. Stinville
The Materials Department, University of California Santa Barbara, Santa Barbara, CA, USA
e-mail: pollock@engineering.ucsb.edu; stinville@engineering.ucsb.edu

M. D. Uchic
Materials and Manufacturing Directorate, Air Force Research Laboratory, Wright-Patterson AFB, Dayton, OH, USA
e-mail: michael.uchic@wpafb.af.mil

C. Woodward
Air Force Research Laboratory/RX, Wright-Patterson Air Force Base, Dayton, OH, USA

S. Ghosh et al. (eds.), *Integrated Computational Materials Engineering (ICME)*,
https://doi.org/10.1007/978-3-030-40562-5_3

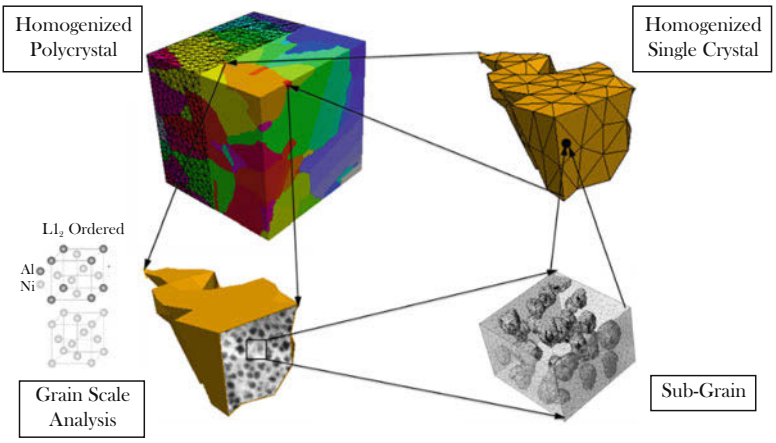

Fig. 1 Schematic representation of multiple scales in the development of a crystal plasticity finite element model for Ni-based superalloys: polycrystalline microstructure, subgrain microstructure in a single grain, discretized subgrain microstructural RVE, and homogenized crystal plasticity FE model for a grain

The continuous γ-matrix phase has a face-centered cubic (FCC) lattice structure and is an alloy of Ni and Cr with a small fraction of other alloying elements. The γ' precipitate phase is a coherent, ordered intermetallic Ni_3Al reinforcing phase of $L1_2$ crystal structure, which appears as a distribution of cuboidal precipitates in a solid solution. The presence of the γ' precipitate phase in the γ matrix causes strengthening mechanisms for the two-phase system. In FCC and $L1_2$ crystal structures, dislocations have Burgers vectors with the same $\langle 101 \rangle$ directions but different magnitudes. A full dislocation in the $L1_2$ structure must transverse twice the distance compared to that of FCC in order to maintain the ordered lattice, which creates many additional consequences for the dislocation core. Figure 1 shows the polycrystalline microstructure, the subgrain $\gamma - \gamma'$ microstructure in a single grain, the discretized subgrain $\gamma - \gamma'$ microstructural representative volume element or RVE, and the homogenized crystal plasticity finite element model for a grain.

The shape and size of the γ'-phase depend largely on the cooling rate and internal stress gradients during processing [3–5]. Slower cooling rates lead to the formation of bimodal populations of large ($\geq$500 nm) secondary and small ($\leq$50 nm) tertiary γ' precipitates, while higher cooling rates yield a predominantly unimodal distribution of secondary γ' precipitates (~50–500 nm). The γ' precipitates act as effective obstacles to the motion of dislocations by virtue of their shape and ordered structure. The volume fraction of γ' precipitates, their mean size, and spacing have a major effect on the mechanical properties of these superalloys [6, 7]. Micro-mechanisms controlling creep in polycrystalline Ni-based superalloys are complex [6, 8]. At intermediate temperatures $650\,^{\circ}\text{C} \leq \theta \leq 800\,^{\circ}\text{C}$ and moderate stress levels 650 MPa, dominant deformation mechanisms include antiphase boundary (APB) shearing and micro-twinning. The probability of occurrence of a given mechanism depends on the load, crystal orientation, and microstructural morphology. At lower

temperatures $\theta \leq 650\,^{\circ}\mathrm{C}$ and higher stresses, creep is governed by different types of dislocation-based shearing processes, while at higher temperatures $\theta \geq 800\,^{\circ}\mathrm{C}$, the creep deformation is controlled by Orowan looping and cross-slip mechanisms [9]. Deformation behavior under various loading and temperature conditions has been studied both for single crystal and polycrystalline Ni-based superalloys [10, 11].

Phenomenological crystal plasticity models, based on the power law or thermally activated models of plasticity, have been implemented to model creep and deformation response of single crystal and polycrystalline Ni-based superalloys in [12–16]. These are generally single-scale models and lack information on the underlying microstructural characteristics at the intragranular or subgrain scale, which affect the single crystal and polycrystalline behavior. Three scales are relevant, when modeling polycrystalline behavior of Ni-based superalloys using crystal plasticity models. They are:

1. Intragranular, subgrain scale, characterized by the size of γ' precipitates and their spacing designated as the γ-matrix channel-width;
2. Grain-scale of single crystals characterized by the grain-boundary distance;
3. Scale corresponding to representative volume elements of polycrystalline aggregates.

It is computationally intractable to simulate the behavior of polycrystalline microstructures with explicit representation of the subgrain-scale microstructure. To represent the effects of lower-scale morphology and deformation mechanisms on higher-scale response models, it is necessary to develop crystal plasticity models that hierarchically incorporate microstructural information from the lower scales. In [17], hardening parameters are expressed as functions of the average size of precipitates. Hierarchical approaches for Ni-based superalloys have been proposed in [18], where artificial neural network algorithms are used to develop grain size and volume fraction-dependent dislocation density-based crystal plasticity models for creep and fatigue. Ghosh et. al. have homogenized subgrain scale response to develop hierarchical grain-scale crystal plasticity models for Ni-based superalloys in [19–23]. Parametric forms of subgrain-scale morphological characteristics are incorporated in grain-level constitutive relations in these models.

An important aspect of hierarchical modeling is the establishment of the "representative volume element" or RVE [24] for conducting direct numerical simulations (DNS) of the micromechanical problem. The RVE is defined as a microstructural domain that optimally represents the morphological characteristics and effective response of the entire microstructure. However, it is difficult to define an RVE in the strictest sense for microstructures with nonuniformly dispersed heterogeneities as shown in Fig. 1, due to the lack of uniformity or periodicity [25]. To facilitate a computational domain for nonuniform microstructures, the statistically equivalent RVE or *SERVE* has been introduced in [26–28]. It is designated as an optimal microstructural domain, for which statistical distribution functions of morphological parameters, as well as material properties converge to those for the entire microstructure. The associated exterior statistics-based boundary conditions are discussed in another chapter of this book.

The SERVE is further classified into a microstructure-based SERVE or *M-SERVE* and a property-based SERVE or *P-SERVE* in [29–31]. Similar clarifications have been proposed in [32]. The M-SERVE is defined as one for which morphological and crystallographic characteristics of the microstructure are the sole determinants of the representative volume. Convergence tests are needed for determining the minimum SERVE size necessary for the statistics of characteristic microstructural descriptors to converge. The M-SERVE is the foundation of the DREAM.3D software [33, 34]. On the other hand, the P-SERVE is determined from convergence of material response functions and properties.

Development of the M-SERVE and P-SERVE is preceded by the creation of 3D statistically equivalent virtual microstructures or *SEVMs*. The statistics of morphological descriptors in SEVMs must be equivalent to those derived from high-fidelity datasets obtained from experiments involving electron backscatter diffraction (EBSD) [34, 35], scanning electron microscopy (SEM), or computed tomography (CT). Deterministic models, e.g., in [36], are not well-suited for microstructures with significant spatial variations. Various methods of generating polycrystalline or polyphase microstructures have been proposed in the literature, e.g., in [37–43]. These methods account for spatial variations in microstructural morphology and represent the microstructure with statistical distributions functions equivalent to those obtained from experimental observations. Conversely, other methodologies rely on a multiphase field approach to generate microstructural statistics for both polycrystalline and polyphase microstructures [44, 45]. These methods focus on the modeling and subsequent statistics of the formation of microstructural geometries and complement the top-down approach of observing and matching the microstructural statistics. In [34, 35], statistically equivalent polycrystalline microstructures have been developed to capture the statistics of grain shape and size, crystallographic orientations, misorientations, and their correlations. The DREAM.3D code resulting from this work [33] is very successful in generating SEVMs for polycrystalline materials.

This chapter is devoted to a discussion on the development of the M-SERVE and P-SERVE of the Ni-based superalloy René 88DT [46] at multiple scales, as depicted in Fig. 1. Section 2 focuses on the M-SERVE and P-SERVE development for intragranular $\gamma - \gamma'$ microstructures at the subgrain scales. It involves a sequence of tasks, viz., serial sectioning, image processing, feature extraction, and statistical characterization, followed by micromechanical analysis and convergence tests for establishing the M-SERVE and P-SERVE. Subsequently the M-SERVE and P-SERVE development for the higher-scale polycrystalline microstructure, characterized by grains containing annealing twins, is discussed in Sect. 3.

2 M-SERVE and P-SERVE for Intragranular Microstructures at the Subgrain Scale

The scanning electron microscopy image of a section of intragranular $\gamma - \gamma'$ microstructure of the Ni-based superalloy René 88DT is shown in Fig. 2a. The following sections discuss the process of experimental image extraction, microstructural characterization, and statistical analysis, followed by micromechanical analysis for establishing the M-SERVE and P-SERVE. Details of these developments are given in [30, 47].

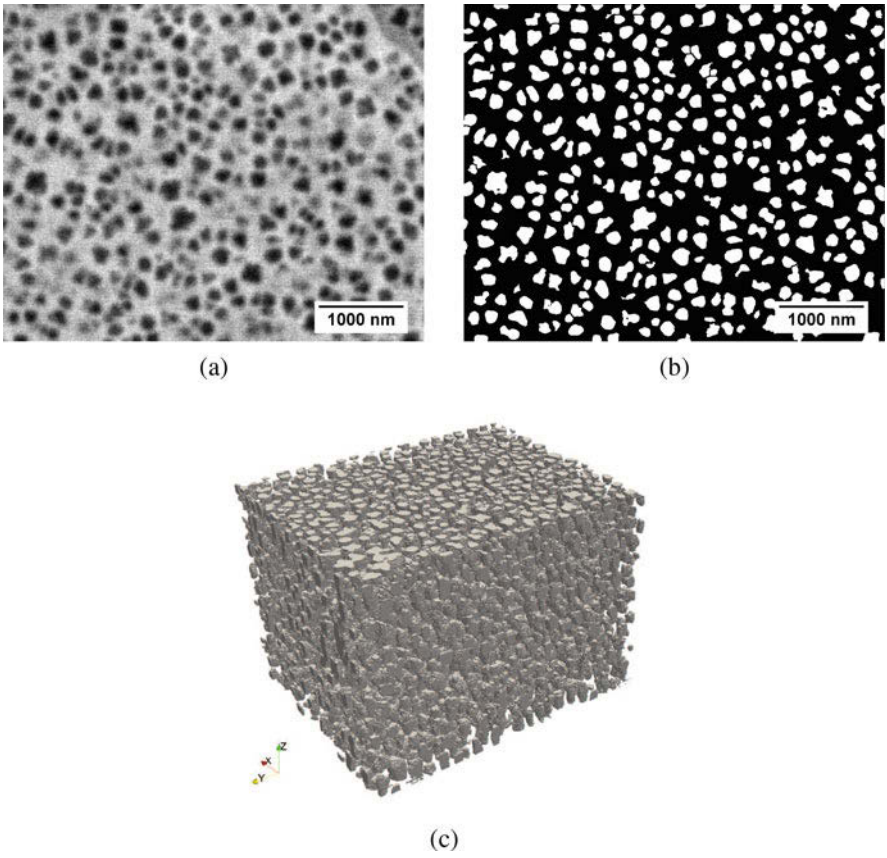

Fig. 2 (**a**) A scanning electron microscope image of Rene'88DT acquired by FIB serial sectioning, (**b**) final segmented image following thresholding and despeckling, and (**c**) visualization of the 3D microstructure by stacking section images after binarization and post-processing. (Reprinted from: Pinz et al. [30], with permission from Elsevier)

2.1 Experimental Data Acquisition and Image Processing

Acquisition of high-fidelity micro- and nano-scale 3D data for a single crystal Rene'88DT superalloy with $\gamma - \gamma'$ microstructure is done using an automated, high-throughput focused ion beam (FIB) coupled with a high-resolution scanning electron microscope (SEM) in a TriBeam system [48]. The resulting dataset used in microstructure reconstruction is available in [46]. The FIB process serially sections layers of the specimen in the [001] direction, ablating approximately 20 nm of material in each pass. Individual section images are subsequently extracted using the SEM with a backscattered electron detector, repeating the process until the desired volume is scanned. The dataset used in the generation of a $3 \times 4 \times 5\,\mu$m virtual material volume is from 182 grayscale section images, each containing 1996×1596 pixels. This yields a resolution of 2.5 nm between pixels and 20 nm between slices.

A pipeline of automated image processing techniques is necessary to generate 3D virtual microstructures from this dataset. This pipeline converts the experimentally derived image stack into a fully segmented 3D voxelized representation following a four-step procedure that includes (i) slice registration and alignment; (ii) voxel level cleanup; (iii) feature segmentation; and (iv) artifact removal. Once a 3D virtual representation of the experimental data is processed and segmented, statistical distributions of microstructural descriptors, viz., feature size, shape, orientation, neighbor distance, etc., are generated from the dataset. The fidelity of the statistical distributions depends on the robustness of the preliminary image processing.

The collection of image slices from serial-sectioning must be assimilated into a 3D voxelized binary structure, representing γ matrix and γ' precipitate phases. To achieve this objective, the slices in the image stack must be aligned, followed by preliminary image processing and thresholding for binarization. Major steps in this process include (i) image slice alignment; (ii) background subtraction; (iii) local smoothing; (iv) contrast enhancement through unsharp masking; (v) minimum cross-entropy thresholding; and (vi) scanning direction normalization with image interpolation. A representative slice, corresponding to the output of the segmentation process, is shown in Fig. 2b. The difference in data resolution between the sectioning direction (z) ($\sim$20 nm) and the in-plane directions (x, y) ($\sim$2.5 nm) necessitates additional image slices to ensure the same distance between voxels in all directions. Consistent resolution in the x, y, and z directions allows the usage of filters that operate with uniform spacing, such as the watershed algorithm and microstructural statistics extraction. The aligned and binarized images should subsequently undergo an image interpolation method to equalize section spacing in all directions. A consistent resolution of 2.5 nm between voxels in all directions is obtained by inserting $(\frac{d_{bp}}{d_{ip}} - 1)$ additional slices between images. Here $d_{bp} = 20$ nm is the resolution between planes, and $d_{ip} = 2.5$ is the in-plane resolution. The surrounding images of the new slices are converted into distance to boundary maps, representing the distance to the nearest boundary of a precipitate. These are then linearly interpolated and thresholded as detailed in [30, 47].

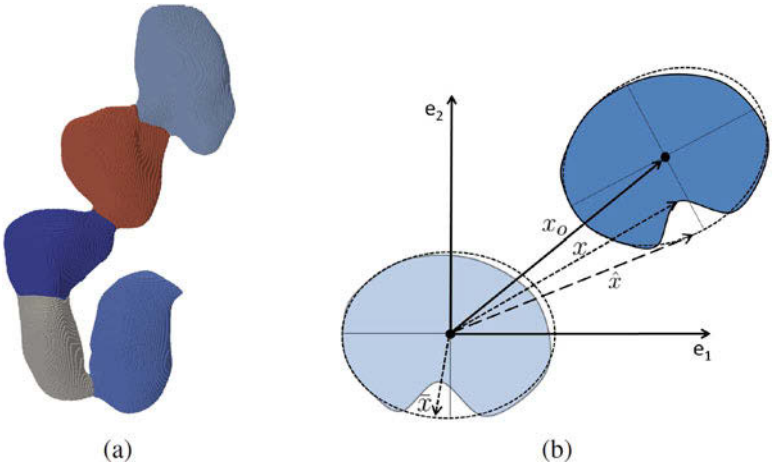

Fig. 3 (**a**) Spurious connectivity ensuing with the 3D SEM-FIB serial sectioning and segmentation process, (**b**) illustration of coordinate systems during ODM mapping algorithm. A single observed point x with its relation to x_o, $\hat{x}$, and $\bar{x}$. The dotted line represents the current iterate of the super-ellipsoid with the surface of the blue object representing a collection of m observed points. (Reprinted from: Pinz et al. [30], with permission from Elsevier)

Due to imperfect image processing, as well as the finite interaction volume of the SEM, spurious connections between precipitates exist as shown in Fig. 3a. A watershed segmentation procedure [49] is employed to eliminate this spurious connectivity and separate conjoined precipitates. The method uses a pseudo-gradient field defined as:

$$\mathcal{G}(i,j,k) = \mathcal{B}_{\text{int}}(i,j,k)\frac{\sum_{\bar{i}=0}^{N_x}\sum_{\bar{j}=0}^{N_y}\sum_{\bar{k}=0}^{N_z}\mathcal{D}_{\text{int}}(\bar{i},\bar{j},\bar{k})e^{-\left[\left(\frac{(\bar{i}-i)^2}{2\sigma^2}\right)+\left(\frac{(\bar{j}-j)^2}{2\sigma^2}\right)+\left(\frac{(\bar{k}-k)^2}{2\sigma^2}\right)\right]}}{\sum_{\bar{i}=0}^{N_x}\sum_{\bar{j}=0}^{N_y}\sum_{\bar{k}=0}^{N_z}e^{-\left[\left(\frac{(\bar{i}-i)^2}{2\sigma^2}\right)+\left(\frac{(\bar{j}-j)^2}{2\sigma^2}\right)+\left(\frac{(\bar{k}-k)^2}{2\sigma^2}\right)\right]}} \tag{1}$$

where N_x, N_y, and N_z represent the number of voxels in the x, y, and z directions, respectively, and $\bar{i}$, $\bar{j}$, $\bar{k}$ are dummy indices. $\mathcal{D}_{\text{int}}$ is a map from each voxel to the value of its distance to the nearest boundary in the plane. It is interpolated to the new slices from the original distance-to-boundary map. $\mathcal{B}_{\text{int}}$ is a binarized map relative to $\mathcal{D}_{\text{int}}$ and is an indicator function of whether a voxel (i, j, k) is in a precipitate or not. The standard deviation σ of the Gaussian blur is set to $\frac{1}{10}$th of the mean particle radius. This gradient field is chosen to reduce disconnected over-segmentation by the watershed algorithm. The 3D Gaussian blur mitigates the effects from voxelization of precipitate edges. After application to initially connected inclusions, the watershed segmentation algorithm produces a final binary voxelized map $\mathcal{B}_{\text{final}}$. The resulting experimentally obtained microstructure from the volume sampled contains approximately 6000 precipitates.

2.2 Parametric Representation of Precipitate Morphology and Statistical Distributions

The morphology of the γ' precipitate phase is generally quite complex that requires a high dimensional shape representation. To avert surface profile representations with large datasets, the order of the precipitate morphology representation is reduced through parametric mapping functions with optimal number of parameters. Such parametrization enables direct incorporation of the morphological parameters in parametrically homogenized constitutive models [19, 20]. For each precipitate, coefficients of the parametrized mapping function are calibrated via an orthogonal distance minimization (ODM) algorithm [50], in which the 3D voxelization is reduced to a list of (x, y, z) coordinates for surface voxels. The equation of a generalized superellipsoid (GSE) is selected to parametrically represent the γ' precipitate morphology, given as:

$$\left(\frac{\bar{x}}{a}\right)^{n_1} + \left(\frac{\bar{y}}{b}\right)^{n_2} + \left(\frac{\bar{z}}{c}\right)^{n_3} = 1 \tag{2}$$

where the set (a, b, c) corresponds to the lengths of principal axes of the GSE and the exponents (n_1, n_2, n_3) manifest the shape of the GSE. The position vector $\{\bar{\mathbf{x}}\} = \{\bar{x}, \bar{y}, \bar{z}\}^T$ describes the location of a GSE surface point $\left\{\hat{\mathbf{x}}\right\} = \left\{\hat{x}, \hat{y}, \hat{z}\right\}^T$ relative to its centroid $\{\mathbf{x}_0\} = \{x_0, y_0, z_0\}^T$ in its principal coordinate system. The latter is represented by the Bunge Euler angles (ϕ_1, Φ, ϕ_2) as shown in Fig. 3b. The relative coordinates are expressed as $\{\bar{\mathbf{x}}\} = [\mathbf{R}]\left\{\hat{\mathbf{x}} - \mathbf{x}_0\right\}$, where the Bunge rotation matrix is defined as:

$$[\mathbf{R}] = \begin{bmatrix} c(\phi_1)c(\phi_2) - s(\phi_1)s(\phi_2)c(\Phi) & s(\phi_1)c(\phi_2) + c(\phi_1)s(\phi_2)c(\Phi) & s(\phi_2)s(\Phi) \\ -c(\phi_1)s(\phi_2) - s(\phi_1)c(\phi_2)c(\Phi) & -s(\phi_1)s(\phi_2) + c(\phi_1)c(\phi_2)c(\Phi) & c(\phi_2)s(\Phi) \\ s(\phi_1)s(\Phi) & -c(\phi_1)s(\Phi) & c(\Phi) \end{bmatrix} \tag{3}$$

where $c = \cos$ and $s = \sin$. The parametrized function in Eq. (2) is capable of adequately describing precipitates of varying size, shape, orientation, aspect ratio, and roundness. An ordered parameter set needs to be evaluated for representing each precipitate, given as:

$$\mathbf{Y}_{\text{par}} = (x_0, y_0, z_0, n_1, n_2, n_3, a, b, c, \phi_1, \Phi, \phi_2) \tag{4}$$

The shape and location of each precipitate in the microstructure is fully characterized by an instantiation of the set $\mathbf{Y}_{\text{par}}$. This parameter set, describing a single GSE, is determined by solving an optimization problem that minimizes the orthogonal distance between N_{points} voxelized surface points of each precipitate and its parametrized representation. For $p \in [1, N_{\text{points}}]$, the orthogonal distance D_p between an observed surface point $\mathbf{x}_p$ of a voxelized precipitate and the conjugate

surface point $\hat{\mathbf{x}}_p$ on the parametrized GSE is given by:

$$D_p = \|\mathbf{x}_p - \hat{\mathbf{x}}_p\| = \sqrt{\left(x_p - \hat{x}_p\right)^2 + \left(y_p - \hat{y}_p\right)^2 + \left(z_p - \hat{z}_p\right)^2} \tag{5}$$

To determine an optimal value of the set $\mathbf{Y}_{\text{par}}$, the minimization problem is stated as:

$$\underset{\mathbf{Y}_{\text{par}}}{\text{Minimize}} \sum_{p=1}^{N_{\text{points}}} D_p^2 \tag{6a}$$

subject to the constraint that each point $\hat{\mathbf{x}}_p$ belongs to the GSE surface

$$\left(\frac{\bar{x}_p}{a}\right)^{n_1} + \left(\frac{\bar{y}_p}{b}\right)^{n_2} + \left(\frac{\bar{z}_p}{c}\right)^{n_3} = 1 \quad \forall\ p \in [1, N_{\text{points}}] \tag{6b}$$

A two-level optimization process is executed to solve the orthogonal distance minimization (ODM) problem, given as:

1. *Level 1*: For every point on the precipitate surface, locate the nearest point on the surface of the test GSE;
2. *Level 2*: Update $\mathbf{Y}_{\text{par}}$ through a Newton-Raphson scheme to determine a new test GSE that reduces the total orthogonal distance over all surface points.

In Level 1, each point $\bar{\mathbf{x}}_p$ on the parametrized surface is identified for a given parameter set $\mathbf{Y}_{\text{par}}$. The constrained minimization problem for the pth point is solved as:

$$\underset{\hat{\mathbf{x}}_\mathbf{p}}{\text{Minimize}}\ D_p^2 = \left(x_p - \hat{x}_p\right)^2 + \left(y_p - \hat{y}_p\right)^2 + \left(z_p - \hat{z}_p\right)^2 \tag{7}$$

subject to the constraint that the point belongs to the known GSE surface given in Eq. (6b). The nonlinear MATLAB solver *fmincon* is used to solve this problem. It avoids instabilities especially as the shape exponents n_1, n_2, n_3 increase [50]. Once all the nearest points $\hat{\mathbf{x}}_p$ are identified, the global optimization problem in Eq. (6) is solved in Level 2 for the next iterate of the parameter set $\mathbf{Y}_{\text{par}}$. The Newton-Raphson iterative solver is implemented to evaluate the update to the test GSE surface. For the ith iteration, the equation to be solved is:

$$\left[\frac{\partial \mathbf{D}}{\partial \mathbf{Y}_{\text{par}}}\right]^i \left\{\mathbf{Y}_{\text{par}}^{i+1} - \mathbf{Y}_{\text{par}}^i\right\} = -\mathbf{D}^i \tag{8}$$

where $\mathbf{D}$ is the vector of D_p for all $p \in [1, N_{\text{slice}}]$. The algorithm is terminated when the update size $\left\{\mathbf{Y}_{\text{par}}^{i+1} - \mathbf{Y}_{\text{par}}^i\right\}$ drops below a convergence threshold.

This method is implemented for the microstructure with 6000 γ' precipitates to generate a database contributing to the 12-dimensional parameter space of $\mathbf{Y}_{\text{par}}$ in Eq. (4). It has been further observed in [30, 47] that the parameter set can be further reduced using the constraint $n = n_1 = n_2 = n_3$ with minimal loss in statistical error. In addition, the principal axis half-lengths are replaced by the normalized aspect ratios $\frac{a}{b}, \frac{b}{c}$ and the half-length of the intermediate principal axis b. These modifications yield the re-parametrization:

$$\hat{\mathbf{Y}}_{\text{par}} = \left(x_0, y_0, z_0, n, \frac{a}{b}, \frac{b}{c}, b, \phi_1, \Phi, \phi_2 \right) \tag{9}$$

Optimally selected analytical forms for the probability density functions of each parameter of $\hat{\mathbf{Y}}_{\text{par}}$ are chosen and fit the experimental data. For example, the aspect ratios are approximately fit to a shifted beta prime distribution function $B'(s) = \frac{s^{-\alpha-\beta}(s-1)^{\alpha-1}}{\bar{B}(\alpha,\beta)}$, where s corresponds to an aspect ratio, (α, β) are fitting parameters, and $\bar{B}$ is the beta function, as shown in Fig. 4a. The shape exponent, on the other hand, is fit to a log-normal distribution function $f(n) = \frac{1}{(n-2)\sqrt{2\pi\sigma}} e^{-\frac{(ln(n-2)-\mu)^2}{2\sigma}}$ with the origin shifted to $n = 2$, and (μ, σ) are fitting parameters as shown in Fig. 4b.

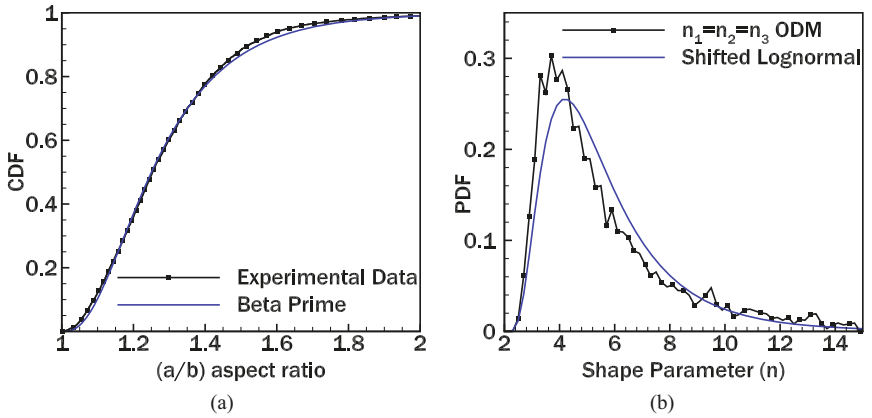

Fig. 4 (**a**) Comparison of the cumulative distribution of the evaluated aspect ratio $\frac{b}{c}$ for 6000 precipitates with the fitted shifted beta prime distribution and (**b**) probability distribution function of the reduced shape exponent n for all 6000 precipitates and a maximum likelihood estimation of a shifted log-normal distribution. (Reprinted from: Pinz et al. [30], with permission from Elsevier)

2.3 Generating Intragranular Statistically Equivalent Virtual Microstructures

The parametrically represented γ' precipitates or GSEs are next dispersed in the computational volume to generate statistically equivalent virtual microstructures or (*SEVMs*). A first step is the initialization of SEVMs with N_p GSE precipitates. For each N_p, distributions of morphological parameters, viz., aspect ratios ($\frac{a}{b}$, $\frac{b}{c}$), the intermediate axis length b, shape exponent n, and the orientation distribution functions (ϕ_1, Φ, ϕ_2), are sampled from the distribution functions created. The aspect ratio $\frac{a}{c}$ can be determined in terms of the other two aspect ratios. However, $\frac{a}{c}$ can be matched to its representative distribution by swapping the relative position of the aspect ratio $\frac{a}{b}$. In a similar manner, the cross-correlations of the sampled parameters are aligned with those of the ODM obtained statistics by a shuffling method. Finally, the N_p precipitates are spatially dispersed inside the cubic computational domain with a volume fraction known from the experimental statistics. The placement of GSEs in the computational domain is done by an iterative algorithm. It initially disperses the statistically equivalent GSE at a very low volume fraction and subsequently conducts gradual dilation and shuffling to avoid precipitate contact, until the target volume fraction is reached.

2.3.1 Finalizing SEVMs Through Optimization of the Two-Point Correlation Function

Following initialization of the SEVM with matching volume fraction, the spatial positions of the γ' precipitates are optimized with respect to the two-point correlation function S_2. A genetic algorithm (GA) optimization method [51] is employed to determine the optimal placement of the GSEs, with the objective of matching S_2 of the SEVM to that of the 6000 precipitates in the experimental microstructure. The 3D correlation function $S_2(r, \theta, \phi)$ in spherical coordinates is a known measure of microstructural heterogeneity [41, 42]. For isotropic microstructures, $S_2(r, \theta, \phi)$ reduces to a r dependent radial distribution function, which may be approximated by a parametrized function as [39]:

$$S_2(r) = {V_f}^2 + V_f(1 - V_f)\frac{\sin\left(\frac{2\pi r}{a_0}\right)}{\frac{2\pi r}{a_0}}e^{-\frac{r}{r_0}} \tag{10}$$

where V_f is the precipitate volume fraction and (a_0, r_0) are parameters to be calibrated. A volume fraction independent, scaled $S_2(r)$ may be obtained as:

$$\bar{S}_2(r) = \frac{S_2(r) - {V_f}^2}{V_f - {V_f}^2} = \frac{\sin\left(\frac{2\pi r}{a_0}\right)}{\frac{2\pi r}{a_0}}e^{-\frac{r}{r_0}} \tag{11}$$

A fitness function is introduced in terms of the variables $(a_0^{\text{target}}, r_0^{\text{target}})$ in $\bar{S}_2(r)$ to assess the fitness of the placement of GSEs in an instantiation of the SEVM.

$$\Psi = \left(\frac{a_o - a_o^{\text{target}}}{a_o^{\text{target}}} \right)^2 + \left(\frac{r_o - r_o^{\text{target}}}{r_o^{\text{target}}} \right)^2 \tag{12}$$

This represents an error metric between the best fit parameters of the experimental microstructure and a candidate SEVM.

The GA search process minimizes Ψ for a given microstructure. Only mutation operators are considered in GA for evolving the population, as crossover operators between microstructures tend to bias the morphological distributions and generate frequent overlaps between precipitates. Candidate microstructures are updated through mutation in one of two possible ways, viz., either perturbation of the GSE centroids or swapping of Euler angles between two GSEs in the microstructure. For viability of the perturbation method, the microstructure is checked for precipitate to precipitate overlap. In the event of an unacceptable overlap, a different random perturbation is attempted. The algorithm is terminated when the fitness function Ψ falls below a threshold. Figure 5 shows examples of reconstructed microstructures for $N_p = 10, 50, 100$, and 200 precipitates corresponding to the same volume fraction.

2.3.2 Validation of SEVM Generation Method by Convergence Tests

The SEVM generation process for the $\gamma - \gamma'$ microstructure invokes minimization of the S_2 best fit equation (12). In [30, 47], it has been shown that the error between the two-point correlation function of the created SEVM and that of the experimental microstructure is reduced with iterations of the GA optimization. The absolute values of $\bar{S}_2(r)$ for the three cases, viz., (i) experimental (FIB-SEM) microstructure, (ii) its best fit equation (10), and (iii) median of an ensemble of 30 SEVMs each with $N_p = 200$, are plotted in Fig. 6b. The figure illustrates that the spatial positioning of γ' precipitates of the virtual microstructure closely match that of the experiment.

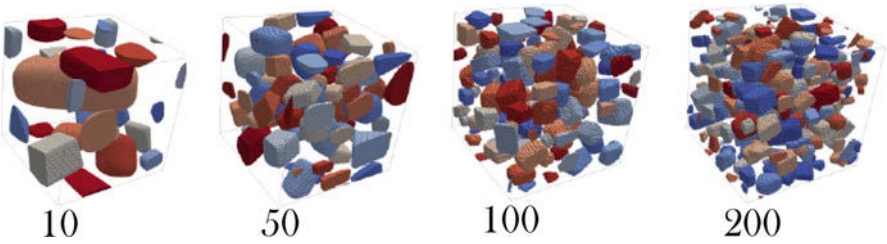

Fig. 5 Statistically equivalent virtual microstructures with $N_p = 10, 50, 100$, and 200 precipitates for the same volume fraction. (Reprinted from: Pinz et al. [30], with permission from Elsevier)

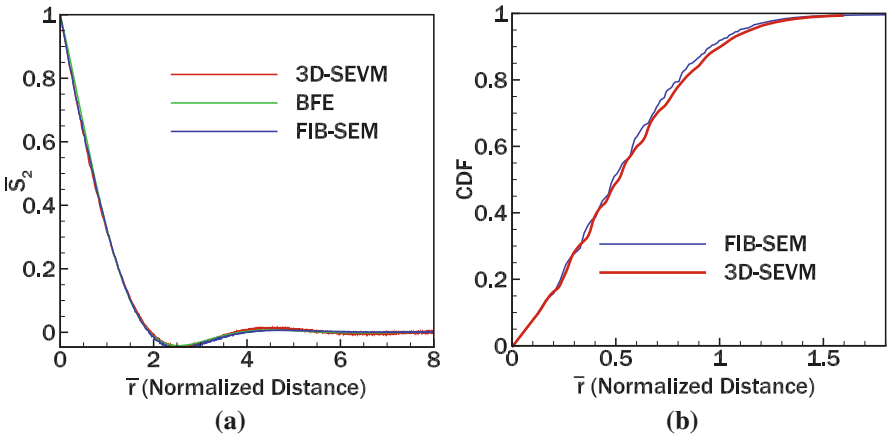

Fig. 6 (**a**) $\bar{S}_2(r)$ of the experimental microstructure, its best fit equation and the median of 30 SEVM instantiations ($N_p = 200$) and (**b**) CDF of the distance to surface distribution for ensemble median of 30 SEVM instantiations and experimental data. (Reprinted from: Pinz et al. [30], with permission from Elsevier)

Additionally, the statistics of the distance to surface distribution is tested against experimental values. This metric is not used in the SEVM generation process. The distance to surface measure corresponds to the distribution of distances from γ voxels to the nearest γ' voxel. The cumulative ensemble distribution of the distance to surface distribution for 30 instantiations of SEVMs with $N_p = 200$ is compared with the experimental FIB-SEM distribution in Fig. 6b. The error in distributions may be estimated by a Kolmogorov-Smirnov (KS) test [52], in which the test statistic is the maximum difference between two cumulative distribution functions. A KS test statistic shows a value of 0.038 between the two distributions in Fig. 6b, demonstrating effective convergence.

2.4 Determining the M-SERVE from Statistical Convergence

The microstructure-based SERVE or M-SERVE is defined in the introduction as a statistically equivalent RVE for which morphological, spatial, and crystallographic characteristics of the microstructure are the sole determinants of the representative volume. Representing the morphological and spatial statistics of a microstructure in a smaller representative volume requires establishment of sufficiency of the volume for equivalence of a variety of statistical distributions. The M-SERVE represents this minimum volume for statistical fidelity of one or more microstructural descriptors. In this context, distributions for shape, size, orientation of precipitates, and grains are referred to as *morphological distributions*, while those for relative positions of material features are referred to as *spatial distributions*. The convergence of

morphological parameters of the GSE is determined by a sampling error associated with finite number of sampling from a distribution, whereas the convergence of spatial microstructural statistics is calculated by generating 30 instantiations of SEVMs with $N_p = 10,\ 50, 100$, and 200 precipitates and subsequently comparing their spatial distribution with those from experimental data.

2.4.1 Convergence of Morphological Distributions

Within the SEVM generation procedure framework, a small sample size may incur large discrepancies between the sampled dataset and representative distributions. This sampling error is reliably determined with respect to N_p by the KS test statistic D_n, defined as the maximum absolute difference between two cumulative distribution functions. By specifying the number of samples N_p and the frequency f_b of observing a D_n or greater, the number of required samples N_p is solved for as:

$$f_b = \frac{\sqrt{2\pi}}{\sqrt{N_p} D_n} \sum_{k=1}^{\infty} \exp\left(\frac{-(2k-1)^2 \pi^2}{8 N_p D_n^2} \right) \tag{13}$$

The cases of $f_b = 0.5, 0.95$ are displayed in Fig. 7a. At $Np \approx 50$, 95% of all sampled datasets have a KS statistic of less than 0.2, corresponding to the minimum acceptable M-SERVE population for morphological distributions.

2.4.2 Convergence of Spatial Distributions

While morphological distributions can all be characterized similarly with the KS test, the spatial distributions are unique, and each test may require a different error metric. Therefore, each test is analyzed independently, and the largest required minimum size is taken to be the M-SERVE for all spatial metrics. Where applicable, a 2% error threshold is applied, and the resultant number of precipitates required for that threshold are given.

For non-ellipsoidal precipitates the local volume fraction is calculated by assigning γ matrix voxels to the nearest γ' precipitate and then by dividing the number of γ' precipitate voxels by the total number of voxels assigned to that precipitate. This method generates N_p data-points per microstructure, which gives rise to large variability across microstructural instantiations of the same statistics. The ensemble statistics of its distribution is employed to estimate convergence. The ensemble distribution of the local volume fraction is computed for the same 30 instantiations of SEVMs for $N_p = 10,\ 20,\ 50,\ 100, 200$. Their cumulative distribution functions are shown in Fig. 7d. The KS test values, computed between distribution for $N_p = 200$ and those for $N_p = 10,\ 20,\ 50,\ 100$, are, respectively, 0.0743, 0.0493, 0.0224, 0.0213. For 2% error, the local volume fraction measure requires $N_p > 100$ to converge.

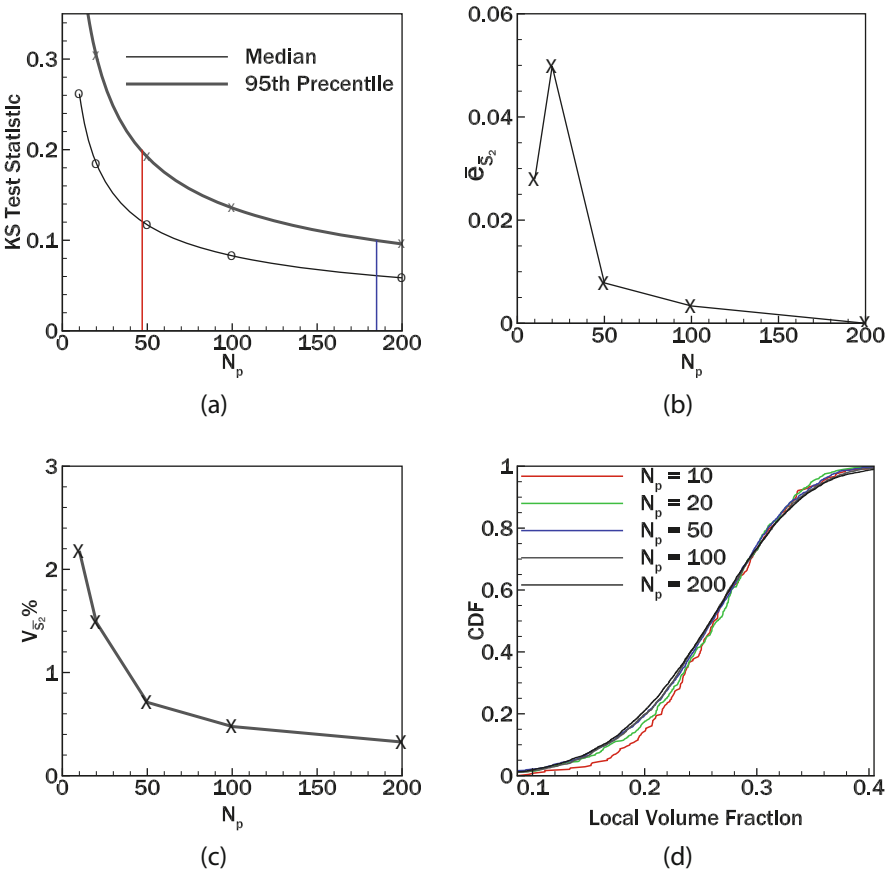

Fig. 7 (**a**) 50th and 95th percentile expected KS test statistic for various N_p (red and blue lines indicate the number of samples required to achieve a 95% probability of observing a KS test statistic of less than 0.2 and 0.1, respectively); (**b**) ensemble error metric between SEVMs with $N_p = 200$ and those with $N_p = 10, 20, 50, 100, 200$ respectively; (**c**) variability related to the differences in S_2; and (**d**) ensemble CDFs of the local volume fraction for SEVMs with $N_p = 10, 20, 50, 100, 200$. (Reprinted from: Pinz et al. [30], with permission from Elsevier)

2.5 Determining the Property-Based Statistically Equivalent RVE (P-SERVE)

The mechanical response of Ni-based superalloys is highly dependent on the subgrain-scale intragranular $\gamma - \gamma'$ microstructure. Microstructural simulations for evolving variables and overall response fields must incorporate large-enough computational RVEs to account for variabilities in evolving fields caused by spatial and morphological heterogeneities. The property-based statistically equivalent representative volume element (P-SERVE) corresponds to the minimum simulation

volume needed for convergence of mechanical properties and response functions to within a prescribed level of accuracy. Such properties may be classified into a spatially averaged and a local category. Spatially averaged properties are mean-field values over the entire SERVE, such as overall yield strength or hardening rate. Local properties on the other hand are described in terms of the spatial distribution or the extreme values of a response variable. Both classes are important when performing a P-SERVE analysis. In this study, the P-SERVE is determined from convergence of evolving fields and properties in the microstructure that are evaluated from dislocation density-based crystal plasticity finite element (DD-CPFE) simulations. While methods like discrete dislocation dynamics may be more appropriate at the *nm* scales of γ channels, their current capabilities are not yet adequate for simulating the large heterogeneous domains required for this problem.

A sequence of steps is executed to generate microstructure realizations and perform dislocation density-based crystal plasticity finite element (CPFE) simulations. The steps are summarized below.

- *Microstructure Generation:* The SEVMs and M-SERVEs of the $\gamma - \gamma'$ microstructure are generated.
- *Precipitate Smoothing and Meshing:* The voxelized precipitates are smoothed using the Simmetrix code [53] to remove spurious artifacts. The cubic SERVE is then meshed with four-noded tetrahedral (TET4) elements, capturing the precipitate geometries.
- *Pre-processing:* FE input files are generated for the microstructure and loading conditions.
- *FE Simulation:* Dislocation density-based crystal plasticity FE simulations with locking-free TET4 elements are performed for multiple SEVMs.
- *Output Extraction:* The averaged and local fields are extracted from the CPFE simulation results for use in analyzing properties.

2.5.1 Crystal Plasticity Models for Ni-Based Superalloys

Finite element simulations of the SEVMs for determining the P-SERVE are conducted with a dislocation density-based crystal plasticity constitutive law, developed for intragranular $\gamma - \gamma'$ microstructures of Ni-based superalloys in [19, 23]. A brief summary of these constitutive equations is provided here. Plastic slip on each slip system α is governed by a flow rule derived from the Orowan equation for thermally activated flow, given as:

$$\dot{\gamma}^{\alpha} = \rho_M^{\alpha} b \lambda \nu \exp\left(-\frac{Q}{k_B T}\right) \sinh\left(\frac{|\tau^{\alpha}| - \tau_{\text{pass}}^{\alpha}}{\tau_{\text{cut}}^{\alpha}}\right) \text{sign}\,(\tau^{\alpha}) \tag{14}$$

where ρ_M^{α} is the mobile dislocation density, b is the Burgers vector, λ is the jump width, ν is the jump frequency, Q is the activation energy for slip, T is the temperature, τ^{α} is the resolved shear stress, $\tau_{\text{pass}}^{\alpha}$ is the passing stress, and $\tau_{\text{cut}}^{\alpha}$

is the cutting stress. The passing and cutting stresses are explicit functions of the dislocation density, whose evolution is governed by the time-rate of dislocation density evolution due to mechanisms like multiplication, locking, and annihilation. In addition to statistically stored dislocations, geometrically necessary dislocations are considered for local closure of the Burgers circuit, derived from the time rate of the Nye tensor. The critical resolved shear stress of the γ' precipitate phase for octahedral slip systems is given as [23]:

$$\tau_c^\alpha = \tau_c^\alpha(\tau_{pe}^\alpha, \tau_{se}^\alpha, \tau_{cb}^\alpha, T, \Gamma_{111}, \Gamma_{100}) \tag{15}$$

where Γ_{111} is the antiphase boundary or APB energy on the octahedral plane, Γ_{100} is the APB energy on the cube plane, and τ_{pe}^α, τ_{se}^α, and τ_{cb}^α are the resolved shear stresses for partial dislocations on the primary, secondary, and cube planes, respectively. This resistance stress for the precipitates accounts for APB shearing and Kear-Wilsdorf locks and manifests non-Schmid effects, tension-compression asymmetry, and anomalous yield strength.

2.5.2 CPFE Simulations for Analyzing Response Variables

The automated computational sequence probes a large number of statistically equivalent virtual $\gamma - \gamma'$ microstructures generated from the experimental dataset. Mechanical response of various intragranular microstructures is analyzed with increasing volume, measured in terms of number of precipitates considered. As with the M-SERVE determinations, 20–25 instantiations of SEVMs are simulated, each with $N_p = 10, 20, 50, 100, 200$ precipitates, respectively. The CPFE simulations are all performed under a constant strain-rate loading of 10^{-4}s^{-1} in the [001] direction at a temperature of 300K, until 10% total strain is attained. These simulations permit the quantification of the diminishing effect of microstructural variations on mechanical properties with increasing material volume.

A number of spatially averaged and local response variables are identified for extraction from the results of CPFE simulations. The spatially averaged quantities are (i) the initial yield strength σ_Y defined as the 0.2% offset yield stress of the overall stress-strain curve and (ii) the hardening rate H that corresponds to the average slope from σ_Y to the stress at 10% strain (relatively constant over this range). The local field variable considered is the equivalent plastic strain ϵ^p at every quadrature point of the FE mesh. This field variable is compared to its bulk mean value through an error metric defined as:

$$e_P = \left| \frac{P - \mu_P}{\mu_P} \right|, \quad P \in \{\sigma_Y, H, \rho, \tau_{1\%}\} \tag{16}$$

where μ_P is the limiting mean of a given property P as the size of the SEVM approaches the bulk behavior. In this study, this value is approximated by calculating the ensemble mean of 200 precipitates.

2.5.3 Spatially Averaged Mechanical Fields

Both the initial yield strength σ_Y and the hardening rate H are computed from the mean stress and strain fields for each microstructural instantiations with different N_p values. Figure 8 demonstrates the convergence of the spatially averaged responses, along with the decaying effect of microstructural variation with increasing size. Even with relatively low number of precipitates, the yield strength varies within only 2.5% of the average. This result implies that the higher moments of precipitate morphology and spatial distribution do not play significant roles for the yield strength. Lower moments like the averaged volume fraction or shape characteristics are sufficient to quantify this property. Analogous effects are also seen for the hardening rate. Bounds on the variation vary from 8% to 2% with increase in N_p

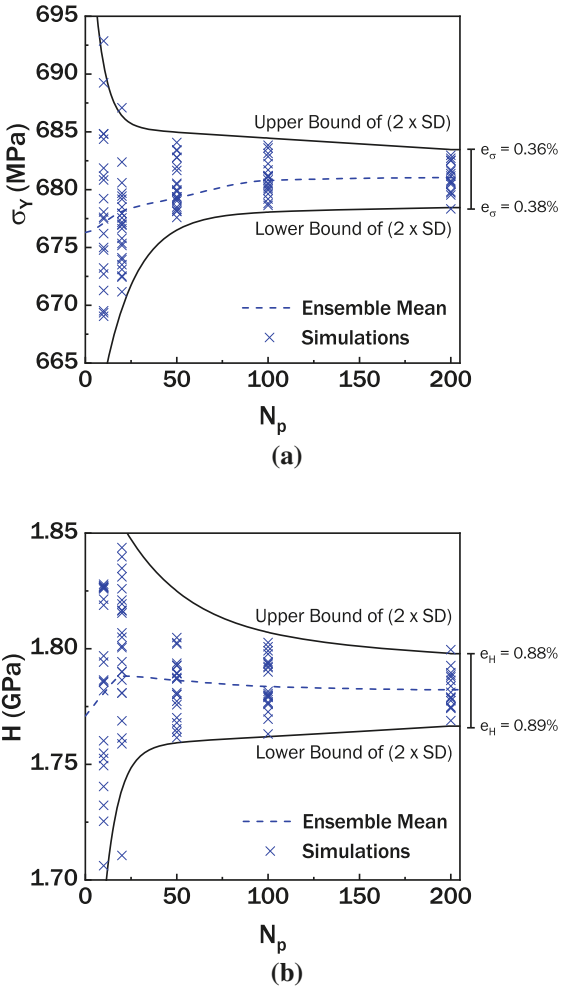

Fig. 8 Convergence of (**a**) the yield strength and (**b**) the hardening rate with increasing N_p. The upper and lower bounding lines represent two standard deviation bounds from the mean for each ensemble, and the scattered markers depict individual simulations. The final bounds on the relative error at 200 precipitates are shown for each case. (Reprinted from: Pinz et al. [30], with permission from Elsevier)

from 10 to 50. As with the yield strength, the hardening rate also converges quickly with microstructural volume. For both these properties, the P-SERVE is estimated at $N_p = 10$–20, where the bounding curves fall below 5% relative error.

2.5.4 Local Response Field Variables

Mechanical response fields, obtained from intragranular crystal plasticity simulations, exhibit significant variations in the microstructure consisting of precipitates and matrix channels. The gradients and extreme values of these fields are often used as indicators of critical events such as fracture. P-SERVEs that represent the computational domain for analyses must be sufficient to depict these local features and gradients. The spatial distribution of three evolving state variables, viz., the equivalent plastic strain, dislocation density, and stress measures like the von Mises stress, are studied here for their influence on the estimation of P-SERVEs.

The equivalent plastic strain $\epsilon^p := \sqrt{\frac{2}{3}\mathbf{E}^p : \mathbf{E}^p}$, where $\mathbf{E}^p := \mathbf{F}^{p\mathrm{T}}\mathbf{F}^p - \mathbf{I}$ and $\mathbf{F}^p$ is the plastic deformation gradient, yields a scalar measure of plasticity experienced at a local site. The probability distribution of the plastic strain field is plotted over the spatial domain in Fig. 9 for N_p varying from 10 to 200 precipitates.

This spatial distribution shows significant variation for different microstructure realizations when the simulation volume is small and is highly dependent on the precipitate configuration. The variance in the tails of the distributions is driven by the largest channel width, accounting for the passage of dislocations through the domain with weak obstacle interactions. A prolonged and heavy distribution tail indicates a relatively large set of regions undergoing large and localized plastic deformation. The spatial distribution of plastic strains converges to approximately a log-normal distribution, with decay in the variance of extreme values. Convergence

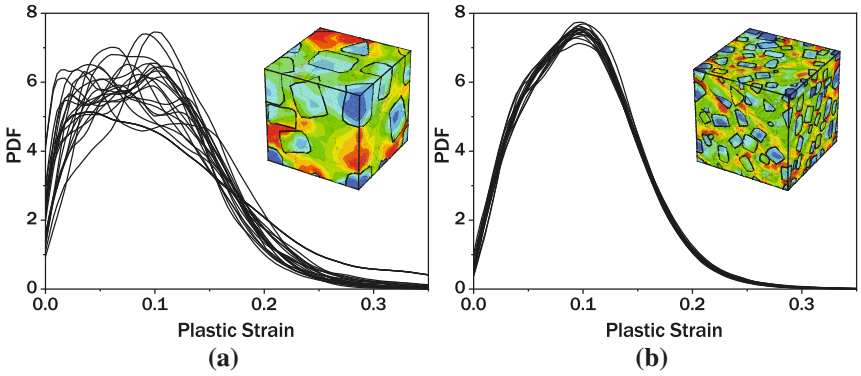

Fig. 9 Convergence of the spatial distribution of the plastic strain field ϵ^p with (**a**) 10 and (**b**) 200 precipitates. The corresponding contour plots are shown in the inset, with plastic strain ranging from 0 to 0.2. (Reprinted from: Pinz et al. [30], with permission from Elsevier)

with a relative error of 5% in the second moment of the distribution corresponds to a P-SERVE of approximately 100–200 precipitates. This is much larger than that for the yield strength and hardening rate, due to the requirements of convergence of higher order moments of the distribution.

2.6 Summary of the Subgrain-Scale Analysis

This section develops the microstructure and property-based SERVEs, viz., M-SERVE and P-SERVE for intragranular microstructures of Ni-based superalloys, characterized by γ-γ' phase distribution. Steps to the development of the M-SERVE and P-SERVE include the development of statistically equivalent virtual microstructures or SEVMs, for which statistical distribution functions are equivalent to those from experimental data. The main difference between the M-SERVE and the SEVMs is that the M-SERVE is the optimal domain with respect to a chosen microstructural feature.

An important outcome of parametric representation of the morphology, e.g., in Eq. (4), is the capability of explicit representation of these parameters in parametrically homogenized constitutive models [20]. These constitutive models can relate the sensitivity of various response fields to these morphological parameters and hence facilitate material design. P-SERVEs are established with respect to a few global and local material properties from evolving variables in dislocation density-based crystal plasticity FE (DD-CPFE) simulations. It is observed that the convergence with respect to the global properties occurs in the vicinity of $\approx$10–20 precipitates for relative error bounds of 5%. When local variables are considered, a higher number of precipitates with $N_p \approx$ 100–200 becomes necessary for convergence. Spatially averaged quantities converge quicker than the local distributions, independent of whether the quantity is microstructure or property-based. The convergence characteristics of the M-SERVE and P-SERVE can generally be used to delineate the relation between morphological characteristics and certain response functions in the microstructure.

3 M-SERVE and P-SERVE for Polycrystalline Microstructures of Ni-Based Superalloys

This section establishes M-SERVEs and P-SERVEs for the scale corresponding to polycrystalline microstructures of Ni-based superalloys, as shown in Fig. 10. This scale is characterized by an ensemble of grains containing annealing twins that are generated as a consequence of the thermomechanical process. An algorithmic development is pursued to generate 3D statistically equivalent virtual polycrystalline microstructures (3D-SEVMs) from experimental observations by employing sta-

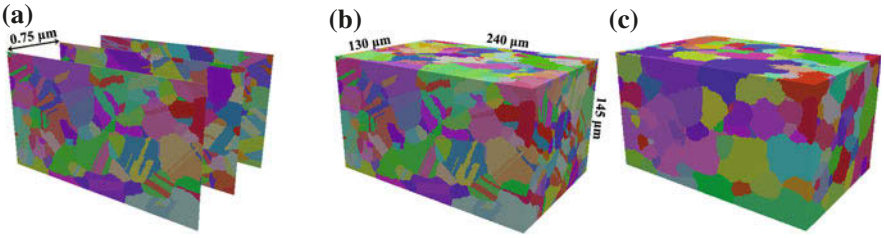

Fig. 10 (**a**) Serial sectioned EBSD images, (**b**) computer assembled sections of EBSD images manifesting polycrystalline microstructure including twins, and (**c**) polycrystalline microstructure of parent grains only after removing twins, for the Ni-based superalloy Ren*é*88-DT. (Reprinted from: Bagri [29], with permission from Springer)

tistical methods, probability distribution functions of parent grains, as well as the correlation of twins and parent grains in EBSD microstructure. The M-SERVE and P-SERVE are consequently established from convergence studies of microstructural statistics and crystal plasticity finite element simulation-based response functions. Details of the methods are available in [29].

3.1 Image Extraction from Electron Backscattered Diffraction Maps

Electron backscattered diffraction or (EBSD) images are used to extract statistical crystallographic and morphological information of the microstructure. The EBSD dataset, described in [46], is collected over a large volume to characterize the structure of twin-related domains. A $10 \times 5 \times 1$ mm sample is sectioned from a forging of the superalloy Ren*é*-88 DT using wire electrical discharge machining (EDM). The sectioning facilitates data collection over a number of parallel sections as shown in Fig. 10a. A series of 600 μm wide pedestals are fabricated with the wire EDM and then mechanically polished to 600 μm thickness, creating a series of 600×600 μm pedestals. The EBSD images are collected from a 240×145 μm area using a 25 kV electron beam and 8×8 camera binning with a 300 nm step size. A total volume of $240 \times 145 \times 130$ μm is collected from 199 ablated slices.

A 3D microstructure is assembled by stacking the EBSD images from all the slices, as shown in Fig. 10b. The grains are segmented with a 2° tolerance. Those smaller than 75 voxels are removed and followed by isotropic neighbor dilation. Twin-related domains are grouped with a 5° tolerance on both the disorientation axis and the disorientation angle. Slices are aligned using the twin domain centroids. The aligned dataset is next re-segmented with a 5° disorientation tolerance, and grains smaller than 75 voxels are removed with isotropic neighbor dilation. Finally twin-related domains are grouped with a 5° tolerance on both the disorientation axis and angle. The resulting stacked and assembled 3D polycrystalline microstructure

containing annealing twins is shown in Fig. 10b. The ensemble contains 440 $\Sigma 3$ type twins in 300 parent grains for a total of 740 twins and grains. The 3D assembly and microstructure reconstruction is performed in the DREAM.3D software [33] in four sequential steps, viz., (i) slice registration and alignment; (ii) voxel level cleanup; (iii) feature segmentation; and (iv) artifact removal. Corresponding to the angular resolution of orientation measures in the EBSD scans, the segmentation tolerance in the DREAM.3D code is chosen to be 1°–5°. Noisy voxels are identified by thresholding misorientations with neighboring voxels and assigning thresholds on the minimum acceptable grain size. If these criteria are not met, morphological dilation of the voxels or small grains into surrounding grains is conducted.

3.2 Statistically Equivalent Virtual Microstructure (SEVM) Generation from Characterization and Statistical Analysis

The EBSD data in Fig. 10a and the assembled 3D microstructure in Fig. 10b show that the Ren*é*88-DT polycrystalline microstructure contains an abundance of large aspect ratio, annealing $\Sigma 3$ twins that develop during material processing. These twins have a 60° misorientation angle with respect to the $< 111 >$ crystal lattice axis, whereas most of the parent grain boundaries are randomly oriented. Microstructure characterization further reveals that the majority of annealing twin boundaries are coherent with boundaries formed along planes with $\{111\}$ Miller-index facet.

The generation of polycrystalline SEVMs proceeds in two stages. Statistics of the parent grain without twins, that have random grain boundary orientations, are first generated. This is followed by the incorporation of twins in the parent grains. The following steps are executed in sequence to generate statistically equivalent volumes of twinned polycrystalline microstructures.

1. Process the EBSD section data and construct the digitally assembled polycrystalline ensemble including twins;
2. Identify and remove twins from the digitally assembled microstructure to manifest the parent grains, shown in Fig. 10c;
3. Extract the statistics of parent grains from the EBSD data;
4. Create statistically equivalent virtual parent grain microstructures from the 3D EBSD data;
5. Extract correlation statistics of twins with respect to parent grains from the EBSD data in the digitally assembled microstructure;
6. Insert twins in the parent polycrystalline microstructure to match the statistical correlations.

The DREAM.3D software [33] is employed in steps 1–4 to create the digital polycrystalline ensembles from EBSD data in Fig. 10b, remove twins in Fig. 10c and subsequently extract statistics of the parent grains. The statistics of characteristic features in the twin-free parent grains in Fig. 10c, including probability distributions

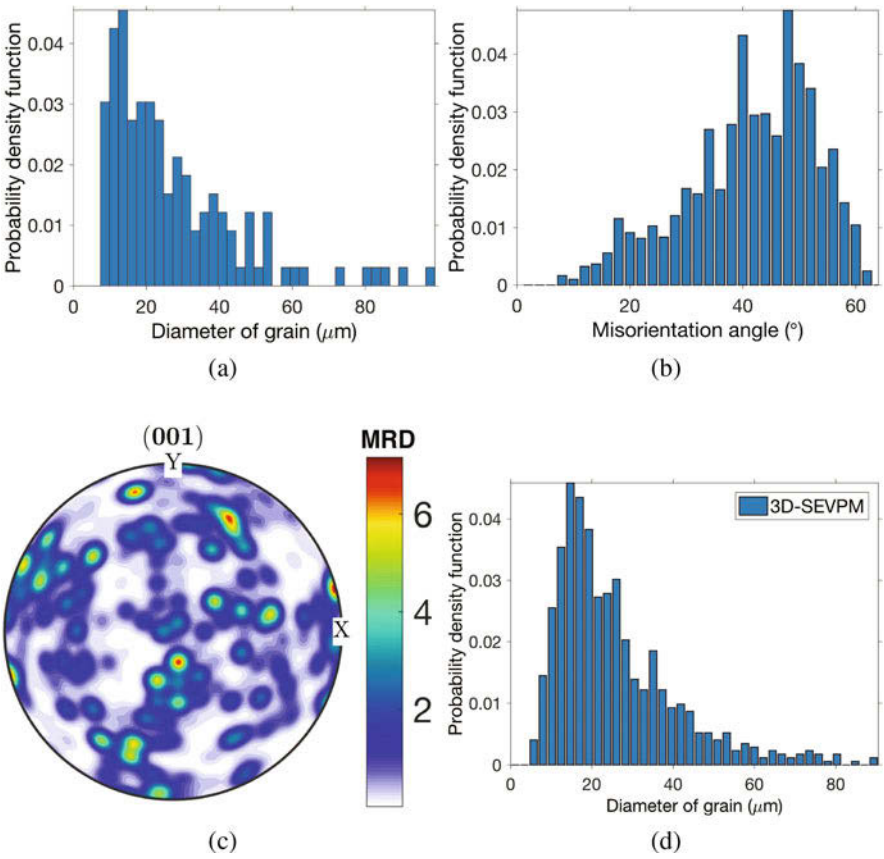

Fig. 11 Statistics of the parent grain microstructure after removing twins: (**a**) grain size distribution, (**b**) misorientation angle distribution, (**c**) orientation distribution of grains along [001] sample axis shown through the pole figure, and (**d**) histogram of parent grain size in a *3D-SEVM* of size $250 \times 250 \times 250\,\mu m$ that is created by DREAM.3D. (Reprinted from: Bagri [29], with permission from Springer)

of grain size, orientation, and misorientation angle, are acquired in this step. The corresponding probability density distributions of grain size, misorientation angle, and orientation (pole figure) are shown in Fig. 11. These distributions are fundamental to the creation of the statistically equivalent virtual parent grain microstructures. A virtual simulated parent grain microstructure is subsequently created from this 3D data [35]. Figure 11d shows a parent grain size histogram in a 3D-SEVM of size $250 \times 250 \times 250\,\mu m$ with a maximum grain size of approximately $90\,\mu m$.

Sample statistics are extracted from the EBSD data to generate probability distribution and correlation functions of twins with respect to parent grains in step 5. These are used to insert twins in the virtual parent microstructure as described

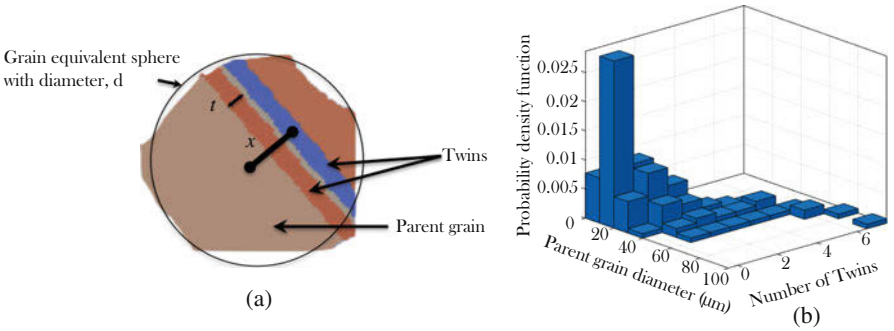

Fig. 12 (**a**) Schematic of the correlation between twins and parent grain; the parent grain has equivalent diameter d and contains twins with thickness of t, located at a distance x from the parent grain centroid, and (**b**) joint probability distribution of the parent grain size (μm) and number of twins. (Reprinted from: Bagri [29], with permission from Springer)

in [29]. A schematic representing the relation of a twin with the parent grain is shown in Fig. 12a. There is a wide range of variation in the size and crystallographic orientations of the twinned grains, as well as the number of twins per grain and their thickness. Statistical analysis identifies four variables are needed to characterize the distributions of twins within grains, viz., the parent grain effective diameter d, the number of twins in parent grain n, the minimum distance x of the twin from the parent grain centroid, and the twin thickness t. A four dimensional joint probability distribution $P_0(x, t, n, d)$ is employed to describe the probability of observing a twin, given these four parameters. Due to the dependency between these twin descriptor variables, this joint probability distribution cannot be easily approximated by sampling from four independent marginal distributions, and therefore, the full joint distribution must be used to capture the appropriate intercorrelations.

A novel algorithm is developed in [29] for inserting twins in parent grain microstructure following the joint and conditional probability distribution functions derived from the 3D EBSD assembly maps. The joint probability distribution of parent grain size and number of twins and the conditional probability distributions of both twin distance from parent centroid and twin thickness are expressed as:

$$P_1(d, n) = \int \int P_0(d, n, t, x)\, dt\, dx \quad \text{joint PD} \tag{17}$$

$$P_2(x|d = D, n = N) \text{ and } P_3(t|d = D, n = N) \quad \text{conditional PD} \tag{18}$$

where PD refers to the probability distribution.

The process first samples the joint probability distribution space for the number of twins and the conditional probability distribution space for the twin thickness and twin distance using statistics from the EBSD data. The four dimensional probability distribution $P_0(d, n, t, x)$ necessitates a large dataset to be constructed. Alternatively, a marginal probability function may be used when a smaller set of

statistical information is available. The marginal probability function corresponds to a joint probability function of the parent grain size and the number of twins and the conditional probability distributions of the twin distance and the twin thickness, respectively. In this step the joint probability distribution in Fig. 12b is used for parent grain and number of twins per parent, while the conditional probability distributions are employed for the twin distance from the parent centroid and twin thickness, respectively. In [29] it is demonstrated that for a given d and n, t is uncorrelated with x and is assumed independent. The four dimensional distribution space may then be approximated as:

$$P_0(d, n, t, x) \approx P_1(d, n)\, P_2(x|d = D, n = N)\, P_3(t|d = D, n = N) \tag{19}$$

where D and N correspond to maximum sample sizes for grain size and number of twins, respectively.

For generating twin descriptors in step 6, the probability distributions P_1, P_2, P_3 are sampled, and a twin is inserted into the parent grain SEVM with selected characteristics described in [29]. The steps in this algorithm are as follows:

1. With an acceptance-rejection algorithm [54], sample the joint probability distribution for the number of twins and grain diameter and the conditional probability distributions for the twin thickness and twin distance, using the statistics obtained from the EBSD data.
2. Upon determination of n, d, t and x, the plane represented by the Miller index (111) at a distance x from the parent centroid is located.
3. The voxels that belong to selected parent grain and are within a distance $\frac{t}{2}$ from the mid-thickness (111) plane are identified via a search algorithm.
4. The rotation matrix of the twin in the specimen frame $\mathbf{R}$ is obtained from the rotation matrix of the parent grain $\mathbf{R}_{\text{parent}}$ and the rotation matrix of the twin with respect to the parent grain $\mathbf{R}_{\text{twin}}$ as:

$$\mathbf{R} = \mathbf{R}_{\text{parent}}\mathbf{R}_{\text{twin}} \tag{20}$$

5. The Bunge Euler angles of voxels that belong to the twins are determined by the components of $\mathbf{R}$.
6. By repeating the above steps, a set of twins is inserted in the parent grain microstructure. Finally, the statistically equivalent virtual microstructure is reconstructed using the new set of voxel Euler angles.

This virtual microstructure generation procedure becomes the basis for the construction of the polycrystalline M-SERVE.

3.2.1 Validation of the SEVM Generation Method

The statistically equivalent virtual microstructure generation algorithm is implemented in a computer code that interfaces with the DREAM.3D software. The model and algorithms are validated using the EBSD data of the Ni-based superalloy

specimen, discussed in Sect. 3.2. 3D statistically equivalent virtual polycrystalline microstructures (3D-SEVM) of various sizes are created using the method. The DREAM.3D generated parent grain microstructure in a $250 \times 250 \times 250\,\mu m$ domain, containing 760 grains is depicted in Fig. 13a. The resulting virtual microstructural domain of size $250 \times 250 \times 250\,\mu m$ consisting of a total of 1700 parent grains and twins is shown in Fig. 13b. The statistical data presented in Figs. 14, 15 and 16 are extracted from this 3D-SEVM.

A few probability distributions are selected to compare the statistics of the 3D-SEVM with the assembled EBSD image data,. The distribution of misorientation angle in the parent grain microstructure only and the grain microstructure with

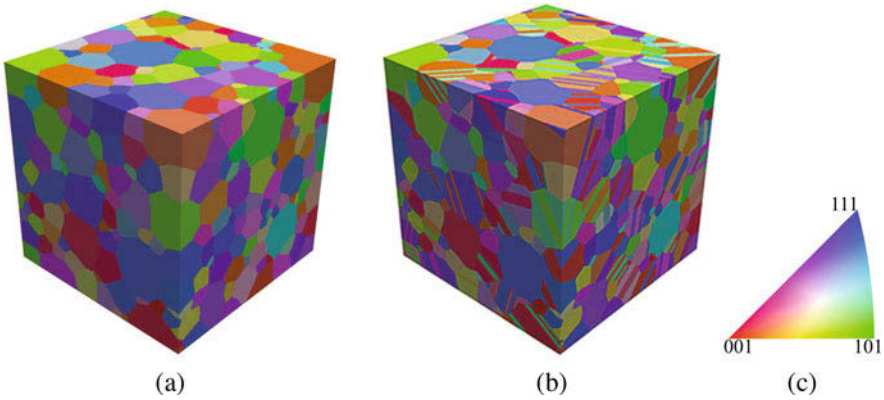

Fig. 13 Simulated 3D statistically equivalent virtual polycrystalline microstructure (3D-SEVM) of a Ni-based superalloy: (**a**) parent grains created by the DREAM.3D software, (**b**) grains with statistically equivalent twins inserted in the parent grains, and (**c**) inverse pole figure (IPF) color scheme for the FCC standard triangle. (Reprinted from: Bagri [29], with permission from Springer)

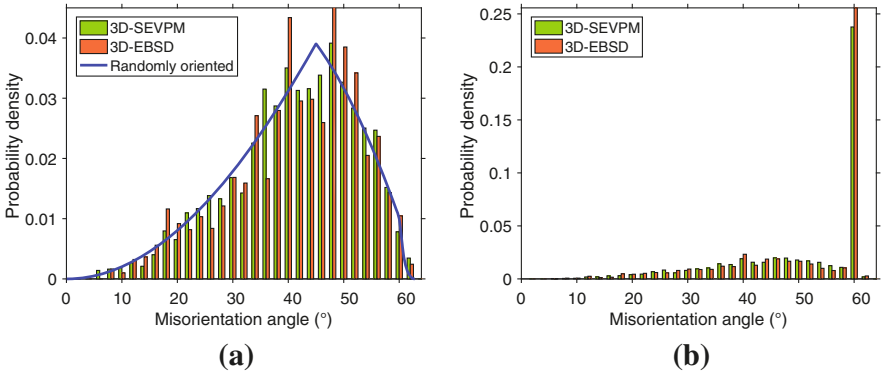

Fig. 14 Probability distribution of (**a**) misorientation angle in parent grain microstructure, (**b**) misorientation angle in microstructure with twins. The 3D-SEVM size is $250 \times 250 \times 250\,\mu m$. (Reprinted from: Bagri [29], with permission from Springer)

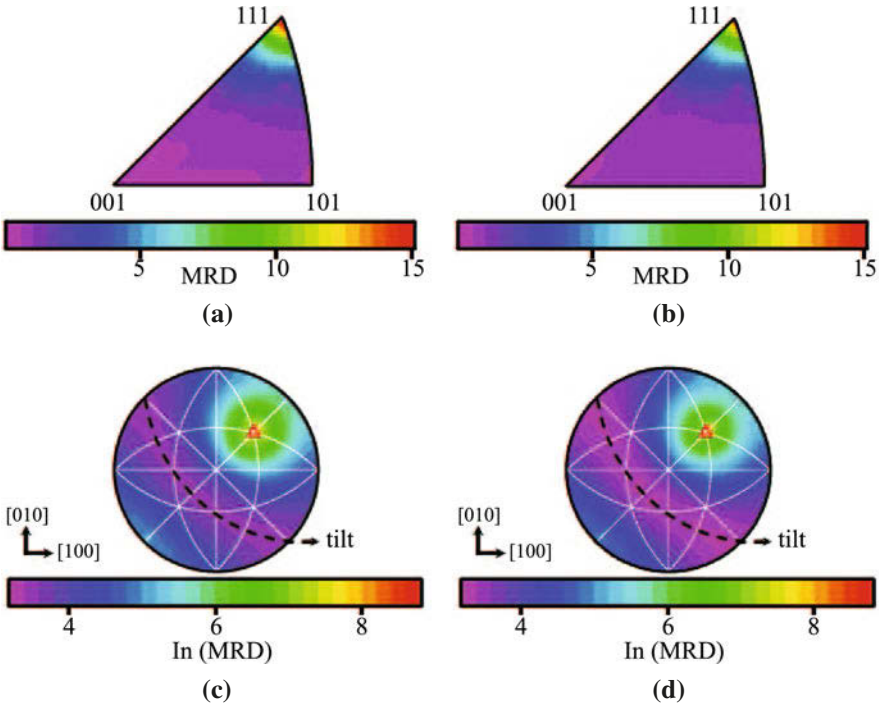

Fig. 15 Misorientation axes for all grain boundaries with misorientation angle of 60° in: (**a**) EBSD images and (**b**) 3D-SEVM of size 250 × 250 × 250 μm; and grain boundary plane normals for Σ3 GBs from the (**c**) EBSD and (**d**) 3D-SEVM. The populations in (**a**, **b**) are represented as multiples of a random distribution (MRD), while they are shown as the natural logarithm of multiples of a random in (**c**, **d**) for clarity. The positions of tilt boundaries in (**c**, **d**) are shown by dashed dark lines and labeled with a "tilt" and the (111) pole is marked by a red triangle. The data are plotted in stereographic projections along [001] axis. (Reprinted from: Bagri [29], with permission from Springer)

twins are compared with the assembled 3D-EBSD data in Fig. 14. For comparison, the Fig. 14a without twins also includes the misorientation angle distribution of a randomly textured cubic material from [55]. A reasonably good agreement is observed between the misorientation distributions of the virtual parent grain microstructure and the 3D EBSD image. For grains with twins in Fig. 14b, the misorientation angle distributions depicts a prominent peak at 60° that reflects the twin orientation. To investigate further the origin of this peak, the inverse pole figure of the stereographic projection of the misorientation axis distribution is plotted for the twin boundaries with the misorientation angles of 60° in Fig. 15a, b. A clear peak exists at the [111] axis for grain boundaries with misorientation angle of 60°. This is an indication of presence of Σ3 twin boundaries in both the 3D-SEVM and 3D EBSD image, not easily reproduced by codes like DREAM.3D. Finally, the distribution of grain boundary plane normals for the Σ3 boundaries on

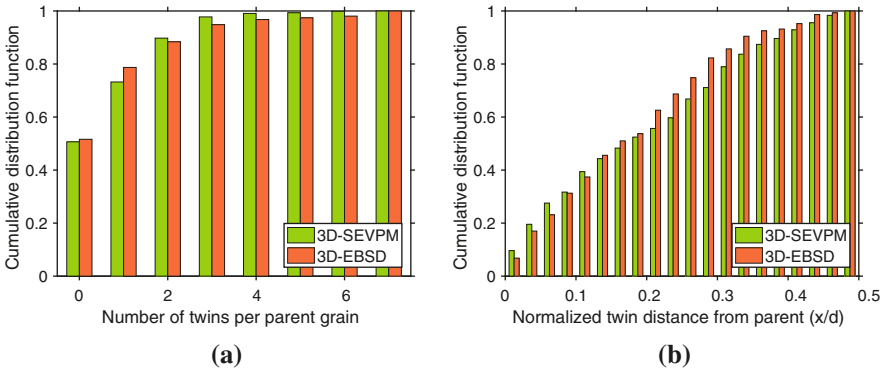

Fig. 16 Comparison of the cumulative distribution function (CDF) of (**a**) number of twins per parent grain n and (**b**) twin distance d from parent centroid in the 3D-SEVM and assembled EBSD with a size of 250 μm. (Reprinted from: Bagri [29], with permission from Springer)

a stereographic projection along the [001] axis are shown in Fig. 15c, d. For clarity, the natural logarithm of the frequency of occurrence is plotted in these figures. The peaks of the distributions in Fig. 15c, d, which appear in small regions of the plotted areas, occur at (111). The strong peak at twist boundaries (111) indicates that the majority of Σ3 boundaries are coherent twins. The population of grain boundaries in Fig. 15 are measured in units of multiples of a random distribution (MRD). Values greater than 1 indicate grain boundaries observed more frequently than those expected in a polycrystalline material with randomly oriented grains [38].

The results can be further validated by comparing the overall distributions in the 3D-SEVM and assembled EBSD data. The cumulative distribution functions (CDFs) of number of twins per parent grain and twin distance from parent centroid are depicted in Fig. 16. Figure 16a implies that about 50% of the parent grains remain untwinned in both the 3D-SEVM and assembled EBSD. With the exception of the twin thickness at higher values, the CDFs are in general very good agreement. The comparison plots of probability distributions in Figs. 14, 15, and 16 validate the virtual generation method for polycrystalline microstructures containing twins.

3.3 Estimating M-SERVEs for Polycrystalline Microstructure with Twins

To estimate the optimal size of a microstructure-based SERVE or M-SERVE that can capture the statistics of the EBSD image data, the CDFs are compared through the Kolmogorov-Smirnov (KS) test [52]. The KS test quantifies the maximum absolute difference in the CDFs for the simulated and experimental volumes. It is a useful tool for seeking the convergence of statistical distributions as a function of the M-SERVE size. The CDFs of n and d are compared in Fig. 16.

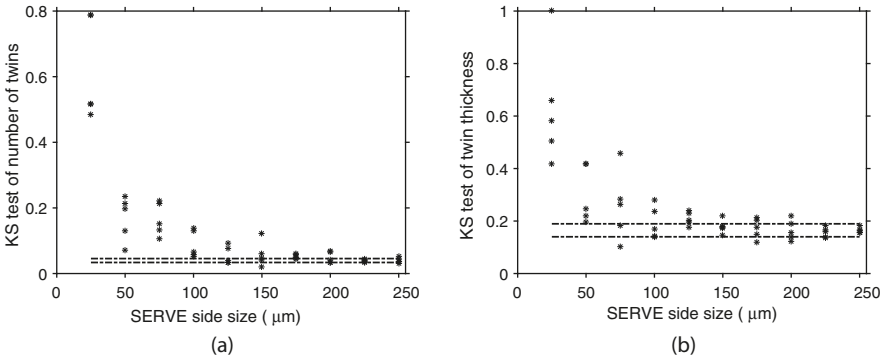

Fig. 17 Results of the Kolmogorov-Smirnov (KS) test for convergence of the probability distributions of (**a**) number of twins n and (**b**) twin thickness t, as a function of the virtual microstructure size for determining the M-SERVE. The dashed lines show the upper and lower bounds of the student t-test. (Reprinted from: Bagri [29], with permission from Springer)

The maximum difference in the CDFs of the simulated and experimental volumes is expected to decrease with increasing the M-SERVE size, as shown in the KS test plots of Fig. 17. At least five different realizations of the virtual polycrystalline microstructure of varying sizes are created to assess the convergence of M-SERVE characteristics. The Student's t-test, where the statistic follows a Student's t-distribution under null hypothesis, is adopted. The convergence of the M-SERVE statistics is determined using a standard 95% confidence interval bound. This translates into having a population of samples at any given size, whose KS-test values are within $\mu \pm 0.1\mu$, where μ is the KS test mean value of a large sample. Using this criterion it is observed that all the CDF's of M-SERVEs converge in the range $150\,\mu\text{m} \rightarrow 250\,\mu\text{m}$. Beyond this range, the probability distributions of morphological and crystallographic parameters of the M-SERVE and EBSD image are in good agreement. It is inferred that the M-SERVE size of this Ni-based superalloy for the adopted characteristics is about $150\,\mu\text{m}$. This volume contains 160 parent grains with a total of 400 parent grains and twins. This is an effective procedure for generating the M-SERVE from 3D-SEVMs that can hence be used in analysis of the microstructure for various response functions.

3.4 Estimating the P-SERVE Through Convergence Studies

As for the subgrain microstructure, the optimal size of the P-SERVE is determined from the convergence of statistics of material properties and response functions. For polycrystalline Ni-based superalloys, crystal plasticity finite element modeling (CPFEM) is performed for estimating the P-SERVE. An activation energy-based crystal plasticity (AE-CP) model developed in [19, 20, 23] is adopted for simulating

the polycrystalline SERVEs. The parameters of the AE-CP constitutive model are calibrated from experimental data on polycrystalline superalloy Rene88-DT. Details of the constitutive model and crystal plasticity parameter calibration are given in [29].

The plastic slip-rate $\dot{\gamma}^\alpha$ in this model is governed by the Orowan's equation, reflecting a thermal activation relationship. For a given slip system,

$$\dot{\gamma}^\alpha = \begin{cases} 0 & \text{for } \tau^\alpha_{\text{eff}} \leq 0 \\ \dot{\gamma}^\alpha_0 \exp\left(-\frac{Q}{k_B T}\left[1 - \left(\frac{\tau^\alpha_{\text{eff}}}{s^\alpha_{*,\text{tot}}}\right)^{p_1}\right]^{p_2}\right) \text{sign}(\tau^\alpha) & \text{for } 0 < \tau^\alpha_{\text{eff}} \leq s^\alpha_{*,\text{tot}} \end{cases} \tag{21}$$

where $\dot{\gamma}^\alpha_0$ is the reference slip rate, Q is the activation energy, k_B is the Boltzmann constant, T is the temperature, and p_1 and p_2 are material constants. The effective shear stress in any slip system, $\tau^\alpha_{\text{eff}} = |\tau^\alpha| - s^\alpha_a$, is defined as the difference of resolved shear stress τ^α and the athermal obstacle resistance s^α_a due to parallel dislocations. The total thermal slip resistance is comprised of two parts, i.e. $s^\alpha_{*,\text{tot}} = s^\alpha_* + s^\alpha_{\text{cross}}$. The thermal slip resistance s^α_* provides an impeding effect of obstacles that can be overcome by thermally activated processes such as forest dislocations. The cross-slip resistance s^α_{cross} develops due to sessile dislocation segments creating pinning points by formation of Kear-Wilsdorf (KW) configurations. The initial values of athermal and thermal resistances, i.e. s^α_{a0} and s^α_{*0} due to the presence of statistically stored dislocations (SSDs) are determined through the experimental calibration process.

The time evolution of the athermal and thermal slip resistances is a function of the plastic slip-rate, in and out of the slip plane, corresponding to the effects of parallel and forest dislocations respectively. The slip resistances evolve as:

$$\dot{s}^\alpha_a = \sum_{\beta=1}^{N} h^{\alpha\beta}_a |\dot{\gamma}^\beta \sin(\mathbf{n}^\alpha, \mathbf{t}^\beta)| \quad \text{and} \quad \dot{s}^\alpha_* = \sum_{\beta=1}^{N} h^{\alpha\beta}_* |\dot{\gamma}^\beta \cos(\mathbf{n}^\alpha, \mathbf{t}^\beta)| \tag{22}$$

where N is the number of slip systems, $\mathbf{m}^\alpha$ is the slip direction, $\mathbf{n}^\alpha$ is the slip plane normal, $\mathbf{t}^\alpha = \mathbf{m}^\alpha \times \mathbf{n}^\alpha$ is the transverse direction. The interaction coefficients are taken to be the same for both the athermal and thermal resistances, i.e. $h^{\alpha\beta} = h^{\alpha\beta}_a = h^{\alpha\beta}_*$. The hardening coefficients for self and latent hardening are expressed as:

$$h^{\alpha\beta} = q^{\alpha\beta} h^\beta \,, \quad \text{where} \quad h^\beta = h_0 \left|1 - \frac{s^\beta}{s^\beta_{\text{sat}}}\right|^r \text{sign}\left(1 - \frac{s^\beta}{s^\beta_{\text{sat}}}\right) \tag{23}$$

where h_0 is a material constant, s^α is the shear resistance, s^α_{sat} is the saturation slip resistance, r is an exponent controlling the rate of saturation, and $q^{\alpha\beta} = q + (1 - q)\delta^{\alpha\beta}$ and $\delta^{\alpha\beta}$ is the Kronecker delta. Parameter $q = 1.4$ in this study. s^α_{cross} is another term contributing to the total thermal slip system resistance. This resistance is associated with the accumulation of pinned screw dislocations after cross slip. The evolution of the cross-slip resistance is computed for both the octahedral and cube slip systems as:

$$s^{\alpha}_{\text{cross}} = \begin{cases} s^{\alpha}_{\text{cross,oct}} = s^{\alpha}_{\text{cross,oct}}(\tau^{\alpha}_{pe}, \tau^{\alpha}_{se}, \tau^{\alpha}_{cb}, T, \Gamma_{111}, \Gamma_{100}) & \text{on octahedral slip systems} \\ s^{\alpha}_{\text{cross,cube}} = s^{\alpha}_{\text{cross,cube}}(T) & \text{on cube slip systems} \end{cases} \tag{24}$$

The cross-slip resistance on the octahedral planes accounts for the non-Schmid shear stresses and anisotropy in the antiphase boundary (APB) energy function and is expressed as:

$$s^{\alpha}_{\text{cross,oct}} = \xi_0 \exp\left(\frac{A}{T - T_c}\right) \mu \sqrt{\rho_0 \exp\left(-\frac{H^{\alpha}}{k_B T}\right)} \tag{25}$$

$$\text{where } H^{\alpha} = c_H \left\{ h + k_1 (t^{\alpha}_{\text{pe}} - k_2 t^{\alpha}_{\text{se}}) + \sqrt{\left(\frac{1}{\sqrt{3}} - \frac{\Gamma^{010}}{\Gamma^{111}} + |t^{\alpha}_{\text{cb}}|\right) \frac{b}{B}} \right\}$$

and ξ_0, A, h, k_1, k_2 are material constants, T_c is the critical temperature, H^{α} is the enthalpy for the cross slip event, and ρ_0 is the initial cross-slipped dislocation density. Furthermore,

$$t^{\alpha}_{xx} = \frac{\tau^{\alpha}_{xx}}{\Gamma^{111}/b}, \quad B = \frac{\mu b^2}{2\pi \Gamma^{111}}, \quad c_H = \frac{\mu b^3}{4\pi} \tag{26}$$

The cross-slip resistance in cube slip system is a function of temperature and is defined as:

$$s^{\alpha}_{\text{cross,cube}} = \begin{cases} s_{cc1} & \text{for } T \leq 915K \\ s_{cc1} - s_{cc2}(T - 915) & \text{for } T > 915K \end{cases} \tag{27}$$

where s_{cc1} and s_{cc2} are material properties. It should be noted that the cube slip systems are only activated when the temperature rises. Details of this model are given in [23].

3.4.1 P-SERVE Convergence Studies with the Crystal Plasticity Model

The size of the P-SERVE is estimated through convergence studies of material properties and response functions. CPFE simulations are conducted for a large number of simulated SERVEs of different sizes with variations in the microstructural statistics using the calibrated material parameters. For each size, at least five realizations are generated for simulations. For smaller sizes, where high scatter in material properties is expected, larger number of SERVEs are simulated. For example, up to 15 samples are simulated with a size of 25 μm.

Results of the CPFE simulations are used to determine the volume-averaged, macroscopic strain energy, yield strength, and the hardening rate. The yield strength is measured as 0.2% flow stress in the stress-strain plot and the hardening rate is derived as average slope of the stress-strain plot in the post-yield plastic deformation. The values of these CPFEM simulated volume-averaged quantities are

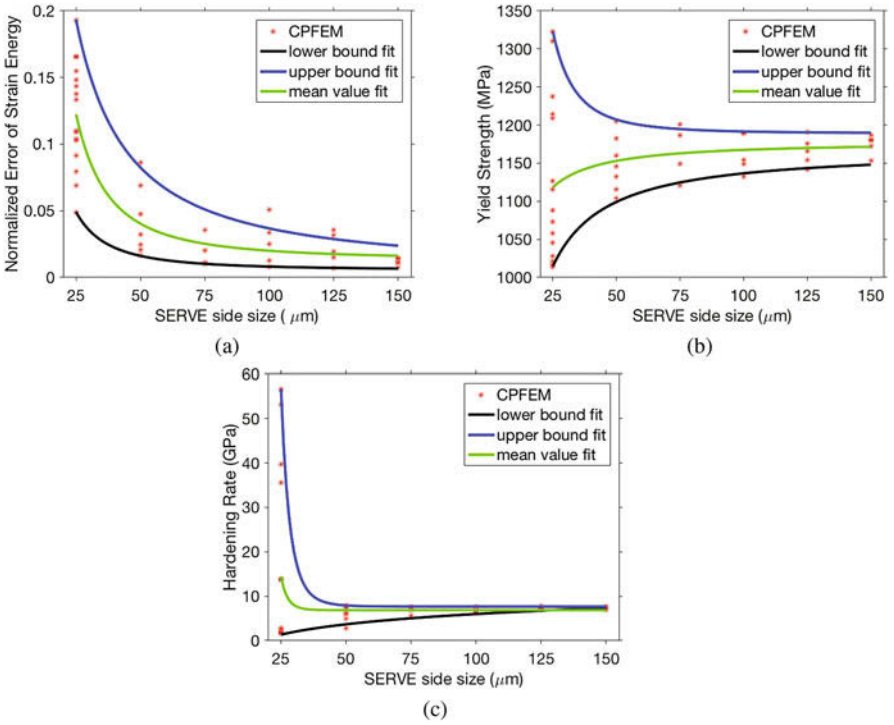

Fig. 18 Convergence of (**a**) normalized difference of the strain energy obtained by CPFEM simulations and experiments, (**b**) yield strength, and (**c**) post-yield hardening rate as a function of the SERVE size. (Reprinted from: Bagri [29], with permission from Springer)

shown in Fig. 18 with discrete points (red stars). The scatter in the data corresponds to variations in the morphological and crystallographic parameters of the SERVEs that are analyzed by CPFEM. For each SERVE size, the upper bound, lower bound, and the mean value of the volume-averaged quantities are also plotted in Fig. 18. Figure 18a plots the normalized difference of strain energy obtained by simulations and experiment as a function of the SERVE size. The normalized error decreases as the SERVE size increases. Additionally, the scatter in simulated values of the strain energy difference reduces with increase in the SERVE size, indicating convergence of the simulated results. This is also implied in the convergence of the upper and lower bounds with increasing SERVE size. Figure 18b, c shows similar convergence trends in the effective yield strength and post-yield hardening rate with SERVE size respectively. The convergence results in Fig. 18 with respect to upper and lower bounds of material properties are consistent with the experimental observations in [32]. Similar lower bound convergence had also been predicted for the yield strength in micro-tensile tests of [56].

A Student's t-test is conducted and convergence of material properties is established using a 95% confidence interval bound. This corresponds to a sample population of a given size, for which material properties are in the range $\mu \pm$

0.1μ, where μ is the mean value property. Reasonable agreement is seen with experimental results. With this criterion, convergence is achieved for SERVEs for which the upper and lower bound values of material properties are within 10% of the mean value. Room temperature simulation results for the largest SERVE with a size of $\sim 150\,\mu$m are used for the identification of the P-SERVE. The results in Fig. 18 indicate that convergence is achieved for a SERVE size of $100\,\mu$m. This implies that the P-SERVE size is $\approx 100\,\mu$m, above which material properties are convergent. This is also corroborated with experimental results. In comparison, the M-SERVE size in Sect. 3.3 is found to be $150\,\mu$m. The smaller P-SERVE compared to the M-SERVE indicates that the characteristic features of twins implemented in determining the M-SERVE are more stringent than those necessary for determining material properties like strength and hardness. This exercise implicitly establishes a relation between the M-SERVE and P-SERVE. Finally, while the M-SERVE and P-SERVE are relatively small compared to the scale of the grain structure for these properties, other properties such as fatigue [57] may require larger volumes of the material to be analyzed.

3.5 Summary of the Polycrystalline Scale Analysis

This section establishes microstructure-based statistically equivalent RVEs or M-SERVEs and property-based statistically equivalent RVEs or P-SERVEs from statistically equivalent virtual polycrystalline microstructures of polycrystalline Ni-based superalloys containing annealing twins. Results from the Kolmogorov-Smirnov (KS) convergence test show that the minimum size of the M-SERVE that captures the experimentally obtained statistics is $\approx 150\,\mu$m. On the other hand, a P-SERVE size of $\approx 100\,\mu$m is adequate to reproduce the macroscopic experimental material response. The smaller P-SERVE size compared to the M-SERVE size implies that the characteristic features of twins needed for determining the M-SERVE are more stringent than those necessary for determining material properties like strength and hardness. This M-SERVE-P-SERVE study implicitly establishes a dependency of a property on the microstructure, i.e., microstructure property relations. In conclusion, the methodologies developed in this paper provide a solid foundation for micromechanical analysis leading to the evaluation of multi-scale properties of complex polycrystalline materials.

In summary, this chapter develops a cogent framework for statistically equivalent virtual microstructures and subsequently M-SERVEs and P-SERVEs of nickel-based superalloy microstructures at multiple scales. The framework couples experimental methods, image extraction, statistical analysis and finite element modeling for establishing a robust methodology that can be applied to a wide variety of heterogeneous materials. This framework lays the foundation for the development of parametrically homogenized constitutive models as functions of the microstructural morphology and crystallography.

Acknowledgements This work has been supported through a grant No. FA9550-12-1-0445 to the Center of Excellence on Integrated Materials Modeling (CEIMM) at Johns Hopkins University awarded by the AFOSR/RSL Computational Mathematics Program (Manager Dr. A. Sayir) and AFRL/RX (Monitors Drs. C. Woodward and C. Przybyla). These sponsorships are gratefully acknowledged. Computing support by the Homewood High Performance Compute Cluster (HHPC) and Maryland Advanced Research Computing Center (MARCC) is gratefully acknowledged.

References

1. M. McLean, R.W. Cahn, *Nickel-Base Superalloys: Current Status and Potential* (Chapman and Hall, London, 1996)
2. D. Furrer, H. Fecht, Ni-based superalloys for turbine discs. J. Miner. Met. Mater. Soc. **51**, 14–17 (1999)
3. T.M. Pollock, S. Tin, Nickel-based superalloys for advanced turbine engines: chemistry, microstructure and properties. J. Prop. Power **22**(2), 361–374 (2006)
4. A. Epishin, T. Link, U. Bruckner, P.D. Portella, Kinetics of the topological inversion of the γ/γ'-microstructure during creep of a nickel-based superalloy. Acta Mater. **49**, 4017–4023 (2001)
5. M. Ignat, J.Y. Buffiere, J.M. Chaix, Microstructures induced by a stress gradient in a nickel-based superalloy. Acta Mater. **41**, 855–862 (1993)
6. G.B. Viswanathan, P.M. Sarosi, D.H. Whitis, M.J. Mills, Deformation mechanisms at intermediate creep temperatures in the Ni-base superalloy Rene 88 DT. Mater. Sci. Eng. A **400**, 489–495 (2005)
7. J.S. Van Sluytman, T.M. Pollock, Optimal precipitate shapes in nickel-base $\gamma - \gamma'$ alloys. Acta Mater. **60**, 1771–1783 (2012)
8. L. Kovarik, R.R. Unocic, J. Li, P. Sarosi, C. Shen, Y. Wang, M.J. Mills, Microtwinning and other shearing mechanisms at intermediate temperatures in Ni-based superalloys. Progr. Mater. Sci. **54**, 839–873 (2009)
9. R.R. Unocic, N. Zhou, L. Kovarik, C. Shen, Y. Wang, M.J. Mills, Dislocation decorrelation and relationship to deformation microtwins during creep of a γ' precipitate strengthened Ni-based superalloy. Acta Mater. **54**, 7325–7339 (2011)
10. J. Cormier, X. Milhet, J. Mendez, Non-isothermal creep at very high temperature of the nickel-based single crystal superalloy. Acta Mater. **55**, 6250–6259 (2007)
11. H.U. Hong, I.S. Kim, B.G. Choi, M.Y. Kim, C.Y. Jo, The effect of grain boundary serration on creep resistance in a wrought nickel-based superalloy. Mat. Sci. Eng. A **517**, 125–131 (2009)
12. Y.S. Choi, T.A. Parthasarathy, D.M. Dimiduk, M.D. Uchic, Microstructural effects in modeling the flow behavior of single-crystal superalloys. Met. Mat. Trans. A **37**(3), 545–550 (2006)
13. C. Allan, *Plasticity of Nickel Base Single Crystal Superalloys*. Ph.D. thesis, Massachusetts Institute of Technology (1995)
14. A. Ma, F. Roters, A constitutive model for FCC single crystals based on dislocation densities and its application to uniaxial compression of aluminium single crystals. Acta Mater. **52**(12), 3603–3612 (2004)
15. A.M. Cuitino, M. Ortiz, Constitutive modeling of $L1_2$ intermetallic crystals. Mater. Sci. Eng. A **170**(1), 111–123 (1993)
16. T. Tinga, W.A.M. Brekelmans, M.G.D. Geers, Cube slip and non-Schmid effects in single crystal Ni-base superalloys. Model. Simul. Mater. Sci. Eng. **18**(1), 015005 (2010)
17. E.P. Busso, K.S. Cheong, Length scale effects on the macroscopic behaviour of single and polycrystalline FCC crystals. Le J. Phys. IV **11**(PR5), 161–170 (2001)

18. J. Zhang, M. Shenoy, D.L. McDowell, Estimating fatigue sensitivity to polycrystalline Ni-base superalloy microstructures using a computational approach. Fatigue Fract. Eng. Mater. Struct. **30**, 889–904 (2007)
19. S. Keshavarz, S. Ghosh, Multi-scale crystal plasticity finite element model approach to modeling nickel-based superalloys. Acta Mater. **61**(17), 6549–6561 (2013)
20. S. Keshavarz, S. Ghosh, Hierarchical crystal plasticity FE model for nickel-based superalloys: sub-grain microstructures to polycrystalline aggregates. Int. J. Sol. Struct. **55**, 17–31 (2015)
21. S. Ghosh, G. Weber, S. Keshavarz, Multiscale modeling of polycrystalline nickel-based superalloys accounting for subgrain microstructures. Mech. Res. Commun. **78**, 34–46 (2016)
22. S. Keshavarz, S. Ghosh, A crystal plasticity finite element model for flow stress anomalies in Ni_3Al single crystals. Philos. Mag. **95**(24), 2639–2660 (2015)
23. S. Keshavarz, S. Ghosh, A. Reid, S. Langer, A non-Schmid crystal plasticity finite element approach to multi-scale modeling of nickel-based superalloys. Acta Mat. **114**, 106–115 (2016)
24. R. Hill, Elastic properties of reinforced solids: some theoretical principles. J. Mech. Phys. Solids **11**(5), 357–372 (1963)
25. I.M. Gitman, H. Askes, L.J. Sluys, Representative volume: existence and size determination. Eng. Fract. Mech. **74**(16), 2518–2534 (2007)
26. S. Swaminathan, S. Ghosh, N.J. Pagano, Statistically equivalent representative volume elements for composite microstructures, Part I: without damage. J. Comput. Mater. **40**(7), 583–604 (2006)
27. S. Swaminathan, S. Ghosh, Statistically equivalent representative volume elements for composite microstructures, Part II: with interfacial debonding. J. Comput. Mater. **40**(7), 605–621 (2006)
28. D. McDowell, S. Ghosh, S. Kalidindi, Representation and computational structure-property relations of random media. JOM J. Miner. Met. Mater. Soc. **63**(3), 45–51 (2011)
29. A. Bagri, G. Weber, J.C. Stinville, W. Lenthe, T. Pollock, C. Woodward, S. Ghosh, Microstructure and property-based statistically equivalent representative volume elements for polycrystalline Ni-based superalloys containing annealing twins. Metall. Mater. Trans. A **49**(11), 5727–5744 (2018)
30. M. Pinz, G. Weber, W.C. Lenthe, M.D. Uchic, T.M. Pollock, S. Ghosh, Microstructure and property based statistically equivalent RVEs for intragranular $\gamma - \gamma$' microstructures of Ni-based superalloys. Acta Mat. **157**, 245–258 (2018)
31. X. Tu, A. Shahba, J. Shen, S. Ghosh, Microstructure and property based statistically equivalent RVEs for polycrystalline-polyphase aluminum alloys. Int. J. Plast. **115**, 268–292 (2019)
32. M. Echlin, W. Lenthe, T. Pollock, Three-dimensional sampling of material structure for property modeling and design. Int. Mater. Manuf. Innov. **3**(1), 21–34 (2014)
33. M.A. Groeber, M. Jackson, DREAM.3D: a digital representation environment for the analysis of microstructure in 3D. Integr. Mater. Manuf. Innov. **3**, 5 (2014)
34. M.A. Groeber, S. Ghosh, M.D. Uchic, D.M. Dimiduk, A framework for automated analysis and representation of 3D polycrystalline microstructures, Part 1: statistical characterization. Acta Mat. **56**(6), 1257–1273 (2008)
35. M.A. Groeber, S. Ghosh, M.D. Uchic, D.M. Dimiduk, A framework for automated analysis and representation of 3D polycrystalline microstructures, Part 2: synthetic structure generation. Acta Mat. **56**(6), 1274–1287 (2008)
36. Y. Bhandari, S. Sarkar, M.A. Groeber, M.D. Uchic, D. Dimiduk, S. Ghosh, 3D polycrystalline microstructure reconstruction from FIB generated serial sections for FE analysis. Comput. Mater. Sci. **41**, 222–235 (2007)
37. S. Niezgoda, D. Turner, D. Fullwood, S. Kalidindi, Optimized structure based representative volume element sets reflecting the ensemble-averaged 2-point statistics. Acta Mat. **58**, 4432–4445 (2010)
38. D.M. Saylor, J. Fridy, B.S. El-Dasher, K.-Y. Jung, A.D. Rollett, Statistically representative 3D microstructures based on orthogonal observation sections. Met. Mat. Trans. A **35**, 1969–1979 (2004)

39. Y. Jiao, F.H. Stillinger, S. Torquato, Modeling heterogeneous materials via two-point correlation functions: basic principles. Phys. Rev. E **76**(3), 031110 (2007)
40. Y. Jiao, E. Padilla, N. Chawla, Modeling and predicting microstructure evolution in lead/tin alloy via correlation functions and stochastic material reconstruction. Acta Mat. **61**(9), 3370–3377 (2013)
41. G. Saheli, H. Garmestani, B.L. Adams, Microstructure design of a two phase composite using two-point correlation functions. J. Comput.-Aided Mater. Des. **11**(2), 103–115 (2004)
42. S. Torquato, G. Stell, Microstructure of two-phase random media. I. the n-point probability functions. J. Chem. Phys. **77**(4), 2071–2077 (1982)
43. J. MacSleyne, M.D. Uchic, J.P. Simmons, M. De Graef, Three-dimensional analysis of secondary γ' precipitates in René-88 dt and UMF-20 superalloys. Acta Mat. **57**(20), 6251–6267 (2009)
44. M. Kühbach, G. Gottstein, L.A. Barrales-Mora, A statistical ensemble cellular automaton microstructure model for primary recrystallization. Acta Mater. **107**, 366–376 (2016)
45. C. Schwarze, R.D. Kamachali, M. Kühbach, C. Mießen, M. Tegeler, L. Barrales-Mora, I. Steinbach, G. Gottstein, Computationally efficient phase-field simulation studies using RVE sampling and statistical analysis. Comp. Mater. Sci. **147**, 204–216 (2018)
46. W. Lenthe, *Twin Related Domains in Polycrystalline Nickel-Base Superalloys: 3D Structure and Fatigue*. Ph.D. thesis, University of California- Santa Barbara (2017)
47. M. Pinz, G. Weber, S. Ghosh, Generating 3D virtual microstructures and statistically equivalent representative volume elements for intragranular nickel-based superalloy microstructures. Submitted 2019.
48. M.P. Echlin, A. Mottura, C.J. Torbet, T.M. Pollock, A new TriBeam system for three-dimensional multimodal materials analysis. Rev. Sci. Instrum. **83**(2), 023701 (2012)
49. F. Meyer. Topographic distance and watershed lines. Signal Process. **38**(1), 113–125 (1994)
50. S.J. Ahn, W. Rauh, H.-J. Warnecke, Least-squares orthogonal distances fitting of circle, sphere, ellipse, hyperbola, and parabola. Pattern Recogn. **34**(12), 2283–2303 (2001)
51. D.E. Goldberg, *Genetic Algorithms in Search, Optimization, and Machine Learning* (Addison-Wesley, Reading, 1989)
52. W.W. Daniel, *Kolmogorov-Smirnov One-Sample Test* (PWS-Kent, Boston, 1990)
53. Simulation Modeling Suite (Simmetrix Inc., 2015). http://www.simmetrix.com/
54. G. Casella, C.P. Robert, M.T. Wells, *Generalized Accept-Reject Sampling Schemes* Lecture Notes: Monograph Series **45**(Institute of Mathematical Statistics. Wiley StatsRef: Statistics Reference Online, John Wiley & Sons Ltd.), 342–347 (2004)
55. J.K. Mackenzie, 2nd Paper on statistics associated with the random disorientation of cubes. Biometrika **45**, 229–240 (1958)
56. Z. Alam, D. Eastman, M. Jo, K. Hemker, Development of a high-temperature tensile tester for micromechanical characterization of materials supporting meso-scale ICME models. JOM **68**(11), 2754–2760 (2016)
57. J.C. Stinville, N. Vanderesse, F. Bridier, P. Bocher, T.M. Pollock, High resolution mapping of strain localization near twin boundaries in a nickel-based superalloy. Acta Mat. **98**(1), 29–42 (2015)

Microscale Testing and Characterization Techniques for Benchmarking Crystal Plasticity Models at Microstructural Length Scales

David W. Eastman, Paul A. Shade, Michael D. Uchic, and Kevin J. Hemker

1 Introduction

The desire to improve the performance and lifetime of polycrystalline components has fueled the development of advanced micromechanical modeling tools. Multiscale modeling approaches, such as Crystal Plasticity Finite Element Methods (CPFEM), now possess the ability to illuminate the link between material processing, microstructure, and properties [1]. Whereas traditional FE modeling relies on convergent macroscale properties, the ability of CPFEM to explicitly represent the morphology and local crystallographic orientations of polycrystalline microstructures requires scale-specific, quantitative microstructural information for both input and validation. The development and implementation of experimental techniques for capturing behavior and microstructural properties at salient length scales are needed to inform the determination of representative volume elements (RVEs). Here, accurately capturing microstructural details and observing size effects on material properties are both important. Simply extrapolating from average microstructure descriptors does not provide information about the relative importance of specific grain size, shape, and configuration with neighbors. These are features that can be captured experimentally through advanced characterization techniques, such as 3D serial sectioning [2].

Whereas traditional modeling efforts have made use of existing data in the literature to model a certain material behavior, the inverse, namely, designing and tailoring experiments to obtain local microstructurally specific benchmarks,

D. W. Eastman (✉) · K. J. Hemker (✉)
Department of Mechanical Engineering, Johns Hopkins University, Baltimore, MD, USA
e-mail: deastma2@jhu.edu; hemker@jhu.edu

P. A. Shade · M. D. Uchic
Materials and Manufacturing Directorate, Air Force Research Laboratory, Wright-Patterson AFB, Dayton, OH, USA

S. Ghosh et al. (eds.), *Integrated Computational Materials Engineering (ICME)*,
https://doi.org/10.1007/978-3-030-40562-5_4

is needed to guide and benchmark corresponding models. The work presented in this chapter was undertaken as part of the Air Force Office of Scientific Research (AFOSR)-sponsored Center of Excellence in Integrated Materials Modeling (CEIMM), and its overall goal was to provide experimental benchmarks and validation routes for multiscale CPFEM models of the Ni-base superalloy René 88DT, specifically through the development of scale-specific mechanical benchmarks by capturing the mechanical response of microtensile samples, in which explicit measures of their microstructure can also be obtained. As part of this effort, multiple test sample geometries were designed to characterize sample volumes that were small enough to be modeled while still providing a true polycrystalline response. Significant effort went into developing machining processes, and the test equipment and techniques required for obtaining the requisite data, at the various length scales that each of these samples represented. In addition, after observing a size effect on yield strength, a further study was done to investigate this phenomenon by testing samples of different sizes and elucidating mesoscale trends in the behavior of René 88DT.

2 Background

The need to connect modeling and experiments is intrinsic to the Integrated Computational Materials Engineering (ICME) paradigm, but the ability to do so has been limited by the need for more computational power as well as more detailed explicit microstructural information from experimental results. In terms of experimentally coupling 3D microstructures with mechanical properties, earlier efforts were limited by their simplicity. This was due not only to limitations with the state of experimental techniques available but also the technology and ability to process the large amounts of data necessary. Becker et al. utilized only the surface orientation data of an Al sample to develop two finite element models: a plane strain model and a quasi-3D model with a mesh that was only one element thick [3]. Cheong et al. performed a similar modeling effort using experimental data collected by Zhang for a polycrystalline sample of Al–0.5% Mg [4]. The model utilized a finite element mesh of $35 \times 31 \times 3$ elements on a subsection of the sample gage and compared distributions of plastic axial strain with experimental measurements of strain as well as the macroscopic stress–strain behavior [5]. These studies are examples of early efforts to connect experiments and modeling; however, the drawback of not being able to model the full 3D structure of the sample is significant.

To avoid the need for full 3D characterization of a sample microstructure, other investigators have focused on materials with microstructures that can be characterized well using only 2D methods. These materials tend to have either very coarse microstructures or columnar structures, achieved by the processing methods used to produce the material (such as directional solidification [6], the extraction of oligocrystals [7], or the use of heat treatments to coarsen the material [8, 9]).

A multitude of ICME studies on oligocrystalline structures have been published on materials that include Zirconium alloys and near-gamma titanium aluminides [10], polycrystalline columnar Al [6, 8, 11], single and bicrystal stainless steel [6], hot worked waspaloy-ingot specimens [12], and coarse-grained tantalum [9]. The ability to model the full sample gage of these samples in 3D had allowed for a more accurate approximation of the true boundary conditions experienced by the sample during an experiment and a more accurate prediction of the deformation response. Another technique that has been utilized when only 2D microstructural data is available is the use of statistics to extrapolate a 3D microstructure from a 2D Electron Backscatter Diffraction (EBSD) scan, such as the work of St-Pierre in modeling TiAl and grade 702 zirconium [13]. This novel modeling approach is however difficult to truly compare one-to-one with experimental results, as even slight changes in the subsurface microstructure can lead to significant deviations in the observed behavior at the sample surface.

The most prevalent experimental technique for building a 3D dataset involves serial sectioning of samples by deconstructing the sample layer by layer and characterizing each newly exposed surface before performing the next sectioning step. The acquired 2D scans can be stitched together to provide a 3D representation of the sample microstructure. Musienko was one of the first to characterize and model a sample using this methodology on a tested Cu microtension sample [14]. A small subsection of the gage, containing about 100 grains, was characterized in this manner and used to generate a finite element simulation of the 3D structure. Although this small subsection did not represent the full physical volume of the sample required to capture requisite boundary conditions for a true one-to-one model, this was one of the first times that a modeling effort was performed on a sample characterized in 3D. Spanos, Lewis, Rowenhorst, and coworkers at the Naval Research Laboratory combined serial sectioning using a Buehler Minimet system and characterization with EBSD to develop 3D datasets of stainless steels and Ti alloys to connect with FEM models [15]. More automated methodologies using mechanical sectioning, such as the Alkemper-Voorhees micromiller, developed at Northwestern University [16], or the Robomet.3D system, developed at the Air Force Research Lab [17, 18], were major advances in streamlining workflows for 3D dataset collection.

Within the last decade or so, the use of more advanced sectioning tools and methods has enabled significant advances in studying microstructure in 3D. In dual beam systems equipped with both a scanning electron microscope (SEM) and focused ion beam (FIB), serial sectioning via FIB and EBSD can be performed and automated in a routine manner. Uchic et al. and Groeber et al. were some of the first to demonstrate this technique in sectioning samples of the nickel-base superalloy IN100 [19, 20]. Shortly thereafter, Zaafarani et al. used FIB serial sectioning to characterize the microstructure surrounding a nanoindent in Cu and to develop a finite element model from the collected data [21]. In terms of utilizing this technique for characterizing and modeling a full sample volume, the applications have been limited by the low material removal rate of the FIB. One study that did yield positive results despite such limitations was carried out by Shade et al.

on microtensile samples of polycrystalline Ni [22, 23]. Using a dual beam FIB-SEM system, multiple samples of a width of 21 μm, a thickness of 38 μm, and a gage length of 80 μm were characterized in 3D and in combination with surface strain maps collected during testing used to later benchmark a finite element model using these explicit representations of microstructure [24]. While these examples demonstrate the ability of the FIB as a sectioning tool, it is clear that sample size and material limitations due to the material removal rate of the FIB can limit what can be done despite the nanometer level of precision that can be achieved.

While the traditional Ga FIB has become a widely used tool in microscale machining and materials research, the more recent development of the Plasma FIB (PFIB), using Xe rather than Ga as in a traditional FIB, allows for material removal rates at orders of magnitude higher. The PFIB can potentially even incur less damage than a traditional FIB, as reported by Kwakman et al., than compared to Ga FIB machining; the damage layer when using Xe FIB could be reduced by up to 25% [25]. Xiao et al. demonstrated that micropillars of Al, a material particularly susceptible to the effects of Ga implantation, machined with a Ga FIB showed a lower yield strength than micropillars fabricated with Xe FIB [26]. Burnett et al. have demonstrated the use of PFIB in serial sectioning and 3D characterization of a $150 \times 120 \times 80\ \mu m^3$ WC-Co sample using 790 slices of 100 nm thickness with a pixel resolution of 30 nm [27]. The step forward that these two tools provide in terms of 3D characterization is very promising, and optimization for sectioning at a smaller length scales could allow for the collection of statistics and 3D datasets for benchmarking at a rate that was previously inaccessible.

A more recently introduced tool for the collection of 3D microstructural data at a larger scale is the TriBeam system, which incorporates a femtosecond laser into a FIB-SEM dual beam platform. The material removal rate of the laser allows for material ablation two orders of magnitude faster than is possible with traditional FIB. In addition, the ablation rate of the femtosecond laser is more materials agnostic [28]. As a result, the TriBeam is an incredibly versatile system in terms of both speed and scale. One successful application of the TriBeam is in its use by Stinville et al. to characterize crack nucleation in René 88DT, in which tested fatigue samples were subsequently sectioned and characterized in the TriBeam to determine what features in the microstructure led to crack nucleation and propagation [29].

Another promising technique for characterizing material in 3D is the nondestructive technique of High-Energy Diffraction Microscopy (HEDM). HEDM utilizes diffraction patterns produced by a monochromatic beam from a synchrotron source to interrogate a volume of material. Two sets of detectors are used to collect information from the sample. One detector is located only a few mm from the sample and is used for near-field HEDM, which provides orientation maps with spatial locations of grains as well as their morphology and misorientation relative to neighboring grains [30]. The second detector is placed much farther away and is used for far-field HEDM, which provides grain centroids and elastic strain tensors [30]. These combined datasets provide a robust representation for the sample microstructure, as well as subgrain information [31]. Many examples of using this technique for 3D characterization have been demonstrated [32–37], and its

benefits are that it is nondestructive and can be used to capture 3D microstructural information in situ rather than from a postmortem sample. For example, Marguiles et al. demonstrated the use of HEDM to investigate deformation of a single grain within a Cu sample during incremental loading and scanning [38]. Oddershede et al. performed an HEDM experiment on a steel sample in a similar manner, but oriented the tensile axis to be vertical with respect to the beam [39]. In addition, this experiment did not simply study a single grain during testing, but rather about 200 grains, demonstrating a marked improvement in this characterization technique. More recently, Schuren et al. and Shade et al. developed a load frame for in situ HEDM experiments, known as the rotation and linear axial motion system (RAMS) [40, 41]. This load frame allows for the use of μ-CT, far-field HEDM, and near-field HEDM concurrently during a tension or compression experiment, while also being able to rotate the sample 360 degrees. In terms of ICME efforts, in one instance, this tool was utilized to collect a HEDM dataset for a Ti-7Al sample, which was then used to instantiate a CPFEM simulation [42]. The model showed a good correlation with experimental results, and this work also highlighted the importance of the stress states of buried grains.

In addition to the determination of global mechanical response and the capturing of an explicit microstructure representation of tested samples to be used for benchmarking, the local deformation behavior needs to be determined for direct comparison with simulation results. Hemker and Sharpe summarized numerous efforts to measure the mechanical response of materials for microscale microelectromechanical systems (MEMS) in their review on small-scale mechanical testing [43]. Espinosa et al. performed tensile tests on very thin films by pushing an Au freestanding film that was fixed at each end, measuring the vertical deflection of the film with interferometry and converting the deflection into elongation. While this is a novel concept, this technique is only able to be applied to a very specific thin film geometry [44, 45]. Haque and Saif constructed a micro-machined test system that combines the load frame and the thin film specimen into a single part that can be tested in an SEM and elongation determined by tracking the displacement of markers deposited on the samples [46].

For a geometry as small as a microtensile specimen, traditional contact methods for measuring strain (such as strain gauges or extensometers) are insufficient, and other methods have developed over time. Attempts to determine strain from grip displacement are made difficult by the compliance of a test machine relative to the small sample geometry being tested, particularly with the large machines used in macroscale testing. Greek and Johansson proposed a method for removing the effects of sample compliance, but use of this technique requires large differences in stiffness and it is generally accepted that strain is better measured in the gage of the specimen rather than corrected grip displacement measurements [47]. As described in the review on small-scale mechanical testing [43], one of the first noncontact methods developed for measuring strain in microtensile samples employed an interferometric strain displacement gage (ISDG). In this technique, two reflective markers are placed on a sample and illuminated with a laser, generating fringe patterns. As the sample changes shape, the motion of the fringe pattern can be

sensed with photodiode arrays and converted into strain [48]. This technique enables measurements of normal and transverse strains and allows for the direct measure of Young's modulus and Poisson's ratio.

The most prominent noncontact method for measuring strain is digital image correlation (DIC), which has been under development since the 1980s [49]. In DIC, markers or speckle patterns are applied to the sample surface and the region of interest is divided into subsets. Each of these subsets is tracked as the sample deforms, and its correlation to the subset in the original image is determined using a grayscale intensity function. The correlation coefficients of subsets of consecutive images are calculated and plotted versus their position. The maximum correlation coefficient is then located that is representative of the optimal fit between the subsets of the two images. From this correlation, displacements can be determined and both local and global strains can be calculated.

Recent progress in developing high-resolution speckle patterns has led to the ability to observe strains at very localized intragranular regions. Kammers et al. used gold nanoparticles to create speckle patterns with features on the order of 30 nm. By imaging these particles in an SEM, DIC with an unprecedented resolution of 4 nm/pixel was reported [50]. One important consideration in performing DIC with high resolution SEM images is distortions in SEM images, which require proper control and the use of high magnification, low accelerating voltages, large spot sizes, long dwell times, and low working distances [50]. Stinville et al. developed a novel technique using the γ' particles after a heat treatment in René 88DT as the speckle pattern [51]. The nanometer-sized features allowed for high resolution DIC in a fatigue sample to observe crack nucleation. Montgomery et al. developed a technique that uses multilayered Au, Ti, and Ag-sputtered coatings reconfigured in an NaCl solution to form DIC speckle patterns, allowing for submicron resolution [52]. This technique was demonstrated to be applicable for multiple classes of materials, including metal alloys, epoxies, and composites. These high-resolution methods along with others provide a way to improve the resolution of DIC measurements, and further improvements to the technique could be made with higher resolution imaging with reduction in noise.

The material that was investigated as part of CEIMM is the polycrystalline Ni-base superalloy René 88DT. The material has a nominal composition (wt %) of: 56.46 Ni, 13 Co, 16 Cr, 4 Mo, 4 W, 2.1 Al, 3.7 Ti, 0.7 Nb, 0.03 C, and 0.015 B. This alloy is processed through a powder metallurgy route and as such contains a high volume fraction of annealing twins. It exhibits exceptional strength, even at very high temperatures, making it ideal for its primary use in turbine engines [53].

René 88DT is an interesting candidate for multiscale modeling because of the features that exist within the material at multiple length scales. At the subgrain, or intragranular, scale, the two-phase microstructure gives rise to properties that affect the higher order scales, especially in terms of the high temperature properties related to dislocation activity [53]. At the polycrystalline scale, the large volume fraction of twins adds complexity in terms of being able to model these finer features as well as the various boundaries that exist. A description of a CPFEM model to approach this multiscale problem is given in [54]. The model endeavors to represent

the morphology of the subgrain structure in order to subsequently homogenize and develop a single crystal model. This single crystal model is then brought up to the polycrystalline scale at which individual grains and twins are organized together to represent the microstructure of the material. The simulation predictions observed at this scale can be directly compared and benchmarked, with the experimental results captured at the mesoscale.

Alongside the ability to machine and test samples at an expanding number of sizes and for a multitude of materials, characterization methods such as DIC to observe strain and local deformation behavior, as well as 3D techniques for characterizing microstructure, have led to the ability to interrogate material behavior at extremely fine length scales. In addition, these advances in property and microstructural characterization have supported the development of more informed models, and modeling techniques such as CPFEM have allowed for the explicit representation of microstructure in silico. Though significant progress has been made in terms of ICME to date, most work has been done on pure materials; structurally complex materials such as René 88DT and other Ni-base superalloys remain a challenge. As such, the continued development of techniques to machine, test, and characterize microtensile samples of commercially relevant materials is needed to promote model development.

3 Machining Methods for Microscale Samples

Miniaturized mechanical testing is fast becoming a widespread technique for capturing the influence of microstructure and measurements of local properties [43, 55, 56]. Capturing these scale-specific properties is critical to benchmarking and development of multiscale CPFEM models. However, at smaller length scales, sample quality has a significant effect on its measured response. Defects and surface roughness can lead to premature failure during tensile loading and inaccurate results, which can be especially troublesome when there is uncertainty in the expected outcome of an experiment. ASTM standards give some guidelines in terms of a target of quality and dimensions of tensile samples, but do not necessarily provide a methodology and best practices for fabricating samples, especially at the microscale [57]. At this length scale, traditional machining methods are not applicable because of inherent limits in the dimensional tolerance of the surface finish.

The three microtensile sample preparation techniques that were utilized in the current study of René 88DT are: focused ion beam (FIB) milling, femtosecond laser machining, and wire electric discharge machining (EDM). Before machining of the final microtensile sample geometries, thin foils were excised from a bulk piece of René 88DT and polished to the proper thickness and surface finish. The foils were prepared to have a specific final thickness that would allow for machining of samples with a square cross section. The initial slices were machined using wire EDM. Due to the recast layer created by the wire EDM, foils were cut to be 100 μm thicker than the final desired thickness and subsequently polished on both sides using SiC

polishing papers ranging from 600 to 1200 grit. This process resulted in precise foil thicknesses, removal of surface defects, and a near-mirror finish, which also made it easier to employ digital image correlation (DIC). Once a foil of the correct thickness was achieved, microtensile samples were machined from it using one of the three techniques. For samples with thicknesses and widths of about 20 μm, FIB machining was employed as the final machining tool, whereas wire EDM was used for samples with thicknesses and widths of 200 μm or larger, and femtosecond laser machining was employed for intermediate samples with thicknesses and widths of 50–100 μm.

3.1 Focused Ion Beam Machining

The focused ion beam (FIB) has become a widely used tool in microscale sample fabrication due to its precise milling capabilities. FIB milling occurs by sputtering, accelerating, and focusing charged ions, typically Ga. The interaction of these ions with atoms in the sample results in ablation at a relatively slow rate, but the nature of this process allows for delicate and precise machining and procedures, such as the extraction of TEM samples using FIB lift out. One of the first major applications of FIB machining for microscale test samples was its use in milling micropillars for compression testing [58]. This methodology, which has inspired many subsequent microscale machining efforts, showed the viability of the FIB as a microscale machining tool and opened the opportunity for the precise machining of samples at the single digit micron scale. FIB-induced damage of microscale samples associated with Ga implantation and amorphization has been reported and shown to vary with material. While this effect is commonly observed, especially in lower atomic mass metals, it has been suggested that it only plays a major role at the outer layer of the sample and with careful control of the beam size and current can be limited to 100 nm or less in most materials [59]. While this level of damage will not play a significant role in microtensile samples with dimensions that are orders of magnitude greater than this, caution is still warranted when FIB milling microsamples.

High throughput use of an FIB as a machining technique for complex geometries and three-dimensional samples, such as micropillars, relies on the ability to automate the machining process. One way in which this can be done is through the use of a fiducial marker and image processing to realign the sample for machining between each cut. For micropillars, a lathe milling process can be used as the sample is rotated around the fiducial marker. A similar process, which will be discussed later in this section, can be used for machining more complex microtensile geometries even though most of the milling is done in a two-dimensional plane [23].

Two of the main parameters that affect the quality of an FIB cut are the beam current, which affects the material removal rate, and the beam focus, which affects the shape of the beam. For bulk milling, a higher beam current is used to increase the rate of material removal, and therefore the focus and shape of the beam become less

important [60]. By contrast, finer milling processes use a lower current and a more sharply focused beam to achieve precision in the final geometry. Combining them in a two-step process provides the most efficient path for machining microtensile samples.

Another technique that can lead to more efficient FIB machining is to design the machining path based on the shape of the ion beam. Even when the focus of the beam is corrected as much as possible, there is still a possibility of beam tails. These regions of the beam can be problematic because material can be removed in undesired regions, which can cause damage or undesired taper, and the sputtering rate in this region can be higher or lower than the rest of the beam [61]. Although it seems like minimizing the tail would be the best method, it can actually be more effective to take advantage of the shape of the beam with the tail in order to simultaneously use a higher current and achieve faster milling rates without sacrificing machining quality. In addition, by calibrating the beam to have the tail occur only on one edge of the beam and having a clean cut with the other edge, it is actually possible to have the beam cut even better than simply minimizing the effect of the tail for a symmetric beam.

In the current study, an automated procedure for machining microtensile samples with the FIB was developed using Python scripts to control a Tescan Lyra dual beam system for both imaging and milling. For each thin foil sample to be machined, a circular fiducial marker was first milled within 200 μm of the edge of the foil to provide a reference of where the top sample grip section was to be located. Using image processing through Python, the fiducial marker was identified and used for automated realignment of the beam as the sample was rotated for cutting. The sample geometry was discretized into a set of cutting steps, with corresponding rotation angles and positions relative to the fiducial marker and beam size, for each cut that was made. The sample stage was rotated to the appropriate angle, where the image was centered on the fiducial marker, and then subsequently moved to where the cut was to be made and the cutting process performed. This procedure was repeated for each step of the sample geometry to complete one pass of the geometry. Each subsequent pass was performed to cut a geometry that approached the final shape and used less current to minimize damage in the final sample. Using a beam current of 3–5 nA for initial bulk passes and then reducing to 500 pA was effective for minimizing surface damage. Images of a sample after the first cut of this machining process and the final sample are shown in Fig. 1.

This combination of using bulk and fine milling, optimizing the beam shape, and taking advantage of the asymmetric shape of the beam rather than working around it provide an effective and automatable method for producing the complex geometries found in microtensile samples, as well as in micropillars and microcantilevers.

Despite the precision and widespread use of FIB milling, it does have limitations. One of the major limitations is the scale at which samples can be fabricated. Slow material removal rates, typically on the order of 1 μm^3/nAs or less, make it impractical to FIB-machine samples with dimensions larger than 50 μm in a reasonable amount of time [59, 61–63]. In addition, machining of larger samples requires more care, as machining across longer distances makes it difficult to

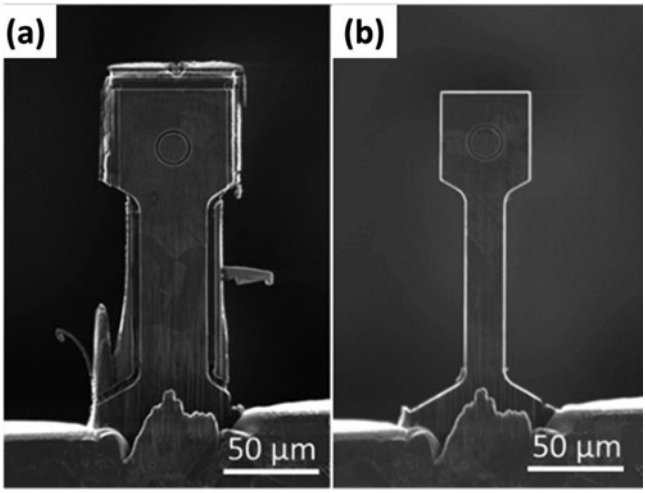

Fig. 1 Images of an FIB cut sample (**a**) after a first cut in the milling procedure and (**b**) cut to the final sample geometry

maintain beam focus, which can lead to taper or curtaining and result in uneven material removal [64]. It is possible to shift the focus of the beam, but that requires more time and effort to reposition the beam multiple times to make one cut.

Another drawback of using the FIB for sample fabrication is the difficulty in machining nonconductive samples. Due to the use of charged particles in both FIB and SEM imaging, it can be difficult to image samples that are not conductive. Charging makes it difficult to perform precise machining and utilize image processing for automated processes. Another aspect that makes working with the FIB difficult, especially with sensitive samples, is that imaging a sample with the FIB can cause ion irradiation damage at the sample surface and can continue to ablate material if the current is too high while imaging. For this reason, most FIB systems are combined with an SEM for imaging to prevent this damage. However, this becomes a challenge when trying to automate machining using a fiducial marker, because the fiducial mark needs to be in the plane of the machining path. The electron column views the fiducial mark at an angle, and image recognition is more difficult in projection. When imaging with the FIB, capturing a single quick image rather than imaging continuously is preferred, if the imaging conditions can be maintained throughout the machining process without damaging the sample.

3.2 Wire EDM Machining

A machining technique that is more commonly used for macroscale component fabrication, but can also be applied at the microscale, is wire electrical discharge machining (EDM). During EDM, the sample and wire are first submerged in a

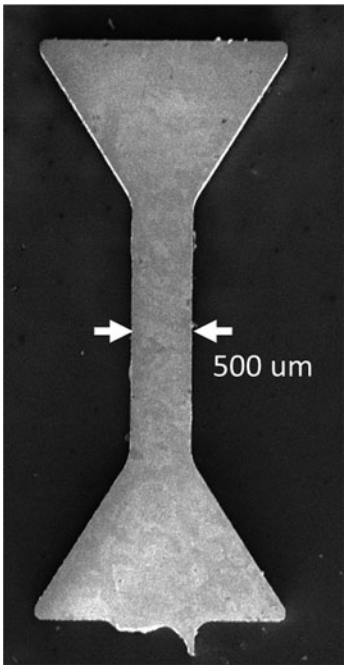

Fig. 2 Image of wire EDM machined René 88 microsample with gage dimensions of 500 × 500 μm

dielectric fluid, usually deionized water. The charged wire is then guided along a programmed path to cut the desired shape, acting as one electrode while the workpiece acts as a second electrode [65, 66].

Due to the nature of the wire EDM, there are limits to the level of quality that can be achieved in sample machining. However, there are multiple ways to improve the quality of samples. The typical EDM cutting process can cause significant surface roughness and damage in the form of a recast layer because of the melting, vaporization, and resolidification of material that occurs. The main parameters that can be adjusted for EDM are the cutting speed, power, and water flow. The wire EDM system used in this study was built by Fanuc Robocut. In initial setup, the user selects a material type and the thickness of object being cut, and the machine provides suggested machine parameters. Although these parameters cut the material well at the macroscale, the surface quality is rarely suitable for microtensile samples. In some cases, if a foil of material being machined is too thin, the machine may not be able to recommend a setting at all or will give an incorrect setting. Figure 2 shows an image of the dogbone sample geometry machined using a wire EDM operating with optimized settings to minimize sample surface roughness. These optimized settings included using multiple passes, starting with a rough cutting pass, followed by a finer cutting pass using less voltage, as well as minimization of water flow to reduce sample vibration during cutting.

As a machine typically used for larger parts, there are drawbacks to the wire EDM as a tool for manufacturing microtensile samples. Samples have to be

conductive in order to be able to pass a current to melt the material. As with the FIB, there is a limit to the scale of microtensile samples that can be machined using wire EDM. It becomes difficult to cut samples below a certain size because of two main factors: the tension of the wire on the sample during the cutting process and the surface roughness. In order for the wire EDM to cut, contact of the wire with the sample must be maintained during machining, and the wire must be kept tight in tension and a flow of water must also be maintained. For smaller, thinner samples or more delicate materials, this can lead to the sample being bent during the EDM process. One means of mitigating this is fixing the sample to a rigid substrate using a conductive epoxy. Doing so protects the sample from bending while still maintaining conductivity. However, there can still be challenges in using this technique, as air gaps in the epoxy or between the epoxy and sample can cause a short that will prevent the wire from cutting. Using a thicker, more rigid substrate also requires more power in order to cut through both materials, which will limit the quality of the actual sample. In addition, if the sample has to be sandwiched between two plates to fully protect it, it can be difficult to align the sample prior to machining.

Figure 3 presents side surface profiles captured using laser confocal microscopy of three samples. Two of these samples were prepared using EDM, one with machine settings and one with optimized settings, and the third is a surface profile from a femtosecond laser-machined sample for reference. Using optimized parameters and employing a multiple pass methodology for machining microtensile samples reduces the average surface roughness from 22 to 2 μm [65, 67–70]. By comparison, the surface roughness of a femtosecond laser-machined sample was less than 1 μm.

The previously demonstrated surface roughness also poses a challenge when machining microtensile samples as this roughness will have a much greater effect at decreased sample sizes, as will be demonstrated in a later section. The roughness can cause artifacts in the experimental data due to premature failure at surface flaws or the creation of local stress concentrations. For most materials, the limit of the sample size that can be created using wire EDM is only a few hundred microns, if the roughness can be controlled and bending avoided. In the current study, the smallest dogbone microtensile samples that were machined had a gage width and thickness of 200 μm.

3.3 Femtosecond Laser Machining

Where the FIB is a valuable tool for machining microtensile samples with dimensions of less than 50 μm, and wire EDM is useful in machining microtensile samples above a few hundred microns to the macroscale, there exists an intermediate length scale where neither technique is effective. One tool that has shown potential for machining samples at this intermediate length scale, however, is the femtosecond laser. The use of femtosecond lasers for various material-removal processes has

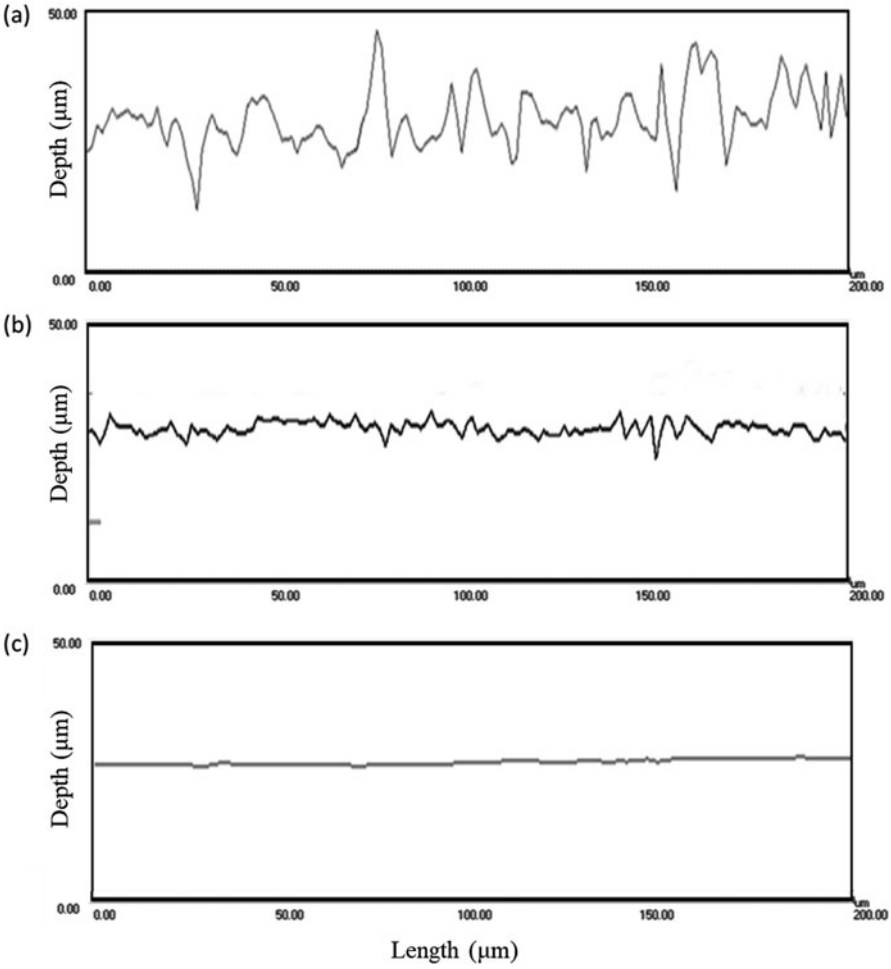

Fig. 3 Surface roughness profiles obtained with confocal laser microscopy for: (**a**) EDM-machined surface with machine recommended parameters, (**b**) EDM-machined surface with optimized parameters, and (**c**) femtosecond laser-machined surface

been demonstrated by multiple groups [2, 71–75], and the use of femtosecond laser for microscale sample fabrication has been demonstrated to be an effective method for precise machining at material removal rates orders of magnitude greater than FIB machining [74–78]. It is also worth noting that, compared to nanosecond and picosecond lasers, femtosecond lasers create much less damage and develop virtually no heat-affected zone in the material being machined [79].

A femtosecond laser-based machining setup was developed as part of CEIMM, in order to fabricate intermediately sized microscale samples. The main component in the setup is a Clark-MXR CPA femtosecond laser which outputs the laser beam

that will be eventually used for ablation of the target material. The maximum output of the laser is 1 W, but the actual power used in machining is 0.1 W or less and can be controlled from the main laser system console. The laser beam is directed into a custom built safety enclosure, where the laser optics and machining components reside. The beam first passes through a waveplate polarizer, which allows for more precise attenuation of the beam as well as the ability to automate the attenuation process. A software interface on the system computer allows for precise rotation of the waveplate to carefully control the laser energy. The beam is then directed within the containment using a series of laser steering mirrors that reflect it to a final dichroic mirror. A dichroic mirror reflects the beam downward to a 10x Mitutoyo NIR objective lens, which focuses the beam to a spot size of about 30 μm for microscale machining. Figures 4 and 5 demonstrate the optical components used from attenuation of laser power and beam steering as well as the optical setup of the camera and dichroic mirror for imaging.

The laser beam has a wavelength of 780 nm, which allows it to be reflected by the dichroic mirror, while visible light still passes through the mirror, allowing for the imaging of the sample with a camera. This makes alignment and positioning of the beam at the beginning of a machining process much easier, as long as the vertical offset between the focal plane of the camera and the focal plane of the laser beam are known. In the current setup, the offset is typically 2.7 ± 0.15 mm. In addition to the various optical components of the setup, there is also a set of Aerotech brand stages that allows for motion on three axes. The objective lens is mounted to a stage that controls the motion in the vertical (Z) direction. The main purpose of this stage is to control the focus of the camera during imaging and the laser during machining. Once the initial height of the objective lens has been established, most stage motion occurs through the two axis X-Y stage. The sample sits on this dual axis stage, and during machining the path that the stage travels is programmed using an Aerobasic

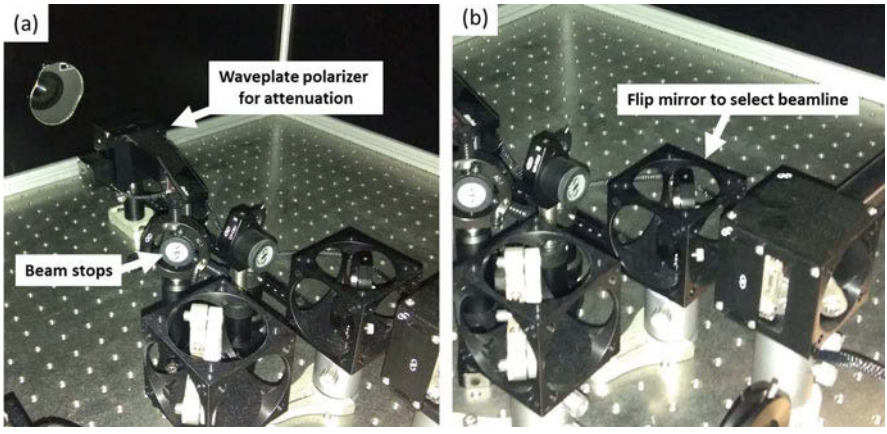

Fig. 4 (**a**) Image of beam ejection site from laser and equipment for beam attenuation and (**b**) optics for switching between laser machining and SEM-based in situ serial sectioning setups

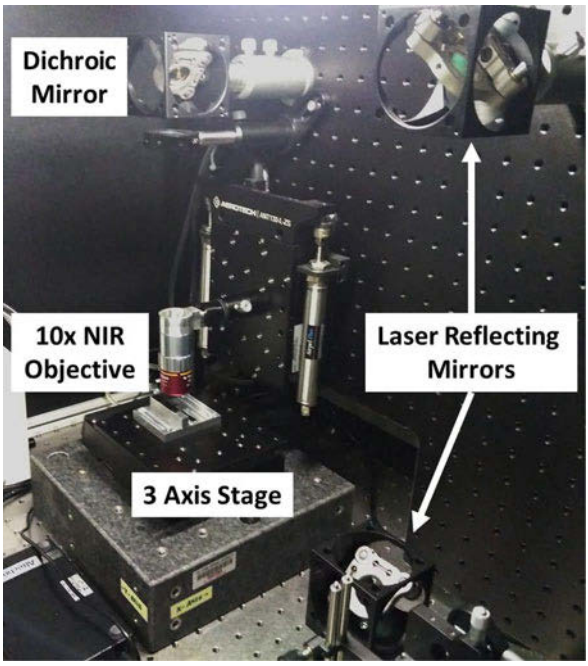

Fig. 5 Image of three-axis stage system and laser machining optics

script in the stage controller software. The laser beam remains focused in the same spot during machining and the sample is moved to trace out the desired shape rather than having the beam move on the sample to perform the machining. The reason for this is that the beam will cut the same way every time since it is stationary, resulting in a consistent machining procedure.

As with any laser system, safety is an important consideration, but especially so in this case because the 780 nm wavelength of the laser beam is invisible to the human eye. Laser safety eyewear must be worn at all times, the laser safety containment box must remain closed during laser machining and a set of safety interlocks installed on the doors to the lab. These interlocks will trip and close the laser shutter if the doors are opened.

As with the other microtensile machining tools described in this chapter, there are many special techniques that can be used with femtosecond laser machining to improve sample quality. Once the spot size of the beam has been properly minimized by adjusting the focal plane, the main parameters that can be changed in the laser machining setup are the energy of the laser and the speed at which the stage moves. The laser energy is a critical aspect to material removal because the ablation threshold must be reached for vaporization of each material [80–83]. Increasing the energy of the beam will result in a higher rate of material removal and a larger effective spot size, because more of the beam at the edges of its Gaussian profile will be above the ablation threshold. However, increasing the energy will also impose more damage in the sample. Care must be taken to select a correct

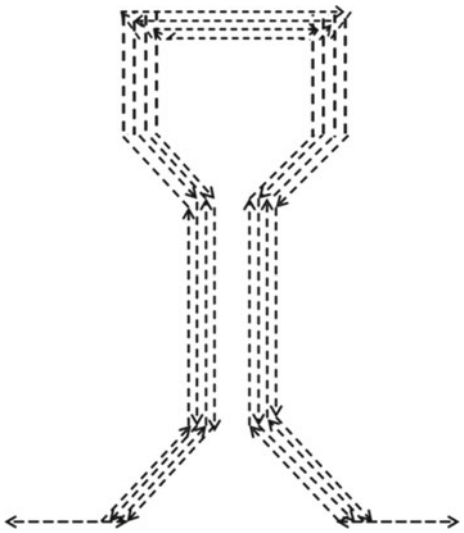

Fig. 6 Schematic of laser machining path for microtensile sample demonstrating trepanning method. Similar to the method presented with the FIB, the sample geometry is cut closer to the final geometry with each pass. For this final shaping of the sample, the laser energy remains the same for each pass and is on the order of 20 μJ for machining René 88DT

energy that is above the ablation threshold of the material, but is not high enough to cause significant damage in the subsurface layer of the material [83–86]. The stage speed and number of passes can also be varied to affect the effective number of laser pulses that hit the sample during machining. A slower speed with fewer passes removes more total material from the sample, but a higher speed with more passes provides a higher quality sample because less redeposited material builds up on it.

Another challenge of laser machining is the taper of the machined sample edges. There are a few techniques that can be used to minimize the effect of taper. One is to use a two-step process, as has been described for FIB and wire EDM machining. An outer series of passes of the sample geometry at higher energy is first used to remove most of the material that needs to be cut away. Then, a series of subsequent passes with less energy is used in a trepanning method in order to achieve the final sample geometry. A diagram showing this trepanning method is shown in Fig. 6. In the current study, each sample was cut using 60 total passes with a beam energy of 50 μJ. Every 10 passes the beam was moved 5 μm closer to the final sample geometry. The first 30 passes were performed using a stage speed of 0.5 mm/s, and the final 30 passes were performed at a faster speed of 2.0 mm/s. This methodology reduces the taper and creates less damage in the final specimen. The taper in a sample can also be reduced by tilting the objective lens that focuses the laser beam on the sample. The objective lens is mounted on a rotator that can be manually adjusted to tilt the incoming beam by about 1 degree, allowing the edge of the beam to cut parallel to the sample edge, rather than at the tapered angle. A drawback of this technique is that changing the cut direction requires changing the tilt of the objective lens on the fly.

Laser machining, and femtosecond laser machining in particular, is a promising technique in sample fabrication with numerous benefits. A main reason the tech-

nique is so promising is that the precision at which samples can be manufactured is close to that of what is possible with an FIB, but laser machining is orders of magnitude faster. The use of a femtosecond laser provides a much cleaner cut than picosecond or nanosecond lasers, because vaporization is more complete and redeposition much lower. The ablation of material through the use of femtosecond laser is difficult to image experimentally, but molecular dynamics (MD) simulations suggest that during femtosecond machining, material is vaporized more rapidly and less heat is stored in the sample, where the former reduces particle redeposition and the latter minimizes the heat-affected zone [79]. Moreover, unlike FIB and EDM, femtosecond laser machining is material agnostic, can be applied to a broad range of materials, and can be used in laboratory air [28].

However, the use of femtosecond laser machining is still under development, and there are drawbacks. One of the most difficult things to control is the redeposition of material that accompanies ablation. A plume of material is released from the sample and tends to redeposit back on the sample or on surrounding surfaces. This can result in redeposited material collecting on other samples or on laser optics. The redeposition can be managed during machining by blowing air over the sample, but this may not be possible for fragile materials or sample geometries. Another option is to use more passes of the sample geometry at a higher speed, which can generate less redeposition, as less material is ejected from the sample and therefore can more easily be removed via vacuum during each pass. In an open-air laboratory setting, environmental effects can also have a nontrivial effect on machining. Fluctuations in temperature and humidity can affect the positioning of optics both internal and external to the laser, which may require recalibration. For this reason, the laser must be maintained within a stable climate to guarantee consistent performance. Additionally, imaging during femtosecond laser machining can be difficult because of the offset between the focal planes of the camera and laser. A second camera and objective could be implemented to observe machining of the sample from the side or at an angle, but it would not provide the best view of the machining process. Finally, as with the FIB, there is a limit to the size of the sample that can be machined using the femtosecond laser. Although ablation rates are significantly higher than with the FIB, there is still a limit at which laser milling becomes inefficient. Making trenches past a certain depth becomes impractical because there is less potential for redeposited material to escape and because of the depth of field of the objective lens. Femtosecond laser machining shows a lot of promise for samples with thickness between 10–300 μm, with great speed and precision at a length scale that is unreachable by other machining techniques, and works for many classes of materials.

3.4 Comparison of Machining Techniques

FIB machining is viable for microtensile samples on the order of tens of microns, laser machining for samples on the order of tens to a few hundreds of microns,

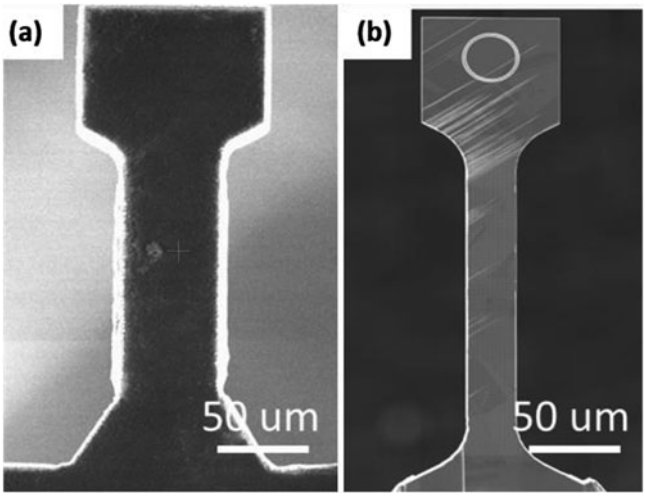

Fig. 7 SEM images of (**a**) bulk-machined microtensile sample of René 88DT with femtosecond laser and (**b**) final milling of the same sample with FIB

and wire EDM for samples larger than that. However, there is some overlap between techniques regarding the scale at which they can be used. In order to better assess how well each technique performs relative to the others, samples of René 88DT machined using each of the techniques were compared. As illustrated by confocal microscopy, the average surface roughness was less than 1 μm for the femtosecond laser, 2 μm for optimized wire EDM cutting, and 20 μm for the commercially recommended wire EDM parameters. Although not measured by confocal microscopy here, the surface roughness of FIB machining was less than 1 μm [63, 87–89]. Although the surface roughness of the laser appears to be minimal in Fig. 3, there is a machining artifact that develops the at the ablated edge of the sample known as Laser Induced Periodic Surface Structures (LIPSS) [90, 91]. The formation of LIPSS is important to note because it limits the scale at which laser machining can be used. LIPSS artifacts, though relatively small, prevent the technique from being used for fine applications, such as TEM foil lift out. The appearance of LIPSS in the material cannot be avoided, but it is possible to affect its orientation by polarization of the laser. The roughness of these structures is on the order of about 100 nm, so for the size of sample being machined in this study it does not impact the mechanical response.

A two-step technique that minimizes the amount of material that must be removed with the FIB can also be employed to produce microtensile samples. An image of a sample that was roughed out of a bulk thin film with the femtosecond laser is shown in Fig. 7a, and that same sample subsequently trimmed using an automated FIB process is shown in Fig. 7b.

It is clear that each of these three machining techniques is relevant at a specific length scale in terms of the rate of material removal, as well as the level of damage

that each imparts. The FIB has been demonstrated to be quite useful for machining sensitive materials or machining at length scales of tens of microns or less with high precision and very low damage. The femtosecond laser, though still a relatively new machining tool, has already been applied in enough cases to demonstrate its utility in machining samples with a thickness ranging from tens of microns to a few hundred microns, with damage scaling with laser beam energy, but able to be controlled to less than a micron in most cases. Although wire EDM is a technique typically applied at the macro scale, with proper optimization it can also be applied at a scale on the order of a few hundred micrometers up to much larger scales, with damage on the order of single-digit microns.

Understanding the capabilities of these three techniques allows a methodology that facilitates machining of materials at multiple length scales in order to study size effects. It can also be applied to develop sample geometries not only for microtensile testing but for developing other microscale samples, such as microcantilevers for studying fatigue or microbending samples for studying fracture toughness. The true benefit of being able to apply these complimentary techniques lies in combining the various techniques to improve the throughput of test samples in a way that has not been achieved previously.

Developing techniques with different material-removal rates and applicable length scales, and optimizing these techniques, is critical to the manufacture and testing of microtensile samples. Sample quality has a significant impact on microtensile results, especially at smaller length scales. There is an inherent stochasticity that arises from testing materials at smaller length scales, specifically in the single crystal and mesoscale regimes where microstructural features give rise to a multitude of material responses. In order to properly study these microstructural and size-scale effects, artifacts from factors such as surface roughness must be mitigated. Due to the variations in the scale of microstructure, it is helpful to have a variety of techniques that can be applied over a range of length scales to provide benchmarks and advance our understanding of microscale mechanical behavior.

4 Sample Size Effects on Strength in René 88DT

It is well known that microstructure plays a significant role in governing the deformation of metals and determining their mechanical properties. Examining the microstructure at different length scales reveals unique mechanisms, such as intragranular interactions of dislocations, phase morphologies at the single crystal scale, and interactions between neighboring grains and twins at the polycrystalline scale. The ability to measure material properties at different length scales is critical to the development of multiscale property prediction models. In this type of modeling, the use of a representative volume element (RVE), which can be further characterized as a property volume element (PVE) or microstructural volume element (MVE), is a key building block for the multiscale framework [92, 93]. These elements represent the volume of material that must be considered to reach a convergence

in a material property, ensuring the results of the model at a larger volume have no side effects with respect to this property of interest. However, there is a lot to be gained in understanding what factors microstructurally affect the convergence of properties to verify that the models capture this behavior at multiple length scales. Observing these trends experimentally and investigating the role of microstructure across length scales are needed to further develop and benchmark well-informed models, such as the crystal plasticity finite element method (CPFEM), that account for the microstructure of materials at the polycrystalline scale [54, 94].

Considerable work has been done to investigate size-scale effects on sample strength in pure metals [95–103], but work on size-scale effects in structural alloys such as René 88DT is more rare. In the current study, samples were tested across multiple length scales, ranging from one grain through the sample thickness up to bulk material, and their yield strengths were determined in order to evaluate the divergence from the bulk strength. It was expected that variability in the data would increase with decreasing sample size as discrete microstructures were realized. Such scatter in mechanical response has been reported in the literature [60] for various experimental designs [2, 93]. Experimentally capturing the size effects over many length scales can provide a systematic approach to defining a RVE, particularly in materials that have not been previously modeled in this manner [99]. The data collected in these experiments provide a better understanding of the role of microstructure and size-scale effects in René 88DT and other FCC materials. Additionally, these methodical studies aid in the development and benchmarking of models that capture mechanical behavior.

Three different sample geometries were manufactured from foils of René 88DT. Each had a uniform gage length, but different gripping strategies were employed. The largest dog bone-shaped samples, with thickness and width ranging from 200–500 μm, were manufactured using wire EDM. Intermediate sized samples, with thicknesses and widths between 50 and 100 μm, were machined using the femtosecond laser. The smallest samples, with thickness and width of 20 μm, were manufactured using automated FIB machining. The volumes tested in the laser and FIB-machined samples provide discrete representation of mesoscale microstructures for René 88DT.

In the Hemker research lab at Johns Hopkins University, there are multiple microtensile testing setups that utilize similar configurations. These load frames have varying load capacities of up to 1200 N and consist of 4 main components: an air bearing, a load cell, a linear actuator, and a mechanism for gripping the samples during a test. The air bearing assures alignment and eliminates friction from the pull bar as it slides during the test. In-line load cells record load data at a rate of 10 points/second, and the screw-driven Zaber linear actuator retracts at a constant speed to achieve nominal strain rate of 10^{-4} per second.

For the dogbone-shaped samples sized 200 μm and larger, a custom set of high strength titanium grips were utilized. One grip was attached to a pull bar that slid within the air bearing while the other grip was mounted on a stationary block. At the beginning of the uniaxial tension test, the sample self-aligned as the shoulders of

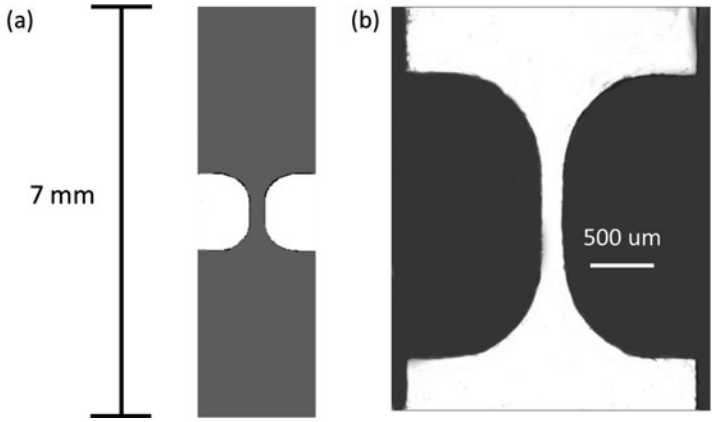

Fig. 8 (**a**) Schematic of femtosecond laser-machined mesoscale sample of René 88 and (**b**) magnified view of sample gage section

the sample slid into place of the custom-designed grips. Once the sample and grips were in full contact, a tensile load was applied by the retraction of the actuator.

For the laser-machined mesoscale samples (2–10 grains through thickness), the same load frame was employed, but a different set of grips was designed for these tests. Despite the gage section of these samples only being 400 μm long, the overall geometry of these samples was 7 mm in length and composed of two large grip sections on either end of the sample. An image of this sample is shown in Fig. 8. This modified grip geometry allowed for the samples to be more easily handled despite the small gage section. Additionally, since the grip geometry remains invariant for these intermediate gage size samples, the same set of grips can be used across all samples machined using this methodology. Unlike the pocket grips used for testing the dogbone samples, the geometry of these grips was plate-like, with a 2 mm alignment ledge cut out at the end. The grips were aligned by placing them in contact with each other, and then the moveable grip was retracted enough to set the sample in place. The sample rests on each end of the cut-out ledges and is affixed to the test plates with Loctite 420 adhesive. The mechanical strength of the dried adhesive is strong enough to hold the sample fixed on each plate as it is pulled in tension.

A 6.6 MP PixeLink camera was mounted above the sample during testing to collect images of the sample during testing that can be postprocessed using digital image correlation (DIC) to calculate strain. Images were acquired once every second during testing for several reasons: to ensure an exposure time of 0.2 s, allow the computer to save images accurately without being slowed down, and simplify the process of obtaining the stress-strain response of tested samples. The latter will be discussed in more detail in this chapter.

For the dogbone-shaped samples, the camera was equipped with an Edmund Optics R-200 rear assembly and OBJ-9 front objective, giving a 5.25×3.86 mm^2 view field. For the laser-machined mesoscale samples, an Edmund Optics R-6 lens

was used in conjunction with a Mitutoyo 10× microscope objective, allowing for a significantly smaller field of view of 1.05 × 0.77 mm^2.

For the 20 μm FIB-machined samples, a separate custom-built load frame was utilized. The frame was displacement-controlled using a piezoelectric actuator, load was measured with a strain gage-based load cell, and mechanical testing was performed in situ in a FEI Quanta SEM. The foil that the samples were machined in was attached to a bulk sample holder that was mounted to an Attocube-controlled x-y-z micro-positioning stage that allowed for precise movement and positioning. The samples were placed into a SiC grip that was 8 mm long and 0.1 mm in diameter and connected directly to a load cell. Stepped quasi-static tests were conducted at an average strain rate of 10^{-4}; the samples were loaded at a constant actuator voltage ramp rate and then held fixed for acquisition of an SEM image. A detailed description of the in-SEM load frame and testing procedure can be found in [104, 105]. The entire process of performing the mechanical testing and collecting SEM images was automated using custom LabVIEW scripts. A periodic grid of 250 nm circular markers, each 200 nm deep with 1 μm spacing, was FIB-milled onto the surface of the samples after final machining [60]. The grid of markers extended along the entire length of the sample gage.

Once the load data from a test was collected, the nominal (engineering) stress was determined from the recorded load and the measured undeformed cross-sectional area of the sample. Each image had a strain and time stamp and each recorded load value had a stress and time stamp, enabling the stress-strain response to be obtained by stitching these two datasets together. To stitch these datasets, the time stamp was matched every 1 s and the associated stress and strain values were extracted. The elastic modulus of the sample was determined from the plot of engineering stress versus strain using the slope of the linear elastic loading of the curve. Alternatively, the elastic modulus can be measured in the plastic region if unload and reload of the sample is performed during testing. The yield strength of each sample was defined by the 0.2% offset.

Figure 9 presents a summary of this yield strength data from the tested samples as a function of the normalized sample width and thickness. This normalized width and thickness was calculated by dividing by the average grain size (20 μm) of the material. Using this parameter gives an idea of the number of grains through the thickness and width of the sample, and thus the total number of grains within a sample gage volume.

The largest samples were 500 μm thick (normalized thickness of 25) and their yield strength is consistent and comparable to bulk values from the literature [51, 106]. As the sample thickness decreases to 300 μm (normalized thickness of 15), the average yield strength decreases slightly but remains consistent from sample to sample, varying by less than 3%. Below this size, however, we begin to see significant variations in sample strength, down to a value of 650 MPa for samples with a normalized thickness of 1.

Two literature values of the bulk strength are compared with the experimental data in Fig. 9 [107, 108], and it was found that the variations in the experimental measurements are much greater, sometimes by an order of magnitude. The error

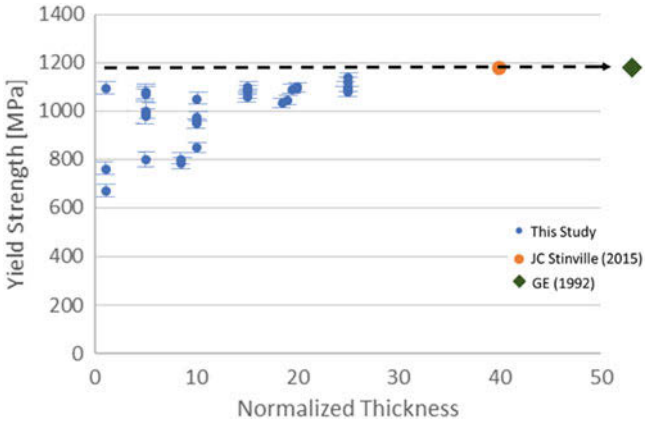

Fig. 9 Plot of sample yield strength vs normalized sample thickness and reference data from literature. The error bars on each data point represent the maximum potential error of each measurement

bars for each sample in Fig. 9 represent the maximum potential error for the measurement. The maximum total error, calculated from the maximum error of all sources of measurement errors in the experimental design, was found to be 6.6%, corresponding to a stress of 40–50 MPa. This indicates that experimental error cannot account for the data scatter, and that the scatter in the experimentally measured yield strengths is an effect of the sampled microstructure. The overall increase in scatter with decreasing sample size matches the expectation that smaller samples are dominated by a limited number of grains, and therefore microstructure plays a more significant role in determining the strength of the sample. By comparison, larger samples have many grains and the microstructural effects are averaged out.

Although the scatter matches the predicted variability of yield strength as a function of sample size, no increase in yield strength was observed at any sample size as was initially expected. In order to understand this behavior in more detail, a numerical study was performed, in collaboration with George Weber et al., to investigate the potential role of grain orientation on the distribution of resolved shear stresses for polycrystalline samples of variable size [60]. This simple model was based on Schmid factor analysis and conducted to gain insight into how finite sampling of grain orientation would affect the measured strength. This is a qualitative approach, since it ignores grain-to-grain interactions and the complex nonuniaxial loading states that may arise within individual grains [20].

For this estimate, the gage volume of a tensile sample was modeled with cubic grains of a uniform size, and the sample was taken to have a square cross-section and a 5:1 aspect ratio. Each grain within the gage was assigned a random orientation and its maximum Schmid factor was calculated, defining the corresponding strength of that grain. The strength of a sample was determined as follows. The individual

strength of each cross-sectional layer, which contains grains loaded in parallel, was defined to be equal to the strength of the grain with the lowest Schmid factor in that layer. Then, the yield strength of the sample was defined using a weakest link approximation along the length of the gage. The strength of the layers loaded serially was taken to be the same as the weakest layer.

In developing this model, an interesting trend with regards to Schmid factor distributions in a randomly textured FCC alloy was observed. When considering <110>{111} FCC slip systems, randomly oriented grains generate a high propensity for high Schmid factors; 50% of grains have a maximum resolved Schmid factor of 0.45 or higher [60]. By contrast, the probability of finding a grain with a low maximum resolved Schmid factor is much smaller. The chance of having a sample with all layers dominated by grains with low maximum resolved Schmid factors (high strength) is in fact very rare and decreases with increasing sample size.

Calculations were conducted for thousands of synthetic samples, from as small as one grain through the thickness to up to 30 grains through the thickness. The results showed that while it is geometrically possible to arrange the grains in small samples such that they have a higher-than-average resolved Schmid factor, and thus a lower-than-average overall strength, the converse is much less likely [60]. This outcome helps explain the increased scatter that is observed in the experimentally measured yield strength with decreasing sample size, as well as why the strength of oligocrystals (with finite numbers of grains) can be weaker, but not stronger, than the bulk strength of the polycrystalline alloy. Although this simple numerical analysis contains many assumptions and ignores the effects of load shedding, free surfaces, and grain size and shape, the qualitative influence of how the finite sampling of grain orientations results in decreasing strength and increasing scatter with decreasing sample size is demonstrated.

Physics-based CPFEM offers a more quantitative approach for modeling the strength of oligocrystals, and the experimentally measured size dependence of strength can be used to benchmark and validate such models. The use of oligocrystals allows for measurements that are much more sensitive to microstructural variations than bulk samples. One such example involves the work of Bagri et al., who employed statistically equivalent representative volume elements (SERVEs) to determine convergence of properties as a function of the size of a sample microstructural volume [109]. This approach is typically used to find a measurement of the proper size RVE needed for convergence of a property and can also be used to predict the effect of sample size on strength. Starting from a large SERVE that produces a bulk value for yield strength, and then decreasing the SERVE size, leads to an increased scatter in strength that is also seen experimentally. However, theses simulations predict that the sample strength will both increase and decrease at smaller sample sizes, while the experiments only documented a decrease in strength at smaller sample sizes. There is a difference in the SERVE geometry as compared to the tested sample geometry, which may account for the difference between simulation and experiment. The SERVE geometry is a cube, whereas the sample geometry has a rectangular shape in order to comply with ASTM tensile testing standards. The influence of microstructure is different for cubes and rectangles, with

the weakest link effect being more prominent in the latter. The cube volume of a SERVE is more likely to capture single crystal-like behavior and show the full range of feasible single crystal orientations and strengths. Conversely, the rectangular microtensile geometry has multiple grains along the sample length and is much less likely to exhibit strength values that exceed the bulk strength. The small cubes also contain a higher fraction of surface grains, which must be properly accounted for in the free boundary condition of the SERVE. These combined factors provide some understanding for the observed discrepancy and may be used to develop more detailed physics-based CPFEM models.

The progress reported in this chapter is summarized as follows. An experimental methodology for machining and testing microtensile samples of Ni-base superalloy René 88DT across multiple length scales was developed, with the intention of studying the effect of sample size on yield strength. The expectation that sample microstructure plays a larger role at smaller sample sizes was confirmed. The yield strength was observed to decrease with sample size, and increased scatter in yield strength values was correlated with decreased sample size. Contrary to initial expectations, none of the tested samples exhibited greater strength than the bulk value for this material. The trends seen in the experimental data were studied using simulations with varying levels of complexity. It was shown that the distribution of maximum Schmid factor for randomly orientated grains in an FCC alloy is biased towards high Schmid factors, and that geometric averaging of these grains in ever smaller volumes leads to decreased strength and increased scatter. The geometry of the sample can also have an effect, as seen by comparison of the SERVE predictions and the experimental results. These results provide insight into the influence of polycrystalline microstructure on the mechanical properties of an alloy and a means of quantifying this behavior to inform selection of RVEs and the creation of multiscale models. Further work on mesoscale oligocrystals shows great promise in facilitating explicit comparisons of CPFEM simulations and experimental results. An end goal for benchmarking the CPFEM models would be the measurement and modeling of an explicit oligocrystalline specimen where every grain orientation, size, and shape is known and can be recreated in silico.

5 Orientation and Deformation Maps

Traditional methods for qualifying structural materials using bulk material testing provide global properties but fail to capture the detailed underlying microstructural dependencies that can now be included in high-fidelity multiscale models. Measured global properties such as yield strength, elastic modulus, or strain to failure are valuable benchmarks for deformation modeling, but recent advances in characterization techniques have made it possible to obtain local microstructural details and scale-specific benchmarks. Here, we focus on efforts undertaken to perform detailed microstructural characterization of René 88DT samples in 2D and 3D. The distribution of local surface strains is a direct output of CPFEM and is also

measurable experimentally through the use of 2D digital image correlation (DIC) surface strain mapping. The creation of strain maps allows for the quantification of strain localization on the sample surface and provides insight into how local microstructural features influence deformation, both of which can be used as explicit benchmarks for CPFEM. Local measurements such as these are needed to inform and benchmark CPFEM modeling efforts.

The procedure for performing DIC on the FIB microtensile samples included tracking of circular markers, machined into the sample surface with the FIB. Femtosecond laser-machined specimens were speckled with 50 nm diameter alumina particles and distortions in the speckle pattern recorded at successive stages of deformation. VIC2D was used to analyze the captured images and make 2D strain maps. Correlating the strain maps with EBSD orientation maps allowed us to identify the features in the microstructure that were present when plastic strain developed and how the plastic deformation spread throughout the sample. Further insights were gained by calculating the Schmid factor and elastic modulus for each grain with the TSL OIM software.

An example of the surface strain evolution of a sample with a 50×50 μm cross section is shown in Fig. 10. The strain plotted on this map is the local axial strain in the loading direction. The snapshots presented in this figure demonstrate how the strain in the sample first starts to nucleate and then eventually concentrates in one location in the sample as the test proceeds. The global strain that the sample experiences is labeled at the corner of each image and can be used to determine how much greater the local strain is at these local hotspots. This behavior captures the heterogeneous distribution of strain in a polycrystalline sample and can provide both a qualitative and quantitative benchmark for CPFEM simulations. Correlating these strain maps with the orientation information obtained from EBSD allows one to identify microstructural characteristics that influence deformation in the sample.

To further look at the deformation behavior of these samples, these strain maps were correlated with orientation information obtained from EBSD to investigate microstructural features that lead to deformation. A summary of results for the sample shown in Fig. 10 is shown in Fig. 11. Starting from the top of Fig. 11 and working down, what is being presented for this sample are: (a) a 2D map of the surface orientation data collected from EBSD with each grain and twin colored according to its out of plane orientation, (b) a 2D map with each grain and twin colored according to its Schmid factor calculated based on the sample loading direction and the EBSD data, (c) a 2D map of each grain and twin colored according to its Young's modulus calculated along the sample loading direction from the EBSD data and the stiffness constants of the material, and (d) an overlay of the 2D strain map from Fig. 12 on an outline of the grain boundaries determined from the EBSD orientation data. Each map is accompanied by a scale for the information plotted on the maps.

The information compiled in Fig. 11 indicates that, in this sample, the strain hotspot shown in Fig. 11d formed in the grain at the center of the sample that is denoted by a blue color in the elastic modulus map of Fig. 11c. This grain had a relatively high Schmid factor of 0.45 (greater than 60% of grains within the sample)

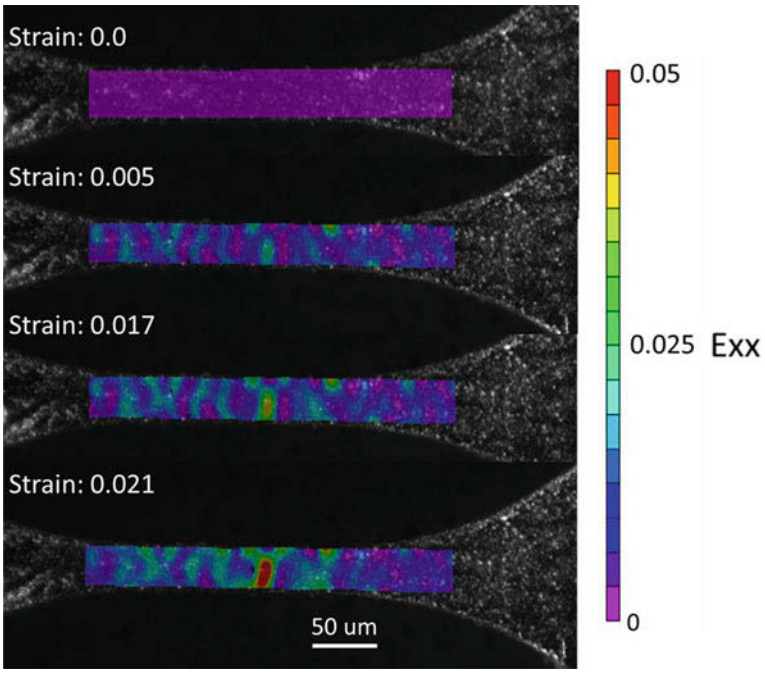

Fig. 10 Progression of surface strain in microsample of René 88 at different levels of global strain

and low elastic modulus of 72 GPa (less than 95% of grains within the sample). The high Schmid factor points to the importance of resolved shear stresses on primary slip systems; however, it is important to note that this is not the grain with the highest Schmid factor, and that simply looking at individual grain orientations is not sufficient. Clearly, other factors such as load sharing or shedding amongst neighboring grains play an important role in strain localization [29, 110, 111].

Closer examination of Fig. 11 indicates that the region of the sample to the left of the strain concentration is composed of a grain that exhibits both a low Schmid factor (0.3) and a high elastic modulus (210 GPa), the opposite characteristics from the grain in which strain is concentrated. In addition, the twins in this grain also exhibit an elastic mismatch with the parent grain. Studies investigating the fatigue behavior of René 88DT, for example, Stinville et al. [29, 51, 112] and Alam et al. [110], have elucidated that crack nucleation occurs in twins in which there is a high Schmid factor and a mismatch in elastic modulus between the twin and the parent grain. These characteristics have been shown to result in a stress concentration and to facilitate the formation of fatigue cracks. Similarly, the mismatches of elastic modulus illustrated in Fig. 11c appear to result in a stress concentration. Modern CPFEM models may be expected to capture and quantify these stress concentrations and predict the onset and propagation of local intragranular plasticity in favorably oriented grains in appropriate neighborhoods.

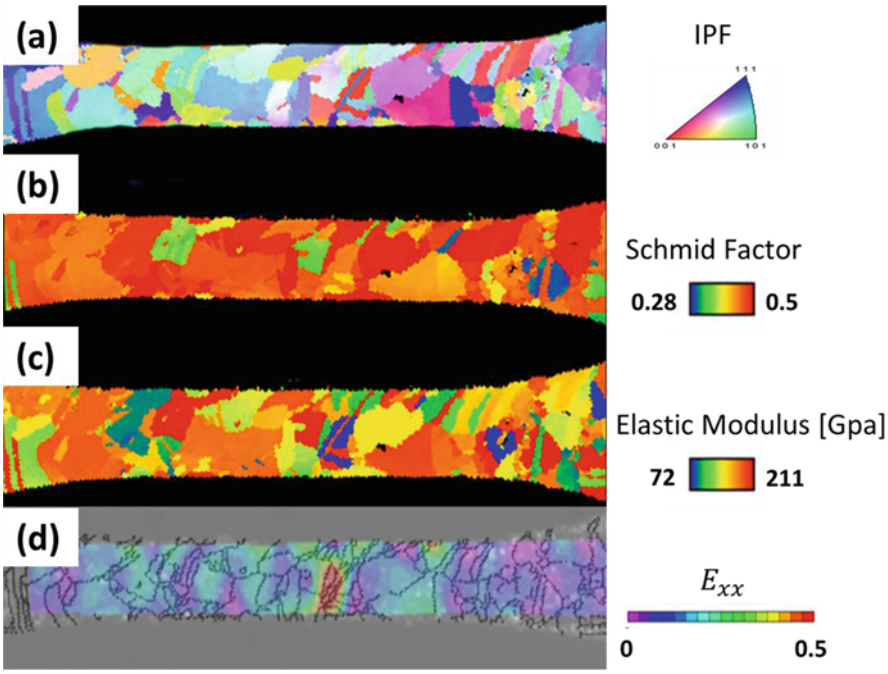

Fig. 11 Surface maps of a 50 × 50 μm tested microsample showing: (**a**) grain orientations using standard IPF coloring for FCC, (**b**) Maximum Schmid factors for each grain, (**c**) the Young's modulus along the loading direction for each grain, and (**d**) a comparison of the surface strain with the grains that make up the polycrystalline microstructure

The combination of 2D surface strain mapping and microstructural characterization is a powerful tool for benchmarking microstructurally dependent models. However, subsurface grains can significantly affect observations made at the sample surface, as shown in microtensile samples of pure Ni [22, 24]. A 3D dataset of the full sample microstructure would avoid such complications, and using explicit 3D microstructural datasets as input for CPFEM simulations would facilitate direct one-to-one comparisons and provide a significant step forward.

Although still in their adolescence, laser-based and mechanical serial sectioning techniques, and emerging nondestructive characterization techniques such as high energy diffraction microscopy (HEDM), provide a means to digitally capture 3D volumes that could be utilized to instantiate a simulation and directly compare with experimental results. Figure 12 presents a roadmap and initial proof-of-concept results for collecting and using 3D digital microstructures to instantiate CPFEM simulations. Once collected, the digital microstructural dataset must be properly segmented in order to properly identify grains and twins. Once identified, each

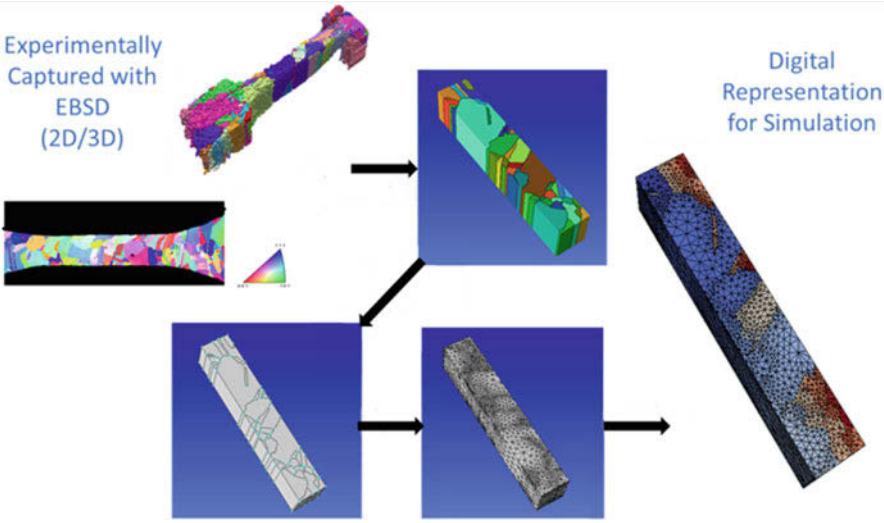

Fig. 12 Progression from experimentally captured digital microstructure to meshed structure ready for simulation. Digital segmentation based on identifying individual features such as grains is performed, followed by assigning properties to each feature and generating a mesh for performing a CPFEM simulation

of these features can be assigned properties based on their orientation, and a finite element mesh can be developed to model the microstructure using the CPFE method.

While this framework for generating explicit benchmarks from combined mechanical testing and 3D dataset generation seems straightforward, the collection of experimental data to instantiate a simulation is nontrivial. Two major limitations reside in the amount of data that can be handled in 3D datasets and the volumes that can be captured in computational models. CPFEM requires a fine mesh to capture grain-level details and an even finer mesh to account for intragranular features such as twins that are common in René 88DT. For René 88DT, this creates the challenge to design and test a sample volume that contains a reasonable number of grains to model at the spatial resolution of about 0.5 μm necessary to accurately capture the twin structures present. Designing and mechanically testing appropriately sized samples is the primary focus of this chapter, but initial attempts at pairing of these tests with explicit 3D datasets of the entire sample shows considerable promise. Realizing this promise will require development of a technique to protect and section freestanding samples using protective layers that eliminate sectioning artifacts. 3D serial sectioning methods and emerging nondestructive characterization techniques like HEDM have considerable promise, especially with the on-going development of infrastructure for big data management.

6 Chapter Summary

Microtensile testing protocols and unique characterization routes have been developed and employed to obtain multiscale, microstructurally dependent benchmarks for CPFEM models of commercial polycrystalline alloys, such as René 88DT. Initial microtensile testing was performed on samples with gage cross sections on the order of a few hundred microns machined via Wire EDM and on much smaller samples with gage cross sections of 20×20 μm machined using a FIB. The samples machined with wire EDM exhibited a mechanical response that was very similar to the bulk material. The much smaller FIB-machined samples were more tractable for CPFEM simulations but were found to be too small to capture a true polycrystalline response. A femtosecond laser machining protocol was developed and used to machine microtensile samples with cross-sectional dimensions of 50–100 microns at a rate that was an order of magnitude faster than FIB milling; machining of samples 25 times larger than could be achieved with the FIB was accomplished in a matter of minutes.

Testing samples of different sizes revealed an inherent effect of sample size on yield strength. It was seen that the sample strength decreased with decreasing sample size and that the variability of the measured strengths increased as the sample size decreased. These variations are attributed to the influence of geometric averaging of oligocrystalline specimens. Combining the microtensile tests with local strain and orientation mapping provided robust microstructural benchmarks for direct comparisons with CPFEM simulations. More than just acquiring the bulk stress-strain response of a sample, investigating local response of the material and the corresponding microstructural features that lead to this behavior provides a new level of benchmarking for ever-improving CPFEM modeling capabilities. Local strain maps can be used to compare directly with simulations instantiated with the microstructural data of these samples. This explicit benchmark is both quantitative in terms of the local magnitudes of strain observed as well as qualitative in terms of where in the microstructure these concentrations are located. Moreover, the correlation of microstructural information with strain maps enhances mechanistic understanding and provides detailed microstructural benchmarks. Ensuring that this behavior is captured in CPFEM simulations should be a key goal of future model development.

The long-term goal of this work was to be able to explicitly characterize tested samples in 3D to be able to instantiate simulations and collect attendant 3D benchmarks of mechanical behavior. The development and availability of advanced characterization and mechanical testing techniques, like the ones outlined in this chapter, make it possible to marry experimental and modeling like never before. While challenges of benchmarking with 3D data within the ICME paradigm still exist, such as error propagation from experimental results and the handling of large datasets, the need and opportunity for making this level of analysis more routine and readily available for model development is clear.

References

1. S. Ghosh, D.M. Dimiduk, *Computational Methods for Microstructure-Property Relationships* (Springer, New York, NY, 2011)
2. M.P. Echlin et al., The TriBeam system: femtosecond laser ablation in situ SEM. Mater. Charact. **100**, 1–12 (2015)
3. R. Becker, S. Panchanadeeswaran, Effects of grain interactions on deformation and local texture in polycrystals. Acta Metall. Mater. **43**(7), 2701–2719 (1995)
4. N. Zhang, W. Tong, An experimental study on grain deformation and interactions in an Al-0.5% Mg multicrystal. Int. J. Plast. **20**(3), 523–542 (2004)
5. K.-S. Cheong, E.P. Busso, Effects of lattice misorientations on strain heterogeneities in FCC polycrystals. J. Mech. Phys. Solids **54**(4), 671–689 (2006)
6. S.R. Kalidindi, A. Bhattacharyya, R.D. Doherty, Detailed analyses of grain–scale plastic deformation in columnar polycrystalline aluminium using orientation image mapping and crystal plasticity models. Proc. R. Soc. Lond. Ser. A **460**(2047), 1935–1956 (2004)
7. C. Rehrl et al., Crystal orientation changes: a comparison between a crystal plasticity finite element study and experimental results. Acta Mater. **60**(5), 2379–2386 (2012)
8. Z. Zhao et al., Investigation of three-dimensional aspects of grain-scale plastic surface deformation of an aluminum oligocrystal. Int. J. Plast. **24**(12), 2278–2297 (2008)
9. H. Lim et al., Grain-scale experimental validation of crystal plasticity finite element simulations of tantalum oligocrystals. Int. J. Plast. **60**, 1–18 (2014)
10. E. Héripré et al., Coupling between experimental measurements and polycrystal finite element calculations for micromechanical study of metallic materials. Int. J. Plast. **23**(9), 1512–1539 (2007)
11. A. Bhattacharyya et al., Evolution of grain-scale microstructure during large strain simple compression of polycrystalline aluminum with quasi-columnar grains: OIM measurements and numerical simulations. Int. J. Plast. **17**(6), 861–883 (2001)
12. T.J. Turner, S.L. Semiatin, Modeling large-strain deformation behavior and neighborhood effects during hot working of a coarse-grain nickel-base superalloy. Model. Simul. Mater. Sci. Eng. **19**(6), 065010 (2011)
13. L. St-Pierre et al., 3D simulations of microstructure and comparison with experimental microstructure coming from OIM analysis. Int. J. Plast. **24**(9), 1516–1532 (2008)
14. A. Musienko et al., Three-dimensional finite element simulation of a polycrystalline copper specimen. Acta Mater. **55**(12), 4121–4136 (2007)
15. A. Lewis et al., Two-and three-dimensional microstructural characterization of a super-austenitic stainless steel. Mater. Sci. Eng. A **418**(1–2), 11–18 (2006)
16. J. Alkemper, P. Voorhees, Quantitative serial sectioning analysis. J. Microsc. **201**(3), 388–394 (2001)
17. J.E. Spowart, H.E. Mullens, B.T. Puchala, Collecting and analyzing microstructures in three dimensions: a fully automated approach. JOM **55**(10), 35–37 (2003)
18. J.E. Spowart, Automated serial sectioning for 3-D analysis of microstructures. Scr. Mater. **55**(1), 5–10 (2006)
19. M.D. Uchic et al., Augmenting the 3D characterization capability of the dual beam FIB-SEM. Microsc. Microanal. **10**(S02), 1136–1137 (2004)
20. M.A. Groeber et al., 3D reconstruction and characterization of polycrystalline microstructures using a FIB–SEM system. Mater. Charact. **57**(4–5), 259–273 (2006)
21. N. Zaafarani et al., Three-dimensional investigation of the texture and microstructure below a nanoindent in a Cu single crystal using 3D EBSD and crystal plasticity finite element simulations. Acta Mater. **54**(7), 1863–1876 (2006)
22. P.A. Shade et al., Micro-tensile testing and 3D-EBSD characterization of pure nickel multi-crystals (preprint). (Air Force Research Lab Wright-Patterson AFB OH Materials and Manufacturing DIR Metals Ceramics and Nondestructive Evaluation DIV/Metals Branch, 2011)

23. P.A. Shade et al., Experimental measurement of surface strains and local lattice rotations combined with 3D microstructure reconstruction from deformed polycrystalline ensembles at the micro-scale. Integr. Mater. Manuf. Innov. **2**(1), 5 (2013)
24. T. Turner et al., The influence of microstructure on surface strain distributions in a nickel micro-tension specimen. Model. Simul. Mater. Sci. Eng. **21**(1), 015002 (2012)
25. L. Kwakman et al., Sample preparation strategies for fast and effective failure analysis of 3D devices, in *39th International Symposium for Testing and Failure Analysis,* San Jose*,* California, 2013
26. Y. Xiao et al., Investigation of the deformation behavior of aluminum micropillars produced by focused ion beam machining using Ga and Xe ions. Scr. Mater. **127**, 191–194 (2017)
27. T.L. Burnett et al., Large volume serial section tomography by Xe plasma FIB dual beam microscopy. Ultramicroscopy **161**, 119–129 (2016)
28. M.P. Echlin et al., A new TriBeam system for three-dimensional multimodal materials analysis. Rev. Sci. Instrum. **83**(2), 023701 (2012)
29. J. Stinville et al., A combined grain scale elastic–plastic criterion for identification of fatigue crack initiation sites in a twin containing polycrystalline nickel-base superalloy. Acta Mater. **103**, 461–473 (2016)
30. H.F. Poulsen, *Three-Dimensional X-Ray Diffraction Microscopy: Mapping Polycrystals and Their Dynamics*, vol 205 (Springer Science & Business Media, New York, NY, 2004)
31. U. Lienert et al., High-energy diffraction microscopy at the advanced photon source. JOM **63**(7), 70–77 (2011)
32. H.F. Poulsen et al., Three-dimensional maps of grain boundaries and the stress state of individual grains in polycrystals and powders. J. Appl. Crystallogr. **34**(6), 751–756 (2001)
33. J.V. Bernier et al., Far-field high-energy diffraction microscopy: a tool for intergranular orientation and strain analysis. J. Strain Anal. Eng. Design **46**(7), 527–547 (2011)
34. H.F. Poulsen et al., Three-dimensional maps of grain boundaries and the stress state of individual grains in polycrystals and powders. J. Appl. Crystallogr. **34**(6), 751–756 (2001)
35. E.M. Lauridsen et al., Tracking: a method for structural characterization of grains in powders or polycrystals. J. Appl. Crystallogr. **34**(6), 744–750 (2001)
36. S. Li, R. Suter, Adaptive reconstruction method for three-dimensional orientation imaging. J. Appl. Crystallogr. **46**(2), 512–524 (2013)
37. R. Suter et al., Forward modeling method for microstructure reconstruction using x-ray diffraction microscopy: single-crystal verification. Rev. Sci. Instrum. **77**(12), 123905 (2006)
38. L. Margulies et al., Strain tensor development in a single grain in the bulk of a polycrystal under loading. Acta Mater. **50**(7), 1771–1779 (2002)
39. J. Oddershede et al., Determining grain resolved stresses in polycrystalline materials using three-dimensional X-ray diffraction. J. Appl. Crystallogr. **43**(3), 539–549 (2010)
40. P.A. Shade et al., A rotational and axial motion system load frame insert for in situ high energy x-ray studies. Rev. Sci. Instrum. **86**(9), 093902 (2015)
41. J.C. Schuren et al., New opportunities for quantitative tracking of polycrystal responses in three dimensions. Curr. Opinion Solid State Mater. Sci. **19**(4), 235–244 (2015)
42. T.J. Turner et al., Crystal plasticity model validation using combined high-energy diffraction microscopy data for a Ti-7Al specimen. Metall. Mater. Trans. A **48**(2), 627–647 (2017)
43. K. Hemker, W. Sharpe Jr., Microscale characterization of mechanical properties. Annu. Rev. Mater. Res. **37**, 93–126 (2007)
44. H. Espinosa, B. Prorok, M. Fischer, A methodology for determining mechanical properties of freestanding thin films and MEMS materials. J. Mech. Phys. Solids **51**(1), 47–67 (2003)
45. H. Espinosa, B. Prorok, B. Peng, Plasticity size effects in free-standing submicron polycrystalline FCC films subjected to pure tension. J. Mech. Phys. Solids **52**(3), 667–689 (2004)
46. M. Haque, M. Saif, In-situ tensile testing of nano-scale specimens in SEM and TEM. Exp. Mech. **42**(1), 123–128 (2002)
47. S. Greek, S.A. Johansson, *Tensile testing of thin-film microstructures, in Micromachined Devices and Components III*, (International Society for Optics and Photonics, Bellingham, WA, 1997)

48. W.N. Sharpe Jr., *An Interferometric Strain-Displacement Measurement System* (National Aeronautics and Space Administration, Langley Research Center, Hampton, 1989)
49. T. Chu, W. Ranson, M.A. Sutton, Applications of digital-image-correlation techniques to experimental mechanics. Exp. Mech. **25**(3), 232–244 (1985)
50. A.D. Kammers, S. Daly, Self-assembled nanoparticle surface patterning for improved digital image correlation in a scanning electron microscope. Exp. Mech. **53**(8), 1333–1341 (2013)
51. J.C. Stinville et al., High resolution mapping of strain localization near twin boundaries in a nickel-based superalloy. Acta Mater. **98**, 29–42 (2015)
52. C. Montgomery, B. Koohbor, N.R. Sottos, A robust patterning technique for electron microscopy-based digital image correlation at sub-micron resolutions. Exp. Mech. **59**(7), 1063–1073 (2019)
53. T.M. Pollock, S. Tin, Nickel-based superalloys for advanced turbine engines: chemistry, microstructure and properties. J. Propuls. Power **22**(2), 361–374 (2006)
54. S. Keshavarz, S. Ghosh, Multi-scale crystal plasticity finite element model approach to modeling nickel-based superalloys. Acta Mater. **61**(17), 6549–6561 (2013)
55. V.T. Srikar, S. Spearing, A critical review of microscale mechanical testing methods used in the design of microelectromechanical systems. Exp Mech **43**, 238–247 (2003)
56. D.S. Gianola, C. Eberl, Micro- and nanoscale tensile testing of materials. JOM **61**(3), 24 (2009)
57. ASTM, E8/E8M-13, *Standard Test Methods for Tension Testing of Metallic Materials* (ASTM International, West Conshohocken, PA, 2013)
58. M.D. Uchic et al., Sample dimensions influence strength and crystal plasticity. Science **305**(5686), 986–989 (2004)
59. L.A. Giannuzzi, F.A. Stevie, A review of focused ion beam milling techniques for TEM specimen preparation. Micron **30**(3), 197–204 (1999)
60. D.W. Eastman et al., Benchmarking crystal plasticity models with microtensile evaluation and 3D characterization of René 88DT, in *Superalloys 2016: Proceedings of the 13th Intenational Symposium of Superalloys*. Wiley Online Library
61. L. Frey, C. Lehrer, H. Ryssel, Nanoscale effects in focused ion beam processing. Appl. Phys. A **76**(7), 1017–1023 (2003)
62. D.P. Adams et al., Micromilling of metal alloys with focused ion beam–fabricated tools. Precis. Eng. **25**(2), 107–113 (2001)
63. J. Orloff et al., High resolution focused ion beams: FIB and its applications. Phys. Today **57**(1), 54–55 (2004)
64. P.R. Munroe, The application of focused ion beam microscopy in the material sciences. Mater. Charact. **60**(1), 2–13 (2009)
65. K.H. Ho, S.T. Newman, State of the art electrical discharge machining (EDM). Int. J. Mach. Tools Manuf. **43**(13), 1287–1300 (2003)
66. S. Mahendran et al., A review of micro-EDM. Proceedings of the international multi conference of engineers and computer scientists, vol. 2, (2010)
67. R. Bobbili, V. Madhu, A.K. Gogia, Effect of wire-EDM machining parameters on surface roughness and material removal rate of high strength armor steel. Mater. Manuf. Process. **28**(4), 364–368 (2013)
68. Y.S. Liao, J.T. Huang, Y.H. Chen, A study to achieve a fine surface finish in wire-EDM. J. Mater. Process. Technol. **149**(1), 165–171 (2004)
69. R. Ramakrishnan, L. Karunamoorthy, Multi response optimization of wire EDM operations using robust design of experiments. Int. J. Adv. Manuf. Technol. **29**(1), 105–112 (2006)
70. P.S. Rao, K. Ramji, B. Satyanarayana, Experimental investigation and optimization of wire EDM parameters for surface roughness, MRR and white layer in machining of aluminium alloy. Procedia Mater. Sci. **5**, 2197–2206 (2014)
71. Q. Feng et al., Femtosecond laser machining of single-crystal superalloys through thermal barrier coatings. Mater. Sci. Eng. A **430**(1), 203–207 (2006)
72. N.H. Rizvi, Femtosecond laser micromachining: current status and applications. Riken review, 2003: p. 107–112

73. S.K. Slaughter et al., High throughput femtosecond-laser machining of micro-tension specimens, in *TMS 2015 144th Annual Meeting & Exhibition*, (Springer, New York, NY, 2015)
74. C.B. Schaffer et al., Micromachining bulk glass by use of femtosecond laser pulses with nanojoule energy. Opt. Lett. **26**(2), 93–95 (2001)
75. M.J. Pfeifenberger et al., The use of femtosecond laser ablation as a novel tool for rapid micro-mechanical sample preparation. Mater. Des. **121**, 109–118 (2017)
76. S.A. Akhmanov, V.A. Vysloukh, A.S. Chirkin, *Optics of Femtosecond Laser Pulses* (Izdatel Nauka, Moscow, 1988)
77. P.P. Pronko et al., Machining of sub-micron holes using a femtosecond laser at 800 nm. Opt. Commun. **114**(1), 106–110 (1995)
78. D. von der Linde, K. Sokolowski-Tinten, J. Bialkowski, Laser–solid interaction in the femtosecond time regime. Appl. Surf. Sci. **109–110**, 1–10 (1997)
79. D. Perez, L.J. Lewis, Molecular-dynamics study of ablation of solids under femtosecond laser pulses. Phys. Rev. B **67**(18), 184102 (2003)
80. S. Preuss, A. Demchuk, M. Stuke, Sub-picosecond UV laser ablation of metals. Appl. Phys. A **61**(1), 33–37 (1995)
81. M.D. Shirk, P.A. Molian, A review of ultrashort pulsed laser ablation of materials. J. Laser Appl. **10**(1), 18–28 (1998)
82. A. Ostendorf, Femtosecond laser machining, in *Technical Digest. CLEO/Pacific Rim 2001. 4th Pacific Rim Conference on Lasers and Electro-Optics (Cat. No.01TH8557)*, 2001
83. S. Ma et al., Femtosecond laser ablation regimes in a single-crystal superalloy. Metall. Mater. Trans. A **38**(13), 2349–2357 (2007)
84. W. Zhang et al., Femtosecond laser machining characteristics in a single-crystal superalloy. Rare Metals **30**(1), 639–642 (2011)
85. N.G. Semaltianos et al., Femtosecond laser ablation characteristics of nickel-based superalloy C263. Appl. Phys. A **94**(4), 999 (2008)
86. E.G. Gamaly et al., Ablation of solids by femtosecond lasers: ablation mechanism and ablation thresholds for metals and dielectrics. Phys. Plasmas **9**(3), 949–957 (2002)
87. D. Di Maio, S.G. Roberts, Measuring fracture toughness of coatings using focused-ion-beam-machined microbeams. J. Mater. Res. **20**(2), 299–302 (2005)
88. J. McCarthy et al., FIB micromachined submicron thickness cantilevers for the study of thin film properties. Thin Solid Films **358**(1), 146–151 (2000)
89. D. Kiener et al., FIB damage of Cu and possible consequences for miniaturized mechanical tests. Mater. Sci. Eng. A **459**(1–2), 262–272 (2007)
90. J. Sipe et al., Laser-induced periodic surface structure. I. Theory. Phys. Rev. B **27**(2), 1141 (1983)
91. J. Bonse et al., Femtosecond laser-induced periodic surface structures. J. Laser Appl. **24**(4), 042006 (2012)
92. R. Hill, Elastic properties of reinforced solids: some theoretical principles. J. Mech. Phys. Solids **11**(5), 357–372 (1963)
93. M.P. Echlin, W.C. Lenthe, T.M. Pollock, Three-dimensional sampling of material structure for property modeling and design. Int. Mater. Manuf. Innov. **3**(1), 21 (2014)
94. A. Ma, F. Roters, D. Raabe, A dislocation density based constitutive model for crystal plasticity FEM including geometrically necessary dislocations. Acta Mater. **54**(8), 2169–2179 (2006)
95. M.D. Uchic, D.M. Dimiduk, A methodology to investigate size scale effects in crystalline plasticity using uniaxial compression testing. Mater. Sci. Eng. A **400-401**, 268–278 (2005)
96. C.H. Suh, Y.-C. Jung, Y.S. Kim, Effects of thickness and surface roughness on mechanical properties of aluminum sheets. J. Mech. Sci. Technol. **24**(10), 2091–2098 (2010)
97. S. Miyazaki, K. Shibata, H. Fujita, Effect of specimen thickness on mechanical properties of polycrystalline aggregates with various grain sizes. Acta Metall. **27**(5), 855–862 (1979)
98. S. Chauhan, A.F. Bastawros, Probing thickness-dependent dislocation storage in freestanding cu films using residual electrical resistivity. Appl. Phys. Lett. **93**(4), 041901 (2008)

99. P. Ghosh, A.H. Chokshi, Size effects on strength in the transition from single-to-polycrystalline behavior. Metall. Mater. Trans. A **46**(12), 5671–5684 (2015)
100. N.L. Okamoto et al., Specimen-and grain-size dependence of compression deformation behavior in nanocrystalline copper. Int. J. Plast. **56**, 173–183 (2014)
101. C.-J. Wang et al., Plastic deformation size effects in micro-compression of pure nickel with a few grains across diameter. Mater. Sci. Eng. A **636**, 352–360 (2015)
102. X.W. Gu et al., Size-dependent deformation of nanocrystalline Pt nanopillars. Nano Lett. **12**(12), 6385–6392 (2012)
103. T. Tsuchiya et al., Specimen size effect on tensile strength of surface-micromachined polycrystalline silicon thin films. J. Microelectromech. Syst. **7**(1), 106–113 (1998)
104. R. Wheeler, P. Shade, M. Uchic, Insights gained through image analysis during in situ micromechanical experiments. JOM **64**(1), 58–65 (2012)
105. P. Shade et al., A combined experimental and simulation study to examine lateral constraint effects on microcompression of single-slip oriented single crystals. Acta Mater. **57**(15), 4580–4587 (2009)
106. S.T. Wlodek, M. Kelly, D.A. Alden, *The Structure of René 88DT*, 1996, pp. 129–136
107. J. Stinville et al., Sub-grain scale digital image correlation by electron microscopy for polycrystalline materials during elastic and plastic deformation. Exp. Mech. **56**(2), 197–216 (2016)
108. D.D. Krueger, R.D. Kissinger, R.G. Menzies, Development and introduction of a damage tolerant high temperature nickel-base disk alloy, René 88DT, in *Superalloys 1992: Proceedings of the 7th International Symposium of Superalloys*, 1992
109. A. Bagri et al., Microstructure and property-based statistically equivalent representative volume elements for polycrystalline Ni-based superalloys containing annealing twins. Metall. Mater. Trans. A **49**(11), 5727–5744 (2018)
110. Z. Alam et al., Microstructural aspects of fatigue crack initiation and short crack growth in René 88DT, in *Superalloys 2016: Proceedings of the 13th International Symposium of Superalloys*, (Wiley, Hoboken), p. 2016
111. W.C. Lenthe et al., Prediction of fatigue-initiating twin boundaries in polycrystalline nickel superalloys informed by TriBeam tomography. Microsc. Microanal. **22**, 1732 (2016)
112. J.C. Stinville et al., Measurement of strain localization resulting from monotonic and cyclic loading at 650 °C in nickel base superalloys. Exp. Mech. **57**(8), 1289–1309 (2017)

Computational Micromechanics Modeling of Polycrystalline Superalloys: Application to Inconel 718

Aitor Cruzado, Javier Llorca, and Javier Segurado

1 Introduction

Ni-based superalloys stand for the state-of-art structural materials for many applications working under high temperature such as parts of energy generation systems or jet engines. Their complex chemical composition and microstructure have been slowly improved during the last 70 years to meet the demands of the operation conditions which require to support high stresses and temperatures (which may vary with time, leading to thermomechanical fatigue) in an aggressive environment. Further developments of Ni-based alloys have been hindered by the complexity of the current alloys, which makes very inefficient the traditional "trial-and-error" approach, and this has led to extensive use of computational tools to guide the development of the next generation of superalloys [49, 56]. Similarly, the design allowables have been established by means of costly experimental campaigns on standard specimens and have to be repeated every time that the alloy composition or microstructure changes, leading to further limitations in the innovation rate. In this respect, approaches that combine simulation tools based on computational homogenization of polycrystals with micromechanical experiments are opening new perspectives to make accurate predictions of the mechanical behavior of complex alloys that can take into account the effect of the microstructure. They will lead to

A. Cruzado
Department of Aerospace Engineering, Texas A& M University, College Station, TX, USA

Center for Intelligent Multifunctional Materials and Structures, TEES, Texas A& M University, College Station, TX, USA

J. Llorca · J. Segurado (✉)
IMDEA Materials Institute, Getafe, Madrid, Spain

Department of Materials Science, Polytechnic University of Madrid, Madrid, Spain
e-mail: javier.segurado@upm.es

S. Ghosh et al. (eds.), *Integrated Computational Materials Engineering (ICME)*,
https://doi.org/10.1007/978-3-030-40562-5_5

a dramatic reduction in the number of experimental tests to characterize new alloys and will also provide more accurate design allowables because the microstructural effects can be accounted for.

Computational homogenization of polycrystals is a simulation strategy in which the effective or macroscopic properties of the polycrystal are obtained by means of the numerical simulation of a representative volume element (RVE) of the microstructure [63]. The two key ingredients to make accurate predictions within this framework are the description of the microstructure (including the grain size and shape distribution and the texture) and the mechanical properties of the single crystals. The former can be easily obtained nowadays using different experimental characterization techniques (including X-ray diffraction, optical and scanning electron microscopy, electron back scattering diffraction, X-ray microtomography), while crystal plasticity provides a very accurate model of the kinematics of the plastic deformation of single crystals. In the case of complex alloys, phenomenological crystal plasticity models are normally used to determine the initial value of the critical resolved shear stress to produce plastic deformation in each slip system as well as the hardening rate. These model parameters have to be estimated using different approaches. For instance, they are optimized from a set of estimated starting values using an inverse optimization strategy by comparison of the predicted mechanical properties with experimental results on polycrystals [17, 27, 29] or on single crystals (extracted from the polycrystal) deformed by nanoindentation [47, 60, 77] or by micropillar compression [14].

In this chapter, a systematic application of computational homogenization of polycrystals to predict the mechanical behavior of IN718 Ni-based superalloy is presented. Section 2 describes the microstructure of the alloy, while the experimental techniques to measure the mechanical properties of the single crystals and of the polycrystals are detailed in Sect. 3. The computational homogenization framework, including the digital representation of the microstructure, the crystal plasticity models, and the details of the numerical simulations, is explained in Sect. 5. Applications to predict the mechanical behavior of IN718 under monotonic tension and fatigue are presented in Sect. 6, while the main conclusions are summarized in Sect. 7.

2 Material Description

Polycrystalline IN718 is a Ni-Fe-based superalloy widely used for structural applications up to 650–700 °C because of its good castability and weldability, high strength, and corrosion resistance. The microstructure of the wrought IN718 is made up by a Ni FCC solid solution which contains a dispersion of nm-sized γ' ($Ni_3(Al,Ti)$) and γ'' (Ni_3Nb) coherent precipitates within the grains together with μm-sized metal carbides and δ phase (Ni_3Nb) particles at grain boundaries (Fig. 1) [55, 68]. The volume fractions of γ' and γ'' phases are in the range 3–5% and 10–

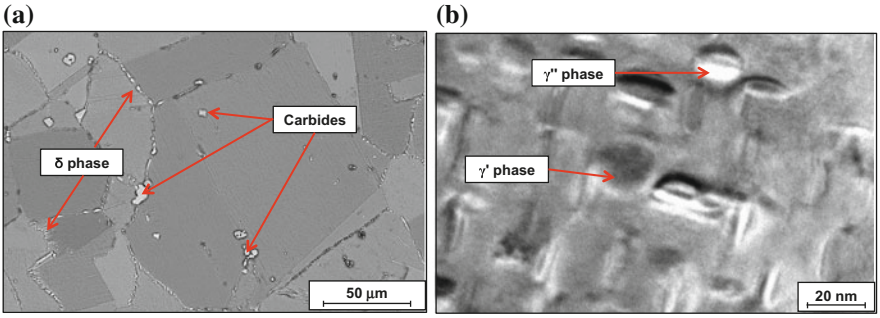

Fig. 1 Microstructure of coarse-grained IN718 Ni-based superalloy. (**a**) Polycrystal grain structure showing the distribution of metal carbides and δ phase at the grain boundaries, (**b**) distribution of γ' and γ'' precipitates within the Ni FCC solid solution. (Reprinted from [14])

20%, respectively, depending on the bulk alloy composition, the heat treatment, and the degree of element segregation [20]. The strength of the alloy in this case (and in the case of many other Ni-based superalloys) is provided by the interaction of the dislocations with the fine distribution of γ' and γ''. The precipitate size and spacing is of the order of 10–20 nm in wrought IN718 (Fig. 1b), which stands for the critical length scale that controls the mechanical behavior.

Two alloys with different average grain size were studied. The grains were equiaxed in both alloys, and the texture was random. The grain size was 8.5 according to the ASTM standard ($\approx$20 μm) in the fine microstructure alloy and 3 ($\approx$125 μm) in the coarse microstructure alloy. The amount of δ phase was $<$1% in the coarse-grained material and around 10% in the fine-grained material. All the other microstructural features were equivalent.

3 Experimental Characterization

The following section aims to describe the results of the mechanical characterization carried out on a wrought Inconel 718 superalloy at two different length scales. At the microscale, room temperature (RT) compression tests were performed on pillars built in grains of the two microstructures considered, coarse and fine. These tests aim to obtain the monotonic single crystal behavior and also to detect differences in the crystal response for the two microstructures considered. At the macroscopic level, uniaxial tensile tests were carried on both microstructures at different temperature ranges, from RT to 550 °C. In addition low cycle fatigue (LCF) tests were performed at 400 °C. This experimental data will be the basis to understand the mechanisms involved in the mechanical response of the superalloy and develop the corresponding computational micromechanics model.

3.1 Micromechanical Characterization

3.1.1 Experimental Procedure

Compression tests were performed on micropillars machined out of grains of a coarse-grained Inconel 718 alloy. The micropillars were milled in the center of selected grains to avoid grain boundary effects, using FIB (FEI Helios Nanolab 600i) following an annular milling strategy, with a final polishing step using a current of 230 pA to minimize FIB surface damage. The micropillar aspect ratio (length/diameter) was selected to be 2.4 to avoid buckling during compression [54]. The annular milling parameters used resulted in a minimum taper ($<1.5°$) of the pillars. The pillars were compressed inside an instrumented nanoindentation system (Hysitron TI950) using a circular diamond flat punch of 10 μm in diameter.

Tests were carried out under displacement control at three different strain rates (10^{-4}, 10^{-3}, and $10^{-2}\,s^{-1}$), and the diameter was varied between 1 and 7.5 μm to determine the effect of the diameter on the mechanical response. Inconel 718 crystals deform according to the lattice structure of the γ phase, along 12 octahedral $\{111\}\ \langle 110\rangle$ slip systems. Therefore, different crystallographic orientations were selected for testing in order to promote single, double (coplanar and noncoplanar), and multiple slip systems. The crystallographic orientation of the pillars was determined by EBSD, using an Oxford AZTEC system. The Sneddon correction [66] was applied in the obtained load displacement curves to account for the extra compliance associated with the elastic deflection of the matrix at the base of the pillar.

3.1.2 Results

The effect of the pillar diameter in the mechanical behavior was first assessed by performing micropillar compression on pillars with diameters ranging between 1 and 7.5 μm built in grains with similar crystallographic orientation. In this study grains favorably oriented for single slip, in either $\langle 245\rangle$ or $\langle 235\rangle$, with Schmid factors (SF) of 0.445 and 0.4512, respectively, were selected.

The corresponding resolve shear stress (RSS) vs. strain curves are shown in Fig. 2a. The pillars ranging between 3 and 7.5 μm present similar response, while the micropillar with diameter of 1 μm presents stiffer and stronger response. A small difference is also presented in the initial slope, which shows a much stiffer behavior as the pillar diameter decreases. This is consequence of the initial contact between the punch and the micropillar, affected by the surface asperities or the incorrect alignment between the flat punch and the head of the pillar, as described in [67]. These results confirm that, opposite to what is found when single crystals of pure metals are tested [73], the micropillar behavior is size independent for diameters above 3 μm. The independence of the pillar response with the diameter size is the consequence of the $\gamma'' + \gamma'$ precipitate spacing (≈50 nm), which is much smaller

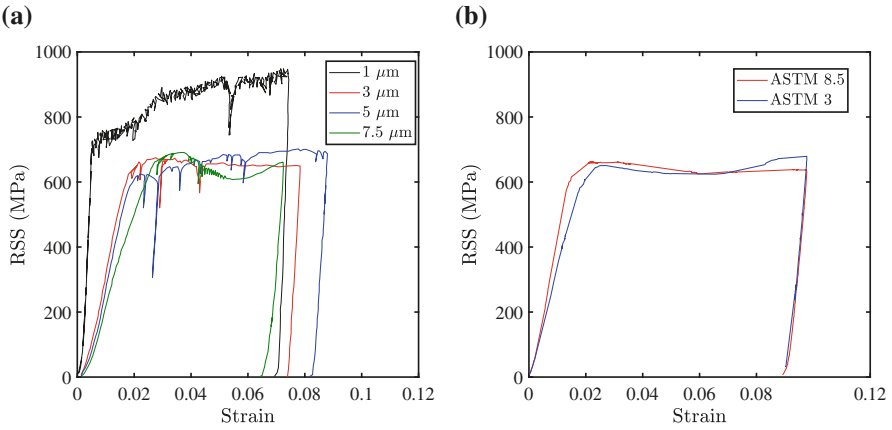

Fig. 2 RSS vs. strain in micropillar compression tests. (**a**) Micropillars of different diameters range from 1 to 7.5 μm oriented for single slip (either ⟨245⟩ or ⟨235⟩). (**b**) Micropillar of 5 μm in diameter oriented in multiple slip (⟨546⟩) for two microstructures with different grain sizes: ASTM 3 and ASTM 8.5

than the pillar dimension, thus being the characteristic length scale that controls the strength. Based on this observation, micropillars of size 5 μm in diameter are selected for the rest of this work to obtain the plastic behavior of Inconel 718 crystals.

The effect of the grain size in the crystal behavior is analyzed using micropillars of 5 μm in diameter milled in grains favorably oriented in ⟨546⟩ for the two microstructures considered, ASTM 3 and ASTM 8.5, as shown in Fig. 2b. Regardless of the initial slope, which is affected by the initial contact, the RSS-strain curves present almost the same behavior. This result confirms that the single crystal behavior is independent of the polycrystalline alloy grain size and can be considered representative of the single crystal bulk behavior. The identical response for pillars built from alloys with different grain sizes confirms the sub-grain microstructure of the crystal (precipitate volume fraction, sizes, shapes, and compositions) which controls the pillar response, and this substructure is almost independent of the grain size of the polycrystalline alloy.

Next, the strain rate sensitivity of Inconel 718 is analyzed testing micropillars favorably oriented in single slip with similar Schmid factor ⟨123⟩ (SF = 0.467) or ⟨235⟩ (SF = 0.451) at strain rates that ranges from 10^{-4} to $10^{-2}\,s^{-1}$ (Fig. 3). To reduce inaccuracies in the elastic behavior and the initiation of plastic yielding (mainly due to the tip-pillar contact), the force-displacement registers obtained in the tests are transformed into plastic strain-resolved shear stress (RSS) following the methodology described in detail in [14, 32]. The RSS-plastic strain rate curves plotted in Fig. 3a show a small strain rate dependency. These curves are then used to obtain the strain rate sensitivity exponent for Inconel 718 grains, assuming that the crystals behave as elasto-viscoplastic solids in which the plastic slip rate $\dot{\gamma}^{\alpha}$ for a

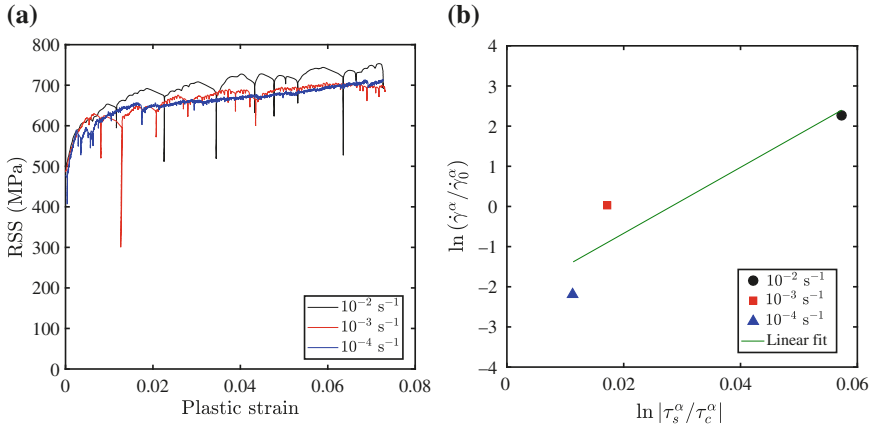

Fig. 3 Strain rate sensitivity analysis of micropillars of 5 μm in diameter oriented for single slip at room temperature. (**a**) RSS *vs.* plastic strain for three different strain rates: 10^{-2}, 10^{-3}, and 10^{-4} s^{-1} and (**b**) linear regression curve to obtain the strain rate sensitivity m parameter

given slip plane α can be expressed as $\dot{\gamma}^\alpha = \dot{\gamma}_0(|\tau^\alpha|/\tau_c^\alpha|)^{1/m}\text{sgn}(\tau^\alpha)$. Here $\dot{\gamma}_0$ is the reference strain rate, τ_c^α the critical resolved shear stress at the reference strain rate, and m the rate sensitivity exponent. Taking the natural logarithm of the viscoplastic flow, the following equation is derived:

$$\ln\left(\frac{\dot{\gamma}^\alpha}{\dot{\gamma}_0^\alpha}\right) = \frac{1}{m}\ln\left|\frac{\tau_s^\alpha}{\tau_c^\alpha}\right| \tag{1}$$

so that the rate sensitivity exponent m can be obtained as the slope of the linear regression between $\ln\left(\frac{\dot{\gamma}^\alpha}{\dot{\gamma}_0^\alpha}\right)$ and $\ln\left|\frac{\tau_s^\alpha}{\tau_c^\alpha}\right|$. The average strain rate $\dot{\gamma}^\alpha$ for each slip system is accounted, and the average strain of the micropillar divided by SF and the corresponding CRSS τ_s^α was taken at a plastic strain of 0.04. These results are normalized against the reference strain rate considered in this work as 10^{-3} s^{-1}. The linear regression performed in Fig. 3b renders a strain rate sensitivity exponent of m = 0.017. This exponent indicates a very small rate sensitivity of the material at room temperature.

The SEM micrographs of micropillars deformed in single and multiple slip orientation are shown in Fig. 4, respectively. The micropillar oriented along ⟨235⟩ clearly deforms through slip in a single plane, while the micropillar ⟨001⟩ shows the activation of multiple slip systems. The rest of the parameters involved in the crystal plasticity model that will be described in Sect. 5 have to be calibrated comparing the results obtained in tests performed on pillars with crystallographic orientations deforming under single and double slip with the corresponding numerical simulations. In particular, this method allowed to identify the critical resolved shear stress and the parameters defining the strain hardening of the crystal [14], accounted here

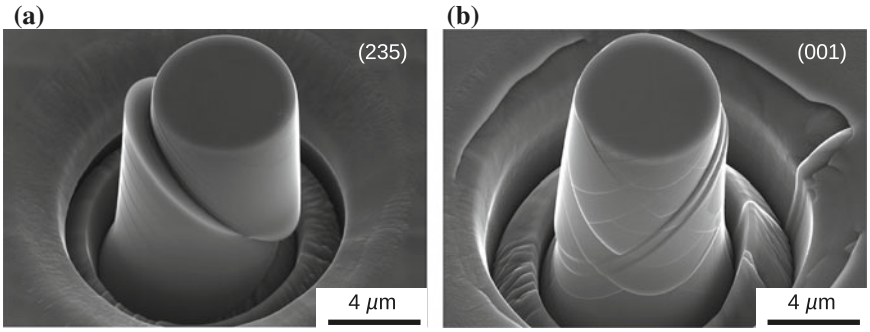

Fig. 4 SEM micrograph of 5 μm diameter deformed micropillar at an average strain rate of $10^{-3}\,s^{-1}$ oriented in: (**a**) ⟨235⟩ showing single slip and (**b**) ⟨001⟩ showing multiple slip

by the Voce hardening law [72]. The resulting values will be reported in Sect. 5, after the presentation of the crystal plasticity model.

3.2 Macromechanical Characterization

3.2.1 Uniaxial Monotonic Tests

Experimental Procedure

Uniaxial tensile tests were performed on a universal testing machine at a constant strain rate of $5\ 10^{-3}\,s^{-1}$. The tests were carried for three different temperatures, RT, 400, and 550 °C for both coarse-grained (ASTM 3) and fine-grained (ASTM 8.5) microstructures. Cylindrical smooth specimens with a diameter of 5.08 mm and a gauge length of 12.7 mm were used for the ASTM 8.5 microstructure, while specimens with a diameter of 6.35 mm and a gauge length of 12.7 mm were used for the ASTM 3 alloy.

Monotonic Behavior

The tensile stress-strain curves for the two microstructures and the three temperatures considered are plotted in Fig. 5. Note that these curves are normalized by a reference stress σ_0 and a reference strain $\Delta\varepsilon_{\min}$ due to the confidential agreement signed with the industrial partners funding this study. σ_0 corresponds to the yield stress of the ASTM 8.5 microstructure at 400 °C ,while $\Delta\varepsilon_{\min}$ corresponds to the smallest of the strain range applied in the experimental campaign. In Fig. 5a, a grain size effect in the alloy strength of the type *smaller is stronger* is clearly observed.

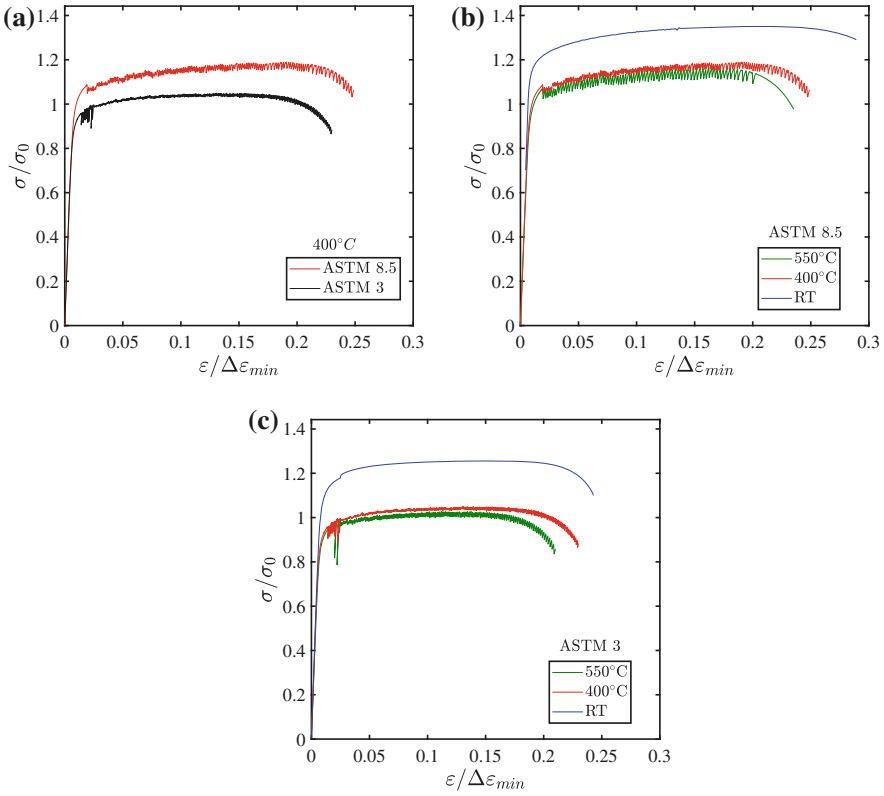

Fig. 5 Experimental uniaxial stress-strain behavior of In 718. (**a**) Effect of the average grain size in the mechanical response of ASTM 3 and ASTM 8.5 alloy at 400 °C. Effect of the temperature in the mechanical response for (**b**) ASTM 8.5 Alloy and (**c**) ASTM 3 Alloy. Stresses are normalized by σ_0 and strains by $\Delta\varepsilon_{\min}$

The tensile yield stress increased by ≈10% as the grain size decreases from ASTM 3 to ASTM 8.5. As shown in Sect. 5, the crystals do not present any grain size dependency, and this phenomenon is attributed to grain boundary strengthening. The grain boundaries act as a barrier which hinders the movement of dislocations between different grains leading to dislocation pileups.

The influence of temperature in the stress-strain for the two microstructures in a temperature range from RT to 550 °C is shown in Fig. 5b, c, respectively. An abrupt decrease in the yield stress ≈18% for the ASTM 3 microstructure and ≈12% for the ASTM 8.5 microstructure is shown from RT to 400 °C. Finally, small differences are presented from 400 to 550 °C, showing the stability of both microstructures in this range of temperature.

3.2.2 Low Cycle Fatigue Tests

Experimental Procedure

A set of uniaxial strain control LCF tests were carried out for the two microstructures analyzed in this work, ASTM 3 and ASTM 8.5, and a fixed temperature of 400 °C. The tests were performed according to the standard ASTM E606-04 on a MTS servo hydraulic fatigue load frame with a 100 kN load cell. Cylindrical smooth specimens with a diameter of 6.35 mm for the ASTM 3 Alloy and a diameter of 5.08 mm for the ASTM8, with a gauge length of 12.7 mm, were used. The axial displacement in the central zone of the specimen was measured with a MTS extensometer directly mounted on the gauge length. The specimens present the same grain size in the surface and in the interior, and the grain sizes observed in both longitudinal and transversal directions were also very similar. A trapezoidal wave form was applied according to 1 s (dwell) – 5 10^{-3} s^{-1} (ramp up) – 1 s (dwell)- 5 10^{-3} s^{-1} (ramp down).

For the ASTM 8.5 Alloy, tests were carried with cyclic strain ranges of $\Delta\varepsilon/\Delta\varepsilon_{\min} = 1$, 1.5, 2, 2.5, 3, and 3.5 for a strain ratio of $R_\varepsilon = -1$ and with cyclic strain ranges of $\Delta\varepsilon/\Delta\varepsilon_{\min} = 1$, 1.25, 1.5, 1.75, 2.25 and 2.75 for a strain ratio of $R_\varepsilon = 0$. The normalizing factor, $\Delta\varepsilon_{\min}$, is the same value used for the monotonic behavior (Fig. 5) and corresponds to the smallest cyclic strain range applied in the experimental tests. For the ASTM 3 alloy, only fully reversed cyclic deformation tests $R_\varepsilon = -1$ under cyclic strain ranges of $\Delta\varepsilon/\Delta\varepsilon_{\min} = 1$, 1.5, 2, 2.5, 3 and 3.5 were performed. The cyclic stress-strain curves derived from these tests are used first to describe the cyclic behavior of Inconel 718.

Cyclic Behavior

The characteristics of the macroscopic cyclic plastic behavior of Inconel 718 are obtained from the cyclic stress-strain response obtained at different number of cycles during a strain-controlled LCF tests. Those characteristics will be described using the particular case of LCF tests at 400 °C for the ASTM 8.5 microstructure. The alloy presents a strong Bauschinger effect [11] or strain-hardening asymmetry (i.e., kinematic hardening). This effect can be observed in Fig. 6a, which shows that yielding in compression starts well before the applied stress has reached $-\sigma_1$, equal to the flow stress in the previous tensile deformation up to ε_1. However, the actual yield stress in compression of Inconel 718 is smaller (in absolute value) than the prediction of pure kinematic hardening. This is associated with an initial softening that suffers the material during the initial unloading [23]. The physical origin of kinematic hardening can be associated with two mechanisms acting at different length scales. At the grain level, back stresses on the mobile dislocations are due to the development of dislocation substructures as a result of the interaction of the dislocations with the shearable γ' and γ'' precipitates as well as with the grain boundaries [38, 65]. At the polycrystal level, kinematic hardening is induced by the

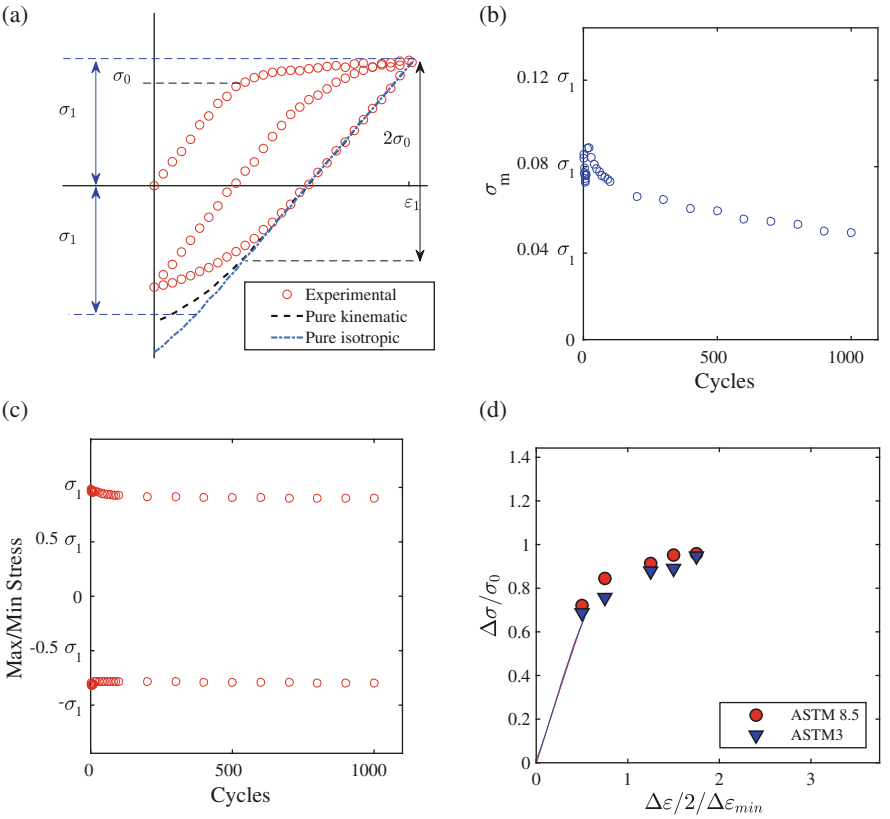

Fig. 6 Experimental cyclic behavior of Inconel 718 alloy at 400 °C deformed under strain control. (**a**) Stress-strain curve of the first cycle with $\varepsilon_{\max} = \varepsilon_1$ and $R_\varepsilon = 0$. (**b**) Evolution of mean stress (σ_m) with the number of cycles N. (**c**) Evolution of maximum ($\sigma_{\max}$) and minimum stress ($\sigma_{\min}$) with the number of cycles N. (**d**) Effect of the mean grain size in the stabilized cyclic stress-strain curve normalized by σ_0 and strains by $\Delta\varepsilon_{\min}$ for obtained from tests performed at different strain ranges and $R_\varepsilon = -1$. σ_0 and σ_1 stand for, respectively, the yield strength in tension and the flow stress at ε_1 in the first cycle

differences in the yield stress between "hard" and "soft" grains depending on the orientation of the slip systems.

Associated to the kinematic hardening, there is another characteristic of the material cyclic response, the mean stress relaxation, that consists in a progressive reduction of the mean stress during a cycle ($\sigma_m = (\sigma_{\max} + \sigma_{\min})/2$) in experiments performed under strain control and nonsymmetric cyclic deformation (e.g., $R_\varepsilon = \varepsilon_{\min}/\varepsilon_{\max} = 0$), Fig. 6b. Under nonsymmetric stress-controlled cyclic loading (mean stress different from 0), the effect of nonlinear kinematic hardening results in cyclic creep or ratcheting [11, 46].

The last characteristic of the cyclic plastic response of Inconel 718 is the progressive reduction of the stress range, $\Delta\sigma = \sigma_{\max} - \sigma_{\min}$, with the number

of cycles shown in Fig. 6c. This mechanism is known as cyclic softening and is attributed to the successive shearing by dislocations of the coherent and ordered γ'' precipitates, during the cyclic deformation. The shearing leads into a progressive reduction of the precipitate size up to a point in which they can no longer offer any resistance to the movement of dislocations [31, 76]. The deformation is thus localized in planar slip bands free of precipitates, and the "mechanical scrambling" of the precipitates is responsible for the cyclic softening. A detailed analyses of the influence of temperature and cyclic plastic strain amplitude on the cyclic softening can be found in various papers [3, 21, 31]. Cyclic hardening was found to take place during a few cycles at ambient temperature and was followed by a continuous cyclic softening until failure. The short period of cyclic hardening disappeared at high temperature and cyclic softening was dominant throughout the test at high temperature.

The effect of the grain size is finally analyzed form the stabilized cyclic stress-strain curve in Fig. 6d. There are two remarkable differences from the monotonic uniaxial tensile stress-strain curves: (1) the size effect found under monotonic loading is strongly reduced being the stabilized curve very similar for the two grain sizes considered and (2) the flow stress under cyclic deformation is below its monotonic counterpart. Note that this second effect is consequence of the cyclic softening previously described.

Low Cycle Fatigue Response

The low cycle fatigue (LCF) performance of the two microstructures studied is represented in Fig. 7, where the cyclic plastic strain range is plotted as function of the number of cycles to have a reduction of 5% in the maximum load during cyclic loading. As suggested by [5, 75], this reduction in the strength can be associated with the nucleation of a fatigue crack, and it has been observed that this number of cycles was very near in all the cases to the final rupture so they can be considered as an estimation of the fatigue life. The results show that this alloy follows a bilinear Coffin-Manson law and the transition between both slopes takes place for $N \approx 2000$. This bilinear Coffin-Manson behavior presented in Inconel 718 has been reported by many researchers [50–52, 61] and has been attributed to many different mechanisms. Recently, using micromechanical models [17] showed that this effect is associated with the transition from highly localized plasticity at low strain ranges to more homogeneous deformation at high cyclic strain ranges.

The influence of the grain size in the fatigue crack nucleation for the two microstructures considered can be observed in Fig. 7a. When the plastic strain range is large, both microstructures present similar fatigue lives. However for small values of the plastic strain range, when the cyclic stress-strain curves are nearly elastic, the fine-grained microstructure exhibits much larger fatigue life. Note that the transition to the grain size-controlled regime coincides with the transition point of the dual slope Coffin-Manson behavior and thus can be associated with the different strain localization observed in the two regimes.

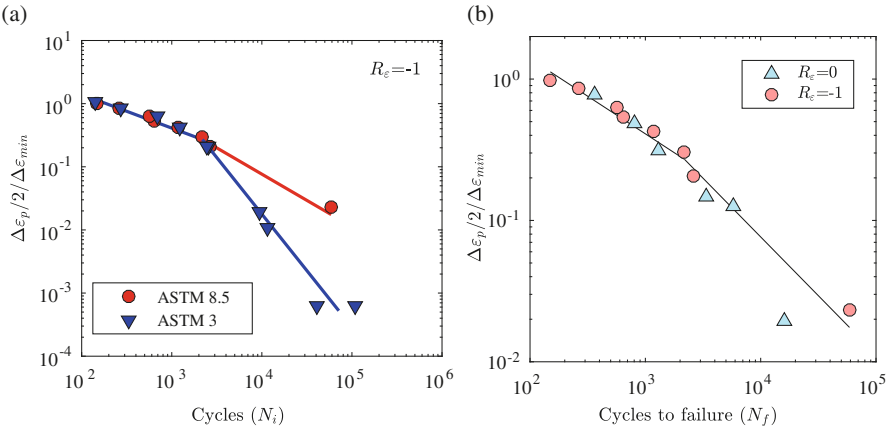

Fig. 7 (**a**) Cyclic plastic strain amplitude, $\Delta\varepsilon_p/2$, *vs.* the number of cycles to crack initiation, N_i, in Inconel 718 alloy at 400 °C. (**a**) Effect of the grain size in the fatigue life of Inconel 718 at $R_\varepsilon = -1$ and (**b**) effect of strain ratio under fully reversed $R_\varepsilon = -1$ and nonsymmetrical strain ratio $R_\varepsilon = 0$ for ASTM 8.5 alloy. The number of cycles for crack initiation N_i corresponds to the 5% load drop. Cyclic plastic strain amplitudes and strain ranges are normalized by $\Delta\varepsilon_{\min}$

Finally the effect of the strain ratio is analyzed in Fig. 7b. It is shown that for the majority of the strain ranges analyzed in this work, there is small influence in the fatigue life. However for the smallest values of the cyclic strain range, the fatigue life for a strain ratio $R_\varepsilon = 0$ is four times smaller than for a strain ratio of $R_\varepsilon = -1$.

4 Polycrystalline Homogenization Framework

The micromechanical framework to establish the relation between the microstructure and crystal behavior of a polycrystalline superalloy Inconel 718 with its macroscopic response is the computational homogenization of polycrystals [63]. Under this approach, the macroscopic response of the alloy and the microscopic fields are obtained from the numerical simulation of the mechanical response of a representative volume element (RVE) of the polycrystalline microstructure. The alloy microstructure is explicitly considered in the RVE that contains a distribution of grain sizes, shapes, and orientations statistically equivalent to the actual microstructure. Although this methodology is computationally expensive – involves the solution of a boundary value problem with a large number of degrees of freedom – it provides more accurate estimations of macroscopic behavior and microstructure evolution than mean-field models such as VPSC [34]. Moreover, it provides very accurate information of the local values of the stress and strain fields as well as of the state variables throughout the microstructure. This information is critical for predicting damage localization and failure of heterogeneous materials.

Three key ingredients are the basis of a successful simulation of a polycrystal using computational homogenization: (1) the numerical approach to solve the boundary value problem, (2) the representation of the microstructure, and (3) the constitutive description of the single crystal behavior. The particular homogenization framework used for the simulation of the mechanical behavior of the alloy Inconel 718 will be reviewed below, attending to these three aspects.

4.1 Boundary Value Problem and Boundary Conditions

Two approaches are normally used to solve the boundary problem in a homogenization problem, the finite element (FE) method or methods based on the fast Fourier transform (FFT). FE is still the most common approach for polycrystalline homogenization and has been profusely used to simulate the behavior of any type of metals [57, 58]. FFT-based homogenization, proposed in the 1990s by [43], soon attracted the attention of the homogenization community for its computational efficiency and because meshing of the RVE is avoided. The use of FFT methods for polycrystalline microstructures was proposed in [33], and the method has been used since then mainly to simulate the response of polycrystalline alloys under monotonic loading [19, 35]. Only very recently these methods have been applied to obtain the cyclic and fatigue response of superalloys like Inconel100 [59] or Inconel 718 [37].

In this work, the micromechanical simulations of the behavior of the alloy Inconel 718 [14–17] have been performed using the FE method. The FE framework for polycrystalline simulations shares many aspects with standard macroscopic plasticity simulations, as the use of the same type of elements, linearization schemes, or linear solvers, and relies very often in the use of commercial FE packages as ABAQUS or MARC. The two main differences with standard plasticity simulations are the constitutive equation used and the boundary conditions. Under the framework of computational homogenization of polycrystals, each material point is modeled using crystal plasticity, and the load history corresponds to the macroscopic stress or strain that is introduced using special boundary conditions as uniform displacement, uniform stress, or periodic boundary conditions.

Periodic boundary conditions are used for the micromechanical simulation of Inconel 718. These boundary conditions fulfill the Hill-Mandel principle of macro-homogeneity [30], and, among the boundary conditions compatible with this principle, the results obtained under these conditions (even in the case of nonperiodic microstructures) show the fastest convergence toward the actual effective response with increasing the RVE size [25]. Periodic boundary conditions assume that the RVE deforms as a jigsaw puzzle. A cubic periodicity of the RVE is assumed (Fig. 8a). Let $\mathbf{l}_i = l_i \mathbf{e}_i$ be the three orthogonal vectors defining the cubic periodicity, and let $\mathbf{e}_i$ be the corresponding unit vectors defining the basis. If x_1, x_2, x_3 are the coordinates of a point in the RVE in the system defined by $\mathbf{e}_i$, the periodic boundary

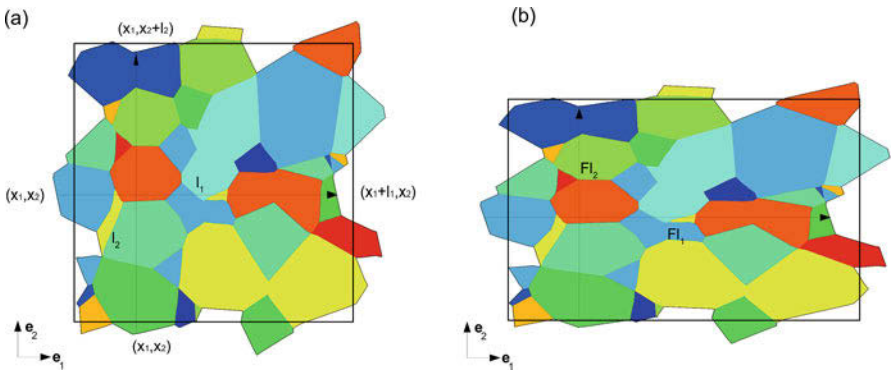

Fig. 8 Deformation of a periodic RVE of a polycrystal under periodic boundary conditions in 2D. (**a**) Undeformed configuration. (**b**) Deformed shape under biaxial deformation

conditions link the local displacement vector $\mathbf{u}$ of the nodes on opposite faces of the RVE with the far-field macroscopic deformation gradient $\bar{\mathbf{F}}$ according to

$$\mathbf{u}(x_1, x_2, 0) - \mathbf{u}(x_1, x_2, L_3) = (\bar{\mathbf{F}} - \mathbf{1})\mathbf{l}_3 \tag{2}$$

$$\mathbf{u}(x_1, 0, x_3) - \mathbf{u}(x_1, L_2, x_3) = (\bar{\mathbf{F}} - \mathbf{1})\mathbf{l}_2 \tag{3}$$

$$\mathbf{u}(0, x_2, x_3) - \mathbf{u}(L_1, x_2, x_3) = (\bar{\mathbf{F}} - \mathbf{1})\mathbf{l}_1 \tag{4}$$

The resulting deformed cell preserves the cubic periodicity, but the new vectors defining the periodicity are given by $\bar{\mathbf{F}}\mathbf{l}_i$, Fig. 8b. When the meshes of opposite faces of the RVE boundaries are identical, periodic boundary conditions are easily implemented coupling the displacements of the boundary nodes with equations (Eq. 4). In particular, a master node M_i $(i = 1, 2, 3)$ is defined for each pair of opposite cube faces, and the value of the far-field macroscopic deformation gradient is imposed to the RVE through the displacement of those master nodes according to

$$\mathbf{u}(M_i) = (\bar{\mathbf{F}} - \mathbf{1})\mathbf{l}_i\,. \tag{5}$$

If some components of the far-field deformation gradient are not known a priori, the corresponding effective stress component $\bar{\sigma}_{ij}$ are set instead (e.g., the transverse components of the stress tensor are set to zero for a uniaxial tensile loading). This task is carried out applying nodal forces P to the corresponding master node i and degree of freedom j according to

$$P_j(M_i) = (\bar{\boldsymbol{\sigma}}\,\mathbf{e}_i)_j A_i \tag{6}$$

where A_i is the *area* of the cell perpendicular to direction $\mathbf{e}_i$. Under small strains, the area A_i corresponds to the undeformed geometry, and Eq. (6) is used to obtain the value of the forces to be applied as function of the target stress.

4.2 Microstructure Representation

In computational homogenization of polycrystals, the RVEs should contain a statistical representation of the most important features of the actual microstructure [63]. For the same composition and precipitate content, the microstructural aspects that mostly influence the elastoplastic response of Inconel 718 are the grain size, shape, and orientation distributions of the alloy. In the case of the fatigue response, the effect of second phases or twin boundaries can also be determinant under small loads (high cycle fatigue). However, for relatively large deformations (low cycle fatigue), range in which we will study Inconel 718, the effect of these microstructural features is negligible compared with the strain localization due to grain orientation and neighborhood. Therefore, all the RVEs generated for this study are representative of the grain distributions experimentally measured but do not explicitly include other microstructural features.

Two wrought microstructures are analyzed in this study, containing both a relatively homogeneous grain size distributions – well represented using log-normal grain size distributions – but with different average grain size. For a given microstructure, the grain size distribution was measured using optical images of cross sections of the material including approximately 300 grains. The experimental 2D grain size distributions were transformed to a 3D distribution assuming spherical grains [26], and these 3D grain radii distribution were approximated by a log-normal function. An example of the resulting 3D grain size distribution obtained for one of the Inconel 718 microstructures studied is represented in Fig. 9, where the parameters obtained for the log-normal distribution were $\sigma = 0.70862$, $\mu = 3.65$ and a correlation coefficient of 0.93 [14].

Two different types of RVEs are generated, tessellation-based RVE with unstructured meshes (Fig. 10a) and voxelized RVEs (Fig. 10b). The first type of RVEs was

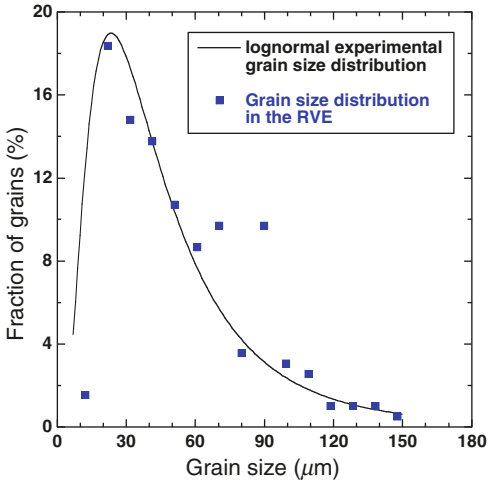

Fig. 9 Log-normal grain size distribution of polycrystalline Inconel 718 (solid line) and the corresponding grain size distribution in the RVE of the microstructure, from [14]

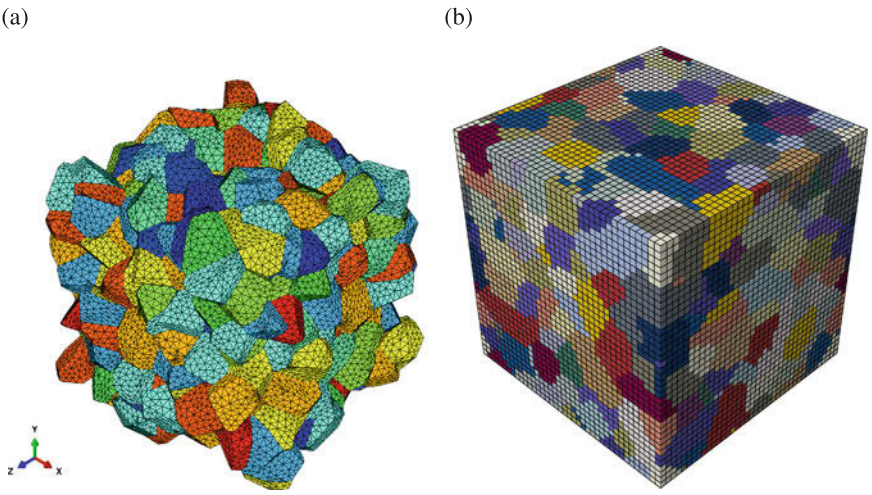

Fig. 10 Representative volume elements (RVEs) of a polycrystalline microstructure. (**a**) Voronoi tessellation-based RVE. (**b**) Voxelized RVE generated using [18]

generated from the tessellation of a set of points, which divided the initial volume in a number of polyhedra. In particular, because the grain size distributions considered in this study are log-normal distributions and grains are equiaxial, simple Voronoi tessellations are used. A Monte Carlo algorithm was developed to generate the position of the set of points used for the tessellation, so the resulting polyhedra in which the RVE is divided fulfill the experimental grain size distribution (e.g., the distribution in Fig. 9). The tessellations during the Monte Carlo process were carried out using an extended cloud of points obtained using periodic copies of the original cloud in the three directions of space in order to preserve the periodicity of the microstructure in the RVE. Although RVEs present cubic periodicity, the final shape of the RVE was not a cube because grains intersecting the cube faces were not cut and copied into the opposite face but were maintained in their original positions. This strategy avoided meshing problems related with the development of very small grains near the cube surfaces. The periodic RVE was finally meshed with the open source program Gmsh [22]. Ten-node quadratic tetrahedral elements (C3D10M with full integration in [1]) were used for the discretization. It must be noted that this strategy leads to planar grain boundaries because the actual geometry defined by the tessellation is preserved in the discretization. The second type of RVEs (Fig. 10b), voxelized RVEs, corresponds to the rasterization of a periodic synthetic microstructure generated in a regular grid by compacting in the RVE volume a set of ellipsoids which sizes fulfill the experimental grain size distribution. These types of synthetic microstructures are generated using the software [18] and do not necessarily correspond to any tessellation of points. After the rasterization, each voxel of the synthetic microstructure was transformed to a linear hexahedral element (C3D8 in Abaqus).

The texture is included in any of the two RVE typologies by assigning to each grain a given initial orientation defined by a rotation tensor. The rotation of each grain is selected to fulfill statistically the orientation distribution function experimentally obtained [27, 62]. In the case of the Inconel 718, all the microstructures studied presented a random texture, and therefore, grain orientations have been randomly generated in the rotation group $SO(3)$.

The computational cost and local accuracy of the two RVEs typologies are different, and their use depends on the application. For simulating the monotonic response, only a small number of different RVEs are needed, and each simulation requires only a limited number of load increments. In this case, Voronoi RVEs are used because they are computationally affordable and the local solution near grain boundaries can be more accurate. On the contrary, for simulating of the cyclic response and fatigue performance, many different RVEs have to be simulated, and each simulation comprises a large number of cycles. In this situation, voxelized RVEs are preferred due to their simple generation and better numerical performance.

4.3 Single Crystal Behavior

The behavior of the Inconel 718 grains is accounted using crystal plasticity theory. A unified kinematic crystal plasticity framework is used for all the regimes studied, but, for simplicity, slightly different flow and hardening rules are used for monotonic and cyclic behavior. In this section, we will review the general equations of the crystal plasticity models used, while the particular flow and hardening rules will be incorporated in each section.

With respect to the number and type of slip systems available in Inconel 718, slip trace analysis performed in [4] and the micromechanical tests presented in the previous section indicate that plastic deformation only takes place in octahedral $111 < 110 >$ slip systems, as in a single-phase FCC alloy. This is due to the low volume fraction (<20%) of γ' and γ'', and, therefore, only those 12 slip systems are considered in the crystal plasticity modeling of the alloy.

The kinematic description of the model is based on the multiplicative decomposition of the deformation gradient, $\mathbf{F}$, into the elastic $\mathbf{F}^{\mathrm{e}}$ and plastic components $\mathbf{F}^{\mathrm{p}}$,

$$\mathbf{F} = \mathbf{F}^{\mathrm{e}}\mathbf{F}^{\mathrm{p}} \tag{7}$$

The plastic velocity gradient in the intermediate configuration, $\mathbf{L}^{\mathrm{p}}$, is given by the sum of the shear rates $\dot{\gamma}^{\alpha}$ on all the slip systems α, according to

$$\mathbf{L}^{\mathrm{p}} = \dot{\mathbf{F}}^{\mathrm{p}}\mathbf{F}^{\mathrm{p}^{-1}} = \sum_{\alpha} \dot{\gamma}^{\alpha}\mathbf{s}^{\alpha} \otimes \mathbf{m}^{\alpha} \tag{8}$$

where $\mathbf{s}^{\alpha}$ and $\mathbf{m}^{\alpha}$ stand for the unit vectors in the slip direction and the normal to the slip plane, respectively, in the reference configuration.

The Green-Lagrange measure of deformation is used to characterize the elastic deformation, $\mathbf{E}^{\mathrm{e}}$,

$$\mathbf{E}^{\mathrm{e}} = \frac{1}{2}\left(\mathbf{F}^{\mathrm{e}T}\mathbf{F}^{\mathrm{e}} - \mathbf{I}\right) \tag{9}$$

being $\mathbf{I}$ the second order identity tensor. The symmetric second Piola-Kirchhoff stress tensor in the intermediate configuration, $\mathbf{S}$, is related with the Green-Lagrange strain tensor according to

$$\mathbf{S} = \mathbb{C} : \mathbf{E}^{\mathrm{e}} \tag{10}$$

where $\mathbb{C}$ is for the fourth-order elastic stiffness tensor of the single crystal. The driving force for the plastic slip is the resolved shear stress τ^{α} on the slip plane α, and it is obtained as the projection of the second Piola-Kirchhoff stress on the slip system according to

$$\tau^{\alpha} = \mathbf{S} : (\mathbf{s}^{\alpha} \otimes \mathbf{m}^{\alpha}) \tag{11}$$

Finally, the Cauchy stress is obtained as

$$\boldsymbol{\sigma} = \frac{1}{J^{e}}\mathbf{F}^{\mathrm{e}}\mathbf{S}\mathbf{F}^{\mathrm{e}T} \tag{12}$$

where J^{e} is the determinant of $\mathbf{F}^{\mathrm{e}}$.

The laws defining the slip rate as function of the resolved shear stress and the internal variables depend on the particular regime considered, monotonic or cyclic, and are included in its respective sections of this chapter.

5 Monotonic Behavior

The mechanical response of Inconel 718 under uniaxial monotonic loading is simulated using the computational homogenization framework presented in the previous section. The grain size distributions extracted from experimental microstructures are used as input for the RVEs. The strategy followed to model the crystal behavior of a coarse-grained Inconel 718 (ASTM 3) was using a simple crystal plasticity model in which the crystal parameters were experimentally measured from micromechanical tests. To extend the model to other microstructures, the crystal plasticity model was modified to include the effect of grain size in the crystal strength combining in this case microscopic data with macroscopic results for different microstructures.

Table 1 Single crystal elastic constants of Inconel 718 at room temperature

C_{11}(GPa)	C_{12}(GPa)	C_{44}(GPa)
259.6	179	109.6

5.1 Elastic Behavior

Inconel 718 crystals present cubic symmetry, and three constants, C_{11}, C_{12}, and C_{44}, are used to reproduce the elastic response of a crystal (Eq. 10). These three constants correspond to the components C_{1111}, C_{1122}, and C_{1212} of the stiffness tensor, and their values are obtained from the literature [40] and given in the next table (Table 1).

5.2 Elastoplastic Behavior

The approach followed to model the behavior of a coarse-grained Inconel 718 alloy consists in using a simple crystal plasticity model and identifies all the crystal parameters from microtesting at the grain level (Sect. 3.1) without using any fitting parameter. The study is performed in an alloy with the grain size distribution shown in Fig. 9. The crystal is assumed to behave as an elasto-viscoplastic solid with isotropic hardening. It is known that the macroscopic behavior presents Bauschinger effect, but since kinematic hardening cannot be distinguished from isotropic in the micropillar compression test results, the hardening is simplified to isotropic. The expression used for the plastic slip rate is a power law according to

$$\dot{\gamma}^{\alpha} = \dot{\gamma}_0 \left(\frac{|\tau^{\alpha}|}{g^{\alpha}} \right)^{\frac{1}{m}} \operatorname{sign}(\tau^{\alpha}) \tag{13}$$

where $\dot{\gamma}_0$ is the reference strain rate, g^{α} the critical resolved shear stress of α slip system, and m the rate sensitivity parameter. The evolution of the CRSS of a given slip system, $\dot{g}^{\alpha}$, is expressed as

$$\dot{g}^{\alpha} = \sum_{\beta} h \, q_{\alpha\beta} \left| \dot{\gamma}^{\beta} \right| \tag{14}$$

where h stands for the self-hardening modulus and $q_{\alpha\beta}$ are the latent hardening parameters that stand for the influence of hardening between different slip systems. The self-hardening was described according to the Voce model [72],

$$h\left(\Gamma\right) = h_s + \left(h_0 - h_s + \frac{h_0 h_s \Gamma}{\tau_s - \tau_0} \right) \exp\left\{ \frac{-\Gamma h_0}{\tau_s - \tau_0} \right\} \tag{15}$$

Table 2 Viscoplastic and hardening parameters obtained from pillar compression

τ_0 (Mpa)	τ_s(MPa)	h_0 (GPa)	h_s (GPa)	$q_{\alpha\beta}$
465.5	598.5	6.0	0.3	1

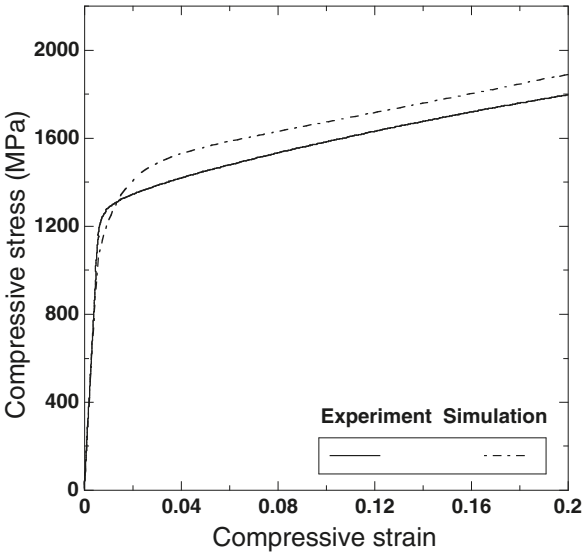

Fig. 11 Experimental result and numerical simulation obtained by computational homogenization of an RVE of the true stress-strain curve in compression of Inconel 718

where h_0 is the initial hardening modulus, τ_0 is the initial yield shear stress, τ_s is the saturation yields shear stress, h_s is the saturation hardening modulus at large strains, and Γ stands for the accumulated shear strain in all slip systems, which is given by

$$\Gamma = \sum_{\alpha} \int |\dot{\gamma}^{\alpha}| \mathrm{d}t. \tag{16}$$

The strain rate sensitivity found from pillar compression was $m = 0.017$, and the Voce hardening parameters obtained also using this technique are given in Table 2.

The crystal plasticity model described was used as constitutive equation in a Voronoi RVE (Fig. 10a) with 210 grains and around 600 finite elements per grain. This RVE size was enough to capture macroscopic behavior, based on volume averaged fields, and only small differences were observed between different realizations of the same size. In order to account for the scatter obtained using several RVEs of the same microstructure, the numerical predictions were obtained using four different realizations of the random grain orientation distribution.

Uniaxial compression was simulated using the framework described, and the stress-strain curve obtained as the average of the four realizations is represented in Fig. 11 together with the experimental result of a compression test performed under the same conditions.

The differences in the mechanical response between the four different models were below 1.3%, that is, an estimation of the error in the prediction of the macroscopic response for a given crystal behavior. The agreement between experimental behavior and simulation results (Fig. 11) was fairly good: the maximum difference in the compressive flow stress was below 4%, and the strain hardening rate predicted was identical to the experimental value. This accurate prediction is remarkable because no fitting parameters have been used being all the crystal parameters obtained from tests at lower length scales (with scatter near 5%). An interesting consequence of this good agreement is that the contribution of the grain boundaries to the strengthening of the alloy is minimal for this coarse-grained microstructure. If dislocation pilling up in front of grain boundaries would play a role, the stress-strain curve of the polycrystal predicted using parameters from micropillar (without grain boundaries) would underestimate the experimental response. The reason of this negligible effect of grain boundaries is probably the small distance between precipitates (tens of nanometers) that controls the dislocation arrangement within the microstructure, minimizing the effect of grain boundaries for this grain size.

The computational homogenization approach presented, based on obtaining all the crystal properties by microtesting, is interesting from the academic viewpoint. However, this strategy implies a very demanding microscopic experimental campaign limiting its technological application since the resulting macroscopic models are only valid for the particular temperature in which the material has been tested and neglect grain boundary effects that might not be negligible for smaller grain sizes. For this reason, the model is extended using a crystal plasticity phenomenological formulation that includes the effect of grain size to provide more general macroscopic predictions.

5.3 Grain Size-Dependent Model

The mechanical behavior of Inconel 718 is mainly controlled by its precipitate sizes and distances, but grain boundaries also play a role for fine-grained microstructures, and in this range, Inconel 718 shows a typical grain size effect of the type *the smaller the stronger* (Fig. 5). This effect has been classically parameterized using Hall-Petch expressions [24, 48] that relates the polycrystalline flow stress with σ_y with the average grain size d as

$$\sigma_y = \sigma_\infty + \frac{H}{\sqrt{d}} \tag{17}$$

being σ_∞ the flow stress of the coarse-grained alloy and H a material parameter. Hall-Petch law reflects the strengthening effect of the alloy due to the accumulation of dislocations in front of grain boundaries, and this effect is accounted at the grain level in the present approach. To this aim, the initial value of the critical resolved shear stress used in the crystal plasticity model (Eq. 13) is modified for each crystal

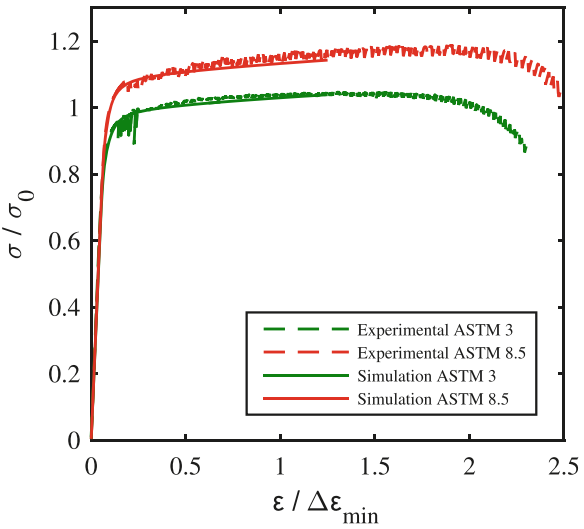

Fig. 12 Experimental result and numerical simulation obtained by computational homogenization of the stress-strain curves at room temperature under uniaxial tension for microstructures with grain sizes ASTM 8.5 and 3. Results are normalized by σ_0 and $\Delta\varepsilon_{\min}$

to include the strengthening due to the dislocations pileups in the grain boundaries as

$$g_\alpha(\Gamma = 0) = \tau_\infty + \frac{h}{\sqrt{d}} \tag{18}$$

being τ_∞ the critical resolved shear stress for a large grain and h a material parameter equivalent to H at the grain level. It must be noted that the value of τ_∞ does not correspond exactly to the value obtained by pillar compression for a coarse-grained microstructure, probably due to the differences in the nanostructure of grains with very different sizes and also to tension/compression asymmetry. For this reason, the Hall-Petch parameters τ_∞ and h and the hardening constants are fitted from experimental results for the two different homogeneous microstructures, ASTM 8.5 and ASTM 3. The resulting polycrystalline model is able to reproduce the grain size effect observed experimentally as it can be observed in Fig. 12.

6 Cyclic Behavior

In this section, polycrystalline computational homogenization will be used to predict the cyclic behavior of Inconel 718. As shown in the experimental characterization (Sect. 3), the alloy presents a strong Bauschinger effect, combination of isotropic and kinematic hardening, and cyclic softening. To model this complex behavior, an alternative flow rule is proposed for the crystal plasticity model [15] including softening and kinematic hardening rules that provide an accurate control of cyclic

softening and mean-stress relaxation with a relatively small number of parameters in comparison with to macroscopic models [10–12, 45].

6.1 Crystal Plasticity Model for Cyclic Behavior

The crystal plasticity framework presented in Sect. 4.3 is used with a plastic slip rate adapted for cyclic loading and given by

$$\dot{\gamma}^{\alpha} = \dot{\gamma}_0 \left(\frac{|\tau^{\alpha} - \chi^{\alpha}|}{g^{\alpha}} \right)^{\frac{1}{m}} \text{sign}(\tau^{\alpha} - \chi^{\alpha}) \tag{19}$$

where $\dot{\gamma}_0$ is the reference strain rate, g^{α} the critical resolved shear stress of α slip system, χ^{α} the back stress and m the rate sensitivity parameter. The back stress term is introduced to account for the effect of the dislocation substructures on the stress necessary to move dislocations when reverting load direction [6, 36, 41, 42, 69]. In this study an evolution law for the back stress is proposed based on a simplification of the Ohno-Wang macroscopic model limited to the first two terms and containing only three material parameters. This relatively simple model at the crystal level is able to reproduce the complex cyclic behavior of the polycrystal because the contribution to kinematic hardening of the residual microstresses due to plastic incompatibilities between grains is naturally accounted for during the homogenization of the polycrystal. The model proposed for kinematic hardening includes two terms. The first one corresponds to the strain hardening [2], and the second one represents the dynamic recovery and is given by

$$\dot{\chi}^{\alpha} = c\dot{\gamma}^{\alpha} - d\chi^{\alpha}|\dot{\gamma}^{\alpha}| \left(\frac{|\chi^{\alpha}|}{c/d} \right)^{k} \tag{20}$$

where c and d are parameters of the Frederick-Armstrong model and k is an extra parameter that controls the mean stress relaxation velocity. The details of the backstress evolution law can be found in [15].

The critical resolved shear stress (g^{α} in Eq. 19) also includes two contributions that determine the amount of hardening or softening under monotonic (g_m^{α}) and cyclic (g_c) deformation according to

$$g^{\alpha} = g_m^{\alpha} + g_c \tag{21}$$

where g_m^{α} controls the evolution under monotonic deformation and g_c determines the cyclic softening due to a progressive reduction of the critical resolved shear stress induced by changes in the direction of plastic shear. The monotonic term, g_m^{α}, has an initial value of τ_0 (the initial critical resolved shear stress), and the evolution with the applied strain, $\dot{g}_m^{\alpha}$, is obtained from the contribution of the shear strain of

all the slip systems β in the crystal according to Eq. 14. The self-hardening rule selected here was the Asaro-Needleman model, given by

$$h\left(\Gamma\right) = h_0 \mathrm{sech}^2 \left| \frac{h_0 \Gamma}{\tau_s - \tau_0} \right| \tag{22}$$

where h_0 is the initial hardening (or softening) modulus, τ_s is the saturation stress, and Γ is the accumulated shear strain in all slip systems of the crystal, (Eq. 16). The second contribution to the evolution of the critical resolved shear stress in Eq. (21) is the cyclic softening, g_c. This softening is caused by the successive shearing of the γ'' precipitates due to the reciprocating movement of the dislocations, and, therefore, it is activated when the shear deformation is reversed. For simplicity, it is considered that the softening induced by this mechanism is the same for all the slip systems. Experimental data on Inconel 718 show that cyclic softening develops very rapidly in the first cycles but the stress amplitude is stabilized afterward. Therefore, the Voce type law [72] (Eq. 15) with a negative slope to consider softening was adopted to simulate this behavior according to

$$g_c = -\left(\tau_s^{cyc} + h_2 \gamma_{cyc}\right)\left(1 - \exp^{\frac{-h_1 \Gamma_{cyc}}{\tau_s^{cyc}}}\right) \tag{23}$$

where τ_s^{cyc} is the saturation softening (the maximum reduction of the critical resolved shear stress due to cyclic softening), h_1 and h_2 are the cyclic softening parameters, and Γ_{cyc}, the cyclic accumulated plastic strain, is an internal variable defined to capture the cyclic softening under a general loading history. Γ_{cyc} is given by

$$\Gamma_{cyc} = \sum_{\alpha} \int_0^t |\dot{\gamma}^{\alpha}| \mathrm{d}t - \sum_{\alpha} \left| \int_0^t \dot{\gamma}^{\alpha} \mathrm{d}t \right|, \tag{24}$$

and is zero under monotonic loading while it increases when the direction of shear plastic strain changes, storing information about the number of changes in the direction of plastic shear and the magnitude of the shear strain accumulated before each change.

6.1.1 Model Parameter Identification

The parameters of the crystal plasticity model for the cyclic behavior are chosen to represent the cyclic response of the fine-grained (ASTM 8.5) Inconel 718 at 400 °C. The reference strain rate, $\dot{\gamma}_0$, and strain rate sensitivity exponent, m, are taken from the micropillar characterization and are independent of the temperature in the range RT-500 °C. The elastic constants of the Inconel 718 single crystals at 400 °C were obtained from the values at room temperature assuming a linear reduction with temperature and can be found in Table 3.

Table 3 Single crystal elastic constants of Inconel 718 at 400C

C_{11}(GPa)	C_{12}(GPa)	C_{44}(GPa)
240	165	101

Table 4 Optimized crystal plasticity parameters for a wrought Inconel 718 at 400 °C

Isotropic hardening	τ_0 (MPa)	τ_s	h_0	$q_{\alpha\beta}$
	τ_0	$0.71\tau_0$	$-57.13\tau_0$	1
Kinematic hardening	c	d	mk	
	$58.9\tau_0$	198.3	17.7	
Cyclic softening	τ_s^{cyc}	h_1	h_2	
	$0.076\tau_0$	$0.07\tau_0$	$2.33\ 10^{-6}\ \tau_0$	

The remaining parameters of the crystal plasticity model were obtained by means of the inverse optimization procedure developed in [27, 28]. This inverse technique is a minimum squares approach based on minimizing the differences between a set of experimental stress-strain curves with respect to the response obtained by means of computational homogenization using the Levenberg-Marquardt method. The experimental data used in the optimization process are the stress-strain loops obtained under uniaxial cyclic tension with strain control at three different strain amplitudes, $\Delta\varepsilon/\Delta\varepsilon_{\min} = 1$, 1.75, and 2.25 (small, medium, and high) with respect to the normalizing value $\Delta\varepsilon_{\min}$ and with $R_\varepsilon = 0$. The details of the fitting procedure can be found in [15], and the resulting parameters are summarized in Table 4, normalized by the initial critical resolved shear stress τ_0.

6.2 Simulation of the Cyclic Behavior

The numerical simulation of the fine-grained Inconel 718 polycrystal alloy at 400 °C was carried out using a voxelized RVE (Fig. 10b) and the crystal plasticity model presented above. The RVE contained $30 \times 30 \times 30$ cubic elements, which ≈300 grains and ≈90 elements per grain. Voxelized RVEs were used (Fig. 10), and the microstructures were synthetically generated using the Dream3D software to fulfill the log-normal distribution obtained from microscope images of the material. Similar to the case of the monotonic behavior, the macroscopic behavior was relatively independent of the particular RVE realization [15], and a set of five different grain realizations was used to obtain the macroscopic cyclic behavior.

The cyclic stress-strain curves under uniaxial tension with cyclic strain amplitudes $\Delta\varepsilon/\Delta\varepsilon_{\min} = 1.25$, 1.5, and 2.75 with $R_\varepsilon = 0$ and $R_\varepsilon = -1$ were simulated using the polycrystalline homogenization approach. The experimental results of the two extremal cases, $\Delta\varepsilon/\Delta\varepsilon_{\min} = 1.25$ and 2.75, are plotted in Fig. 13 together with the numerical predictions provided by computational homogenization. Figure 13 includes the cyclic stress-strain curves in the first cycle and in a cycle at ≈75% of the fatigue life as well as the evolution of the stress amplitude, $\Delta\sigma$, and of the mean

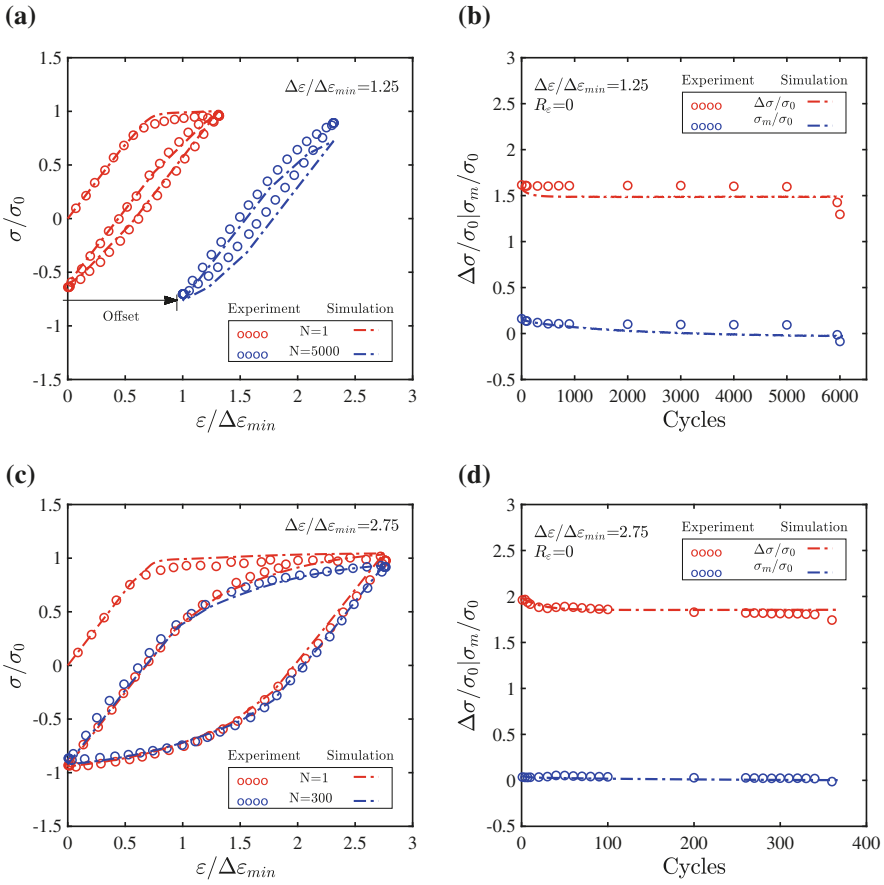

Fig. 13 Experimental results and numerical predictions of the cyclic response of Inconel 718 at 400 °C tested under uniaxial tension with $R_\varepsilon = 0$. (**a**) Cyclic stress-strain loops for $\Delta\varepsilon/\Delta\varepsilon_{\min} = 1.25$. (**b**) Evolution of the stress amplitude, $\Delta\sigma/\tau_0$, and of the mean stress, σ_m/τ_0, with the number of cycles for $\Delta\varepsilon/\Delta\varepsilon_{\min} = 1.25$. (**c**) *Idem* as (**a**) for $\Delta\varepsilon/\Delta\varepsilon_{\min} = 2.75$ (**d**) *Idem* as (**b**) for $\Delta\varepsilon/\Delta\varepsilon_{\min} = 2.75$. Experimental data are given by open circles, while the results provided by computational homogenization using the crystal plasticity parameters obtained with the inverse optimization method are shown by the broken lines

stress, σ_m, (normalized by σ_0) with the number of fatigue cycles. The results show that the computational homogenization approach was able to predict very accurately the hysteresis cycle when $\Delta\varepsilon/\Delta\varepsilon_{\min} = 1.5$ and 2.75, while the stresses are slightly underestimated when $\Delta\varepsilon/\Delta\varepsilon_{\min} = 1.25$. The predictions of the evolution of stress amplitude and of the mean stress with the number of cycles were also very accurate until failure in all cases. Thus, the simulation strategy was able to capture the shape of the hysteresis loops as well as the Bauschinger effect, the cyclic softening, and the mean stress relaxation of Inconel 718 as a function of the fatigue cycles.

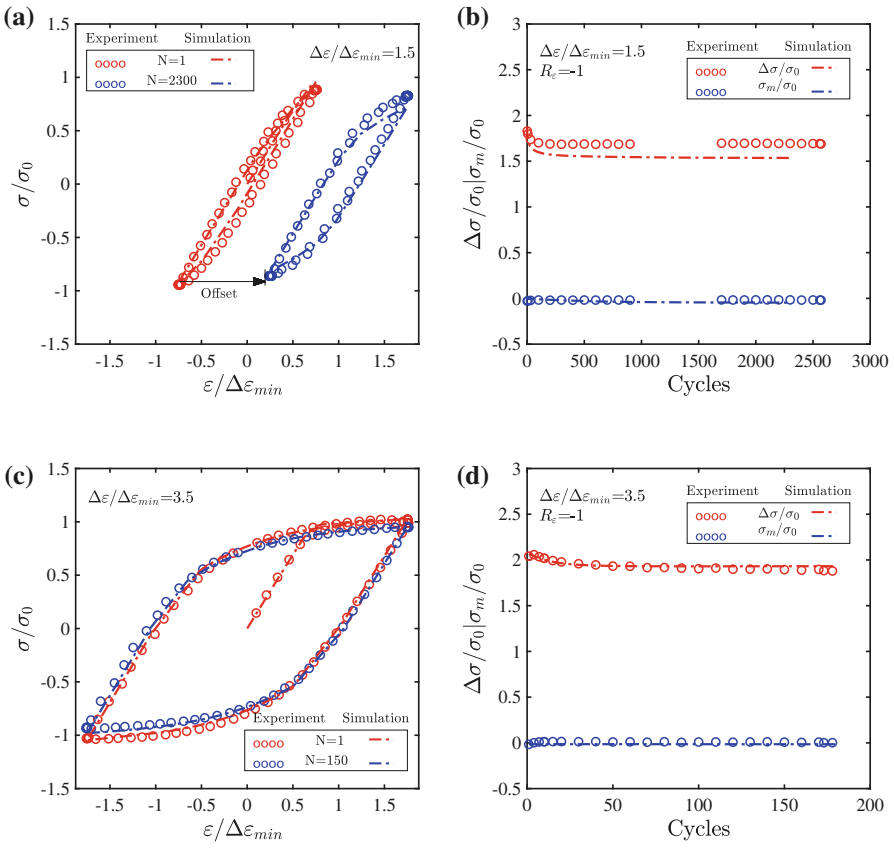

Fig. 14 Experimental results and numerical predictions of the cyclic response of Inconel 718 at 400 °C tested under uniaxial tension with $R_\varepsilon = -1$. (**a**) Cyclic stress-strain loops for $\Delta\varepsilon/\Delta\varepsilon_{\min} = 1.5$. (**b**) Evolution of the stress amplitude, $\Delta\sigma/\sigma_0$, and of the mean stress, σ_m/σ_0, with the number of cycles for $\Delta\varepsilon/\Delta\varepsilon_{\min} = 1.5$. (**c**) *Idem* as (**a**) for $\Delta\varepsilon/\Delta\varepsilon_{\min} = 3.5$ (**d**) *Idem* as (**b**) for $\Delta\varepsilon/\Delta\varepsilon_{\min} = 3.5$. Experimental data are given by open circles, while the results provided by computational homogenization using the crystal plasticity parameters obtained with the inverse optimization are shown by the broken lines

A second test of the predictive capabilities of the model was attempted by simulating the cyclic behavior of the same alloy under strain control at $R_\varepsilon = -1$ also at 400 °C and three different strain ranges $\Delta\varepsilon/\Delta\varepsilon_{\min} = 1.5$, 3, and 3.5. The experimental cyclic stress-strain curves with $R_\varepsilon = -1$ are plotted for two different cycles (the first one and another at ≈75% of the fatigue life) in Fig. 14a, c for the tests carried out at $\Delta\varepsilon/\Delta\varepsilon_{\min} = 1.5$ and 3.5, respectively. In addition, the evolution of the stress amplitude, $\Delta\sigma$, and of the mean stress, σ_m, (normalized by σ_0) with the number of fatigue cycles is plotted in Fig. 14b, d for the tests carried out at $\Delta\varepsilon/\Delta\varepsilon_{\min} = 1.5$ and 3.5, respectively. The corresponding numerical results are plotted in these figures, and the agreement between the experiments

and the simulations is excellent in all cases, with the only exception of the cyclic stress amplitude in the tests carried out at $\Delta\varepsilon/\Delta\varepsilon_{\min} = 1.5$, which was slightly underestimated.

6.3 Grain Size-Dependent Cyclic Behavior

The approach followed to include grain size dependency in the cyclic behavior of Inconel 718 alloy is an extension of the phenomenological approach introduced to reproduce grain size dependency in the monotonic behavior. In this case, in addition to the modification of the initial CRSS (Eq. 18), the dependency on the grain size D is also introduced in the backstress. The parameters c and d controlling the kinematic hardening evolution, given by Eq. (20), are redefined as

$$c = c' + \frac{k_c}{\sqrt{D}} \tag{25}$$

$$\frac{c}{d} = \left(\frac{c}{d}\right)' + \frac{k_{c/d}}{\sqrt{D}} \tag{26}$$

where c' and $(c/d)'$ stand for the direct hardening modulus and saturation hardening, respectively, corresponding to a very large grain (where no dislocation pileups are formed) and k_c and $k_{c/d}$ stand for the Hall-Petch parameters that introduce the effect of grain size. The fitting procedure and resulting values of these new parameters can be found in [16]. The result of the cyclic deformation simulations for two different strain ranges ($\Delta\varepsilon/\Delta\varepsilon_{\min} = 3$ and $\Delta\varepsilon/\Delta\varepsilon_{\min} = 1.5$) at $T = 400\,^{\circ}\mathrm{C}$ and the two different grain sizes considered, ASTM 3 and ASTM 8.5, are represented in Fig. 15 together with the experimental results.

The stabilized stress-strain hysteresis loops predicted by the model were able to accurately reproduce the experimental behavior for both strain ranges. This agreement supports the simplistic strategy to account for the grain size effect by introducing Hall-Petch-type relations in both the initial critical resolved shear stress and back stress evolution. Moreover, it is expected that the small effect of the grain size at the macroscale level will be amplified at the microscopic level, providing a non-negligible effect of grain size in the fatigue response.

7 Microstructure-Dependent Fatigue Life Simulation

7.1 Microstructure-Sensitive Crack Initiation Model

The prediction of crack initiation of Inconel 718 alloy as a function of its microstructure is carried out using a micromechanics-based fatigue life estimation approach. This approach consists first in simulating the cyclic response of the alloy considered using computational homogenization until reaching the stabilized

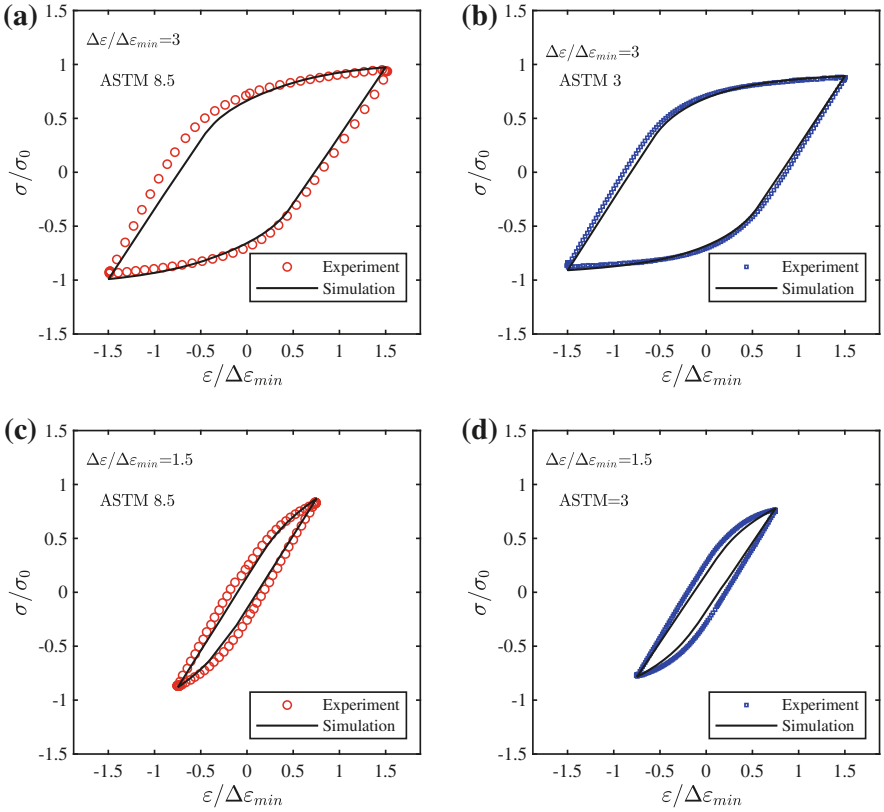

Fig. 15 Experimental results and numerical predictions of the stabilized cyclic stress-strain loops of Inconel 718 alloy at 400 °C tested under uniaxial cyclic deformation with $R_\varepsilon = -1$. (**a**) $\Delta\varepsilon/\Delta\varepsilon_{\min} = 3$ for ASTM 8.5 grain size. (**b**) *Idem* as (**a**) for ASTM 3 grain size. (**c**) $\Delta\varepsilon/\Delta\varepsilon_{\min} = 1.5$ for ASTM 3 grain size. (**d**) *Idem* as (**c**) for ASTM 3 grain size

cycle. The simulation accounts for the alloy microstructure through the RVE and is performed for the particular cyclic loading condition studied (strain/stress range, strain rates, R ratio, etc.). The evolution during the stable cycle of the mechanical fields and internal variables at the microscopic level is used then to obtain some fatigue indicator parameters (FIP) which describe the main driving force that controls crack formation. These parameters are finally linked, using phenomenological relations, to some stage of the fatigue life of the alloy under study. Opposite to the homogenization of the averaged response, a large set of RVEs should be used since the microscopic fields are very sensitive to the particular RVE [64]. The reason is that the FIP of a RVE is based on the extreme value of the FIP distribution inside that RVE, and the tail of this distribution is strongly dependent on the particular RVE. This RVE ensemble is sometimes called SVE (statistical volume element, [64]) or M-SERVES (microstructure representative

volume elements [13]) depending on the author. Therefore, the phenomenological expression for life predictions will be applied to all the RVE ensemble, resulting in a statistical distribution of fatigue lives.

The simulation of the cyclic response using computational micromechanics was covered in the previous section, and the microscopic fields resulting of these simulations are used here to obtain the FIP distributions. Among the different FIPs proposed in the literature for the study of the fatigue life [7, 8, 39, 44, 53, 64, 69–71, 74, 75], the local crystallographic strain energy dissipated per cycle W^b_{cyc} was used in this study to obtain the fatigue life on Inconel 718 alloy. This FIP is expressed as

$$W^{\alpha}_{cyc}(\mathbf{x}) = \int_{cyc} \tau_{\alpha}(\mathbf{x})\dot{\gamma}_{\alpha}(\mathbf{x})\mathrm{d}t \tag{27}$$

where τ_α and $\dot{\gamma}_\alpha$ are the resolved shear stress and the shear strain rate on the slip system α, respectively, for a given location $\mathbf{x}$ in the polycrystal. The local value of the FIP, as described in Eq. 27, is calculated in the centroid of each element in the RVE. However, this local value is not representative of a fatigue damage region, as the formation of persistent slip bands which leads into crack incubation affects a particular finite volume of the material. To overcome this issue, the local FIPs are averaged along narrow bands parallel to the slip planes, similar to the approach proposed by Castelluccio et al. [9]. Under these assumptions, the FIP representative of an RVE subjected to cyclic deformation, W^b_{cyc}, is obtained as the maximum of the band-averaged local FIP throughout the RVE, according to

$$W^b_{cyc} = \max_{i=1,nb} \left\{ \max_{\beta_i} \frac{1}{V_i} \int_{V_i} W^{\beta_i}_{cyc}(\mathbf{x})\mathrm{d}V_i \right\} \tag{28}$$

where β_i (= 1, 2, 3) corresponds to the three different slips systems contained in the slip plane parallel to the band i, V_i is the volume of that band, and nb is the total number of bands considered, which is four times the number of elements in the RVE. This volume-averaging approach also presents the advantage of mitigating spurious stress concentrations and mesh size effects.

The fatigue crack initiation is then related to the stabilized value of the cyclic FIP W^b_{cyc}. Cruzado et al. [17] showed that a linear relation between the number of cycles for crack nucleation and the FIP value – approach followed in many microstructure-based models [39, 71, 74] – did not work for Inconel 718. The deficient predicting capacity of a linear law in Inconel 718 was attributed to the dual slope Coffin-Manson behavior, described in Sect. 3.2.2, which is a consequence of a change in the deformation mechanism that controls the nucleation of fatigue cracks from localized deformation in a few grain at small cyclic strain amplitudes to homogeneous plastic deformation at large cyclic strain amplitudes. Under these conditions, a power law relation of the fatigue life N_i with W^b_{cyc} was proposed

$$N_i = \frac{W_{crit}^{NL}}{(W_{cyc}^{b})^m} \tag{29}$$

where the fatigue life depends on the stabilized cyclic FIP, W_{cyc}^{b}, through two material parameters, W_{crit}^{NL} and m. In order to obtain the stabilized cyclic FIP, it was observed that 5 cycles were enough, except for the smallest strain range $\Delta\varepsilon/\Delta\varepsilon_{\min} = 1$ and the strain ratio of $R_\varepsilon = -1$ in which cyclic simulations were extended up to ≈12% of the fatigue life. This slow convergence to the stable cyclic behavior is a consequence of the cyclic softening that, for the small amount of plasticity accommodated in each cycle, extends the reduction of the stress range until a large number of cycles. It must be noted that the parameters of the crack initiation law should be in principle independent of the alloy microstructure and therefore the effect of the grain size distribution and other microstructural features enter in the model through the FIP values, obtained in the polycrystalline simulations.

7.2 Results

The parameters of the fatigue initiation law described in Eq. 29 were fitted using two different fatigue tests ($\Delta\varepsilon/\Delta\varepsilon_{\min} = 1$ and 3.5) performed in an alloy with fine-grained microstructure (ASTM 8.5). The cyclic FIP, W_{cyc}^{b}, for the two loading conditions was obtained from the average value of the simulation of a RVE ensemble (SVE) with 20 different RVEs. The resulting parameters are $W_{crit}^{NL} = 4.8485 \times 10^4$ MJ/m^3 and $m = 1.4755$.

As in the rest of the chapter, two microstructures are considered, ASTM 3 and ASTM 8.5, in order to check the ability of the model to reproduce size effects in the fatigue life. The cyclic response of four different RVEs (selected to be representative of the SVE distribution of FIPs) for each strain range and microstructure is simulated using the framework previously presented. A value of the FIP, W_{cyc}^{b}, is obtained from each simulation. The life estimation for each RVE and load condition is obtained then by introducing the FIP in Eq. (29), so four different values are computed for each loading conditions that represent somehow the scatter in life.

The resulting fatigue life initiation predictions for the two grain sizes considered are summarized in Fig. 16. Figure 16a, b shows the predictions of the LCF life for the fine-grained microstructure and $R_\varepsilon = -1$ and $R_\varepsilon = 0$, respectively. The bars in the graph represent the scatter of the 20 models used for fitting the fatigue life initiation law, and the stars represent each of the 4 individual realizations of a fatigue simulation. It is shown that the model is able to predict very accurately the fatigue life for very different strain ranges and also under different strain ratios. Moreover, considering that the two tests necessary for fitting the model were obtained from tests at $R_\varepsilon = -1$, the results with $R_\varepsilon = 0$ are pure predictions and perfectly capture the experimental response.

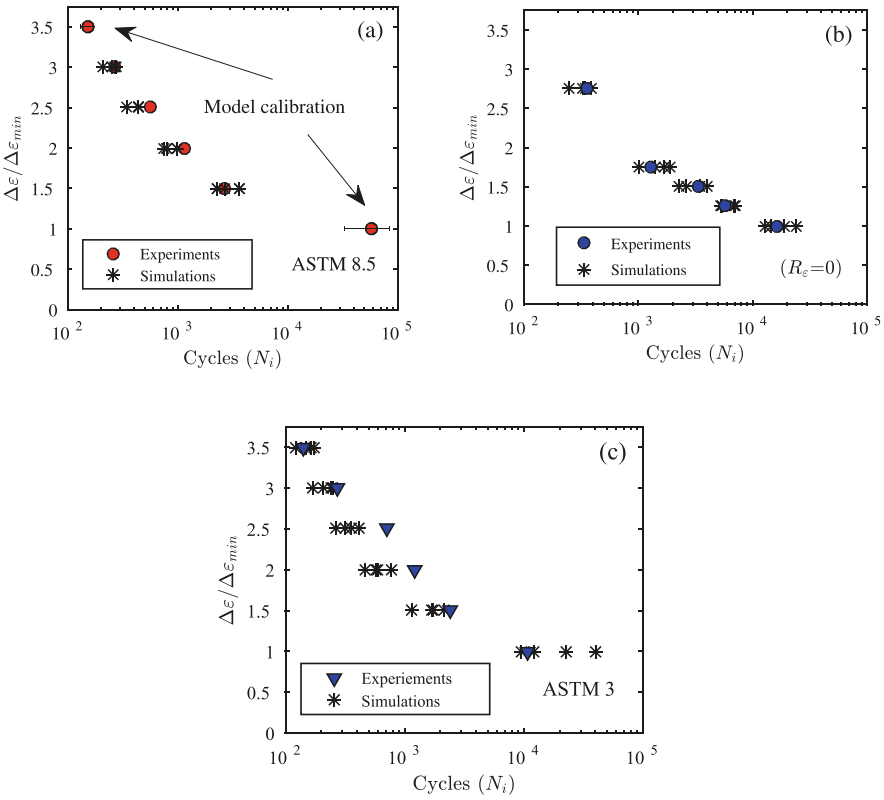

Fig. 16 Experimental results and numerical predictions of the number of cycles for fatigue crack initiation in Inconel 718 alloy at 400 °C as a function of the strain range $\Delta\varepsilon$ normalized by the minimum cyclic strain range $\Delta\varepsilon_{\min}$. (**a**) For $R_\varepsilon = -1$ and ASTM 8.5 grain size. (**b**) For $R_\varepsilon = 0$ and ASTM 8.5. (**c**) *Idem* as (**a**) for ASTM 3 grain size

The fatigue model fitted with the fine-grained LCF experiments was then used to predict the fatigue life of the coarser microstructure, ASTM 3. The results obtained are represented in Fig. 16c. The fatigue initiation predictions are in general very accurate, with only a slight underestimation of life for strain ranges in the middle of the range explored. It must be noted that this material microstructure has not been used to fit the fatigue life initiation and the effect of grain size is a direct consequence of the differences in the plastic response.

Figure 17 presents together the results of the simulations obtained for the two grain sizes considered. It can be observed that the model is able to capture the grain size effect in crack initiation observed in the experiments; for the largest values of the cyclic strain range (where the accumulated plasticity is homogeneous), the scatter is low, and the fatigue lives were independent of the grain size. Nevertheless, at the lowest strain ranges, where the localization of strain in the most favorable

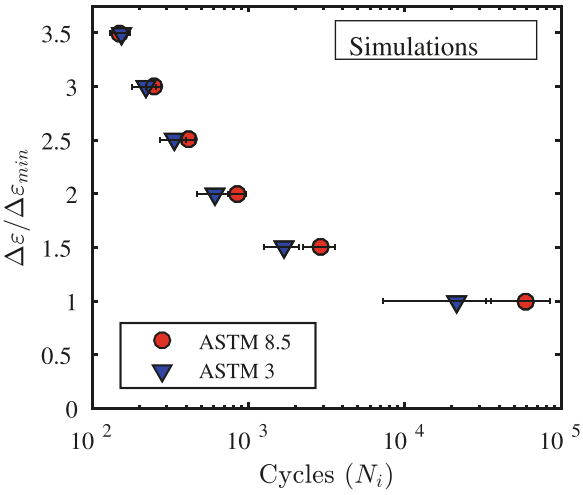

Fig. 17 Effect of the grain size in the predicted number of cycles for fatigue crack initiation (mean and standard deviation) as a function of the applied cyclic strain range, $\Delta\varepsilon$ (normalized by $\Delta\varepsilon_{\min}$)

grain takes place, the scatter in fatigue life is larger, and the microstructure with smallest grain size (ASTM 8.5) presents a better performance.

The ability of the model to accurately predict the crack initiation for different strain ranges, strain ratios, and grain sizes is a consequence of the microstructural basis of the approach used in this work. The resolution of the local fields allows to capture the different localization patterns presented in this material taking into account the effect of this distribution in the fatigue life estimations.

8 Conclusions

The application of a virtual testing methodology, based on the principles of integrated computational materials engineering, has been presented and demonstrated for an Inconel 718 Ni-based superalloy. The mechanical behavior of the polycrystal is obtained by means of computational homogenization of a representative volume element of the microstructure. The microstructural information (grain size distribution and texture) to generate the representative volume element was obtained from standard metallographic characterization techniques. The properties of each crystal were given by a phenomenological crystal plasticity model, whose parameters were obtained using two different strategies, depending on the particular behavior considered. Micropillar compression tests were used to determine the single crystal properties under monotonic deformation, while an inverse optimization strategy using the experimental results of the cyclic stress-strain curve was used in the case of cyclic deformation.

The results of the simulations for the effective properties of the polycrystals under monotonic and cyclic deformation were in good agreement with the experimental data. Moreover, the values of the local fields (resolved stresses, accumulated

plastic strains, etc.) throughout the representative volume element were used to generate fatigue indicator parameters, which were able to determine the most critical points in the microstructure to initiate a fatigue crack. These fatigue indicator parameters were calibrated by comparison with a few experimental fatigue tests and then used to predict the effect of loading conditions (different strain ratios) and microstructure (small and coarse grain size) on the fatigue life of the superalloy. Overall, the strategy shows how a balanced combination of micromechanical tests and macromechanical tests together with the application of computational homogenization strategies can be used to predict the mechanical behavior of Ni-based superalloys taken into account the influence of the microstructure.

References

1. Abaqus (2013) Analysis User's Manual, version 6.13. Dassault Systems
2. P. Armstrong, C.A. Frederick, Mathematical representation of the multiaxial bauschinger effect. CEGB Report rd/b/n731, Berkeley nuclear laboratories, Berkeley (1966)
3. A. Banerjee, J.K. Sahu, C.D. Fernando, R.N. Ghosh, Micromechanisms of cyclic plastic deformation of alloy IN718 at 600 °C. Fatigue Fract. Eng. Mater. Struct. **39**, 877–885 (2016)
4. C. Boehlert, H. Li, L. Wang, Slip system characterization of in 718 using in-situ scanning electron microscopy. Adv. Mater. Process. **168**, 41–45 (2010)
5. R. Brommesson, M. Ekh, M. Hörnqvist, Correlation between crack length and load drop for low-cycle fatigue crack growth in ti-6242. Int. J. Fatigue **81**, 1–9 (2015)
6. G. Cailletaud, A micromechanical approach to inelastic behaviour of metals. Int. J. Plast. **8**, 55–73 (1992)
7. G.M. Castelluccio, D.L. McDowell, A mesoscale approach for growth of 3D microstructurally small fatigue cracks in polycrystals. Int. J. Damage Mech. **23**, 791–818 (2013)
8. G.M. Castelluccio, D.L. McDowell, Mesoscale modeling of microstructurally small fatigue cracks in metallic polycrystals. Mater. Sci. Eng. A **598**, 34–55 (2014)
9. G.M. Castelluccio, D.L. McDowell, Microstructure and mesh sensitivities of mesoscale surrogate driving force measures for transgranular fatigue cracks in polycrystals. Mater. Sci. Eng. A **639**, 626–639 (2015)
10. J. Chaboche, On some modifications of kinematic hardening to improve the description of ratchetting effects. Int. J. Plast. **7**, 661–678 (1991)
11. J. Chaboche, D. Nouailhas, D. Pacou, P. Paulmier, Modeling of the cyclic response and rattchening effects on inconel 718 alloy. Eur. J. Mech. A/Solids **10**, 101–102 (1991)
12. J. Chaboche, P. Kanouté, F. Azzouz, Cyclic inelastic constitutive equations and their impact on the fatigue life predictions. Int. J. Plast. **35**, 44–66 (2012)
13. P. Chakraborty, S. Ghosh, Accelerating cyclic plasticity simulations using an adaptive wavelet transformation based multitime scaling method. Int. J. Numer. Methods Eng. **93**(13), 1425–1454 (2013)
14. A. Cruzado, B. Gan, M. Jiménez, D. Barba, K. Ostolaza, A. Linaza, J. Molina-Aldareguia, J. Llorca, J. Segurado, Multiscale modeling of the mechanical behavior of inconel 718 superalloy based on micropillar compression and computational homogenization. Acta Mater. **98**, 242–253 (2015)
15. A. Cruzado, J. Llorca, J. Segurado, Modeling cyclic deformation of inconel 718 superalloy by means of crystal plasticity and computational homogenization. Int. J. Solids Struct. **122**, 1521–1542 (2017)
16. A. Cruzado, S. Lucarini, J. Llorca, J. Segurado, Crystal plasticity simulation of the effect of grain size on the fatigue behavior of polycrystalline inconel 718. Int. J. Fatigue **113**, 236–245 (2018)

17. A. Cruzado, S. Lucarini, J. Llorca, J. Segurado, Microstructure-based fatigue life model of metallic alloys with bilinear coffin-manson behavior. Int. J. Fatigue **107**, 40–48 (2018)
18. Dream.3D, Website. http://dream3d.bluequartz.net (2012)
19. P. Eisenlohr, M. Diehl, R.A. Lebensohn, F. Roters, A spectral method solution to crystal elasto-viscoplasticity at finite strains. Int. J. Plast. **46**, 37–53 (2013)
20. Y.C. Fayman, Microstructural characterization and element partitioning in a direct – aged superalloy (DA718). Mater. Sci. Eng. A **92**, 159–171 (1987)
21. D. Fournier, A. Pineau, Low cycle fatigue behavior of inconel 718 at 298 k and 823 k. Metall. Trans. A **8**(7), 1095–1105 (1977)
22. C. Geuzaine, J.-F. Remacle, GMSH: a 3-D finite element mesh generator with built-in pre- and post-processing facilities. Int. J. Numer. Methods Eng. **79**(11), 1309–1331 (2009)
23. D. Gustafsson, J. Moverare, K. Simonsson, S. Sjöström, Modeling of the constitutive behaviour of inconel 718 at intemediate temperatures. J. Eng. Gas Turbines Power **133**, 1–4 (2011)
24. E.O. Hall, The deformation and ageing of mild steel: III discussion of results. Proc. Phys. Soc. Sect. B **64**, 747–753 (1951)
25. S. Hazanov, C. Huet, Order relationships for boundary condition effects in heterogeneous bodies smaller that the representative volume. J. Mech. Phys. Solids **42**, 1995–2011 (1994)
26. R. Heilbronner, D. Bruhn, The influence of three-dimensional grain size distributions on the rheology of polyphase rocks. J. Struct. Geol. **20**(6), 695–705 (1998)
27. V. Herrera-Solaz, J. Llorca, E. Dogan, I. Karaman, J. Segurado, An inverse optimization strategy to determine single crystal mechanical behavior from polycrystal tests: application to AZ31 Mg alloy. Int. J. Plast. **57**, 1–15 (2014)
28. V. Herrera-Solaz, J. Segurado, J. Llorca, On the robustness of an inverse optimization approach based on the Levenberg-Marquardt method for the mechanical behavior of polycrystals. Eur. J. Mech./A **53**, 220–228 (2015)
29. P. Hidalgo-Manrique, V. Herrera-Solaz, J. Segurado, J. Llorca, F. Gálvez, O.A. Ruano, S. Yi, M.T. Pérez-Prado, Origin of the reversed yield asymmetry in Mg-rare earth alloys at high temperature. Acta Mater. **92**, 265–277 (2015)
30. R. Hill, A self consistent mechanics of composite materials. J. Mech. Phys. Solids **13**, 213–222 (1965)
31. S. Kalluri, K.B.S. Rao, G.R. Halford, M.A. McGaw, Deformation and damage mechanisms in inconel 718 superalloy. in *Superalloys 718, 625, 706 and Various Derivatives*, The Minerals, Metals and Materials Society, pp. 593–606 (1994)
32. D. Kupka, N. Huber, E. Lilleodden, A combined experimental-numerical approach for elasto-plastic fracture of individual grain boundaries. J. Mech. Phys. Solids **64**, 455–467 (2014)
33. R.A. Lebensohn, N-site modelling of a 3D viscoplastic polycrystal using fast fourier transform. Acta Mater. **49**, 2723–2737 (2001)
34. R.A. Lebensohn, C.N. Tomé, A self-consistent anisotropic approach for the simulation of plastic deformation and texture development of polycrystals: application to zirconium alloys. Acta Metall. et Mater. **41**, 2611–2624 (1993)
35. R.A. Lebensohn, A.K. Kanjarla, P. Eisenlohr, An elasto-viscoplastic formulation based on fast fourier transforms for the prediction of micromechanical fields in polycrystalline materials. Int. J. Plast. **32–33**, 59–69 (2012)
36. F. Lu, Z. Guang, Z. Ke-shi, Discussion of cyclic plasticity and viscoplasticity of single crystal nickel-based superalloy in large strain analysis: comparison of anisotropic macroscopic model and crystallographic model. Int. J. Mech. Sci. **46**(8), 1157–1171 (2004)
37. S. Lucarini, J. Segurado, On the accuracy of spectral solvers for micromechanics based fatigue modeling. Comput. Mech. **63**, 365–382 (2019)
38. K. Maciejewski, H. Ghonem, Isotropic and kinematic hardening as functions of gamma prime precipitates in a nickel-based superalloy. Int. J. Fatigue **68**, 123–135 (2014)
39. A. Manonukul, F.P.E. Dunne, High– and low–cycle fatigue crack initiation using polycrystal plasticity. Proc. R. Soc. Lond. A Math. Phys. Eng. Sci. **460**(2047), 1881–1903 (2004)

40. G. Martin, N. Ochoa, K. Sai, E. Herve-Luanco, G. Cailletaud, A multiscale model for the elastoviscoplastic behavior of directionally solidified alloys: application to fe structural computations. Int. J. Solids Struct. **51**(5), 1175–1187 (2014)
41. D. McDowell, Viscoplasticity of heterogeneous metallic materials. Mater. Sci. Eng. R Rep. **62**(3), 67–123 (2008)
42. L. Méric, P. Poubanne, G. Cailletaud, Single crystal modeling for structural calculations: part 1 model presentation. ASME J. Eng. Mater. Technol. **113**, 162–170 (1991)
43. H. Moulinec, P. Suquet, A fast numerical method for computing the linear and nonlinear mechanical properties of composites. Comptes Rendus de l'Académie des Sci. **318**, 1417–1423 (1994)
44. W.D. Musinski, D.L. McDowell, Microstructure-sensitive probabilistic modeling of {HCF} crack initiation and early crack growth in ni-base superalloy {IN100} notched components. Int. J. Fatigue **37**, 41–53 (2012)
45. N. Ohno, J.-D. Wang, Kinematic hardening rules with critical state of dynamic recovery, part ii: application to experiments of ratchetting behavior. Int. J. Plast. **9**(3), 391–403 (1993)
46. S. Park, K. Kim, H. Kim, Ratcheting behaviour and mean stress considerations in uniaxial low-cycle fatigue of inconel 718 at 649 °C. Fatigue Fract. Eng. Mater. Struct. **30**(11), 1076–1083 (2007)
47. D.K. Patel, S.R. Kalidindi, Estimating the slip resistance from spherical nanoindentation and orientation measurements in polycrystalline samples of cubic metals. Int. J. Plast. **92**, 19–30 (2017)
48. N.J. Petch, The cleavage strength of polycrystals. J. Iron Steel Inst. **174**, 25–28 (1953)
49. T.M. Pollock, Alloy design for aircraft engines. Nat. Mater. **15**, 809–815 (2016)
50. N. Prasad, A. Paradkar, G. Malakondaiah, V. Kutumbarao, An analysis based on plastic strain energy for bilinearity in coffin-manson plots in an Al-Li alloy. Scripta Metall. et Mater. **30**(12), 1497–1502 (1994)
51. K. Praveen, V. Singh, Effect of heat treatment on coffin–manson relationship in {LCF} of superalloy {IN718}. Mater. Sci. Eng. A **485**(1–2), 352–358 (2008)
52. K. Praveen, G. Sastry, V. Singh, Room temperature LCF behaviour of superalloy in 718. Trans. Indian Inst. Metals **57**(6), 623–630 (2004)
53. C.P. Przybyla, W.D. Musinski, G.M. Castelluccio, D.L. McDowell, Microstructure-sensitive {HCF} and {VHCF} simulations. Int. J. Fatigue **57**, 9–27 (2013). Fatigue and microstructure: a special issue on recent advances
54. D. Raabe, D. Ma, F. Roters, Effects of initial orientation, sample geometry and friction on anisotropy and crystallographic orientation changes in single crystal microcompression deformation: a crystal plasticity finite element study. Acta Mater. **55**(13), 4567–4583 (2007)
55. J.F. Radavich, The physical metallurgy of cast and wrought alloy 718. in *Superalloy 718 – Metallurgy and Applications*, The Minerals, Metals and Materials Society, pp. 229–240 (1989)
56. C. Rae, Alloys by design: modelling next generation superalloys. Mater. Sci. Technol. **25**, 479–487 (2009)
57. F. Roters, P. Eisenlohr, T.R. Bieler, D. Raabe, *Crystal Plasticity Finite Element Methods: In Materials Science and Engineering*. Wiley-VCH, Weinheim, Germany (2010)
58. F. Roters, P. Eisenlohr, L. Hantcherli, D.D. Tjahjanto, T.R. Bieler, D. Raabe, Overview of constitutive laws, kinematics, homogenization and multiscale methods in crystal plasticity finite-element modeling: theory, experiments, applications. Acta Mater. **58**, 1152–1211 (2010)
59. A. Rovinelli, R.A. Lebensohn, M.D. Sangid, Influence of microstructure variability on short crack behavior through postulated micromechanical short crack driving force metrics. Eng. Fract. Mech. **138**, 265–288 (2015)
60. R. Sánchez-Martín, M.T. Pérez-Prado, J. Segurado, J. Bohlen, I. Gutiérrez-Urrutia, J. Llorca, J.M. Molina-Aldareguia, Measuring the critical resolved shear stresses in Mg alloys by instrumented nanoindentation. Acta Mater. **71**, 283–292 (2014)
61. T.H. Sanders, R. Frishmuth, G.T. Embley, Temperature dependent deformation mechanisms of alloy 718 in low cycle fatigue. Metall. Mater. Trans. A **12**(6), 1003–1010 (1981)

62. J. Segurado, J. Llorca, Simulation of the deformation of polycrystalline nanostructured Ti by computational homogenization. Comput. Mater. Sci. **76**, 3–11 (2013)
63. J. Segurado, R.A. Lebensohn, J. Llorca, Computational homogenization of polycrystals. Adv. Appl. Mech. **51**, 1–114 (2018). Elsevier
64. M. Shenoy, J. Zhang, D. McDowell, Estimating fatigue sensitivity to polycrystalline ni-base superalloy microstructures using a computational approach. Fatigue Fract. Eng. Mater. Struct. **30**(10), 889–904 (2007)
65. M. Shenoy, Y. Tjiptowidjojo, D. McDowell, Microstructure-sensitive modeling of polycrystalline {IN} 100. Int. J. Plast. **24**(10), 1694–1730 (2008). Special issue in honor of Jean-Louis Chaboche
66. I.N. Sneddon, The relation between load and penetration in the axisymmetric boussinesq problem for a punch of arbitrary profile. Int. J. Eng. Sci. **3**(1), 47–57 (1965)
67. R. Soler, J.M. Molina-Aldareguia, J. Segurado, J. Llorca, Effect of misorientation on the compression of highly anisotropic single-crystal micropillars. Adv. Eng. Mater. **14**(11), 1004–1008 (2012)
68. Y.S. Song, M.R. Lee, J.T. Kim, Effect of grain size for the tensile strength and the low cycle fatigue at elevated temperature of alloy 718 cogged by open die forging press. in *Superalloys 718, 625, 706 and Derivatives*, ed. by E.A. Loria (TMS, Warrendale, 2005), pp. 539–549
69. C. Sweeney, P. McHugh, J. McGarry, S. Leen, Micromechanical methodology for fatigue in cardiovascular stents. Int. J. Fatigue **44**, 202–216 (2012)
70. C.A. Sweeney, B. O'Brien, P.E. McHugh, S.B. Leen, Experimental characterisation for micromechanical modelling of CoCr stent fatigue. Biomaterials **35**(1), 36–48 (2014)
71. C. Sweeney, B. O'Brien, F. Dunne, P. McHugh, S. Leen, Micro-scale testing and micromechanical modelling for high cycle fatigue of CoCr stent material. J. Mech. Behav. Biomed. Mater. **46**, 244–260 (2015)
72. C. Tome, G. Canova, U. Kocks, N. Christodoulou, J. Jonas, The relation between macroscopic and microscopic strain hardening in F.C.C. polycrystals. Acta Metall. **32**(10), 1637–1653 (1984)
73. M.D. Uchic, D.M. Dimiduk, J.N. Florando, W.D. Nix, Sample dimensions influence strength and crystal plasticity. Science **305**(5686), 986–989 (2004)
74. V. Wan, D. MacLachlan, F. Dunne, A stored energy criterion for fatigue crack nucleation in polycrystals. Int. J. Fatigue **68**, 90–102 (2014)
75. V. Wan, J. Jiang, D. MacLachlan, F. Dunne, Microstructure-sensitive fatigue crack nucleation in a polycrystalline Ni superalloy. Int. J. Fatigue **90**, 181–190 (2016)
76. L. Xiao, D. Chen, M. Chaturvedi, Shearing of γ" precipitates and formation of planar slip bands in inconel 718 during cyclic deformation. Scr. Mater. **52**(7), 603–607 (2005)
77. C. Zambaldi, C. Zehnder, D. Raabe, Orientation dependent deformation by slip and twinning in magnesium during single crystal indentation. Acta Mater. **91**, 267–288 (2015)

Non-deterministic Calibration of Crystal Plasticity Model Parameters

Jacob Hochhalter, Geoffrey Bomarito, Saikumar Yeratapally, Patrick Leser, Tim Ruggles, James Warner, and William Leser

1 Introduction

The use of crystal plasticity (CP) to model grain-scale mechanical behavior of metallic microstructures has become widely used, especially in the finite element context. A major motivation has been observations made during experiment regarding the microstructure dependence of crack initiation on microstructural features and the general understanding that microstructure variation underpins variability observed at larger length scales. CP models aid in the fundamental understanding of those observations through their capability to model the effect of microscale heterogeneity by capturing the orientation-dependent behavior of each grain in a polycrystalline material. The aggregate effect of each grain, assembled in a polycrystal model, can then be analyzed upon CP model implementation within numerical methods for the solution of differential equations with complex geometry and imposed boundary conditions, e.g., finite element or fast Fourier transform methods.

J. Hochhalter (✉)
Department of Mechanical Engineering, University of Utah, Salt Lake City, UT, USA
e-mail: jacob.hochhalter@utah.edu

G. Bomarito · P. Leser · J. Warner · W. Leser
Durability, Damage Tolerance and Reliability Branch, NASA Langley Research Center, Hampton, VA, USA
e-mail: geoffrey.f.bomarito@nasa.gov; patrick.e.leser@nasa.gov; james.e.warner@nasa.gov@nasa.gov; william.leser@nasa.gov

S. Yeratapally · T. Ruggles
Durability, Damage Tolerance and Reliability Branch, National Institute of Aerospace, Hampton, VA, USA
e-mail: saikumarreddy.yeratapally@nasa.gov; timothy.ruggles@nasa.gov

S. Ghosh et al. (eds.), *Integrated Computational Materials Engineering (ICME)*,
https://doi.org/10.1007/978-3-030-40562-5_6

Recently, the importance of CP-based models for engineering applications has been highlighted, especially in aerospace applications where increased demands on efficiency and speed are driving increased complexity in structural configuration and reductions in thickness for fracture-critical components [31, 36]. While this change in paradigm is exciting and is enabling a new era in aerospace vehicles, it also defines specific challenges for researchers. A major challenge currently is that traditional standard practice models for material constitutive behavior and crack growth rates become invalidated for these next-generation applications. For example, the application of traditional fracture mechanics approaches does not apply when crack growth is in the microstructurally small regime throughout life with only several grains through thickness.

At the center of these engineering challenges is CP-based modeling for grain-scale constitutive and cracking behavior. An ultimate goal of the Integrated Computational Materials Engineering community is to provide physics-based models for materials, enabled through multiscale modeling of fundamental material behavior, propagated to a continuum representation of a material. However, until CP model parameters can be provided without a need for any experimental measurements, calibration will play a fundamental role in the application of CP models for engineering applications.

Simply put, parameter calibration is an inverse problem that aims to determine a set of material model parameters that minimize some measure of error between a model, which is a function of the parameters, and measured data. The field of applying inverse problem methodologies for the calibration of material parameters is broad. Many of the approaches to date are based on the same variational and virtual work principles upon which the fundamental principles of continuum solid mechanics are based, such as the reciprocity gap or error in constitutive equations methods. For an overview of the more general area of inverse problem methodologies applied to material parameter calibration, see [3]. For understanding the work in this chapter, it is important to identify the additional complexities imposed by working with CP models specifically. As the material model becomes more complex or requires more parameters, which is characteristic of CP models, the computational demand of calibration increases. Additionally, more data is required in such cases to mitigate issues of uniqueness. This notion becomes especially important upon consideration of the need to identify distributions of material parameters, where it is expected that the parameters are not single deterministic values.

The current literature, pertaining to discussion in this chapter, typically involves a hybrid approach to CP model parameter calibration, in which local strains from digital image correlation (DIC) and global (homogenized) stresses from testing are combined to form a cost function. An interesting approach to calibration using such data is the integrated DIC (IDIC) method. Early work of Leclerc et al. [24] formulated a two-stage process, whereby the correlation and parameter identification optimization was solved simultaneously. While the formulation is general, that work studied identification of elastic material parameters and presented a study of the effect of signal-to-noise ratio on the calibrated parameters. That initial work was later extended to the calibration of elastic-plastic material model parameters,

with comparison to the commonly used finite element model updating (FEMU) method [26]. Local DIC strain data was also used to calibrate spatial variations of yield stress within a weld nugget and heat-affected zone using uniform stress and virtual fields methods [39]. Recently, Rokoš et al. [32] addressed the known issue of boundary condition sensitivity within the IDIC method, by formulating a procedure to combine material parameters with kinematic boundary conditions as degrees of freedom at the model boundary. For an in-depth description of parameter identification methods using local DIC strain and global stress data, see [1].

The application of parameter identification methods to CP models is relatively limited. Early work of Hoc et al. [17] studied the calibration of CP parameters for an ARMCO oligocrystal specimen using deterministic optimization. In that work, the local DIC strain field was homogenized to produce a statistical distribution of their component values. Additionally, global stress values were measured during experiment. A cost function was formed by a weighted sum of both sets of data: summing the differences between the measured and computed strain distributions, at eight sampling points, and the measured and computed global stresses. More recently, local DIC strain and global stress data have been used to calibrate CP parameters from in situ tensile tests. By comparing two different CP models with experimental data at various length scales (global stress-strain curve and strain map from DIC), Sangid et al. [37] showed that although the two CP models agreed with each other and the experimental data with regard to the global stress-strain behavior, their local agreement was relatively poor at the spatial length scale of the slip system. Guery et al. [15] used FEMU to calibrate CP parameters for AISI 316LN steel using 2D simulations of microstructures with varying grain size. Grain size-dependent CP parameters were calibrated and illustrated the ability to reproduce the expected Hall-Petch behavior. Bertin et al. [2] also studied CP parameter calibration, using the IDIC method. In comparison with the study previously mentioned, the work of Bertin et al. was on a smaller scale, focused on the deformation of a bicrystal tensile sample fabricated using a focused ion beam (FIB).

The use of CP models within the finite element framework has largely focused on the propagation of uncertainty via representative volume elements (RVEs), formed by statistical instantiations of microstructure morphology. In these studies, the CP model parameters are, however, deterministic, and their variations are not considered in the ultimate prediction of variation in mechanical behavior. This is likely due to two fundamental difficulties. First, there are currently no proven methods for the non-deterministic identification of CP model parameters, and preliminary developments are required. Second, the inclusion of CP model parameter uncertainties adds to an already computationally intensive problem, when considering variations in microstructure morphology. A goal of this chapter is to illustrate that there are now methods available for the non-deterministic calibration of CP model parameters and that those parameters can be considered in the forward propagation from microscale uncertainties to predicted variation in component scale mechanical behavior.

This chapter first covers the common methods for acquiring and processing experimental data, when calibrating CP model parameters. The methods are organized into global and local approaches. Subsequently, a brief introduction to CP is given, mainly to provide sufficient understanding of the CP parameters to be calibrated and how they are involved in the model. Common numerical methods for CP model parameter calibration are then discussed in context of the global and local data that can be acquired and processed. The fundamental concepts of uncertainty quantification, with focus on the context of CP model parameter calibration, are then provided. Lastly, each of the discussed methods for calibration is evaluated on a simulated experiment with known CP parameters. This provides a clear quantification of the practical issues of uniqueness of the identified parameters.

2 Acquiring and Processing Experiment Data

The experimental measurements that must be made and post-processing methods to prepare the acquired data are overviewed here. There are two general categories, global and local, by which the acquiring and processing methods can be binned. The fundamental definitions for each of these types of acquired data are given here because they are important for understanding of the subsequently described calibration methods.

2.1 Global Data

Global data here is defined by any measurement or post-processing method that quantifies the bulk behavior of a mechanical test coupon. An example of a directly measured global data set would be the applied or reaction force provided by a load cell during testing. Similarly, this data could then be post-processed to produce either the engineering or true stress by considering the initial or current cross-section area, respectively. While displacements can similarly be obtained from the stroke of the test stand during testing, typically a displacement or strain gauge is attached to the test coupon for this data. Using gauges in this way means that any test-stand compliance is inherently filtered out of the displacement or strain data. Because these gauges homogenize underlying coupon deformation over their length, they are also considered global data.

2.2 Local Data

Local data here is defined as any measurement or post-processing method that extracts data as a field across the coupon surface or volume. An example of a directly

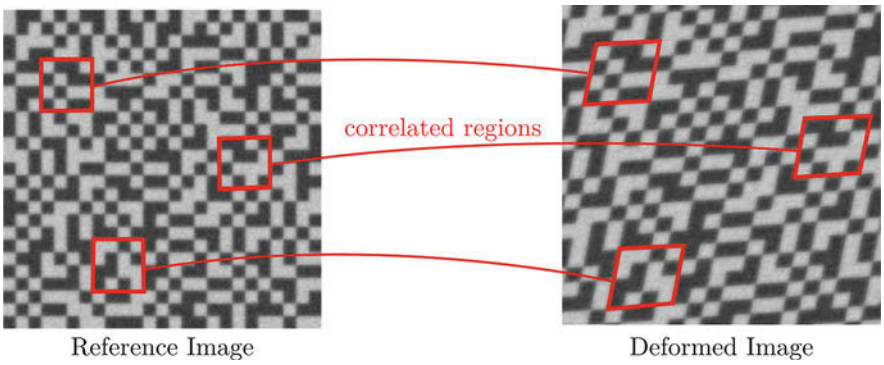

Fig. 1 Digital image correlation example

measured local data set would be displacements or strain obtained through the use of DIC, which is explained in Sect. 2.2.1. The full-field data could also be used to produce global data by extracting displacements or strains from virtual strain gauges, which extract averaged values over their length during post-processing of the DIC data. In the context of deformation of polycrystalline materials, local DIC data can be used to quantify deformations within each grain in the polycrystalline aggregate. This approach requires that the underlying microstructural features be aligned with the DIC data. The underlying microstructure morphology can be measured using electron backscatter diffraction (EBSD), which provides quantification of the surface grain shapes and their orientations. Additionally, high-resolution EBSD (HREBSD) can be used to compute the elastic deformation gradient locally on the surface of a specimen. An overview of EBSD and HREBSD is provided in Sect. 2.2.2.

2.2.1 Digital Image Correlation

DIC is a metrological tool used for quantifying motion/deformation that occurs between a reference image $f(x, y)$ and a deformed image $g(x', y')$ (see Fig. 1). By maximizing the correlation of features within f and g, a mapping can be found between (x, y) and $(x'y')$. Ultimately, that mapping comes in the form of a displacement field (usually a spatial array of displacements) [28, 40]. The displacements can be further processed to give estimates of local strains. A limitation in the above-described two-dimensional DIC is that displacements can only be measured in the plane of the image, i.e., displacements and strains with components in the Z-direction are not identified. Stereo-DIC is able to identify out-of-plane motion with the use of a two-camera setup. However, because images can only be taken of the surface of a specimen, strains with respect to the through-thickness dimension, i.e., into the specimen, are still not identified.

A fundamental aspect of DIC is that the specimen surface must contain sufficient features such that obtained images can be used to perform the correlation. While there are examples of using natural surface variation for DIC in the literature, cf. [19, 46], it is more common that a pattern must be applied to the specimen to make up for sparse natural features. The applied surface pattern plays a large role in DIC, namely, it affects the possible spatial resolution and accuracy of the measurements. There are several patterning options available for measurements of deformations at the grain scale, e.g., microstamping, lithography, and nanoparticle placement. For a full review of available techniques, the reader is referred to the recent review article of Dong and Pan [10]. Most importantly, the pattern needs to be visible to the image capturing device; optical cameras and scanning electron microscopes (SEM) are the two most common means of image capture for appropriately scaled DIC of polycrystalline metals. Furthermore, those methods require different pattern characteristics, e.g., pattern features must be opaque to electrons for optimal image contrast in SEM and opaque to visible light with optical cameras.

2.2.2 High-Resolution EBSD

EBSD is a well-established scanning electron microscope-based diffraction technique that may be used to determine local crystallographic orientation on a specimen surface. With respect to modeling, it may be used to determine the grain structure of a specific specimen [47] or to acquire statistical data about grain texture and morphology for a given material [8, 45]. HREBSD is a means of extracting the elastic deformation gradient of one diffraction pattern compared to another via cross-correlation [44]. This deformation gradient, $\mathbf{F}$, is related to a feature shift between the patterns measured by cross-correlation, $\mathbf{q}$, as follows:

$$\mathbf{q} = \mathbf{F}(\mathbf{x} - \mathbf{PC}) \frac{-\mathbf{PC} \cdot \hat{z}}{\mathbf{F}(\mathbf{x} - \mathbf{PC}) \cdot \hat{z}} - \mathbf{x} + \mathbf{PC}, \tag{1}$$

where $\mathbf{x}$ is the location of the feature on the reference pattern, $\mathbf{PC}$ is the location of origin of the diffraction pattern relative to the detector (also known as the pattern center), and $\hat{z}$ is a unit vector normal to the detector surface. If shifts are measured from four or more non-collinear points, eight of the nine components of $\mathbf{F}$ may be calculated via least squares. The missing degree of freedom is approximately the relative dilatory strain (it may not be recovered as a consequence of projecting the diffraction pattern onto a 2D detector) and is recovered by assuming zero traction or by determining only the deviatoric component of the strain. Note that HREBSD recovers the relative deformation gradient between two patterns. In order to determine the absolute deformation gradient of a material, it is necessary to simulate a strain-free reference pattern of known orientation [18, 20]. This method is more sensitive to error in $\mathbf{PC}$ and requires careful calibration [5]. Once recovered, the local elastic deformation gradient may be used to determine a number of useful variables concerning the local material state, including elastic strain, orientation

(much more accurately than conventional EBSD), and stress via Hooke's law (if the elastic parameters of the material are well-known). By looking at the curl of the deformation gradient, HREBSD measurements may even be used to calculate Nye's tensor, a continuum representation of geometrically necessary dislocation density [34].

2.2.3 Combining DIC and HREBSD

Recently, a new measurement method has been developed which allows for the simultaneous acquisition of DIC and HREBSD on a specimen surface. The integration of these two, previously mutually exclusive, experimental methods is made possible by the application of an amorphous DIC-pattern material, such as urethane rubber [35], that provides good contrast for DIC in a SEM at low acceleration voltage (at about 5 keV) using secondary electron imaging, but has negligible interference with the primary electrons that form diffraction patterns at high-accelerating voltage (20 keV). An example of this stamp, imaged in two different modes, is shown in Fig. 2. This combination of methods enables decomposition of deformation within the same surface domain during loading. In other words, DIC can be used to quantify the total deformation, while HREBSD can be used to quantify the elastic part of that total deformation, allowing for a decomposition of the elastic and plastic parts. Note that the current feature size of the stamp is approximately 1 micron and the spatial resolution of the patterning technique is expected to improve with further development. The implications of this new measurement method on calibration methods are provided in Sect. 6.3.

3 Crystal Plasticity

As motivated in Sect. 1 of this chapter, CP models are becoming increasingly used when microstructure dependence in engineering use cases is observed. There are at least two driving factors for that increased adoption. First, CP models are reaching maturity where even complex micromechanism multiphysics simulations can be completed in a reasonable amount of time and with well-supported computational toolsets. Second, in many engineering applications, component size reduction is common. Examples of such applications are microelectromechanical systems, electronic devices, and thinning of structural components in aerospace vehicle components. Furthermore, material processing of Ni- and Al-based metals in aerospace applications, e.g., turbine blades and pressure vessels, can result in grain growth resulting in grain sizes approaching the structural scale. In these cases, and others like them, the micromechanics plays a governing role in the behavior, size effect, and variability in component performance and reliability and, hence, must be considered during design and certification.

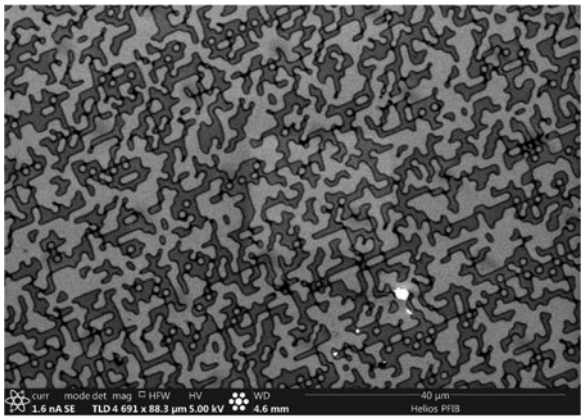

(a)

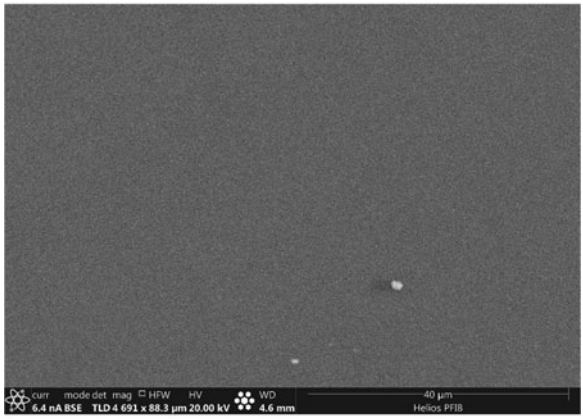

(b)

Fig. 2 Images on of a urethane residual layer stamp applied to an aluminum oligocrystal sample imaged at 5 keV using secondary electron imaging (**a**) and at 20 keV using backscattered electrons (**b**)

While the general area of CP modeling and their applications is large, a focus here is given to phenomenological models. Such models are characterized by the consideration of the shear stress resolved on each crystallographic slip system, τ^{α}, and its current strength, g^{α}, that causes plastic slip, γ^{α}, to occur. Similarly, the discussion is limited to CP models that represent a single phase with lattice dislocations as the sole deformation mechanism. The objective of this section is to provide sufficient background for CP modeling such that the subsequent discussion of non-deterministic calibration of CP parameters can be understood. For an encompassing review of CP modeling, see [33].

3.1 Concepts

For the remainder of this chapter, consideration is given to CP as a model for the homogenization of the underlying motion of dislocations on each slip system. As such, the primary parts of a CP model are the kinematics of slip and a constitutive model relating the external forces to slip rates through resolved shear stress. The mathematical model of the kinematics of finite deformation relates the original reference configuration of a continuum to a current configuration that is obtained through the application of external loads and displacements. The total deformation gradient, F, relates the reference and current configurations directly.

The decomposition of F into its elastic and plastic parts can be thought of as a multiplicative transformation, Eq. 3. Therein, F_e represents the reversible component of deformation, while F_p represents the deformation that remains upon removal of the external forces and displacements. If irreversible deformation is present, an intermediate configuration is obtained upon removal of external forces and displacements. This intermediate configuration is related to the reference configuration by F_p. Furthermore, the lattice orientation remains unchanged in the intermediate configuration, resulting in a stress-free configuration. Effectively, this relies on an assumption that any dislocations formed must be passed beyond its local neighborhood. The intermediate and current configurations are related by F_e, where lattice distortions lead to material stresses. This concept that the stress is induced by the elastic portion of the deformation is fundamental both to the development of the following constitutive equations and to the calibration method presented in Sect. 4.4.

$$F = F_e F_p. \tag{2}$$

However, this decomposition does not yet have information regarding the underlying crystallography essential for CP modeling. To capture crystallographic kinematics, the plastic velocity gradient, L_p, is defined as a tensor that transforms the plastic deformation gradient, F_p, to its time rate of change:

$$\dot{F}_p = L_p F_p. \tag{3}$$

Since the consideration here is limited to dislocation slip as the only plastic deformation process, L_p is formulated as the sum of rates of slip on each system, $\dot{\gamma}^\alpha$, along with the slip direction for each system, m^α, and its corresponding plane normal, n^α:

$$L_p = \sum_{\alpha=1}^{n} \dot{\gamma}^\alpha m^\alpha \otimes n^\alpha. \tag{4}$$

It is with this definition that the crystallographic kinematics are modeled.

The constitutive models in CP relate F_e to the resolved shear stress on each system, τ^α, through the elastic stiffness tensor, C, using second Piola-Kirchhoff stress and Green elastic strain:

$$\tau^\alpha = 0.5C[F_e^T F_e - I] : m^\alpha \otimes n^\alpha, \tag{5}$$

where T denotes the transpose. With τ^α computed, the rate of slip on each system, $\dot{\gamma}^\alpha$, is computed herein as:

$$\dot{\gamma}^\alpha = \dot{\gamma}_o \frac{\tau^\alpha}{g^\alpha} \left| \frac{\tau^\alpha}{g^\alpha} \right|^{\frac{1}{m}-1}. \tag{6}$$

And, lastly, the evolution of hardening on each system, $\dot{g}^\alpha$, is integrated as a function of the current hardness, g^α; the saturation hardness, g_s; and the initial hardness, g_o.

$$\dot{g}^\alpha = G_o \left(\frac{g_s - g^\alpha}{g_s - g_o} \right) \left| \dot{\gamma}^{\text{tot}} \right|. \tag{7}$$

In Eq. 7, $\dot{\gamma}^{\text{tot}}$ refers to the total slip rate across all the slip systems and can be represented mathematically per Eq. 8:

$$\dot{\gamma}^{\text{tot}} = \sum_{\alpha=1}^{N_{SS}} \dot{\gamma}^\alpha, \tag{8}$$

where N_{SS} refers to the number of slip systems, which is 12 for an FCC system. Since Eq. 7 incorporates the total accumulated slip rate, the hardening on each system is equivalent.

Further, the saturation hardness term, g_s, in Eq. 7 can be expressed as:

$$g_s = g_{so} \left| \frac{\dot{\gamma}^{\text{tot}}}{\dot{\gamma}_s} \right|^\omega, \tag{9}$$

where g_{so}, $\dot{\gamma}_s$, and ω are three input parameters for the reference saturation hardness, the reference saturation slip rate, and the saturation rate exponent, respectively.

For the purpose of simplicity and tractability of both global-local and local calibration studies, the saturation hardness, g_s, can further be expressed as:

$$g_s = (g_o + g_s^*) \left| \dot{\gamma}^{\text{tot}} \right|^\omega, \tag{10}$$

where g_s^* is a normalized reference saturation hardness. Although g_s^* is a function of both g_{so} and $\dot{\gamma}_s$, for the purpose of calibration studies, it is expressed as an independent variable. Additionally, parameters $\dot{\gamma}_o$ and ω are treated as "fixed parameters" – not included as calibration parameters – as their respective influence on slip rates and hardening of each slip system can be emulated by parameters m and

g_s^*, respectively. Therefore, the set of calibration parameters involved in the current work include g_o, m, G_o, and g_s^*.

The CP model presented in this section is used throughout the remainder of the chapter. First, the model is used to represent a collection of grains, Sect. 4.2, within a Taylor model where the grains deform independently. Subsequently, in Sects. 4.3 and 4.4, these equations are implemented within a finite element framework for higher-fidelity modeling of the interaction among grains in a polycrystal. This aggregation of the deformation of multiple grains with varying crystallographic orientations leads to an anisotropic behavior with heterogeneous stress and strain fields throughout the continuum. As discussed in the subsequent sections, these heterogeneities are important aspects of the calibration process.

Finally, model selection is an important preliminary step to calibrating parameters. In other words, no calibration process can function adequately if an inaccurate or invalid model is selected. Consequently, care should be taken in identifying an appropriate model, before the calibration process is considered. In this chapter, simulated experiments are completed to serve as a surrogate for physical test data. As such, the model selection is inherently prescribed, which allows for a focus on issues regarding non-deterministic calibration (and not model selection).

4 Calibration

In this section, an overview of the general methods for CP material model calibration is provided in the context of local and global, measured and computed, data. Subsequently, in Sect. 6, issues of uniqueness and precision are illustrated through application of several calibration methods, using a simulated experiment.

4.1 General Process

The core of model calibration is the inference of model parameters, θ, adjusted to match some set of measured data. The inference is centered on the comparison of the predicted model response and measured response, where the model is subjected to some measured loading (see the flowchart in Fig. 3). To put this in context of the uncertainty quantification framework, which is described in Sect. 5, the comparison is used in the calculation of the likelihood of a set of calibration parameters.

The measurements, model, and comparison parts of the process are where customization for a particular calibration method are made. The experimental measurements, which provide loading and geometry input to the model, can be global, local, or a combination. Similarly, the model itself can be global, local, or a combination in its scale. The comparison of the model and measured response can be either deterministic or non-deterministic in its formulation. In this section, a discussion of available experimental measurement and modeling approaches are

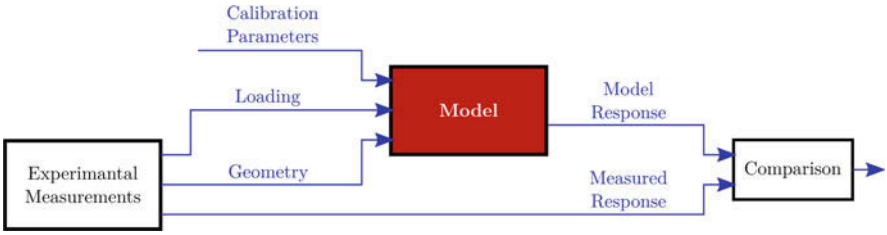

Fig. 3 Model calibration flowchart

discussed in the context of global and local variations. Subsequently, in Sect. 5, a method for non-deterministic comparison is presented.

Model choice plays an important role in the ability to generate accurate and precise calibrations. The inability of a model to fit a given data set during calibration suggests that the model is missing necessary physics and will exhibit poor predictive performance. This is known as model discrepancy and is discussed in detail in [22]. It is the responsibility of the analyst to check for model discrepancy as part of the calibration process.

In the context of CP calibration, three general categories of models can be used. The categories are differentiated by the types of data that are used for both the input loading and output response. Global and local calibration methods are differentiated by their use of global and local data, respectively (see Sect. 2). Global-local methods use a combination of global and local data.

4.2 Global Methods

In the case of isotropic materials, calibrating material parameters is readily achieved using a uniaxial, one-dimensional, stress-strain curve. However, because of the anisotropic nature of CP models, the resulting yield surface being evolved during computational simulation is six-dimensional. In the case of anisotropic material models, as is the focus here, the reduction of a six-dimensional yield surface to a measured scalar (one-dimensional) surface can be problematic. For example, Fig. 4 illustrates global uniaxial tension stress-strain behavior measured on a pure Al coupon. Also shown are the computed stress-strain results, using a Taylor model, from two disparate sets of CP parameters; see Table 1. Note, the parameters in Table 1 are chosen to illustrate this issue of uniqueness, where ω is permitted to vary (unlike other calibration exercises in this chapter). Upon studying the goodness of fit produced by either set of CP parameters, it would be reasonable to accept either set as accurately reproducing the measured data because both produce a nearly identical aggregate response. Consequently, more advanced methods should be considered for calibration of CP parameters to resolve this issue of uniqueness.

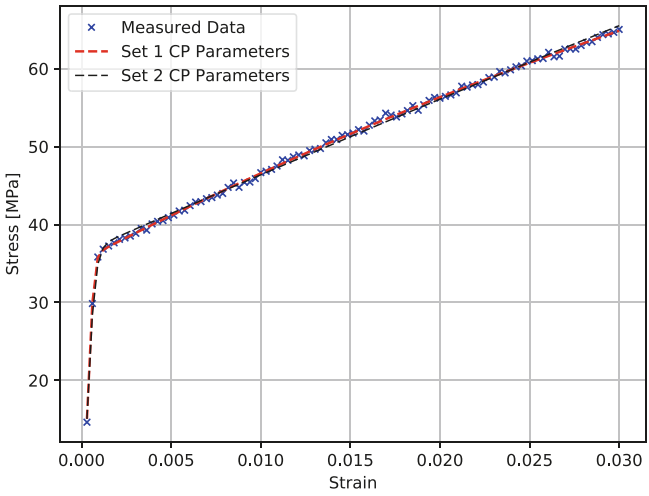

Fig. 4 Multiple CP parameters sets with nearly identical one-dimensional stress-strain response

Table 1 Two disparate sets of CP model parameter definitions. These sets were used to produce the global stress-strain curves in Fig. 4

Parameter (units)	Set 1	Set 2
m	0.037	0.121
g_o (MPa)	19.477	30.460
G_o (MPa)	292.28	365.89
ω	2.682×10^{-4}	3.343×10^{-4}
g_s^* (MPa)	47.912	419.168
Mean absolute error (MPa)	0.19	0.35

Nonetheless, global methods are commonly used for CP model calibration. It is largely the practicality of these methods that make them attractive: less sample preparation and specialized equipment is required to complete the calibrations. In the most typical form, calibration is performed based on the stress-strain relationship of a polycrystalline coupon in uniaxial tension. In cases where only bulk behavior is of interest, the lack of uniqueness poses no real issue. However, when local, microstructurally controlled quantities are of interest, the lack of uniqueness becomes more problematic. The fundamental problem is that the local response may be very different between predictions made with two sets of CP parameters despite the fact that their global response is similar.

4.2.1 Data Flow

In a global calibration method, both the measured and computed data are the result of a homogenization; see Fig. 5. Typically, the experimental measurement is force and displacement over the gauge length for a uniaxial mechanical test. This provides a one-dimensional slice of the larger yield surface. To inform the CP model,

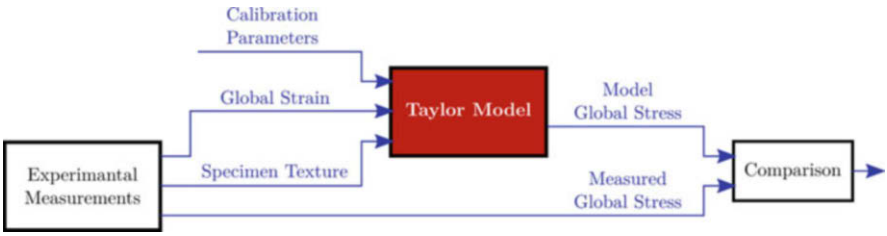

Fig. 5 Example of a global calibration based on a Taylor model

crystallographic texture must also be measured, for example, using EBSD. The measured force or displacement (or stress and strain) is used, along with the current iterate for material parameters as input to the computational model, discussed in Sect. 4.2.2. The output of the model must produce data that is directly comparable to the measured data to enable the computation of difference and drive updates to iterated material parameters.

4.2.2 Computational Model

In global calibration methods, two approaches can be used. First, simplified (not explicitly representing specific grain structure or compatibility) models, like that developed by Taylor [41], are often used because of their relative simplicity and computational efficiency. In this case, the equations presented in Sect. 3 are integrated using the measured strains and texture as input. Orientations are then sampled for each material point to be modeled with the measured strain applied to each sampled orientation. After integrating the constitutive equations, to evolve slip rates and resistance to slip, stresses are computed for each material point. Those stresses are then averaged to compute an homogenized, global scalar value to be compared to the measured stress-strain curve.

Second, a higher-fidelity model of the polycrystalline aggregate can be generated using finite element (FE) models. In this approach, either a statistically representative volume can be instantiated by sampling measured microstructure morphology distributions, or a replicated volume can be produced by measuring the specific microstructure of the coupon. The advantage of these models, over the Taylor model, is that the complex interactions among grains in the polycrystal is inherently captured. The disadvantage is that these models are computationally more demanding. Consequently, calibration will take longer, will require additional computational resources, and limits the number of grains that can be modeled. Upon an iterative update to the CP material parameters being calibrated, the global forces and displacements are post-processed from reactions at the boundary for comparison with measured data.

Taylor approximations and FE models represent bounding scenarios between ease of use (Taylor) and high fidelity (FE). However, approaches such as the

visco-plastic self-consistent (VPSC) model [23] can provide accurate results by accounting for the effect of grain shape while maintaining a tractable computational effort. Additionally, while not exercised in this chapter, it is important to note that stress-strain curves could be extracted from a variety of directions with respect to the bulk material texture. This additional data would serve to improve the global calibration approach.

4.3 Global-Local Methods

Like purely global methods, hybrid global-local methods use homogenized stress as a target for the calibration method. A major difference, and improvement, comes from the acquiring and integration of full-field displacement or strain data from DIC. This additional full-field data fundamentally changes the numerical aspects of the calibration. Instead of fitting a relatively simple (approximately a second-order polynomial) global stress-strain curve using many (often greater than 5) CP parameters, the DIC dataset helps alleviate the issue of uniqueness that plagues global methods. Because of this, global-local methods are an improvement over global methods.

4.3.1 Data Flow

In a global-local calibration method, the measured global force is combined with local DIC data; see Fig. 6. Consequently, compared to the standard global methods, global-local methods require additional DIC hardware and software to acquire and process the acquired images. To inform the CP model, it is ideal to measure the particular microstructure throughout the test coupon. Most commonly, this data is acquired before mechanical testing using EBSD. While acquiring EBSD data provides data beneficial to the calibration process, it is incomplete in the sense that only surface microstructure is measured, leaving uncertainty about the underlying microstructure. This not only means that subsurface grain orientations are unknown but further means that subsurface defects could also influence the acquired surface strain data. While volumetric methods for measuring microstructure are possible, their availability is currently lacking in general common usage and less commonly used for calibration.

4.3.2 Computational Model

Because the DIC data acquired in this method is local, local values for displacement or strain must be computed using a FE model. To most closely match the acquired DIC data, the FE model should be constrained on its boundaries with measured DIC displacement data within a region of interest (ROI). Rokoš et al. [32] have recently

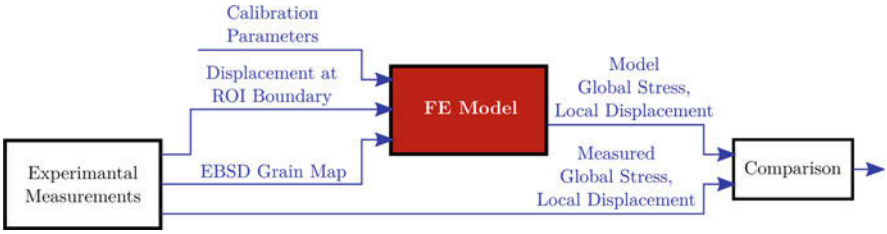

Fig. 6 Example of a global-local calibration based on a finite element model

studied the high sensitivity of calibrated CP parameters on applied boundary conditions and investigated methods to mitigate this source of noise. The FE model should also be defined to replicate the measured grains and their orientations. Upon simulation of the FE model, the computed global stress can be homogenized and compared in the same manner as global methods. Additionally, the local displacement or strain data should also be compared and requires the spatial alignment of the measured and computed displacement or strain data. Alignment of multiple data sets in this context is typically done using fiducial markers as discussed in Lim et al. [25] and Chen et al. [9]. The relative error is typically defined mathematically as a weighted summation of the global and local components.

4.4 Local Methods

Purely local methods are characterized by utilization of local DIC data and local stress data. These methods are somewhat specific to calibrating CP models for crystalline structures in that HREBSD is used to compute local stress; recall Sect. 2.2.2. This improves upon both previously discussed methods in that no global homogenization of mechanical behavior is required. Also, since local stresses and strains are acquired coincidentally, there is no need to generate a FE model to compute homogenized stress. The main disadvantage of the purely local approach is that acquiring and processing HREBSD data is time-consuming, which means that the test must be periodically paused for relatively long periods to acquire the data, which can have implications for rate-dependent materials.

4.4.1 Data Flow

The local calibration method requires that the mechanical test be paused periodically to acquire and process HREBSD and compute local stress at various microstructure locations; see Fig. 7. At the same time, DIC data is acquired to provide local strain data. The DIC data is used as input to the CP model, where each local strain tensor is used to drive deformation. The CP model is then used to compute stress at each coincident point. Those computed stress values are compared directly with

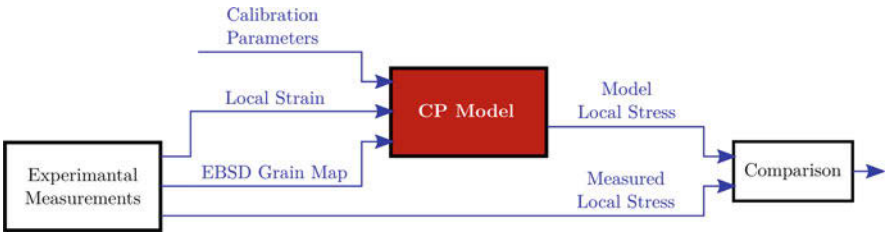

Fig. 7 Example of a local calibration based on a direct use of a CP model

the local stress values acquired by HREBSD. In this process, the CP model must be constrained to follow the same local strain and strain rate as the test. This way, there is no discrepancy in the history between acquired and computed data. Lastly, because acquiring HREBSD data is relatively time-consuming, it is practical to repeat this measurement only several times during loading. The increment in time between these measurements will likely be large relative to the numerical integration time stepping required by the CP model. However, the CP model need not increment in one step to times where DIC data was acquired, but may instead subdivide that increment into sufficiently small time steps to achieve convergence.

4.4.2 Computational Model

Since no FE model is required for the local method, there is also no need to extract boundary conditions from DIC for application to the FE model, and the previously discussed issues regarding sensitivity of calibrated CP parameters to boundary conditions in the global and global-local methods are precluded. Instead, each material point is completely defined, in terms of deformation gradient and stress, as decoupled material tests. Because these material points exist throughout a heterogeneous stress-strain field, each of these decoupled material behavior datasets is under different loading scenarios, with respect to their local crystallography. In effect, this is equivalent to running many mechanical tests and measuring the stress-strain response.

5 Uncertainty Quantification Model for Calibration

Model calibration in the presence of uncertainty requires a non-deterministic approach to parameter estimation. For cases where measurement errors, ε_i, are unbiased, independent, and identically distributed (iid), the statistical model describing the relationship between measurements, model, and errors can be defined as:

$$\mathrm{Y}_i = \mathcal{M}_i(\Theta) + \varepsilon_i, \tag{11}$$

for $i = 1, \ldots, M$, where Y_i, Θ, and ε_i are random variables representing the measurements, model parameters, and measurement errors, respectively. In the context of the CP model calibration herein, $\Theta = [g_0, m, G_0, g_s^*]$ and the measurements are local or global observations, as discussed in previous sections. M is the total number of measurements available, and $\mathcal{M}_i(\Theta)$ denotes the model response corresponding to a time and location, represented by i, at which the measurements were obtained.

The goal of model calibration is to solve the inverse problem posed by Eq. 11; that is, determine the probability distribution of the model parameters given a set of measurements. Formally, this involves determining the posterior density, $\pi(\theta|y)$, where y and θ are realizations of the random variables Y and Θ, respectively. Using Bayes' theorem, the posterior density can be expressed as:

$$\pi(\theta|y) = \frac{\pi(y|\theta)\pi(\theta)}{\pi(y)} = \frac{\pi(y|\theta)\pi(\theta)}{\int_{\mathbb{R}^p} \pi(y|\theta)\pi(\theta)d\theta}. \tag{12}$$

The numerator of Eq. 12 is a multiplication of two densities, the likelihood function, $\pi(y|\theta)$, and the prior density, $\pi(\theta)$. The latter represents any a priori knowledge regarding the parameters, Θ. The prior density is assumed to be known and is often derived from expert knowledge or previous experiments. If unknown, a noninformative prior can be used such that the prior is an improper uniform density over the known parameter support; e.g., a parameter known to be positive would be distributed uniformly over the space bounded by zero and infinity.

The likelihood function is dependent on assumptions about the errors in Eq. 11. A common assumption is that errors are iid and $\varepsilon_i \sim N(0, \sigma^2)$ where the variance, σ^2, is fixed. In this case, the likelihood function becomes:

$$\pi(y|\theta) = \frac{1}{(2\pi\sigma^2)^{M/2}} \exp\left(-\frac{1}{2\sigma^2} \sum_{i=1}^{M} \left[y_i - \mathcal{M}_i(\theta) \right]^2 \right), \tag{13}$$

which is a function of the sum of squared errors between the model and the measurements. Therefore, both the prior density and the likelihood function can be evaluated at any given point in the parameter space.

The denominator, on the other hand, is more complex as it involves integration over the entire parameter space, with $\theta \in \mathbb{R}^p$ and p denoting the dimensionality of θ. Computing this denominator and, hence, the posterior density can be challenging if not intractable, especially as p increases. While classical quadrature can be used in some cases, an alternative is to construct a Markov chain through the parameter space that has a stationary distribution equal to the posterior density. This approach is called Markov chain Monte Carlo (MCMC) and was chosen in this work to obtain an approximation of the posterior density, $\pi(\theta|y)$.

A detailed explanation of MCMC is beyond the scope of this section, but interested readers are referred to [21, 38] for more information on implementation.

In short, MCMC avoids computing the denominator of Eq. 12 and instead utilizes the proportionality:

$$\pi(\theta|y) \propto \pi(y|\theta)\pi(\theta), \tag{14}$$

which can be computed at any point $\theta \in \mathbb{R}^p$. An iterative sampling procedure is implemented to form the Markov chain. Since realizations of the chain are samples of the posterior by definition, a sample-based approximation of the posterior density can be obtained. As with standard Monte Carlo sampling, this sample-based estimate of the posterior density converges as the number of samples in the chain, $N \to \infty$. In practice, $N << \infty$, and thus MCMC yields an approximation of the posterior density.

A multitude of algorithms exist for forming this Markov chain. In general, they involve a proposal distribution, $J(\theta^*|\theta^{k-1})$, that depends only on the previous sample in the chain, θ^{k-1}. A common choice is $J(\theta^*|\theta^{k-1}) = N(\theta^{k-1}, V)$, a normal distribution centered at the previous sample with some covariance, V. The candidate sample, θ^*, is either accepted or rejected based on the value of the acceptance ratio:

$$\mathcal{A}(\theta^*, \theta^{k-1}) = \frac{\pi(\theta^*|y)}{\pi(\theta^{k-1}|y)} = \frac{\pi(y|\theta^*)\pi(\theta^*)}{\pi(y|\theta^{k-1})\pi(\theta^{k-1})}. \tag{15}$$

A new sample yielding $\mathcal{A}(\theta^*, \theta^{k-1}) > 1$ is always accepted into the chain as it has a high posterior probability than the previous sample. Accepting a sample implies $\theta^k = \theta^*$. If not, the new sample is accepted with probability $\mathcal{A}(\theta^*, \theta^{k-1})$, meaning that the sample is more likely to be accepted the closer $\pi(\theta^*|y)$ is to $\pi(\theta^{k-1}|y)$. If rejected, $\theta^k = \theta^{k-1}$. This process is iterated until chain convergence.[1]

The dependence of $J(\cdot)$ on θ^{k-1} means MCMC algorithms require initialization. In this work, a least squares optimization was conducted to deterministically fit the model parameters to available data and generate an initial guess in a region of high posterior probability. This method accelerates chain convergence by reducing the time spent searching for this region of high probability by a random walk over the parameter space. Adaptive tuning of the proposal covariance V is typically required during the initial stage of chain development as well. The resulting, non-stationary period of searching and tuning is referred to as the burn-in period. The end of the burn-in is defined by the point at which the Markov chain reaches a stationary condition. By definition, samples obtained from the burn-in period are not drawn from the targeted posterior distribution. In practice, an initial percentage of the chain is attributed to burn-in and discarded.

[1] Diagnosing chain convergence can be challenging, and readers are referred to [6, 13] for more information.

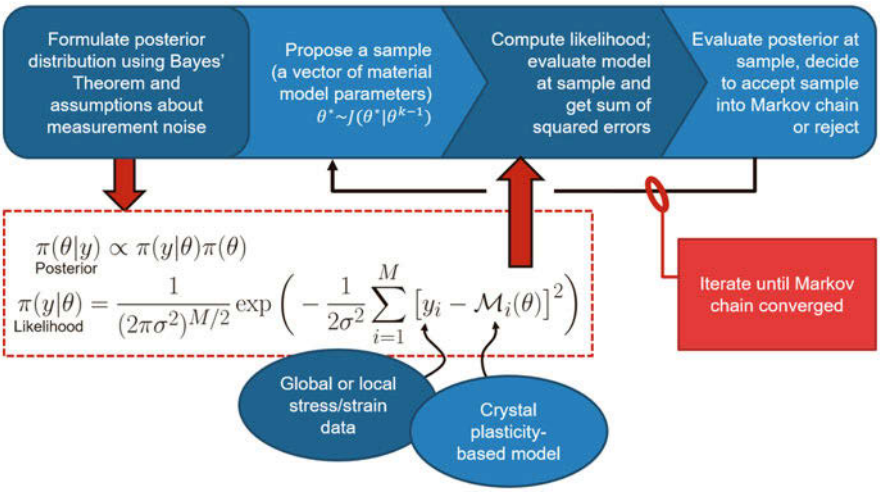

Fig. 8 Flowchart of the MCMC-based model calibration

A flowchart of the calibration process is shown in Fig. 8. Upon completion of MCMC sampling, approximations of Θ are available. If the variance in the assumed measurement error distribution is unknown, it can be included in the parameter vector and estimated; e.g., $\Theta = [g_0, m, G_0, g_s^*, \sigma^2]$. The end result is a non-deterministic calibration of the CP model as well as an estimate of measurement noise. Then, according to Eq. 11, samples drawn from the joint posterior parameter density can be fed through the model to form a non-deterministic prediction of a given quantity of interest via Monte Carlo simulation. Examples of a quantity of interest in the context of CP model calibration might be mechanical response at a larger scale or under new boundary conditions.

6 Demonstration Using Simulated Experiments

A numerical experiment was performed in order to generate a synthetic dataset on which a calibration can be performed. An advantage to a numerical experiment and synthetic data is that the true values of the parameters will be known. The proceeding calibration demonstrations can thus be judged relative to the known values.

A coarse-grain microstructure model representing an aluminum oligocrystal was created using DREAM.3D [14], an open-source microstructure modeling and analysis package. Zhao et al. [47] observed that a significant portion of grain boundaries in an oligocrystal sample remained perpendicular to the surface of the sample, thereby maintaining a nearly columnar shape. For simplicity, an idealized perfectly columnar grain structure is considered in the current study, thereby

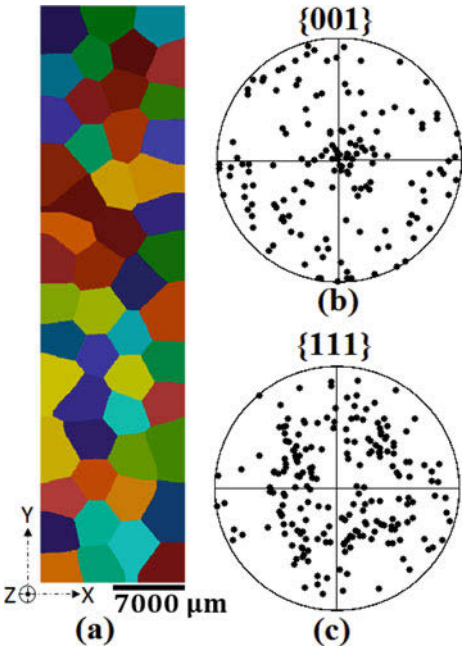

Fig. 9 (**a**) Front view of the 2.5D microstructure model used in the current work. Each unique color represents an individual grain. (**b**) {001} pole figure showing the overall orientation distribution of all the grains in the polycrystal model. (**c**) {111} pole figure showing the overall orientation distribution of all the grains in the polycrystal model

resulting in the generation of a 2.5D microstructure. The columnar grain assumption serves to reduce a source of uncertainty that arises due to the through-thickness variation in grain structure [30, 42]. Based on the observations of Zhao et al. [47], the texture of the microstructure was assumed to be random, and an average grain size of 3.5 mm was used in creating the microstructure model. A 2.5D microstructure model of an aluminum oligocrystal (shown in Fig. 9a) was used in the current study. Figure 9b, c are the {001} and {111} pole figures, respectively, showing the orientations assigned to the 51 grains in the microstructure model. The dimensions of the microstructure model shown in Fig. 9a are $200 \times 800 \times 20$ voxels, with each voxel having a resolution of 70 µm.

To prepare the geometry for finite element simulation, the "quick mesh" filter in DREAM.3D is applied to convert the grid geometry of the voxelated microstructure to a triangle geometry by inserting a pair of triangles on the face of each voxel or cell. Following the "quick mesh" filter, the "Laplacian smoothing" filter is applied to smooth out the stair stepped grain boundary profiles. The smoothed surface mesh of each grain is then output to a binary stereolithography file. Surface meshes of all the grains were input into Gmsh [12] to generate a volume mesh of the microstructure. The finite element volume mesh of the microstructure model was discretized into 5.837 million quadratic tetrahedral elements and contained 8.509 million nodes. The volume mesh is then input into the finite element code, ScIFEi [43], to carry out the computationally intensive CP simulations to solve for the heterogeneous stress and strain state within the microstructure.

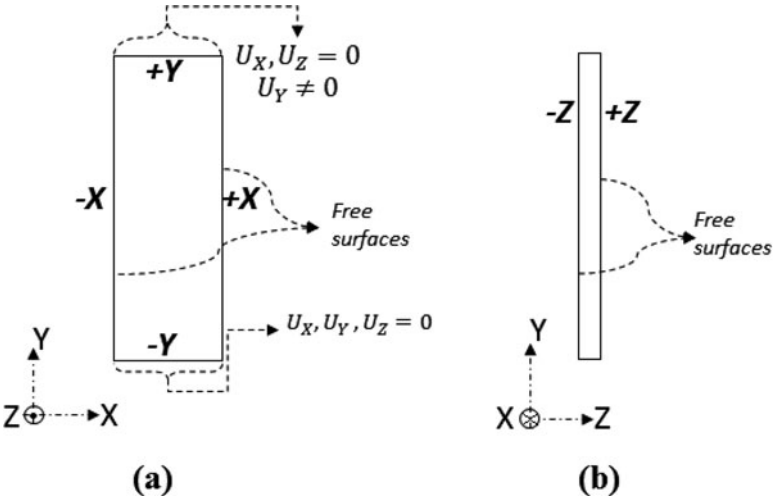

Fig. 10 (**a**) Front view of the microstructure domain showing the boundary conditions on +X, +Y, −X, and −Y faces. (**b**) Side view of the microstructure domain showing the boundary conditions on the +Z and −Z faces

The microstructure model is subjected to a 1% global strain by prescribing displacement-controlled loading conditions along with the other boundary conditions as depicted schematically in Fig. 10. Fully fixed constraints were applied on the bottom (−Y) face, whereas the top (+Y) face, on which the displacement was prescribed, was constrained from any displacements in the X- and Z-directions. The remaining four faces (+X, −X, +Z, and −Z) of the cuboidal microstructure domain were set to deform freely. The simulation was run in parallel on 400 processors using NASA Langley's K cluster for about 38 h.

The complex heterogeneous stress and strain fields developed within the microstructure are computed using a built-in anisotropic elasticity and CP framework in ScIFEi, Sect. 3.1. The grains were assigned anisotropic elastic properties, through three cubic elastic constants C_{11},C_{12}, and C_{44}, which were assigned the values 101.9, 58.9, and 26.3 GPa, respectively. Rate-dependent and length scale-independent CP kinematics (flow and hardening laws), discussed in Sect. 3, were assigned to the grains. The values of the calibration constants used for the CP model were chosen in such a way that they are in the range of the values assigned for corresponding parameters in CP models of aluminum alloys [4, 47], but do not pertain to any specific study.

As discussed in Sect. 3, the six fitting parameters present in the CP equations shown in Eq. 6 through Eq. 10 include g_o, ω, G_o, $\dot{\gamma}_o$, g_s^*, and m. The values of the six fitting parameters that serve as the target for calibration studies are shown in Table 2. It must be noted that since the non-deterministic local calibration model is insensitive to the values of the fitting parameters used, the chosen values will not influence the output of the calibration model. In order to mimic the lower yield strength of oligocrystal alloy, g_o and G_o were assigned lower values compared to the

Table 2 Fitting parameters used in the CP model

Parameter (units)	Value
m	0.05
g_o (MPa)	130.0
$\dot{\gamma}$ $(\frac{1}{s})$	1.0
G_o (MPa)	100.41
g_s^* (MPa)	113.91
ω	0.001

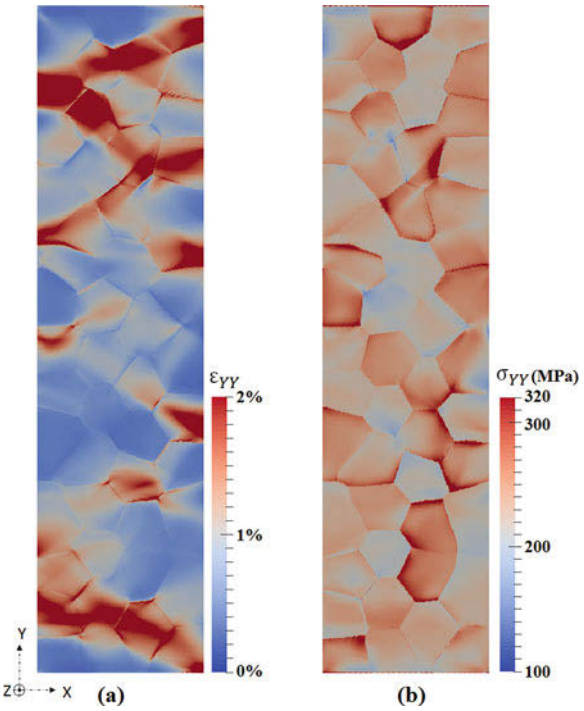

Fig. 11 (**a**) Strain map on the free surface of the microstructure model showing the strain component in the loading direction obtained at a global strain of 1%. (**b**) Stress map on the free surface of the microstructure model showing stress component in the loading direction obtained at a global strain of 1%

relatively finer grain material, Al 7075-T651 [4]. The lower g_o and G_o signify the lower yield strength of the aluminum oligocrystal, which is the material of choice in the current study.

The heterogeneous distributions of stress and strain components in the loading direction, obtained at 1% global strain, are shown in Fig. 11. The stress and strain data obtained from the free surface of the microstructure model serves as the simulated DIC data.

In all of the proceeding calibration demonstrations, model inputs that are derived from the simulated experiments (i.e., geometry and loading) are noise-free. Measurement noise has been lumped into the measurement fields Y_i. For example, the stress-strain curve used in the global calibration has Gaussian noise added to the homogenized stress with a standard deviation of 0.5% of the maximum stress, Fig. 12. The strain values and the grain orientations for that case are noise-free and

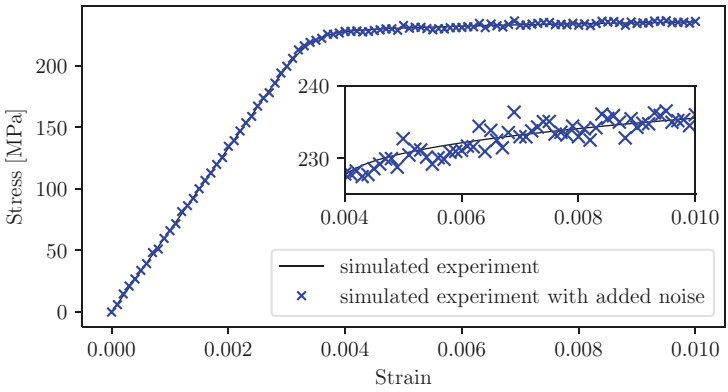

Fig. 12 Stress-strain curve from simulated experiment, including added measurement noise

taken directly from the simulation. Gaussian noise with standard deviations of 0.07 microns and 5 MPa are added to each component of the simulated experiment's DIC displacement and HREBSD stress, respectively, when these are used as data for model calibration. Note that the stress fields in simulated HREBSD have more added noise than the homogenized stress (standard deviation of 5 MPa compared to about 1.2 MPa, respectively) to reflect higher measurement error in the local method.

6.1 Using Global Calibration

The demonstration of non-deterministic global calibration was performed using the Taylor model (see Sect. 4.2.2) and the uncertainty quantification framework described in Sect. 5. In this case, the measurements, Y_i, are the homogenized stresses from the simulated experiment. The model response $\mathcal{M}_i(\Theta)$ is the homogenized stresses of the Taylor model.

Before approximating the posterior parameter distribution with MCMC sampling, a deterministic optimization was performed to initialize the Markov chain. A Broyden-Fletcher-Goldfarb-Shanno (BFGS) [27] optimization was chosen with the initial guesses of the parameters at 105% of their true values. The open-source python package PyMC [29] was used to perform MCMC sampling with the delayed rejection adaptive Metropolis (DRAM) [16] step method. In total, 25,000 samples were generated, with the first 10,000 samples discarded as burn-in. The covariance of the proposal distribution was adapted every 1,000 accepted samples to accelerate convergence of the Markov chain to a stationary condition. The calibration took about 82 h on a single core of a 3.50 GHz Intel Xeon E5-1650 v3 CPU, corresponding to about 12 s per sample, although it should be noted that up to two samples can be evaluated for each new addition to the Markov chain due to the delayed rejection aspect of the DRAM algorithm.

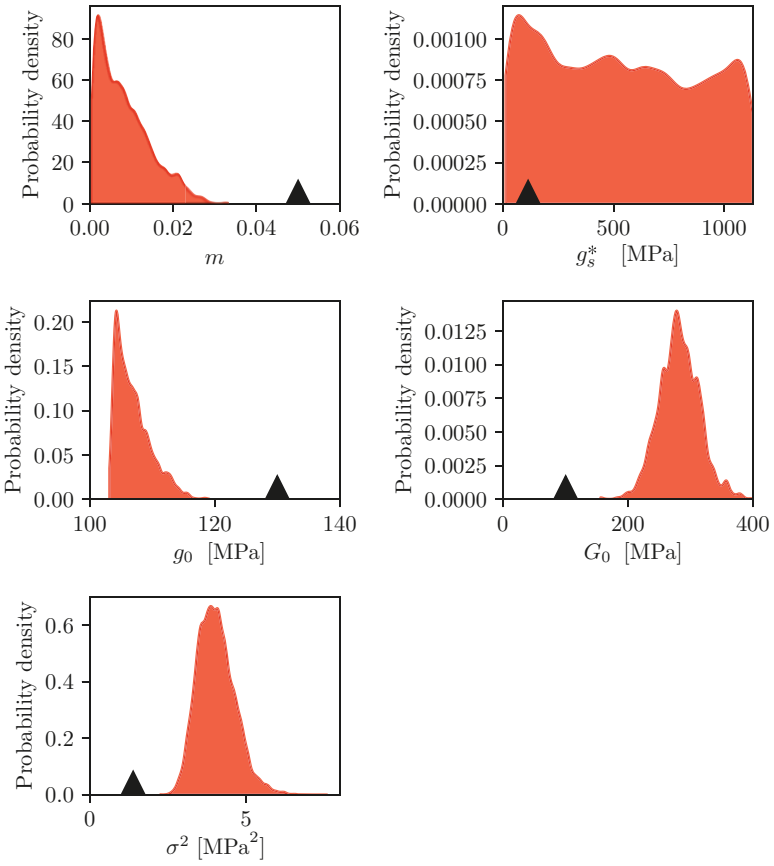

Fig. 13 The result of global calibration. The marginal probability density functions of the calibration parameters, including the estimate of the variance of the error. The triangle denotes the true values of each calibration parameter

The resulting marginal probability density functions of Θ are illustrated in Fig. 13. In general and with respect to the initial bounds, the distributions of the parameters are wide, corresponding to high uncertainty in the parameter values. Also, all of the distributions of the calibrated parameters are biased away from the true values (black triangles). This bias has been linked to model discrepancy [7], which generally leads to a violation of assumptions made in Sect. 5. The overestimation of the measurement noise variance supports this and points toward an inability of the Taylor model to accurately reproduce the measurements. Additionally, the lack of uniqueness of the calibration parameters and their corresponding high degree of correlation also plays a part in the large uncertainty in the parameters.

The marginal probability density function for g_s^* is relatively flat and spans the complete range specified by the bounds of the uninformative (uniform) prior.

Essentially, the uncertainty in g_s^* is similar to the prior, which indicates that the test used in the calibration did not provide significant insight on g_s^*. Because g_s^* is related to saturation hardness, the above might indicate that the applied strain loading of the experiment was too small to see saturation; repeating the test to higher strains might help identify g_s^*. It is worth noting that, if a deterministic calibration was performed, a single value of g_s^* would result, without knowing that the parameter was essentially unidentifiable by the test. Apart from gathering additional data to aid identification, a more informative prior could have been used to regularize the inverse problem. However, this was beyond the scope of this work, and the uncertainty in the calibrated g_s^* was accepted as uniform over the given bounds.

6.2 Using Global-Local Calibration

The global-local calibration was set up using a finite element model with the same geometry as the simulated experiment. In order to remove the effect of erroneous boundary conditions, the same boundary conditions were applied as the simulated experiment.

The model was coarsened to decrease the model evaluation time. The coarse mesh contained 25,500 quadratic tetrahedral elements and 45,700 nodes. The time discretization of the model was also decreased by a factor of 2 compared to the simulated experiment. Model evaluation of the coarsened finite element model took approximately 9 min on 40 cores of a Dual socket 20 core 2.40 GHz Intel Gold 6148 Skylake Processor. Because a non-deterministic calibration akin to the one in Sect. 6.1 would take at least 156 days, a deterministic optimization was pursued instead. This means that a single deterministic set of calibration parameters is obtained, without an idea of how certain that calibration is.

The error metric for the optimization was the weighted sum of the error norms of the global (homogenized stress) and local (displacement) fields. The weighting was performed in the fashion of [26] which weights the errors at each scale based on the resolution of the measurement technique. In this case, the magnitude of the added measurement noise was used. After normalization of the two fields, equal weight was placed on global and local measurements.

The optimization was performed via Nelder-Mead simplex method [11] with the initial guesses of the parameters at 105% of their true values. The optimization took about 50 h to complete. The resulting optimal parameters are shown in Table 3. Example comparisons of the global and local response from the simulated experiment and optimal parameters are shown in Figs. 14 and 15. The global response is close to the simulated data with a slight under prediction. Presumably the bias seen in the global response was compensated by a more accurate local field, i.e., a balance of the global and local errors would be found.

From Figs. 14 and 15, it can be seen that overall the calibration was somewhat successful in matching the global and local behavior of the model; however, it is difficult to place confidence in the calibration without a measure of uncertainty.

Table 3 Results of global-local deterministic calibration

Parameter	Optimized value	True value	Relative error
m	0.04837	0.05	3.2%
g_s^*	350.1	113.9	207%
g_0	128.1	130.0	1.4%
G_0	41.55	100.4	58%

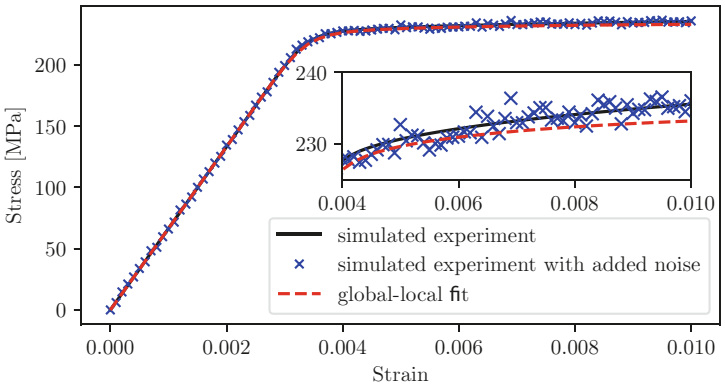

Fig. 14 Global response comparison of the global-local optimization using finite element model updating. For these data, the mean absolute error is 1.32 MPa

Furthermore, there is no guarantee that the optimized values represent global optimal values; it is possible they only correspond to a local optimum. No insight on g_s^* is gained besides a single optimum value.

6.3 Using Local Calibration

The demonstration of non-deterministic local calibration was performed by directly integrating the CP model given a local grain orientation from EBSD and local deformation gradients stemming from simulated DIC. In this case, the measurements, Y_i, are the deviatoric stresses fields from the simulated experiment (i.e., simulated HREBSD). The model response, $\mathcal{M}_i(\Theta)$, is the deviatoric part of the stress resulting from the CP model integration. It is worth noting that in this demonstration, the full deformation gradient is imposed on the CP model, which assumes unrealistically that all components of strain can be identified with DIC. With addition of a plane-stress constraint, the result is not expected to be altered significantly by the restriction of the DIC information to the planar strains.

The local calibration was again non-deterministic. As in the global calibration, a deterministic optimization was performed to initialize the Markov chain prior to MCMC sampling. The same optimization and MCMC options were used for this

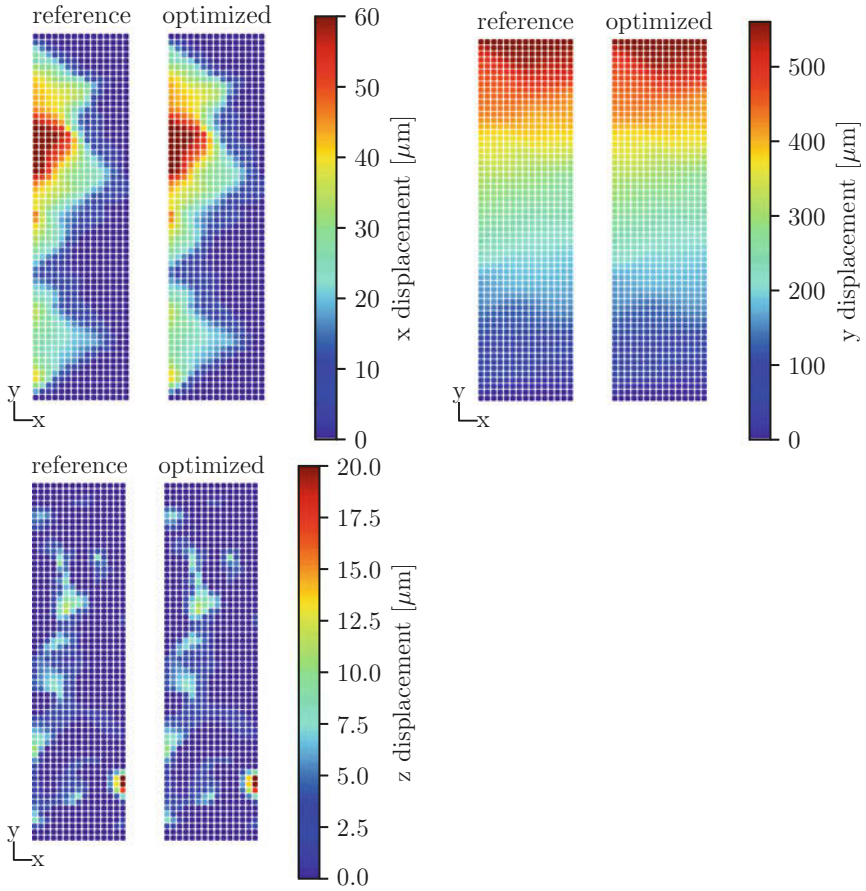

Fig. 15 Local response comparisons for the global-local optimization using finite element model updating. Displacement fields are shown at the point locations of the simulated DIC (reference)

local calibration as before. This includes the generation of 25,000 samples with a 10,000 sample burn-in. The calibration took about 116 h to run on a single core of a 3.50 GHz Intel Xeon E5-1650 v3 CPU, corresponding to about 17 s per sample. Again, the effect of rejection on this per-sample estimate should be noted.

The resulting marginal probability density functions of Θ are illustrated in Fig. 16. The distributions are now much tighter when compared to the global posterior. More importantly, these distributions now encompass the true values. The local calibration is better able to identify the parameters for two reasons: first, an increased amount of data acquired and second, the CP model is directly probed rather than utilizing homogenized values, which diminishes the model discrepancy. As in the local calibration, the probability density function of g_s^* looks similar to the uniform prior, illustrating that the simulated experiment was not very informative

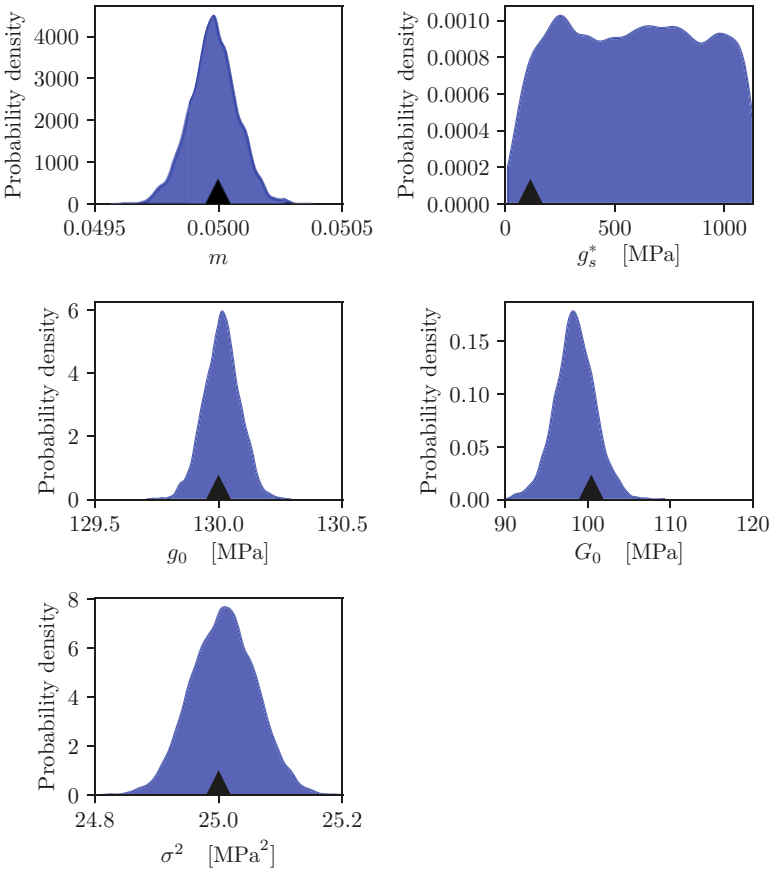

Fig. 16 The results of local calibration. The marginal probability density functions of the calibration parameters, including the estimate of the variance of the error. The triangle denotes the true values of each calibration parameter

for this parameter. The σ^2 probability density functions in Fig. 16 should not be compared to those shown in Fig. 13 because they correspond to noise estimates of different data sets (i.e., noise in homogenized stress vs. noise in HREBSD stress).

7 Summary

The objective of this chapter is to motivate the use of CP models in microstructure-dependent engineering problems and to provide a comprehensive study of calibrating CP model parameters. Historical perspective and background is provided for understanding what methods have been published, in terms of both generalized

parameter identification methods and specific methods studied for use with CP models. A review of the literature illustrates that the methods for CP parameter calibration studied to date have largely focused on global-local methods, where a combination of global (homogenized) stresses are combined with local DIC displacements or strain to form the comparison between measured and computed data.

Various methods for acquiring and post-processing data are also overviewed. Global data, as would come directly from test-stand data or attached gauges, are relatively cheap and easy to apply. Consequently, especially when many tests are being performed, acquiring global data may be the only affordable method. Acquiring local DIC displacement and strain data provides a significant improvement on the measured data set. But, this comes with a cost of additional equipment and setup time. Additionally, application of this data in the global-local approach also implies the need to acquire EBSD data before testing. Local stress data can also be measured using HREBSD to analyze shifts in diffraction patterns. Combining both local methods, DIC and HREBSD, is now possible with selectively transparent stamping as the means to apply a DIC speckle pattern to the test specimen surface. However, this method requires the highest level of infrastructure and time since both HREBSD and DIC must be completed multiple times during testing.

Three classes of calibration methods can be used, differing by the type of acquired data. While global data is the easiest and cheapest to acquire, CP model parameter calibration using that data has fundamental issues. Namely, because many sets of CP model parameters can reproduce nearly equivalent global stress-strain curves, there should be no expectation that the calibrated parameters are unique. Adding local DIC displacement data aids in the mitigation of this uniqueness issue, but there are still local minima that exist in this case. Because of the hybrid approach, with both global and local data, the computational model in this case must represent the particular microstructure being tested. Running these full simulations, for example, as a finite element model, is computationally intensive and intractable for a non-deterministic approach. Additionally, this leads to the need for assumptions or direct measurement of the microstructure underlying the surface and high sensitivities to applied boundary conditions. Purely local data enables a computationally tractable method for non-deterministic calibration. Furthermore, this method precludes issues of generating a model of the microstructure aggregate, does not incorporate boundary conditions, and helps resolve the issue of uniqueness. However, as illustrated by the calibration of g_s^*, the model parameters cannot be determined accurately without adequate data that has sensitivity to the parameter.

As complexity in acquiring data is added, the computational cost of the calibration and issues surrounding uniqueness can be resolved. The combination of the results from Fig. 13, Table 3, and Fig. 16 is shown in Fig. 17; it illustrates the calibrated parameters from each approach. The two distributions represent the calibrated parameters for the purely global (red) and purely local (blue) methods. This clarifies the relative uncertainty and inaccuracy in calibrating CP model parameters using only global data. On the other hand, the purely local method results in very little uncertainty and accurately reproduces the correct parameters (black triangles).

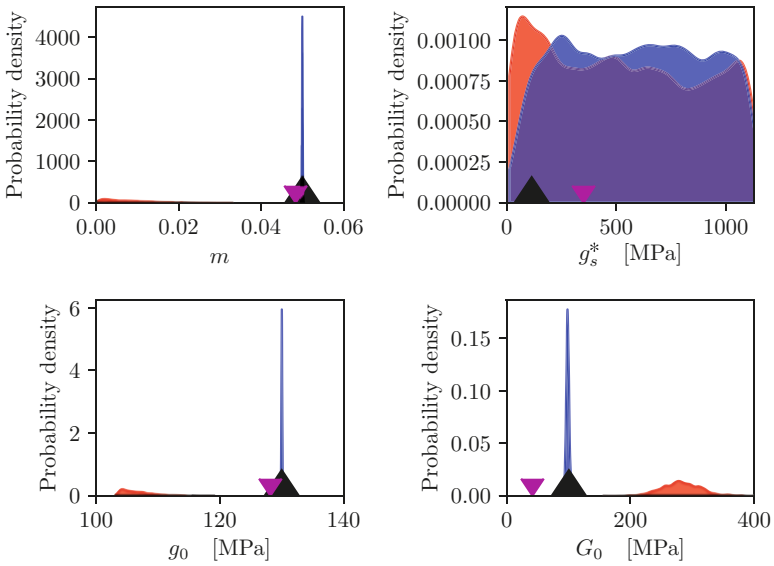

Fig. 17 The results of all calibrations. The marginal probability density functions of the calibration parameters for the global calibration (red) and local calibration (blue). The upward-pointing black triangle denotes the true values of each calibration parameter. The downward-pointing magenta triangle denotes the deterministic result of global-local optimization

Because it is computationally intractable to run the global-local calibration because of the costly computational model required, the single deterministic value for each parameter is shown (downward-pointing magenta triangle). As mentioned above, the inclusion of local DIC data improves significantly the calibrated result of a purely global approach, but still suffers from inaccuracy because of local minima.

8 Outlook

The ability to make high-resolution and volumetric observations and measurements of material microstructures is ever-increasing. The measurement techniques described in this chapter were chosen to represent methods that could be employed in a common materials research laboratory at the present. Consequently, data acquisition methods were mainly focused on high-resolution surface measurements, EBSD and DIC, along with load-displacement data acquired through mechanical testing. However, volumetric acquisition methods, such as X-ray computed tomography (CT) and high-energy X-ray diffraction (HEDM), are becoming increasingly valuable and available.

With these improved data acquisition methods, the various global and local calibration methods presented in this chapter may still be used. Utilizing only

surfaced-based approaches includes uncertainties to the calibration process due to unknown subsurface features, such as grain variations and defects. For example, a subsurface defect can influence the local strain on the surface as measured by DIC. Using only a surface-based approach, this would manifest as additional (inaccurate) variation in the calibrated parameter distribution. However, if that same subsurface feature was detected using X-ray CT and included in the computational model, a more accurate calibrated parameter distribution would be expected. Consequently, an important next step is to quantify the improvement in calibration that can be expected with volumetric acquisition methods and weigh those against the added costs and time associated with acquiring that data.

References

1. S. Avril, M. Bonnet, A.S. Bretelle, M. Grédiac, F. Hild, P. Ienny, F. Latourte, D. Lemosse, S. Pagano, E. Pagnacco, F. Pierron, Overview of identification methods of mechanical parameters based on full-field measurements. Exp. Mech. **48**(4), 381 (2008)
2. M. Bertin, C. Du, J.P. Hoefnagels, F. Hild, Crystal plasticity parameter identification with 3D measurements and integrated digital image correlation. Acta Mater. **116**, 321–331 (2016)
3. M. Bonnet, A. Constantinescu, Inverse problems in elasticity. Inverse Prob. **21**(2), R1 (2005). http://stacks.iop.org/0266-5611/21/i=2/a=R01
4. J.E. Bozek, J.D. Hochhalter, M.G. Veilleux, M. Liu, G. Heber, S.D. Sintay, A.D. Rollett, D.J. Littlewood, A.M. Maniatty, H. Weiland, R.J. Christ, J. Payne, G. Welsh, D.G. Harlow, P.A. Wawrzynek, A.R. Ingraffea, A geometric approach to modeling microstructurally small fatigue crack formation: I. Probabilistic simulation of constituent particle cracking in AA 7075-T651. Model. Simul. Mater. Sci. Eng. **16**(6), 065007 (2008)
5. T. Britton, C. Maurice, R. Fortunier, J. Driver, A. Day, G. Meaden, D. Dingley, K. Mingard, A. Wilkinson, Factors affecting the accuracy of high resolution electron backscatter diffraction when using simulated patterns. Ultramicroscopy **110**, 1443–1453 (2010)
6. S.P. Brooks, G.O. Roberts, Convergence assessment techniques for markov chain Monte Carlo. Stat. Comput. **8**(4), 319–335 (1998)
7. J. Brynjarsdóttir, A. O'Hagan, Learning about physical parameters: the importance of model discrepancy. Inverse Prob. **30**(11), 114007 (2014)
8. G.M. Castelluccio, D.L. Mcdowell, A mesoscale modeling of microstructurally small fatigue cracks in metallic polycrystals. Mater. Sci. Eng. A **598**, 34–55 (2014)
9. Z. Chen, W. Lenthe, J.C. Stinville, M. Echlin, T.M. Pollock, S. Daly, High-resolution deformation mapping across large fields of view using scanning electron microscopy and digital image correlation. Exp. Mech. **58**(9), 1407–1421 (2018)
10. Y. Dong, B. Pan, A review of speckle pattern fabrication and assessment for digital image correlation. Exp. Mech. **57**(8), 1161–1181 (2017)
11. F. Gao, L. Han, Implementing the Nelder-Mead simplex algorithm with adaptive parameters. Comput. Optim. Appl. **51**(1), 259–277 (2012)
12. C. Geuzaine, J.F. Remacle, GMSH: a 3-D finite element mesh generator with built-in pre- and post-processing facilities. Int. J. Numer. Methods Eng. **79**(11), 1309–1331 (2009)
13. J. Geweke et al., Evaluating the accuracy of sampling-based approaches to the calculation of posterior moments, vol. 196. Federal Reserve Bank of Minneapolis, Research Department Minneapolis (1991)
14. M. Groeber, M. Jackson, DREAM.3D: a digital representation environment for the analysis of microstructure in 3D. Integr. Mater. Manuf. Innov. **3**(1), 5 (2014)

15. A. Guery, F. Hild, F. Latourte, S. Roux, Identification of crystal plasticity parameters using DIC measurements and weighted FEMU. Mech. Mater. **100**, 55–71 (2016)
16. H. Haario, M. Laine, A. Mira, E. Saksman, Dram: efficient adaptive MCMC. Stat. Comput. **16**(4), 339–354 (2006)
17. T. Hoc, J. Crèpin, L. Gèplèrt, A. Zaoui, A nonprocedure for identifying the plastic behavior of single crystals from the local response of polycrystals. Acta Mater. **51**(18), 5477–5488 (2003)
18. B.E. Jackson, J.J. Christensen, S. Singh, M. De Graef, D.T. Fullwood, E.R. Homer, R.H. Wagoner, Performance of dynamically simulated reference patterns for cross-correlation electron backscatter diffraction. Microsc. Microanal. **22**(4), 789–802 (2016)
19. H. Jin, W. Lu, J. Korellis, Micro-scale deformation measurement using the digital image correlation technique and scanning electron microscope imaging. J. Strain Anal. Eng. Des. **43**(8), 719–728 (2008)
20. J. Kacher, C. Landon, B.L. Adams, D. Fullwood, Bragg's law diffraction simulations for electron backscatter diffraction analysis. Ultramicroscopy **109**(9), 1148–1156 (2009)
21. J. Kaipio, E. Somersalo, *Statistical and Computational Inverse Problems* (Springer Science & Business Media, New York, 2006)
22. M.C. Kennedy, A. O'Hagan, Bayesian calibration of computer models. J. R. Stat. Soc. Ser. B (Stat. Methodol.) **63**(3), 425–464 (2001)
23. R. Lebensohn, C. Tomé, A self-consistent anisotropic approach for the simulation of plastic deformation and texture development of polycrystals: application to zirconium alloys. Acta Metall. et Mater. **41**(9), 2611–2624 (1993)
24. H. Leclerc, J.N. Périé, S. Roux, F. Hild, Integrated digital image correlation for the identification of mechanical properties, in *Proceedings of the 4th International Conference on Computer Vision/Computer Graphics Collaboration Techniques* (Springer, 2009), pp. 161–171
25. H. Lim, J. Carroll, C. Battaile, T. Buchheit, B. Boyce, C. Weinberger, Grain-scale experimental validation of crystal plasticity finite element simulations of tantalum oligocrystals. Int. J. Plast. **60**, 1–18 (2014)
26. F. Mathieu, H. Leclerc, F. Hild, S. Roux, Estimation of elastoplastic parameters via weighted FEMU and integrated-DIC. Exp. Mech. **55**(1), 105–119 (2015)
27. J. Nocedal, S. Wright, *Numerical Optimization*, Springer Series in Operations Research and Financial Engineering, 2nd edn. (Springer-Verlag, New York, 2006). http://dx.doi.org/10.1007/978-0-387-40065-5
28. B. Pan, K. Qian, H. Xie, A. Asundi, Two-dimensional digital image correlation for in-plane displacement and strain measurement: a review. Meas. Sci. Technol. **20**(6), 062001 (2009)
29. A. Patil, D. Huard, C.J. Fonnesbeck, PyMC: bayesian stochastic modelling in Python. J. Stat. Softw. **35**(4), 1–81 (2010)
30. P.L. Phillips, A. Brockman, R. John, Modelling strategies for property identification based on full-field surface displacement data. Strain **48**, 143–152 (2011)
31. R.S. Piascik, N.F. Knight Jr., Re-tooling the agency's engineering predictive practices for durability and damage tolerance. NASA/TM-2017–219621, 60 (2017)
32. O. Rokoš, J. Hoefnagels, R. Peerlings, M. Geers, On micromechanical parameter identification with integrated dic and the role of accuracy in kinematic boundary conditions. Int. J. Solids Struct. **146**, 241–259 (2018)
33. F. Roters, P. Eisenlohr, L. Hantcherli, D. Tjahjanto, T. Bieler, D. Raabe, Overview of constitutive laws, kinematics, homogenization and multiscale methods in crystal plasticity finite-element modeling: theory, experiments, applications. Acta Mater. **58**(4), 1152–1211 (2010)
34. T. Ruggles, D. Fullwood, J. Kysar, Resolving geometrically necessary dislocation density onto individual dislocation types using EBSD-based continuum dislocation microscopy. Int. J. Plast. **76**, 231–243 (2016)
35. T.J. Ruggles, G.F. Bomarito, A.H. Cannon, J.D. Hochhalter, Selectively electron-transparent microstamping toward concurrent digital image correlation and high-angular resolution electron backscatter diffraction (EBSD) analysis. Microsc. Microanal. **23**(6), 1091–1095 (2017)

36. R. Russell, D. Dawicke, J. Hochhalter, Composite overwrapped pressure vessel (COPV) life test, in *European Conference on Spacecraft Structures, Materials and Environmental Testing (ECSSMET)*. Electrostatics Society of America (ESA) (2018), pp. 1–6
37. M. Sangid, S. Yeratapally, A. Rovinelli, Validation of microstructure-based materials modeling, in *55th AIAA/ASME/ASCE/AHS/ASC Structures, Structural Dynamics, and Materials Conference*. American Institute of Aeronautics and Astronautics (2014). http://arc.aiaa.org/doi/10.2514/6.2014-0462
38. R.C. Smith, *Uncertainty Quantification: Theory, Implementation, and Applications* (SIAM, Philadelphia, 2013)
39. M.A. Sutton, J.H. Yan, S. Avril, F. Pierron, S.M. Adeeb, Identification of heterogeneous constitutive parameters in a welded specimen: uniform stress and virtual fields methods for material property estimation. Exp. Mech. **48**(4), 451–464 (2008)
40. M.A. Sutton, J.J. Orteu, H. Schreier, *Image Correlation for Shape, Motion and Deformation Measurements: Basic Concepts, Theory and Applications* (Springer Science & Business Media, New York, 2009)
41. G. Taylor, Plastic strain in metals. J. Inst. Met. **62**, 307–324 (1938)
42. T.J. Turner, P.A. Shade, J.C. Schuren, M.A. Groeber, The influence of microstructure on surface strain distributions in a nickel micro-tension specimen. Model. Simul. Mater. Sci. Eng. **21**, 015002 (2013)
43. J.E. Warner, G.F. Bomarito, J.D. Hochhalter, Scalable Implementation of Finite Elements by NASA _ Implicit (ScIFEi), NASA/TM – 2016-219180. Technical Report April, NASA, Hampton (2016)
44. A.J. Wilkinson, G. Meaden, D.J. Dingley, High resolution mapping of strains and rotations using electron back scatter diffraction. Mater. Sci. Technol. **22**(11), 1–11 (2006)
45. S.R. Yeratapally, M.G. Glavicic, M. Hardy, M.D. Sangid, Microstructure based fatigue life prediction framework for polycrystalline nickel-base superalloys with emphasis on the role played by twin boundaries in crack initiation. Acta Mater. **107**, 152–167 (2016)
46. X. Zhang, Y. Wang, J. Yang, Z. Qiao, C. Ren, C. Chen, Deformation analysis of ferrite/pearlite banded structure under uniaxial tension using digital image correlation. Opt. Lasers Eng. **85**, 24–28 (2016)
47. Z. Zhao, M. Ramesh, D. Raabe, A.M. Cuitino, R. Radovitzky, Investigation of three-dimensional aspects of grain-scale plastic surface deformation of an aluminum oligocrystal. Int. J. Plast. **24**, 2278–2297 (2008)

Local Stress and Damage Response of Polycrystal Materials to Light Shock Loading Conditions via Soft Scale-Coupling

C. A. Bronkhorst, P. W. Marcy, S. A. Vander Wiel, H. Cho, V. Livescu, and G. T. Gray III

1 Introduction

Research in the past six decades has shown tremendous progress in the ability to represent the process of ductile damage under dynamic loading conditions. Even though good progress has been made, many challenges remain in effectively representing this complex physical process accurately, and without numerical artifacts. Work discussed in this chapter is a current representation of developments which have taken place over several years, beginning with the work of Johnson [31] and the development of a constitutive model for shock loaded copper representing nonlinear elasticity, plasticity, and evolution of local porosity. Johnson [31] recognized the significance of the aggregate nature of polycrystalline metallic materials and used a unit cell analysis of the elastic–plastic response of the material under rapidly loaded conditions. Inertial effects were recognized as important but were not included in the analysis of copper presented. The model was applied to problems of plate

C. A. Bronkhorst (✉)
Theoretical Division, Los Alamos National Laboratory, Los Alamos, NM, USA

Department of Engineering Physics, University of Wisconsin, Madison, WI, USA
e-mail: cbronkhorst@wisc.edu

P. W. Marcy · S. A. Vander Wiel
Computer, Computational, and Statistical Sciences Division, Los Alamos National Laboratory, Los Alamos, NM, USA

H. Cho
School of Mechanical and Aerospace Engineering, Korea Advanced Institute of Science and Technology, Daejeon, Republic of Korea

V. Livescu · G. T. Gray III
Materials Science and Technology Division, Los Alamos National Laboratory, Los Alamos, NM, USA

S. Ghosh et al. (eds.), *Integrated Computational Materials Engineering (ICME)*,
https://doi.org/10.1007/978-3-030-40562-5_7

impact, explosively loaded material, and an expanding ring. Much later, this model was also applied to the study of loading pulse duration in copper [33]. Addessio and Johnson [1] adapted the work of Johnson [31, 32] by proposing a modified Gurson [26]-type model, which also employed an overstress equation for the plastic flow rule of the material. This equation introduces a length scale into the series of equations and assists in regularizing the problem. This helps to alleviate issues of numerical stability and severe mesh sensitivity. The authors also clearly recognized the possibility that relying upon deformation rate sensitivity within the model would not always solve the regularization issue, but that additional length scales (e.g., spatial gradients in physically based internal state variables) may be required in general. A void nucleation model was not proposed, and the model was tested against copper plate impact experiments. It was demonstrated that for the problems examined, the use of the overstress model reduced the mesh sensitivity of the simulated results. The model of Addessio and Johnson [1] was expanded upon by Maudlin et al. [40] to include the effect of nonisotropic plastic flow. They also included the ability to account for the anisotropic nature of the void as it grows, but this capability is not exercised in the work presented here. Significant advancements were made to the solution algorithm to improve the numerical efficiency. This model was used on several dynamic loading boundary value problems with success. The numerical algorithm initially developed in this work was later published by Zuo and Rice [48]. Bronkhorst et al. [10] demonstrated the limitations of such a model and general computational limitations for ductile damage against differing shock loading conditions. Recently, Versino and Bronkhorst [46] proposed a computational framework to facilitate material variability for representation of porosity nucleation more accurately within a macroscale continuum setting.

Material microstructure has long been known to play a key role in the process of ductile damage where porosity is the dominant damage mechanism (e.g. [43, 47]). Polycrystalline metallic materials at a local scale produce highly inhomogeneous deformation fields upon mechanical loading (e.g. [8, 12]) and provide the conditions for establishing a pore field. There remains tremendous potential to bring to bear computational crystal plasticity tools to explore the physics of porosity-based ductile damage in ways which are not approachable through experimental means alone. This chapter has a focus on the ductile damage response of tantalum for lightly loaded shock conditions. Tantalum is a body-centered cubic material whose plastic deformation is dominated by the motion of screw dislocations. The natural state of the screw dislocation within tantalum is not planar as in other cubic materials but rather the core is split along additional planes [2, 3]. Recently a model for representation of the deformation behavior of tantalum single crystals was proposed [16] and will be employed to explore here the micromechanics of deformation leading to the onset of porosity initiation in tantalum polycrystals.

The purpose of this chapter is to present the above discussion in the context of a theoretical framework for models of porosity-based damage and failure. Numerical results are presented in the context of experimental results presented by Gray et al. [24]. This chapter begins by first presenting a simple macroscale ductile damage

model for metallic materials and the representation of the abovementioned tantalum on tantalum plate impact experiment. A single crystal model is then discussed for representation of tantalum with non-Schmid effects. Numerical models of tantalum are then presented, and load coupling with the macroscale model is described. Numerical results of polycrystal calculations are then presented with an analysis of the results in the context of relationship with shock loading conditions. Finally, the results are discussed and concluding statements are offered.

2 Nomenclature

Standard direct notation is used throughout this paper. Second rank tensors are denoted by boldface uppercase letters. Fourth rank tensors are denoted by underscored boldface uppercase letters. The following variables are used: **I** identity, **F** deformation gradient, **D** stretch, **T** Cauchy stress, ρ density, and θ temperature. The prime symbol $\mathbf{A}'$ indicates a deviatoric quantity. The inner product of two second rank tensors **A** and **B** is defined by $\mathbf{A}\cdot\mathbf{B} = \text{trace}(\mathbf{A}^{\mathrm{T}}\mathbf{B})$. The over-tilde $\tilde{\mathbf{A}}$ represents the quantity **A** in the undamaged material.

3 Experimental Overview

The dynamic behavior of materials under shock loading conditions is commonly studied with plate impact experiments. These are conceptually simple in that a stationary circular disk (the target sample) is impacted by another circular disk (the flyer) moving at high velocity. The flyer is accelerated through a gun barrel by either compressed gas or in some cases gunpowder. The flyer is soft-mounted on a sabot, which travels through the barrel. The primary diagnostic used in plate impact experiments is the measurement of the velocity of the back of the target sample subsequent to the impact of the two plates – free-surface velocity. Under certain conditions, it is possible to recover the deformed sample for subsequent metallographic analysis. Both of these sources of information are used in the present work. Details of the plate impact experiment technique and focus on tantalum can be found in Gray [19, 20], Gray and Vecchio [21], and Gray et al. [22, 23].

Here we focus on a single experiment where both the flyer plate material and the sample plate material were fabricated from the same high-purity tantalum. The details of the experiments and the conditions under which they were conducted can be found in Gray et al. [24] and Bronkhorst et al. [10]. The flyer plate velocity was 249 m/s. The free-surface velocity trace for this experiment is given in Fig. 1. The cross-sectional image of the recovered sample showing the porosity field is given in Fig. 2. A higher magnification view of a region of the cross-sectioned sample which displays early-stage coalescence behavior within the incipient spalled region of the sample is given in Fig. 3. Although discussion of these details is outside the scope

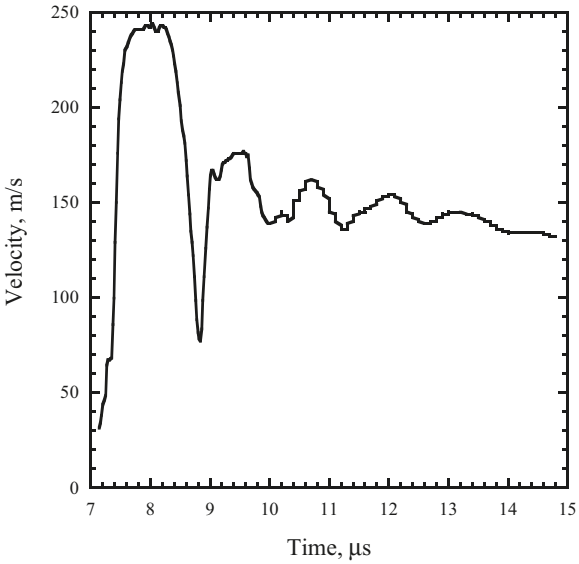

Fig. 1 Free-surface velocity versus time trace for the tantalum on tantalum plate impact experiment considered in this study

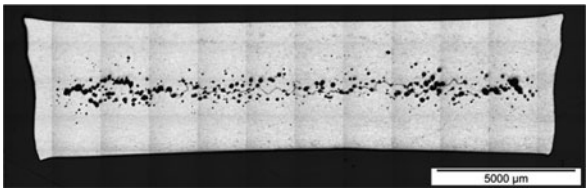

Fig. 2 Cross-section image of the soft-recovered tantalum sample showing the field of damage developed in the sample. The dark regions are voided areas

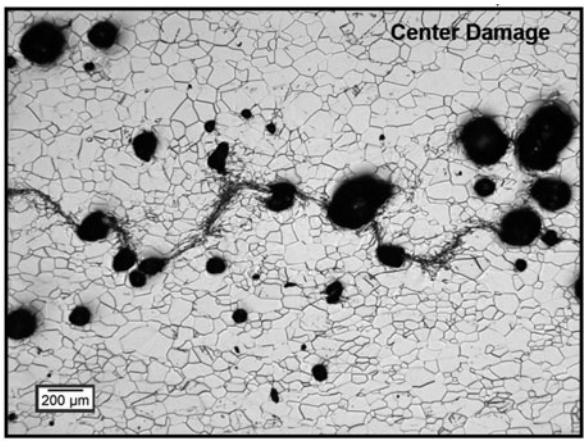

Fig. 3 Local-scale damage field (dark regions are pores) on the cross-sectional view of the recovered sample showing the beginning of the coalescence process between existing voids via localized deformation regions

of the current chapter, the results clearly indicate that pore locations are dominated at grain boundaries within the high-purity tantalum material used in this study.

4 Macroscale Damage Modeling

The model presented here is in the long line of modified Gurson-Tvergaard-Needleman [7, 26, 44]-type models for the representation of porosity-based ductile damage. The model presented here has been adapted for application to shock loading situations with high stress triaxiality conditions.

4.1 Damage Constitutive Model

The constitutive model used in this study is derived from the work of Addessio and Johnson [1], Maudlin et al. [39, 40], Zou [49], and Bronkhorst et al. [10]. The model is applied to tantalum plate impact loading as presented earlier and is summarized here.

The Cauchy stress in the damaged state is given by

$$\mathbf{T} = \underline{\mathbf{M}}\tilde{\mathbf{T}}, \tag{1}$$

where the stress in the undamaged material is $\tilde{\mathbf{T}}$ and the general fourth rank isotropic damage tensor is given by

$$\underline{\mathbf{M}} = (1 - \phi)\,\underline{\mathbf{I}}, \tag{2}$$

with the scalar internal state variable ϕ representing the isotropic state of porosity at the material point used in this study. In general, the tensor $\underline{\mathbf{M}}$ allows for the anisotropic representation of damage evolution within the material. However, for the present study, this dependence is assumed to remain isotropic given that pores remain close to spherical. Time integration is performed in the unrotated frame relative to the current configuration defined by the rotation $\mathbf{R}$ given by the polar decomposition

$$\mathbf{F} = \mathbf{RU} = \mathbf{VR}. \tag{3}$$

The Cauchy stress time rate of change defined in the unrotated frame relative to the current configuration is given by

$$\dot{\mathbf{T}} = \underline{\mathbf{M}\tilde{\mathbf{L}}'}\left(\mathbf{D}' - \mathbf{D}^{p\prime}\right) + \underline{\mathbf{M}}\left(\mathrm{J}\tilde{\mathrm{K}}_s \mathrm{tr}\mathbf{D}^e - \frac{\tilde{\rho}}{\rho}\tilde{\Gamma}\mathbf{T}\cdot\mathbf{D}^p\right)\underline{\mathbf{I}} + \underline{\dot{\mathbf{M}}\mathbf{M}}^{-1}\mathbf{T}, \tag{4}$$

where $\tilde{\underline{\mathbf{L}}}$ is the fourth order elastic stiffness tensor, $J = \tilde{\rho}_0/\tilde{\rho}$, $\tilde{K}_s$ is the isentropic solid bulk modulus, $\tilde{\Gamma}$ is the Gruneisen coefficient and

$$\tilde{P} = -\frac{1}{3}\mathrm{tr}\tilde{\mathbf{T}}. \tag{5}$$

Equation (4) contains four terms defining the time evolution of Cauchy stress, each with a specific physical significance. The first term is the contribution to the evolution of the stress due to deviatoric elastic deformation. The second term is due to the influence of mean volumetric elastic deformation in the material given that finite elastic strains and substantial pressures must be accounted for. The third term is due to the thermal expansion or contraction of the material through the Gruneisen parameter and thermal energy produced via plastic work. The fourth and final term is due to the evolution of stress due to the effects of damage evolution. The deformation rate $\mathbf{D}$ is additively decomposed as

$$\mathbf{D} = \mathbf{D}^e + \mathbf{D}^p = \mathbf{D}^e + \left(\mathbf{D}^d + \mathbf{D}^{p'}\right), \tag{6}$$

where the plastic contribution ($\mathbf{D}^p$) to the rate of deformation is separated into spherical ($\mathbf{D}^d$) and deviatoric ($\mathbf{D}^{p'}$) components. The spherical component and the contribution due to damage [1] is given by

$$\dot{\phi} = (1-\phi)\,\mathrm{tr}\mathbf{D}^d. \tag{7}$$

The plastic flow rule is given by

$$\mathbf{D}^p = \frac{1}{\tau_r}\left(\mathbf{T} - \mathbf{T}^{\mathrm{proj}}\right). \tag{8}$$

This overstress style approach uses a relaxation constant τ_r, with the tensorial quantity $\mathbf{T}^{\mathrm{proj}}$ being the current Cauchy stress projected onto the plastic flow surface given below in Eq. (10). Based upon Addessio and Johnson [1] and Maudlin et al. [40], the approximate length scale implied by τ_r is given by

$$l = \frac{\tau_r}{\sqrt{\rho_0\left(K + \frac{4}{3}G\right)}}, \tag{9}$$

where K and G are the ambient condition solid bulk and shear moduli, respectively, and l is the implied length scale represented by the overstress expression Eq. (8) for equation regularization.

Therefore Eq. (8) allows for the possibility of states of stress external to the flow surface. The porosity-modulated plastic flow surface employed here is that

developed by Gurson [26] and extended by Addessio and Johnson [1] and Maudlin [40] and given by

$$\tau - \sigma_f\left(\dot{\bar{\varepsilon}}_p, \theta\right)^2 \left[1 + q_3\phi^2 - 2q_1\phi\cosh\delta\right] = 0, \tag{10}$$

where

$$\tau = \frac{1}{2}\mathbf{T}' \cdot \underline{\boldsymbol{\alpha}}\mathbf{T}' \tag{11}$$

is a quadratic relationship allowing for plastic anisotropy using the anisotropy tensor $\underline{\boldsymbol{\alpha}}$ and $\sigma_f\left(\dot{\bar{\varepsilon}}_p, \theta\right)$ is the rate and temperature sensitive scalar flow stress with

$$\dot{\bar{\varepsilon}}_p = \sqrt{\frac{2}{3}\mathbf{D}^{p\prime} \cdot \mathbf{D}^{p\prime}}, \tag{12}$$

$$\delta = -\frac{3q_2\tilde{P}}{2\sigma_s}. \tag{13}$$

The quantities q_1, q_2, and q_3 are material parameters, and the saturation flow stress σ_s is defined below (Eq. (26)).

The criterion for computational cell failure as a function of porosity and plastic strain is a modified Hancock-Mackenzie [29] relationship and is defined as

$$F = \left(\frac{\phi}{\phi_f}\right)^2 + \left(\frac{\overline{\varepsilon}_p}{\gamma_f}\right)^2 \geq 1, \tag{14}$$

where $\overline{\varepsilon}_p = \int \dot{\bar{\varepsilon}}_p dt$, ϕ_f is the failure porosity and

$$\gamma_f = \gamma_0 + \gamma_1 e^{\gamma_2 \frac{\tilde{P}}{\tau}}, \tag{15}$$

where $\overline{P}$ is the tensile hydrostatic pressure and γ_0, γ_1, and γ_2 are material parameters evaluated from notched bar tensile experiments.

Equation (14) represents combined effects of porosity and plastic deformation so that when F reaches a value of 1.0, the material at that particular material point no longer retains load bearding ability. We only consider monotonic states of damage; recompaction of damaged regions is not considered here. A polynomial Mie-Gruneisen equation of state is used for the volumetric component of compressive states of stress as a function of density

$$\tilde{P} = \left(K_1\tilde{\beta} + K_2\tilde{\beta}^2 + K_3\tilde{\beta}^3\right)\left(1 - \tilde{\Gamma}\tilde{\beta}/2\right) + \tilde{\Gamma}\tilde{E}_s\left(1 + \tilde{\beta}\right), \tag{16}$$

where

$$\tilde{\beta} = \frac{\tilde{\rho}}{\tilde{\rho}_0} - 1, \tag{17}$$

$$\rho = (1 - \phi)\,\tilde{\rho}, \tag{18}$$

$$\tilde{E}_s = \int \left(\overline{\sigma}\dot{\overline{\varepsilon}} - \tilde{P}\mathrm{tr}\left(\mathbf{D}^e + \mathbf{D}^d \right) \right) J dt, \tag{19}$$

$$\overline{\sigma} = \sqrt{\frac{3}{2}\mathbf{T}' \cdot \mathbf{T}'}. \tag{20}$$

K_1, K_2, and K_3 are coefficients.

The rate and temperature sensitivity of the plastic deformation response is represented through the flow stress. The deformation of tantalum at rates observed here has been shown to be well represented by several constitutive models [11, 12, 15, 38, 41] which are based upon the thermal activation kinetics developed by Kocks et al. [36]. We employ here the isotropic mechanical threshold strength (MTS) model, which has been well established for tantalum and is evolved from the work of Follansbee and Kocks [18], Chen and Gray [15], and Maudlin et al. [39]. The MTS model is based on the concept of a superposition of resistances to the glide of dislocations. Generally, they are grouped as athermal barriers (e.g., grain boundaries) and thermally influenced barriers (e.g., Peierls stress – intrinsic lattice resistance, forest dislocations, dislocation structure, solute atoms). The mechanical threshold stress is the deformation resistance at 0 K. The flow stress used here is the stress adjusted to current temperature and strain rate. The reader is referred to Follansbee and Kocks [18] and Chen and Gray [15] for more details.

The relationship for the solid material flow stress is given by

$$\sigma_f\left(\dot{\bar{\varepsilon}}_p, \theta\right) = \sigma_a + \frac{\mu}{\mu_0}\left(S_i\left(\dot{\bar{\varepsilon}}_p, \theta\right)\hat{\sigma}_i + S_\varepsilon\left(\dot{\bar{\varepsilon}}_p, \theta\right)\hat{\sigma}_\varepsilon \right), \tag{21}$$

where σ_a is the constant athermal resistance, $\hat{\sigma}_i$ is the constant intrinsic lattice resistance at 0 K, and $\hat{\sigma}_\varepsilon$ is the resistance due to dislocation structure at 0 K, which evolves with deformation. The relationship for shear modulus as a function of temperature is given [45] as

$$\mu = \mu_0 - \frac{D_0}{\exp\left(\frac{\theta_0}{\theta}\right) - 1}, \tag{22}$$

The rate and temperature kinetics are represented by the two premultiplying terms

$$S_i\left(\dot{\bar{\varepsilon}}_p, \theta\right) = \left(1 - \left[\frac{k\theta}{\mu b^3 g_{0i}} \ln\left(\frac{\dot{\varepsilon}_{0i}}{\dot{\bar{\varepsilon}}_p}\right)\right]^{1/q_i}\right)^{1/p_i}, \tag{23}$$

and

$$S_\varepsilon\left(\dot{\bar{\varepsilon}}_p, \theta\right) = \left(1 - \left[\frac{k\theta}{\mu b^3 g_{0\varepsilon}} \ln\left(\frac{\dot{\varepsilon}_{0\varepsilon}}{\dot{\bar{\varepsilon}}_p}\right)\right]^{1/q_\varepsilon}\right)^{1/p_\varepsilon}, \tag{24}$$

and k is Boltzmann's constant, b is the magnitude of the Burgers vector, g_0 are normalized activation energies, $\dot{\varepsilon}_0$ are reference strain rates, and p and q are exponents which determine the shape of the energy barrier profile. Kocks et al. [36] suggest that $p \in [0, 1]$ and $q \in [1, 2]$.

The resistance due to the evolution of the dislocation structure changes with strain as

$$\frac{d\hat{\sigma}_\varepsilon}{d\bar{\varepsilon}_p} = h_0\left(1 - \frac{\hat{\sigma}_\varepsilon}{\hat{\sigma}_{\varepsilon s}}\right)^\kappa, \tag{25}$$

where the saturation stress as a function of rate and temperature is given by Kocks [37]

$$\hat{\sigma}_{\varepsilon s} = \hat{\sigma}_{\varepsilon s_0}\left(\frac{\dot{\bar{\varepsilon}}_p}{\dot{\varepsilon}_{0_{\varepsilon s}}}\right)^{\frac{k\theta}{\mu b^3 g_{0_{\varepsilon s}}}}. \tag{26}$$

The saturation stress σ_s, used in Eq. (13), is taken as the current value of the flow stress given in Eq. (21), with the quantity $\hat{\sigma}_\varepsilon$ replaced by its saturation value $\hat{\sigma}_{\varepsilon s}$, given by Eq. (26). The local mechanical work done to the material changes the local temperature by the following relationship

$$\dot{\theta} = \frac{1}{\rho C_p}\dot{\tilde{E}}_s, \tag{27}$$

where $\tilde{E}_s$ is the internal energy in the undamaged material (Eq. (19)) and C_p is the specific heat at constant pressure. The material parameters for this model used in the calculations presented here can be found in Bronkhorst et al. [10].

4.2 Numerical Simulation Results

Simulations of the tantalum on tantalum plate impact experiment described above were performed with the explicit finite element code EPIC-06 [30]. The two-dimensional simulations assumed axi-symmetry and preserved the anisotropy of the geometry. Since cross-sectional metallography of the recovered samples was an integral part of this study, simulation of the full experimental geometry, with radial momentum trapping rings [19], was necessary. The exact geometry of the experimental impact and sample plates was replicated numerically. Frictionless contact surfaces between each of the independent members of the assembly were assumed and have generally been found to be an accurate assumption for these types of loading conditions. The details of the simulation used here can be found in Bronkhorst et al. [10]. The simulation result with a computational cell size of 50 μm is used in our analysis here. The comparison between simulation and experiment is shown in Fig. 4. The numerical results represent well the response of the material through the region of interest here, which is up to the first pullback in the velocity signal.

Using the numerical results shown in Fig. 4, we can derive an estimate of the time in the simulation where the macroscale model indicates an appreciable increase in porosity. The time indicated by the results is at a simulation time of 2.166 μs. Since the experimental conditions are designed in a way such that the maximum tensile stress will occur at the center of the sample, we can use that location in the computational model to also derive the stress history within the material up to this point in time. At the simulation time of 2.166 μs, the stress in the direction of shock

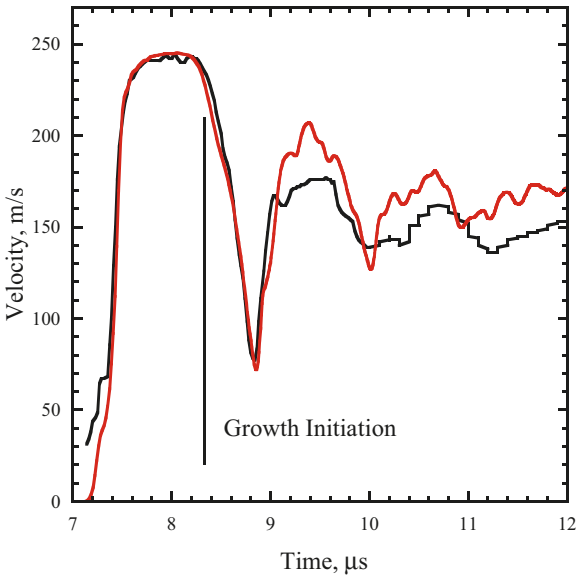

Fig. 4 Experimental (black) and macroscale simulation (red) free-surface velocity vs time curves for the tantalum on tantalum flyer plate experiment. The time in the profile where porosity growth initiation in the macroscale model simulations is indicated. Note that zero time for this plot is arbitrary

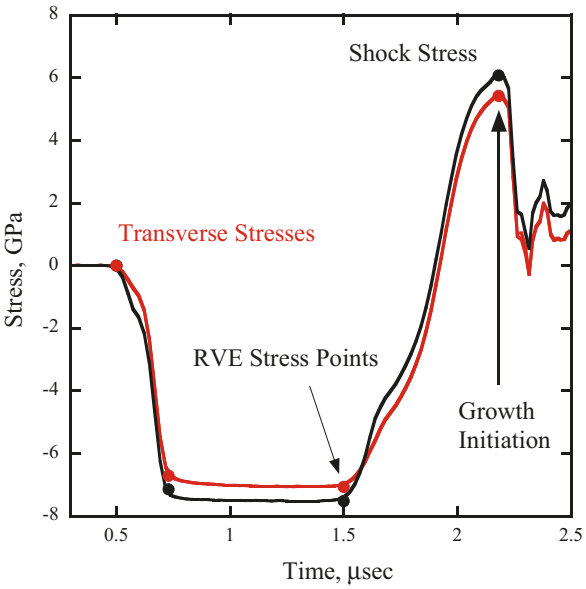

Fig. 5 Stress profile derived from the macroscale model simulation of the tantalum on tantalum flyer plate case up to the point of porosity growth initiation. The points superposed on the curves indicate the piece-wise linear stress profile applied to the local-scale statistical volume element

loading was computed to be 6.083 GPa, and in both principal directions transverse to the shock direction the value of stress was 5.402 GPa. The computed stress-time profile for this loading history at the center of the sample is given in Fig. 5.

5 Local-Scale Modeling

Using the results of the macroscale simulations of the plate impact experiment, we now seek to probe the micromechanics of deformation within a series of polycrystal calculations. The loading profiles given in Fig. 5 will be the applied stress boundary conditions for the polycrystal models discussed later and represent the soft-scale coupling procedure advocated herein. To enable this, we first discuss a single crystal model for tantalum that has been developed to also represent the non-Schmid effects in that material.

5.1 Single Crystal Model

The single crystal model used in this work is one, which has been developed over a number of years and is cast in a large deformation framework. The formulation outlined here is derived from prior work by Asaro and Rice [5], Acharya and Beaudoin [6], Kothari and Anand [38], Busso [13], Busso and McClintock [14], Kocks [37], Kalidindi et al. [34], Bronkhorst et al. [9], Anand [4], Bronkhorst et al. [12], Gurtin [27], Gurtin et al. [28], and Cho et al. [16] (Fig. 6).

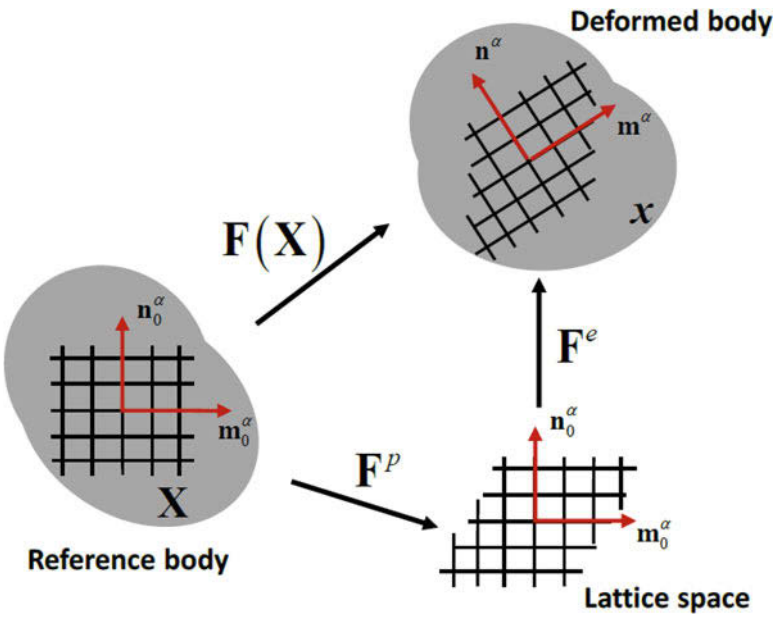

Fig. 6 Schematic of the kinematical structure used in the current single crystal model

Within a finite deformation kinematical framework, the deformation gradient is decomposed as

$$\mathbf{F} = \mathbf{F}^{e}\mathbf{F}^{p} \tag{28}$$

The second Piola-Kirchoff stress is given as a function of the energy conjugate Green-Lagrange elastic strain and the thermal expansion term

$$\mathbf{T}^{*} = \underline{\mathbf{C}}\left[\mathbf{E}^{e} - \mathbf{A}\left(\theta - \theta_0\right)\right], \tag{29}$$

where in relation to the Cauchy stress, $\mathbf{T}^{*}$ in the deformed configuration

$$\mathbf{T}^{*} = \left(\det \mathbf{F}^{e}\right)\mathbf{F}^{e^{-1}}\mathbf{T}\mathbf{F}^{e^{-\mathrm{T}}}. \tag{30}$$

The elastic stiffness tensor as a function of temperature θ is given as a linear expression with temperature

$$C_{ijkl} = C_{ijkl_0} + m_{C_{ijkl}}\theta. \tag{31}$$

The elastic Green-Lagrange strain is given by

$$\mathbf{E}^{e} = \frac{1}{2}\left(\mathbf{F}^{e^{\mathrm{T}}}\mathbf{F}^{e} - \mathbf{1}\right). \tag{32}$$

The thermal expansion coefficient is given by

$$A_{ij} = \alpha \delta_{ij}. \tag{33}$$

The plastic velocity gradient is given as a function of the plastic slip rates $\dot{\gamma}^{\alpha}$ on the α slip systems

$$\mathbf{L}^{p} = \dot{\mathbf{F}}^{p} \mathbf{F}^{p^{-1}} = \sum_{\alpha} \dot{\gamma}^{\alpha} \mathbf{S}_{0}^{\alpha}, \tag{34}$$

where the Schmid tensor in the reference configuration via the slip direction $\mathbf{m}_{0}^{\alpha}$ and slip plane normal $\mathbf{n}_{0}^{\alpha}$ is given by

$$\mathbf{S}_{0}^{\alpha} = \mathbf{m}_{0}^{\alpha} \otimes \mathbf{n}_{0}^{\alpha}. \tag{35}$$

The plastic slip rate is given by an expression which represents the thermally activated motion of dislocations and also accounts for the non-Schmid behavior of the screw dislocations in BCC materials

$$\dot{\gamma}^{\alpha} = \dot{\gamma}_{0} \exp\left(-\frac{\Delta G}{k_{B}\theta} \left\langle 1 - \left\langle \frac{\tau_{\text{eff}}^{\alpha}}{\tilde{s}_{l}^{\alpha}} \right\rangle^{p} \right\rangle^{q} \right) \text{ for } \tau^{\alpha} > 0, \quad \text{otherwise } \dot{\gamma}^{\alpha} = 0, \tag{36}$$

where $\dot{\gamma}_{0}$ is the reference shear rate, ΔG is the activation energy, k_{B} is Boltzmann's constant, $p \in [0, 1]$, $q \in [1, 2]$ are exponents which define the shape of the atomic level energy barrier to dislocation motion, and $\tau^{\alpha} = \mathbf{T}^{*} : \mathbf{S}_{0}^{\alpha}$. The effective resolved shear stress on slip system α is given by

$$\tau_{\text{eff}}^{\alpha} = \tilde{\tau}^{\alpha} - \tilde{s}^{\alpha}, \tag{37}$$

$$\tilde{s}^{\alpha} = s^{\alpha} \frac{\mu}{\mu_{0}}, \quad \tilde{s}_{l}^{\alpha} = s_{l}^{\alpha} \frac{\mu}{\mu_{0}}, \tag{38}$$

where s^{α} is the dislocation structure dependent resistance, s_{l}^{α} is the intrinsic lattice resistance, and the temperature-dependent shear modulus μ is given by

$$\mu(\theta) = \sqrt{C_{44}(\theta) \frac{C_{11}(\theta) - C_{12}(\theta)}{2}}, \tag{39}$$

and μ_{0} is the shear modulus at 0 K. The resolved shear stress is now inclusive of both the traditional Schmid tensor $\mathbf{S}_{0}^{\alpha}$ and additional terms $\tilde{\mathbf{S}}_{0}^{\alpha}$ representing the non-Schmid effects of the split core of screw dislocations in BCC materials

$$\tilde{\tau}^{\alpha} = \mathbf{T}^{*} : \left(\mathbf{S}_{0}^{\alpha} + \tilde{\mathbf{S}}_{0}^{\alpha} \right), \tag{40}$$

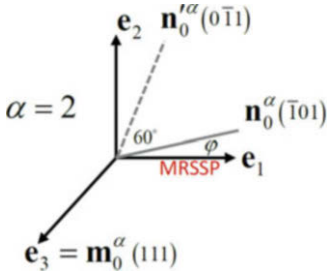

Fig. 7 Spatial relationship of the three vectors used in the non-Schmid terms of Eqs. 41 and 42 for a single slip system in tantalum

$$\tilde{\mathbf{S}}_0^{\alpha} = \sum_{i=1}^{3} \omega_i \tilde{\mathbf{S}}_0^{i,\alpha}, \tag{41}$$

$$\tilde{\mathbf{S}}_0^{1,\alpha} = \mathbf{m}_0^{\alpha} \otimes \mathbf{n}'^{\alpha}_0, \tilde{\mathbf{S}}_0^{2,\alpha} = \left(\mathbf{n}_0^{\alpha} \times \mathbf{m}_0^{\alpha}\right) \otimes \mathbf{n}_0^{\alpha}, \tilde{\mathbf{S}}_0^{3,\alpha} = \left(\mathbf{n}'^{\alpha}_0 \times \mathbf{m}_0^{\alpha}\right) \otimes \mathbf{n}'^{\alpha}_0. \tag{42}$$

The quantities ω_i in Eq. (41) are weighting factors for each of the three terms defined in Eq. (42). The additional plane represented by normal vector $\mathbf{n}'^{\alpha}_0$ is shown schematically in Fig. 7.

Within BCC materials in general, there are three different close-packed planes {110}, {112}, and {123} with the common ⟨111⟩ direction. In keeping with observations made by a number of authors [12, 38, 39, 42], we will restrict ourselves to the {110} and {111} planes in our single crystal model for BCC materials. Values for all material parameters and slip systems used for this study can be found in Cho et al. [16].

5.2 *Polycrystal Numerical Results*

We employ here 10 statistical volume elements that were constructed based upon the tools and methodology reported by Knezevic et al. [35]. The tantalum material microstructure was characterized by electron-backscatter diffraction (EBSD) metallography of the three principal plate directions. These EBSD data sets were then used within the open-source code Dream.3D [25] to construct statistically equivalent 3D numerical microstructure cubes with between 65 and 100 grains represented within each volume. The methodology discussed in Knezevic et al. [35] uses STL files produced by Dream.3D [17] and representing each grain to construct tetrahedral mesh tessellations of each grain and allows for grain boundary conforming representation. This is important in our study of damage in polycrystalline materials. A cross-sectional example of one of the 10 such numerical realizations used for the polycrystal simulations is given in Fig. 8. Each of the 10 polycrystal realizations was loaded by applying the stress profile computed using the

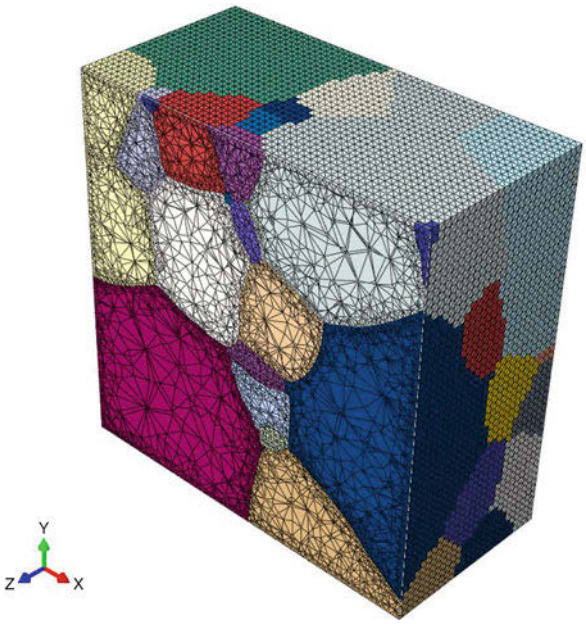

Fig. 8 Cross-sectional image of one of the polycrystal numerical realizations used for the simulations in this work. This particular realization contained a total of 70 grains

macroscale damage model representing the plate impact experiment in the previous section (Fig. 5) and applied to the primary faces of each cube. These results are presented below.

Combining the results from all 10 numerical realization calculations, the pressure distribution at all computational points is given in Fig. 9 for the cases where non-Schmid effects are accounted for. This plot compares results between calculations without non-Schmid effects on both {110} and {112} plane slip systems and calculation with the non-Schmid effects applied to the {110} without slip on the {112} plane systems. In the same way, vonMises stress results are shown in Fig. 10, giving the same two comparisons. These results are at the maximum tensile stress point in the loading profile given in Fig. 5. These results then account for the deformation history for that loading profile. The density estimates (smoothed histograms) given in both Figs. 9 and 10 are derived from a combined total of approximately 8.5 million computational (Gauss) points.

Two individual grains within one of the 10 realizations are examined in more detail through the results presented in Figs. 11, 12, 13, and 14 and are shown for calculations performed without the non-Schmid effect accounted for with slip on {110} and {112} plane systems. The results in Figs. 11 and 12 show the magnitude of vonMises stress versus distance from grain boundary surface and distance from grain boundary triple line, respectively, for a single grain (grain 45). Each point in these figures represents a single computational point. Figures 13 and 14 show the same information for another grain in the simulation (grain 53). These results are interesting in that they clearly demonstrate and quantify the influence of these two

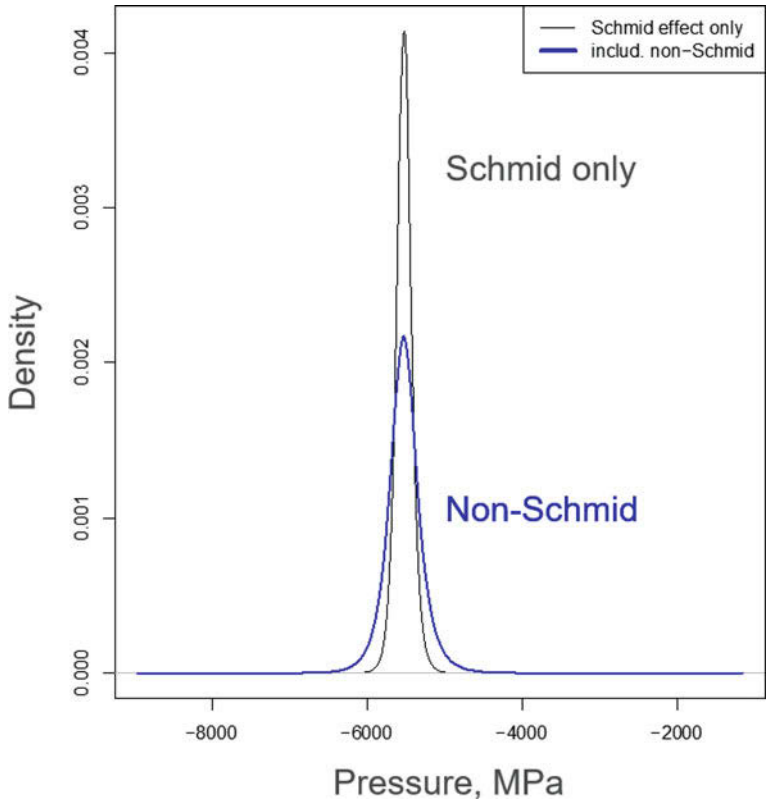

Fig. 9 Density estimates (smoothed histograms) of pressure at all computational points in the 10 statistical volume element polycrystal simulations at the conclusion of the loading profile given in Fig. 5

structural features on the stress variability within the grain. These results suggest that the variation of vonMises stress within the grain is much more heterogeneous in the vicinity of the grain boundary with some locations about 40% higher than the more stable mean value towards the grain center. The variability drop is more rapid in the case of the grain boundary surface than for the grain boundary triple line. It is also interesting to note that the converging vonMises stress magnitude is different for the two grains. This magnitude is approximately 740 MPa for grain 45 and approximately 800 MPa for the case of grain 53. This is likely due to neighborhood effects within the polycrystal and also differences in crystallographic orientation between the two grains. The results shown in Fig. 5 show that the loading is not purely hydrostatic, but the stress magnitude in the shock direction is 10% higher than the two other principal directions.

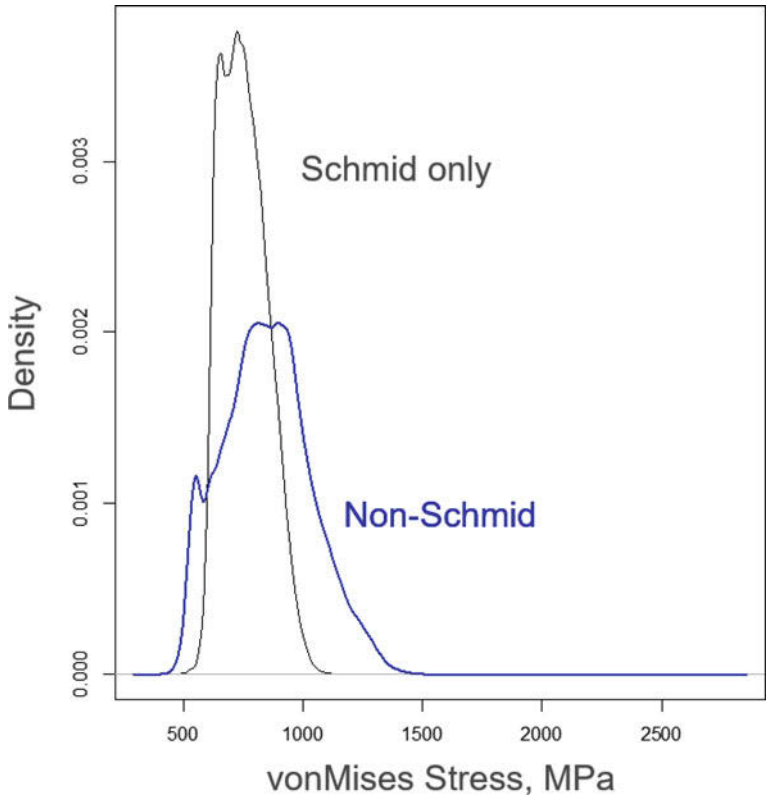

Fig. 10 Density estimates of vonMises stress at all computational points in the 10 statistical volume element polycrystal simulations at the conclusion of the loading profile given in Fig. 5

The experimental results shown earlier suggest that grain boundaries can provide the conditions to enable pore formation for lightly loaded shock conditions. Certainly, there is much which we do not yet understand about grain boundaries which leads to grain boundaries being critical defects in some high purity materials. The results given in Figs. 11, 12, 13, and 14 demonstrate high stress conditions at some points on grain boundaries computed for the 10 statistical volume elements used in this study. The results given in Figs. 15 and 16 feature the normal and shear components of traction stresses on all grain boundaries within the 10 polycrystal calculations as a function of angle of inclination of the grain boundary segment relative to the shock direction. In both figures, angles of 0 and 180 are the points on the curves where the grain boundary normal is parallel to the direction of shock. The results in Fig. 15 show that the normal traction on grain boundaries perpendicular to the shock direction display a high-tensile traction loading. Since the loading for the shock conditions is overall hydrostatic, the results demonstrate that the normal traction is tensile on all grain boundary surfaces. The shear traction component

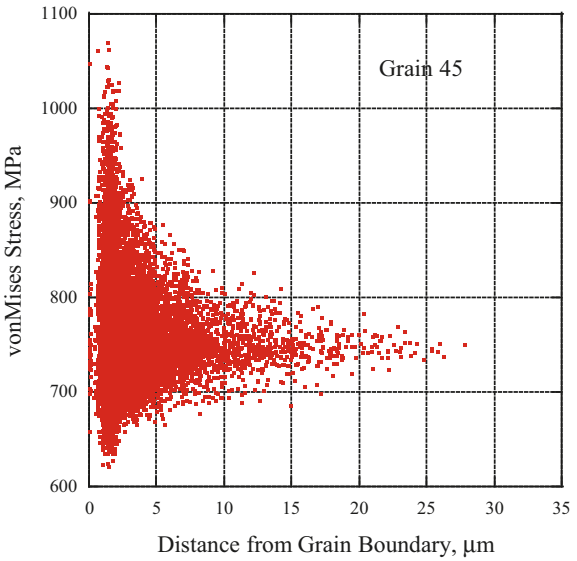

Fig. 11 vonMises stress versus distance from grain boundary surface within grain 45 in one of the 10 polycrystal realizations. Each point represents the stress conditions at a single computational point

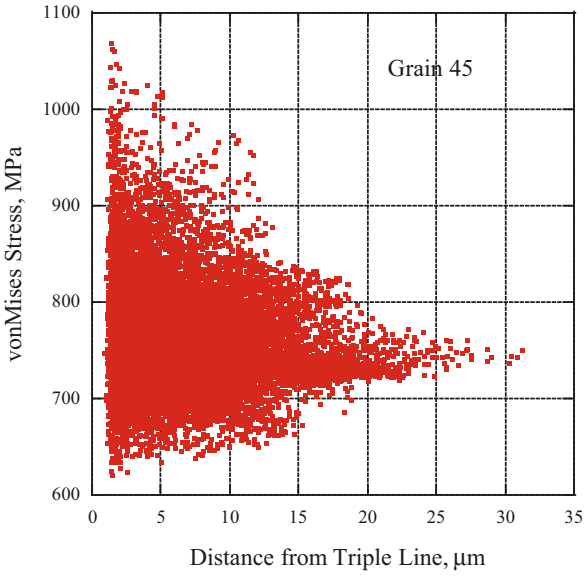

Fig. 12 vonMises stress versus distance from a grain boundary triple line within grain 45 in one of the 10 polycrystal realizations. Each point represents the stress conditions at a single computational point

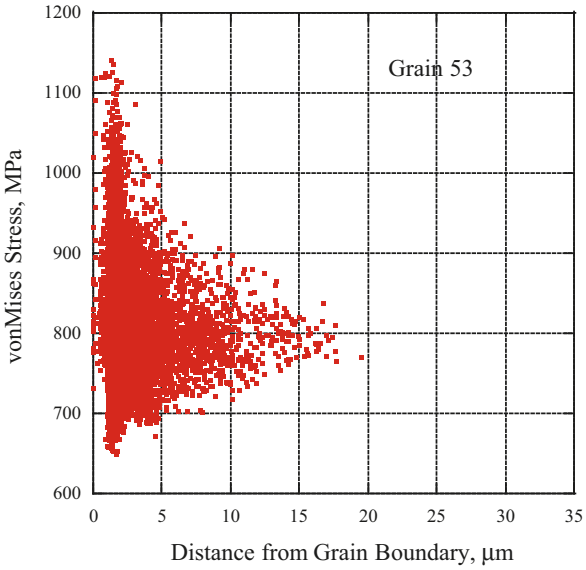

Fig. 13 vonMises stress versus distance from grain boundary surface within grain 53 in one of the 10 polycrystal realizations. Each point represents the stress conditions at a single computational point

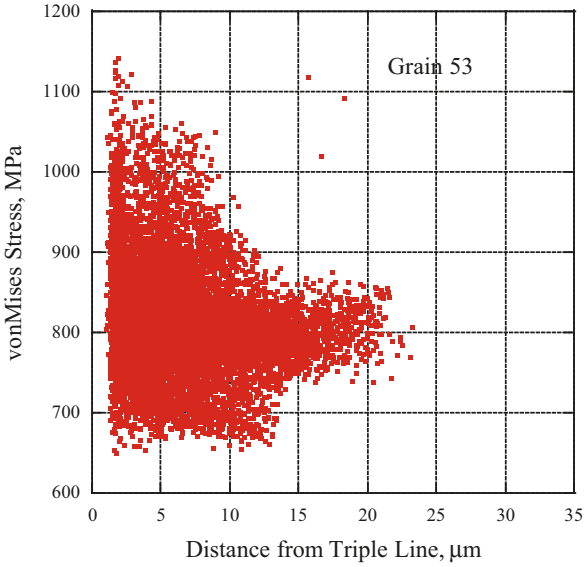

Fig. 14 vonMises stress versus distance from a grain boundary triple line within grain 53 in one of the 10 polycrystal realizations. Each point represents the stress conditions at a single computational point

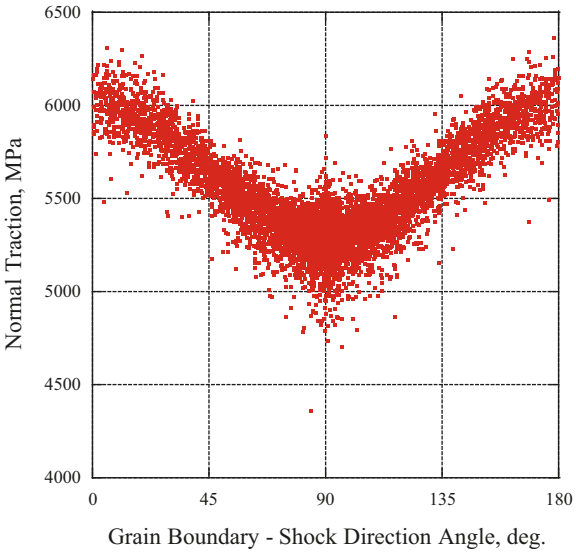

Fig. 15 Normal component of traction at all grain boundary mesh elements in the 10 statistical volume element polycrystal simulations at the conclusion of the loading profile given in Fig. 5. Each point represents the stress conditions at a single computational point near the centroid of a grain boundary. Angles 0 and 180 degrees are grain boundary orientations where the grain boundary normal is parallel with the shock direction

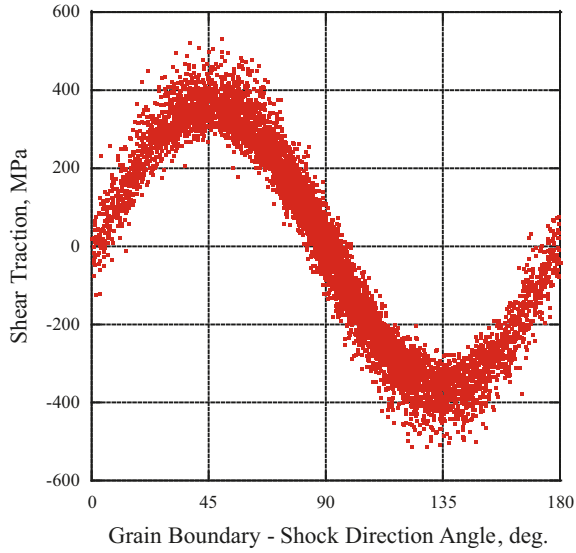

Fig. 16 Shear component of traction at all computational points in the 10 statistical volume element polycrystal simulations at the conclusion of the loading profile given in Fig. 5. Each point represents the stress conditions at a single computational point on a grain boundary. Angles 0 and 180 degrees are grain boundary orientations where the grain boundary normal is parallel with the shock direction

of loading results is given in Fig. 16. These results show that shear traction is maximum at 45 and 135 degrees and zero at the grain boundary orientation angles of 0, 90, and 180 degrees. At any given angle in both Figs. 15 and 16, the variability in stress magnitude is significant. This is currently being studied in more detail; however, we expect that different misorientation angles for different grain boundaries and neighborhood effects influencing details of local stress conditions as being responsible for this high degree of variability.

6 Conclusion

The microstructure of polycrystalline metallic materials is known to affect the nature of porosity-based damage initiation and growth for shock loading conditions. Experimental results have suggested that for high-purity materials, such as the tantalum of interest here, grain boundaries are prominent locations for pore nucleation. The polycrystal calculations performed for this study have provided insight into the stress conditions within the microstructure and the conditions at the grain boundaries. Each of the polycrystal realizations are soft-coupled to the macroscale model via the computed stress conditions predicted for a tantalum on tantalum plate impact experiment. The computational results presented can provide information which is supplemental to those derived by experiment due to the diagnostic limitation of current experimental capability. This information can then in turn be used to further advance our macroscale ductile damage models to improve both physical and computational performance for component scale simulations.

Acknowledgments This work was performed at Los Alamos National Laboratory and funded through the Laboratory Directed Research and Development program via projects 20170033DR and 20150594ER. The authors also wish to acknowledge the assistance provided by Dr. M. Ardeljan in constructing the SVEs used in this study.

References

1. F.L. Addessio, J.N. Johnson, Rate-dependent ductile failure model. J. Appl. Phys. **74**, 1640–1648 (1993)
2. C. Alleman, S. Ghosh, D.J. Luscher, C.A. Bronkhorst, Evaluating the effects of loading parameters on single crystal slip in tantalum using molecular mechanics. Phil. Mag. **94**, 92–116 (2013)
3. C. Alleman, D.J. Luscher, C.A. Bronkhorst, S. Ghosh, Distributed-enhanced homogenization framework and model for heterogeneous elasto-plastic problems. J. Mech. Phys. Solids **85**, 176–202 (2015)
4. L. Anand, Single-crystal elasto-viscoplasticity: application to texture evolution in polycrystalline metals at large strains. Comput. Methods Appl. Mech. Eng. **193**, 5359–5383 (2004)
5. R.J. Asaro, J.R. Rice, Strain localization in ductile single crystals. J. Mech. Phys. Solids **25**, 309–338 (1977)
6. A. Acharya, A.J. Beaudoin, Grain size effect in viscoplastic polycrystal at moderate strains. J. Mech. Phys. Solids **48**, 2213–2230 (2000)
7. R. Becker, Ring fragmentation predictions using the Gurson model with material stability conditions as failure criteria. Int. J. Sol. Struct. **39**, 3555–3580 (2002)
8. R. Becker, Effects of crystal plasticity on materials loaded at high pressures and strain rates. Int. J. Plasticity **20**, 1983–2006 (2004)
9. C.A. Bronkhorst, S.R. Kalidindi, L. Anand, Polycrystal plasticity and the evolution of crystallographic texture in FCC metals. Phil. Trans. R. Soc. Lond. A **341**, 443–477 (1992)
10. C.A. Bronkhorst, G.T. Gray III, F.L. Addessio, V. Livescu, N.K. Bourne, S.A. MacDonald, P.J. Withers, Response and representation of ductile damage under varying shock loading conditions in tantalum. J. Appl. Phys. **119**, 085103 (2016)

11. C.A. Bronkhorst, E.K. Cerreta, Q. Xue, P.J. Maudlin, T.A. Mason, G.T. Gray III, An experimental and numerical study of the localization behavior of tantalum and stainless steel. Int. J. Plasticity **22**, 1304–1335 (2006)
12. C.A. Bronkhorst, B.L. Hansen, E.K. Cerreta, J.F. Bingert, Modeling the microstructural evolution of metallic polycrystal materials under localization conditions. J. Mech. Phys. Solids **55**, 2351–2383 (2007)
13. E.P. Busso, Cyclic deformation of monocrystalline nickel aluminide and high temperature coatings, Ph.D. Thesis, MIT, 1990
14. E.P. Busso, F.A. McClintock, A dislocation mechanics-based crystallographic model of a B2-type intermetallic alloy. Int. J. Plasticity **12**, 1–28 (1996)
15. S.R. Chen, G.T. Gray III, Constitutive behavior of tantalum and tantalum-tungsten alloys. Met. Mat. Trans. A **27A**, 2994–3006 (1996)
16. H. Cho, C.A. Bronkhorst, H.M. Mourad, J.R. Mayeur, D.J. Luscher, Anomalous plasticity of body-centered-cubic crystals with non-Schmid effects. Int. J. Solids Struct. **139–140**, 138–149 (2018)
17. Dream.3D version 4.2, BlueQuartz Software, Springboro OH, USA, 2013
18. P.S. Follansbee, U.F. Kocks, A constitutive description of the deformation of copper based on the use of the mechanical threshold stress as an internal state variable. Acta Metall. **36**, 81–93 (1988)
19. G.T. Gray III, Shock wave testing of ductile materials, in *ASM Handbook*, (ASM International, Materials Park, 2000)
20. G.T. Gray III, High-strain-rate deformation: mechanical behavior and deformation substructures induced. Annu. Rev. Mater. Res. **42**, 285–303 (2012)
21. G.T. Gray III, K.S. Vecchio, Influence of peak pressure and temperature on the structure/property response of shock-loaded Ta and Ta-10W. Met. Mat. Trans. A **26**, 2555–2563 (1995)
22. G.T. Gray III, N.K. Bourne, J.C.F. Millett, Shock response of tantalum: Lateral stress and shear strength through the front. J. Appl. Phys. **94**, 6430–6436 (2003)
23. G.T. Gray III, N.K. Bourne, K.S. Vecchio, J.C.F. Millett, Influence of anisotropy (crystallographic and microstructural) on spallation in Zr, Ta, HY-100 steel, and 1080 eutectoid steel. Int. J. Fract. **163**, 243–258 (2010)
24. G.T. Gray III, N.K. Bourne, V. Livescu, C.P. Trujillo, S. MacDonald, P. Withers. The influence of shock-loading path on the spallation response of Ta. in *Proceedings of APS Topical Group of Shock Compression of Condensed Matter*, Seattle, 7–12 July 2013
25. M. Groeber, S. Ghosh, M.D. Uchic, D.M. Dimiduk, A framework for automated analysis and simulation of 3D polycrystalline microstructures. Part 2: Synthetic structure generation. Acta Mat. **56**, 1274–1287 (2008)
26. A.L. Gurson, Continuum theory of ductile rupture by void nucleation and growth: Part 1 – Yield criteria and flow rules for porous ductile media. J. Eng. Mat. Tech. **99**, 2–15 (1977)
27. M.E. Gurtin, On the plasticity of single crystals: free energy, microforces, plastic-strain gradients. J. Mech. Phys. Solids **48**, 989–1036 (2000)
28. M.E. Gurtin, E. Fried, L. Anand, *The Mechanics and Thermodynamics of Continua* (Cambridge University Press, Cambridge, 2010)
29. J.W. Hancock, A.C. Mackenzie, On the mechanisms of ductile failure in high-strength steels subjected to multi-axial stress-states. J. Mech. Phys. Solids **24**, 147–169 (1976)
30. G.R. Johnson, S.R. Beissel, C.A. Gerlach, R.A. Stryk, T.J. Holmquist, A.A. Johnson, S.E. Ray, J.J. Arata, *User Instructions for the 2006 Version of the EPIC Code* (Network Computing Services Inc., Minneapolis, 2006)
31. J.N. Johnson, Dynamic fracture and spallation in ductile solids. J. Appl. Phys. **52**, 2812 (1981)
32. J.N. Johnson, F.L. Addessio, Tensile plasticity and ductile fracture. J. Appl. Phys. **64**, 6699 (1988)
33. J.N. Johnson, G.T. Gray III, N.K. Bourne, Effect of pulse duration and strain rate on incipient spall fracture in copper. J. Appl. Phys. **86**, 4892 (1999)

34. S.R. Kalidindi, C.A. Bronkhorst, L. Anand, Crystallographic texture evolution in bulk deformation processing of FCC metals. J. Mech. Phys. Solids **40**, 537–569 (1992)
35. M. Knezevic, B. Drach, M. Ardeljan, I.J. Beyerlein, Three dimensional predictions of grain scale plasticity and grain boundaries using crystal plasticity finite element models. Comput. Methods Appl. Mech. Eng. **277**, 239–259 (2014)
36. U.F. Kocks, A.S. Argon, M.F. Ashby, *Thermodynamics and Kinetics of Slip. Progress in Materials Science* (Pergamon, Oxford, 1975)
37. U.F. Kocks, Laws for work-hardening and low-temperature creep. J. Eng. Mater. Technol. **98**, 76–85 (1976)
38. M. Kothari, L. Anand, Elasto-viscoplastic constitutive equations for polycrystalline metals: application to tantalum. J. Mech. Phys. Solids **46**, 51–83 (1998)
39. P.J. Maudlin, J.F. Bingert, J.W. House, S.R. Chen, On the modeling of the Taylor cylinder impact test for orthotropic texture materials: experiments and simulations. Int. J. Plasticity **15**, 139–166 (1999)
40. P.J. Maudlin, E.N. Harstad, T.A. Mason, Q.H. Zuo, F.L. Addessio. TEPLA-a: coupled anisotropic elastoplasticity and damage, the Joint DoD/DOE Munitions Technology Program progress report, LA-UR-14015-PR (2003)
41. S. Nemat-Nasser, J.B. Isaacs, Direct measurement of isothermal flow stress of metals at elevated temperatures and high strain rates with application to Ta and Ta-W alloys. Acta Mater. **45**, 907–919 (1997)
42. D.J. Savage, I.J. Beyerlein, M. Knezevic, Coupled texture and non-Schmid effects on yield surfaces on body-centered cubic polycrystals predicted by a crystal plasticity finite element approach. Int. J. Solids Struct. **109**, 22–32 (2017)
43. P. Shanthraj, M.A. Zikry, Dislocation-density mechanisms for void interactions in crystalline materials. Int. J. Plasticity **34**, 154–163 (2012)
44. V. Tvergaard, A. Needleman, Analysis of the cup-cone fracture in a round tensile bar. Acta Metall. **32**, 157–169 (1984)
45. Y.P. Varshni, Temperature dependence of the elastic constants. Phys. Rev. B **2**, 3952–3958 (1970)
46. D. Versino, C.A. Bronkhorst, A computationally efficient ductile damage model accounting for micro-inertia. Comp. Meth. Appl. Mech. Engr. **333**, 395–420 (2018)
47. Q. Wu, M.A. Zikry, Dynamic fracture predictions of microstructural mechanisms and characteristics in martensitic steels. Eng. Frac. Mech. **145**, 54–66 (2014)
48. Q.H. Zuo, J.R. Rice, An implicit algorithm for a rate-dependent ductile failure model. J. Appl. Phys. **104**, 083526 (2008)
49. Q.H. Zuo, Modified formulation of a rate-dependent damage model for ductile materials. J. Appl. Phys. **107**, 053513 (2010)

A Framework for Quantifying Effects of Characterization Error on the Predicted Local Elastic Response in Polycrystalline Materials

Noah Wade, Michael D. Uchic, Amanda Criner, and Lori Graham-Brady

1 Introduction

Advances in integrated computational materials engineering (ICME) are fundamentally dependent on acquisition of quality microstructural material information in three dimensions (3D). DeHoff emphasized the importance of characterizing microstructures in 3D in 1983, and since then a number of other authors have illustrated the benefits of collecting detailed 3D microstructural data sets [1, 2]. This recognition has spurred the development of a whole suite of tools and methods for collecting data across many different length scales [3], which in turn has led to the development of more integrated material property-structure relationships. While simplified microstructures are commonly applied to computational models [4], more recent advances in computational power and automated sectioning techniques have allowed the ICME community to begin exploring property-structure relationships which were previously unattainable. This has encouraged significant investment of equipment and time in collecting detailed 3D microstructures.

One example of this has been the development of focused ion beam (FIB) milling within a scanning electron microscope (SEM) for rapid collection of 3D electron backscatter diffraction (EBSD) data sets. Many papers have been published about the development and advantages of this technique [5–11]. Uchic et al. highlighted one of the main advantages of FIB-SEM as filling a critical length-scale gap between mechanical serial sectioning and electron tomography [12], and this technology has

N. Wade · L. Graham-Brady (✉)
Department of Civil Engineering, Johns Hopkins University, Baltimore, MD, USA
e-mail: nwade2@jhu.edu; lori@jhu.edu

M. D. Uchic · A. Criner
Materials and Manufacturing Directorate, Air Force Research Laboratory, Wright-Patterson AFB, Dayton, OH, USA
e-mail: micheal.uchic@us.af.mil; amanda.criner.1@us.af.mil

S. Ghosh et al. (eds.), *Integrated Computational Materials Engineering (ICME)*,
https://doi.org/10.1007/978-3-030-40562-5_8

enabled the study of many fine- and ultrafine-grained alloys. Materials scientists have been tasked with the challenge of using this improved resolution to evaluate materials that have property-structure relationships that scale across several orders of magnitude. For example, Rene-88 DT has parent grain sizes on the order of 20–100 μm but has features that exist at smaller length scales, like annealing twins that are approximately 100 nm–1 μm thick and precipitate phases that are approximately 10 nm–1 μm in diameter. Previous work has shown that all of these features, as well as the overall grain boundary networks, play a role in crack initiation and propagation [13], meaning that microstructural data needs to be collected at 100 nm–1 μm resolutions across 1 mm length scales, pushing the limits of FIB and mechanical serial sectioning.

As research continues to advance this technology, there is a growing tendency toward generating large data sets, without a full understanding of the associated limitations. For example, high-resolution data sets provide more detailed information about small-scale features, but they may not capture a representative volume due to resource limitations. This trade-off must be reconciled in the context of the properties one hopes to infer from the data set. In fact, a whole field of research has emerged studying the effects of various properties as a function of the representative volume element from which they are derived, with the ultimate goal of determining the minimum volume from which to collect data without bias. Early data collection efforts provided rough guidelines such as collecting enough slices to encompass a volume at least twice the diameter of the largest grain [14], although more recent efforts have suggested that larger volumes than this are needed. One common statistical approach is to compare the variance of apparent properties through a Monte Carlo (MC) simulation of increasing RVE sizes [15, 16] or stochastic characterization of response quantities [17].

Other efforts have looked at how the spatial resolution should be selected to ensure good convergence of properties, with some suggesting a minimum of ten samples across a feature diameter is a reasonable resolution to resolve statistical properties [18]. A later study looked at the effect of voxel resolution on the accuracy of ensemble statistics by systematic downsampling of a synthetic microstructure, suggesting different values for various types of desired statistics [19].

In other circumstances, researchers have looked at ways to improve interpretation of the data, thereby reducing the overall experimental cost. For example, DeGraef et al. introduced a dictionary-based indexing of diffraction patterns, which reduces the number of unindexed or misindexed pixels resulting from the lack of clearly identifiable Kikuchi bands [20].

In summary, each of these efforts has tried to identify ways of optimally allocating resources to obtain the highest-quality data sets. This can be recast as an effort to reduce the error in collecting data from a physical sample and building a digital reconstruction of the material. Any error introduced during the generation of these digital reconstructions is propagated to the material model. Understanding the effects of this error will help in the effort to develop more accurate computational models.

Throughout these studies, several authors have noted that estimation of the uncertainty of 3D microstructures has been underdeveloped and is key to implementing ICME [19, 21]. This work aims to introduce a framework for which the error associated with a given choice of characterization parameters is evaluated. Ultimately, such a framework will enable identification of the optimal data collection and cleanup parameters for a given class of materials. The approach makes use of synthetically generated phantom microstructures that represent "ground truth" specimens. Section 2 describes the method for simulating the data collection process. Section 3 evaluates the error in the resulting reconstructed microstructures, resulting from variations in four sources of error: resolution, interaction volume, random noise, and data processing parameters. Section 4 addresses the effect of data collection errors on the predictions from computational models developed from the associated reconstructed microstructure, specifically for linear elastic stresses. Section 5 provides some conclusions and thoughts on possible future work.

2 Methods

The overall framework for the current work is shown in Fig. 1. A synthetic microstructure that is presumed to be reasonably representative of the material of interest serves as the basis for the analysis, providing a phantom microstructure that is viewed as the "ground truth." The serial-sectioned EBSD data collection process is represented by simulations that capture the effects of noise, resolution, and interaction volume. The resulting data from this virtual collection process is cleaned up using standard protocols in DREAM.3D [22]. A comparison between this virtually reconstructed microstructure and the phantom microstructure provides a number of possible measures of microstructural error, including volumetric mismatch or differences in grain size distribution. Finally, the virtually reconstructed microstructure is meshed and modeled using ABAQUS [23], to predict elastic stress. Because the phantom microstructure can be modeled directly, there is a set of

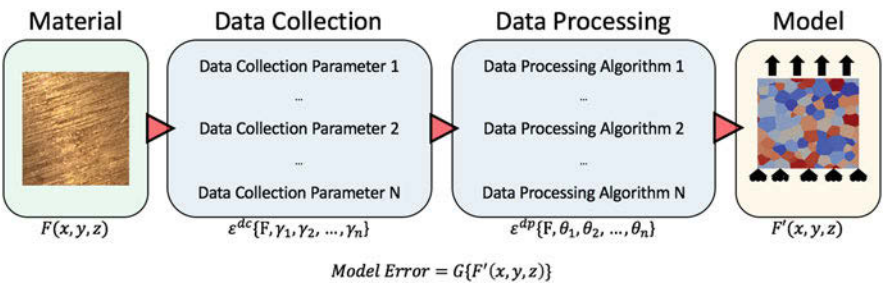

Fig. 1 A general workflow of the main stages of the framework. The three stages are highlighted starting with the generation of a synthetic material (green), material data collection and processing modeling (blue), and model evaluation and error computation (yellow)

"ground truth" results to which the virtually reconstructed results are compared. This provides a quantitative way to measure the error associated with different choices of data collection and processing parameters on computational models associated with the microstructure. This framework is meant to be general and can be adapted for a number of serial sectioning techniques and/or computational models of interest. Each of these steps is described in greater detail in the subsequent subsections.

2.1 Step 1: Synthetic Material Generation – Phantoms

One of the challenges associated with 3D serial sectioning techniques is the inherently destructive nature of the process. Reevaluation of the sample is impossible, which makes comparisons between measurement strategies difficult. This motivates our use of a virtual material which can be copied and resampled repeatedly [19]. This virtual material, or phantom, should reasonably represent the true physical material of interest through statistical similarities of key microstructural properties, such as the grain size, orientation distributions, neighbor distributions, etc. The intention is that while the phantom may not be an exact instantiation of a physical material, its properties are presumed to be similar enough that it can be assumed that parameter studies based on the phantom will generalize to the material of interest.

The generation of synthetic volumes has seen many developments. A review of several possible techniques for polycrystalline materials can be found in [24]. For the examples described in this work, phantoms are generated using a DREAM.3D [22] synthetic microstructure generation pipeline. A simple example of this process can be found in the DREAM.3D software tutorials [25]. Various phantoms were used but in general phantoms featured on the order of 1000's of grains and typically 5000 voxels per grain. Figure 2 is a visual representation of a typical phantom, with some basic statistical information. Additional phantom microstructures of various types can also be seen in Fig. 6.

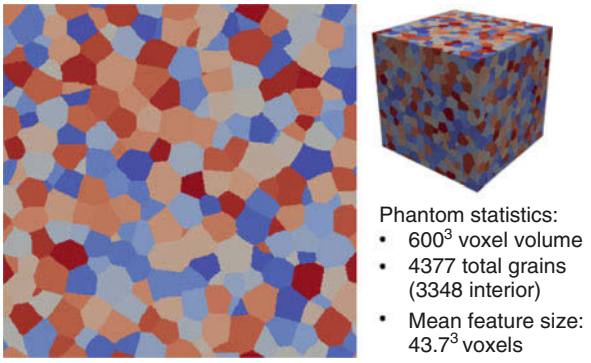

Fig. 2 An example of a typical equiaxed phantom generated using DREAM.3D. Typical grain sizes range between 10^3–80^3 voxels

2.2 Step 2: Simulation of Data Collection

To model the serial sectioning data collection process, a simulation-based model is employed. Some efforts have been made to model more specific aspects of the EBSD process [18–20]; however, these efforts focused primarily on a single aspect such as simulating the diffraction pattern. In the current work, the efforts focus on the effects of resolution, sample size, interaction volume, and random noise. Of course, the framework allows expansion to any number of data collection parameters.

2.2.1 Resolution

One of the most important experimental determinations to be made is assessing where to collect data and at what resolution. To model this, the EBSD simulation allows users to individually vary sample spacing in the $x-$, $y-$ and $z-$ directions. The sampling points are not limited to uniform spacing. A common example of this could be randomly varying the slice thicknesses removed from the sample due to variations in the serial sectioning process, for example, as often observed in metallographic polishing.

2.2.2 Interaction Volume

The physics of EBSD is a complicated but well-understood process [26]. In short, the diffraction process occurs within a region of material in which electrons from an incident beam are forward scattered out of the sample, with some of these electrons collected on a detector. The pattern of scattered electrons, comprised of what are known as Kikuchi bands, is analyzed to assign a crystallographic orientation to the interrogation point. It is important to note that the diffraction pattern represents a finite volume of the material (known as the interaction volume), and it is not truly a point process. This interaction volume is related to the incident beam energy, which is one of the tuned parameters available to the user in serial-sectioned EBSD. One common method of approximating this interaction volume was proposed by Kanaya and Okayama in 1972. Their estimate of the interaction volume was given as the radius of a hemisphere centered on the beam impact point and can be modeled as:

$$R_{ko} = 27.6(A/Z^{0.89}\rho)E_o^{1.67} \tag{1}$$

where A is the atomic weight, Z is the atomic number, ρ is the density, and E_o is the incident beam energy [27]. The Kanaya-Okayama model provides good estimates for interaction volumes in pure metals exposed to a perpendicular electron source, the results of which can be seen for various metals in Table 1.

Table 1 The Kanaya-Okayama equation evaluated for various metals. Typical interaction volumes range from 80 nm–10 μm[27]

	5 KeV	10 Kev	20 KeV	30 KeV
C	450 nm	1.4 μm	4.5 μm	8.9 μm
Al	413 nm	1.3 μm	4.2 μm	8.2 μm
Fe	159 nm	505 nm	1.6 μm	3.2 μm
Ni	138 nm	438 nm	1.4 μm	2.7 μm
Au	85 nm	270 nm	860 nm	1.7 μm

Because the current work is attempting to present an overall framework that is not specific to a particular material, the integration volume is left as a free parameter which defines the semi-ellipsoid over which the EBSD process operates. In simplifying the Kanaya-Okayama model, we removed the inherent accounting of differing absorption properties of metals and replaced it with a single variable, the equivalent material radius. In reality, the interaction volume is a semi-ellipsoid because of the angle of the incident beam relative to the surface of the sample. For the purposes of the analysis performed here, however, an equivalent radius representing this semi-ellipsoidal interaction volume is a reasonable representation. This equivalent material radius could be calibrated to reflect a specific material's absorption properties, but for the current work, interaction volumes were selected to be consistent with the ranges shown in Table 1.

2.2.3 Random Noise

Another parameter that affects the interpretation of EBSD data is the dwell time, a key factor in the ability to correctly index an interrogation point through clearly identifiable Kikuchi bands. During EBSD, data collection error can be grouped into two primary types: (1) geometric noise, which results from double diffraction near grain boundaries or where too much surface damage or deformation has disrupted the regular crystal structure, and (2) random noise, where indexing was not possible due to poor diffraction patterns or pseudosymmetry, leading to misindexing [28]. Different levels of random noise for one microstructure are illustrated in Fig. 3, where the unindexed pixels are shown in black. The number of unindexed pixels can be shown to be inversely related to the dwell time of the electron beam. Figure 4 shows an estimate of the unindexed pixels as a function of dwell time, based on data collected on a Tescan Vega SEM with Bruker eFlash 1000 EBSD detector at AFRL. By fitting a curve to this data, a noise model was developed for the simulated EBSD data collection process, where unindexed pixels are randomly generated. To reflect a decrease in dwell time, increased random noise is included in the simulation (see Fig. 3).

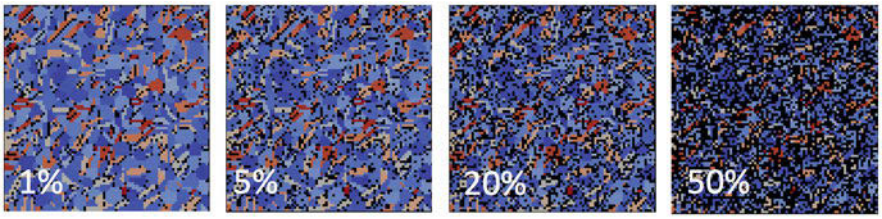

Fig. 3 Effect of increasing random error on simulated microstructures. Pixels shown in black represent bad data points where no orientation assignment is made

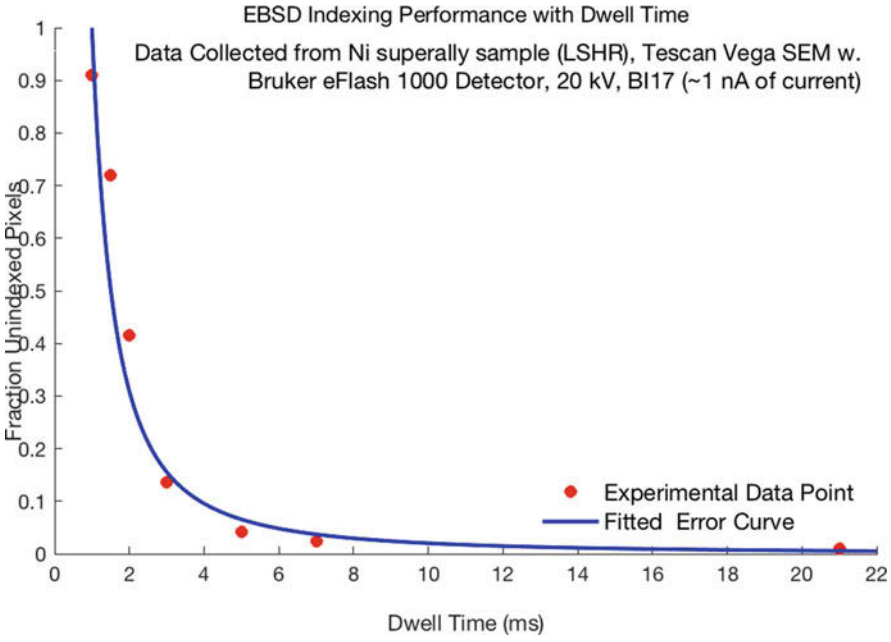

Fig. 4 Data collected with various interrogation point dwell times, showing the nonlinear relationship between the ability to compute orientation data and the time spent collecting a diffraction pattern

2.2.4 Summary of Data Collection Model

The primary goal of the EBSD model is to develop a computationally cheap approximation of the data collection process. By evaluating different combinations of parameters, the process allows for both a general estimate of the magnitude of the expected error and a quantitative means to evaluate the cost/benefits of different experimental resource allocations. The detail to which the processes are analyzed can easily be scaled through user inputs, by adding new modules or fixing certain parameters which are of less interest. The relatively cheap approximations used here

were chosen to demonstrate the utility of modeling processes for error estimation and to allow for the incorporation of many different parameters to be analyzed within a reasonable time frame. Nonetheless, the results presented in the following sections can offer some insights into important trends and will serve to demonstrate the potential of the framework.

2.3 Additional Notes on Methodology

One goal in developing the framework was to create a simple tool which can help inform the choice of data collection parameters, even in an in situ manner. It provides an outline for analyzing how changes to the data collection and data processing of microstructural data sets, and to do so it was necessary to develop simple models relying on several simplifying assumptions. However, additional capabilities or refined models can easily be implemented to meet the desires of the user. If users feel model assumptions may not generally hold for their specific application, models can easily be calibrated and/or refined to more accurately model the process in any given system. For example, the data collected as part of Sect. 2.2.3 is instrument specific, and users might want to collect data to develop a model for their specific instrument setup. Similarly, an improved physics-based model of the interaction volume (Sect. 2.2.2) that accounts for chemical compositions could also be implemented. Ultimately, the model framework was designed to allow for the variation of individual input variables. As such, any doubt surrounding the effects of a certain quantitative input (e.g., the size interaction volume) can be studied through direct variation of said parameter. By varying a parameter of interest over a range of reasonable values, and examining the output, a sensitivity to said parameter can be developed. Model assumptions relating to parameters with high sensitivity can then be refined as needed.

Additionally, the framework is intended to be able to incorporate computational models in its evaluation of the error between true and measured microstructures. For this a third step is added where the computational model is applied. An example of such an evaluation is included as part of Sect. 4.

3 Individual Parameter Variation Examples

One benefit of the framework is that it is possible to quantitatively analyze the effect of various characterization parameters. This allows for the sensitivity to be quantified and compared for any parameter, allowing for a more detailed study of the evolution and propagation of error in the sample. In this section, several simulations of EBSD data collection are conducted over a range of typical values for the parameters of interest. Each simulation was analyzed and compared directly to the phantom, using only the interior non-biased features. The exact size of the

simulation and the total number of features varied, but typically ∼1000 features were used for the determination of error, ensuring good statistical convergence. The results illustrate several key observations and demonstrate how the framework is useful in analyzing different types of error.

3.1 Step 3: Error Measurements

One of the primary motivations of the proposed framework is the ability to explicitly compute various error metrics. Using the phantom microstructure as a baseline, one measure of error is the percent of mismatched voxels (MMV) defined as:

$$MMV = \frac{\sum_{i=1}^{l}\sum_{j=1}^{m}\sum_{k=1}^{n} P(i,j,k) \neq S(i,j,k)}{lmn} \tag{2}$$

where, P, the phantom, and S, the simulation, are $l \times m \times n$ matrices of general microstructural properties voxel such as crystal orientation or phase assignments. Other measures can address error in statistical quantities that describe features of the microstructure, such as the grain size distribution:

$$L_2 = \frac{\sqrt{\sum_{i=1}^{n}[P_{gs}(x_i) - S_{gs}(x_i)]^2}}{\sqrt{\sum_{i=1}^{n} P_{gs}(x_i)^2}} \tag{3}$$

where $P_{gs}(x_i)$ and $S_{gs}(x_i)$ are the CDFs of grain size x_i for the phantom and simulation, respectively, and n is the total number of grain sizes considered. Another measure of error is the number of lost features, which occurs when none of the voxels in the reconstructed microstructure are assigned the address associated with a feature in the phantom microstructure.

As an example, Table 2 shows the three measures of error resulting from a comparison between the phantom microstructure in Fig. 5a and a simulated reconstruction of the microstructure in Fig. 5b. In this table, the resulting errors are separated into four different groups based on the percentile value associated with the grain size. Because the smallest grains are the most poorly resolved, it is not

Table 2 Changes in various error metrics across various percentiles of grain size. More error is found in the smallest 25% of grains, for all 3 error measures

Percentile range	MMV	L_2 grain size	Lost features
0–25th	13.62%	0.054	1
25th–50th	1.12%	0.015	0
50th–75th	0.58%	0.010	0
75th–100th	0.53%	0.0044	0
Total	5.02%	0.034	1

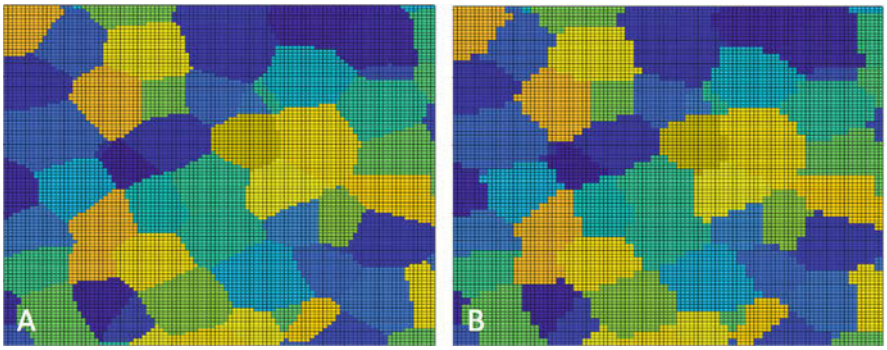

Fig. 5 Slice of (**a**) Phantom microstructure and (**b**) simulation sampled with normalized resolution of 0.14

surprising that these grains exhibit the most error, in terms of mismatched volume, grain size distribution, and lost features.

More complex error metrics can be defined such as the PDF of the grain aspect ratio distribution. For most data sets, the most appropriate error metric is typically dependent on the desired application. For data collection, efforts seeking to identify unique sites within a microstructure might prefer a counting metric, such as the number of triple lines or quad points where three or more grains meet. In each case any desired error metric can be computed directly by examining the difference between phantom and simulation volumes. For microstructures collected to support computational models, the best error metric might be differences between the predicted response from the model based on the phantom and the model based on the simulated microstructure, as will be described in Sect. 4.

3.2 Resolution

One of the most important parameters in data collection is the resolution at which data is collected. The resolution or spacing between interrogation points sets a minimum feature size threshold, which in practice should be larger than the spacing itself, in order to resolve that feature. The accuracy resolving shape, size, and feature boundaries is dependent on the resolution. Moreover, the appropriate resolution should be determined relative to microstructural features of interest, and for this reason the current discussion normalizes resolution by the average feature size. Often a minimum of ten samples across a feature diameter is recommended to resolve statistical properties [18]. By varying the spacing of interrogation points, we can examine in more detail this rule of thumb and develop an estimate of the error associated with changing resolution.

Figure 6 shows the effect of varying resolution in a single coordinate direction for various material types. This is analogous to varying the slice thickness during serial

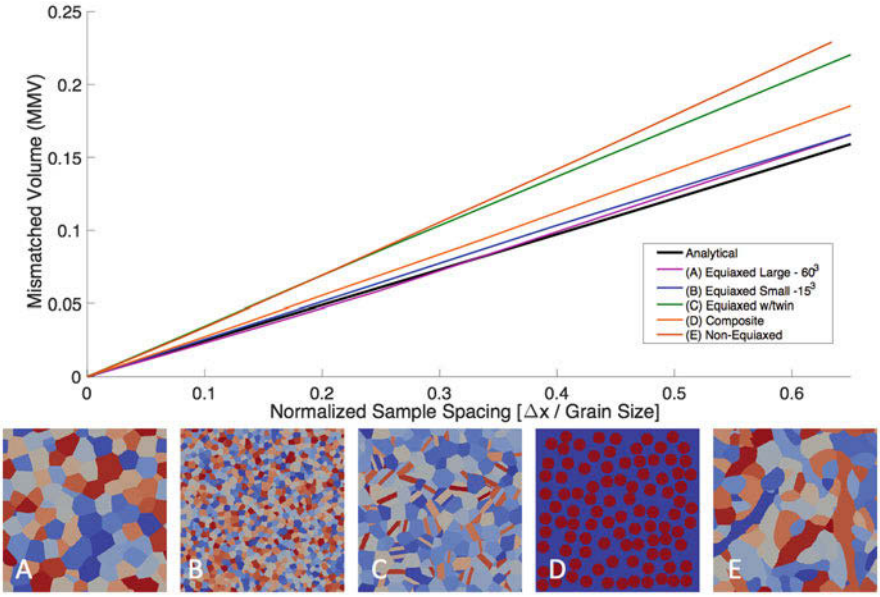

Fig. 6 Plot of mismatched volume (MMV) vs. normalized 1D sample spacing, based on simulations from various types of microstructures: (**a**) large-grained equiaxed structure, (**b**) fine-grained equiaxed structure, (**c**) large-grained equiaxed structure with inserted twins, (**d**) composite with circular fiber inclusions, and (**e**) non-equiaxed structure. Images of a single slice of each phantom are shown for comparison. Results from the 1D analytical model described in Sect. 3.2.1 are included for comparison

sectioning. In each simulation the in-plane resolution is one-to-one resampling of the phantom. In other words, the sample spacing in the 1D out-of-plane direction is the sole source of error. When averaged over a large number of phantoms (30), an approximately linear trend of increasing mismatched volume (MMV) with increasing sample spacing is clearly present. Normalizing by the average feature size, this trend can be generalized for various material types. In Fig. 6 large (60^3 voxels) and small (15^3 voxels) equiaxed materials all show the same dependence on increasing resolution along one direction. Considering the general rule of thumb of ten samples across a feature diameter (0.1 normalized resolution), this translates to an estimated 2–3% error in the geometric volume. Other less equiaxed microstructure types showed similar linearly increasing trends, although with different slopes. This can be attributed to the various length scales that exist within the microstructure, which may not be reflected through normalization by the average feature size. For example, in a composite microstructure (see Fig. 6d), the mean fiber size is used as the normalizing feature size; however, the distance to the nearest neighbor fibers can be smaller than the fiber diameter. This would create a smaller relative length scale where sampling resolution is not sufficient to resolve matrix between fibers, leading to a larger error.

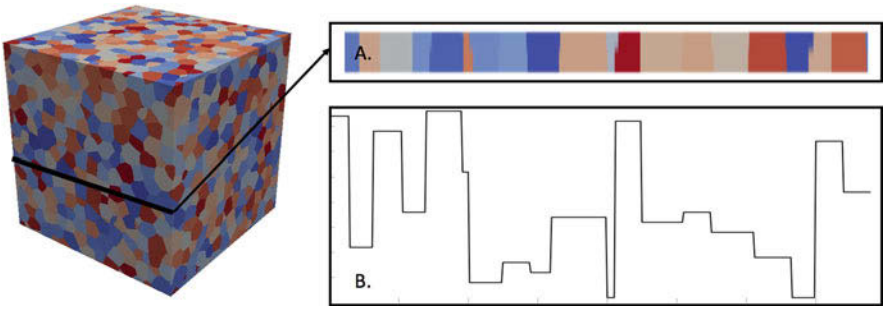

Fig. 7 Illustration of how a line slice of a phantom (**a**) could be represented as a 1D piecewise function (**b**)

The general linear trend for various material types suggests that resolving resolution is geometrically dependent on an underlying length scale. To evaluate this, a simplified analytical model is described in the next section.

3.2.1 Analytical Model of Error Associated with Sample Spacing

In order to develop an analytical model based on sample spacing, we start by considering 1D samples of the microstructure. Specifically, consider the grain identification number (grain ID) along a line through the microstructure. The grain ID along this line is represented by a piecewise constant function, where the value within each constant region is the identification number of the grain through which the line travels (see Fig. 7b). The measured grain ID along this line is a function of the sample spacing. If the sample spacing approaches zero, then the microstructure is captured exactly, although the required number of sample points becomes infinite. If the sample spacing is very large, then there is significant misassignment of grain ID along the line.

The analysis is further simplified by assuming that all grains are of equal length L_g. If the sample spacing Δx is equal to the grain size, then the fraction of mismatched volume is derived following the illustrations in Fig. 8. If the sample points happen to fall in the middle of the grains, then the microstructure is captured with zero mismatch (Fig. 8a). At the other extreme, if the sample points happen to fall on the grain boundaries (either just to the left or just to the right of the grain boundary), then there will be a 0.5 mismatch in the sampled microstructure (Fig. 8b). If the sample points fall somewhere between the grain boundary and the grain center, then the mismatch will scale linearly with the distance from the grain center (Fig. 8c). Therefore, the lineal fraction of mismatched grain ID is a function of the sample location x^*:

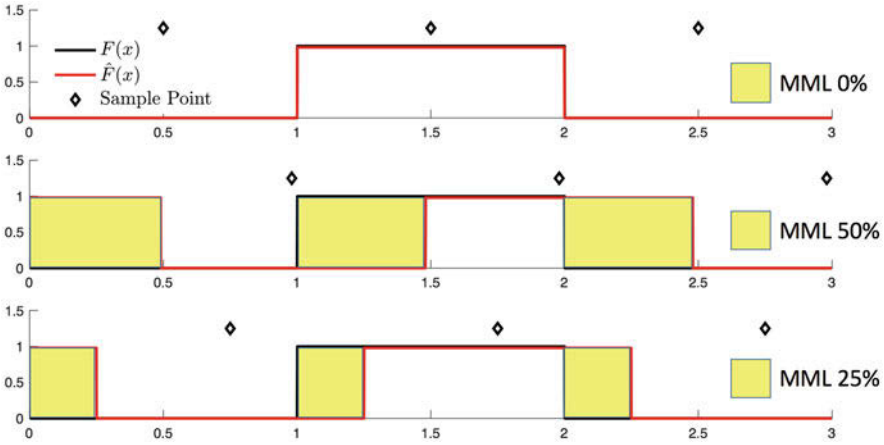

Fig. 8 Detailed view illustrating how the location of a sample point relative to the feature will produce varying amounts of mismatched length. By integrating over all possible locations relative to the feature, the expected mismatch length can be determined in 1D

$$m(x^*) = 0.5\frac{|x^* - X_g^c|}{L_g/2} \tag{4}$$

where X_g^c is the location of the nearest grain center to x^*. Assuming that x^* is a uniform random variable on the interval $[-L_g/2, L_g/2]$, then the average fraction of the line with mismatched grain ID (MML) is derived as:

$$MML = \frac{0.5}{L_g}\int_{-L_g/2}^{L_g/2}\frac{|x^* - X_g^c|}{L_g/2}dx^* = 0.25 \tag{5}$$

The mismatch is zero when sample spacing $\Delta x = 0$, which corresponds to exact resolution. Assuming that the mismatch scales linearly with the sample spacing, then a reasonable approximation to the probability of mismatch is therefore:

$$P_m = 0.25\frac{\Delta x}{L_g} \tag{6}$$

where L_g is the average grain size and Δx is the sample spacing. Noting that this 1D model of MML is the equivalent to a 3D model of MMV if we assume full resolution in the other two dimensions, these results are compared to the MMV that is obtained when performing 1D sampling from lines extracted from the microstructures in Fig. 6. This figure shows that the results from this simple 1D analytical approximation are a good match to those from the simulations for equiaxed microstructures, though it is not as good an approximation for twinned, non-equiaxed, and composite microstructures.

Assuming finite sampling occurs in only one coordinate direction is not physically realistic, since infinite sampling in the other two directions is infeasible. The analytical model is therefore extended to consider the effect of sample spacing in all three coordinate directions in a 3D microstructure. This is enabled by assuming that the probability of a correctly assigned grain ID is independent in all three directions. In other words, the grain ID at a point is only matched correctly if there is no mismatch due to sample spacing in any of the 3 coordinate directions. Therefore, the probability p_3 of a correctly matched value at a given 3D location is the cubed probability of a correctly matched grain ID at a 1D location:

$$p_3 = \left(1 - 0.25\frac{\Delta x}{L_g}\right)^3 \tag{7}$$

The probability of an incorrectly matched grain ID at a 3D location (or the mismatched volume MMV) is simply the complement of p_3:

$$MMV = 1 - p_3 = 0.75\frac{\Delta x}{L_g} - 0.1875\left(\frac{\Delta x}{L_g}\right)^2 + .015625\left(\frac{\Delta x}{L_g}\right)^3 \tag{8}$$

Figure 9 shows a comparison between this approximation and simulated mismatched volume, indicating reasonable agreement. While the analytical model

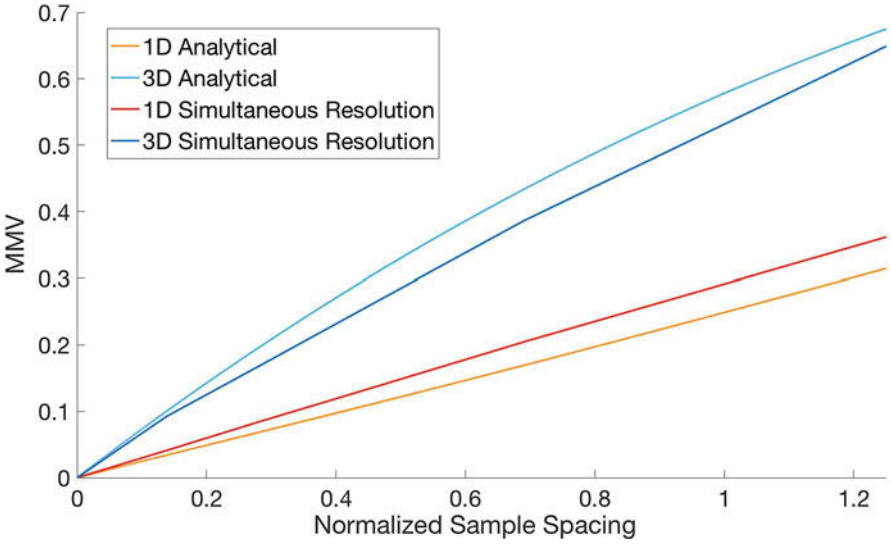

Fig. 9 Mismatched volume (MMV) vs. normalized sample spacing based on one- and three-dimensional sampling, from both the simulations and the analytical models. The simulated values were obtained from an equiaxed microstructure. The 1D model predicts a slope of 0.25, while the simulated values are 0.266. The 3D model predicts a less linear function than that found from the simulated values, but the values from both compare reasonably well

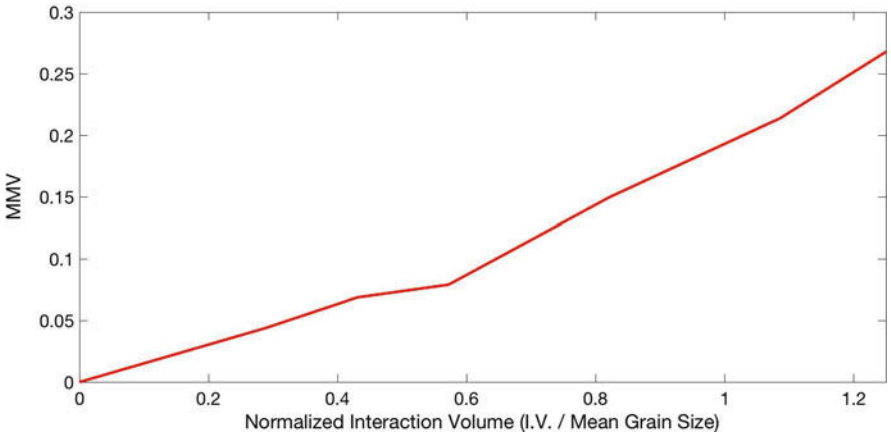

Fig. 10 Mismatched volume (MMV) as a function of the interaction volume normalized by the average feature size, assuming that sample spacing ~0 so that resolution error is zero

is based on a number of assumptions, it provides a useful approximation that can be applied to determine a reasonable resolution without undergoing lengthy simulations.

3.3 Interaction Volume

As discussed in Sect. 2, changing the size of the interaction volume (IV) in the simulation is a representation of changing beam energy. More realistic predictions of the relationship between interaction volume and beam energy in a specific SEM configuration for a given material require calibration or the use of simplified models such as Eq. 1. The example shown here serves only to illustrate how relative increases or decreases in interaction volume affect error.

As was done in the resolution study, the size of the interaction volume is normalized by the average feature size. Figure 10 shows the mismatched volume MMV as a function of the normalized interaction volume, with zero resolution error. It is worth mentioning that for large features (>10 μm) interaction volumes on the order of 10–25% are infeasible in modern SEM; however, for small features they are certainly possible. The MMV values for the smaller values of normalized interaction volume are lower than the typical MMV values associated with typical sampling resolution, suggesting that the error due to interaction volume may be lower than that due to resolution in many situations.

3.4 Unindexed Pixels

During EBSD data collection, it is common that some interrogation points will return diffraction patterns that are unable to be indexed to the local crystal orientation. These points become unindexed pixels or "bad data" which often needs to be accounted for after data collection is completed. As described in Sect. 2.2.3, the primary way that these unindexed pixels enter our model is through the assignment of a dwell time which produces a corresponding level of random noise. A second means by which unindexed pixels can be accounted for is through the assignment of a threshold to the interaction volume (i.e., if a certain percentage of the interaction volume is not dominated by a single grain, an unindexed pixel is assigned). As both of these methods are dependent on user input, quantifying the resulting error is trivial. For example, an assigned dwell time associated with 10% noise produces 10% mismatched volume. However, the incorporation of unindexed pixels into the simulation is very important, since this supports a study of how well these pixels are corrected during the data processing step.

3.5 Data Processing Parameters

Data processing algorithms come in many forms. There are algorithms for addressing known errors in the collected data set, e.g., assigning values to unindexed interrogation points, and those which transform or alter the data to be used in other ways, e.g., creating a meshing for finite element analysis (FEM). Depending on the data, and its desired use, different algorithms may be applied, with each algorithm potentially having many of its own parameters. Figure 11 highlights some details in the data processing section of the outlined framework (see Fig. 1), focusing on one

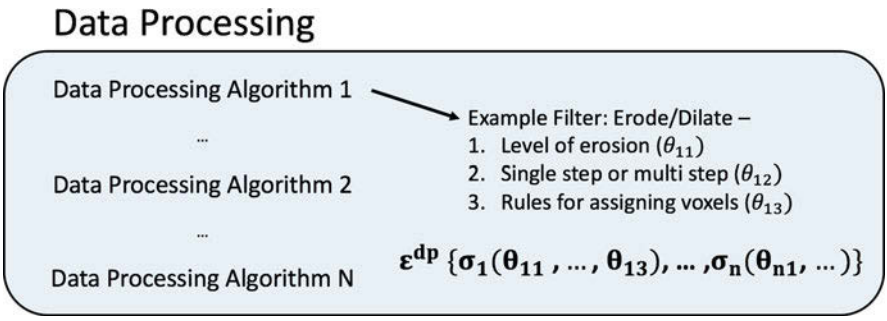

Fig. 11 Details of how data processing error ε^{dp} is categorized. Erode/dilate is a data cleaning process whereby small noisy elements are shrunk in size and then filled in by their nearest neighbor elements. Items 1–3 are some of the parameters which can be used to define the process and are provided as examples for what parameters could be changed

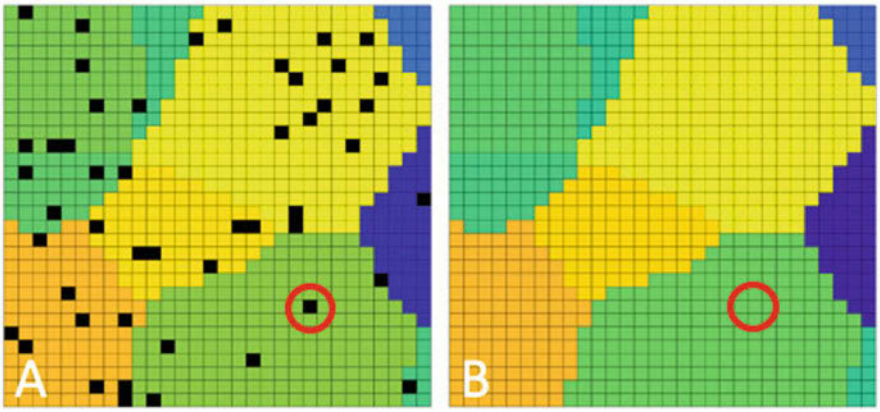

Fig. 12 A partial slice of an equiaxed phantom simulated with 7% random noise, (**a**) before and (**b**) after the DREAM.3D erode/dilate filter was applied. Each black pixel represents a data point where an orientation assignment could not be made. Each of these points has been "cleaned" by the filter, resulting in a reduction of the mismatched volume, from 7.1% to 0.3%

common post processing technique known as erode/dilate, which is used to assign values to missing or incorrectly assigned points in the data set. In the context of the framework for analyzing errors introduced through data processing, each algorithm and its parameters are varied and individually applied to simulated data sets. The reconstructed data sets are then compared in order to determine which algorithms and parameter combinations are most effective in correcting data collection errors.

The erode/dilate filters can effectively remove unindexed pixels and spurious data points. Classical versions of these filters typically work by first eroding feature surfaces, effectively creating an unassigned property region between features, and then dilating features to fill these regions with data assignments from the closest feature to each voxel. DREAM.3D offers an erode/dilate filter that essentially does the reverse, first dilating the bad data and then eroding the bad data through feature assignment (for details see [25]). The effect is that features smaller than the half erosion length, such as those resulting from a single bad data point, vanish and are replaced with the assignment of their surrounding feature (see Fig. 12).

For data with less than 10% noise that is evenly distributed over the volume, nearly all noise can be removed by erode/dilate filters. However, in certain microstructures with small or highly asymmetric features and/or with noise more prevalent in local regions such as grain boundaries, erode/dilate filters can introduce more error. Figure 13 shows results from two different simulations where 7% noise was added to an equiaxed and twinned microstructure. An isotropic erode/dilate filter was applied to assign orientations to the unindexed pixels. The result was that for the equiaxed microstructure (largely isotropic), almost no noticeable error in the grain size distribution was observed, while the twinned microstructure (strongly anisotropic) had many of its small plate-like features removed, altering the feature size distribution significantly. This resulted in a total MMV for the twinned

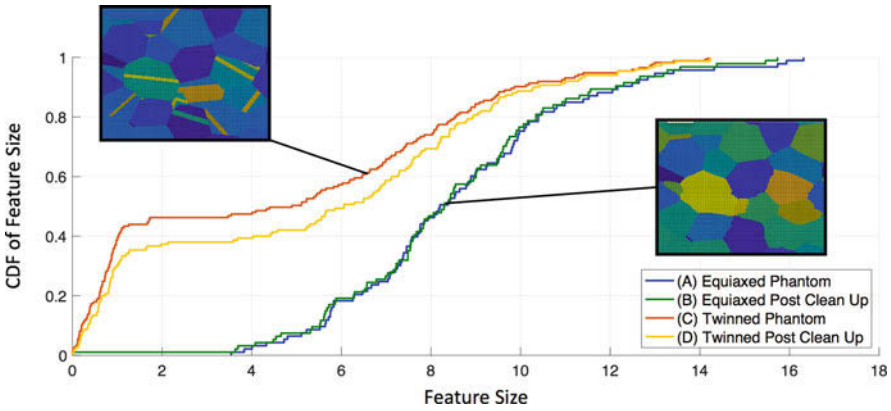

Fig. 13 Comparison of the cumulative distribution function (CDF) of feature size, before and after 7% random noise was cleaned from an equiaxed and a twinned microstructure, using erode/dilate filters

microstructure of 7.2%, which is significantly higher than the MMV of 0.3% for the equiaxed microstructure.

These results demonstrate how the erode/dilate filters can introduce error, despite being effective in removing random noise. Application of the filter was able to reduce noise error although a biasing toward parent grains was observed during reassignment.

3.6 Brief Discussion on Data Collection and Processing Error

The selection of experimental parameters is important to data collection, and the ability to study the individual effects of varying parameters will undoubtedly prove useful. The observation of linear dependence of mismatched volume on resolution is useful for estimating expected errors or biases. Furthermore, the application of data processing filters, which is highly dependent on the needs of a collected data set, can have both positive and negative effects. The ability to quantify the application of different filters to compare their outputs to an expected norm will prove useful for analyzing which filters to use and where new filters need to be developed.

While examining the relative effects and magnitudes of individual parameters is of interest, some of these conclusions can be trivial and misleading without the context of the data collection process as a whole. Changing a data collection parameter to address one source of error may require different choices of other data collection parameters that lead to new sources of error. For example, electron beam energy is indirectly related to the dwell time, as the overall strength of a diffraction pattern is related to both. The electron beam energy can be reduced in order to reduce the interaction volume, which would decrease the error that

arises from potential ambiguity in the diffraction pattern associated with a finite sampling volume. However, if the dwell time is not increased, then this would result in a decrease in the overall strength of the output signal, which will diminish the quality of the diffraction patterns. If there are resource limitations that limit the total characterization time, then the choice to increase dwell time would have to be offset by a decreased number of interrogation points. This could be achieved by decreasing resolution or decreasing sample size, both of which can increase error. Given typical constraints on instrumentation time, this interaction illustrates the balance and trade-offs that must be made during the data collection process.

4 Case Study: Application to Finite Element Model

To this point the work has focused on purely geometric measures of the error of the simulated microstructure compared to the ground truth phantom. While this form of error is important, it might not fully reflect how these reconstructions are ultimately used. In practice these reconstructions are often used to inform computational models, either as direct inputs or through the extraction of key statistics. To analyze this interaction requires extending the analysis to apply the microstructural data to a computational model. The extension is relatively straightforward, because data processing tools such as DREAM.3D that perform meshing allow direct modeling of the simulated microstructures. This addition allows computational models to serve as the context for measuring error. Given that the results from computational models are the primary outcome, evaluating their sensitivity to microstructural data set inputs and subsequently the data collection processes used to collect them is clearly of interest. This is shown in this section through an example case study.

To illustrate how the proposed framework can help in determining the error associated with resolution, a simple example was performed. An outline of the computational framework is shown in Fig. 14. For this example, a $500 \times 500 \times 500$ voxel equiaxed phantom encompassing $\sim$1500 interior grains, with an average grain diameter of 18.2 voxels, was generated using DREAM.3D. Data collection was then performed at various interrogation point spacings, over various volumes, and with different levels of noise. A pictorial representation of the problem is shown in Fig. 15. Each simulated microstructure and the larger phantom were meshed using standard DREAM.3D filters and exported as ABAQUS input files. Individual grains were assigned elastic material properties based on their crystallographic orientation. The average von Mises stress in each interior grain at a global strain of 2% was evaluated. The error in this average grain stress between the phantom microstructure and the simulated microstructure was then averaged across all interior grains. Results are shown in Fig. 16 for various normalized sample sizes and resolutions.

Figure 16 shows a greater dependence of the mean average stress on the total number of grains resolved (i.e., sample size). In small samples, boundary conditions dominate the grain-averaged stresses. For this reason, increasing the total number of interrogation points without also increasing the volume over which they were placed

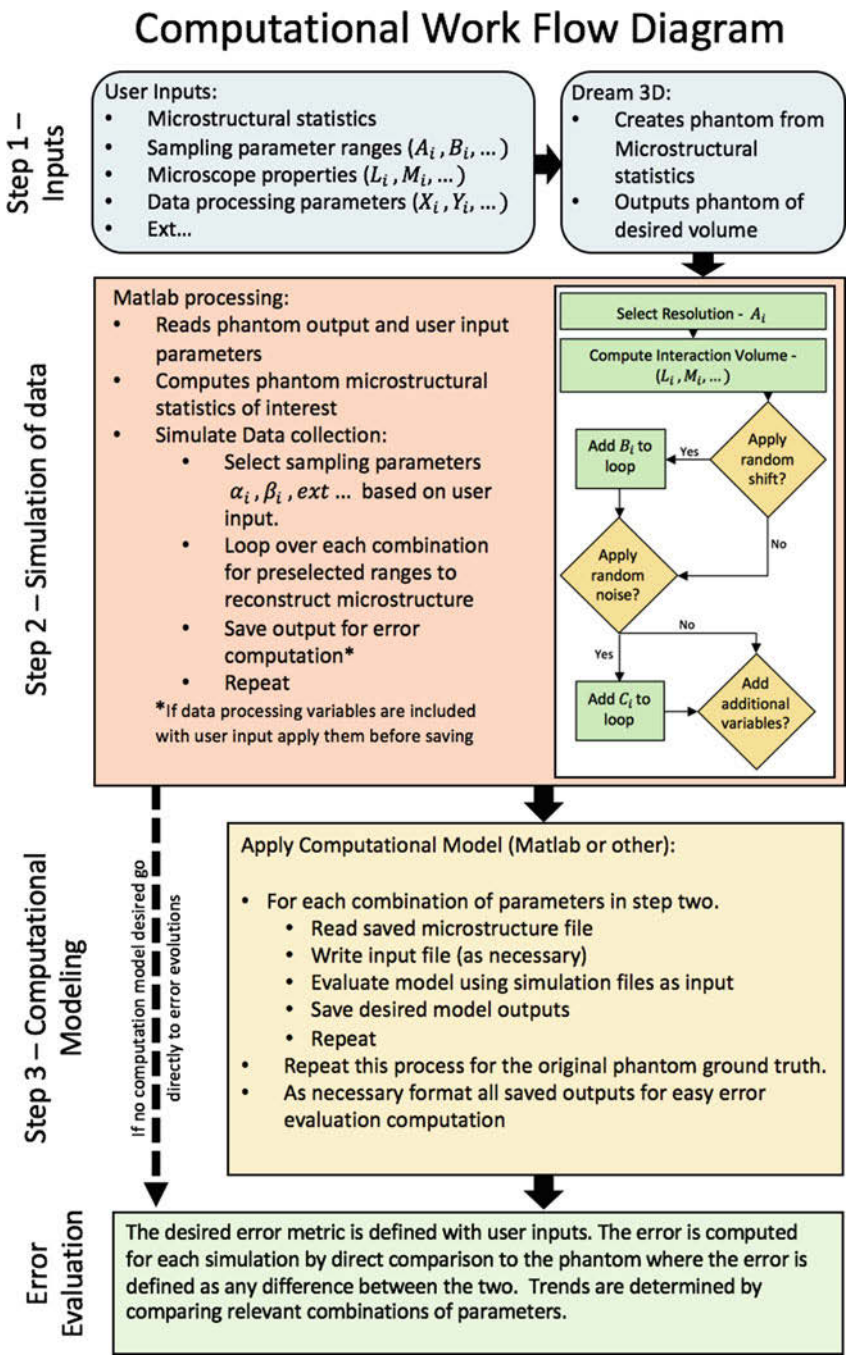

Fig. 14 Outline of the computational framework for error evaluation. The total number of parameters to be evaluated is left open, as well as the inclusion/choice of computational model

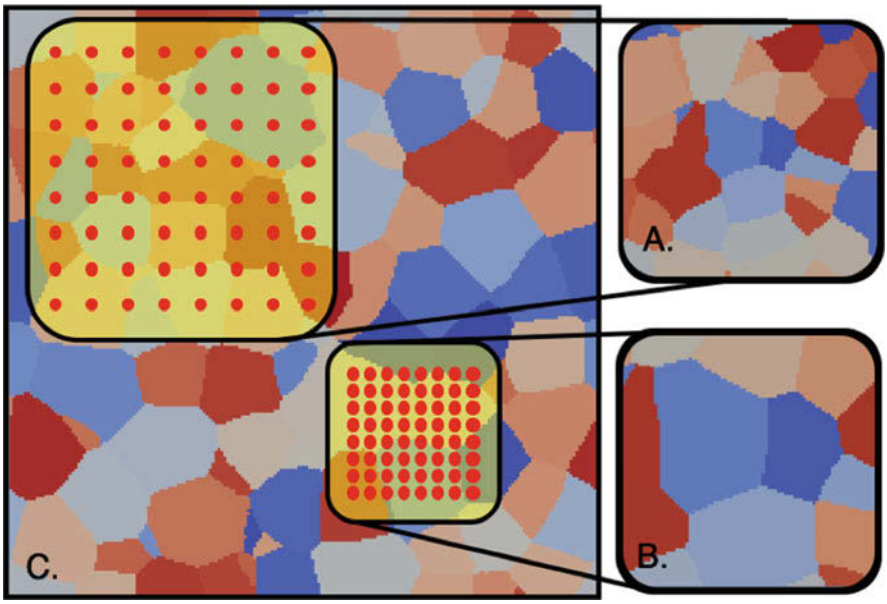

Fig. 15 An illustration of data collection over at different resolutions. (**a**) Shows wide interrogation point spacing over a large volume, (**b**) shows the same number of interrogation points with a narrower spacing over the same area of (**c**), the phantom

does not result in any significant improvement in the error. Similarly, increased or decreased dwell times (as reflected by random noise) had no meaningful effect on computed error (see Table 3).

There are several arguments for these findings. First, the Laplacian smoothing applied to the mesh in DREAM.3D resulted in a partial correction of the error introduced through limited resolution. Second, Fig. 17 shows a 2D projection of nodes from the 3D mesh. The lower resolution mesh (shown in blue) has minimal differences within the region of overlap from the high-resolution mesh (shown in red); meaning that within this region, both simulations had similar representation of the volume. Third, the effectiveness of the data cleanup algorithms in removing bad data points where orientation could not be assigned neutralized the effects of random noise. This was possible in part because of the equiaxed nature of the phantom and may not be true for other mircostructure types. Finally, the choice of a linear elastic model leads to minimal localizations and other behaviors that would increase the sensitivity of the computational model to local microstructural features such as grain boundary geometry.

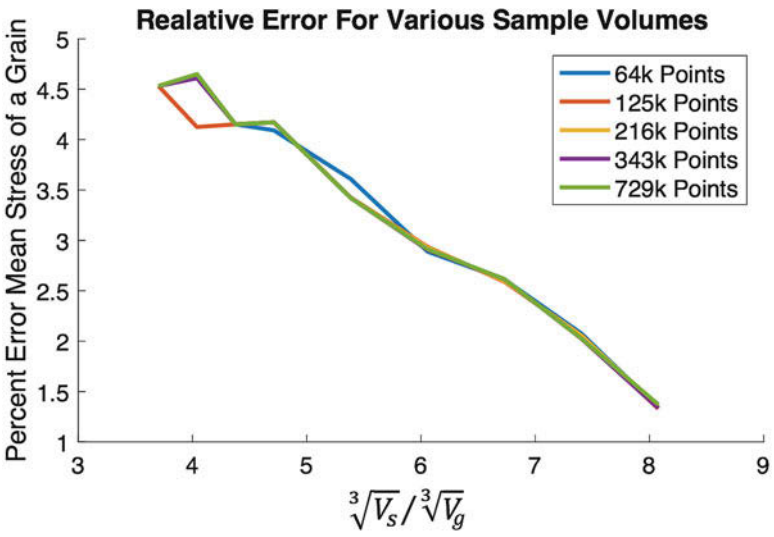

Fig. 16 Percentage of error in grain-averaged elastic von Mises stress as a function of the volume of the sample (V_s) normalized by the average grain size (V_g). Various simulations on a single phantom highlighted the importance of selecting a sufficient sample size in reducing error

4.1 Conclusions from the Case Study

Several conclusions can be drawn from this case study. First, the potential for oversampling can be mitigated. While it's not universally true, in this case little is gained by Herculean efforts to collect highly resolved data. As shown, collecting data at over 10× the number of interrogation points did not ultimately have any meaningful effect on the error in the mean grain stress. Second, proper data processing can be very effective at reducing errors introduced during data collection. Finally, the size of the sample has a strong influence on the predicted elastic stresses.

The mean elastic stress of interior grains is a relatively simple measure from the computational model, and it is highly insensitive to the details of the microstructure. While other measures could be used in future studies, this averaged elastic stress serves as a reasonable baseline measure. For example, a failure to represent the mean elastic stress values would lead to decreased accuracy for more complicated models of inelastic behavior.

These conclusions may not hold for different microstructural data collection efforts, but they are an example of how a priori analysis of the data collection process as a whole can inform data collection efforts. Using the results of this study, efficient data collection parameters such as a large sample volume, short dwell times, and wide resolution spacing could be selected, resulting in a more efficient use of experimental resources. Given the relatively low cost in terms of

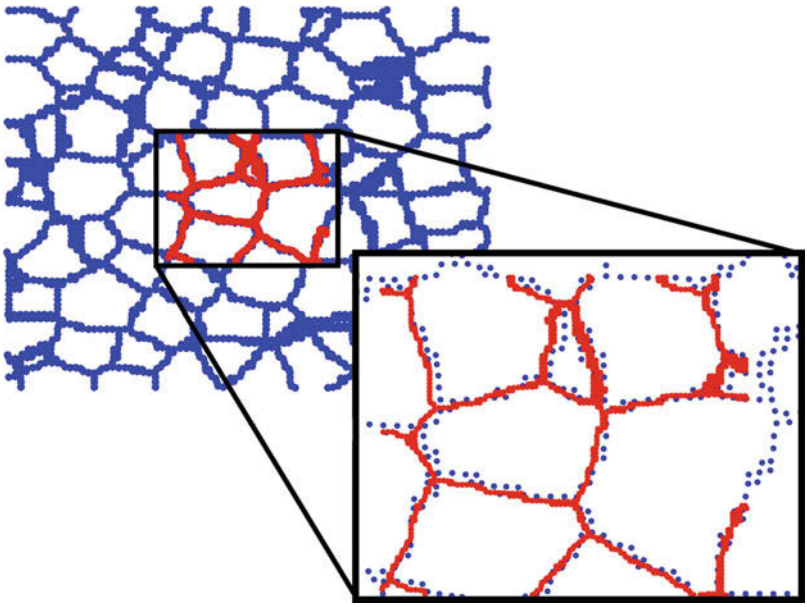

Fig. 17 2D projections of two meshes based on 729,000 interrogation points, collected across a sample of 8 full grains across the face (blue) and across a sample of 4 full grains across the face (red). Even though smaller mesh is better resolved, the resulting meshes are very similar

Table 3 Results for variation of random noise levels (associated with dwell time). Changes in the level of random noise had negligible effect on total error compared to the sample size

	Sample size 1–4.4 grains	Sample size 2–8.1 grains
Level of random noise	Total error after simulation	
3 percent	4.181%	1.384%
5 percent	4.182%	1.384%
15 percent	4.185%	1.389%

computational effort and physical time that such an analysis requires, there are certainly gains to be made in the efficiency and accuracy of microstructural data set collection.

5 Conclusions

Growth in the capabilities to collect 3D microstructural data and apply this information to computational models has been a key research focus, but quantitative analysis of error propagation to the models from data collection has lagged behind. The proposed framework based on a phantom microstructure provides a means for analyzing the error associated with individual data collection and data processing

parameters all the way through to computational models. The approach can easily introduce new modules and/or additional complexity as needed.

We show how the framework can provide detailed insight into the influence of data collection parameters, such as resolution, electron beam energy, and dwell time. The resolution study showed that increasing sample point spacing results in an approximately linear increase in mismatched volume, and an analytical model was developed that provides basic insights into this behavior. Additional studies showed how changes to the interaction volume (i.e., electron beam energy) or increased levels of random noise (i.e., shorter dwell times) also affect error. It was also demonstrated that through proper data processing parameters, much of this error can be mitigated; however, an improperly applied erode/dilate data processing filter can increase error for certain microstructural types. Finally, an example was provided in which the framework was used to analyze the propagation of error from characterization through to a simple finite element model based on the characterized microstructure. For the particular study here, it was shown that sample size was more critical to accurate evaluation of mean elastic stress in each grain than either resolution or integration volume. Such conclusions provide input as to the most efficient data collection parameters that will lead to accurate results from the associated computational models.

A natural extension of the framework presented here will be more formal optimization of data collection parameters, balancing cost, and accuracy. Defining an objective function based on costs, subject to the constraints of acceptable error levels, such an optimization is feasible. Furthermore, the framework can be extended to more detailed physically based characterization parameters and/or to more challenging computational models, such as those that attempt to predict the onset and growth of fatigue cracks.

References

1. R.T. DeHoff, Quantitative serial sectioning analysis: preview. J. Microsc. **131**(3), 259–263 (1983)
2. M. Uchic, *Serial Sectioning Methods for Generating 3D Characterization Data of Grain- and Precipitate-Scale Microstructures* (Springer, Boston, 2011), pp. 31–52
3. X. Lui, D. Furrer, J. Kosters, J. Holmes, Vision 2040: a roadmap for integrated, multiscale modeling and simulation of materials and systems. Technical report, NASA Glenn Research Center (2018)
4. M. Groeber, *Digital Representation of Materials Grain Structure* (Springer, Boston, 2011), pp. 53–97
5. T. Sakamoto, Z. Cheng, M. Takahashi, M.Owari, Y. Nihei, Development of an ion and electron dual focused beam apparatus for three-dimensional microanalysis. Jpn. J. Appl. Phys. **37**(4R), 2051 (1998)
6. M. Uchic, M. Groeber, D. Dimiduk, J.P. Simmons, 3D microstructural characterization of nickel superalloys via serial-sectioning using a dual beam fib-sem. Scr. Mater. **55**(1), 23–28 (2006). Viewpoint set no. 41 “3D Characterization and Analysis of Materials” Organized by G. Spanos

7. S. Zaefferer, S. Wright, D. Raabe, Three-dimensional orientation microscopy in a focused ion beam–scanning electron microscope: a new dimension of microstructure characterization. Metall. Mater. Trans. A **39**(2), 374–389 (2008)
8. J. Guyon, N. Gey, D. Goran, S. Chalal, F. Pérez-Willard, Advancing fib assisted 3D EBSD using a static sample setup. Ultramicroscopy **161**, 161–167 (2016)
9. T.L. Burnett, R. Kelley, B. Winiarski, L. Contreras, M. Daly, A. Gholinia, M.G. Burke, P.J. Withers, Large volume serial section tomography by Xe plasma FIB dual beam microscopy. Ultramicroscopy **161**, 119–129 (2016)
10. S. Monteiro, S. Paciornik, From historical backgrounds to recent advances in 3D characterization of materials: an overview. JOM **69**(1), 84–92 (2017)
11. M. Echlin, A. Mottura, C.J. Torbet, T. Pollock, A new tribeam system for three-dimensional multimodal materials analysis. Rev. Sci. Instrum. **83**(2), 023701 (2012)
12. M. Uchic, L. Holzer, B. Inkson, E. Principe, P. Munroe, Three-dimensional microstructural characterization using focused ion beam tomography. MRS Bull. **32**(5), 408–416 (2007)
13. W.C. Lenthe, Twin related domains in polycrystalline nickel-base superalloys: 3D structure and fatigue. Ph.D. thesis, UCSB. Copyright – database copyright ProQuest LLC; ProQuest does not claim copyright in the individual underlying works; Last updated – 28 Apr 2018 (2017)
14. F. Rhines, K. Craig, D. Rousse, Measurement of average grain volume and certain topological parameters by serial section analysis. Metall. Trans. A **7**(11), 1729–1734 (1976). Cited By 31
15. T.H. Hoang, M. Guerich, J. Yvonnet, Determining the size of RVE for nonlinear random composites in an incremental computational homogenization framework. J. Eng. Mech. **142**(5), 04016018 (2016)
16. M. Pinz, G. Weber, W.C. Lenthe, M.D. Uchic, T.M. Pollock, S. Ghosh, Microstructure and property based statistically equivalent RVEs for intragranular $\gamma - \gamma'$ microstructures of Ni-based superalloys. Acta Mater. **157**, 245–258 (2018)
17. K. Teferra, L. Graham-Brady, A random field-based method to estimate convergence of apparent properties in computational homogenization. Comput. Methods Appl. Mech. Eng. **330**, 253–270 (2018)
18. M. Groeber, S. Ghosh, M. Uchic, D. Dimiduk, A framework for automated analysis and simulation of 3D polycrystalline microstructures: part 1: statistical characterization. Acta Mater. **56**(6), 1257–1273 (2008)
19. G. Loughnane, M. Groeber, M. Uchic, M. Shah, R. Srinivasan, R. Grandhi, Modeling the effect of voxel resolution on the accuracy of phantom grain ensemble statistics. Mater. Charact. **90**, 136–150 (2014)
20. F. Ram, S. Wright, S. Singh, M. De Graef, Error analysis of the crystal orientations obtained by the dictionary approach to EBSD indexing. Ultramicroscopy **181**, 17–26 (2017)
21. G. Spanos, J. Allison, B. Cowles, J. DeLoach, T. Pollock, Implementing integrated computational materials engineering (ICME) in the aerospace, automotive, and maritime industries. Technical report, The Minerals, Metals, and Materials Society, http://www.tms.org/icmestudy (2013)
22. M. Groeber, M. Jackson, Dream.3D: a digital representation environment for the analysis of microstructure in 3D. Integr. Mater. Manuf. Innov. **3**(1), 5 (2014)
23. Dassault Systèmes. Abaqus (2017)
24. K. Teferra, L.Graham-Brady, Tessellation growth models for polycrystalline microstructures. Comput. Mater. Sci. **102**, 57–67 (2015)
25. BlueQuartz, http://dream3d.bluequartz.net/. Dream.3D User Manual – Erode/Dilate Bad Data
26. J. Goldstein, D. Newbury, J. Michae, N. Ritchie, J. Scott, D. Joy, *Scanning Electron Microscopy and X-Ray Microanalysis* (Springer, New York, 2018)
27. K. Kanaya, S. Okayama Penetration and energy-loss theory of electrons in solid targets. J. Phys. D Appl. Phys. **5**(1), 43 (1972)
28. V. Randle, Electron backscatter diffraction: strategies for reliable data acquisition and processing. Mater. Charact. **60**(9), 913–922 (2009)

Material Agnostic Data-Driven Framework to Develop Structure-Property Linkages

Dipen Patel, Triplicane Parthasarathy, and Craig Przybyla

1 Introduction

Integration of advanced material systems into most engineering applications requires a detailed understanding of the structural and functional behavior of such materials. Most advanced materials such as metallic alloys, ceramics, polymers, hybrids, and composites exhibit hierarchical internal structure with rich details at multiple length scales of interest. Such microstructures have significant impact on their behavior. Relating the processing variables, structure and behavior is the objective of most materials models, which are directed towards use in design or in optimization, as envisioned by Integrated Computational Materials Engineering (ICME) [1]. A reliable and robust material modelling framework is required that satisfies the goals of ICME, captures the physics behind structure-property relationships at every length scale, accounts for the effects of interactions between different length scales, and provides a way to integrate these into a computationally efficient macro-level model. Current physics-based, multiscale models are limited in their use due to their computational expense, and when constraints are imposed, they capture only partial interactions. For accelerated design and material optimization, computationally efficient models that can capture all the salient effects are needed.

In this review, we explore the status of data science as an approach that could play a significant role in the current and future of ICME-based materials engineering. As the name implies this approach relies on data. Thus, it is important to understand the availability of materials data in current engineering practice and identify areas

D. Patel · T. Parthasarathy
UES, Inc, Dayton, OH, USA

C. Przybyla (✉)
Air Force Research Laboratory/RX, Wright-Patterson Air Force Base, Dayton, OH, USA
e-mail: craig.przybyla@us.af.mil

S. Ghosh et al. (eds.), *Integrated Computational Materials Engineering (ICME)*,
https://doi.org/10.1007/978-3-030-40562-5_9

where data science may be best applicable. The current state-of-the-art materials engineering practice relies on reliable synthesis and/or manufacturing process with quality control checks and extensive laboratory data on performance characteristics as a metric to guide design processes. The material structure is mostly characterized via nondestructive tests, rather than traditional microscopy. X-ray CT, eddy current test, and ultrasound imaging are some of these techniques. On the other hand, most materials models require detailed microstructural information at all length scales using optical, SEM, and TEM imaging techniques. When required, the industry employs such destructive methods on coupons from each batch of material manufactured. In some cases, processing-microstructure-property relationships are semi-empirically derived (physics-based but fast acting) and used in engineering design to achieve desired properties. This is especially true for applications that can benefit significantly from ICME. It is those applications that are best suited for the use of data science or machine learning (ML) [2]. In this work we focus on such applications, and we show that the ML approach has potential as a structure-property linkage model and is materials agnostic. It must be noted that the ML framework can incorporate the physics behind the linkages, despite staying materials agnostic.

We review the data-driven, material agnostic framework towards possible use in ICME-based applications. We illustrate the application of the framework across different materials, without sacrificing the physics behind the linkages. In particular, the data-driven methods are shown to successfully establish the process-structure or structure-property (P-S-P) linkages applied to a wide range of materials, including metallic alloys [3], ceramics [4], composites [5], and polymeric materials [6].

2 Material Agnostic Data-Driven Framework to Process-Structure-Property Linkages

A key element to data science in materials science is a inherent versatile framework which is amenable to data acquisition, curation, dissemination, and reuse of high-value knowledge in a highly efficient compact manner at a desirable cost at the relevant length scale. The reason the approach is material agnostic is that the treatment is entirely mathematical in how data is represented and relationships are established. The physics are captured in the preprocessing stage. With respect to microstructure, preprocessing involves representation, data reduction, feature extraction, and/or simulations. With respect to properties, this involves use of physics-based simulations to generate sufficient data for ML learning. The same is true for processing-structure relations. While the physics-based simulations carry the computationally expensive physics, the ML tool derived from them is fast acting and amenable for inverse solutions.

The approach can be easily coupled with multiscale materials' modeling effort where the data-driven (P-S-P) models can be integrated to reduce the computational cost associated with the physics-based model while improving the efficacy of the

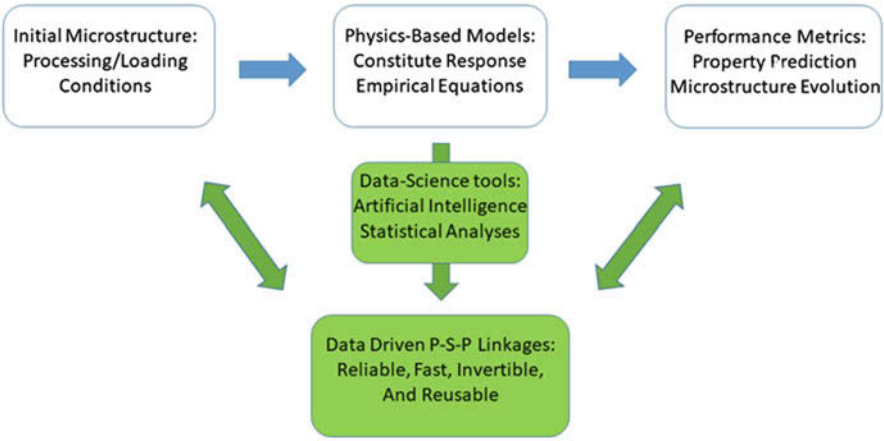

Fig. 1 A general schema of the framework illustrating the data science approach enhancing/augmenting the current materials science effort to explore the process-structure-property linkages

surrogate models being built. A general strategy/schema of data-driven framework is described in Fig. 1. The current approach to developing P-S-P linkages in computational material science explores physics-based models, as described in Fig. 1, top row. Physics-based models entail the use of highly complex physics coupled with an iterative numerical solver, which in turn drastically increases the computational cost to explore the space.

As depicted in Fig. 1, data science tools can be utilized to learn the structure-property relationships between the inputs parameters that describe the structure and the simulated output. In the context of multiscale modeling effort, the calibration of data-driven models to processing-structure-property (P-S-P) linkages is carried out via rigorous mathematical form utilizing advance machine learning techniques.

The P-S-P linkages form surrogate models (or metamodels) which enable inversion due to their relatively simple mathematical representation compared to the complex physics-based nonlinear models. This in turn implies the development of formal data science methods as refining and reusing P-S-P linkages from available ensembles of simulated datasets.

It is important to note that with all data-driven approaches, the underlying physics of the structure-property relationships modeled are not always clear or interpretable based on the resulting surrogate model. However, when coupled with experiments or physics-based models, these data-driven techniques can provide meaningful insights on the connection between the structure and its derived properties. The approach allows one to seek physical understanding of the structural-property linkages derived through machine learning if the variables employed in the machine learning algorithms are able to completely define the state of the system. However, such a rigorous definition is not always necessary or readily available in order to understand the underlying physics.

The broad implementation of data-driven approach requires validated and widely adopted methods to describe and quantify hierarchical material structure(s) referred to as microstructure(s). The performance behavior of materials is largely characterized and governed by the microstructure of the sample material; hence, microstructure plays a significant role in the formulation of P-S-P linkages and forms an input and/or output to the surrogate models. Accurate quantification of microstructure is essential to determining the macroscopic constitutive response of the materials subjected to various loading/processing conditions. It is imperative to seek proper quantification of microstructures before addressing the formulation of P-S-P linkages.

2.1 Microstructure Quantification

The success of materials design efforts hinges on how the salient microstructural features of materials are quantified and tracked during various process/loading conditions. Conventionally, the approach to microstructure quantification is motivated largely by our current partial understanding of physics, which includes measures such as mean volume fraction, average grain size (and sometimes shape), and rarely ensemble distributions. It is now increasingly recognized that there are significant variations of all these parameters and they also miss important topological information. Therefore, it is increasingly recognized that the statistical information about the structure that includes topology is important to predict the design allowables that depend on the variability of properties of interest.

Recently, various methods have been proposed and applied to quantify the microstructure of heterogeneous materials at relevant length scales. For example, correlation functions such as pair correlation functions [7], radial distribution functions [8], chord length distribution functions [9, 10], and n-point spatial correlation functions [3, 9–12] at different length scales have been utilized to represent diverse material systems ranging from solids to gaseous phases. A correlation function of a variable of interest is a measure of the spatial order/disorder in a system with respect to that variable. In addition, correlation functions quantify how different variables covary with one another spatially. Studies have shown that these spatial correlation functions are the microstructural features that naturally emerge in some of the most sophisticated composite models/theories for effective, homogenized, properties [13].

Although the quantification of microstructures using various correlation functions provides a means to capture the salient features and its interactions, the statistical representation of the microstructure often span an unwieldy dimensional space in comparison to the other variable(s) in the P-S-P linkages formulation [3, 5, 10–12]. From a practical perspective, the statistical representation of microstructure needs to be cast in a compressed form for it to serve any useful purpose in order to produce simple and easily applicable P-S-P linkages. Traditional approaches to

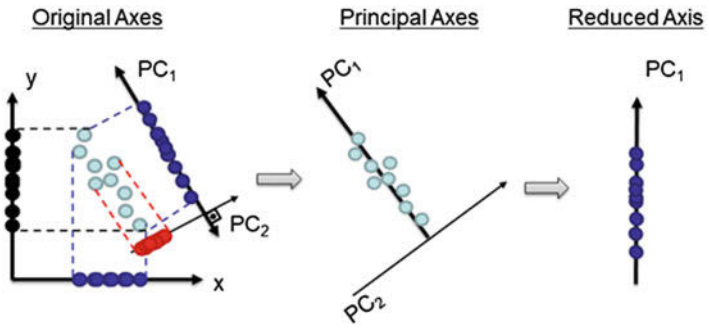

Fig. 2 A schematic representation of PCA analysis summarizing the procedural logic of dimensionality reduction based on variance of data

data reduction involve hand-selecting features based on scientific insight. As an example, one might quantify the polycrystalline microstructure using grain size or shape distributions while studying yield strength in metals due to Hall-Petch effect [14]. However, such approaches do not have a common set of low-dimensional representations that can be applied universally across all material systems.

The recent explosion of dataset size, in terms of both number of records and number of features/attributes, has triggered the advancement of dimensionality reduction algorithms [2]. Dimensionality reduction techniques, such as Random Forest/Ensemble Trees, Principal Component Analysis, and Backward/Forward Feature Elimination, are extensively employed for image analysis in computer vision technology as well as other scientific fields. One such data dimensionality reduction technique heavily employed in material science field is principal component analysis (PCA), extensively used in formulating P-S-P linkages. PCA is a statistical analysis that transforms the original k coordinates of datasets into a new set of n coordinates called principal components. As a result of the transformation, the first principal component has the largest possible variance; each succeeding component has the highest possible variance under the constraint that it is orthogonal (i.e., uncorrelated) to the preceding components. In other words, PCA is a distance-preserving linear map, which involves the derivation of a new set of orthonormal feature vectors (basis) that are linear combinations of existing feature vectors, whose optimization is determined by maximizing the variance of the data along the principal component vectors (see Fig. 2). PCA, as a statistical modeling tool, is capable of efficient representation of complex, nonlinear data without the need for a separate identification of the parameter typically required for conventional modeling. For example, Cord et al. employed PCA to reduce pixel texture descriptions of metallic surfaces and then employ a supervised learning approach to distinguish between nominal background and anomalous or defect structures on the imaged surfaces [15].

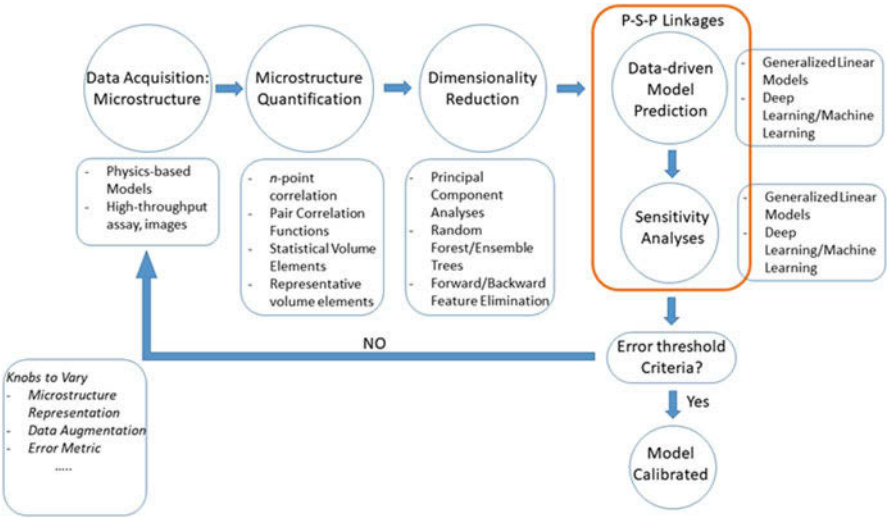

Fig. 3 A generic workflow to extracting process-structure-property linkages using data-science AI tools. Circles describe step-by-step protocol, while the corresponding rectangle box lists the possible approach employed within each step

2.2 Data-Driven Workflow for Extracting P-S-P Linkages

The data-driven workflow is a four-step protocol designed for establishing process-structure and structure-property linkages (see Fig. 3). The main steps are listed in blue circles. The accompanying boxes show specific methods and/or procedures that might be employed in that step.

This workflow has been designed to serve as a generic template that is applicable to the broad class of microstructure evolution phenomena that are likely to be studied by a variety of techniques (these could include modeling techniques such as phase-field models, cellular automata, and level-set methods or experimental techniques such as X-ray computed tomography) as well as to predict property given microstructure.

The data-driven workflow is a four-step protocol designed for establishing process-structure and structure property linkages (see Fig. 3). The main steps are listed in blue circles. The accompanying boxes show specific methods and/or procedures that might be employed in that step.

This workflow has been designed to serve as a generic template that is applicable to the broad class of microstructure evolution phenomena that are likely to be studied by a variety of techniques (these could include modeling techniques such as phase-field models [16], cellular automata [17], and level-set methods [18] or experimental techniques such as X-ray computed tomography).

The first step in the workflow is a preprocessing step aimed at ensuring quality and consistency of the dataset. While the identification of the phases, boundaries, or

other features of interest in simulated data is trivial in most cases, experimental data often requires segmentation of images to properly identify a given feature of interest. As needed, one might set criterion to eliminate spurious or questionable data (e.g., the data that does not conform to known physics). In this step, the inputs (process parameters) are also clearly associated with the outputs (microstructure data).

It is acknowledged that the robustness of this preprocessing step is a direct function of the uncertainties introduced during data collection, experimentation, and data processing techniques. For example, measurement uncertainty is immediately introduced with data collection due to instrument accuracy and human error. Additional uncertainty is introduced as these data are processed into human and computer interpretable forms using various data processing algorithms. For example, the uncertainty associated with imaging and image processing of microscopic data has been studied and published for a variety of techniques. Uncertainty is introduced at each stage of the processes depending on the methods and algorithms employed. While understanding these uncertainties is important to the success of the framework proposed here, there is much ongoing research in this area, and this topic is not addressed in detail here but in another chapter in this volume.

In the second step, microstructures are quantified to obtain salient statistical measures of microstructures. In a data science approach, it is desirable to capture a very large set of measures at this stage. Consequently, it is preferable to adopt a microstructure quantification framework that allows one to increase systematically the numbers of potential features included in the analyses. In this regard, the framework of n-point spatial correlations offers tremendous promise because of its scalability (ability to define an infinite number of microstructural features) and organization (value of n can start with one and increase).

The third step in the workflow focuses on reducing the dimensionality of microstructure representation using data science approaches. Some of the established dimensionality reduction techniques include principal component analysis, factor analysis, projection pursuit, and independent component analysis, among others. These methods are designed to reduce dataset dimensions, while losing only the smallest amounts of information. The use of dimensionality reduction leads to savings in both computational time and storage and identification of salient features that can be used to establish models. For example, in prior work, PCA has proven to be remarkably efficient in producing high-value, low-order representation of microstructures that are ideally suited to establishing P-S-P linkages in a broad variety of material systems.

The last step of the workflow focuses on establishing and validating a reliable and robust process-structure (P-S) or structure-property (S-P) linkage. This step typically involves an iterative process of model selection. The first part of this step requires establishing a model using a variety of machine learning techniques ranging from simple regression to sophisticated M5 model trees and support vector machines. It is important to recognize that the models developed are indeed dependent on the available data. Therefore, the model itself can change as one adds more data. Validation of the model established in this step is typically performed using accuracy estimation methods. Cross-validation has been found to be quite

effective in avoiding over-fitting of the data to the model. Data splitting is another validation method in which each ensemble dataset is generally split into calibration and test subsets. Data splitting was shown to be an effective technique, where a collection of new validation data is avoided. In this step, a model selection is accomplished iteratively based on the optimization of error parameters. Error metrics therefore play an important role in the model selection process. Popular choices have included various combinations and variants of the mean of absolute error (MAE), the standard deviation of error (SDE), the coefficient of correlation (R), and the explained variance (R2) [10–12, 19].

Once a physics guided data-driven model is obtained, a new data point, not in the calibration dataset, is tested/validated. If the errors are not satisfactory, it is important to identify the step contributing to the unreliable model to allow suitable modification for the next iteration. For instance, one might select a different learning algorithm or select/identify new features via different data reduction techniques. The modular nature of the framework allows exploration of a number of machine learning models in a highly computationally efficient manner to best capture the phenomena being studied.

3 Application of the Material Agnostic Framework to Different Material Systems

In this section, the data-driven, process- structure, and structure-property linkages applied to materials are reviewed. Microstructure plays an important role in the formulation of P-S-P linkages and requires a higher dimensional representation compared to other input/output (i.e., process parameters, properties) variables. As microstructure quantification and representation form the bedrock to the material agnostic models, the section is focused on various quantification techniques to P-S and S-P linkages for diverse material systems.

3.1 Composites

Recent advancements in the development of composite materials systems sparked the use of such material system in turbine engines replacing heavy metals parts. Arguably, performance of composites, mainly ceramic matrix composites (CMCs), is largely affected by its internal microstructure. At the scale of the microstructure, the characteristic response of CMCs depends on the heterogeneous distribution of local constituents (i.e., fiber, coating, crack, voids, and matrix itself) as seen in Fig. 4. Thus, the damage response is sensitive to the local microstructure within a CMC. The material agnostic, data-driven framework is ideal for exploring the microstructural variabilities and their effects on performance.

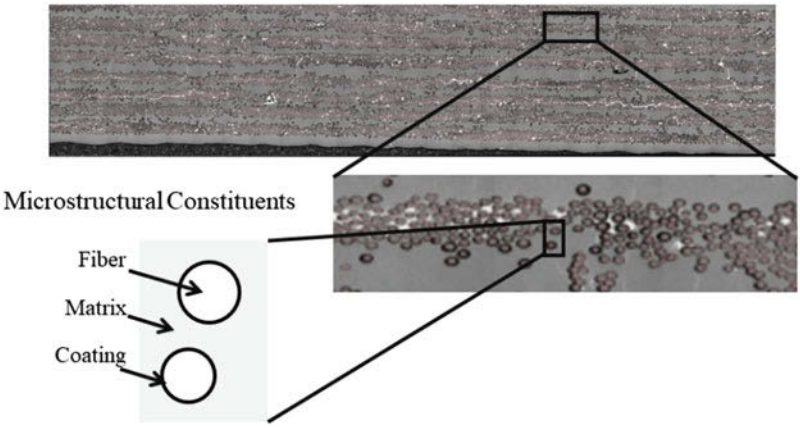

Fig. 4 A CMC sample material illustrating microstructural features: fiber, coating, crack, voids and matrix itself

Various methods have been applied to quantify the structure of random heterogeneous materials such as CMCs. Oda et al. developed several metrics for spherical granules in a sample instead of fibers [20]. These metrics were derived from the contacts between granules because it is at those points where forces are transmitted under load. Fast et al. [21] characterized the microscale statistics of the filaments in the fiber tow bundles based on topological and Euclidean metrics. As observed here, the fibers naturally meander within and outside of tows during processing and tend to run together as bundled fibers running in smooth parallel pathways relative to each other. By focusing on how the fibers meander through the column in relation to the other fibers in their neighborhood, Fast et al. were able to parameterize the variation using metrics such as the changes in the neighborhood per unit distance of the fibers such that the neighborhood here refers to the connecting vertices of the Delaunay Triangulation where the positions of the fiber centers are at the vertices. If the neighborhood of a fiber changes consistently, this indicates that there is misalignment of a particular fiber relative to its surrounding neighborhood. Sherman et al. [22] developed a continuous field quantity of chirality to quantify the substructing of groups of fibers within fiber bundles as these groups of fibers on a scale less than that of a fiber tow tended to twist in migrate through the volume in relative unison.

Focusing on the characterization of stochastic textile composites at tow scale (i.e., mesoscale), Bale et al. and Vanaerschot et al. [23] developed metrics based on ellipses that were automatically fitted to fiber tow cross sections, with some manual corrections, to describe variance in textile structure. This allowed for the study of variability in each tow's centroid coordinates, aspect ratio, area, and tow reinforcement. Their method for gathered statistical information on tows is constructed so that the data can be used to instantiate and simulate performance characteristics for synthetically generated microstructures via micromechanical finite element analysis needed to extract metamodels for their data-driven framework.

The data-driven framework discussed here has been employed to study the effect of fiber architecture on the transverse matrix cracking. Patel et al. [24] have utilized two-point correlations to quantify the microstructure at submicron length scales where the constituents (i.e., fiber, matrix, coating, fiber interfaces) are distinctly identifiable. More specifically, the two-point spatial correlations are defined by

$$f\left(h, h' \,|\boldsymbol{r}\right) = \frac{1}{S}\sum_{s}^{S} m_s^h m_{s+\boldsymbol{r}}^{h'} \tag{1}$$

where $\boldsymbol{r}$ enumerates all possible discretized vectors that can be defined on the adopted uniform grid size describing the microstructure volume. The variable m_i^h is defined such that it is equal to one if the argument h belongs to the bin label i and zero otherwise. The spatial correlation is defined as the conditional probability of finding a local state h and $h^{'}$ at the head and tail, respectively, of a vector $\boldsymbol{r}$ arbitrarily placed in microstructure. The local states considered for the study are fiber, coating, and matrix. PCA was performed on the full set of two-point statistics to reduce the dimensionality. In this case cited here, it was seen that the PCA efficiently reduced the dimensionality from 10^7 to mere 5 to 10 basis vectors, capturing the ~99% of variance (see Fig. 5) in the dataset.

This work illustrates the capabilities of machine learning the complex multiparametric interaction among the various microstructural features of SiC/SiC ceramic composites leading to damage imitation. The machine learned parameter was then employed to generate a probability map of transverse crack initiation as a function of the fiber spacing in PC space.

More specifically, data-driven models were utilized to capture the effect of fiber architecture on the transverse matrix-cracking tendencies. The approach applied here included the calibration of the finite element response of several instantiated classes of microstructures (see Fig. 6) via a neural network. The microstructures and the FEA results (maximum principal stresses) were captured using a two-point correlation and a two-parameter statistical Gumbel distribution (Fig. 7), respectively.

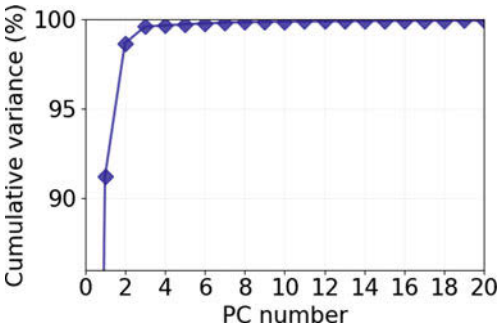

Fig. 5 Illustration of the individual variance of the principal components

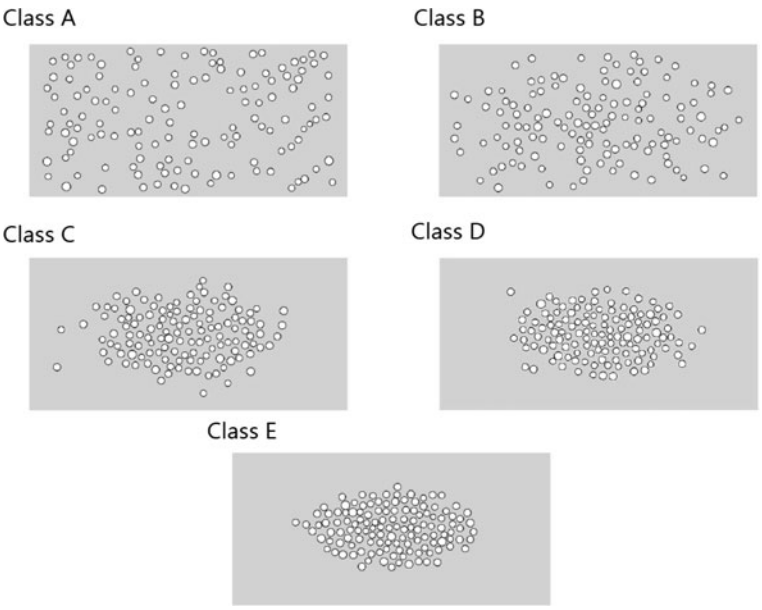

Fig. 6 Microstructure classes generated using bivariate Gaussian distribution to obtain difference in fiber spatial distribution

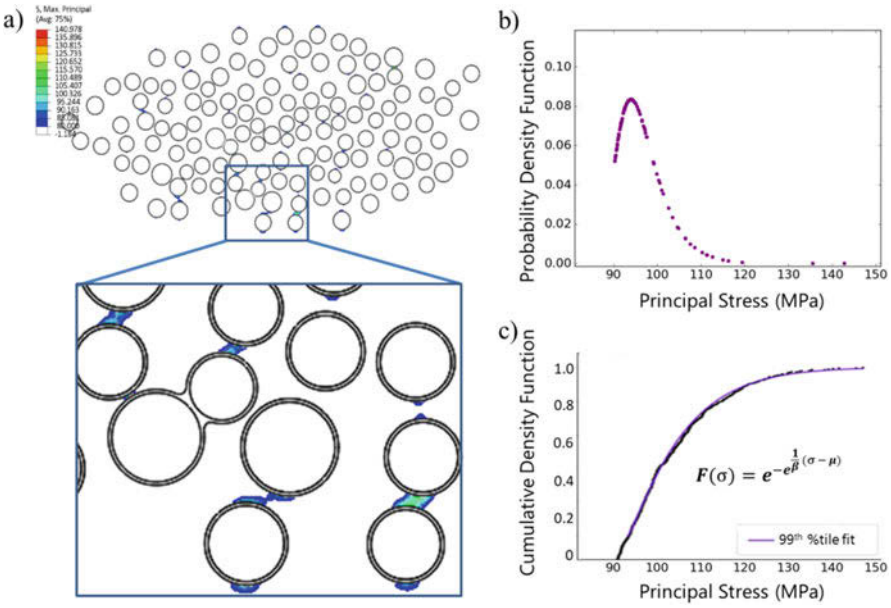

Fig. 7 (**a**) Top 1% of the maximum principal stress contours for a microstructure subjected to transverse load. (**b**) PDF of the selected 1% extreme values of maximum principal stress. (**c**) Two-parameter CDF of Gumbel distribution fitted to obtain PDF in **b**

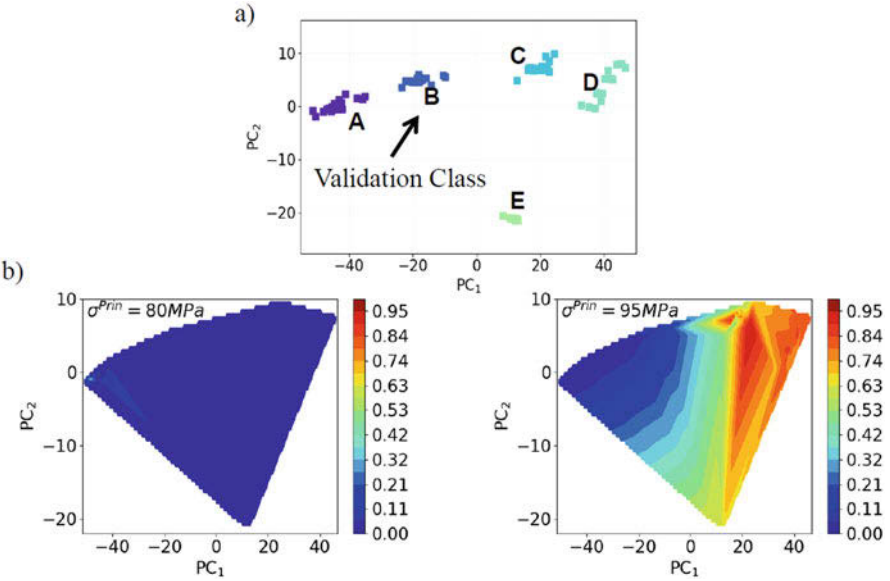

Fig. 8 (**a**) Microstructure classes delineated in the PC features space. Note Class B was not included in the calibration process. (**b**) Probability predictions of cumulative damage (volume percent of top 1% of pixels) at varying maximum principal stresses as a function of microstructural features in principal component space using ML

Using a partial dataset for training and then predicting the rest, the feasibility of using machine learning to predict the transverse cracking initiation probability for a given microstructure was demonstrated. Further, by applying a failure criterion, the trained machine learning model can be employed to generate probability map of damage initiation as a function of the microstructural features, as shown in Fig. 8.

3.2 Polycrystalline Metallic Materials

Many metallic materials exhibit a crystalline phase. Local properties of crystalline phases may not be considered isotropic. That is, local anisotropic, elastic-plastic properties (i.e., effective modulus, yield strength, fatigue parameters) depend not only on the phase but also on the ordered atomic orientation of lattice plane described by Bunge-Euler angles, as shown in Fig. 9, for example, structural materials exhibiting polycrystalline microstructures, where spatial distribution of crystal lattice orientation at microscale plays an important role in controlling the measured effective properties.

Local features for a generic class of polycrystalline metals may include descriptors such as crystal symmetry, dislocation density, and chemical composition

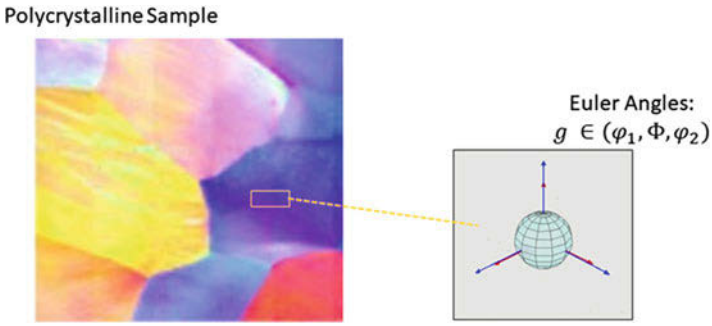

Fig. 9 A polycrystalline sample material illustrating a dominant microstructural feature, grain orientation described by a set of Bunge-Euler angles

(among others). However, a prevalent feature for most polycrystals is the crystal lattice orientation, g, which spans the orientation space. A primitive approach of binning the orientation space leads to an inefficient representation, that is, a large number of bins are needed to represent the orientation space.

As an alternative, generalized spherical harmonics functions are utilized as an efficient, continuous Fourier basis for the computation of two-point spatial correlations in polycrystalline materials [3, 11, 12, 25]. For a single phase, annealed, polycrystalline material, the main local state of interest at the grain-scale is the crystal lattice orientation. The corresponding local state space is simply the orientation space. Based on the concepts discussed thus far, a simple approach to addressing polycrystalline microstructures is to simply bin the fundamental zone of orientation space. As a specific example, the fundamental zone of orientation space for cubic crystals is expressed as

$$FZ = \left\{ g = (\varphi_1, \Phi, \varphi_2) \;\middle|\; \begin{array}{c} 0 \le \varphi_1 < 2\pi, \\ \cos^{-1}\left(\frac{\cos\varphi_2}{\sqrt{1+\cos^2\varphi_2}}\right) \le \Phi \le \frac{\pi}{2}, \\ \text{and } 0 \le \varphi_2 \le \frac{\pi}{4} \end{array} \right\} \tag{2}$$

In this approach, the microstructure function, which can now be expressed as

$$m_s^h = m\,(g, \boldsymbol{x}) \approx \sum_{s=1}^{S} \sum_{\mu,n,l} M_{ls}^{\mu n} \dot{T}_l^{\mu n *}(g) \chi_s\,(\boldsymbol{x}) \tag{3}$$

where $\dot{T}_l^{\mu n}(g)$ denotes the symmetrized GSH functions for cubic-triclinic symmetry (in this notation, the first symmetry refers to crystal symmetry and the second one to the sample symmetry) and * denotes a complex conjugate. $M_{ls}^{\mu n}$ are referred to as the GSH coefficients. As a special case, when there is a single crystal of lattice

orientation g_o in a spatial bin s, the corresponding GSH coefficients are simply given by

$$M_{ls}^{\mu n} = (2l+1)\,\dot{\dot{T}}_{l}^{\mu n*}(g_o) \tag{4}$$

For simplicity of notation, we will simply map every distinct combination of (l, μ, n) to a single index L in all of the ensuing equations. As a result of this simplification, $M_{ls}^{\mu n}$ will be henceforth denoted simply as M_{s}^{L}. Extending the concept above to the description of the two-point spatial (Eq. 1) correlations, the orientations in the polycrystalline microstructure can be expressed as

$$f\left(g,\, g' \middle| \boldsymbol{r}\right) \approx \sum_{K} \sum_{L} \sum_{t=1}^{S} F_{t}^{LK}\, \dot{\dot{T}}^{L}(g) \dot{\dot{T}}^{K}\left(g'\right) \chi_{t}\left(\boldsymbol{r}\right) \tag{5}$$

As mentioned earlier, the set of two-point statistics yields a large and unwieldy dataset. A lower dimensional representation can similarly be sought using PCA. Over the past decade, numerous structure-property linkage studies are illustrated to predict the bulk properties of polycrystalline microstructure using the framework. Specifically, the framework leverages the comprehensive description of microstructure based on n-point correlations coupled with the data-driven framework. The viability and advantages of the data-driven framework were demonstrated in the prediction of the elastic and inelastic bulk properties of titanium polycrystals, elastic strain fields in cubic and hexagonal poly-crystals, and high-cycle fatigue predictions of fatigue indicator parameters (FIPs) for alpha-titanium polycrystalline alloys within 2–5% prediction errors in comparison with the physics-based models (see Fig. 10) [3].

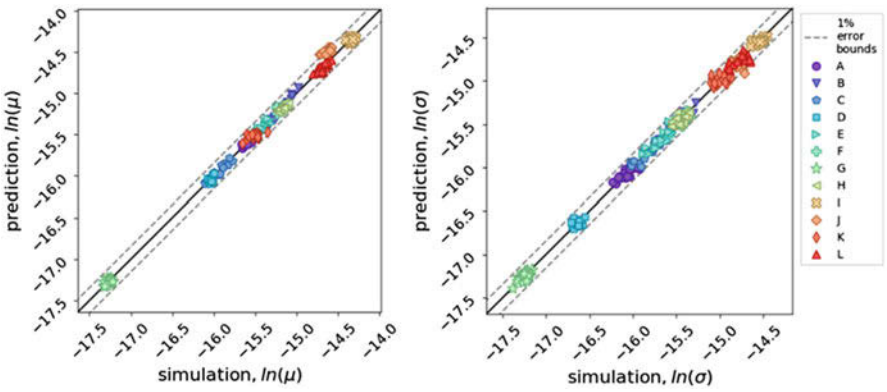

Fig. 10 The simulated versus predicted fatigue indicator parameters, commonly referred to as FIPs. (Taken from Paulson et al.)

This data-driven framework has also been applied to polymeric materials as well. In particular, the transport properties of porous microstructures used in fuel cell applications were linked to the microstructural features of polymers, a gas diffusion layer (GDL), and the microporous layers (MPL) [6]. It was clearly shown that the diffusivity coefficient prediction from the data-driven model outperforms the conventional semi-empirical correlations.

Further, the data-driven framework was applied to inverse design problems to extract single crystal elastic-plastic properties of a polycrystalline sample. A data-driven model was calibrated using a physics-based model of nanoindentation to establish the relationship between the input parameters, that is, elastic constants, yield strength, and hardening parameters on the indentation stress-strain response [19, 26]. In particular, a functional dependence (i.e., calibrated model) of respective elastic-plastic properties extracted from the indentation stress-strain curve on its input parameters (e.g., elastic stiffness constants and initial slip resistance) was established. An inverse protocol is formulated to extract the single crystal elastic-plastic parameters from nanoindentation measurements. More specifically, a large number of data points, i.e., indentation stress-strain curves, were accumulated from the finite element model predictions for a wide range of material properties for cubic polycrystalline metals covering a range of cubic anisotropy ratio, $0 < A < 8$, as shown in Fig. 11, over the fundamental zone as defined in Eq. 2 for a total of 2700 FE simulations.

The calibrated model was used to estimate the single crystal elastic stiffness and slip resistance parameters for Fe-3%Si for which indentation measurements on differently oriented single crystals were available from literature. The single crystal

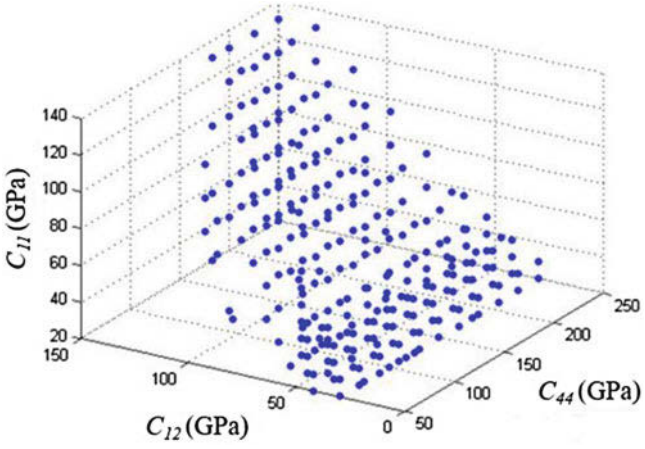

Fig. 11 Three hundred distinct sets of independent elastic stiffness constants for cubic polycrystalline materials selected to calibrate the data-driven model. (see [26])

elastic stiffness constants and the initial slip resistance parameters obtained using the inverse solution approach were within 5% of the typical values reported in literature for Fe-3%Si.

4 Challenges

The availability of data and the use of data-driven protocols allows us to objectively quantify the uncertainty associated with the information gathered and knowledge gained. The quantity of experimental data generated by a single material research group is typically relatively small and may not be enough to tackle the engineering material's design problems.

This framework has been demonstrated on a variety of problems. Structure-property relations were developed capable of the prediction of the extreme value elastic stresses hypothesized to be associated with transverse crack formation at the scale of the filaments in ceramic matrix composites. The elastic and inelastic bulk properties of titanium polycrystals were predicted, including the elastic strain fields in cubic and hexagonal polycrystals and high-cycle fatigue predictions of fatigue indicator parameters (FIPs). The transport properties of porous microstructures used in fuel cell applications were linked to the microstructural features of polymers. Additionally, the framework has been applied to inverse design problems to extract single crystal elastic-plastic properties of a polycrystalline metal.

The practical realization of the framework is only feasible with the accumulation of substantially large libraries of materials data that capture the relevant multiscale spatiotemporal information about materials internal structures for a very broad class of materials. It is practically impossible for a single research group or an organization to take on the monumental task given the information required. Further, the domain expertise needed to mine and curate the materials knowledge needed to accelerate the material development of new and improved materials lie well outside the traditional skill sets of materials scientists and engineers. Currently, the materials community does not have the skill set needed to fully enable the materials data science revolution. Hence, an intimate collaboration of teams with specific domain knowledge are needed to facilitate the ICME approach.

5 Summary

A novel workflow template is presented to extract process-structure linkages in microstructure evolution problems through the utilization of advanced data science techniques. The presented workflow is scalable, expandable, and can be applied to a broad variety of microstructure evolution datasets. This workflow consists of four modular steps: (1) data preprocessing, (2) microstructure quantification, (3) dimensionality reduction, and (4) extraction and validation of process-structure

linkages. Each step of the workflow allows selection and utilization of readily accessible codes from a large library of repositories.

Emerging toolsets in materials data science and informatics have demonstrated tremendous promise in addressing some of the key challenges in materials engineering. It is now possible to generate a large ensemble of datasets (inputs and outputs) from a simulation toolset and publicly share these with the broader scientific community in an open access data repository. Once this is accomplished, it is possible to engage the broader scientific community in the extraction of the embedded knowledge of these datasets. If this activity is guided in a suitable framework for P-S-P, it could lead to an accelerated and robust curation of the knowledge, while simultaneously ensuring the highest levels of access, sharing, and dissemination for reuse.

References

1. National Research Council, *Integrated Computational Materials Engineering: A Transformational Discipline for Improved Competitiveness and National Security* (The National Academies Press, Washington, DC, 2008), p. 152
2. C. Bishop, *Pattern Recognition and Machine Learning (Information Science and Statistics)*, 1st edn. (Springer-Verlag, New York, 2006), p. XX, 738
3. N.H. Paulson et al., Reduced-order structure-property linkages for polycrystalline microstructures based on 2-point statistics. Acta Mater. **129**, 428–438 (2017)
4. Z. Yang et al., Deep learning approaches for mining structure-property linkages in high contrast composites from simulation datasets. Comput. Mater. Sci. **151**, 278–287 (2018)
5. A. Gupta et al., Structure–property linkages using a data science approach: application to a non-metallic inclusion/steel composite system. Acta Mater. **91**, 239–254 (2015)
6. A. Çeçen et al., A data-driven approach to establishing microstructure–property relationships in porous transport layers of polymer electrolyte fuel cells. J. Power Sources **245**, 144–153 (2014)
7. A.J. Schwartz, M. Kumar, B.L. Adams, D.P. Field, *Electron Backscatter Diffraction in Materials Science*, 2nd edn. (Springer, US, 2009), p. XXII, 403
8. A.P. Lyubartsev, A. Laaksonen, Calculation of effective interaction potentials from radial distribution functions: a reverse Monte Carlo approach. Phys. Rev. E **52**(4), 3730 (1995)
9. B.S. Fromm et al., Grain size and orientation distributions: application to yielding of α-titanium. Acta Mater. **57**(8), 2339–2348 (2009)
10. A. Cecen et al., 3-D microstructure analysis of fuel cell materials: spatial distributions of tortuosity, void size and diffusivity. J. Electrochem. Soc. **159**(3), B299–B307 (2012)
11. S.R. Kalidindi, S.R. Niezgoda, A.A. Salem, Microstructure informatics using higher-order statistics and efficient data-mining protocols. JOM **63**(4), 34–41 (2011)
12. S.R. Kalidindi, J.R. Houskamp, Application of the spectral methods of microstructure design to continuous fiber-reinforced composites. J. Compos. Mater. **41**(8), 909–930 (2007)
13. S. Torquato, H. Haslach, *Random Heterogeneous Materials: Microstructure and Macroscopic Properties* (American Society of Mechanical Engineers Digital Collection, 2002)
14. N. Hansen, Hall–Petch relation and boundary strengthening. Scr. Mater. **51**(8), 801–806 (2004)
15. A. Cord, F. Bach, D. Jeulin, Texture classification by statistical learning from morphological image processing: application to metallic surfaces. J. Microsc. **239**(2), 159–166 (2010)
16. A.A. Wheeler, W.J. Boettinger, G.B. McFadden, Phase-field model for isothermal phase transitions in binary alloys. Phys. Rev. A **45**(10), 7424 (1992)

17. S. Wolfram, Statistical mechanics of cellular automata. Rev. Mod. Phys. **55**(3), 601 (1983)
18. J.A. Sethian, A fast marching level set method for monotonically advancing fronts. Proc. Natl. Acad. Sci. **93**(4), 1591–1595 (1996)
19. D.K. Patel, H.F. Al-Harbi, S.R. Kalidindi, Extracting single-crystal elastic constants from polycrystalline samples using spherical nanoindentation and orientation measurements. Acta Mater. **79**, 108–116 (2014)
20. M. Oda, S. Nemat-Nasser, M.M. Mehrabadi, A statistical study of fabric in a random assembly of spherical granules. Int. J. Numer. Anal. Methods Geomech. **6**(1), 77–94 (1982)
21. M.N. Rossol et al., Characterizing in-plane geometrical variability in textile ceramic composites. J. Am. Ceram. Soc. **98**(1), 205–213 (2015)
22. S. Sherman, J. Simmons, C. Przybyla, Mesoscale characterization of continuous fiber reinforced composites through machine learning: Fiber chirality. Acta Mater. **181**, 447–459 (2019). https://doi.org/10.1016/j.actamat.2019.10.001
23. H. Bale et al., Characterizing three-dimensional textile ceramic composites using synchrotron X-ray micro-computed-tomography. J. Am. Ceram. Soc. **95**(1), 392–402 (2012)
24. D.K. Patel, T. Parthasarathy, C. Przybyla, Predicting the effects of microstructure on matrix crack initiation in fiber reinforced ceramic matrix composites via machine learning. Compos. Struct. **236** (2020). https://doi.org/10.1016/j.compstruct.2019.111702
25. Y.C. Yabansu, D.K. Patel, S.R. Kalidindi, Calibrated localization relationships for elastic response of polycrystalline aggregates. Acta Mater. **81**, 151–160 (2014)
26. D.K. Patel, S.R. Kalidindi, Estimating the slip resistance from spherical nanoindentation and orientation measurements in polycrystalline samples of cubic metals. Int. J. Plast. **92**, 19–30 (2017)

Multiscale Modeling of Epoxies and Epoxy-Based Composites

Xiawa Wu and Jaafar A. El-Awady

1 Introduction

Epoxies are thermoset polymers with highly cross-linked molecular structures [1]. They are synthesized in a curing process, which involves chemical reactions between epoxy resins with or without curing agents [2]. Cured epoxies are typically characterized by their high elastic modulus, mechanical strength, thermal stability, electrical and chemical resistance, and a strong adhesion to other solid surfaces. Thus, epoxies are often used as adhesives, coatings, and matrix phases in fiber-reinforced composites for a wide range of industrial applications [3].

Epoxy resins usually have low molecular weight and weak thermal and mechanical properties. The curing process transforms the epoxy resins into a three-dimensional network with improved macroscale properties [4]. Some major factors that affect the curing process include the combination of epoxy resins and curing agents, the curing temperature and pressure, the cooling rate, and the presence of other materials, such as fiber reinforcements or nanoparticles [3, 5–11]. Many experimental studies (e.g., [12–16]) have aimed to quantify the structural, thermal (e.g., glass transition temperature, thermal conductivity, and the coefficient of thermal expansion), and mechanical (e.g., elastic modulus, mechanical strength, strain to failure, and failure modes) properties of different epoxy systems. In

X. Wu
Department of Mechanical Engineering, Whiting School of Engineering, The Johns Hopkins University, Baltimore, MD, USA

Mechanical Engineering, The Pennsylvania State University, The Behrend College, Erie, PA, USA

J. A. El-Awady (✉)
Department of Mechanical Engineering, Whiting School of Engineering, The Johns Hopkins University, Baltimore, MD, USA
e-mail: jelawady@jhu.edu

S. Ghosh et al. (eds.), *Integrated Computational Materials Engineering (ICME)*,
https://doi.org/10.1007/978-3-030-40562-5_10

addition, experimentally, the structure of bulk epoxies has been characterized using measurements such as material density, degree of cross-linking, averaged length between cross-linking sites, and distribution of free volume holes (e.g., [8, 17–19]). However, such measurements provide average quantities and do not give precise characterization of the local molecular structure, which is sometimes needed to establish fundamental structure-property relationships [20, 21]. This is particularly important when characterizing the interphase regions in epoxy-based composites. These regions are of significant importance since they exhibit strong structural and chemical variations within a relatively small volume and these variations greatly influence the performance of the overall composites [8, 22]. Furthermore, while scanning electron microscopy (SEM) and transmission electron microscopy (TEM) techniques can be used to analyze the distribution of fibers within the epoxy matrix and they have an adequate resolution to identify whether there are cracks at the fiber/matrix interface [23], a direct experimental measurement of the local molecular structure of the epoxy or the strength at the fiber/epoxy interface is still lacking.

On the other hand, simulations of the epoxy curing process are generally simplified by only including the material constituents to create a neat cross-linked network [24–26]. Such simulations are usually based on fully atomistic molecular dynamics (MD) simulations with inputs from either density functional theory (DFT) to calculate the chemical reactions during curing [27] or by utilizing reactive force fields to create a cross-linked epoxy structure [28, 29]. Additionally, MD simulations can also be utilized to provide an atomic level understanding of the local variations of the molecular structure and properties in the bulk epoxy or near/at interface regions as well as provide an avenue to establish structure-property relationships for epoxies [23]. The main challenge for such atomistic-based simulations is that the material properties do not directly match the experimentally measured macroscale properties [30], which can be attributed to the small length and time scales probed in the simulations [31]. On the opposite end of length scales, the finite element method (FEM) is often used to predict the mechanical properties and deformation/failure of epoxy and epoxy-based composites at the macroscale [32–35]. In conventional FEM, the material parameters and the constitutive rules are typically based on empirical observations coming from experimental measurements. Thus, these simulations lack information from small scales, such as the variations in local molecular structure and properties (e.g., in the interphase region). One of the promising approaches to overcome some of the limitations of MD and FEM simulations and to bridge between them is coarse-grained (CG) methods.

All in all, the study of epoxies and epoxy-based composites is motivated by their advanced properties and applications. In order to achieve desirable properties of epoxies, the relationships between the curing process (in bulk and at interphase) and their molecular structure, as well as their thermal and mechanical properties, need to be established. If these process-structure-property relationships were well established, one would be able to create different epoxy systems and probe their properties effectively and efficiently. Current experimental investigations alone can hardly reveal the structure-property relationships in epoxy systems. Thus, simulation methods, especially multiscale simulations, are in need of development.

This also highlights the need to develop a multiscale modeling approach in which information is upscaled from the appropriate length scale to the next one, either hieratically or concurrently, to better predict the deformation and failure of epoxies and composites. This would provide a promising avenue to greatly accelerate the design of advanced epoxy-based materials.

While a number of comprehensive review articles on epoxies and epoxy-based composites have been published in the last 10 years [36–38], there is still a lack of a comprehensive review focused on multiscale epoxy modeling efforts. Thus, in this chapter, recent research on multiscale simulations of epoxies and epoxy-based composites are discussed. In Sect. 2, common simulation methods are briefly discussed for the purpose of outlining the building blocks of a multiscale framework. In Sect. 3, various models that predicte the molecular structure and thermomechanical properties of epoxies are reviewed. The majority of studies discussed in this paper are on two of the most common epoxies, diglycidyl ether of bisphenol A (DGEBA) and diglycidyl ether of bisphenol F (DGEBF). The properties of epoxy-based composites, coatings, and adhesives are then discussed in Sect. 4. Finally, a summary and conclusions are given in Sect. 5.

2 Overview of Multiscale Simulation Methods for Epoxies

2.1 Molecular Dynamics Simulation

Molecular dynamics simulations are based on modeling many-body dynamics at the atomic scale using Newton's second law. Atomic structures and force fields are two important inputs for an MD simulation, and both can be obtained from DFT calculations.

The commonly used force fields in classical MD simulations include CVFF, PCFF, COMPASS, Dreiding, and other modified and mixed potentials [16, 39, 40]. Many studies have been performed using classical (nonreactive force fields) MD simulations to explore the molecular topology, degree of cross-linking, water absorption, strain rate, temperature, and effects of force fields on the density, modulus, fracture, glass transition temperature, and coefficient of thermal expansion of various epoxy systems [16, 31, 40–49]. In these simulations, nonreactive force fields are utilized, and bonds are created or broken based on criterion upscaled from DFT simulations. In addition, reactive force fields (i.e., ReaxFF) are also widely used when the chemical reactions are of interest in the epoxy simulations [28, 29, 50]. Different types of force fields used in various epoxy studies are listed in Table 1.

The MD simulations can typically model epoxy systems that are up to tens of nanometers in edge lengths and reach time scales of up to a few nanoseconds. As the examples in Table 1 show, the size of the MD simulation cells often consists of few hundreds of combined prepolymer and curing agents, and a simulation system that is larger than a few thousand molecules is rare due to the high computational cost demands associated with such simulations.

Table 1 Summary of different MD (including the force field method used) and CG-MD simulations of DGEBA and DGEBF epoxy systems alongside the number of prepolymers and curing agents. The size column is expressed in terms of (# prepolymers, # curing agents)

Epoxy system	Method and force field	Size	Refs
DGEBF+DETDA	MD+CVFF	(128, 64)	[51]
DGEBF+DETDA	MD+Dreiding	(256, 128)	[31]
DGEBF+DETDA	MD+OPLS	(432, 216)	[49]
DGEBF+DETDA	MD+ReaxFF	(72, 36)	[28]
DGEBF+DETDA	MD+COMPASS	na	[41]
DGEBF+DETA	MD+ReaxFF	(1120, 920)	[50]
DGEBA+DETDA	MD+ReaxFF	na	[29]
DGEBA+DETA	MD+COMPASS	(100, 40)	[42]
DGEBA+DETA	CG-MD	(325, 150)	[52]
DGEBA+IPD	MD+Dreiding+COMPASS	(16, 8)	[40]
DGEBA+IPD	MD+ReaxFF	na	[29]
DGEBA+IPD	MD+PCFF	na	[44]
DGEBA+T403	MD+ReaxFF	na	[29]
DGEBA+33DDS	MD+Dreiding	(1024, 512)	[16]
DGEBA+MDA	MD+COMPASS	(492, 246)	[45]
DGEBA+DAB	CG-MD	(3888, 1944)	[27]

One of the main applications of MD simulation in multiscale modeling is the modeling of the curing process and to study the epoxy system's response under different thermomechanical loading conditions. Generally, thermosets have been less studied compared to thermoplastics partly due to the difficulty of constructing a 3D structure having a high degree of cross-linking. Nevertheless, the rapid developments in molecular modeling and computing power in the last 10 years enabled all-atom studies of thermoset materials.

In addition to modeling neat epoxy systems, MD simulations were also used to investigate nanocomposites that consist of a single reinforcement nanoparticle and its surrounding epoxy matrix. Such simulations have been used to investigate interfacial bonding and damage initiation in carbon nanotube (CNT)/epoxy [53], SiO_2/epoxy [54], and graphene/epoxy [55] nanocomposites. Some MD simulations of epoxies were also integrated with higher length/time scale models to enable comparison to experiments. As an example, MD simulations and a homogenization-based continuum model were used to predict the stress-strain behavior of epoxy nanocomposites [22, 56], while combined MD and FEM simulations were used to study the alumina/epoxy nanocomposites' mechanical properties [57].

Similar to nanocomposite simulations, epoxy coating/substrate systems have also been commonly studied using MD simulation. Examples include studying the deformation and failure mechanisms of Cu/epoxy bi-materials [58], predicting interfacial bonding between carbon steel and epoxy systems [59], simulating fracture and adhesive properties of epoxy/solid wall systems [60], modeling epoxy coating on inorganic substrate [39], and investigating silica/epoxy interface with the presence of water molecules [61].

2.2 Coarse-Grained Molecular Dynamics Methods

One of the most commonly used length/time scale bridging methods for epoxy simulations is coarse-grained molecular dynamics simulations (CG-MD). Generally, there are two steps in developing a CG-MD model for epoxies. The first step is to map groups of atoms into coarser particles, commonly known as super-atoms, and the second step is to define the interactions between these coarse particles [62]. It should be noted that the individual atoms grouped into super-atoms typically have much less significant motion with respect to each other as compared to the whole molecule. In addition, the interactions between super-atoms are modeled by spring-like bonds, as well as angular and torsional potentials that properly average the high-frequency internal degrees of freedom of the molecules.

The CG-MD simulations are roughly two orders of magnitude faster than all-atom MD simulations [63]. Thus, CG-MD simulations can model time scales of up to microseconds depending on the degree of coarse-graining implemented [62]. Additionally, a CG-MD model can include thousands of prepolymers and curing agents.

The highest level of coarsening reduces a single polymer chain into one "CG" bead. However, this is not popular for epoxy modeling due to the loss of major details of the epoxy structures (e.g., the lengths of monomers), which can strongly influence the epoxy response. The lowest level of coarsening usually involves grouping hydrogen with other atoms to create united-atom force fields. One such low-level CG method that has been used in literature to simulate epoxy behavior is the OPLS united-atom force field method [49, 55]. In this method, CH_3, CH_2, CH, and alkyl groups were grouped into single united atoms [49].

In mid-level epoxy CG methods, a few non-hydrogen atoms are also grouped into a single super-atom. An example of coarsening a DGEBA monomer based on its full atomic structure is shown in Fig. 1. This mid-level CG model was used by Aramoon et al. to study the curing structure evolution and thermal properties of a DGEBA epoxy [27, 64]. Other examples for the utilization of mid-level CG models include creating high degree of cross-linked epoxy systems using a dynamic curing process with very long bonds [65]; studying the failure mechanism of general thermoset and thermoplastic materials [30]; coarse-graining EPN-3mer, EPN-4mer, and BPA molecules and predicting various thermomechanical properties including their tensile failure [66, 67]; studying the cross-linking process of an epoxy under Couette and Poiseuille flow conditions [68]; studying the interfacial failure and microstructural evolution at interphase in epoxy/Cu [69] and epoxy/rigid walls [62, 70] systems; as well as studying the glass transition temperature [52, 64].

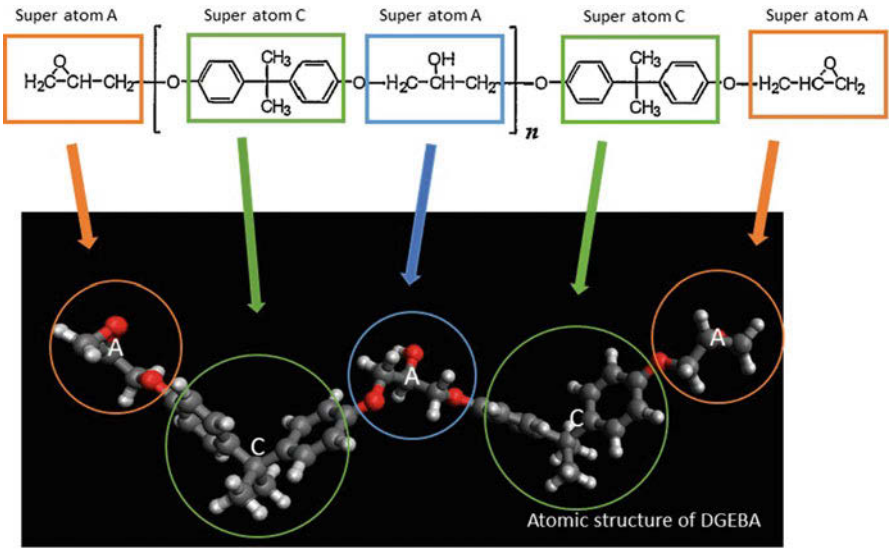

Fig. 1 CG mapping between an all-atom structure of a DGEBA monomer and coarse particles [27]

2.3 Finite Element Method

FEM simulations are based on numerically solving conservation laws expressed in terms of the material constitutive laws to predict the material continuum response. The advantage of FEM simulations in epoxy studies is that it can explicitly model a large length scale of epoxy-based composites, with detailed description of the reinforcement fiber size, shape, orientation, distribution, and their interactions with the epoxy matrix [71–74]. Commercial FEM packages, such as ABAQUS (Dassault Systemes, 2016 [75]), offer a number of material models to describe the elastic and plastic deformation, as well as brittle and ductile failure of bulk epoxies. The cohesive zone element model is also commonly utilized to simulate fracture and delamination at the interface region between the fiber and matrix [76–78]. However, the material parameters that are used as inputs to FEM models highly depend on experimental measurements. As discussed in Sect. 1, current experimental methods are limited in measuring small-scale structures and properties, and it is a common practice to assign homogeneous properties for the polymer matrix across the simulation volume with a damage model that does not account for the effect of local variations in the molecular structure or the multiscale damage mechanisms of epoxies [79, 80]. Furthermore, this approach ignores the differences between the molecular structure of the matrix and the interphase region, which can be substantially different.

In literature, a number of multiscale simulations combining MD and FEM models have been proposed to study epoxy-based nanocomposites/composites. For

example, Mortazavi et al. studied graphene reinforced DGEBA epoxy composites to understand their thermal conduction and dependence on geometry and volume fraction of the fiber reinforcements [55, 74]. Subramanian et al. simulated the damage and fracture of CNT/epoxy nanocomposites using MD and FEM models [53]. In these studies, the MD simulation predictions were upscaled into FEM simulations to develop homogenized properties based on microscale representative volume elements (RVEs). Additionally, Choi et al. studied the size effects of carbon nanotubes in SWNT/epoxy systems using a combined MD/FEM model [81]. In this approach, the interphase geometric boundaries and mechanical response were predicted from FEM through matching of homogenization and deformation energy from MD simulations [82].

It should be noted that the MD and FEM models are at the nano- and microscales, respectively; thus, there is a need for developing homogenization methods to bridge the length-scale gap between both models. The CG-MD models provide such an approach. Since CG-MD models can simulate large-scale domains (i.e., up to the microscale), it is feasible to explicitly simulate the fiber/matrix regions with dynamically created CG epoxy structures, and the resulting material properties can be directly upscaled to FEM models, which will enable a one-way information flow. In particular, CG-based bridging methods can be beneficial to epoxy and epoxy-based composite modeling.

3 Multiscale Simulations of Epoxies and Their Properties

3.1 Modeling the Curing Process of Epoxies

A first step in any epoxy molecular modeling simulation is to create a structure that represents a true epoxy material. Many simulations have been devoted to simulate the dynamic curing process of highly cross-linked epoxies [27, 40, 65, 83, 84]. The creation of an epoxy system is highly dependent on the epoxy resin, the cross-linker, and the force field employed to describe the system dynamics. Generally, a mixture of monomers and curing agents are placed in a simulation cell with periodic boundary conditions in all directions. The functional groups on the prepolymers are allowed to form covalent bonds according to a pre-defined distance-based bond creation rule [85]. The cross-linking process is considered complete when a certain degree of conversion is achieved or there are no more bonds to create in the system. This general curing process is adopted in both MD and CG simulations with a few modifications to achieve a good epoxy structures. The main modification occurs in the cross-linking step. Wu and Xu [40] developed an algorithm that employed repeated MD and molecular mechanics (MM) simulation steps during the curing process and were able to achieve an epoxy network with conversion up to 93.7% with less computing time and much flexibility. Additionally, Varshney et al. [51] proposed a multistep robust procedure that includes a relaxation period during the polymer network buildup and noted that the relaxation time between each step of

Table 2 Different epoxy systems (system), the highest achieved degree of cross-linking (CL), the material density at room temperature (density), volume shrinkage (VS), and gel point (GP) from various MD and CG-MD simulations

System	CL (%)	Density (g/cm^3)	VS (%)	GP (%)	Refs.
DGEBF+DETDA	95	1.12	7	60–65	[51]
DGEBF+DETDA	86	1.13	na	60–70	[31]
DGEBF+DETDA	76	1.21	12	na	[49]
DGEBF+DETDA	85	1.2	na	na	[28]
DGEBF+DETDA	90	1.2	na	na	[41, 87]
DGEBA+DETDA	84	1.159	na	na	[29]
DGEBA+DETA	81	1.15	na	na	[42]
DGEBA+DETA	72	1.10	na	na	[52]
DGEBA+IPD	93.7	1.116	na	na	[40]
DGEBA+IPD	82	1.147	na	na	[29]
DGEBA+IPD	92	1.13	5–7	60–80	[44]
DGEBA+T403	72	1.155	na	na	[29]
DGEBA+33DDS	85	1.17	14	65–70	[16]
DGEBA+DAB	95	1.16	5	65–70	[27]

creating new bonds helps to create an epoxy with a high degree of cross-linking and good structure stability.

To reach a high degree of cross-linking in CG-MD simulations millions of simulation time steps are usually required, and for degrees of cross-linking higher than 80%, the mobility of the curing agents rapidly decreases due to trapping by the formation of the 3D network, which can as well inhibit the simulation from reaching the desired degree of cross-linking in a realistic simulation time [27]. Table 2 summarizes the degree of cross-linking in different simulation studies for reference. Thus, to reduce computational cost in a large CG-MD simulation domain, Aramoon et al. developed a new curing algorithm that can reach high degrees of cross-linking faster than traditional ones and creates a more uniformly cross-linked epoxy structure [27]. In this new approach, groups of partially cross-linked chains with random lengths from 3 to 6 monomers were used as prepolymers, and they were mixed with curing agents in a simulation cell. During the curing process, curing agents were actively redistributed to sub-volumes where high reactive monomers exist. The rate of curing in local areas was actively controlled based on the local degree of cross-linking. This algorithm design ensures a cross-linked network with a uniform degree of cross-linking can be achieved in a relatively short amount of simulation time.

Figure 2a shows the degree of cross-linking reached as a function of the number of simulation time steps as predicted using this new curing model for a DGEBA/DAB system containing 5,832 super-atoms in a 75 nm periodic cube simulation cell [27]. This new curing algorithm can reach a higher degree of cross-linking (∼95%) compared to the traditional curing method after 1 million simulation steps. An additional benefit of this new curing algorithm is that a uniform degree of cross-linking was achieved throughout the simulation domain, which also

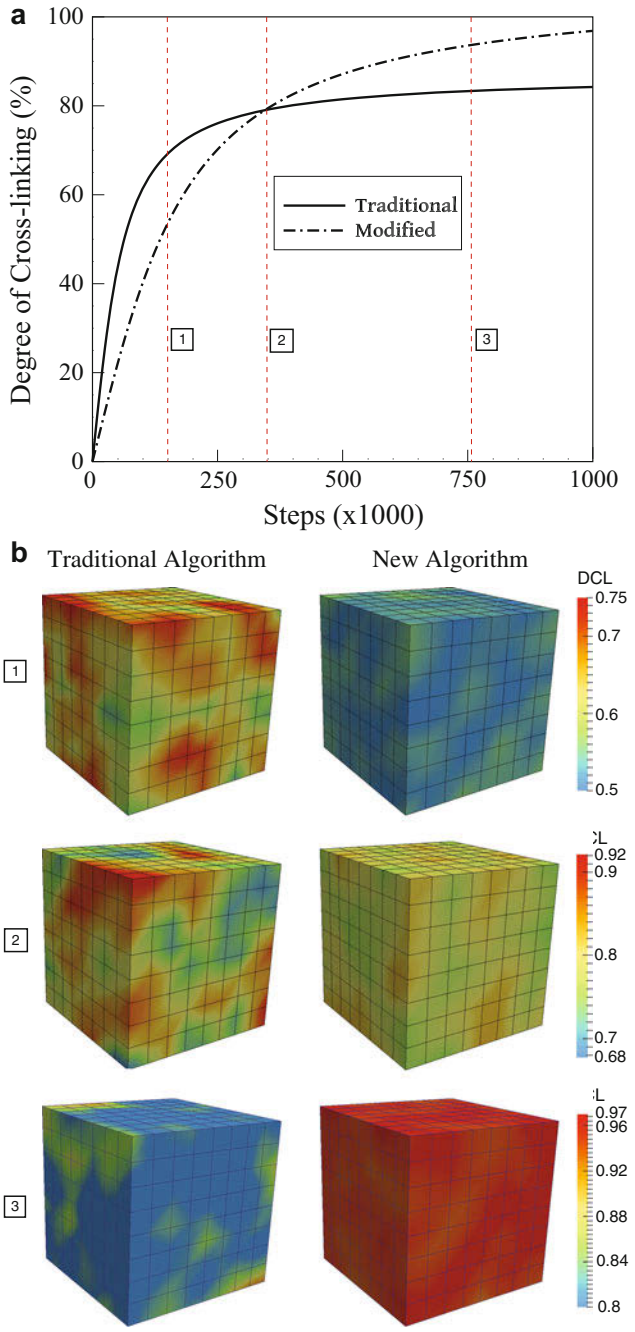

Fig. 2 (**a**) Comparison between the degree of cross-linking as a function of the number of simulation time steps as predicted from a traditional algorithm [40] and the curing algorithm proposed by [27]. (**b**) Comparison of the uniformity of cross-linking in CG simulation domains at different steps, as indicated in (**a**). (Reprint with permission from [27])

contributes to the stability of the cured structure [27]. Figure 2b shows the epoxy structure created using the new curing algorithm (right column) has a more uniform degree of cross-linking than the ones created using the traditional method (left column).

The degree of cross-linking is a well-controlled parameter in a simulated curing process. Theoretically this value can be quantitatively compared to experiments. However, the lack of experimental evaluation of the molecular structure of epoxies has led to uncertainties in how well a constructed atomistic model represents the true material structure. Accordingly, the molecular structure produced from curing simulations is indirectly validated by computing other properties as discussed in the following subsections.

3.2 Epoxy Density and Volume Shrinkage

Table 2 shows a summary of three common structural properties used to validate the molecular structures predicted from MD and CG-MD simulations. As an example, the predicted density of DGEBF systems is commonly in the range of 1.12–1.21 g/cm^3, while that for DGEBA systems is in the range of 1.1–1.169 g/cm^3. The variation in the predicted density is a result of the different curing agents and force fields used (see Table 1), as well as the degrees of cross-linking reached (see Table 2). These predicted values are qualitatively in agreement with experimental measurements, which are in the range of 1.111–1.142 g/cm^3 for the DGEBA systems with different curing agents [86]. Generally speaking, the error in the molecular-based simulation-predicted densities versus the experimental measured ones for various DGEBA based-epoxies is in the range of 1.0–5.3%.

An exact agreement between experiments and simulation is hard to achieve due to the following: (1) the force fields used in most simulation are generic polymer potentials without specific tailoring to the simulated system and, thus, may introduce systematic errors in describing the atomic interactions in the material; (2) the simulated volume is small, and the curing process in the simulations is significantly simplified as compared to experiments; and (3) the epoxy density is a function of the degree of cross-linking, and the difference between the conversion degree of a simulation system (72–95% conversion) and real materials (usually considered to be close to 100% conversion) can also contribute to the differences between the predicted and measured densities.

In addition to the static density of the cured epoxy at room temperature, the dynamic change of density, i.e., volume shrinkage, during the curing process is also commonly used to validate the accuracy of the predicted molecular structure. Figure 3a shows a linear relationship between volume and the degree of conversion from a CG-MD simulation of DGEBA/DAB epoxy [27]. The predicted volume shrinkage from some MD and CG-MD simulations is also summarized in Table 2. A volume shrinkage of 5–12% is typically predicted for different epoxy systems [39].

It should be noted that the slope of the volume shrinkage is a function of the curing temperature [83]. Additionally, the volume shrinkage often causes internal

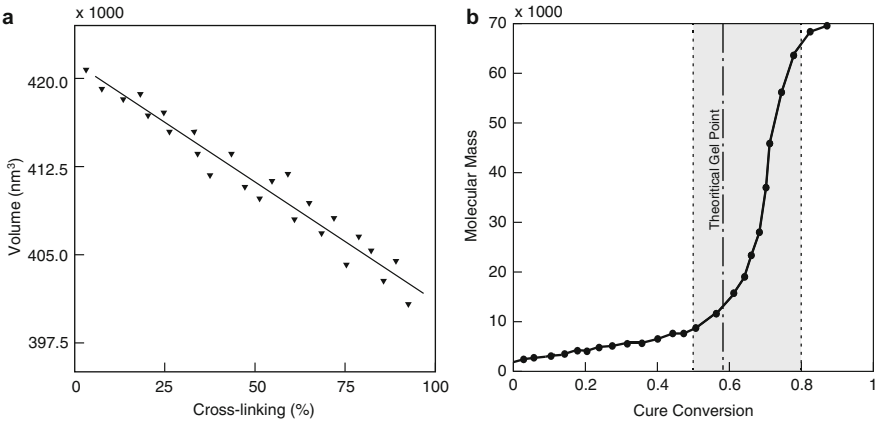

Fig. 3 Coarse-grained MD simulation predictions of the curing process of a DGEBA/DAB system: (**a**) volume change versus the degree of cross-linking (a 5% volume shrinkage is predicted when the degree of cross-linking reaches 95%) and (**b**) molecular mass buildup versus the cure conversion. The shaded area in (**b**) represents the range of gel point from experiments, and the dashed line indicates the theoretical value. (Reprint with permission from [27])

residual stresses and interfacial stresses when the epoxy is in contact with solid surfaces [39], which may lead to performance issues for epoxy coatings, adhesives, and composites. Thus, it is desired that the volume shrinkage be kept at minimum by choosing a lower curing temperature or a smaller degree of conversion.

Gel point is another structure property that measures the molecular weight of the largest molecule during a curing process. The gel point can be experimentally measured using dynamic mechanical analysis (DMA), and some simulation studies report it for the purpose of validating the simulations. Figure 3b shows a profile of the molecular mass of the largest DGEBA polymer increasing with the degree of cross-linking in a CG-MD study of a DGEBA/DAB system. The molecular mass rapidly increases during 65–70% conversion, and the calculated gel point is around 67%, which is in agreement with the experimental measurements that are in the range of 50–80% and the theoretical prediction of 58% [27]. Some additional measurements of the gel point from different simulations are also summarized in Table 2, and they are in a 60–80% range.

3.3 Glass Transition Temperature

The glass transition temperature, T_g, is directly linked to the chemical composition and the degree of cross-linking of a polymer. In epoxy simulations, T_g is often used as a validation characteristic to tune the developed models, since its experimental value is reported in literature for a wide range of polymers. Figure 4a shows the specific volume versus temperature as predicted from CG-MD simulation of DGEBA/DAB epoxy with 85% degree of cross-linking [27]. Two straight lines were

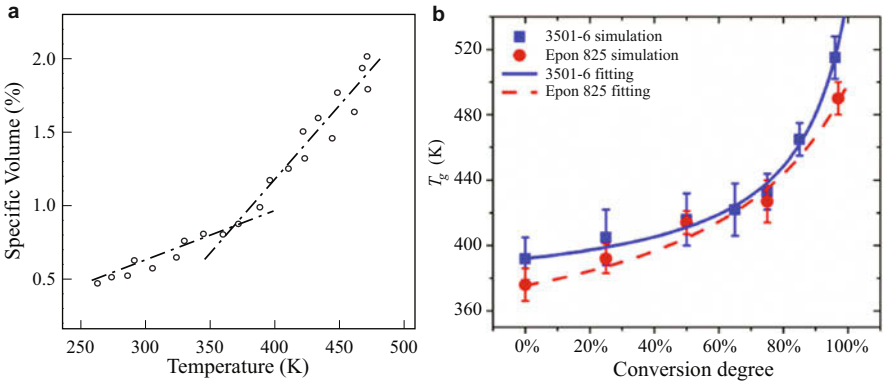

Fig. 4 (**a**) The specific volume versus temperature as predicted from CG-MD simulations of a DGEBA/DAB epoxy with a 85% degree of cross-linking. The intersect of the two dashed lines represents the predicted glass transition temperature, which is $T_g = 385.0$ K [27]. (Reprint with permission from [27].) (**b**) The glass transition temperature as a function of conversion degree. DiBenedetto equation is fitted for both 3501–6 and Epon 825 systems [47]. (Reprint with permission from [47])

Table 3 The glass transition temperature, T_g, and elastic modulus, E, as predicted for different degrees of cross-linking (CL) from different molecular-based simulations

System	CL (%)	T_g (°C)	E (GPa)	Refs
DGEBF+DETDA	95	105	na	[51]
DGEBF+DETDA	86	172	2.8–3.2	[31]
DGEBF+DETDA	76	151.2	2.258	[49]
DGEBF+DETDA	100	109	na	[24]
DGEBF+DETDA	na	na	2.76	[88]
DGEBF+DETDA	na	na	2.46	[89]
DGEBF+DETDA	90	113–161	2.5	[41, 87]
DGEBA+DETDA	90	177–190	5.5–8.5	[90]
DGEBA+DETA	72	87	1.10	[52]
DGEBA+DETA	81	na	3.82	[42]
DGEBA+IPD	82	153	3.0–3.4	[29]
DGEBA+IPD	93.7	na	5.198	[40]
DGEBA+IPD	92	107	2.953	[44]
DGEBA+T403	72	88	3.7–4.7	[29]
DGEBA+T403	na	96	2.88	[91]
DGEBA+33DDS	85	242	1.3	[16]
DGEBA+DAB	95	116	na	[27]

fitted for the low- and high-temperature regions in the calculated specific volume and temperature profile. The cross point of the two lines indicate the predicted T_g value. Table 3 summarizes the predicted T_g and elastic modulus of various epoxy systems and their corresponding degrees of cross-linking. The experimentally measured T_g for DGEBA systems is in the range of 110–155 °C, which is in agreement with simulation predictions [86].

It should be noted that T_g is strongly dependent on many factors, including the degree of cross-linking, curing temperature, length of the monomers, the size of the simulation system, cooling rate, etc. [83]. Many simulation studies report that T_g increases with increasing degree of conversion, which can be attributed to the high degree of cross-linking in the epoxy that leads to lower mobility for the molecular chains, leading to a stable epoxy network [31, 49, 54, 84]. Figure 4b shows the dependence of T_g on the conversion degree for two epoxy systems. As most epoxies are cured to high conversion degrees, a slight difference in degree of cross-linking may cause a big variation in the predicted T_g.

3.4 *Free Volume Distribution*

Free volume (FV) holes are defined as the empty volume between polymer chains, and the size of FV holes is related to the connectivity and mobility of the surrounding molecules. Positron annihilation lifetime spectroscopy (PALS) is commonly used to experimentally measure the size distribution of FV holes in a polymer material [92, 93]. The drawback of PALS experiments is that it measures averaged values over large volumes and lacks the resolution to characterize local material structure (e.g., the interphase region). On the other hand, MD and CG-MD models can capture both the average material property and local distributions.

To validate the molecular structure predicted from CG-MD simulations, Aramoon et al. developed a computational algorithm to measure FV distribution using spherical or ellipsoidal shapes fitted to the empty volumes between connected epoxy molecules [64]. Figure 5 shows the predicted probability distribution function of FV in DGEBA/DAB at different pressures as predicted from CG-MD simulations [94] and those from PALS experiments [95]. These results indicate

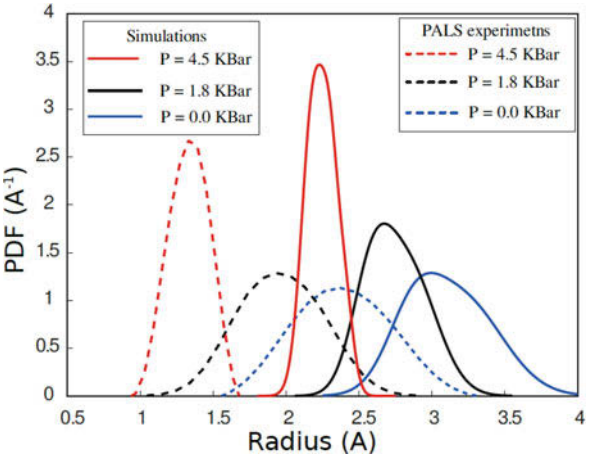

Fig. 5 The probability distribution function (PDF) of FV holes as computed from PALS experiments and predicted from CG-MD simulations at different pressuress (P) [94]

a good agreement between the CG-MD simulations and PALS measurements. The simulations also show that the average FV radius and the standard deviation of the FV distribution both decrease with increasing pressure. However, it should be noted that the predicted average FV radius from the CG-MD simulations is larger than the experimental values under all conditions. This can be attributed to the way the FV is predicted in the simulations as compared to the experiments. The PALS experiments measure the annihilation time of orthopositronium (o-Ps) particles created by the reaction of positrons and electron cloud of the surrounding atoms [96], while in the simulations the FVs are calculated by fitting the largest ellipsoids in the empty space and reaching the surface of surrounding atoms without considering the effects of the electron cloud. Thus, simulation predictions are systemically larger than experiments.

Because FV holes are sensitive to temperature and pressure, it can be correlated to the polymer properties that are temperature and pressure dependent. Aramoon et al. predicted the T_g for different degrees of cross-linking and prepolymer lengths based on the calculated FV distributions obtained from CG-MD simulations of DGEBA epoxies [64]. Figure 6a shows the density ρ and the average radius of FV holes, Γ, as functions of temperature for a 85% cured DGEBA/DAB system as predicted from those simulations. The sharp turns observed in density, ρ, and in the average FV hole radius, Γ, both coincide with the same predicted glass transition temperature. While conventionally T_g is measured according to the

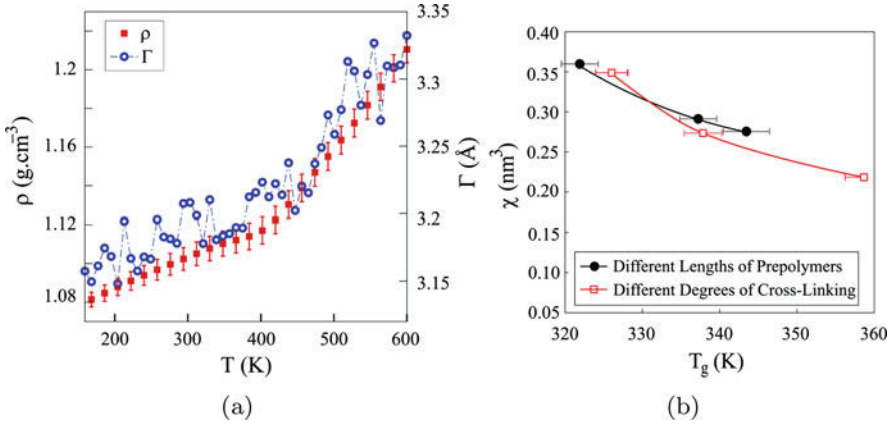

Fig. 6 (**a**) The density (left axis) and average FV radius (right axis) as a function of temperature as predicted from CG-MD simulations of a DGEBA/DAB system having an initial length of 5 monomers, a degree of cross-linking of 85%, and a pressure of 0 kbar. The sharp turns observed in the density and in the average FV hole radius curves both coincide with the same predicted glass transition temperature. (**b**) Effects of prepolymer length, the degree of cross-linking, and the average volume of free volume holes (χ) on the predicted glass transition temperature. Results labeled by black circles and red squares are calculated using a 85% cross-linking system and a 5-monomer system, respectively. Both systems are measured under 0 pressure. (Reprint with permission from [64])

changes in density or specific volume, Fig. 6a demonstrates that the average FV radius can also be used to calculate T_g in CG-MD simulations [64].

Figure 6b also shows the effect of the average FV hole volume, degree of cross-linking, and length of prepolymers on the predicted T_g. The average volume of FV holes, χ, decreases with the increase in the degree of cross-linking and an increase of prepolymer length. For smaller average volumes of FV holes, the T_g becomes higher, which indicates a low mobility of the polymer chains and a more stable molecular structure. An analytical predictive model was also developed from CG-MD simulations, and the model was shown to be able to predict T_g based only on the initial FV distribution that is calculated from simulations or measured experimentally [64].

3.5 Elastic Modulus

Two approaches are commonly used to calculate the elastic modulus from molecular-scale simulations [40]. In the first approach, molecular mechanics (MM), which is a static method, is used to predict the elastic tensor of epoxies [40, 42]. In this approach, the predicted elastic tensor is usually non-symmetric, and non-zero off-diagonal components are common due to the fact that the simulated system has relatively small dimensions to be considered a perfect isotropic material. This method was employed by Wu and Xu [40] to predict the bulk, elastic, and shear modulus of DGEBA/IPD epoxies, which were 15% higher than experimental predictions. This discrepancy is systematically observed between MM simulations and experiments. It is attributed to the ideally constructed epoxy structure and the chosen force field in the MM simulations. In the second approach, the epoxy moduli in different directions can be predicted from MD simulations. As summarized in Table 3, the elastic modulus of DGEBF systems as predicted from MD simulations is in the range of 2.258–3.2 GPa, and that of DGEBA systems is in the range of 1.10–8.5 GPa, which are in reasonable agreement with experimental measurements that are in the range of 2.34–3.1 GPa [5, 86].

It should be noted that there are conflicting reports in literature on the effect of the high strain rate imposed in MD simulations on the predicted elastic modulus [28, 31, 45, 83]. Moller et al. showed a log-linear dependence of the elastic modulus and yield strength on strain rate in an MD simulation of DGEBA [45]. Odegard et al. also showed that the elastic properties are over predicted in MD simulations due to the high strain rate discrepancy between simulation and experiments [28]. On the contrary, Li and Strachan indicate that in various thermoset systems, the elastic modulus is insensitive to strain rate, while the yield strength was strongly affected by it [83]. They argue that this is mainly due to the short relaxation time required for solid materials to relax in a small deformation region. Because of such conflicting reports on the effects of strain rate on the elastic response of epoxies, further research is needed on this topic. Nevertheless, the effect of strain rate usually plays a more important role in large deformation of epoxies [97].

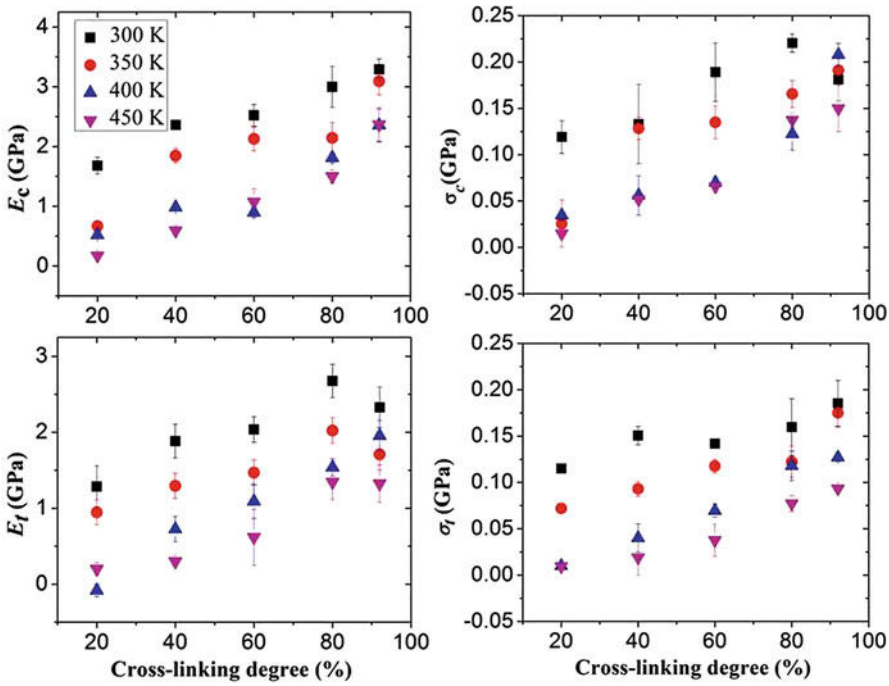

Fig. 7 Elastic modulus and yield stress, in compression (E_c, σ_t) and tension (E_t, σ_t) as a function of degree of cross-linking and temperature. (Reprint with permission from [44])

The elastic properties are also strongly correlated to the degree of cross-linking. Bandyopadhyay et al. predicted that the elastic mechanical properties increase with the increase in the degree of cross-linking for a DGEBF/DETDA system [49]. A similar trend was also observed for DGEBA/IPD systems [22, 44, 57] and DGEBF/TETA systems [22]. Bandyopadhyay et al. proposed that there exists a threshold in the degree of cross-linking, beyond which elastic property of epoxy has minimal effects. In their system the threshold was at 63% degree of cross-linking. Fu et al. also showed a slowed increment in modulus change at high degree of cross-linking as compared to lower degrees of cross-linking, as shown in Fig. 7.

3.6 Failure Properties

An MD simulation-predicted stress-strain curve in large deformation of an Epon 825 epoxy under tension loading is shown in Fig. 8. The stress-strain curve can be divided into three regimes before the failure point. This is a representative stress-strain curve from MD and CG-MD simulations of epoxies, with the extent of each regime changing depending on the epoxy system modeled, temperature, and strain

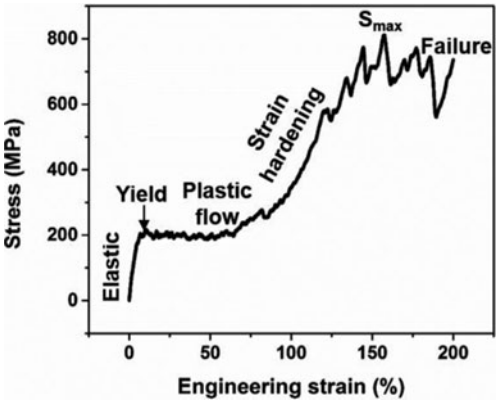

Fig. 8 A stress-strain curve of epoxy Epon 825 using a MD model. (Reprint with permission from [47])

rate imposed. In the first regime is an initial elastic deformation region, where stress arises mainly from Lennard-Jones attractive forces. In the second regime is a plateau regime, i.e., plastic flow, where stress is mostly constant over a range of strains. Here, the compact packed molecules are stretched in the deformation direction until they are mostly taut. Finally, in the third regime, strain hardening is induced by the stretch in covalent bonds. Covalent bonds start to break near the end of this stage and ultimately lead to the failure of the epoxy, which is indicated by the rapid decreasing stress at the end of the stress-strain curve [31, 45, 47].

It should be noted that to model fracture in large deformation from MD and CG-MD simulations, realistic bond breaking criteria should be upscaled from DFT simulations. For example, Barr et al. created a hybrid DFT/MM concurrent multiscale model to simulate bond breaking events in epoxy without predetermined bond breaking sites [98]. An alternative way of determining bond breaking sites is to use reactive MD methods such as ReaxFF force field [28, 47]. Furthermore, MD simulations indicate that the bonds around cross-linking sites are the ones most likely to break under deformation [45, 46, 62, 98].

It is important to note that both MD and CG-MD simulations generally show an extended plastic deformation and ductile failure for epoxies a [30, 31, 45, 47, 98], which is very different from the brittle failure mode observed in experiments (tensile failure strain is typically less than 7%) [86, 99, 100]. To explain this, Li et al. attributed the over 100% strain required for local failure of an epoxy system in MD simulations to the small simulation cell size and small time steps in the simulations [31]. On the other hand, Koo et al. proposed that the temperature caused rapid re-equilibrium of the deformation structure, which leads to the observed plastic flow and strain hardening stages. They conduct an MD study to deform a DGEBF/DETA system at absolute zero temperature to eliminate the temperature effect and predicted a stress-strain profile of an epoxy system with a yield strain below 10% and no strain hardening phase [50]. They further took strain rate effect into consideration and predicted a brittle failure of CNT/epoxy composites at near zero temperature and a high strain rate using RVE methods [53]. However, Tsige

and Stevens [60] argued that their molecular models were fully flexible (there is no stiffness of the strands), which allows for a higher packing density of the strands than in a realistic material, which explained the large strain of failure.

On the other hand, Wu et al. attributed the discrepancies between MD and CG-MD simulations with experiments to the frequency at which bonds are checked if they satisfy the bond breaking criterion or not and the percentage of bonds that are allowed to break during a given time step in the simulations [101]. They have shown that with increasing bond breaking percentage and bond checking frequency in the simulations, a more realistic response is achieved. However, performing the bond breaking checking every time step adds a significant computational cost in large simulations [101]. Additionally, at any given time step, if a large number of bonds that satisfy the bond breaking criteria are all allowed to break, then a large amount of energy would be instantaneously released into the system leading to an instability in the simulations [101]. Thus, overcoming these issues is important for predicting realistic responses of epoxies at high strain levels.

4 Multiscale Simulations of Epoxy Interfacial Properties

The advantages of using a multiscale simulations approach are demonstrated in predicting epoxy's interphase dominated properties and performances [52, 70]. Understandably the interphase strength depends on various factors, ranging from material chemistry in the interphase region to the operating conditions [102–104]. Finite element simulations (FEM) are usually the common method to simulate the overall material properties of epoxies with interfaces. The elastic-plastic constitutive formula used in FEM models requires input data not only of the bulk epoxy but also of the interphase region, and the latter are not commonly available in experimental measurements. In the following, multiscale simulation studies that account for the epoxy interphase region are reviewed in two general applications, nanocomposites/composites and coatings/adhesives.

4.1 Epoxy-Based Composites and the Interphase Region

Advanced polymer matrix composites (PMCs) are usually used for structural applications in aerospace, automotive, and marine industries. An in-depth understanding of the interphase region is especially crucial for PMC applications because the polymer matrix transfers load to the reinforcement fibers through these interphase regions. Most mechanical damage initiates in the interphase region and eventually leads to failure of the whole material. Thus, the interphase region is typically considered the weakest link in a PMC structure, and its properties largely determine the performance and failure of advanced PMCs.

Glass- and carbon-fiber reinforced epoxy composites have been widely studied both experimentally and computationally [8, 105]. One example is single and multiwall carbon nanotube (CNT)-reinforced nanocomposites, which are of interest because of their wide potential applications [23, 106, 107]. Although there is no chemical bonding between the CNT and epoxy, the electrostatic and van der Waals forces are strong enough to create a tightly bonded interface [23].

Putz et al. conducted dynamic scanning calorimetry (DSC) testing and showed that introducing multiwall CNTs in an epoxy matrix alters the T_g depending on the degrees of cross-linking of the matrix [8]. In particular, the inclusion of nanoparticles results in an increase/decrease in T_g at low/high degrees of cross-linking. From their observation, the authors proposed three mechanisms that can be used to explain the interphase phenomenon (see Fig. 9): (1) incomplete curing of the network near the interphase region induced by the limited mobility of the prepolymers and cross-linker leads to the formation of dangling unreacted end groups of epoxide chains; (2) the epoxy curing process is disrupted at the interphase region, and the formed network is different than the bulk epoxy; and (3) there is a retarded dynamic at the interphase so that epoxy forms a distinguished structure involving physical and/or chemical interactions with the fiber surfaces. All three mechanisms can happen at the interface region, and various simulation efforts have been conducted to understand the exact mechanisms, not only for T_g but also for structural and mechanical properties as well. Note that fiber/epoxy interface is different from fiber/plastic interface, as the latter has relatively long un-cross-linked polymer molecules and physical adsorption and wrapping are most likely to happen at the interface [108].

All-atom MD and CG-MD simulations of nanocomposites typically include one nano-sized fiber/particle and a surrounding epoxy matrix to represent a small region of the nanocomposites. The resulting material properties obtained from these simulations can be considered as local properties of the nanocomposites. Langeloth et al. [52] studied a DGEBA/DETA epoxy system as a bulk material and with a solid surface using CG-MD models. They found that T_g is a function of the conversion degree and it is a local material property that changes at a 3 nm region around the fiber (the interphase region). A multiscale study from Choi et al. [81] showed that a soft and slippery layer of a polymer at the CNT/DGEBA interface reduces the mechanical strength in the transverse and shear directions compared to neat epoxies. They have also bridged between the MD and FEM models using an iterative matching process to obtain key parameters (i.e., interphase thickness of 1.14–1.92 nm and strain energy density) for the FEM model (see Fig. 10a). Kim et al. also used a matching process between MD and a continuum model to create an effective interphase region between silica particle and epoxy matrix [22]. They found the interface structural conformation to depend on the degree of cross-linking of the epoxy. Liu et al. proposed a novel multiscale simulation approach that combined MD and CG-MD simulations to create a cured epoxy network with a carbon fiber substrate and investigated the diffusion effect on the cured structure [109]. Based on Koo et al.'s work of neat epoxy [50], Subramanian et al. created an MD simulation of CNT/epoxy nanocomposites and modeled its fracture behaviors

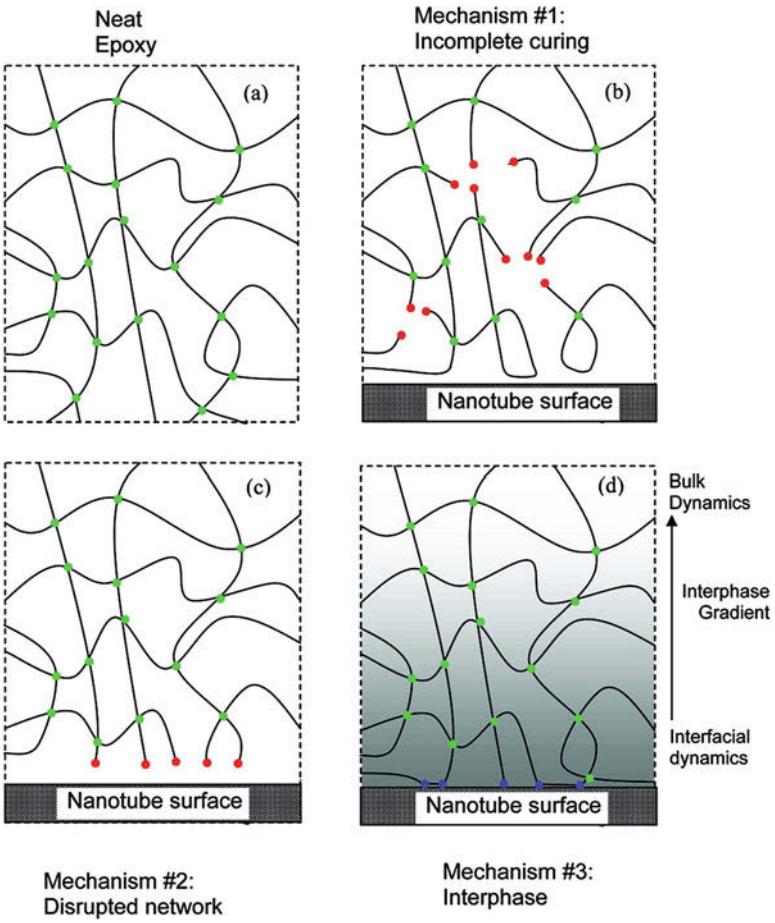

Fig. 9 Schematic representations of three proposed mechanisms that control T_g changes in epoxy nanocomposites [8]. (**a**) The fully cured neat epoxy. The green dots represent covalent cross-links. (**b**) Mechanism #1: incomplete curing of the network near the interphase region. Dangling unreacted end groups of epoxide chains are shown by red dots. (**c**) Mechanism #2: the epoxy curing process is disrupted at the interphase region leading to a different network than the bulk epoxy. (**d**) Mechanism #3: retarded dynamic at the interphase so that epoxy forms a distinguish structure involves physical and/or chemical interaction with the fiber surfaces. (Reprint with permission from [8])

via incorporating the bond disassociation energy from MD to a damage mechanics model for a microscale simulation [53]. Buyukozturk et al. used an MD model to understand the debonding between silica and epoxy at the molecular level and found the influence of the water environment [61]. Yu and et al. [57] focused their study on the nanoparticle size effects on the mechanical properties of alumina reinforced epoxy matrix nanocomposites.

Based on the above literature, interphase thickness and their corresponding properties (i.e., interface stiffness) are key factors in creating a multiscale simulation model [110]. The interphase thickness can be determined from density variation near the fiber surface. At the interface of the polymer matrix and nanoparticles, there is usually a layered mass distribution (as shown in Fig. 10b), from which the interphase thickness can be calculated [22, 69]. Schadler [111] points out the interfacial depth depends on the reinforcement particle size and the interaction between the matrix and particle [54]. For example, the reported interface of DGEBF epoxy nanocomposites is 0.64–0.69 nm, comparable to the 0.6–1.0 nm Al_2O_3 particle size [57]. The interface of a DGEBF matrix is 0.29–0.34 nm, comparable to the 0.7–1.4 nm CNT particle size [81]. The interphase of a DGEBF system is 2.2 nm and is comparable to the size of the silica particles 1.01 nm [22]. Depending on the configuration of the simulated system, an interface can be as large as 250 nm, which is half of the spacing between particles in some cases [111].

After determining the thickness and properties of the interphase region, material properties predicted from MD or CG-MD can then be upscaled into FEM models via a numerical homogenization method, i.e., representative volume element (RVE) method. An RVE model can effectively account for the structure variation through a large material size and bring small localized material properties predicted by all-atom MD or CG-MD models into microscale and macroscale level continuum models [53, 112]. The basic concept of an RVE is to discretize a cubic FEM matrix domain into unit cells, and each unit cell is corresponding to a fiber/epoxy system. Stochasticity is considered in the FEM model via a random sampling process, so that each unit cell has different fiber fractions and degrees of cross-linking of epoxies. The overall FEM model thus can be used to simulate a macroscale material with various local material properties. Figure 11a shows a work conducted by Mortazavi et al., where they used the RVE method to incorporate MD-simulated thermal conductivity of graphene/epoxy nanocomposites to a FEM microscale composite model with 10% volume fraction of unidirectional graphene fibers and predict its anisotropic thermal conductivity. The macroscale thermal properties of graphene reinforced epoxy composites were then predicted using a larger FEM model with 20^3 elements and randomly assigned thermal properties predicted from RVEs in each element, as shown by different colors in Fig. 11b. The latter model predicted isotropic thermal properties of the material and demonstrated that RVE method can be used to achieve homogenization in nanocomposite modeling [55, 74]. Kim et al. also used the RVE method combined with MD simulation and simulated mechanical deformation of a SiC/epoxy nanocomposites [22, 56]. Subramanian et al. used RVE method simulating the fracture of CNT/epoxy nanocomposites [53]. Other analytical-based homogenization methods are also used in many multiscale simulation of polymer composites, but they are not yet commonly used for epoxy systems [63].

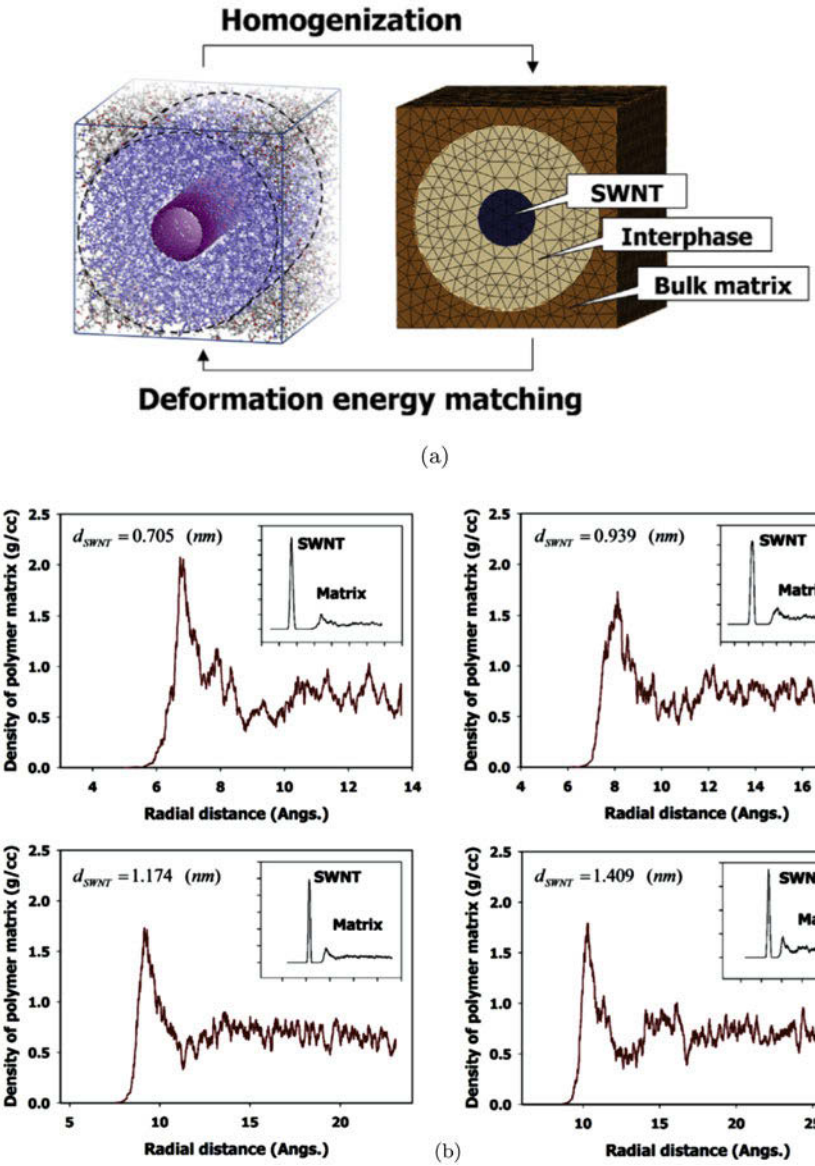

Fig. 10 (**a**) An MD-FEM bridged multiscale simulation method characterizing the thickness and strain energy density of an effective interphase of CNT/epoxy nanocomposites. (**b**) Radial density distribution of epoxy matrix in a nanocomposite unit cell with CNT particles of different radii. The inset in each figure is the overall density distribution. (Reprint with permission from [81])

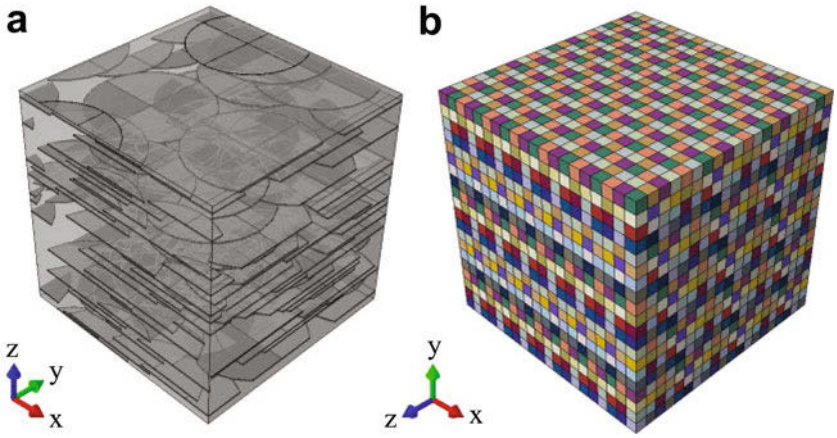

Fig. 11 An example of using the RVE method to bring MD simulation results into macroscale FEM models. (**a**) A finite element RVE model of graphene/DGEBA epoxy nanocomposite is created, and MD-predicted interphase properties are incorporated using thermal conductance contact elements. (**b**) The anisotropic thermal conductivity predicted by RVE models are randomly assigned to a larger FEM model with discretized unit cells. This model then predicts isotropic thermal properties of the epoxy-based composites, which represents macroscale materials. (Reprint with permission from [55])

4.2 Coatings and Adhesives

Coating and adhesives are two other application examples where the interphase region plays an important role. Yarovsky and Evans used MD simulations to predict the interface properties between low molecular weight water-soluble epoxy primer coating and inorganic alumina substrates [39]. They reported that the shrinkage of CYMEL epoxy leads to a high density coating, which prevents the penetration of molecules and reduced the damage to the coated metal substrates. The increased adhesion between epoxy and alumina was caused by interfacial hydrogen bonds. Stevens [62, 113] studied the interphase strength, particularly the fracture mechanics and failure mode at the interface between bisphenol A (BPA) epoxy and silicon wafer. Yang et al. simulated EPN epoxy coating on copper using both MD and CG-MD models. In neat epoxy, they found the polymer stands were stretched to their taut positions before fracture, which is in agreement with Stevens' theory [62, 66, 67]. Yang et al. also found a brittle failure of this substrate/coating system which was caused by the debonding of epoxy from the copper substrate [58]. Using CG model, they further observed that plastic deformation is localized to the epoxy region near the epoxy/copper interface [69]. Bahlakeh and Ramezanzadeh [59] simulated DGEBA as a coating on a steel (Fe) surface via MD simulation and compared adhesion properties to experiments. Their results provided useful information on surface treatment selection for the purpose of enhancing the interfacial bonding and minimizing the underlying cause of weak surface bonding.

Finally, Tsige and Stevens showed that the density of interfacial bonds determines the fracture mode of DGEBA/solid surface system, and the tensile and shear stresses were predicted as functions of interfacial bonds [60].

5 Summary and Conclusions

In summary, all-atom MD and CG-MD simulations are the most common modeling approaches to investigate the molecular structural and the thermal and mechanical properties of epoxy bulk materials. However, when the desired simulation length and time scales are large (e.g., simulations of epoxy-matrix composites), multiscale simulation methods are required [83].

The most common multiscale approach involves first the utilization of DFT simulations to quantify the bond breaking conditions (i.e., critical length) [98], as well as to create molecular force fields [27]. These results provide inputs for all-atom MD or CG-MD simulations. All-atom MD simulations are commonly used to predict epoxy properties at the atomic scale with the goal to use the predicted values as inputs to larger length/time scale models [44], or to reveal quantify relevant molecular-scale mechanisms in order to explain macroscale observed phenomena [43, 61]. However, the common challenges facing all-atom MD simulations is how to interpret the results in the relevant length/time scales and compare the simulated properties directly with macroscale experiments. On the other hand, CG-MD simulations are ideal to create larger simulation domains on the scale of the spacing between fibers/particles in composites [52, 70, 109]. In plastics, soft matter, and biomaterial simulations, CG-MD simulations have been very popular in modeling material mesoscale structures [114–116]; however, it is still in the development stages for epoxy simulations. Finally, FEM simulations have the advantage of simulating a microscale material with heterogeneous local properties, with the RVE method used commonly to help bring atomic information to continuum models.

The advantages of multiscale simulation of epoxy can be summarized as follows:

1. Provide mechanistic understanding of the molecular-scale origins of observed macroscopic material properties, which enriches our understanding of epoxy materials.
2. For specific nanoscale materials, such as nanocomposites, accurate and well-validated simulation models provide a less expensive means to study and test materials than experiments and with a high resolution.
3. Simulation at all scales can be used for examining material response under extreme condition including temperature and pressure, where lab setup of such tests can be difficult or time-consuming.
4. For the purpose of screening, design, and optimization of new materials, and tailoring material properties of existing materials, simulation is a very effective method and compliments well to experiments.

The last two points are in fact the main driving forces behind the research and development of multiscale modeling of epoxy. Future development of multiscale simulation of epoxy should focus on continuing developing computational models at all relevant scales and pushing the limits in bridging different scales to simulate microscale epoxy-based systems.

References

1. R.A. Dickie, S.S. Labana, R.S. Bauer (eds.), *Cross-Linked Polymers: Chemistry, Properties, and Applications* (American Chemical Society, Washington DC 1988)
2. C. May, *Epoxy Resins: Chemistry and Technology* (CRC Press, New York 1988)
3. F.-L. Jin, X. Li, S.-J. Park, Synthesis and application of epoxy resins: a review. J. Indus. Eng. Chem. **29**, 1–11 (2015)
4. K. Dušek, Network formation in curing of epoxy resins, in *Epoxy Resins and Composites III* (Springer, 1986), pp. 1–59
5. O. Becker, Y.-B. Cheng, R.J. Varley, G.P. Simon, Layered silicate nanocomposites based on various high-functionality epoxy resins: the influence of cure temperature on morphology, mechanical properties, and free volume. Macromolecules **36**(5), 1616–1625 (2003)
6. J. Jordan, K.I. Jacob, R. Tannenbaum, M.A. Sharaf, I. Jasiuk, Experimental trends in polymer nanocomposites'a review. Mater. Sci. Eng. A **393**(1–2), 1–11 (2005)
7. J. Jancar, J.F. Douglas, F.W. Starr, S.K. Kumar, P. Cassagnau, A.J. Lesser, S.S. Sternstein, M.J. Buehler, Current issues in research on structure–property relationships in polymer nanocomposites. Polymer **51**(15), 3321–3343 (2010)
8. K.W. Putz, M.J. Palmeri, R.B. Cohn, R. Andrews, L.C. Brinson, Effect of cross-link density on interphase creation in polymer nanocomposites. Macromolecules **41**(18), 6752–6756 (2008)
9. A.A. Azeez, K.Y. Rhee, S.J. Park, D. Hui, Epoxy clay nanocomposites–processing, properties and applications: a review. Compos. Part B Eng. **45**(1), 308–320 (2013)
10. T.A. Nguyen, T.H. Nguyen, T.V. Nguyen, H. Thai, X. Shi, Effect of nanoparticles on the thermal and mechanical properties of epoxy coatings. J. Nanosci. Nanotechnol. **16**, 9874–9881 (2016)
11. J. Arbaoui, H. Moustabchir, J.R. Vigué, F.-X. Royer, The effects of various nanoparticles on the thermal and mechanical properties of an epoxy resin. Mater. Res. Innov. **20**, 145–150 (2016)
12. J.B. Enns, J.K. Gillham, Effect of the extent of cure on the modulus, glass transition, water absorptio, and density of an amine-cured epoxy. J. Appl. Polym. Sci. **28**(9), 2831–2846 (1983)
13. M. Cizmecioglu, A. Gupta, R.F. Fedors, Influence of cure conditions on glass transition temperature and density of an epoxy resin. J. Appl. Polym. Sci. **32**(8), 6177–6190 (1986)
14. E.D. Crawford, A.J. Lesser, Brittle to ductile: fracture toughness mapping on controlled epoxy networks. Polym. Eng. Sci. **39**(2), 385–392 (1999)
15. C. Czaderski, E. Martinelli, J. Michels, M. Motavalli, Effect of curing conditions on strength development in an epoxy resin for structural strengthening. Compos. Part B Eng. **43**(2), 398–410 (2012)
16. C. Li, G.A. Medvedev, E.-W. Lee, J. Kim, J.M. Caruthers, A. Strachan, Molecular dynamics simulations and experimental studies of the thermomechanical response of an epoxy thermoset polymer. Polymer **53**(19), 4222–4230 (2012)
17. Q. Deng, Y.C. Jean, Free-volume distributions of an epoxy polymer probed by positron annihilation: pressure dependence. Macromolecules **26**, 30–34 (1988)
18. S.J. Wang, C.L. Wang, B. Wang, Microstructure and mechanical properties of polymers studied by positron annihilation. J. Radioanal. Nucl. Chem. **210**, 407–421 (1996)

19. T. Yang, Mechanical and swelling properties of hydrogels. Ph.D. thesis, Royal Institute of Technology in Stockholm (2012)
20. C.L. Sherman, R.C. Zeigler, N.E. Verghese, M.J. Marks, Structure–property relationships of controlled epoxy networks with quantified levels of excess epoxy etherification. Polymer **49**(5), 1164–1172 (2008)
21. S. Morsch, Y. Liu, S.B. Lyon, S.R. Gibbon, Insights into epoxy network nanostructural heterogeneity using afm-ir. ACS Appl. Mater. Interfaces **8**(1), 959–966 (2015)
22. B. Kim, J. Choi, S. Yang, S. Yu, M. Cho, Multiscale modeling of interphase in crosslinked epoxy nanocomposites. Compos. Part B **120**, 128–142 (2017)
23. M. Wong, M. Paramsothy, X.J. Xu, Y. Ren, S. Li, K. Liao, Physical interactions at carbon nanotube-polymer interface. Polymer **44**(25), 7757–7764 (2003)
24. H.B. Fan, M.M.F. Yuen, Material properties of the cross-linked epoxy resin compound predicted by molecular dynamics simulation. Polymer **48**(7), 2174–2178 (2007)
25. C.F. Wu, W.J. Xu, Atomistic molecular modelling of crosslinked epoxy resin. Polymer **48**, 6004 (2006)
26. S. Yang, Z. Cui, J. Qu, A coarse-grained model for epoxy molding compound. J. Phys. Chem. B **118**, 1660–1669 (2014)
27. A. Aramoon, T.D. Breitzman, C. Woodward, J.A. El-Awady, Coarse-grained molecular dynamics study of the curing and properties of highly cross-linked epoxy polymers. J. Phys. Chem. B **120**(35), 9495–9505 (2016)
28. G.M. Odegard, B.D. Jensen, S. Gowtham, J. Wu, J. He, Z. Zhang, Predicting mechanical response of crosslinked epoxy using reaxff. Chem. Phys. Lett. **591**, 175–178 (2014)
29. A. Vashisth, C. Ashraf, C.E. Bakis, A.C.T. van Duin, Effect of chemical structure on thermo-mechanical properties of epoxy polymers: comparison of accelerated reaxff simulations and experiments. Polymer **158**, 354–363 (2018)
30. M. Panico, S. Narayanan, L.C. Brinson, Simulations of tensile failure in glassy polymers: effect of cross-link density. Model. Simul. Mater. Sci. Eng. **18**(5), 055005 (2010)
31. C. Li, A. Strachan, Molecular dynamics predictions of thermal and mechanical properties of thermoset polymer epon862/detda. Polymer **52**(13), 2920–2928 (2011)
32. K. Friedrich, T. Goda, K. Varadi, B. Wetzel, Finite element simulation of the fiber–matrix debonding in polymer composites produced by a sliding indentor: Part I – normally oriented fibers. J. Compos. Mater. **38**(18), 1583–1606 (2004)
33. A.R. Maligno, N.A. Warrior, A.C. Long, Finite element investigations on the microstructure of fibre-reinforced composites. Express Polym. Lett. **2**(9), 665–676 (2008)
34. D. Esqué-de los Ojos, R. Ghisleni, A. Battisti, G. Mohanty, J. Michler, J. Sort, A.J. Brunner, Understanding the mechanical behavior of fiber/matrix interfaces during push-in tests by means of finite element simulations and a cohesive zone model. Comput. Mater. Sci. **117**, 330–337 (2016)
35. M.M. Moure, S.K. Garcí-a-Castillo, S. Sánchez-Sáez, E. Barbero, E.J. Barbero, Matrix cracking evolution in open-hole laminates subjected to thermo-mechanical loads. Compos. Struct. **183**, 510–520 (2018)
36. G. Allegra, G. Raos, M. Vacatello, Theories and simulations of polymer-based nanocomposites: from chain statistics to reinforcement. Prog. Polym. Sci. **33**(7), 683–731 (2008)
37. A. Karatrantos, N. Clarke, M. Kröger, Modeling of polymer structure and conformations in polymer nanocomposites from atomistic to mesoscale: a review. Polym. Rev. **56**(3), 385–428 (2016)
38. Q.H. Zeng, A.B. Yu, G.Q. Lu, Multiscale modeling and simulation of polymer nanocomposites. Prog. Polym. Sci. **33**(2), 191–269 (2008)
39. I. Yarovsky, E. Evans, Computer simulation of structure and properties of crosslinked polymers: application to epoxy resins. Polymer **43**(3), 963–969 (2002)
40. C. Wu, W. Xu, Atomistic molecular modelling of crosslinked epoxy resin. Polymer **47**(16), 6004–6009 (2006)

41. J.L. Tack, D.M. Ford, Thermodynamic and mechanical properties of epoxy resin DGEBF crosslinked with DETDA by molecular dynamics. J. Mol. Graph. Model. **26**(8), 1269–1275 (2008)
42. A. Shokuhfar, B. Arab, The effect of cross linking density on the mechanical properties and structure of the epoxy polymers: molecular dynamics simulation. J. Mol. Model. **19**(9), 3719–3731 (2013)
43. L. Gao, Q. Zhang, H. Li, S. Yu, W. Zhong, G. Sui, X. Yang, Effect of epoxy monomer structure on the curing process and thermo-mechanical characteristics of tri-functional epoxy/amine systems: a methodology combining atomistic molecular simulation with experimental analyses. Polym. Chem. **8**(13), 2016–2027 (2017)
44. Y. Fu, J.G. Michopoulos, J.-H. Song, On investigating the thermomechanical properties of cross-linked epoxy via molecular dynamics analysis. Nanoscale Microscale Thermophys. Eng. **21**(1), 8–25 (2017)
45. J.C. Moller, S.A. Barr, E.J. Schultz, T.D. Breitzman, R.J. Berry, Simulation of fracture nucleation in cross-linked polymer networks. JOM **65**(2), 147–167 (2013)
46. J.C. Moller, G.S. Kedziora, S.A. Barr, T.D. Breitzman, R.J. Berry, Atomistic prediction of plane stress behavior of glassy thermosets. Comput. Mater. Sci. **128**, 257–277 (2017)
47. Z. Meng, M.A. Bessa, W. Xia, W. Kam Liu, S. Keten, Predicting the macroscopic fracture energy of epoxy resins from atomistic molecular simulations. Macromolecules **49**(24), 9474–9483 (2016)
48. T. Okabe, Y. Oya, K. Tanabe, G. Kikugawa, K. Yoshioka, Molecular dynamics simulation of crosslinked epoxy resins: curing and mechanical properties. Eur. Polym. J. **80**, 78–88 (2016)
49. A. Bandyopadhyay, P.K. Valavala, T.C. Clancy, K.E. Wise, G.M. Odegard, Molecular modeling of crosslinked epoxy polymers: the effect of crosslink density on thermomechanical properties. Polymer **52**(11), 2445–2452 (2011)
50. B. Koo, N. Subramanian, A. Chattopadhyay, Molecular dynamics study of brittle fracture in epoxy-based thermoset polymer. Compos. Part B Eng. **95**, 433–439 (2016)
51. V. Varshney, S.S. Patnaik, A.K. Roy, B.L. Farmer, A molecular dynamics study of epoxy-based networks: cross-linking procedure and prediction of molecular and material properties. Macromolecules **41**(18), 6837–6842 (2008)
52. M. Langeloth, T. Sugii, M.C. Böhm, F. Müller-Plathe, The glass transition in cured epoxy thermosets: a comparative molecular dynamics study in coarse-grained and atomistic resolution. J. Chem. Phys. **143**(24), 243158 (2015)
53. N. Subramanian, B. Koo, A. Rai, A. Chattopadhyay, Molecular dynamics-based multiscale damage initiation model for cnt/epoxy nanopolymers. J. Mater. Sci. **53**(4), 2604–2617 (2018)
54. Z. Wang, Q. Lv, S. Chen, C. Li, S. Sun, S. Hu, Effect of interfacial bonding on interphase properties in sio2/epoxy nanocomposite: a molecular dynamics simulation study. ACS Appl. Mater. Interfaces **8**(11), 7499–7508 (2016)
55. B. Mortazavi, O. Benzerara, H. Meyer, J. Bardon, S. Ahzi, Combined molecular dynamics-finite element multiscale modeling of thermal conduction in graphene epoxy nanocomposites. Carbon **60**, 356–365 (2013)
56. B. Kim, J. Choi, H. Shin, M. Cho, Multiscale study on load transfer of epoxy nanocomposites, in *21st International Conference on Composite Materials* (2017)
57. S. Yu, S. Yang, M. Cho, Multi-scale modeling of cross-linked epoxy nanocomposites. Polymer **50**(3), 945–952 (2009)
58. S. Yang, F. Gao, J. Qu, A molecular dynamics study of tensile strength between a highly-crosslinked epoxy molding compound and a copper substrate. Polymer **54**(18), 5064–5074 (2013)
59. G. Bahlakeh, B. Ramezanzadeh, A detailed molecular dynamics simulation and experimental investigation on the interfacial bonding mechanism of an epoxy adhesive on carbon steel sheets decorated with a novel cerium–lanthanum nanofilm. ACS Appl. Mater. Interfaces **9**(20), 17536–17551 (2017)

60. M. Tsige, M.J. Stevens, Effect of cross-linker functionality on the adhesion of highly cross-linked polymer networks: a molecular dynamics study of epoxies. Macromolecules **37**(2), 630–637 (2004)
61. O. Büyüköztürk, M.J. Buehler, D. Lau, C. Tuakta, Structural solution using molecular dynamics: fundamentals and a case study of epoxy-silica interface. Int. J. Solids Struct. **48**(14–15), 2131–2140 (2011)
62. M.J. Stevens, Interfacial fracture between highly cross-linked polymer networks and a solid surface: effect of interfacial bond density. Macromolecules **34**(8), 2710–2718 (2001)
63. Y. Li, B. Abberton, M. Kröger, W. Liu, Challenges in multiscale modeling of polymer dynamics. Polymers **5**(2), 751–832 (2013)
64. A. Aramoon, T.D. Breitzman, C. Woodward, J.A. El-Awady, Correlating free-volume hole distribution to the glass transition temperature of epoxy polymers. J. Phys. Chem. B **121**(35), 8399–8407 (2017)
65. K.S. Khare, R. Khare, Directed diffusion approach for preparing atomistic models of crosslinked epoxy for use in molecular simulations. Macromol. Theory Simul. **21**(5), 322–327 (2012)
66. S. Yang, J. Qu, Coarse-grained molecular dynamics simulations of the tensile behavior of a thermosetting polymer. Phys. Rev. E **90**(1), 012601 (2014)
67. S. Yang, Z. Cui, J. Qu, A coarse-grained model for epoxy molding compound. J. Phys. Chem. B **118**(6), 1660–1669 (2014)
68. Y. Fu, J. Michopoulos, J.-H. Song, Coarse-grained molecular dynamics simulations of epoxy resin during the curing process. Comput. Mater. Sci. **107**, 24–32 (2015)
69. S. Yang, J. Qu, An investigation of the tensile deformation and failure of an epoxy/cu interface using coarse-grained molecular dynamics simulations. Model. Simul. Mater. Sci. Eng. **22**(6), 065011 (2014)
70. A.V.S.S. Prasad, T. Grover, S. Basu, Coarse–grained molecular dynamics simulation of cross–linking of dgeba epoxy resin and estimation of the adhesive strength. Int. J. Eng. Sci. Technol. **2**(4), 17–30 (2010)
71. A.J.M. Jasso, J.E. Goodsell, A.J. Ritchey, R.B. Pipes, M. Koslowski, A parametric study of fiber volume fraction distribution on the failure initiation location in open hole off-axis tensile specimen. Compos. Sci. Technol. **71**(16), 1819–1825 (2011)
72. H.W. Wang, H.W. Zhou, R.D. Peng, L. Mishnaevsky Jr, Nanoreinforced polymer composites: 3D FEM modeling with effective interface concept. Compos. Sci. Technol. **71**(7), 980–988 (2011)
73. J. Bienias, H. Debski, B. Surowska, T. Sadowski, Analysis of microstructure damage in carbon/epoxy composites using FEM. Comput. Mater. Sci. **64**, 168–172 (2012)
74. B. Mortazavi, J. Bardon, S. Ahzi, Interphase effect on the elastic and thermal conductivity response of polymer nanocomposite materials: 3D finite element study. Comput. Mater. Sci. **69**, 100–106 (2013)
75. Dassault Systemes (2016) Abaqus. Retrieve from http://www.3ds.com/products-services/simulia/products/abaqus/
76. P.P. Camanho, C.G. Dávila, Mixed-mode decohesion finite elements for the simulation of delamination in composite materials. NASA/TM-2002–211737 (2002)
77. S. Li, M.D. Thouless, A.M. Waas, J.A. Schroeder, P.D. Zavattieri, Use of mode-i cohesive-zone models to describe the fracture of an adhesively-bonded polymer-matrix composite. Compos. Sci. Technol. **65**(2), 281–293 (2005)
78. G. Giuliese, R. Palazzetti, F. Moroni, A. Zucchelli, A. Pirondi, Cohesive zone modelling of delamination response of a composite laminate with interleaved nylon 6,6 nanofibres. Compos. Part B Eng. **78**, 384–392 (2015)
79. J. Fish, Q. Yu, K. Shek, Computational damage mechanics for composite materials based on mathematical homogenization. Int. J. Numer. Methods Eng. **45**(11), 1657–1679 (1999)
80. G.Z. Voyiadjis, P.I. Kattan, Z.N. Taqieddin, Continuum approach to damage mechanics of composite materials with fabric tensors. Int. J. Damage Mech. **16**(3), 301–329 (2007)

81. J. Choi, H. Shin, M. Cho, A multiscale mechanical model for the effective interphase of SWNT/epoxy nanocomposite. Polymer **89**, 159–171 (2016)
82. J. Choi, H. Shin, S. Yang, M. Cho, The influence of nanoparticle size on the mechanical properties of polymer nanocomposites and the associated interphase region: a multiscale approach. Compos. Struct. **119**, 365–376 (2015)
83. C. Li, A. Strachan, Molecular scale simulations on thermoset polymers: a review. J. Polym. Sci. B Polym. Phys. **53**(2), 103–122 (2015)
84. P.V. Komarov, C. Yu-Tsung, C. Shih-Ming, P.G. Khalatur, P. Reineker, Highly cross-linked epoxy resins: an atomistic molecular dynamics simulation combined with a mapping/reverse mapping procedure. Macromolecules **40**(22), 8104–8113 (2007)
85. D.R. Heine, G.S. Grest, C.D. Lorenz, M. Tsige, M.J. Stevens, Atomistic simulations of end-linked poly (dimethylsiloxane) networks: structure and relaxation. Macromolecules **37**(10), 3857–3864 (2004)
86. F.G. Garcia, B.G. Soares, V.J.R.R. Pita, R. Sánchez, J. Rieumont, Mechanical properties of epoxy networks based on dgeba and aliphatic amines. J. Appl. Polym. Sci. **106**(3), 2047–2055 (2007)
87. J.L. Tack, Thermodynamic and mechanical properties of EPON 862 with curing agent detda by molecular simulation. Technical report, Texas A and M University College Station, Department of Chemical Engineering (2006)
88. L. Sun, G.L. Warren, J.Y. O'reilly, W.N. Everett, S.M. Lee, D. Davis, D. Lagoudas, H.-J. Sue, Mechanical properties of surface-functionalized swcnt/epoxy composites. Carbon **46**(2), 320–328 (2008)
89. Y. Zhou, F. Pervin, L. Lewis, S. Jeelani, Experimental study on the thermal and mechanical properties of multi-walled carbon nanotube-reinforced epoxy. Mater. Sci. Eng. A **452**, 657–664 (2007)
90. N.B. Shenogina, M. Tsige, S.S. Patnaik, S.M. Mukhopadhyay, Molecular modeling approach to prediction of thermo-mechanical behavior of thermoset polymer networks. Macromolecules **45**(12), 5307–5315 (2012)
91. B. Burton, D. Alexander, H. Klein, A. Garibay-Vasquez, A. Pekarik, C. Henkee, Epoxy formulations using jeffamine polyetheramines (2005)
92. H.J. Zhang, S. Sellaiyan, T. Kakizaki, A. Uedono, Y. Taniguchi, K. Hayashi, Effect of free-volume holes on dynamic mechanical properties of epoxy resins for carbon-fiber-reinforced polymers. Macromolecules **50**(10), 3933–3942 (2017)
93. G. Dlubek, E.M. Hassan, R. Krause-Rehberg, J. Pionteck, Free volume of an epoxy resin and its relation to structural relaxation: evidence from positron lifetime and pressure-volume-temperature experiments. Phys. Rev. E **73**(3), 031803 (2006)
94. A. Aramoon, A multiscale ccomputational framework to predict deformation and failure in polymer matrix composites. Ph.D thesis, Johns Hopkins University (2016)
95. Q. Deng, Y.C. Jean, Free-volume distributions of an epoxy polymer probed by positron annihilation: pressure dependence. Macromolecules **26**(1), 30–34 (1993)
96. Y.C. Jean, Q. Deng, Direct measurement of free-volume hole distributions in polymers by using a positronium probe. J. Polym. Sci. B Polym. Phys. **30**(12), 1359–1364 (1992)
97. S. Tamrakar, R. Ganesh, S. Sockalingam, B.Z. Haque, J.W. Gillespie, Experimental investigation of strain rate and temperature dependent response of an epoxy resin undergoing large deformation. J. Dyn. Behav. Mater. **4**(1), 114–128 (2018)
98. S.A. Barr, G.S. Kedziora, A.M. Ecker, J.C. Moller, R.J. Berry, T.D. Breitzman, Bond breaking in epoxy systems: a combined qm/mm approach. J. Chem. Phys. **144**(24), 244904 (2016)
99. B. Fiedler, M. Hojo, S. Ochiai, K. Schulte, M. Ando, Failure behavior of an epoxy matrix under different kinds of static loading. Compos. Sci. Technol. **61**(11), 1615–1624 (2001)
100. A. Gilat, R.K. Goldberg, G.D. Roberts, Strain rate sensitivity of epoxy resin in tensile and shear loading. J. Aerosp. Eng. **20**(2), 75–89 (2007)
101. X. Wu, A. Aramoon, J.A. El-Awady, A hierarchical multiscale approach for modeling the deformation and failure of epoxy-based polymer matrix composites. Under Review (2019)

102. A.T. DiBenedetto, Tailoring of interfaces in glass fiber reinforced polymer composites: a review. Mater. Sci. Eng. A **302**(1), 74–82 (2001)
103. D.G.D. Galpaya, J.F.S. Fernando, L. Rintoul, N. Motta, E.R. Waclawik, C. Yan, G.A. George, The effect of graphene oxide and its oxidized debris on the cure chemistry and interphase structure of epoxy nanocomposites. Polymer **71**, 122–134 (2015)
104. Y. Gan, Effect of interface structure on mechanical properties of advanced composite materials. Int. J. Mol. Sci. **10**(12), 5115–5134 (2009)
105. M. Wang, N. Pan, Predictions of effective physical properties of complex multiphase materials. Mater. Sci. Eng. R. Rep. **63**(1), 1–30 (2008)
106. J. Zhu, H. Peng, F. Rodriguez-Macias, J.L. Margrave, V.N. Khabashesku, A.M. Imam, K. Lozano, E.V. Barrera, Reinforcing epoxy polymer composites through covalent integration of functionalized nanotubes. Adv. Funct. Mater. **14**(7), 643–648 (2004)
107. Z. Wang, Z. Liang, B. Wang, C. Zhang, L. Kramer, Processing and property investigation of single-walled carbon nanotube (SWNT) buckypaper/epoxy resin matrix nanocomposites. Compos. Part A Appl. Sci. Manuf. **35**(10), 1225–1232 (2004)
108. M. Yang, V. Koutsos, M. Zaiser, Interactions between polymers and carbon nanotubes: a molecular dynamics study. J. Phys. Chem. B **109**(20), 10009–10014 (2005)
109. H. Liu, M. Li, Z.-Y. Lu, Z.-G. Zhang, C.-C. Sun, T. Cui, Multiscale simulation study on the curing reaction and the network structure in a typical epoxy system. Macromolecules **44**(21), 8650–8660 (2011)
110. S. Kari, H. Berger, U. Gabbert, R. Guinovart-Dıaz, J. Bravo-Castillero, R. Rodrıguez-Ramos, Evaluation of influence of interphase material parameters on effective material properties of three phase composites. Combust. Sci. Technol. **68**(3–4), 684–691 (2008)
111. L. Schadler, Nanocomposites: model interfaces. Nat. Mater. **6**(4), 257 (2007)
112. N. Subramanian, A. Rai, A. Chattopadhyay, Atomistically informed stochastic multiscale model to predict the behavior of carbon nanotube-enhanced nanocomposites. Carbon **94**, 661–672 (2015)
113. M.J. Stevens, Manipulating connectivity to control fracture in network polymer adhesives. Macromolecules **34**(5), 1411–1415 (2001)
114. E. Brini, E.A. Algaer, P. Ganguly, C. Li, F. Rodríguez-Ropero, N.F.A. van der Vegt, Systematic coarse-graining methods for soft matter simulations–a review. Soft Matter **9**(7), 2108–2119 (2013)
115. A.J. Liu, G.S. Grest, M.C. Marchetti, G.M. Grason, M.O. Robbins, G.H. Fredrickson, M. Rubinstein, M.O. De La Cruz, Opportunities in theoretical and computational polymeric materials and soft matter. Soft Matter **11**(12), 2326–2332 (2015)
116. S.O. Nielsen, C.F. Lopez, G. Srinivas, M.L. Klein, Coarse grain models and the computer simulation of soft materials. J. Phys. Condens. Matter **16**(15), R481 (2004)

Microstructural Statistics Informed Boundary Conditions for Statistically Equivalent Representative Volume Elements (SERVEs) of Polydispersed Elastic Composites

Somnath Ghosh, Dhirendra V. Kubair, and Craig Przybyla

1 Introduction

The representative volume element or *RVE* of a heterogeneous material is an optimally representative microstructural subdomain, with morphological characteristics and effective response similar to that of the entire microstructure [1–5]. Direct numerical simulations of the RVE are essential for determining higher length-scale homogenized constitutive models without having to solve the larger microstructural domains. Homogenization involves averaging principles like the Hill-Mandel condition [6] with assumptions of scale separation, along with energy equivalence of the microstructural RVE and the homogenized medium under equivalent loading conditions. Computational homogenization from micromechanical analysis of complex microstructures is now quite common [7–10]. Most of the analyses assume periodic repetition of the RVE to uncouple governing equations at different scales. Furthermore, the uncoupling process requires specific boundary conditions like uniform displacement, traction, or periodicity on the RVE boundaries. Asymptotic expansion-based computational homogenization methods with assumptions of macroscopic homogeneity and microscopic periodicity have found extensive applications in [9, 11–16]. Analogously, the FE^2 multi-scale methods [17]

S. Ghosh (✉)
Departments of Civil, Mechanical Engineering and Materials Science & Engineering, Johns Hopkins University, Baltimore, MD, USA
e-mail: sghosh20@jhu.edu

D. V. Kubair
Department of Civil Engineering, Johns Hopkins University, Baltimore, MD, USA
e-mail: dkubair1@jhu.edu

C. Przybyla
Air Force Research Laboratory/RX, Wright-Patterson Air Force Base, Dayton, OH, USA
e-mail: craig.przybyla@wpafb.af.mil

S. Ghosh et al. (eds.), *Integrated Computational Materials Engineering (ICME)*,
https://doi.org/10.1007/978-3-030-40562-5_11

also solve micro-mechanical RVE models at every macroscopic element integration point to obtain homogenized properties.

In practice, however, actual composite microstructures are seldom uniform or periodic. They generally comprise nonuniform dispersion of heterogeneities with clusters and matrix-rich regions as shown in the unidirectional composite micrographs of Fig. 1a, b. To account for the nonuniform distribution of heterogeneities, the concept of statistically equivalent RVE or *SERVE* was proposed in [9, 18, 19].

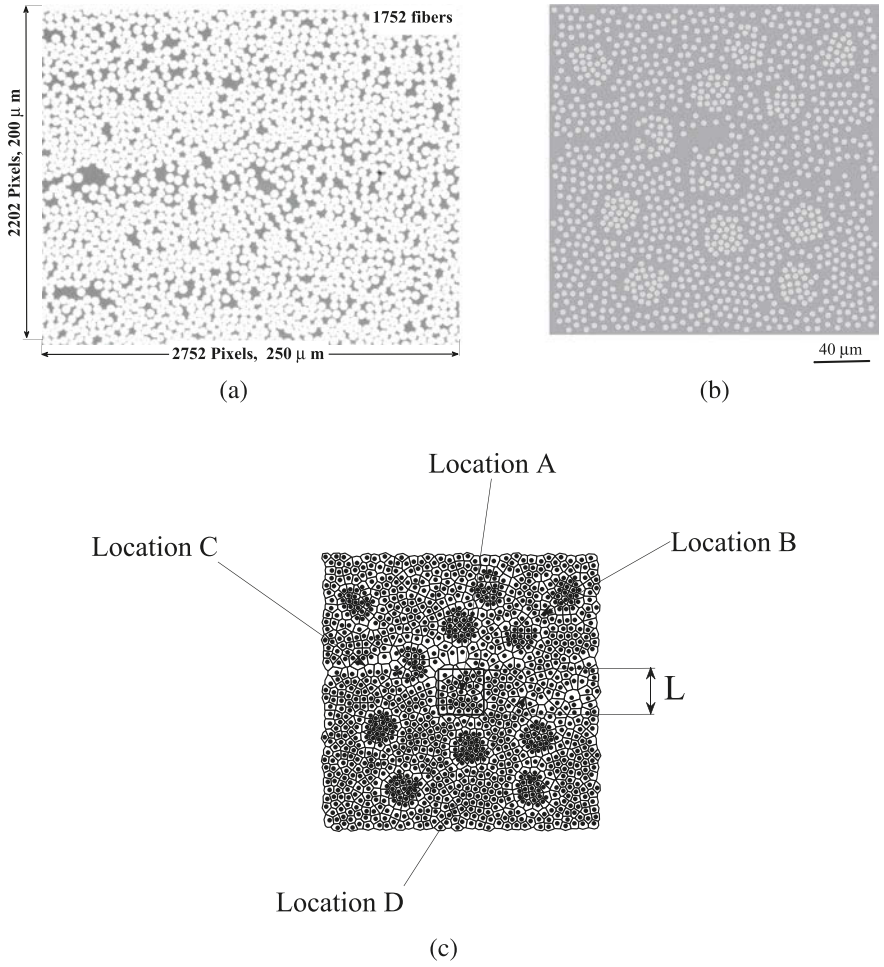

Fig. 1 (**a**) Experimental micrograph of a carbon fiber epoxy matrix unidirectional composite; (**b**) micrograph of a composite containing fiber clusters; and (**c**) microstructure tessellated into Voronoi cells showing regions of potential microstructural SERVE. (Reprinted from: Kubair and Ghosh [35])

A SERVE is defined as the smallest microstructural domain with the following characteristics:

1. Distribution functions of morphological parameters in the SERVE should be statistically equivalent to those for the overall microstructure. This is classified as a microstructure-based SERVE or *M-SERVE* [20–22].
2. Effective material properties and response functions for the SERVE should be equivalent to those of the entire microstructure. This is classified as a property-based SERVE or *P-SERVE* [20–22].
3. The SERVE should not depend on the location in the microstructure, e.g., A,B,C, and D in Fig. 1c, or the applied loading. The size of the SERVE should be optimal in terms of representing deformation mechanisms and overall response. A smaller than necessary SERVE size may not include all possible deformation mechanisms and lead to erroneous estimation of effective properties, while a larger than required size can require exorbitant computational resources. A variety of methods have been developed for estimating RVE sizes of random media, where direct numerical simulations are performed with different boundary conditions [23–25]. Various statistical descriptors have been used to estimate the RVE size to be sampled for obtaining the bulk material response [23, 26–29]. These descriptors include distributions of the local fiber volume fraction, nearest neighbor distance, radial basis functions, and n-point correlation functions, e.g., in [30–34].

While methods of RVE estimation have generally focused only on the effective microstructural domain and its volume, little consideration has been given to the appropriateness of the *boundary conditions*. Three types of boundary conditions have been conventionally applied on the RVE for solving the micromechanics problem. These are:

1. Affine transformation-based displacement boundary condition (ATDBC), expressed as:

$$u_i^A = \epsilon_{ij}^0 x_j \text{ on } \Gamma_{RVE}$$

   Here, ϵ_{ij}^0 is a constant applied far-field strain, and x_j are the boundary coordinates measured with respect to the geometrical centroid of the RVE. This condition provides the lower or *Voigt* bound of the solution.
2. Uniform traction boundary condition (UTBC) given as:

$$T_i = \sigma_{ij}^0 n_j \text{ on } \Gamma_{RVE}$$

   T_i is the applied traction on the RVE boundary resulting in a constant stress σ_{ij}^0, where n_j is the unit normal to the RVE boundary. This condition provides the upper or *Reuss* bound of the solution.

3. Periodic boundary condition (PBC), expressed as:

$$u_i^P = \epsilon_{ij}^0 x_j + u_i^{pd} \quad \text{on } \Gamma_{RVE}$$

The periodic additional displacement u_i^{pd} is equal on opposite faces of the RVE, which requires the boundary to be homologous.

The underlying assumption of the ATDBC and UTBC is that strains and stresses immediately outside the simulated RVE are constant [36, 37]. These boundary conditions assume that the RVE is immersed in a continuum (exterior to the RVE) with a spatially invariant strain energy density. They typically ignore the presence of fibers exterior to the RVE and their interaction with those in the interior. The periodic boundary condition, on the other hand, assumes the deformation patterns in the domain exterior to the RVE to be homologous. However, for composites with nonuniform distributions, these assumptions of strain energy invariance or periodicity are invalid in the vicinity of the RVE boundary. All of the above boundary conditions result in an overestimation of the RVE region from convergence requirements.

The proper definition of the SERVE is incomplete without the application of appropriate boundary conditions, reflecting microstructural statistics of the domain. Ghosh et al. [35, 38, 39] have overcome these limitations by prescribing a new class of exterior statistics-based boundary conditions or *ESBCs*. ESBCs are constructed as a modification to the affine transformation-based displacement boundary conditions (ATDBCs) in this work. They are expected to mimic periodic boundary conditions (PBCs) when the dispersion of heterogeneities is periodic.

ESBCs are very effective boundary conditions when modeling linear elastic heterogeneous materials with nonuniform distributions of heterogeneities. They account for the interaction of heterogeneities in the region exterior to the SERVE with those in its interior and how this interaction affects its response. The boundary conditions incorporate the statistics of the exterior microstructure resulting in an optimal volume for the converged SERVE. In [35, 38, 39], statistically informed Green's functions with the 2-point correlation function $S_2(r, \theta)$ and the Eshelby equivalent inclusion method have been derived to describe the interactions between the exterior and interior domains. Excellent convergence rates have been observed for elastic stiffness components in comparison with other boundary conditions or with statistical volume elements or SVEs.

This chapter reviews major developments in [35, 38, 39] for establishing the novel exterior statistics-based boundary conditions or *ESBCs* for the statistically equivalent RVE or SERVE. The first part discusses the formulation and numerical implementations. Validation tests and convergence of the SERVE with ESBCs are subsequently studied. The SERVE with ESBCs is compared with emerging methods of homogenization, viz., those with statistical volume elements (SVEs) and weighted statistical volume elements (WSVE).

2 Formulation of the Exterior Statistics-Based Boundary Conditions for a SERVE

A summary of the exterior statistics-based boundary condition formulation that has been detailed in [35, 38] is given in this section. A microstructural volume element or *MVE* for a given macroscopic point occupies a infinite microstructural region $\Omega^{\text{mve}} \rightarrow \Omega^{\infty}$ as depicted in Fig. 2a. The MVE consists of nonuniformly dispersed heterogeneities, e.g., fibers, particulates, etc. with clusters and matrix-rich regions as shown in Fig. 1.

The homogenized constitutive response for a linear elastic material with MVE occupying a domain Ω^{mve} is expressed as:

$$\bar{\sigma}_{ij}^{\text{mve}} = \bar{C}_{ijkl}^{\text{mve}} \bar{\epsilon}_{kl}^{\text{mve}} \tag{1}$$

where $\bar{C}_{ijkl}^{\text{mve}}$ is the homogenized stiffness tensor, and the homogenized stresses and strains are, respectively, written as:

$$\bar{\sigma}_{ij}^{\text{mve}} = \frac{1}{\Omega^{\text{mve}}} \int_{\Omega^{\text{mve}}} \sigma_{ij}^{\text{mve}}(\mathbf{x})\, d\Omega \tag{2}$$

$$\bar{\epsilon}_{ij}^{\text{mve}} = \frac{1}{\Omega^{\text{mve}}} \int_{\Omega^{\text{mve}}} \epsilon_{ij}^{\text{mve}}(\mathbf{x})\, d\Omega \tag{3}$$

where $\sigma_{ij}^{\text{mve}}(\mathbf{x})$ and $\epsilon_{ij}^{\text{mve}}(\mathbf{x})$ are, respectively, the spatially varying microscopic stresses and strains in the MVE. In a finite element formulation of the microstructural MVE problem for static problems in the absence of body forces, the weak form corresponding to the principle of virtual work form is written as:

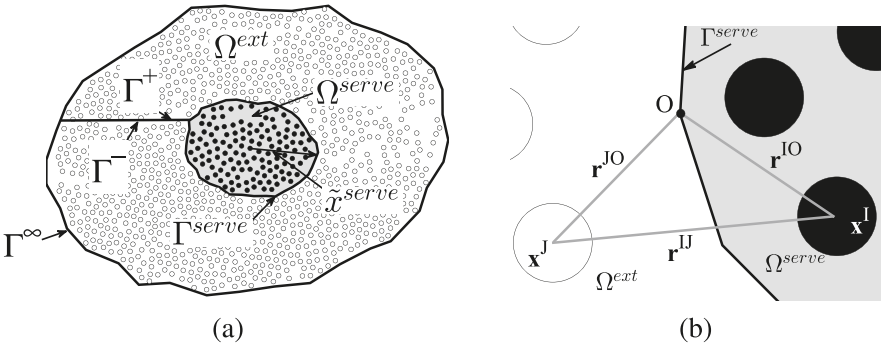

Fig. 2 (**a**) Schematic view of the MVE containing the SERVE and its complementary exterior domain, i.e., $\Omega^{\text{mve}} = \Omega^{\text{serve}} \cup \Omega^{\text{ext}}$, and (**b**) effect of an interacting fiber pair I-J on a field point O at the P-SERVE boundary Γ^{serve}. (Reprinted from: Kubair and Ghosh [35])

$$\int_{\Omega^{\text{mve}}} \sigma_{ij}^{\text{mve}}(\mathbf{x}) \delta\epsilon_{ij}^{\text{mve}}(\mathbf{x}) d\Omega = 0 \tag{4}$$

subject to the affine transformation-based displacement boundary conditions

$$u_i^A(\mathbf{x}^\infty) = \epsilon_{ij}^0 x_j^\infty \text{ on } \Gamma^\infty \tag{5}$$

Here, $\delta\epsilon_{ij}$ is the virtual strain, and x_j^∞ are the coordinates of a point on the MVE boundary Γ^∞ relative to a reference point, such as the centroid of Ω^{mve}. Since the MVE typically consists of a large population of heterogeneities, the solution of the weak form (4) is computationally prohibitive. To avert this, only a statistically equivalent subset of the MVE domain with explicit representation of dispersed heterogeneities is identified as the SERVE for detailed micromechanical analyses. A candidate SERVE is highlighted in Fig. 2a. This domain should be optimally small to make it computationally tractable. Thus, the ratio of the length scales of the MVE (L^{mve}) to that of the SERVE (L^{serve}) should be sufficiently large, i.e., $\frac{L^{\text{mve}}}{L^{\text{serve}}} >> 1$.

For reducing the MVE boundary value problem in equation (4) to that of the SERVE, the MVE domain Ω^{mve} is partitioned into two complementary domains, i.e., a SERVE domain Ω^{serve} and its exterior domain Ω^{ext}, such that $\Omega^{\text{mve}} = \Omega^{\text{ext}} \cup \Omega^{\text{serve}}$. The effect of the exterior domain Ω^{ext} is manifested through equivalent conditions on the SERVE boundary Γ^{serve}, adequately reflecting the interaction of Ω^{ext} with Ω^{serve}. It should result in the same invariant strain energy for the SERVE as for the entire MVE with the applied affine displacement conditions on Γ^∞. To achieve this, the equation of principle of virtual work (4) is written as the sum of the respective virtual work terms in the complementary domains of Fig. 2a as:

$$\int_{\Omega^{\text{ext}}} \sigma_{ij}^{\text{ext}}(\mathbf{x}) \, \delta\epsilon_{ij}^{\text{ext}}(\mathbf{x}) \, d\Omega + \int_{\Omega^{\text{serve}}} \sigma_{ij}^{\text{serve}}(\mathbf{x}) \, \delta\epsilon_{ij}^{\text{serve}}(\mathbf{x}) \, d\Omega = 0 \tag{6}$$

Applying the divergence theorem to the first term containing the integral over Ω^{ext}, incorporating equilibrium conditions in the absence of body forces, i.e., $\sigma_{ij,j}(\mathbf{x}) = 0$, and with $\bar{\epsilon}_{ij}^{\text{mve}} = \epsilon_{ik}^0$ on Γ^∞, the principle of virtual work (6) reduces to that of the SERVE as:

$$\int_{\Omega^{\text{serve}}} \sigma_{ij}^{\text{serve}}(\mathbf{x}) \, \delta\epsilon_{ij}^{\text{serve}}(\mathbf{x}) \, d\Omega - \int_{\Gamma^{\text{serve}}} T_i^{\text{ext}}(\mathbf{x}) \, \delta u_i^{\text{ext}}(\mathbf{x}) \, d\Gamma = 0 \tag{7}$$

$T_i^{\text{ext}}(\mathbf{x})$ is the traction on Γ^{serve} resulting from the stresses in the domain Ω^{ext} exterior to the SERVE. The second term in equation (7) will drop out if an effective displacement field can be prescribed on Γ^{serve}, since $\delta u_i^{\text{ext}} = 0$ on Γ^{serve}. This can be incorporated through the augmentation of the affine transformation-based boundary displacement field $u_i^A(\mathbf{x}^{\text{serve}}) = \epsilon_{il}^0 x^{\text{serve}}$ by an additional perturbation term, which represents the effects of heterogeneities in Ω^{ext} on Γ^{serve}. Since the solution process will not involve an explicit numerical solution of the exterior domain problem in Ω^{ext}, a special analytical solution that involves the statistics of the exterior domain

may be developed. Hence the term exterior statistics-based boundary conditions or u_i^{ESBC}. It is expressed as:

$$u_i^{ESBC}(\mathbf{x}^{\text{serve}}) = u_i^A(\mathbf{x}^{\text{serve}}) + u_i^*(\mathbf{x}^{\text{serve}}) \text{ on } \Gamma^{\text{serve}} \tag{8}$$

where u_i^* is an enhancement due to the interaction of the exterior domain Ω^{ext} with the interior of the SERVE.

Among a plethora of available statistical functions, the n-point correlation functions for characterizing multivariate point sets have been shown to effectively describe arbitrary distributions in [27, 30]. In [40], it has been proved that the anisotropic spatial statistics of a two-phase medium generally can be described by the 2-point correlation function $S_2\left(r^{IJ}, \theta^{IJ}\right)$. Alternately termed as the joint distance and orientation-based 2-point correlation function, it is defined as the probability that two points at positions $\mathbf{x}^I$ and $\mathbf{x}^I$ and separated by a distance r^{IJ} at an orientation θ^{IJ} lie in the same phase α. With location-dependent indicator functions for the matrix phase M and Ith, inclusion phase F_I among n_p inclusions, expressed as:

$$\iota^M(\mathbf{x}) = \begin{cases} 1 & \forall\, \mathbf{x} \in \Omega^M \\ 0 & \forall\, \mathbf{x} \notin \Omega^M \end{cases} \text{ and } \iota^{F_I}(\mathbf{x}) = \begin{cases} 1 & \forall\, \mathbf{x} \in \Omega^{F_I} \\ 0 & \forall\, \mathbf{x} \notin \Omega^{F_I} \end{cases} \quad I = 1 \cdots n_p \tag{9}$$

the joint distance and orientation-based, 2-point correlation function for Ω^{mve} is defined as:

$$S_2(\mathbf{r}) = \frac{1}{\Omega^{\text{mve}}} \int\limits_{\Omega^{\text{mve}}} \iota^F(\mathbf{x})\, \iota^F(\mathbf{x} + \mathbf{r}) d\Omega \tag{10}$$

where $\mathbf{r} = \mathbf{x} - \mathbf{x}^I$ is the position vector separating two points in the domain. This vector can be represented in a parametric form as (r, θ), where the parameter $r = |\mathbf{r}|$ is the separation distance and $\theta = \angle\mathbf{r}$ is the orientation of the line joining these points with a reference direction. In unidirectional composites containing equi-radius fibers, the fiber centroids can represent these points. For isotropic distributions, this correlation function reduces to a distance-based, radial distribution function $S_2(r)$. The 1-point correlation function, which corresponds to the volume fraction, is expressed as:

$$S_1 = \frac{1}{\Omega^{\text{mve}}} \int\limits_{\Omega^{\text{mve}}} \iota^F(\mathbf{x}) d\Omega \tag{11}$$

The displacements u_i^{ESBC} on the SERVE boundary for heterogeneous microstructures containing inclusion clusters and matrix-rich regions are discussed next.

2.1 Exterior Statistics-Based Perturbed Fields

The presence of heterogeneities in the form of inclusions or fibers alters the spatially invariant, homogeneous state of the matrix stress σ_{ij}^M, the matrix strain ϵ_{ij}^M, and the displacement u_i^M fields in the MVE domain Ω^{mve}. The perturbed stress σ_{ij}^*, strain ϵ_{ij}^*, and displacement u_i^* fields due to heterogeneities depend on the morphological characteristics of the microstructure, viz., inclusion geometry and location. The total stress σ_{ij}, strain ϵ_{ij}, and displacement u_i fields in the heterogeneous MVE domain may be defined as the sum of the homogeneous and perturbed parts as:

$$\sigma_{ij}(\mathbf{x}) = \sigma_{ij}^M + \sigma_{ij}^*(\mathbf{x}), \quad \epsilon_{ij}(\mathbf{x}) = \epsilon_{ij}^M + \epsilon_{ij}^*(\mathbf{x}), \quad u_i(\mathbf{x}) = u_i^M + u_i^*(\mathbf{x}) \quad \in \ \Omega^{\text{mve}} \tag{12}$$

Since the homogeneous stress σ_{ij}^M is divergence-free, the equilibrium condition for the perturbed stress fields (in the absence of body forces) is $\sigma_{ij,j}^*(\mathbf{x}) = 0$.

The solution to the problem of a heterogeneous medium can be simplified by introducing an equivalent inclusion approach, where an eigenstrain $\epsilon_{ij}^{\Lambda}(\mathbf{x})$ is introduced in the inclusion domain to account for the constraint that the matrix imposes on the inclusion due to autonomous deformation. Correspondingly, the perturbation stress inside the inclusion F_I can be written as:

$$\sigma_{ij}^*(\mathbf{x}^{F_I}) = C_{ijkl}^M \left(\epsilon_{kl}^*(\mathbf{x}) + \iota^{F_I}(\mathbf{x})\epsilon_{kl}^{\Lambda}(\mathbf{x})\right) \tag{13}$$

where C_{ijkl}^M is the elastic stiffness of the matrix material, and $\iota^{F_I}(\mathbf{x})$ is the inclusion indicator function, defined in equation (9). The eigenstrain $\epsilon_{kl}^{\Lambda}(\mathbf{x}^{F_I})$ represents the effect of distributed point source on the perturbed solution $u_i^*(\mathbf{x})$, where $\mathbf{x}^{F_I}$ represent the location of any source point in Ω^{F_I}. Using an infinite-space Green's function solution $G_{ij}(\mathbf{x}, \mathbf{x}^{F_I})$, the perturbed displacement field in Ω^{MVE} with n_p dispersed inclusions can be derived as a summed integral, given as:

$$u_i^*(\mathbf{x}) = \sum_{I=1}^{n_p} \int_{\Omega^{F_I}} C_{klmn}^M G_{ik,l}(\mathbf{x}, \mathbf{x}^{F_I})\epsilon_{mn}^{\Lambda}(\mathbf{x}^{F_I})d\Omega \tag{14}$$

The integral over Ω^{F_I} corresponds to the contribution from individual inclusions. The perturbed strains can be derived from equation (14) in terms of eigenstrains as:

$$\epsilon_{ij}^*(\mathbf{x}) = \frac{1}{2}\sum_{I=1}^{n_p} \int_{\Omega^{F_I}} C_{klmn}^M (G_{ik,lj}\left(\mathbf{x}, \mathbf{x}^{F_I}\right) + G_{jk,lj}\left(\mathbf{x}, \mathbf{x}^{F_I}\right))\epsilon_{mn}^{\Lambda}\left(\mathbf{x}^{F_I}\right) d\Omega \tag{15}$$

For isotropic, linear elastic matrix materials, the Green's function has been derived in [41] as:

$$G_{ij}(\mathbf{x}, \mathbf{x}^{F_I}) = \frac{1}{4\pi\mu}\left[\frac{\delta_{ij}}{r^I} - \frac{1}{4(1-\nu)} r^I_{,ij}\right] \tag{16}$$

where $r^I = |\mathbf{x} - \mathbf{x}^{F_I}|$ is the separation distance between a source point $\mathbf{x}^{F_I}$ and a generic field point $\mathbf{x}$.

Closed form expressions for the integrals in equations (14) and (15) have been derived using elliptic integrals [42] with spatially invariant eigenstrains inside ellipsoidal inclusions. The perturbed strains due to any isolated (noninteracting) inclusion F_I in the MVE are expressed as:

$$\epsilon^*_{ij}(\mathbf{x}) = \int_{\Omega^{\text{mve}}} H_{ijkl}\left(\mathbf{x}, \hat{\mathbf{x}}\right) \epsilon^{\Lambda}_{kl}\left(\hat{\mathbf{x}}\right) d\hat{\mathbf{x}} \tag{17}$$

where $\hat{\mathbf{x}}$ is a point in the inclusion. H_{ijkl} corresponds to a unified 2-point Eshelby tensor given as:

$$H_{ijkl}\left(\mathbf{x}, \hat{\mathbf{x}}\right) = \iota^{F_I}(\mathbf{x})\, S^{F_I}_{ijkl} + \left(1 - \iota^{F_I}(\mathbf{x})\right) \hat{G}^{F_I}_{ijkl}\left(\mathbf{x}, \hat{\mathbf{x}}\right) \tag{18}$$

where $S^{F_I}_{ijkl}$ and $\hat{G}^{F_I}_{ijkl}\left(\mathbf{x}, \hat{\mathbf{x}}\right)$ are the interior and exterior Eshelby tensors. The corresponding perturbed displacements are written in terms of the Eshelby tensors as:

$$u^*_i(\mathbf{x}) = \int_{\Omega^{\text{mve}}} L_{ikl}\left(\mathbf{x}, \hat{\mathbf{x}}\right) \epsilon^{\Lambda}_{kl}\left(\hat{\mathbf{x}}\right) d\hat{\mathbf{x}} \tag{19}$$

where

$$L_{ikl}\left(\mathbf{x}, \hat{\mathbf{x}}\right) = \iota^{F_I}(\mathbf{x})\, T^{F_I}_{ikl}\left(\mathbf{x}, \hat{\mathbf{x}}\right) + \left(1 - \iota^{F_I}(\mathbf{x})\right) D^{F_I}_{ikl}\left(\mathbf{x}, \hat{\mathbf{x}}\right) \tag{20}$$

Expression for the interior and exterior Eshelby tensors $S^{F_I}_{ijkl}$ and $\hat{G}^{F_I}_{ijkl}\left(\mathbf{x}, \hat{\mathbf{x}}\right)$, as well as the displacement-transfer tensors $T^{F_I}_{ikl}\left(\mathbf{x}, \hat{\mathbf{x}}\right)$ and $D^{F_I}_{ikl}\left(\mathbf{x}, \hat{\mathbf{x}}\right)$ for a circular cylindrical fiber are given in the Appendix. For identical fibers in Ω^{mve}, the following reductions hold:

$$S^{F_I}_{ijkl} = S^{F_J}_{ijkl} = S_{ijkl}$$
$$M_{ijkl}\left(\mathbf{x}^I\right) = M_{ijkl}\left(\mathbf{x}^J\right) = M_{ijkl}$$
$$\hat{G}^{F_I}_{ijkl}(\mathbf{r}) = \hat{G}^{F_J}_{ijkl}(\mathbf{r}) = \hat{G}_{ijkl}(r, \theta)$$

where S_{ijkl} and M_{ijkl} are spatially invariant, and $\hat{G}_{ijkl}$ is position dependent and describes interactions between fibers.

The perturbed strain in an inclusion is influenced by its interactions with other inclusions in the MVE. For a population of inclusions represented by the 2-point probability distribution function $S_2(\mathbf{r})$ in equation (9), the perturbed strain in the fiber F_I, $(I = 1 \cdots n_p)$ due to the interactions of fibers dispersed in Ω^{mve} is expressed as:

$$\epsilon_{ij}^{*}\left(\mathbf{x}^{F_I}\right) = S_{ijkl}(\mathbf{x}^{I})\epsilon_{ij}^{\Lambda}\left(\mathbf{x}^{I}\right) + \int\limits_{\Omega^{\text{mve}}\setminus\Omega^{F_I}} S_2(\mathbf{r})\,\hat{G}_{ijkl}(\mathbf{r})\,\epsilon_{ij}^{\Lambda}(\mathbf{r})\,d\Omega \tag{21}$$

where $S_2(\mathbf{r})$ is the 2-point correlation function defined in equation (10). The second integral term represents the interaction effect of all fibers with the Ith fiber, and the integrand may be denoted as a *statistically informed Green's function* or *SIGF*.

The eigenstrains with n_p interacting inclusions are evaluated by applying the Eshelby's stress consistency condition, which requires the total stress inside the fiber Ω^{F_I} to be equal to the total stress in the equivalent matrix domain. For the domain Ω^{mve} consisting of interacting fibers with a distribution represented by the 2-point correlation function $S_2(\mathbf{r})$, the eigenstrain ϵ_{ij}^{Λ} in a reference fiber occupying a domain Ω^{F} may be derived using equation (13) as:

$$\begin{aligned}
&\epsilon_{ij}^{\Lambda}(\mathbf{x}) = \Bigg[\iota^{F}(\mathbf{x})\left(S_{ijab} + M_{ijab}\right) - \int\limits_{\Omega^{\text{mve}}\setminus\Omega_F} S_2(\mathbf{r})\,\hat{G}_{ijmn}(\mathbf{r}) \\
&\left(S_{mnpq} + M_{mnpq}\right)^{-1}\hat{G}_{pqab}(\mathbf{r})\,d\Omega\Bigg]^{-1} \\
&\left[\left((S_{abmn} + M_{abmn})^{-1}\int\limits_{\Omega^{\text{mve}}\setminus\Omega_F} S_2(\mathbf{r})\,\hat{G}_{mnkl}(\mathbf{r})\,d\Omega\right) - \tfrac{1}{2}\left(\delta_{ak}\delta_{bl} + \delta_{al}\delta_{bk}\right)\right]\epsilon_{kl}^{M} \\
&= A_{ijkl}(\mathbf{x})\epsilon_{kl}^{M} \quad \forall \mathbf{x} \in \Omega^{\text{mve}}
\end{aligned} \tag{22}$$

where $M_{ijkl} = \left(C_{ijpq}^{F_I} - C_{ijpq}^{M}\right)^{-1} C_{pqkl}^{M}$, $C_{ijkl}^{F_I}$ is the elastic stiffness of the inclusion material and $\mathbf{r}$ is the distance between a source and field point. The perturbed displacements at an observation point O in Fig. 2b can be obtained in terms of the matrix strain ϵ_{ij}^{M} by substituting equation (22) into equation (19) as:

$$u_i^{*}(\mathbf{x}) = \left(\int\limits_{\Omega^{\text{mve}}\setminus\Omega_F} S_2\left(\mathbf{r}'\right) L_{imn}\left(\mathbf{r}'\right) A_{mnkl}\left(\mathbf{r}'\right) d\Omega\right)\epsilon_{kl}^{M} \tag{23}$$

Finally, using equation (8), the affine transformation-based displacement fields can be superposed on the above perturbed displacements to prescribe the exterior statistics-based boundary conditions (ESBCs).

2.2 Implementation of the Exterior Statistics-Based Boundary Conditions (ESBCs)

The ESBCs are implemented on the boundary Γ^{serve} of a SERVE domain Ω^{serve} of size L using the following steps:

1. Discretize the SERVE domain Ω^{serve} into a finite element mesh. For the 3D domains considered in this study, 4-noded tetrahedral elements are used.
2. Extract the positions and coordinates x_i of all the boundary nodes on Γ^{serve}.
3. Compute the affine transformation-based displacements $u_i^A(\mathbf{x})$ on all the boundary nodes with the applied far-field strain ϵ_{ij}^0 as $u_i^A(\mathbf{x}) = \epsilon_{ij}^0 x_j$, where x_j is measured relative to the centroid of the SERVE.
4. Compute the 2-point correlation function $S_2(r, \theta)$ for the entire MVE domain Ω^{mve} using equation (10).
5. Compute the perturbed displacements u_i^* using equation (19) incorporating $S_2(r, \theta)$ for all the boundary nodes, using the following steps:
   - Each radial orientation is discretized into N_r number of equally spaced segments with increment $\Delta r = \frac{R-a}{N_r}$, where a is the radius of the fibers, R is the radius of horizon that corresponds to the extent of the MVE, and the lower limit of the integration is $r = a$. The αth radial point is given as $r_\alpha = \alpha \frac{R-a}{N_r}$.
   - The angular orientation is discretized into N_θ equally spaced points of $\Delta\theta = \frac{2\pi}{N_\theta}$. The βth angular point is $\theta_\beta = \beta \frac{2\pi}{N_\theta}$.
   - At a SERVE boundary node at x_i, the discrete perturbed displacement components in equation (23) are evaluated for an applied strain ϵ_{ij}^0 as:

$$u_i^*(\mathbf{x}) = [\ \frac{2\pi(R-a)}{N_r N_\theta} \sum_{\alpha=1}^{N_r} \sum_{\beta=1}^{N_\theta} \alpha L_{imn}\left(\mathbf{x} - (\alpha\Delta r, \beta\Delta\theta)\right) \tag{24}$$

$$A_{mnkl}\left(\mathbf{x} - (\alpha\Delta r, \beta\Delta\theta)\right) S_2\left(\mathbf{x} - (\alpha\Delta r, \beta\Delta\theta)\right)\ ]\,\epsilon_{ij}^0$$

6. The ESBCs on the boundary nodes are computed and applied as:

$$u_i^{ESBC}(\mathbf{x}) = u_i^A(\mathbf{x}) + u_i^*(\mathbf{x}) \tag{25}$$

3 Validation of ESBCs for SERVEs in Nonhomogeneous Microstructures with Clustering

The exterior statistics-based boundary conditions (ESBCs) developed in Sect. 2.1 are validated in this section. Finite element simulations are conducted for a MVE with section size $240 \times 240 \times 10\,\mu\text{m}$ and consisting of 1152 fibers with clusters. The MVE shown in Fig. 1b is generated from data on real glass-fiber epoxy matrix composites that have been characterized in [43]. The fibers have a uniform $4\,\mu\text{m}$

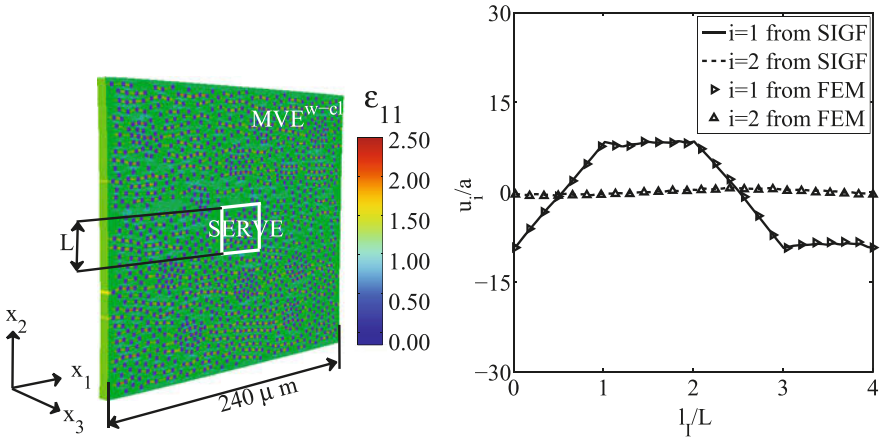

(a) (b)

Fig. 3 (**a**) Contour plot of the FE solution ϵ_{11} in the clustered MVE (obtained from data provided in [43]) subjected to a far-field applied strain $\epsilon^0_{11} = 1$, (**b**) comparison of displacements on the $40 \times 40\,\mu$m SERVE obtained by the SIGF equation (25) with that from the finite element simulation of the MVE. (The abscissa marks (0–1) correspond to the bottom edge, (1–2) to the left edge, (2–3) to the top edge, and (3–4) to the right edge of the Γ_{SERVE}.) (Reprinted from: Kubair and Ghosh [35])

diameter. A candidate SERVE cross-section of $40 \times 40 \times 10\,\mu$m encompassing 38 fibers is highlighted by the white square boundary in Fig. 3a. The computational domains are discretized into meshes of 4-noded tetrahedral elements of a minimum size of $0.8\,\mu$m and with 13 elements in the z-direction. The Young's modulus and Poisson's ratio of the epoxy matrix are $E^M = 3.2$ GPa and $\nu^M = 0.4$, while those for the e-glass fibers are $E^F = 80$ GPa and $\nu^F = 0.25$, respectively. The first set of simulations correspond to the affine transformation-based applied displacement boundary condition $u^A_i = \epsilon^0_{ij} x_j$, with an applied far-field strain $\epsilon^0_{11} = 1$.

Contour plots of ϵ_{11} from the finite element solution are shown on the deformed configuration in Fig. 3a. The strain inside the fibers is smaller than in the matrix due to the larger fiber Young's modulus. The FE displacement solution along the white line is extracted from FE simulations of the MVE. This is compared with the displacement solution $u_i = u^A_i + u^*_i$ used in ESBC, in which u^*_i is the perturbed displacement solution from equation (25) using the statistically informed Green's function or SIGF approach. The displacement solutions, normalized by the fiber radius, are plotted in Fig. 3b. The abscissa corresponds to the total length along the sides of the white SERVE boundary in Fig. 3a. The markers (0–1) correspond to the bottom edge, (1–2) to the left edge, (2–3) to the top edge, and (3–4) to the right edge. Excellent agreement is seen between results of the FE simulations of the MVE (shown with markers) and the displacement solutions $u^A_i + u^*_i$ (shown in solid lines). This provides a validation of the ESBC formulation. The SIGF-augmented solutions show that even though the far-field strain is $\epsilon^0_{11} = 1$, the u_2

component is not zero on the white SERVE boundary due to fiber interactions. It will be shown in the following sections that the affine transformation-based displacement boundary conditions (ATDBCs) or periodic boundary conditions (PBCs) applied on the SERVE boundary suffer from poor accuracy.

3.1 *Comparing ESBCs Generated by the 2-Point Correlation and Radial Distribution Functions*

Figure 4 plots the perturbation displacements u_i^*/a normalized by the fiber radius a. The figure compares plots generated using the radial distribution function $S_2(r)$ and the 2-point correlation function $S_2(r, \theta)$. The abscissa shows the normalized length along the bottom (edge 0–1), right (edge 1–2), top (edge 2–3), and left (edge 3–4) edges of the 40 μm square SERVE in sequence, in Fig. 3. The applied far-field strain ϵ_{11}^0 affects the perturbation displacements in the x_1 direction, but not much in the x_2 direction. The difference in the perturbation displacement alters the ESBCs applied on the SERVE and hence the computed homogenized stiffness $\bar{C}_{ijkl}$.

Furthermore, the effect of ATDBCs and ESBCs using $S_2(r)$ and $S_2(r, \theta)$ on a candidate SERVE of size $L = 40\,\mu\text{m}$ containing 38 fibers is illustrated in Figs. 5, 6 and 7, respectively. In this paper, the boundaries of the SERVEs Γ^{serve} are assumed not to intersect the inclusions, for the sake of simplicity. However the developed ESBCs are capable of being prescribed on boundaries that intersect inclusions. The plots in Figs. 5a, 6a and 7a show the displacement components in the 1 and 2 directions applied as boundary conditions along the four sides of the SERVE boundary. Perturbations in the ESBCs $u_1 = u_1^A + u_1^*$ are pronounced on the right and left edges of Figs. 6a, 7a. While $u_2^A = 0$ for $\epsilon_{11}^0 = 1$ on the boundary, $u_2 = u_2^*$ is nonzero along the edges with the ESBC. Unlike for PBCs, the deformed edges with the ESBCs are not homologic. Contour plots of the strain ϵ_{11} for the different

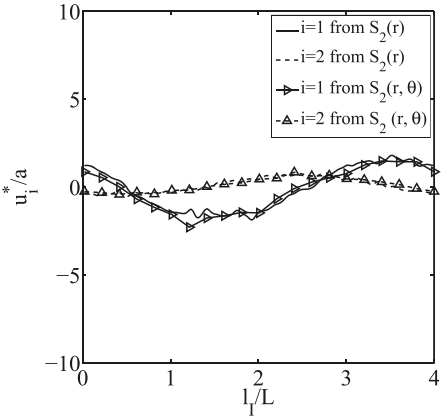

Fig. 4 Perturbation displacements u_i^*/a obtained for a clustered MVE using the $S_2\,(r)$ and $S_2\,(r, \theta)$ statistical functions in SIGF. (Reprinted from: Kubair and Ghosh [35])

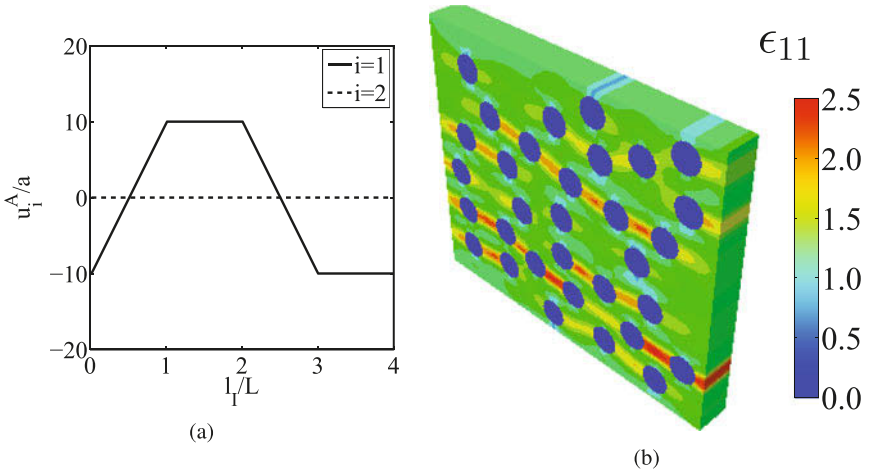

Fig. 5 Results from SERVE simulation with ATDBC: (**a**) displacements on the boundary of the SERVE, (**b**) contour plot of ϵ_{11} in the SERVE. (Reprinted from: Kubair and Ghosh [35])

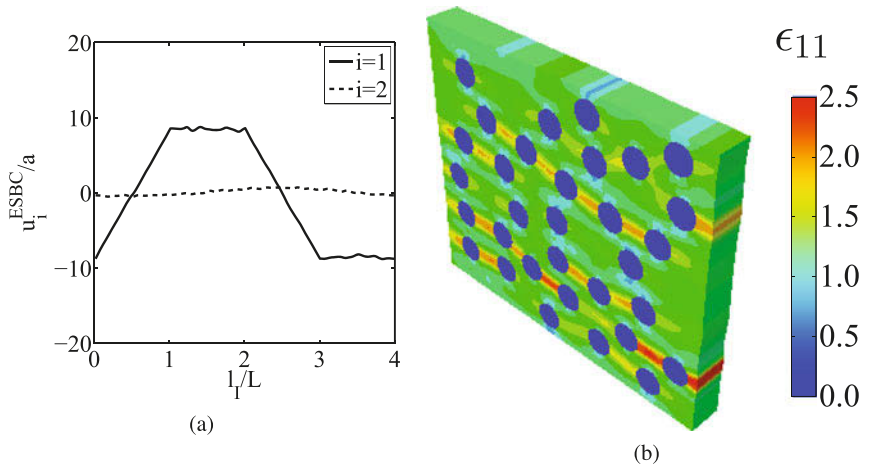

Fig. 6 Results from SERVE simulation with ESBC generated by radial distribution function $S_2(r)$: (**a**) displacements along the SERVE boundary, (**b**) contour plot of ϵ_{11} in the SERVE. (Reprinted from: Kubair and Ghosh [35])

boundary conditions are shown in Figs. 5b, 6b and 7b. While regions of strain localization are observed for all the boundary conditions, the intensity is less with ESBCs.

The homogenized stiffness for the entire composite MVE $\bar{C}_{ijk}^{\text{mve}}$ is evaluated using equation (1), together with the averaged stresses from equation (3) corresponding to an applied averaged strain. The same stiffness can be obtained from the averaged stresses in the SERVE domain with the applied ESBCs generated by applying the

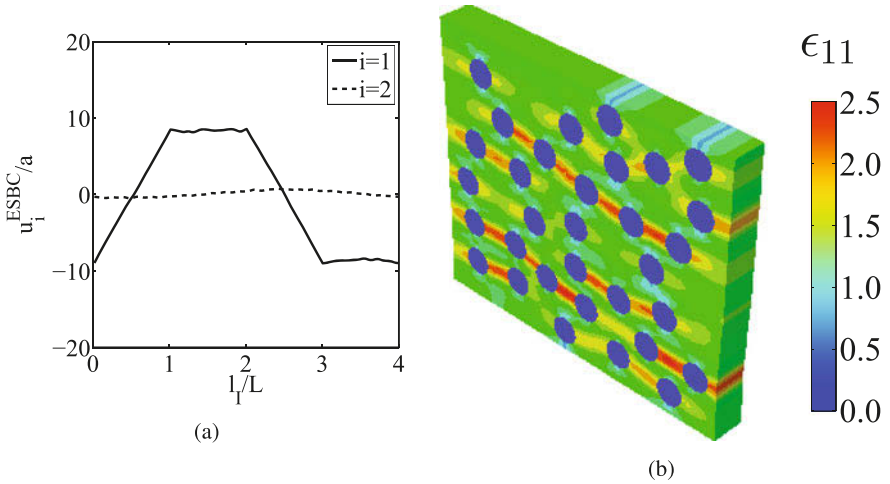

Fig. 7 Results from SERVE simulation with ESBC generated with the 2-point correlation function $S_2(r, \theta)$: (**a**) displacement along the SERVE boundary, (**b**) contour plot of the ϵ_{11} in the SERVE. (Reprinted from: Kubair and Ghosh [35])

Table 1 Homogenized stiffness $\bar{C}_{1111}/E^M$ in SERVEs subjected to different boundary conditions

Figure	Boundary condition	$\bar{C}_{1111}/E^M$	% error $\left(\frac{\lvert\bar{C}^{mve}_{1111}-\bar{C}^{serve}_{1111}\rvert}{\bar{C}^{mve}_{1111}}\right)\times 100$
(L = 240 μm) 3	ATDBC	2.8836	0.0000
5	ATDBC	2.9406	1.9767
6	ESBC using $S_2(r)$	2.9056	0.7620
7	ESBC using $S_2(r, \theta)$	2.8813	0.0798

SIGF to the applied averaged strains. Table 1 tabulates the normalized homogenized stiffness $\bar{C}_{1111}/E^M$ from the entire MVE simulations, as well as from simulating a 40 μm SERVE subjected to ATDBC and ESBCs. For the ESBCs, both the radial distribution $S_2(r)$ in Fig. 6a and the joint 2-point correlation function $S_2(r, \theta)$ in Fig. 7a are considered. The homogenized stiffness obtained from the SERVE simulations with the $S_2(r, \theta)$-based ESBCs are the closest to those obtained from entire MVE simulations. This illustrates the excellent desired performance of the applied ESBCs.

The contour plot of the difference in the maximum principal stress obtained by applying the ATDBC and ESBC with $S_2(r, \theta)$ is shown in Fig. 8a. The difference is pronounced in ligaments between fibers that are in close proximity. The maximum principal stresses are larger with ATDBCs than with ESBCs for the same far-field strain energy density. Analogously, the contour plot of the difference in the maximum principal stress by ESBCs using the $S_2(r)$ and $S_2(r, \theta)$ functions is shown in Fig. 8b. While the perturbation displacements in Fig. 4 by using the $S_2(r)$ and $S_2(r, \theta)$-based ESBCs are comparable in magnitude, the stresses are significantly

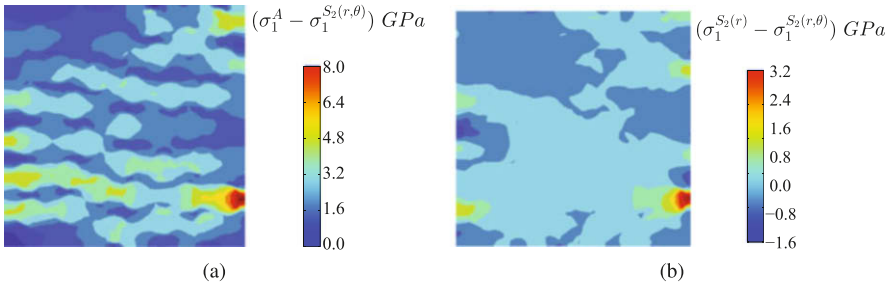

Fig. 8 Contour plot showing the difference in the maximum principal stresses in the SERVE for: (**a**) ATDBC and ESBC using $S_2(r, \theta)$ (**b**) ESBCs using $S_2(r)$ and $S_2(r, \theta)$, normalized by the matrix modulus. (Reprinted from: Kubair and Ghosh [35])

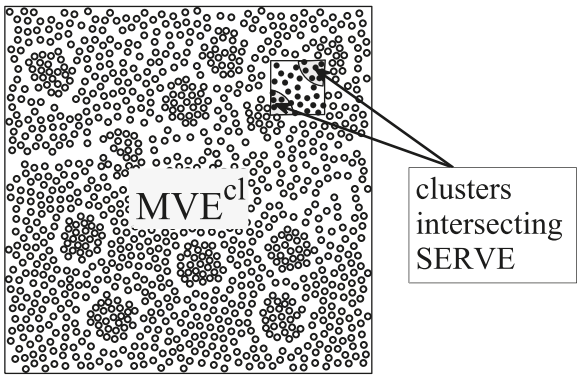

Fig. 9 Intersection of clusters in the MVE with the edges of a SERVE. (Reprinted from: Kubair and Ghosh [35])

different. The $S_2(r, \theta)$-based ESBCs are accurate as they account for the presence of fiber clusters in the exterior domain.

3.2 ESBCs for SERVEs Intersecting Clustered Regions

In certain microstructural volume elements, the SERVE can intersect clustered regions in the microstructure. This will affect the ESBCs on SERVEs that intersect clusters. A $40 \times 40\,\mu$m SERVE intersecting two clusters in the MVE is illustrated in Fig. 9. The intersection of the clusters with the SERVE boundaries results in a few fibers, belonging to the cluster, to be present inside the SERVE. Regions that belong to the clusters are highlighted in gray. The prescribed $S_2(r, \theta)$-based ESBCs are shown in Fig. 10a. The ϵ_{11} strain contour in the SERVE is depicted in Fig. 10b. Strain concentrations are larger due to the reduction of inter-fiber spacing inside the clusters. The homogenized stiffness of the SERVE is $\bar{C}_{1111} = 2.8823E^M$, which is almost equal to that obtained from the entire MVE $\bar{C}^{\infty}_{1111} = 2.8836E^M$ is given in

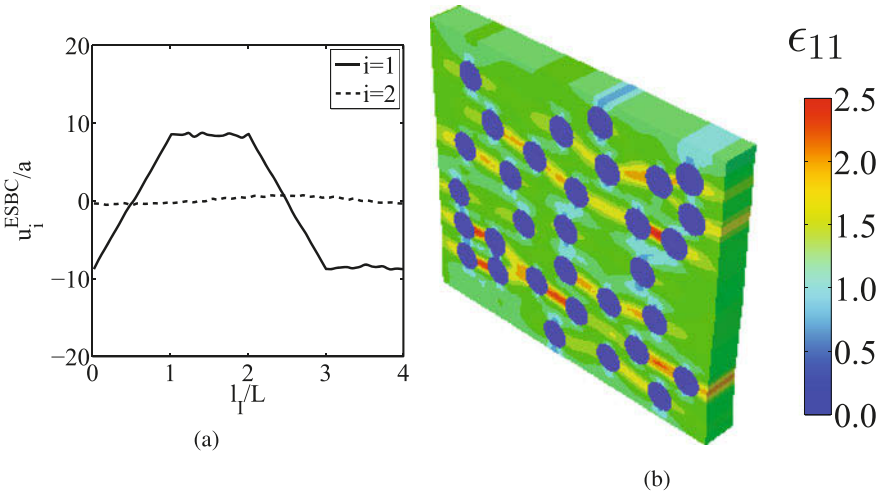

Fig. 10 Results from ESBC from SERVE with edges intersecting clusters: (**a**) displacement along the SERVE boundary, (**b**) contour plot of ϵ_{11} in the SERVE. (Reprinted from: Kubair and Ghosh [35])

Table 1. This example illustrates the effectiveness of the ESBCs for SERVEs with intersecting clusters.

4 Convergence of Elastic Homogenized Stiffness

4.1 Selection of SERVE Size from Convergence Characteristics

Figure 11 shows a set of concentric square cross-sections that are candidate SERVEs that can be extracted from the MVE domain. The candidate SERVEs are chosen to consist of an increasing number of fibers. The different SERVE sizes considered are depicted in Fig. 11(i–vii). The thickness of the composite domain is 10μm. The FE model is discretized into 4-noded tetrahedral elements with 13 elements in the z-direction. Details of the SERVE size L and the number of fibers N_f contained are listed in Table 2.

The candidate SERVEs are subjected to either ATDBCs, PBCs, or $S_2(r,\theta)$-based ESBCs that correspond to a far-field unit uniaxial strain $\epsilon_{11}^0 = 1$. All other strain components are kept to zero. Three-dimensional finite element simulations of the SERVEs are performed, and the homogenized stiffness $\bar{C}_{ijkl},\ i,j,k,l = 1,2,3$ are obtained by post-processing. Details of obtaining the homogenized moduli have been discussed in [18, 38]. The convergence in homogenized stiffness with increasing SERVE size is used as a metric to determine the necessary SERVE size. In particular, the dominant stiffness component $\bar{C}_{1111}$ is used to

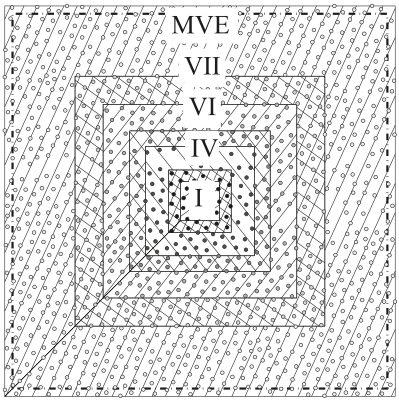

Fig. 11 Concentrically increasing candidate SERVE domains in the MVE generated from data in [43]

Table 2 Parameters in the selection of the SERVE

SERVE	I	II	III	IV	V	VI	VII	MVE
L (μm)	35	40	70	90	124	160	250	300
N_f	13	38	120	176	313	498	1292	1746

determine the effect of the applied boundary conditions on the converged SERVE size.

The homogenized stiffness component $\bar{C}_{1111}$ is plotted as a function of increasing SERVE size L in Fig. 12. In the plots, $L = 0$ corresponds to the matrix alone, for which the SERVE size is a material point of zero volume. The error in Fig. 12b is calculated as the difference between the homogenized stiffness component for the SERVEs and that for the entire MVE with L=300 μm. Figure 12a clearly shows that the homogenized modulus obtained with the ESBCs converges at a SERVE size of approximately $L = 40\,\mu$m consisting of 38 fibers. In contrast, much larger SERVE sizes of approximately $L \approx 220\,\mu$m are required when subjected to the ATDBC or PBC. The error plots in Fig. 12b consolidate this conjecture that convergence with ESBCs is much faster than with the other boundary conditions. This example elucidates the role of exterior statistics on the boundary condition of the SERVE.

Next, the effect of the 2-point correlation functions $S_2(r)$ or $S_2(r, \theta)$ on the optimal SERVE size is examined. The variation of the volume-averaged stiffness is plotted as a function of the SERVE size in Fig. 13a. The $S_2(r)$-based ESBCs exhibit much slower convergence leading to larger SERVEs in comparison to SERVEs by the $S_2(r, \theta)$-based ESBCs. In the example shown, the SERVE size by the latter boundary condition is less than half of that obtained by the former boundary condition. The plot of error in the homogenized stiffness, shown in Fig. 13b, also corroborates this conclusion.

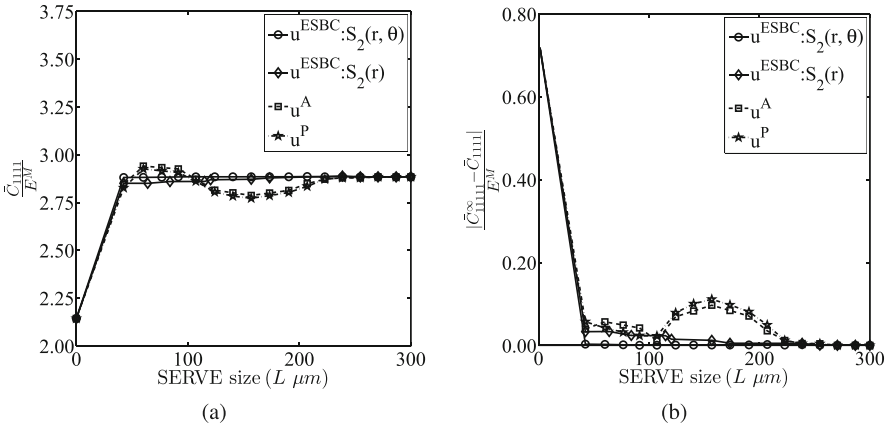

Fig. 12 Variation of (**a**) the normalized homogenized stiffness tensor $\bar{C}_{1111}/E^M$ and (**b**) error in $\bar{C}_{1111}$, as a function of increasing SERVE size. (Reprinted from: Kubair and Ghosh [35])

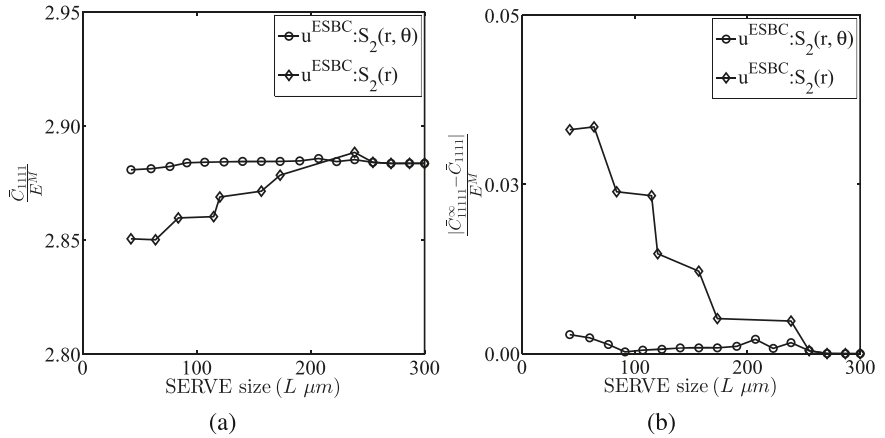

Fig. 13 Convergence of homogenized stiffnesses for $S_2(r)$ and $S_2(r, \theta)$-based ESBCs with increasing SERVE size: (**a**) variation of the normalized homogenized stiffness tensor $\bar{C}_{1111}/E^M$ and (**b**) variation of the normalized error. (Reprinted from Kubair and Ghosh [35])

4.2 Comparing Convergence of ESBC-Based SERVE with Statistical Volume Elements (SVEs)

Statistical volume elements (SVEs) are based on the ergodicity hypothesis that the composite microstructure with dispersed heterogeneities is statistically homogeneous, and hence, its volume averages are identical to the ensemble averages [44, 45]. In this approach, the homogenized modulus for the MVE is expected to be equal to the mean of the volume-averaged modulus obtained from a large

number of instantiations of a much smaller analysis volume. The ensemble average of any spatially varying field quantity $\Psi(\mathbf{x})$ over the SVE is expressed in terms of the homogenized value over the MVE as:

$$\bar{\Psi} = \frac{1}{\Omega^{\text{mve}}} \int\limits_{\Omega^{\text{mve}}} \Psi\left(\mathbf{x}\right) d\Omega = \frac{1}{N} \sum_{I=1}^{I=N} \left(\frac{1}{\Omega^{\text{sve}_I}} \int\limits_{\Omega^{\text{sve}_I}} \Psi\left(\mathbf{x}\right) d\Omega \right), \tag{26}$$

where $\bar{\Psi}$ is the volume-averaged value, Ω^{sve_I} is the domain of the Ith SVE instantiation, and N corresponds to the number of sample SVEs in the ensemble. In general, the volume of any SVE is much smaller than that of the RVE, i.e., $\Omega^{\text{sve}_I} < \Omega^{rve}$.

For comparison with the SERVE predictions, the SVE problem is set up with individual square SVEs of size $L^I = 60\,\mu\text{m}$, $100\,\mu\text{m}$ and $200\,\mu\text{m}$. One hundred candidate SVEs are chosen from the much larger MVE for each SVE size. Two-dimensional plane strain analysis of the candidate SVEs is performed subjected to ATDBCs and PBCs. The ensemble-averaged stiffness components $\bar{C}_{ijkl}$ are obtained for the population of N SVEs as:

$$\bar{C}_{ijkl} = \frac{1}{N} \sum_{I=1}^{I=N} \bar{C}^I_{ijkl} \tag{27}$$

where $\bar{C}^I_{ijkl}$ are the volume-averaged stiffness components for the $I-$th SVE. With increasing number of instantiations in the ensemble population N, the ensemble-averaged stiffness components are expected to converge to their respective homogenized values for the MVE ($\bar{C}^{\infty}_{ijkl}$). The convergence criterion is defined in terms of the minimum number of instantiations or SVEs N required in the ensemble to attain a steady-state, invariant value of the homogenized stiffness in equation (27). Convergence is ascertained from the plot of the cumulative mean (CM) of the normalized stiffness as a function of the ensemble population size N, as shown in Fig. 14a. The cumulative mean of a stiffness component $\bar{C}_{ijkl}$, normalized by the matrix Young's modulus E^M, is defined as:

$$CM\left(\frac{\bar{C}_{ijkl}}{E^M}\right)_N = \frac{1}{N} \sum_{I=1}^{I=N} \frac{\bar{C}^I_{ijkl}}{E^M}$$

For an ergodic microstructure, the cumulative mean (CM) of the volume-averaged stiffness is expected to converge to that of the entire MVE $\bar{C}^{\infty}_{ijkl}$. The CM of $\bar{C}_{1111}$, obtained from the three SVE sizes, are shown in Fig. 14a. For SVE size $L^{\text{sve}} = 60\,\mu\text{m}$, the ensemble-averaged stiffness even with 100 instantiations does not converge to the accurate value obtained from the SERVE analysis. For the SVE size of $L^{\text{sve}} = 200\,\mu\text{m}$, the cumulative mean converges for ensembles consisting of more than 15 SVE instantiations. The corresponding error in CM, defined as

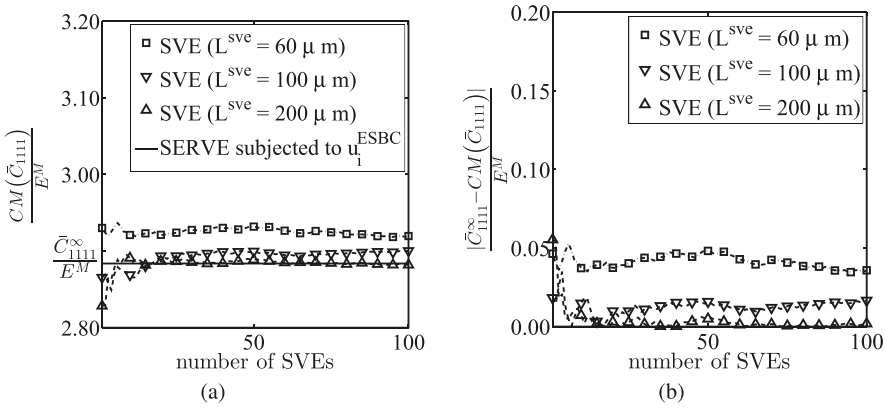

Fig. 14 (**a**) Cumulative mean (CM) of the ensemble-averaged stiffness component $\bar{C}_{1111}$as a function of the number of SVEs for different SVE sizes (L^{sve}); (**b**) error in CM of the stiffness as a function of the number of SVEs. (Reprinted from: Kubair and Ghosh [35])

the difference from the stiffness $\bar{C}^{\infty}_{1111}$, is plotted as a function of the number of SVEs in Fig. 14b. This confirms the lack of convergence for smaller size SVEs. SERVEs subjected to ESBCs require only one instantiation of size $L^{\text{serve}}40\,\mu\text{m}$ for convergence, as illustrated in Fig. 12.

5 ESBCs for Polydispersed Microstructures of Carbon Fiber Polymer Matrix Composites

The efficacy of the ESBC-based SERVEs is examined in this section for a unidirectional polymer matrix composite (IM7/977-3 PMC) with a polydispersed microstructure containing a nonuniform distribution of IM7 carbon fibers of varying sizes in a 977-3 epoxy matrix.

5.1 Microstructure Imaging, Characterization, and Mechanical Testing

The unidirectional polymer matrix composite (IM7/977-3 PMC) has a composition of IM7 carbon fibers of varying sizes (mean radius of 2.43 μm and standard deviation of 0.11 μm) nonuniformly distributed in a 977-3 epoxy matrix. Details of processing this composite are given in [39]. A 200 × 250 μm montage, acquired by the software autofocus with a 500× objective lens, is depicted in Fig. 1a. The overall fiber volume fraction of this microstructure is ∼62%. Mechanical tests on the PMC are performed following the ASTM-D3039 standardized test protocols

Table 3 Experimentally obtained elastic properties of the IM7/977-3 polymer matrix composite [46]

Property	Mean	St. Dev.
Tens. longitudinal modulus (E_{1T})	164 GPa	4.12
Comp. longitudinal modulus (E_{1C})	137 GPa	0.608
Tens. transverse modulus (E_{2T})	8.98 GPa	0.284
Compressive transverse modulus (E_{2C})	8.69 GPa	0.367
In-plane shear modulus (G_{12})	5.01 GPa	0.249
Major Poisson's ratio (ν_{12})	0.320	0.0266

and have been reported in [46]. The elastic properties of the IM7/977-3 polymer matrix composite are selectively documented in Table 3. The effective stiffness coefficient can be calculated from values in Table 2. For example, the transverse stiffness component $\bar{C}^{\text{exp}}_{1111} = 11.4 \pm 0.3597$ GPa, which is of the same order as E_{2T}.

For micromechanical analysis, material properties of the microstructural constituents are obtained from various sources. The Young's modulus and Poisson's ratio of the isotropic 977-3 epoxy matrix are $E^M = 2.5$ GPa and $\nu^M = 0.43$, respectively. The IM7 carbon fibers are assumed to be transversely isotropic, for which the modulus in the longitudinal direction is recorded in the manufacturer database [47] as $E^F_{\text{long}} = 276$ GPa. The transverse direction modulus of the IM7 carbon fibers has been experimentally obtained in the Sottos group [48] as $E^F_{\text{trans}} = 19.5$ GPa, while the Poisson's ratio is $\nu^F = 0.23$.

5.2 *Statistical Characterization of the Polydispersed Microstructure*

An image-processed micrograph of the cross-section of the unidirectional PMC is shown in Fig. 1a. A large region in the micrograph is designated as the MVE and tessellated into a network of Voronoi cells [9], based on the fiber centroids, as shown in Fig. 15a. The selected MVE consists of 1239 fibers with a median fiber radius of 2.4624 μm. Voronoi cells provide a basis for microstructural characterization. The local fiber volume fraction Φ is defined as the ratio of the fiber cross-sectional area to the area of the associated Voronoi cell, and the shading represents the level of Φ. Brighter cells with lower values of Φ indicate regions that are matrix rich, while darker cells with large Φ indicate regions of fiber clustering.

The probability density functions (PDF) of the local volume fraction Φ and the fiber size of the MVE are, respectively, plotted in Fig. 15b, c. The median volume fraction is evaluated to be $\Phi = 0.63$. The distribution of the normalized 2-point correlation function $\frac{S_2(r,\theta)}{S_1^2}$ is shown in Fig. 15d, where S_1 is the 1-point correlation function corresponding to the overall volume fraction, and $S_2(r, \theta)$ is the radial distance and orientation-dependent, 2-point correlation function [30]. The function $\frac{S_2(r,\theta)}{S_1^2}$ has a peak near the center and reaches a far-field value of S_1^2 with some oscillations.

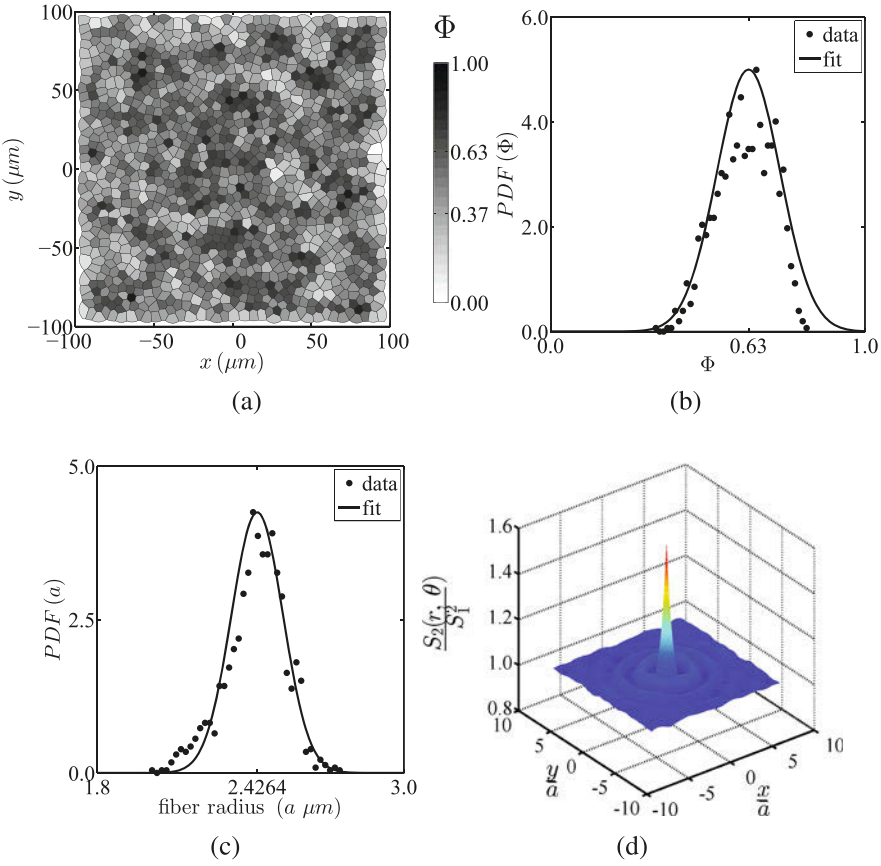

Fig. 15 (**a**) Voronoi tessellation of the polydispersed microstructural volume element (MVE) with gray-scale shading corresponding to the local volume fraction Φ (coordinates x (or 1) and y (or 2) correspond to transverse directions in the section, while z (or 3) corresponds to the longitudinal direction of the fibers); probability distribution functions of (**b**) volume fraction Φ; (**c**) fiber size, and (**d**) the radial distance and orientation-dependent 2-point correlation function $S_2(r, \theta)$ of the polydispersed MVE

5.3 *Creating Statistically Equivalent MVEs from Experimental Micrographs*

Prior to conducting DNS of the SERVE for effective properties, it is important to create *statistically equivalent microstructural volume elements* (SE-MVEs) that are representative of the entire experimental micrograph as in Fig. 1a with identical statistical distributions. The SE-MVE forms the parent domain from which SERVEs may be extracted. The SE-MVEs are obtained by a Monte Carlo-type reconstruction method using the 2-point correlation function S_1, 2-point correlation function S_2, and the probability distribution of fiber radius in the PMC micrograph, depicted

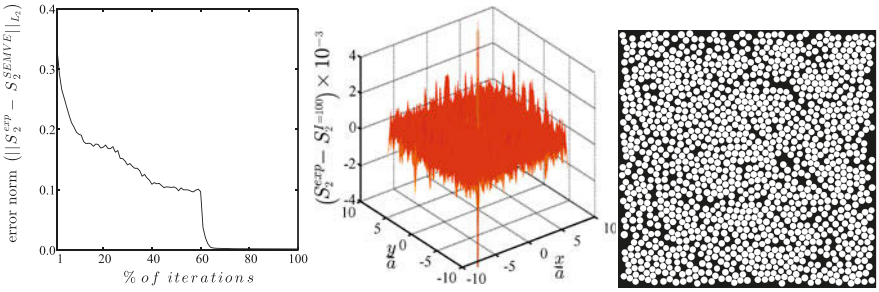

Fig. 16 (**a**) Convergence with respect to the L_2-norm of error with progressive iterations and (**b**) map of error in the $S_2\,(r, \theta)$ field between the experimental MVE and reconstructed SE-MVEs and (**c**) square window containing the final SE-MVE microstructure with $N_f \sim 2000$ fibers

in Fig. 15. The process initializes the positions of N_f chosen fibers in hexagonal close packing arrangements within the MVE, with the initial spacing between fibers determined from the global volume fraction S_1. The radii of these fibers are assigned by randomly sampling from the fiber size distribution in Fig. 15c. Values of parameters used to start the process are $N_f \approx 2000$, $S_1 = 0.65$, mean fiber radius $= 2.43\,\mu$m, and standard deviation of $= 0.11\,\mu$m. The reconstruction process executes a large number of iterations ($\sim 1000 N_f$). The centroid of a randomly selected fiber is perturbed in each iteration to transform the hexagonal arrangement to an amorphous microstructure. Nonoverlapping perturbations are accepted for the first $\sim$60% of the iterations toward this amorphization. The subsequent 40% iterations optimize the configuration of the SE-MVE by minimizing the L_2-norm of the difference between the SE-MVE instantiation and the reference MVE.

$$||S_2^{\text{exp}}\,(r,\theta) - S_2^{SEMVE}\,(r,\theta)||_{L_2} = \sqrt{\int_{\Omega^{MVE}} \left(S_2^{\text{exp}}\,(r,\theta) - S_2^{SEMVE}\,(r,\theta)\right)^2 d\Omega} \tag{28}$$

After each nonoverlapping fiber shuffle, $S_2(r, \theta)$ of the SE-MVE is evaluated, and the resulting L_2-norm is compared with that for the unperturbed state. The move is accepted only if there is an improvement with respect to the L_2-norm. Figure 16a shows the convergence in $S_2\,(r, \theta)$ as a function of iterations. The rate of convergence is rapid in the beginning of the amorphization. At $\sim$60% of iterations, the optimization algorithm begins with a sharp increase in convergence rate and stabilizes at around 70% of the iterations. The map of error in the $S_2\,(r, \theta)$ field, between the experimental MVE and the reconstructed final SE-MVE of Fig. 16c, is given in Fig. 16b. Figure 16c shows the square window containing the SEMVE represented by the fibers.

5.4 Micromechanical Analysis of the Polydispersed SERVE with ESBCs

The ESBCs for the statistically nonhomogeneous microstructures in Sect. 2 are extended for polydispersed microstructures in this section. For polydispersed fibers, the distribution of fiber radius a is represented by the probability density function of the fiber size $PDF(a)$. A relative position vector $\mathbf{r} = \mathbf{x} - \mathbf{x}^I$, where $\mathbf{x}$ is a generic spatial point and $\mathbf{x}^I$ is a reference point, is used to represent the 2-point kernel functions. The eigenstrain ϵ_{ij}^{Λ} in a reference fiber occupying a domain Ω^F given in equation (22) is correspondingly modified as:

$$\epsilon_{ij}^{\Lambda}(\mathbf{x}) = [\ \iota^F(\mathbf{x})\left(S_{ijab} + M_{ijab}\right) - \int\limits_{\Omega^{\text{mve}}\setminus\Omega^F} PDF(a) S_2(\mathbf{r}) \hat{G}_{ijmn}(\mathbf{r}, a)\left(S_{mnpq} + M_{mnpq}\right)^{-1}$$

$$\hat{G}_{pqab}(\mathbf{r}, a) d\Omega\ ]^{-1}\ [\ (\ (S_{abmn} + M_{abmn})^{-1} \int\limits_{\Omega^{\text{mve}}\setminus\Omega^F} PDF(a) S_2(\mathbf{r}) \hat{G}_{mnkl}(\mathbf{r}, a) d\Omega\ ) -$$

$$\frac{1}{2}\left(\delta_{ak}\delta_{bl} + \delta_{al}\delta_{bk}\right)\ ]\epsilon_{kl}^M = A_{ijkl}(\mathbf{x})\epsilon_{kl}^M \quad \forall \mathbf{x} \in \Omega^{\text{mve}} \tag{29}$$

S_{ijkl} are the spatially invariant interior, $\hat{G}_{ijkl}(\mathbf{r}, a)$ are the position- dependent exterior Eshelby tensors, respectively, and ι is a phase-based unit function. Furthermore, $M_{ijkl} = \left(C_{ijpq}^F - C_{ijpq}^M\right)^{-1} C_{pqkl}^M$, with C_{ijkl}^M and C_{ijkl}^F being the elastic stiffness of the matrix and inclusion materials, respectively. The perturbed displacements at an observation point O in Fig. 2b are written in terms of the matrix strain as:

$$u_i^*(\mathbf{x}) = \left[\int\limits_{\Omega^{\text{mve}}\setminus\Omega^F} PDF(a)\, S_2\left(\mathbf{r}'\right) L_{imn}\left(\mathbf{r}', a\right) A_{mnkl}\left(\mathbf{r}'\right) d\Omega\right] \epsilon_{kl}^M \tag{30}$$

where $L_{ikl}(\mathbf{r})$ is a unified displacement-transfer tensor. Finally, using equation (8), the affine transformation-based displacement fields are superposed on the perturbed displacements to prescribe the exterior statistics-based boundary conditions. The ESBCs are applied on the boundary Γ^{serve} of a SERVE domain Ω^{serve} of size L using the steps given in Sect. 2.2 with a few modifications.

In step 5, the perturbed displacements u_i^* are computed using equation (30) incorporating $PDF(a)$ and $S_2(r, \theta)$ for all the boundary nodes, using the following steps:

- Each radial orientation is discretized into N_r number of equally spaced segments with increment $\Delta r = \frac{R-a}{N_r}$, where a is the fiber radius, R is the radius of horizon (extent of the MVE), and the lower limit of the integration is $r = a$. The αth radial point is given as $r_\alpha = \alpha \frac{R-a}{N_r}$.

- The angular orientation is discretized into N_θ equally spaced points of $\Delta\theta = \frac{2\pi}{N_\theta}$. The βth angular point is $\theta_\beta = \beta\frac{2\pi}{N_\theta}$.
- The fiber size distribution is discretized into N_a equally spaced bins with $\Delta a = \frac{a_{\max}-a_{\min}}{N_a}$, $a_{\max}$ and $a_{\min}$ being the maximum and minimum fiber size.
- At a SERVE boundary node at x_i, the discrete perturbed displacement components in equation (30) are evaluated for an applied strain ϵ^0_{ij} as:

$$u_i^*(\mathbf{x}) = [\sum_{\gamma=1}^{N_a} \frac{2\pi(R-\gamma\Delta a)}{N_r N_\theta} \sum_{\alpha=1}^{N_r}\sum_{\beta=1}^{N_\theta} \alpha L_{imn}\,(\mathbf{x} - (\alpha\Delta r, \beta\Delta\theta, \gamma\Delta a)) \times$$
$$A_{mnkl}\,(\mathbf{x} - (\alpha\Delta r, \beta\Delta\theta))\, S_2\,(\mathbf{x} - (\alpha\Delta r, \beta\Delta\theta))\, PDF\,(\gamma\Delta a)\,]\,\epsilon^0_{ij} \tag{31}$$

The ESBCs on the boundary nodes are computed using equation (25).

5.5 Candidate SERVE Selection from Stiffness Convergence

Candidate SERVEs are extracted from the SE-MVE domain in Fig. 16c for simulations leading to the homogenized stiffness evaluation. Figure 17a shows a set of five concentric cross-sections (i-v) with increasing number of fibers in the SE-MVE that can be used as candidate SERVEs. The SERVE boundaries coincide with the Voronoi cell boundaries at the edges of the MVE, and hence Γ^{serve} does not intersect any fiber. The thickness of the composite domain is considered to be 10μm. The FE model is discretized into four-noded tetrahedral elements with ten elements in the z-direction.

The composite system is assumed to be the weakest in transverse loading, as corroborated by the transverse modulus E_{2T} in Table 3. Hence the analyses are performed in the transverse direction. The SERVEs are subjected to both ATDBCs and ESBCs, corresponding to a far-field unit uniaxial strain in the transverse direction $\epsilon^0_{11} = 1$. The axes 1 (or x) and 2 (or y) in Fig. 17a correspond to the transverse directions, and the fiber axis is in the 3 (or z) direction. All other strain components are set to zero. 3D finite element simulations of the SERVEs are performed, and the homogenized stiffness $\bar{C}_{ijkl},\ i, j, k, l = 1, 2, 3$ are evaluated by averaging the stress and strain fields. The analyses represent tensile loading in the critical transverse direction, for which the tensile strength is the least. Convergence in the homogenized stiffness with increasing SERVE size is used as a metric to determine the optimal SERVE size. In this study, the critical stiffness component $\bar{C}_{1111}$ is used to determine the effectiveness of the applied boundary conditions on the converged SERVE size.

The homogenized stiffness component $\bar{C}_{1111}$, normalized by the matrix stiffness, is plotted as a function of the P-SERVE size L in Fig. 17b. The figure shows that the

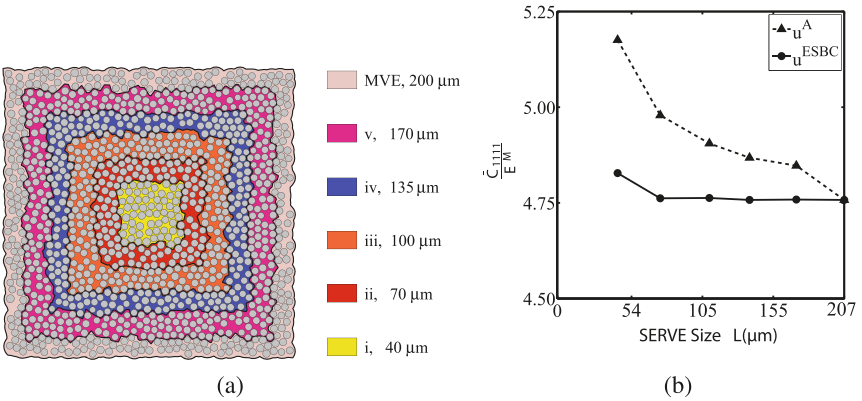

(a) (b)

Fig. 17 (**a**) Concentrically increasing candidate SERVE domains in the MVE for micromechanical simulations and (**b**) convergence of the normalized homogenized stiffness tensor $\bar{C}_{1111}/E^M$ with SERVE size

Table 4 Comparison of convergence conditions for different cases

	Bound. Cond.	Size	# instantiations
SERVE	ATDBC	200 µm	1
SVE	ATDBC	200 µm	10
SERVE	ESBC	70 µm	1

homogenized modulus obtained with the ESBCs (superscript ESBC) converges at a SERVE size of approximately $L = 70\,\mu\text{m}$ consisting of 179 fibers. In contrast, a much larger P-SERVE sizes of approximately $L \approx 200\ \mu\text{m}$ is necessary for convergence when subjected to the ATDBC.

5.6 *Comparing the SERVE and SVE Stiffness with Experimental Observations*

Results of mechanical tests in [46] have been discussed in the section on characterization and testing. The dominant stiffness coefficient is evaluated as $\bar{C}^{\text{exp}}_{1111} = 11.4 \pm 0.3597\,\text{GPa}$. The homogenized stiffness is obtained from finite element simulations of the SERVEs subjected to both ATDBCs and ESBCs. In addition, the homogenized stiffness is also computed from SVEs subjected to ATDBCs as discussed in Sect. 4.2. All the cases in their respective converged situations yield $\bar{C}^{\text{serve}}_{1111} = \bar{C}^{\text{sve}}_{1111} = 11.9\,\text{GPa}$, which is within the acceptable range of the experimental error. The conditions for convergence of the different cases are given in Table 4. The SERVEs with ESBCs require the smallest volume Ω^{serve} for convergence with only one iteration. This is a significant advantage over the other methods proposed in the literature.

6 Summary and Conclusions

This chapter discusses the development of the exterior statistics-based boundary conditions or ESBCs, for statistically equivalent RVEs of elastic composites with a nonuniform distribution of fibers [35, 38, 39]. Boundary conditions are complementary to the micromechanical SERVE domain for micromechanical simulations. The ESBCs overcome deficiencies with conventionally applied boundary conditions, such as the affine transformation-based displacement boundary conditions (ATDBCs) or periodic boundary conditions (PBCs) in evaluating homogenized material properties. These deficiencies arise from overlooking the actual statistics of heterogeneities in nonuniform microstructures, where the effect of the exterior microstructure on the SERVE can be significant. The SERVE-ESBC model is capable of resulting in an optimal SERVE domain due to the representation of realistic boundary conditions. This results in significant computational efficiency. Development of the ESBCs for the large exterior region needs characterization for statistical analysis, which is efficiently accomplished for most material systems. Validation results clearly show the significant advantage and potential of this method, both in terms of the volume to be modeled for determining effective mechanical properties and the number of iterations. In the case of high fiber volume fractions, higher-order correlation functions such as S_3, convoluted with the proper three-body polarization tensor, may be helpful. In conclusion, the ESBCs are very effective boundary conditions when modeling linear elastic heterogeneous materials with nonuniform distributions of heterogeneities. Extension to nonlinear materials will however require a different formulation due to the use of superposition methods in this approach. Alternative approaches are in consideration for nonlinear heterogeneous materials.

Appendix: Eshelby Tensors for Circular Cylindrical Fibers

For a cylindrical fiber of circular cross-section with a radius a and centroid at $\mathbf{x}^I$, let $\mathbf{r} = \mathbf{x} - \mathbf{x}^I$, $\mathbf{x}$ being a generic field point. Let $\rho = \frac{a}{r}$ with $r = |\mathbf{x} - \mathbf{x}^I|$ and $\theta = \angle(\mathbf{x} - \mathbf{x}^I)$. Then the interior and exterior Eshelby tensors S_{ijkl} and $\hat{G}_{ijkl}\left(\mathbf{x}, \mathbf{x}^I\right)$ have been given in [41] as:

$$S_{ijkl} = \{\alpha\}^T \{\Theta_{ijkl}\}(\theta) \quad \text{and} \quad \hat{G}_{ijkl}\left(\mathbf{x}, \mathbf{x}^I\right) = \{\beta\}^T(r)\{\Theta_{ijkl}\}(\theta) \tag{32}$$

The material-dependent vectors $\{\alpha\}$ and $\{\beta\}$ are:

$$\{\alpha\} = \frac{1}{8\left(1-\nu^M\right)} \begin{Bmatrix} 4\nu^M - 1 \\ 3 - 4\nu^M \\ 0 \\ 0 \\ 0 \end{Bmatrix}, \quad \{\beta\}(r) = \frac{\rho^2}{8\left(1-\nu^M\right)} \begin{Bmatrix} -2\left(1+2\nu^M\right) + 9\rho^2 \\ 2 - 3\rho^2 \\ 4(1+2\nu^M) - 12\rho^2 \\ 4 - 12\rho^2 \\ 16 - 24\rho^2 \end{Bmatrix}$$

The parameter ν^M is the Poisson's ratio of the matrix material. The circumference basis tensor is given as:

$$\{\Theta_{ijkl}\}(\theta) = \begin{Bmatrix} \delta_{ij}\delta_{kl} \\ \delta_{ik}\delta_{jl} + \delta_{il}\delta_{jk} \\ \delta_{ij}n_k n_l \\ n_i n_j \delta_{kl} \\ n_i n_j n_k n_l \end{Bmatrix}, \quad \text{where} \begin{Bmatrix} n_1 \\ n_2 \\ n_3 \end{Bmatrix} = \begin{Bmatrix} \cos\theta \\ \sin\theta \\ 1 \end{Bmatrix}$$

For the cylindrical fiber of circular cross-section, the interior and exterior displacement-transfer tensors are given by:

$$T_{ijk}\left(\mathbf{x}, \mathbf{x}^I\right) = \{\eta\}^T(r)\{\Psi_{ijk}\}(\theta) \quad \text{and} \quad D_{ijk}\left(\mathbf{x}, \mathbf{x}^I\right) = \{\gamma\}^T(r)\{\Psi_{ijk}\}(\theta) \tag{33}$$

where

$$\{\eta\}(r) = a\frac{\rho}{8\left(1-\nu^M\right)} \begin{Bmatrix} 4\nu^M - 1 \\ 3 - 4\nu^M \\ 0 \end{Bmatrix}, \quad \{\gamma\}(r) = a\frac{\rho}{8\left(1-\nu^M\right)} \begin{Bmatrix} -2\left(1-2\nu^M\right) + \rho^2 \\ 2\left(1-2\nu^M\right) + \rho^2 \\ 4\left(1-\rho^2\right) \end{Bmatrix}$$

and

$$\{\Psi_{ijk}\}(\theta) = \begin{Bmatrix} n_i\delta_{jk} \\ n_j\delta_{ik} + n_k\delta_{ij} \\ n_i n_j n_k \end{Bmatrix}$$

Acknowledgements This work has been supported through a grant No. FA9550-12-1-0445 to the Center of Excellence on Integrated Materials Modeling (CEIMM) at Johns Hopkins University awarded by the AFOSR/RSL Computational Mathematics Program (Manager Dr. A. Sayir) and AFRL/RX (Monitors Drs. C. Woodward and C. Przybyla). These sponsorships are gratefully acknowledged. Computing support by the Homewood High-Performance Compute Cluster (HHPC) and Maryland Advanced Research Computing Center (MARCC) is gratefully acknowledged.

References

1. R. Hill, Elastic properties of reinforced solids: some theoretical principles. J. Mech. Phys. Solids **11**, 357–372 (1963)
2. Z. Hashin, S. Shtrikman, A variational approach to the theory of the elastic behaviour of multiphase materials. J. Mech. Phys. Solids **11**(2), 127–140 (1963)
3. M. Stroeven, H. Askes, L.J. Sluys, Numerical determination of representative volumes for granular materials. Comput. Methods Appl. Mech. Eng. **193**(30–32), 3221–3238 (2004)
4. M. Thomas, N. Boyard, L. Perez, Y. Jarny, D. Delaunay, Representative volume element of anisotropic unidirectional carbon-epoxy composite with high-fibre volume fraction. Compos. Sci. Technol. **68**(15–16), 3184–3192 (2008)
5. C. Heinrich, M. Aldridge, A.S. Wineman, J. Kieffer, A.M. Waas, K. Shahwan, The influence of the representative volume element (RVE) size on the homogenized response of cured fiber composites. Model. Simul. Mater. Sci. Eng. **20**(7), 075007 (2012)
6. R. Hill, The essential structure of constitutive laws for metal composites and polycrystals. J. Mech. Phys. Solids **15**, 79–95 (1967)
7. H.J. Böhm, A short introduction to continuum micromechanics, in *Mechanics of Microstructured Materials: CISM Courses and Lectures*, ed. by H.J. Böhm, vol. 464 (Springer, Wien, 2004), pp. 1–40
8. P.W. Chung, K.K. Tamma, R.R. Namburu, A finite element thermo-viscoelastic creep for heterogeneous structures with dissipative correctors. Finite Elem. Anal. Des. **36**, 279–313 (2000)
9. S. Ghosh, *Micromechanical Analysis and Multi-scale Modeling Using the Voronoi Cell Finite Element Method* (CRC Press/Taylor & Francis, Boca Raton, 2011)
10. N. Willoughby, W.J. Parnell, A.L. Hazel, I.D. Abrahams, Homogenization methods to approximate the effective response of random fibre-reinforced composites. Int. J. Solids Struct. **49**(13), 1421–1433 (2012)
11. J. Fish, K. Shek, Multiscale analysis of composite materials and structures. Compos. Sci. Technol. **60**, 2547–2556 (2000)
12. S. Ghosh, K. Lee, S. Moorthy, Multiple scale analysis of heterogeneous elastic structures using homogenization theory and Voronoi cell finite element method. Int. J. Solids Struct. **32**(1), 27–62 (1995)
13. S. Ghosh, K. Lee, S. Moorthy, Two scale analysis of heterogeneous elastic-plastic materials with asymptotic homogenization and Voronoi cell finite element model. Comput. Methods Appl. Mech. Eng. **132**(1–2), 63–116 (1996)
14. J.M. Guedes, N. Kikuchi, Preprocessing and postprocessing for materials based on the homogenization method with adaptive finite element methods. Comput. Methods Appl. Mech. Eng. **83**, 143–198 (1991)
15. V. Kouznetsova, M.G.D. Geers, W.A.M. Brekelmans, Multi-scale constitutive modelling of heterogeneous materials with a gradient-enhanced computational homogenization scheme. Int. J. Numer. Methods Eng. **54**, 1235–1260 (2002)
16. K. Terada, N. Kikuchi, Simulation of the multi-scale convergence in computational homogenization approaches. Int. J. Solids Struct. **37**, 2285–2311 (2000)
17. F. Feyel, J.H. Chaboche, FE^2 multiscale approach for modelling the elastoviscoplastic behaviour of long fibre SiC/Ti composite materials. Comput. Methods Appl. Mech. Eng. **183**, 309–330 (2000)
18. S. Swaminathan, S. Ghosh, N.J. Pagano, Statistically equivalent representative volume elements for unidirectional composite microstructures: part I-without damage. J. Compos. Mater. **40**(7), 583–604 (2006)
19. S. Swaminathan, N.J. Pagano, S. Ghosh, Statistically equivalent representative volume elements for unidirectional composite microstructures: part II-with interfacial debonding. J. Compos. Mater. **40**(7), 605–621 (2006)

20. M. Pinz, G. Weber, W. Lenthe, M. Uchic, T.M. Pollock, S. Ghosh, Microstructure and property based statistically equivalent RVEs for intragranular $\gamma - \gamma'$ microstructures of Ni-based superalloys. Acta Mater. **157**(15), 245–258 (2018)
21. A. Bagri, G. Weber, J.-C. Stinville, W. Lenthe, T. Pollock, C. Woodward, S. Ghosh, Microstructure and property-based statistically equivalent representative volume elements for polycrystalline Ni-based superalloys containing annealing twins. Metall. Mater. Trans. A **49**(11), 5727–5744 (2018)
22. X. Tu, A. Shahba, J. Shen, S. Ghosh, Microstructure and property based statistically equivalent RVEs for polycrystalline-polyphase aluminum alloys. Int. J. Plast. **115**, 268–292 (2019)
23. T. Kanit, S. Forest, I. Galliet, V. Mounoury, D. Jeulin, Determination of the size of the representative volume element for random composites: statistical and numerical approach. Int. J. Solids Struct. **40**(13–14), 3647–3679 (2003)
24. P. Trovalusci, M. Ostoja-Starsewski, M.L. De Bellis, A. Murrali, Scale-dependent homogenization of random composites as micropolar continua. Eur. J. Mech. A Solids **49**, 396–407 (2015)
25. E. Recciaa, M.L. De Bellis, P. Trovalusci, R. Masiani, Sensitivity to material contrast in homogenization of random particle composites as micropolar continua. Compos. Part B **136**, 39–45 (2018)
26. R. Pyrz, Correlation of microstructure variability and local stress-field in 2-phase materials. Mater. Sci. Eng. A-Struct. Mater. Prop. Microstruct. Process. **177**(1–2), 253–259 (1994)
27. S. Torquato, Effective stiffness tensor of composite media-I. exact series expansions. J. Mech. Phys. Solids **45**(9), 1421–1448 (1997)
28. S.E. Wilding, D.T. Fullwood, Clustering metrics for two-phase composites. Comput. Mater. Sci. **50**(7), 2262–2272 (2011)
29. E.-Y. Guo, N. Chawla, T. Jing, S. Torquato, Y. Jiao, Accurate modeling and reconstruction of three-dimensional percolating filamentary microstructures from two-dimensional micrographs via dilation-erosion method. Mater. Charact. **89**, 33–42 (2014)
30. Y. Jiao, F.H. Stillinger, S. Torquato, Modeling heterogeneous materials via two-point correlation functions: basic principles. Phys. Rev. E **76**, 031110 (2007)
31. Y. Jiao, F.H. Stillinger, S. Torquato, A superior descriptor of random textures and its predictive capacity. Proc. Nat. Acad. Sci. USA **106**(42), 17634–17639 (2007)
32. A Tewari, A.M Gokhale, J.E Spowart, D.B Miracle, Quantitative characterization of spatial clustering in three-dimensional microstructures using two-point correlation functions. Acta Mater. **52**(2), 307–319 (2004)
33. D.T. Fullwood, S.R. Niezgoda, S.R. Kalidindi, Microstructure reconstructions from 2-point statistics using phase-recovery algorithms. Acta Mater. **56**, 942–948 (2008)
34. S.R. Niezgoda, D.T. Fullwood, S.R. Kalidindi, Delineation of the space of 2-point correlations in a composite material system. Acta Mater. **56**(18), 5285–5292 (2008)
35. D.V. Kubair, S. Ghosh, Exterior statistics based boundary conditions for establishing statistically equivalent representative volume elements of statistically nonhomogeneous elastic microstructures. Int. J. Solids Struct. **112**, 106–121 (2017)
36. T.I. Zohdi, P. Wriggers, *An introduction to Computational Micromechanics* (Springer-Verlag Berlin, Heidelberg, 2004). https://doi.org/10.1007/978-3-540-32360-0
37. M. Ostoja-Starzewski, *Microstructural Randomness and Scaling in Mechanics of Materials* (Chapman and Hall/CRC, Boca Raton, 2007)
38. S. Ghosh, D.V. Kubair, Exterior statistics based boundary conditions for representative volume elements of elastic composites. J. Mech. Phys. Solids **96**, 1–24 (2016)
39. D. V. Kubair, M. Pinz, K. Kollins, C. Przybyla, S. Ghosh, Role of exterior statistics-based boundary conditions for property-based statistically equivalent RVEs of polydispersed elastic composites. J. Comput. Mech. **52**(21), 2919–2928 (2018)
40. S. Torquato, *Random Heterogeneous Materials; Microstructure and Macroscopic Properties* (Springer, New York, 2002)
41. T. Mura, *Micromechanics of Defects in Solids*, 2nd edn. (Kluwer Academic Publishers and Martinus Nijhoff, Dordrecht, 1987)

42. J.D. Eshelby, The determination of the elastic field of an ellipsoidal inclusion and related problems. Proc. R. Soc. Lond. **A241**, 376–396 (1957)
43. W. Lenthe, C. Pollock, Microstructural characterization of unidirectional composites. Private Communications (2014)
44. X. Yin, A. To, C. McVeigh, W.K. Liu, Statistical volume element method for predicting microstructure–constitutive property relations. Comput. Methods Appl. Mech. Eng. **197**, 3516–3529 (2008)
45. D.L. McDowell, S. Ghosh, S.R. Kalidindi, Representation and computational structure-property relations of random media. JOM, TMS **63**(3), 45–51 (2011)
46. S.W. Clay, P.M. Knoth, Experimental results of quasi-static testing for calibration and validation of composite progressive damage analysis methods. J. Compos. Mater. **10**, 1333–1353 (2016)
47. HEXCEL, Composite materials and structures (2017)
48. C. Montgomery, N. Sottos, Experiments for properties of composites. Unpublished work. Private communication (2017)

Transverse Failure of Unidirectional Composites: Sensitivity to Interfacial Properties

Scott Zacek, David Brandyberry, Anthony Klepacki, Chris Montgomery, Maryam Shakiba, Michael Rossol, Ahmad Najafi, Xiang Zhang, Nancy Sottos, Philippe Geubelle, Craig Przybyla, and George Jefferson

1 Introduction

In fiber-reinforced polymer-matrix composite laminates, transverse plies are needed to provide stiffness and strength under multiaxial loading. However, unidirectional plies typically have a relatively low transverse strength [1]. Transverse cracking in these plies results in degraded material properties and often leads to further

The original version of this chapter was revised: Missed out co-author name has been added. The correction to this chapter is available at https://doi.org/10.1007/978-3-030-40562-5_15

S. Zacek · D. Brandyberry · A. Klepacki · P. Geubelle (✉)
Department of Aerospace Engineering, University of Illinois, Urbana, IL, USA
e-mail: brandyb2@illinois.edu; geubelle@illinois.edu

C. Montgomery · M. Rossol · N. Sottos
Department of Materials Science and Engineering, University of Illinois, Urbana, IL, USA
e-mail: cbmontg2@illinois.edu; n-sottos@illinois.edu

M. Shakiba
Department of Civil and Environmental Engineering, Virginia Tech., Blacksburg, VA, USA
e-mail: mshakiba@vt.edu

A. Najafi
Department of Mechanical Engineering and Mechanics, Drexel University, Philadelphia, PA, USA
e-mail: arn55@drexel.edu

X. Zhang
Department of Mechanical Engineering, University of Wyoming, Laramie, WY, USA
e-mail: xiang.zhang@uwyo.edu

C. Przybyla · G. Jefferson
Air Force Research Laboratory/RX, Wright-Patterson Air Force Base, Dayton, OH, USA
e-mail: craig.przybyla@wpafb.af.mil; george.jefferson.1@us.af.mil

S. Ghosh et al. (eds.), *Integrated Computational Materials Engineering (ICME)*,
https://doi.org/10.1007/978-3-030-40562-5_12

degradation of the laminate, such as induced delamination between plies and fiber breakage [2]. Characterizing and modeling the transverse failure of composites are complicated by the variability present not only in the material microstructure (i.e., the fiber size distribution and placement) but also in the local constitutive and failure properties of the constituents. The interaction between failure mechanisms such as fiber/matrix interface debonding and matrix cracking further complicates the prediction of the transverse strength of the composite laminate [1].

Multiple analytical and numerical models have been developed over the past decades to predict transverse cracking in composite laminates. In analytical models, it is often assumed that sequential cracks occur midway between existing cracks [3, 4], while numerical models, which tend to rely on periodic boundary conditions, simulate only a small portion of the experimental microstructure [5–7] and/or assume a uniform, structured packing [8, 9]. However, there is an increasing need to model larger, more realistic composite microstructures, as complex interactions between phases result in effective properties that are highly dependent on microstructural details [10].

In unidirectional composites with a high fiber volume fraction under transverse tensile loading, failure typically occurs at the interfaces between the fibers and the matrix. One of the most successful numerical methods used to capture this type of failure relies on a cohesive failure law relating the cohesive traction to the displacement jump along the fiber/matrix interfaces [11, 12]. This approach is also the basis of the present study, which relies on a nonlinear, discontinuous extension of a recently introduced interface-enriched generalized finite element method (IGFEM) [13, 14] that allows for the modeling of transverse failure in realistic virtual composite microstructures with hundreds of fibers discretized with nonconforming finite element meshes. Beyond the development of this special form of the IGFEM, a key goal of this work is to compute the sensitivity of the transverse failure response of the transverse ply to the cohesive properties of the fiber/matrix interfaces. To that effect, we present an analytic material sensitivity formulation based on the direct differentiation method and implement it in the nonlinear, cohesive IGFEM solver. Related work on IGFEM-based sensitivity analysis in the context of multi-scale material design can be found in [15, 16].

The manuscript is organized as follows: in Sect. 2, the material system of interest and experimental observations are presented. Next, Sect. 3 summarizes the computational method used to simulate the initiation and propagation of the transverse cracks. Section 4 describes the sensitivity analysis adopted in this work to capture the dependence of the transverse failure response of the transverse ply on the cohesive failure properties of the fiber/matrix interfaces. Additional derivations of the sensitivity to the critical displacement jumps are provided in the Appendix. The sensitivity formulations are verified against finite difference approximations in Sect. 5, while Sect. 6 summarizes the results of a sensitivity analysis performed on a virtual composite laminate composed of hundreds of fibers.

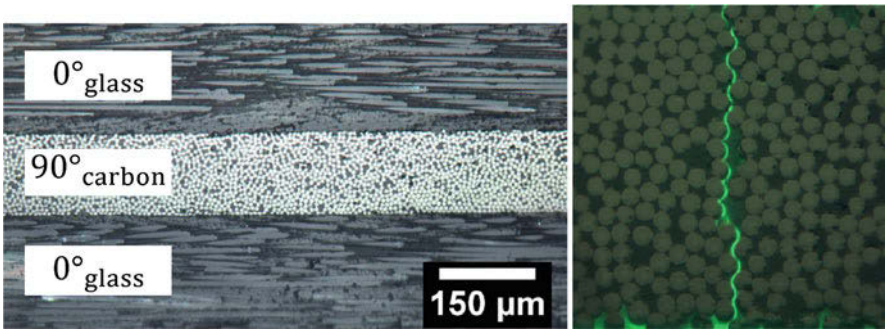

Fig. 1 Left: Optical image of the $[0/90/0]_T$ composite laminate used in the transverse failure experiments. The 0° plies are glass/epoxy, while the 90° ply consists of carbon fibers embedded in the epoxy matrix. Right: Representative image of a transverse crack spanning the 90° ply. The crack path was identified visually after unloading by the introduction of a fluorescent penetrant, while the specimen is under loading. As apparent from this optical image, the transverse cracks extend primarily along fiber/matrix interfaces

2 Experimental Observations

The material system under investigation is a $[0/90/0]_T$ composite laminate (Fig. 1). The 90° ply is made of AS4 carbon fibers (Hexcel Corporation, Stamford, CT) embedded in an Araldite/Aradur 8605 epoxy system, while the 0° plies, which serve as barriers to the transverse cracks propagating in the 90° ply, consist of glass fibers (PPG industries, Pittsburgh, PA) in the same epoxy matrix. Glass fibers are used in the top and bottom layers to allow for the initiation of transverse cracks in the carbon/epoxy ply at lower loads. The manufacturing of the composite specimen involves using an in-house pre-impregnator to create pre-preg plies from a carbon fiber or glass fiber spool. The composites are consolidated under vacuum bag pressure and temperature according to manufacturer-recommended cure cycle. The composite panels are then cut into rectangular coupons.

Six composite samples with thickness 0.7 mm, width 2 mm, and a gauge length of 25 mm were tested in an Instron loadframe. The composite specimens were subjected to quasi-static longitudinal tension at a displacement rate of 5 μm/sec (SEMtester, MTI Instruments, Albany, NY) to obtain the composite stress-strain response. A custom LabVIEW virtual instrument was used to record load and displacement data. Samples were loaded under an optical microscope (DMR-R, Leica Microsystems, Buffalo Grove, IL) to record failure mechanisms in the transverse ply optically during the test.

The main failure mechanisms in this composite system are fiber/matrix debonding and matrix cracking, and a typical transverse crack from these experiments is shown in Fig. 1. A detailed analysis of the fracture surface indicates that transverse cracks predominantly (in excess of 95% of the crack path) extend

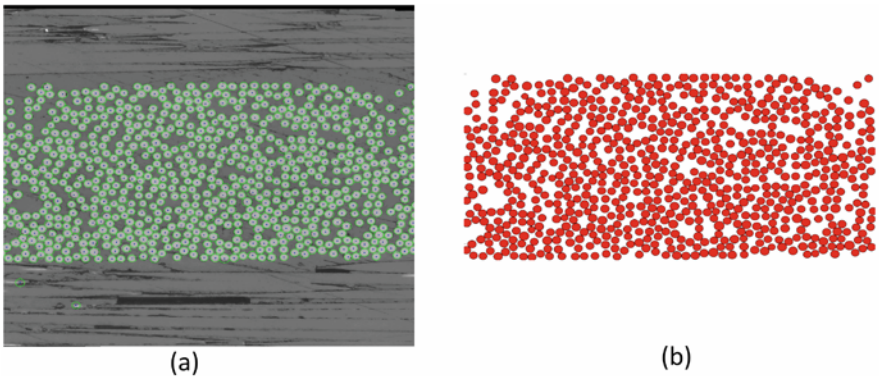

Fig. 2 Reconstruction of fiber placement in 90° ply: (**a**) Optical image of [0/90/0] hybrid laminate; (**b**) Extraction of fiber distribution

along the fiber/matrix interfaces, in agreement with results reported in [17, 18]. This observation motivates the emphasis placed in this computational work on the cohesive modeling of the fiber/matrix interface failure, as described in Sect. 3.

Small windows of the 90° ply were imaged using a Leica DMR optical microscope with 50X objective to capture the microstructure with enough resolution (9.3 pixels/μm) to make morphological reconstruction possible. Otsu's method for thresholding [19] was used to reduce the image to a binary representation. This method computes an optimum threshold intensity level to separate the pixels in the image into two pixel classes following a bimodal histogram to minimize intra-class variance. Computing a single global threshold value may not be appropriate in large images due to nonuniform contrast across the image, which makes it difficult to classify pixels as foreground or background based on pixel intensity [20]. For this reason, local threshold intensity values were used to threshold smaller portions of the microstructure.

The reconstruction of the microstructure used generalized Hough transforms, which have been adopted by multiple previous studies to find geometric parameters describing instances of geometric shapes [21, 22]. We adopted the circular Hough transform to identify individual fibers in the experimental micrographs [23], as illustrated in Fig. 2a. To avoid the stress singularity associated with direct fiber-fiber contact, a one-pixel minimum spacing between fibers is enforced, which is of the order of 100 nm (or about 1/70 of a typical fiber diameter) for the image presented.

The microstructure from Fig. 2b, which is used in the simulations presented in Sect. 3, is composed of 751 fibers and has a fiber volume fraction of 55%. The fiber radius distribution is shown in Fig. 3a, while the nearest-neighbor distance distribution is presented in Fig. 3b, with the majority of fibers having a nearest neighbor closer than 135 nm.

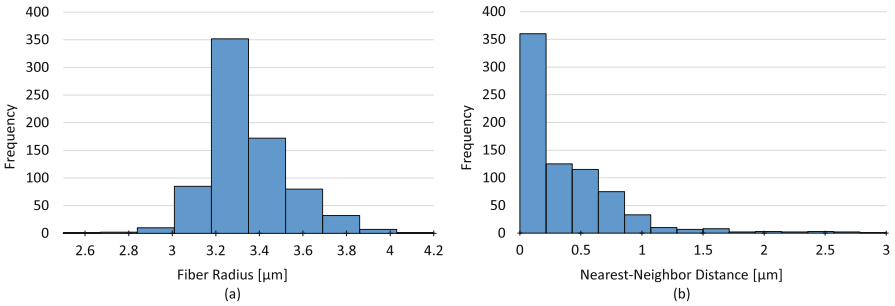

Fig. 3 Fiber radius (**a**) and nearest-neighbor distance (**b**) distributions of the reconstructed composite microstructure taken from Fig. 2b

3 Modeling

To simulate the initiation and propagation of transverse cracks in the 90° ply, a plane strain finite element model is constructed directly from the reconstructed microstructure. As indicated earlier, the transverse cracks predominantly extend along the fiber/matrix interfaces, thereby motivating the use of a cohesive failure law to describe the progressive failure of the fiber/matrix interfaces.

One of the key challenges in modeling transverse failure in composite plies with high fiber volume fractions is associated with the very small distance between adjacent fibers. Using a conventional finite element method that relies on elements that conform to the fiber/matrix interfaces leads to extremely fine meshes and therefore prohibitively expensive models. To address this challenge, which has limited most existing numerical analyses to small computational domains and/or unrealistically low fiber volume fractions, we have adopted a special form of a recently introduced IGFEM that allows for the modeling of nonconforming elements containing multiple cohesive interfaces.

Details on the numerical method adopted in this study are provided hereafter, together with the results of a typical mesoscale analysis of transverse failure in the $[0/90/0]_T$ laminate described in Sect. 2.

3.1 Cohesive Zone Model

For the cohesive failure of the fiber/matrix interfaces, we adopt the modified trilinear traction-separation law of Scheider et al. [24]. Five material properties characterize the cohesive response: the cohesive strength (σ_c), the three critical opening displacements (δ_{c1}, δ_{c2}, and δ_{c3}), and the ratio between shear and normal critical tractions (β). Defining the scalar effective displacement δ by

$$\delta = \sqrt{\beta^2 \delta_s^2 + \delta_n^2}, \tag{1}$$

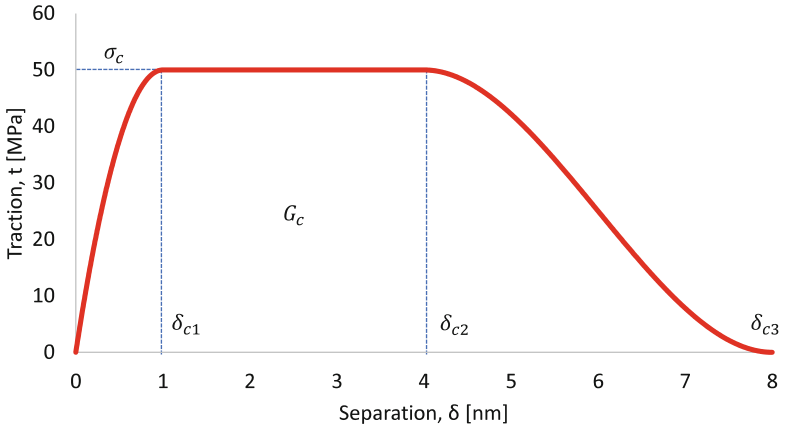

Fig. 4 Smooth "trilinear" cohesive law corresponding to $\sigma_c = 50$ MPa, $\delta_{c1} = 1$ nm, $\delta_{c2} = 4$ nm, and $\delta_{c3} = 8$ nm. The area under the curve G_c denotes the cohesive fracture toughness of the fiber/matrix interface

where δ_s and δ_n are the shear and normal components of the displacement jump vector ($\boldsymbol{\delta}$), the cohesive traction vector $\mathbf{t}$ takes the form

$$\mathbf{t} = \frac{t}{\delta}[\beta^2 \boldsymbol{\delta} + (1 - \beta^2)(\boldsymbol{\delta} \cdot \boldsymbol{n})\boldsymbol{n}], \tag{2}$$

where $\mathbf{n}$ is the normal vector of the interface and the scalar effective traction t is

$$t(\delta) = \sigma_c \begin{cases} 2(\frac{\delta}{\delta_{c1}}) - (\frac{\delta}{\delta_{c1}})^2 & \text{if } 0 \le \delta < \delta_{c1}, \\ 1 & \text{if } \delta_{c1} \le \delta < \delta_{c2}, \\ 2(\frac{\delta-\delta_{c2}}{\delta_{c3}-\delta_{c2}})^3 - 3(\frac{\delta-\delta_{c2}}{\delta_{c3}-\delta_{c2}})^2 + 1 & \text{if } \delta_{c2} \le \delta < \delta_{c3}, \\ 0 & \text{if } \delta \ge \delta_{c3}. \end{cases} \tag{3}$$

For unloading, when $\delta \le \delta$max, a linear cohesive relation is adopted:

$$t = \frac{\delta}{\delta_{\max}} t^*, \tag{4}$$

where $t^* = t(\delta_{\max})$.

As shown in Fig. 4, the nonlinear relations in the first and third segments of the cohesive law are introduced to ensure the C^1 continuity of the traction-separation law. The area under the traction-separation law, which denotes the cohesive fracture toughness, G_c, of the interface is given by

$$G_c = \sigma_c \left(\frac{\delta_{c2}}{2} + \frac{\delta_{c3}}{2} - \frac{\delta_{c1}}{3} \right). \tag{5}$$

The initial slope of the cohesive law, which describes the initial compliance of the cohesive interface prior to failure (i.e., for $\delta < \delta_{c1}$), is given by $2\sigma_c/\delta_{c1}$.

Finally, a numerical damping scheme is used to stabilize the solution [25]:

$$t = f(\sigma_c, \delta_{c1}, \delta_{c2}, \delta_{c3}, \beta) + \xi \frac{\sigma_c}{\delta_{c1}} \frac{d\delta}{dt}, \tag{6}$$

where the first term on the right-hand side denotes the modified trilinear cohesive model described in Fig. 4. To minimize the impact of the numerical damping term (ξ) on the solution, an adaptive scheme is adopted in which the damping parameter is progressively increased to the point where the solution is stabilized and decreased thereafter.

3.2 Interface-Enriched Generalized Finite Element Method (IGFEM)

One of the key challenges in the modeling of transverse failure in composite layers with high fiber volume fraction is associated with the very small distance separating adjacent fibers. To address this challenge and allow for the simulation of transverse failure in realistic virtual models of a composite layer consisting of hundreds of closely packed fibers, we have adopted a special form of IGFEM. The method was originally introduced in [13, 14] to simulate the thermal and structural response of heterogeneous materials with meshes that do not conform to the material interfaces by using enrichment functions and generalized degrees of freedom that allow for capturing the gradient discontinuity present across these material interfaces.

For the present application, the method is modified in two ways. Firstly, while the traditional IGFEM utilizes C^0 enrichment functions to capture the gradient discontinuity of the solution across "intact" material interfaces, the method is extended hereafter to the use of C^{-1} enrichment functions to capture the discontinuity in the displacement solution field associated with the cohesive failure of the fiber/matrix interfaces [26]. In this discontinuous extension of the IGFEM, two enrichment nodes are placed at every intersection of the material interface with an element edge. Generalized degrees of freedom are then associated with the original enrichment node and its "mirror" node, allowing for the introduction of a cohesive failure model used to describe their progressive normal and tangential separations.

Beyond the ability to model cohesive failure with nonconforming discontinuous elements, the second modification to the conventional IGFEM used in this study consists of the introduction of enriched elements with two cohesive interfaces which are used to model the potential failure of two very close fiber/matrix interfaces when they intersect the same element [27].

The remainder of the implementation of the nonlinear IGFEM solver is relatively conventional and consists of a Newton-Raphson scheme with adaptive load stepping and a parallel C++ framework using the Message Passing Interface (MPI). PETSc [28] is used to solve the linearized system of equations using Krylov subspace methods.

3.3 Mesoscale Simulations

The mesoscale computational model, created from the reconstructed microstructure shown previously in Fig. 2b, is presented schematically in Fig. 5, together with details of the nonconforming IGFEM mesh. The model, which spans the entire thickness of the 90° ply, contains 751 fibers. The width (L_1) is approximately 325 μm, the height of the 90° ply (H_2) is 162 μm, and each of the 0° plies (H_1) has a height of 28 μm. The nonconforming triangular elements intersected by the fiber/matrix interfaces contain one or two cohesive interfaces. The other elements are conventional three-node linear elements. The IGFEM computational model is made of 512, 025 elements, 321, 975 nodes, and 643, 950 degrees of freedom.

The in-plane properties of the various constituents are summarized in Table 1. The cohesive properties used to model the failure of the fiber/epoxy matrix interfaces are derived from a numerical analysis of microbond experiments [29]. The homogenized properties used in the 0° plies are obtained using the classical Halpin-Tsai relations [1, 30], with a fiber volume fraction of 69% in these 0° plies.

Under the effect of a 0.43% transverse strain, a complex heterogeneous stress state and transverse cracking pattern develop in the composite laminate, as illustrated in Fig. 6a, in which the deformations have been scaled by a factor of 5. The figure clearly shows distinct transverse cracks consisting of failed cohesive

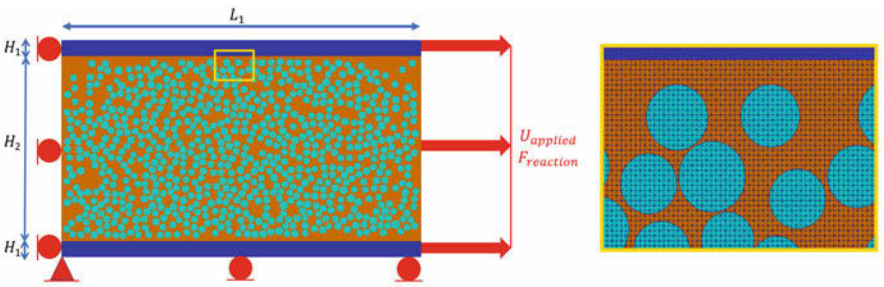

Fig. 5 (Left) Schematic of mesoscale computational model used to simulate the transverse failure of the reconstructed microstructure shown in Fig. 2b, with (right) details of the IGFEM mesh consisting of nonconforming triangular elements. Cohesive interfaces are placed along each fiber/matrix interface

Table 1 Material properties used in the mesoscale simulations

Carbon fibers	$E = 19.5$ GPa,	$\nu = 0.45$	
Epoxy matrix	$E = 2.38$ GPa,	$\nu = 0.43$	
Cohesive interfaces	$\sigma_c = 50$ MPa,	$\delta_{c1} = 1$ nm,	$\delta_{c2} = 4$ nm,
	$\delta_{c3} = 8$ nm,	$\beta = 1$	
0° glass-epoxy plies	$E_1 = 49.2$ GPa,	$E_2 = 7.21$ GPa,	$\nu_{12} = 0.298$,
	$G_{12} = 3.96$ GPa,	$G_{23} = 2.08$ GPa	

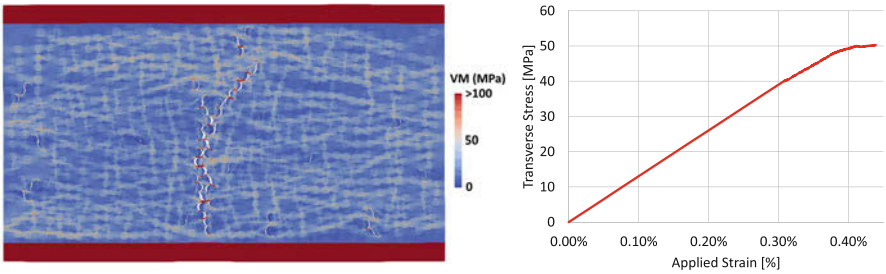

Fig. 6 (Left) Von Mises stress distribution in the composite laminate subjected to a 0.43% applied transverse strain with the deformations scaled by a factor of 5, showing the appearance of a transverse crack spanning the width of the 90° ply. (Right) Corresponding transverse stress-strain curve

interfaces that span the 90° ply. Due to stiffness of the 0° plies, the corresponding evolution of the transverse stress (Fig. 6b) computed from the reaction forces along the right edge of the computational domain remains almost linear up to the point where the cohesive elements in the vicinity of the crack path begin to fail and subsequently reduce the overall modulus of the composite.

3.4 Validation

The IGFEM model for transverse composite failure was validated by comparing the statistical distribution of the predicted linear elastic response and onset of failure with experimental measurements. A reconstructed microstructure of approximately 6000 fibers was split into 9 and 18 sections of about 700 and 350 fibers, respectively. These results are compared with experimental measurements of the initial stiffness and of the strain at the first transverse crack obtained from tensile tests performed on the same $[0/90/0]_T$ carbon/glass-epoxy system, with the onset of transverse cracking captured through acoustic emission.

These virtual specimens were subjected to a tensile loading up to a transverse strain of about 0.5%. The resulting stress-strain curves are plotted in Fig. 7 with the characteristic first crack marked for each computational case. The cohesive traction-separation law for this set of validation simulations is the same as outlined in Table 1 and the previous example of a mesoscale simulation using the IGFEM computational model. Table 2 presents a comparison between experimental and numerical values of the initial composite stiffness and the strain corresponding to the formation of the first transverse crack, measured through decreases in the macroscopic stress-strain curve, and indicates good agreement between measured and predicted values.

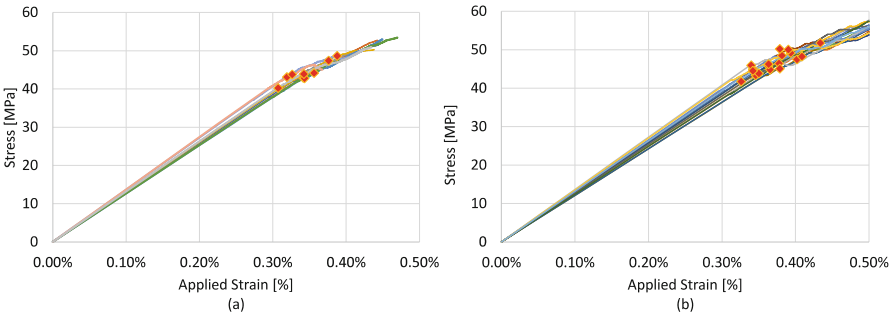

Fig. 7 Numerical stress-strain curves associated with 9 (**a**) and 18 (**b**) virtual microstructures composed of approximately 700 and 350 fibers, respectively. The diamond-shaped symbols denote the strains at which the first transverse crack for each microstructure is predicted

Table 2 Validation of computational model based on the initial composite stiffness and the strain at the onset of transverse cracking. N denotes the number of sections into which the large composite sample was split for the mesoscale validation. The experimental values of the initial stiffness are obtained by scaling the measured data using an isostrain relation of the $[0/90/0]_T$ laminate to reflect the reduced thickness of the simulated 0° plies

	Initial stiffness [GPa]	Initial stiffness error [%]	Strain at first crack [%]	First crack error [%]
Experimental	14.03 ± 0.363	N/A	0.34 ± 0.06	N/A
IGFEM ($N = 9$)	13.06 ± 0.396	6.91	0.345 ± 0.026	1.47
IGFEM ($N = 18$)	12.80 ± 0.266	8.77	0.358 ± 0.022	5.29

4 Sensitivity Analysis: Formulation

Beyond the simulation of transverse failure in realistic composite layers reconstructed directly from optical images, a key objective of this work is the analytical extraction of the sensitivity of the transverse failure response on the parameters defining the cohesive failure of the fiber/matrix interfaces. In particular, we derive the IGFEM-based analytic material sensitivity of the macroscopic transverse stress (denoted hereafter simply as σ) with respect to the interface variables (denoted as η_i). A direct method is used here because of the costly nature of the nonlinear simulations which would make finite difference extremely expensive, while the direct method allows us to compute sensitivities at very low cost.

For this problem, the response functional at every load step n can be written as

$$ {}^{n}\sigma = \mathbf{L}^{T\,n}\mathbf{F}_{p}^{\text{ext}} \frac{1}{2H_1 + H_2}, \tag{7} $$

where $\mathbf{L}^T$ is a constant vector of 0s and 1s to select the correct degrees of freedom from the external force vector $\mathbf{F}^{\text{ext}}$, the subscript p denotes the prescribed degrees of freedom, and H_1 and H_2 are the ply thicknesses introduced in Fig. 5. Unit depth

is assumed here. The sensitivity of the macroscopic transverse stress at load step n with respect to the design variable η_i can then be expressed as

$$\frac{d^n\sigma}{d\eta_i} = \mathbf{L}^T \frac{d^n \mathbf{F}_p^{\text{ext}}}{d\eta_i} \frac{1}{2H_1 + H_2}. \tag{8}$$

The partitioned system of nonlinear equations,

$${}^n\mathbf{F}^{\text{int}}\left(\eta_i, {}^{n-1}\boldsymbol{\delta}_{\max}(\eta_i), {}^n\mathbf{U}(\eta_i, {}^{n-1}\boldsymbol{\delta}_{\max}(\eta_i))\right) = \begin{bmatrix} {}^n\mathbf{F}_f^{\text{int}} \\ {}^n\mathbf{F}_p^{\text{int}} \end{bmatrix} = \begin{bmatrix} 0 \\ {}^n\mathbf{F}_p^{\text{ext}} \end{bmatrix} = {}^n\mathbf{F}^{\text{ext}}, \tag{9}$$

where the subscript f denotes the free degrees of freedom, is solved incrementally. Because no external loads are applied, ${}^n\mathbf{F}_f^{\text{ext}}$ vanishes. ${}^n\boldsymbol{\delta}_{\max}$ denotes the vector of internal state variables computed at each cohesive integration point:

$${}^n\delta_{\max} = \begin{cases} \sqrt{\beta^2\, {}^n\delta_s^2 + {}^n\delta_n^2} & \text{if loading,} \\ {}^{n-1}\delta_{\max} & \text{if unloading.} \end{cases} \tag{10}$$

Differentiation of (9) yields

$${}^n\mathbf{K}^{ff} \frac{d^n\mathbf{U}^f}{d\eta_i} = -\left(\frac{\partial {}^n\mathbf{F}_f^{\text{int}}}{\partial \eta_i} + \frac{\partial {}^n\mathbf{F}_f{}^{\text{int}}}{\partial {}^{n-1}\boldsymbol{\delta}_{\max}} \frac{d^{n-1}\boldsymbol{\delta}_{\max}}{d\eta_i} \right) \tag{11}$$

and

$$\frac{d^n\mathbf{F}_p^{\text{ext}}}{d\eta_i} = {}^n\mathbf{K}^{pf} \frac{d^n\mathbf{U}^f}{d\eta_i} + \frac{\partial {}^n\mathbf{F}_p^{\text{int}}}{\partial \eta_i} + \frac{\partial {}^n\mathbf{F}_p{}^{\text{int}}}{\partial {}^{n-1}\boldsymbol{\delta}_{\max}} \frac{d^{n-1}\boldsymbol{\delta}_{\max}}{d\eta_i}. \tag{12}$$

Note that $\frac{d^n\mathbf{U}^p}{d\eta_i} = 0$ since ${}^n\mathbf{U}^p$ is a prescribed value applied at each load step. ${}^n\mathbf{K}^{ff}$ and ${}^n\mathbf{K}^{pf}$ are the partial derivatives of the free and prescribed internal force vectors with respect to the free displacements, respectively.

To compute $\frac{d^n\sigma}{d\eta_i}$ in Equation (8), the right-hand side of Equation (12) must be evaluated which requires the solution of the linear system given by Equation (11) to compute $\frac{d^n\mathbf{U}^f}{d\eta_i}$. The right-hand sides of Equations (11) and (12) contain the partial derivative of the internal force with respect to the internal variables ${}^{n-1}\boldsymbol{\delta}_{\max}$, which is computed only over the cohesive elements. The elemental internal force vector contribution from a cohesive element has the form

$${}^n\mathbf{F}_{\text{elem}}^{\text{int},\{\text{cohesive}\}} = \sum_{gp=1}^{n_{gp}} w_{gp} \mathbf{N}_{gp}^T {}^n\mathbf{t}_{gp} dA, \tag{13}$$

where w_{gp} is the Gauss integration weight, $\mathbf{N}_{gp}$ is a matrix arrangement of the discontinuous enrichment functions used to compute the displacement jump vector, and ${}^{n}\mathbf{t}_{gp}$ is the traction vector defined in Equation (2). Differentiating Equation (13) with respect to the internal variables yields

$$\frac{\partial \mathbf{F}_{gp}^{\text{int,\{cohesive\}}}}{\partial^{n-1}\delta_{\max}^{gp}} = w_{gp}\mathbf{N}_{gp}^{T}\frac{\partial^{n}\mathbf{t}_{gp}}{\partial^{n-1}\delta_{\max}^{gp}}dA,$$

$$\frac{\partial^{n}\mathbf{t}_{gp}}{\partial^{n-1}\delta_{\max}^{gp}} = \begin{cases} 0 & \text{if loading,} \\ \frac{1}{{}^{n-1}\delta_{\max}^{gp}}\left(\frac{dt^{*}}{d^{n-1}\delta_{\max}^{gp}} - \frac{t^{*}}{{}^{n-1}\delta_{\max}^{gp}}\right)\times & \\ \left[\beta^{2}\boldsymbol{\delta} + (1-\beta^{2})(\boldsymbol{\delta}\cdot\boldsymbol{n})\boldsymbol{n}\right] & \text{if unloading,} \end{cases} \tag{14}$$

where t^{*} is defined in Equation (4) and $\frac{dt^{*}}{d^{n-1}\delta_{\max}}$ is easily computed from Equation (3).

The right-hand sides of Equations (11) and (12) also contain the derivatives of the internal variables with respect to the parameters from the previous load step. These derivatives are simply stored as additional internal variables for each quadrature point and initialized as $\frac{d^{0}\delta_{\max}}{d\eta_i} = 0$. For subsequent steps, the components of the vector are updated using

$$\frac{d^{n}\delta_{\max}}{d\eta_i} = \begin{cases} \frac{1}{2\,{}^{n}\delta}\left(2\beta^{2}\,{}^{n}\delta_{s}\frac{d^{n}\delta_{s}}{d\eta_i} + 2\,{}^{n}\delta_{n}\frac{d^{n}\delta_{n}}{d\eta_i}\right) & \text{if loading,} \\ \frac{d^{n-1}\delta_{\max}}{d\eta_i} & \text{if unloading,} \end{cases} \tag{15}$$

where

$$\frac{d^{n}\delta_{gp}}{d\eta_i} = \mathbf{N}_{gp}\frac{d^{n}\mathbf{U}_{\text{elem}}}{d\eta_i}. \tag{16}$$

In Equation (16), $\frac{d^{n}\mathbf{U}_{\text{elem}}}{d\eta_i}$ can be solved using Equation (11). These updated internal variable derivatives are then used in the sensitivity analysis at the end of the next load step.

The last missing term is the partial derivative of the internal force with respect to specific interface parameters. The sensitivity derivations presented in the remainder of this section are specific to $\eta_i = \sigma_c$, leaving a summary of the derivations of the sensitivity with respect to the critical displacement jumps δ_{ci} $(i = 1, 2, 3)$ for the Appendix.

Again, the contributions from the linear elastic bulk elements to the partial derivative vanish as the stress does not depend explicitly on the cohesive internal strength. The partial derivative of Equation (13) with respect to σ_c is

$$\frac{\partial^{n}\mathbf{F}_{\text{elem}}^{\text{int,\{cohesive\}}}}{\partial\sigma_c} = \sum_{gp=1}^{n_{gp}} w_{gp}\mathbf{N}_{gp}^{T}\frac{\partial^{n}\mathbf{t}_{gp}}{\partial\sigma_c}dA. \tag{17}$$

The explicit partial derivative of Equation (2) with respect to σ_c yields

$$\frac{\partial^n \mathbf{t}_{gp}}{\partial \sigma_c} = \frac{\partial^n t}{\partial \sigma_c} \frac{1}{{}^n\delta} [\beta^2 \, {}^n\boldsymbol{\delta} + (1 - \beta^2)({}^n\boldsymbol{\delta} \cdot \boldsymbol{n})\boldsymbol{n}], \tag{18}$$

where $\frac{\partial t}{\partial \sigma_c}$ is readily obtained from Equation (3) as

$$\frac{\partial t}{\partial \sigma_c} = \begin{cases} 2(\frac{\delta}{\delta_{c1}}) - (\frac{\delta}{\delta_{c1}})^2 & \text{if } 0 \leq \delta < \delta_{c1}, \\ 1 & \text{if } \delta_{c1} \leq \delta < \delta_{c2}, \\ 2(\frac{\delta - \delta_{c2}}{\delta_{c3} - \delta_{c2}})^3 - 3(\frac{\delta - \delta_{c2}}{\delta_{c3} - \delta_{c2}})^2 + 1 & \text{if } \delta_{c2} \leq \delta < \delta_{c3}, \\ 0 & \text{if } \delta \geq \delta_{c3}. \end{cases} \tag{19}$$

5 Sensitivity Analysis: Verification

To verify the material sensitivity analysis described in Sect. 4, the simple problem shown in Fig. 8 is solved. The verification problem consists of a small square domain containing two fibers of different sizes. The larger and smaller fibers have a diameter of 8 and 6 μm, respectively, which correspond to the upper and lower sizes of the carbon fibers used in the experiments.

The cohesive properties for this simulation are chosen as $\sigma_c = 50\,\text{MPa}$, $\delta_{c1} = 10\,\text{nm}$, $\delta_{c2} = 40\,\text{nm}$, $\delta_{c3} = 80\,\text{nm}$, and $\beta = 1$. The domain is subjected to a 2% traverse strain and the results computed by the direct analytic sensitivity formulation described in the previous section are compared to those obtained with a central finite difference scheme.

As shown in Fig. 9, there is a very good agreement between the analytic and finite difference sensitivity results for both the sensitivities with respect to the cohesive strength and to δ_{c1}. The first and second peaks observed in the sensitivity curves are

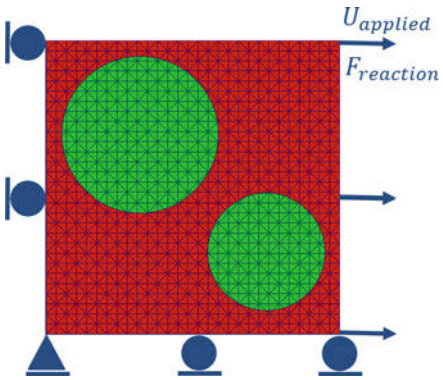

Fig. 8 Schematic of two-fiber problem used to verify the analytic sensitivity formulation

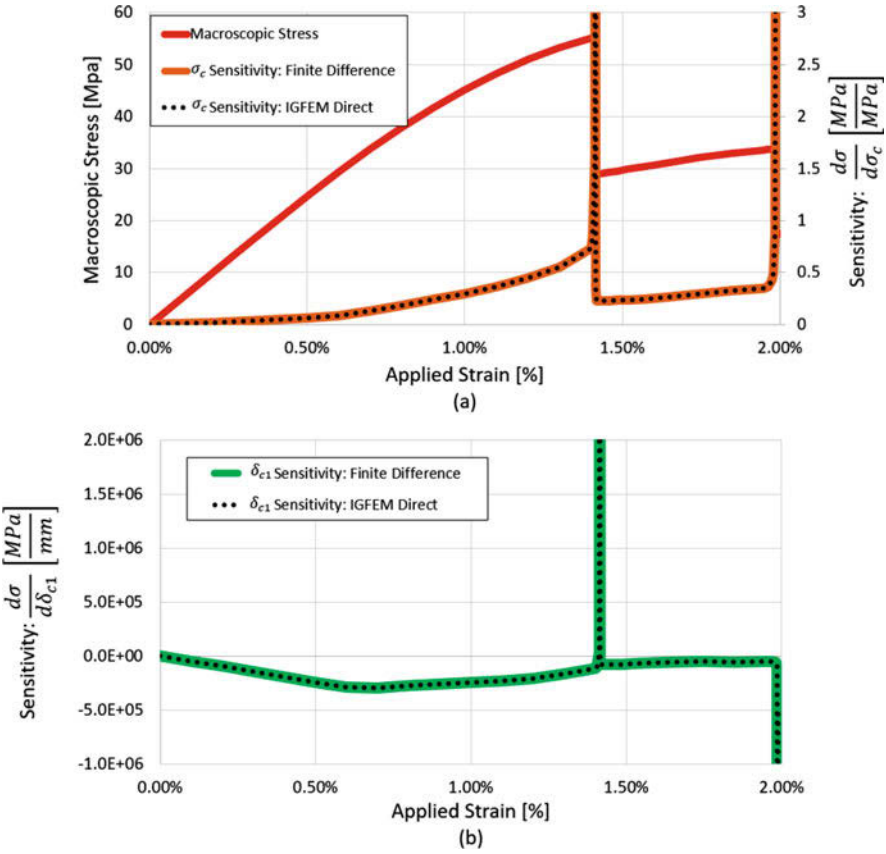

Fig. 9 Verification of the material sensitivities for the two-fiber problem shown in Fig. 8. (**a**) Transverse stress-strain response and sensitivity of the transverse stress with respect to σ_c; (**b**) Sensitivity with respect to δ_{c1}

associated with the debonding failure of the larger and smaller fibers, respectively. As expected, the sensitivity of the transverse stress with respect to σ_c remains positive through the entire range of applied strains as the incremental increase of the cohesive strength leads to an overall increase of σ over the entire traction-separation curve as seen in Fig. 10 which shows the effect of differential changes in both σ_c and δ_{c1} on an example traction-separation curve. The sensitivity of the transverse stress with respect to δ_{c1} is first negative, as a higher value of the critical displacement jump for a fixed cohesive strength leads to a more compliant cohesive model, and therefore a decrease in σ. Once the interfaces start to fail, the δ_{c1} sensitivity of σ switches sign, as a larger value of δ_{c1} leads to a delayed failure and therefore a higher value of σ for a given applied strain.

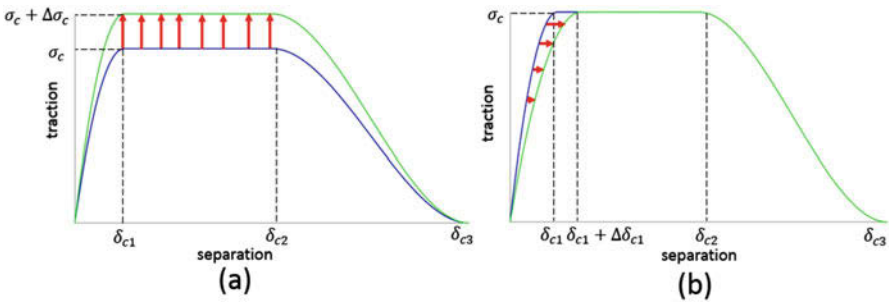

Fig. 10 Schematic illustration of the impact on the cohesive traction-separation curve for an incremental increase in σ_c (**a**) and in δ_{c1} (**b**)

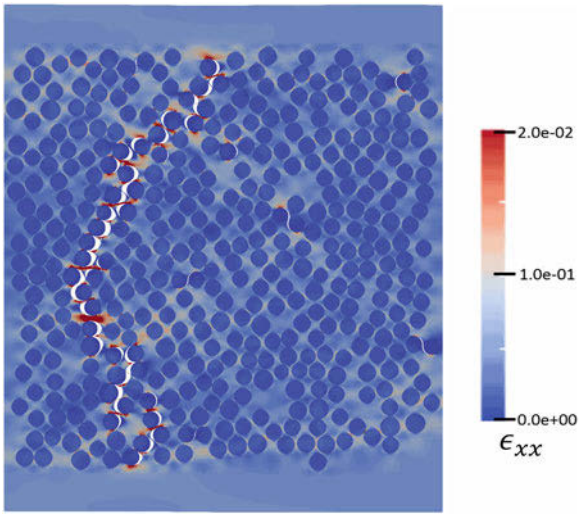

Fig. 11 Formation of a large transverse crack at 0.5% strain in the 90° ply of the $[0/90/0]_T$ composite laminate. The 90° ply is composed of 406 fibers. The deformation has been scaled by a factor of 5

6 Sensitivity Analysis: Results

In this section, a 406-fiber microstructure is simulated to extract the sensitivity of the transverse stress with respect to the cohesive strength and the critical displacement jumps. The simulated microstructure is presented in Fig. 11 at $\epsilon_{\text{applied}} = 0.5\%$ showing a large transverse crack. The macroscopic transverse stress curve, along with the evolution of the sensitivity with respect to the cohesive strength, is plotted against the applied strain in Fig. 12, and the sensitivities with respect to the critical displacement jumps are presented in Fig. 13.

As apparent in Fig. 12, the sensitivity of the transverse stress-strain curve with respect to σ_c remains positive throughout the transverse failure process. This result can be again explained by the effect of differential changes in σ_c on the cohesive law illustrated in Fig. 10a.

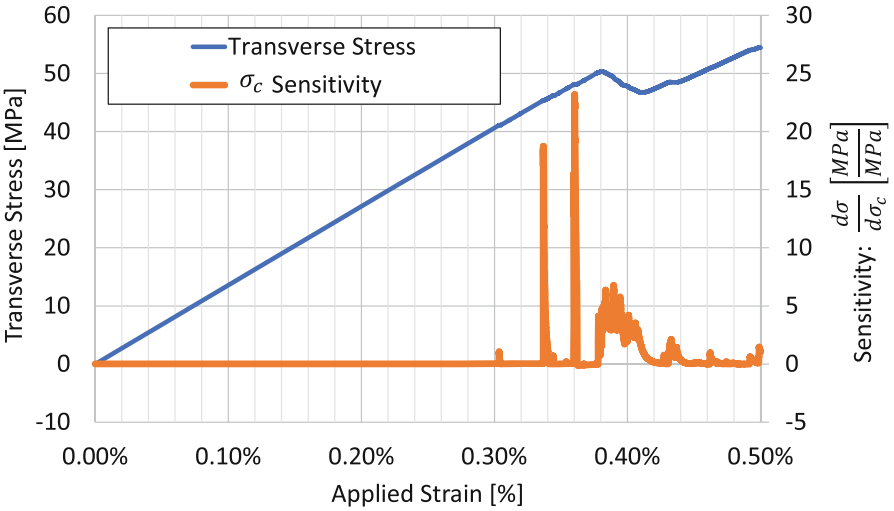

Fig. 12 Evolution of the transverse stress σ and of the σ_c-sensitivity of σ versus the applied transverse strain for the 406-fiber problem shown in Fig. 11

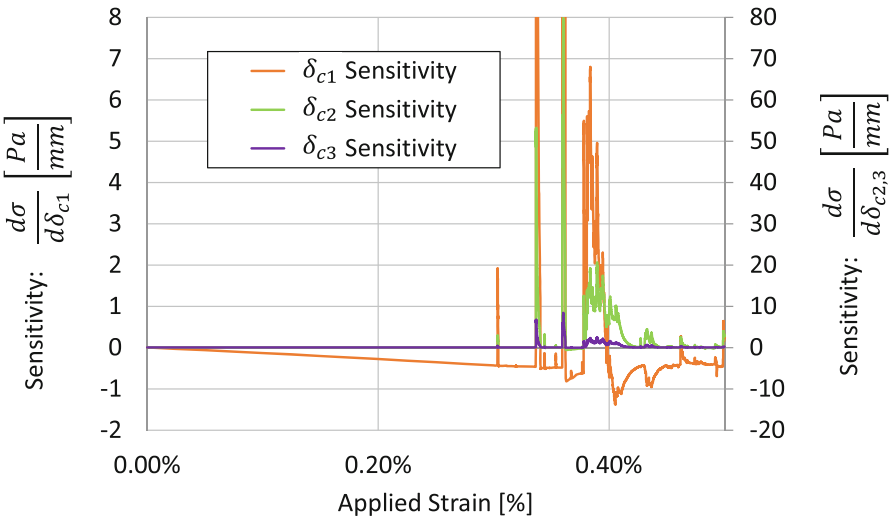

Fig. 13 Evolution of the sensitivities of the transverse stress σ with respect to the critical displacement jumps δ_{ci} for the trilinear cohesive law versus the applied transverse strain for the 406-fiber problem

The sensitivity of the transverse stress with respect to δ_{c1} is initially negative due to the increased cohesive compliance of the interfaces, as illustrated in Fig. 10b. During the failure events, the δ_{c1}-sensitivity becomes positive due to the delayed failure response. The sensitivities with respect to δ_{c2} and δ_{c3} initially vanish

before becoming positive during the failure events. It should also be noted that the sensitivity with respect to δ_{c3} is substantially smaller than the sensitivity with respect to δ_{c2}.

Due to the complexity of the large 406-fiber microstructure and of the stress field in the 90° ply, the failure of the fiber/matrix interfaces is a complex function of the applied strain, rendering a precise determination of the onset of transverse cracking difficult when only inspecting the stress-strain response or deformed geometry. However, the evolution of the sensitivities of the transverse stress with respect to the cohesive parameters provides a clear insight on the correlation between applied strain and the onset of transverse cracking.

7 Conclusion

A computational framework has been presented for the modeling of transverse cracking in realistic virtual microstructures of 90° composite plies reconstructed directly from optical images. The underlying numerical method relies on a discontinuous, multi-interface extension of an interface-enriched generalized finite element method, which allows for the simulation of fiber/matrix debonding in composite layers with high fiber volume fractions. This computational model has been validated against strain measurements of the onset of transverse cracking performed on a $[0/90/0]_T$ carbon/glass-epoxy laminate. Also included in the computational framework is the analytic extraction of the sensitivity of the macroscopic transverse stress with respect to the parameters that define the cohesive failure law. By monitoring the evolution of these sensitivities, the onset and propagation of transverse cracks can be assessed. It should be noted, however, that in the present study, all fiber/matrix interfaces are assumed to have the same cohesive properties. The next steps include relaxing that assumption and deriving individual interface property sensitivities, i.e., extracting how sensitive the transverse stress is to the critical stress of individual fibers. With these individual sensitivities, one could study the sensitivity to the parameters that define the distributions of the interface properties, e.g., the sensitivity to the average and standard deviation of the interface strength.

Appendix: Sensitivity to Critical Displacement Jumps

For completeness, a summary of the sensitivity formulation with respect to the critical displacement jumps δ_{c1}, δ_{c2}, and δ_{c3} is included hereafter, starting from Equation (18) in Sect. 4.

For linearly elastic volumetric elements, again there is no explicit dependence of the internal force contribution on δ_{ci} and no displacement discontinuity. Therefore, Equation (18) simply becomes

$$\frac{\partial^n \mathbf{t}_{gp}}{\partial \delta_{ci}} = \frac{\partial^n t}{\partial \delta_{ci}} \frac{1}{{}^n\delta} [\beta^2 {}^n\boldsymbol{\delta} + (1-\beta^2)({}^n\boldsymbol{\delta} \cdot \boldsymbol{n})\boldsymbol{n}]. \tag{20}$$

From Equation (3), the partial derivatives of the scalar effective traction are

$$\frac{\partial t}{\partial \eta_i} = \begin{cases} \begin{cases} -2\sigma_c \left(1 - \frac{\delta_e}{\delta_{c1}}\right)\left(\frac{\delta_e}{\delta_{c1}^2}\right) & 0 \le \delta_e < \delta_{c1} \\ 0 & \text{else} \end{cases} & \text{for } \eta_i = \delta_{c1} \\ \begin{cases} 6\sigma_c \left(\frac{\delta_e - \delta_{c2}}{\delta_{c3} - \delta_{c2}} - 1\right)\left(\frac{\delta_e - \delta_{c2}}{\delta_{c3} - \delta_{c2}}\right)\left(\frac{\delta_e - \delta_{c3}}{(\delta_{c3} - \delta_{c2})^2}\right) & \delta_{c2} \le \delta_e < \delta_{c3} \\ 0 & \text{else} \end{cases} & \text{for } \eta_i = \delta_{c2} \\ \begin{cases} -6\sigma_c \left(\frac{\delta_e - \delta_{c2}}{\delta_{c3} - \delta_{c2}} - 1\right)\left(\frac{\delta_e - \delta_{c2}}{\delta_{c3} - \delta_{c2}}\right)\left(\frac{\delta_e - \delta_{c2}}{(\delta_{c3} - \delta_{c2})^2}\right) & \delta_{c2} \le \delta_e < \delta_{c3} \\ 0 & \text{else.} \end{cases} & \text{for } \eta_i = \delta_{c3} \end{cases} \tag{21}$$

Acknowledgements This work has been supported through a grant No. FA9550-12-1-0445 to the Center of Excellence on Integrated Materials Modeling (CEIMM) at Johns Hopkins University (partners JHU, UIUC, UCSB), awarded by the AFOSR/RSL (Computational Mathematics Program, Manager Dr. A. Sayir) and AFRL/RX (Monitors Dr. C. Woodward and C. Przybyla).

References

1. I. Daniel, O. Ishai, *Engineering Mechanics of Composite Materials* (Oxford University Press, New York, 2005)
2. J. Nairn, Matrix microcracking in composites, *Polymer Matrix Composites*, **2**, 403–432 (2000)
3. K. Garrett, J. Bailey, Multiple transverse fracture in 90° cross-ply laminates of a glass fibre-reinforced polyester. J. Mater. Sci. **12**, 157–168 (1977)
4. J. Mayugo, P. Camanho, P. Maimi, C. Davila, Analytical modelling of transverse matrix cracking of $[\pm\theta/90_n]_s$ composite laminates under multiaxial loading. Mech. Adv. Mater. Struct. **17**, 237–245 (2010)
5. L. Canal, J. Segurado, J. Llorca, Failure surface of epoxy-modified fiber-reinforced composites under transverse tension and out-of-plane shear. Int. J. Solids Struct. **46**, 2265–2274 (2009)
6. D. O'Dwyer, N. O'Dowd, C. McCarthy, Numerical micromechanical investigation of interfacial strength parameters in a carbon fibre composite material. J. Compos. Mater. **48**(6), 749–760 (2014)
7. A. Louhghalam, S. Arwade, Prediction of incipient damage sites in composites using classifiers. Int. J. Damage Mech. **19**, 233–260 (2010)
8. T. Okabe, M. Nishikawa, H. Toyoshima, A periodic unit-cell simulation of fiber arrangement dependence on the transverse tensile failure in unidirectional carbon fiber reinforced composites. Int. J. Solids Struct. **48**, 2948–2959 (2011)
9. T. Okabe, H. Sekine, K. Ishii, M. Nishikawa, N. Takeda, Numerical method for failure simulation of unidirectional fiber-reinforced composites with spring element model. Compos. Sci. Technol. **65**, 921–933 (2005)
10. S. Torquato, *Random Heterogeneous Materials, Microstructure and Macroscopic Properties* (Springer, New York, 2002)
11. T. Vaughan, C. McCarthy, Micromechanical modelling of the transverse damage behaviour in fibre reinforced composites. Compos. Sci. Technol. **71**, 388–396 (2011)

12. V. Kushch, S. Shmegera, P. Brondsted, L. Mishnaevsky, Numerical simulation of progressive debonding in fiber reinforced composite under transverse loading. Int. J. Eng. Sci. **49**, 17–29 (2011)
13. S. Soghrati, A. Aragón, C. Duarte, P. Geubelle, An interface-enriched generalized finite element method for problems with discontinuous gradient fields. Int. J. Numer. Methods Eng. **89**(8), 991–1008 (2012)
14. S. Soghrati, P. Geubelle, A 3D interface-enriched generalized finite element method for weakly discontinuous problems with complex internal geometries. Comput. Methods Appl. Mech. Eng. **217**–**220**, 46–57 (2012)
15. A. Najafi, M. Safdari, D. Tortorelli, P. Geubelle, A gradient-based shape optimization scheme using an interface-enriched generalized FEM. Comput. Methods Appl. Mech. Eng. **296**, 1–17 (2015)
16. A. Najafi, M. Safdari, D. Tortorelli, P. Geubelle, Material design using a NURBS-based shape optimization scheme, in *In 57th AIAA/ASCE/AHS/ASC Structures, Structural Dynamics, and Materials Conference* (American Institute of Aeronautics and Astronautics Inc, AIAA, 2016)
17. T. Hobbiebrunken, M. Hojo, T. Adachi, C.D. Jong, B. Fiedler, Evaluation of interfacial strength in CF/epoxies using FEM and in-situ experiments. Compos. A: Appl. Sci. Manuf. **37**, 2248–2256 (2006)
18. E. Gamstedt, B. Sjogren, Micromechanisms in tension-compression fatigue of composite laminates containing transverse plies. Combust. Sci. Technol. **59**, 167–178 (1999)
19. N. Otsu, A threshold selection method from gray-level histograms. IEEE IEEE Trans. Syst. Man Cybern. **9**, 62–66 (1979)
20. M. Chandrakala, P. Devi, Threshold based segmentation using block processing. Int. J. Innov. Res. Comput. Commun. Eng. **4**, 821–826 (2016)
21. D. Ballard, Generalizing the Hough transform to detect arbitrary shapes. Pattern Recogn. **13**, 111–122 (1981)
22. T. Atherton, D. Kerbyson, Size invariant circle detection. Image Vis. Comput. **17**, 795–803 (1999)
23. C. Przybyla, T. Godar, S. Bricker, J. Simmons, M. Jackson, L. Zawada, J. Pearce, Statistical characterization of SiC/SiC ceramic matrix composites at the filament scale with bayesian segmentation, Hough transform feature extraction, and pair correlation statistics, in *International SAMPE Technical Conference* (2013), pp. 859–878
24. I. Scheider, W. Brocks, The effect of the traction separation law on the results of cohesive zone crack propagation analyses. Key Eng. Mater. **251**, 313–318 (2003)
25. Y.F. Gao, A.F. Bower, A simple technique for avoiding convergence problems in finite element simulations of crack nucleation and growth on cohesive interfaces. Model. Simul. Mater. Sci. Eng. **12**(3), 453 (2004)
26. A. Aragón, A. Simone, The discontinuity-enriched finite element method. Int. J. Numer. Methods Eng. **112**, 1589–1613 (2017)
27. S. Zacek, Exploring the link between microstructure statistics and transverse ply fracture in carbon/epoxy composites. Master's thesis, University of Illinois – Urbana-Champaign (2017)
28. S. Balay, S. Abhyankar, M.F. Adams, J. Brown, P. Brune, K. Buschelman, L. Dalcin, V. Eijkhout, W.D. Gropp, D. Kaushik, M.G. Knepley, L.C. McInnes, K. Rupp, B.F. Smith, S. Zampini, H. Zhang, H. Zhang, PETSc Web page. http://www.mcs.anl.gov/petsc (2016)
29. S. Potukuchi, Fracture analysis of carbon fiber/epoxy matrix interface through microbond and cruciform tests. Master's thesis, University of Illinois – Urbana-Champaign (2016)
30. J. Halpin, J. Kardos, The Halpin-Tsai equations: a review. Polym. Eng. Sci. **16**, 344–352 (1976)

Geometric Modeling of Transverse Cracking of Composites

Angel Agrawal, Scott Zacek, Kyle Nixon, Chris Montgomery, Philippe Geubelle, Nancy Sottos, Craig Przybyla, and George Jefferson

1 Introduction

Continuous-fiber laminated composites have been shown to be a valuable material option when high specific stiffness and strength are desired, particularly in the aerospace industry [1]. However the random nature of the composite microstructure complicates the experimental and analytical study of their failure response. The primary objective of this research project is to develop a set of multiscale analytical and experimental tools to investigate the link between the geometrical and material parameters that define the microstructure and one of the failure modes of composite laminates, i.e., the cracking taking place in 90° plies due to the transverse loading of the laminate. Emphasis is placed on transverse cracking as this failure mode is often considered as a precursor to other more critical failure modes such as delamination and fiber breaking.

On the experimental side, transverse failure tests have been conducted using a specially designed hybrid composite laminate composed of a carbon/epoxy transverse (90°) ply sandwiched between two glass/epoxy 0° plies [2]. On the analytical side, a cohesive interface-enriched generalized finite element method (IGFEM) combined with analytical sensitivity analysis has been formulated and implemented

A. Agrawal · S. Zacek · K. Nixon · P. Geubelle (✉)
Department of Aerospace Engineering, University of Illinois, Urbana, IL, USA
e-mail: aagrawa5@illinois.edu; geubelle@illinois.edu

C. Montgomery · N. Sottos
Department of Materials Science and Engineering, University of Illinois, Urbana, IL, USA
e-mail: cbmontg2@illinois.edu; n-sottos@illinois.edu

C. Przybyla · G. Jefferson
Air Force Research Laboratory/RX, Wright-Patterson Air Force Base, Dayton, OH, USA
e-mail: craig.przybyla@wpafb.af.mil; george.jefferson.1@us.af.mil

S. Ghosh et al. (eds.), *Integrated Computational Materials Engineering (ICME)*,
https://doi.org/10.1007/978-3-030-40562-5_13

to simulate transverse failure in realistic virtual models of the composite laminate and extract the sensitivity of the transverse failure response on the material and geometrical parameters that define the microstructure of the transverse ply [3–5]. While the IGFEM scheme allows for the detailed simulation of transverse failure in virtual models composed of hundreds of fibers, larger models of the composite laminate are needed to further explore statistical effects on the transverse failure response. To that effect, we develop in this manuscript a geometric model that combines large reconstructed models of the transverse ply taken from optical images with a simplified model of transverse crack initiation and a shear lag model of crack shielding. This work builds on the theoretical studies of Garret and Bailey [6] and Parvizi and Bailey [7], who used a homogenized model of the transverse ply in their prediction of the relation between applied transverse loading of the laminate and the evolution of transverse cracking in the 90° ply. In contrast, the present study incorporates details of the transverse ply microstructure extracted from optical images of the composite laminates used in the experiments [2].

Figure 1 shows the material system of interest. As indicated earlier, the two outside plies contain 0° oriented glass fibers embedded in an epoxy matrix, while the interior ply contains 90° oriented fibers in the same epoxy matrix. The figure also provides details of the microstructure and of its reconstruction, which was achieved using local thresholding techniques and a circular Hough transform [3].

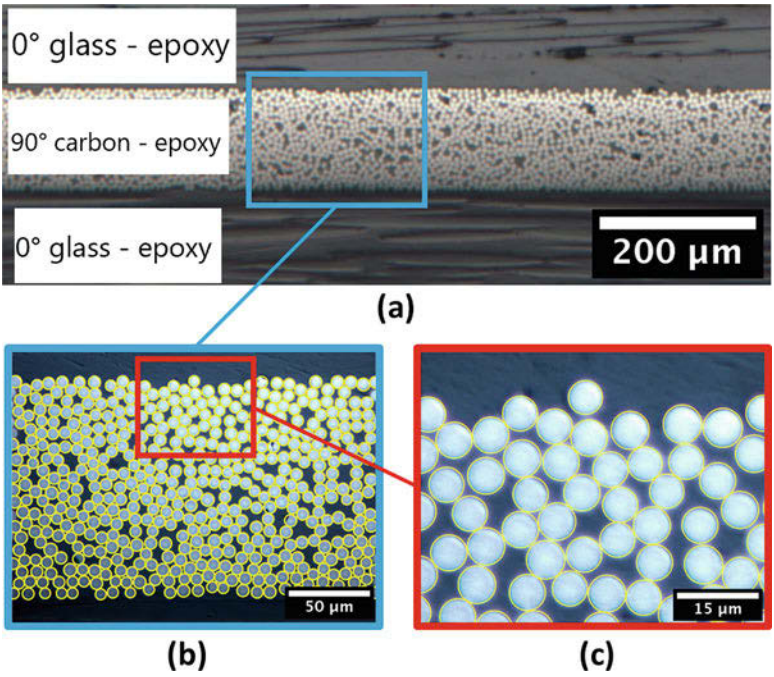

Fig. 1 (**a**) Hybrid glass/carbon/epoxy composite laminate used in the experimental study. (**b**) Focused view of carbon/epoxy transverse ply. (c) Detailed view of the carbon-fiber microstructure

The proposed geometric model consists of three components, which are described in the next three sections. Firstly (Sect. 2), realistic virtual specimens are constructed based on spatial statistics of the actual composite system. Secondly (Sect. 3), estimates of the stress concentration associated with a pair of adjacent fibers on the distance between them and their relative orientation with respect to the loading direction are used to identify potential points of failure initiation. Lastly (Sect. 4), an iterative process is adopted to determine the location of successive cracks, taking into account the shielding associated with previously introduced transverse cracks. Section 5 summarizes the results of a convergence and calibration analysis of the proposed model. In Sect. 6, we apply the geometric model to a statistical investigation of the impact of some of the microstructural parameters on the predicted transverse cracking response.

2 Problem Description

Multiple statistical metrics can be extracted from the optical images of the composite microstructure similar to that shown in Fig. 1. Two of these statistical measures are presented in Fig. 2: the distribution of fiber diameter (top figure) and the distribution of the projected nearest-neighbor distance (NND) (bottom figure), defined as the NND projected onto the direction of the transverse loading. The latter parameter is used in the next section in the estimation of the stress concentration factor that drives the crack initiation process. Due to the high fiber volume fraction of the composite laminate of interest, the measured NND for the system of interest is approximately 0.3 μm [3]. For reference, the diameter for a typical carbon fiber is approximately 7.5 μm.

In the experiments, the monitoring of transverse cracking process is achieved using two distinct methods. As shown in Fig. 3, optical images augmented by a fluorescent dye show that the failure process takes place primarily along the fiber/matrix interfaces. Another, more global approach based on acoustic emission is illustrated in Fig. 4, which also presents the transverse constitutive response dominated by the stiff, linear response of the 0° plies. Video observations of the failure process show that the transverse cracks initiate inside the 90° ply, propagate dynamically across the transverse layer, and are arrested by the adjacent 0° plies, as illustrated in Fig. 4 (top). More details on the experimental aspects of the project can be found in [2].

Once the virtual model of the laminate, built in this work directly from optical images, is defined in terms of the number, diameter, and placement of the fibers in the transverse ply, the problem description is completed by specifying the interfacial strength distribution. It should be noted here that virtual models of the microstructure can also be built numerically using a variety of statistical metrics, such as the fiber diameter and NND distributions or the one- and two-point correlation functions, combined with an optimization scheme aimed at matching the numerically computed and experimentally measured values of these distributions.

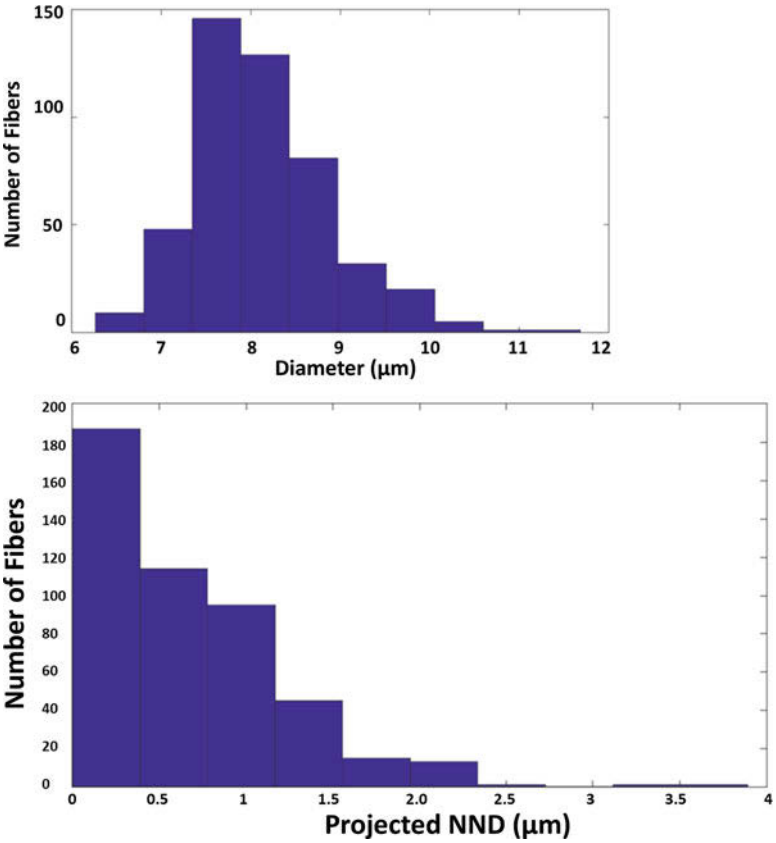

Fig. 2 Top: Fiber size distribution, showing an average fiber diameter around 7.5 μm. Bottom: Histogram of the projected nearest neighbor distance (NND) between the fibers of the transverse ply emphasizing the close packing of the fibers

An example of this virtual model construction based on the simulated annealing method [8] specially adapted for composite with high fiber volume fractions can be found in [9] and is illustrated in Fig. 5.

As described in the next section, the geometric model utilizes the fiber-matrix interface strength to evaluate the required load to initiate failure. In this work, we adopt a Weibull distribution of the interfacial strength, defined by the scale (λ) and shape (k) parameters as

$$\begin{cases} f(s,k,\lambda) = \frac{k}{\lambda}(\frac{s}{\lambda})^{k-1} e^{-(\frac{s}{\lambda})^k} & s \geq 0, \\ f(s,k,\lambda) = 0 & s < 0, \end{cases} \tag{1}$$

with both λ and k greater than zero, and s denotes some strength measure in this work. These two parameters are related to the mean (μ) and variance (σ^2) by

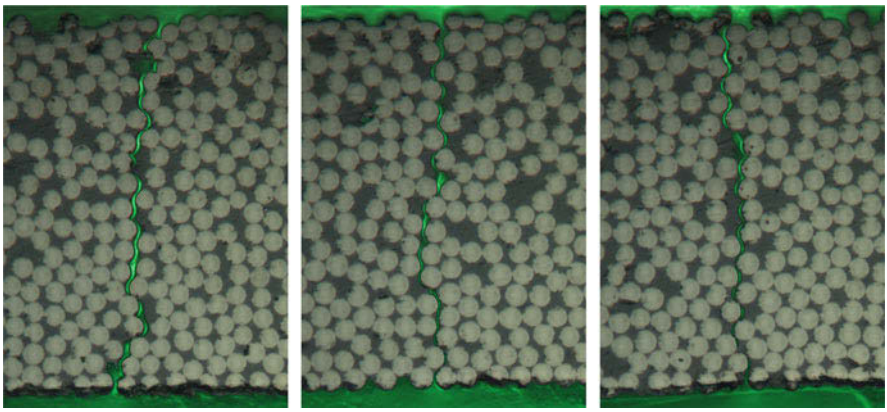

Fig. 3 Three typical transverse cracks, showing that fiber/matrix debonding accounts for most of the crack path

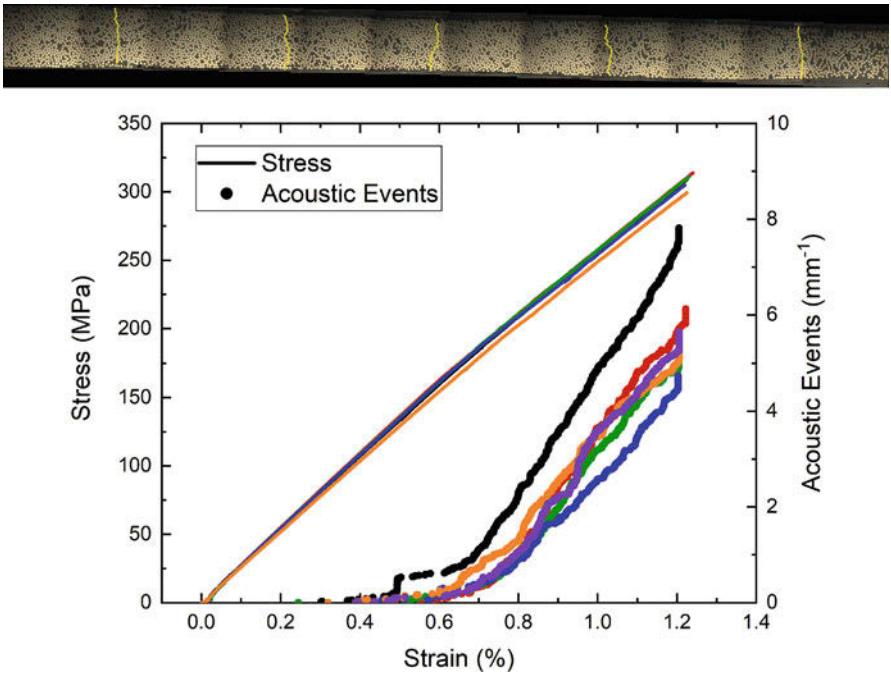

Fig. 4 Top: Multiple cracks across the transverse ply. Bottom: Measured transverse stress-strain curves and acoustic signatures associated with six transverse failure tests. Although multiple cracks are created, the constitutive response, dominated by the stiff 0° plies, is mostly linear

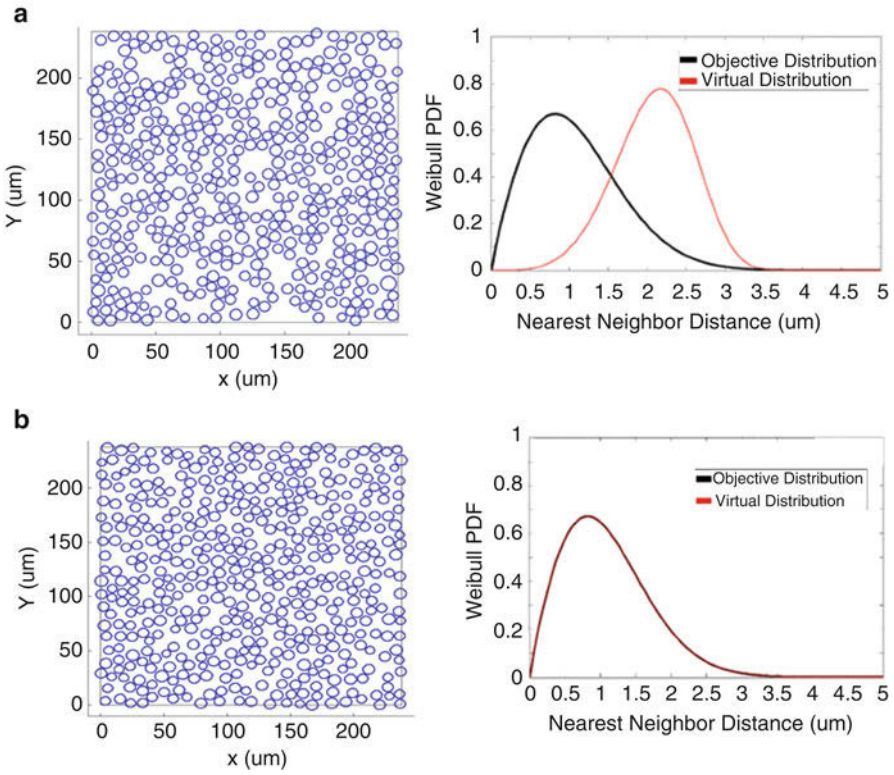

Fig. 5 Numerical building of a virtual model of the transverse ply by on the matching of the NND distribution extracted from optical images. The right figures compare the numerical (red curve) and experimental (black curve) distributions (captured with a Weibul distribution) at the start (**a**) and completion (**b**) of the optimization process. (Taken from [9])

$$\mu = \lambda\Gamma(1 + \frac{1}{k}), \tag{2}$$

and

$$\sigma^2 = \lambda^2(\Gamma(1 + \frac{2}{k}) - \Gamma(1 + \frac{1}{k})^2), \tag{3}$$

where $\Gamma(.)$ is the Gamma function. Equations (2) and (3) lead to

$$\frac{\sigma^2}{\mu^2} = \frac{\Gamma(1 + \frac{2}{k})}{\Gamma(1 + \frac{1}{k})^2} - 1. \tag{4}$$

Figure 6 illustrates how k and λ affect the cumulative probability distribution.

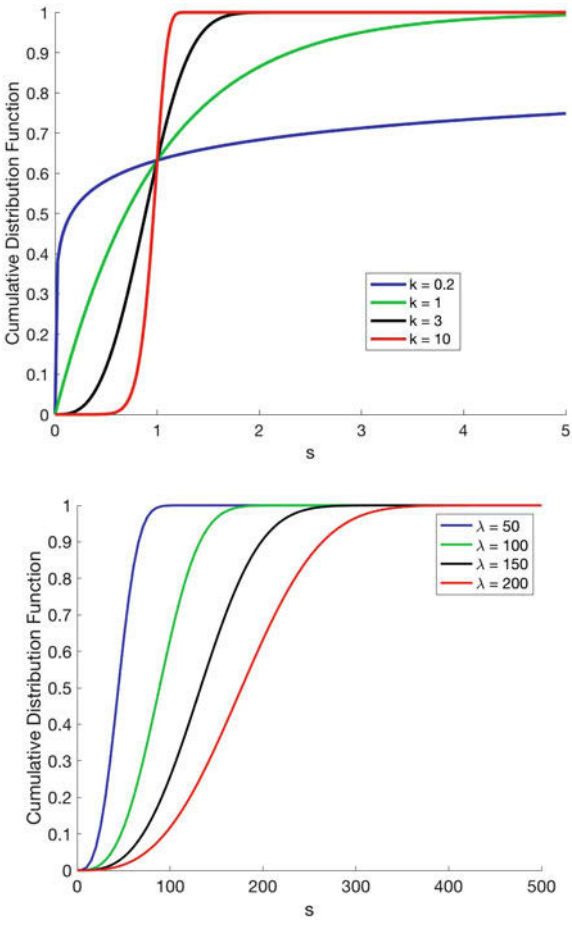

Fig. 6 Effect of the shape parameter k (for $\lambda = 1$) (top) and of the scale parameter λ (for $k = 3$) (bottom) on the cumulative Weibull distribution used to describe the fiber/matrix interface strength distribution

An example of interfacial strength distribution with an average value of 80 MPa and a variance σ of about 3 MPa is shown in Fig. 7.

In the crack initiation component of the model, each fiber/matrix interface is assigned randomly a strength value based on the distribution shown in Fig. 7, and transverse cracking is assumed to occur, and then the stress concentration (see Sect. 3) associated with each fiber pair reaches the lesser of the two strength values. This critical value associated with each fiber pair is pre-computed based on the fiber placement and assigned strength values.

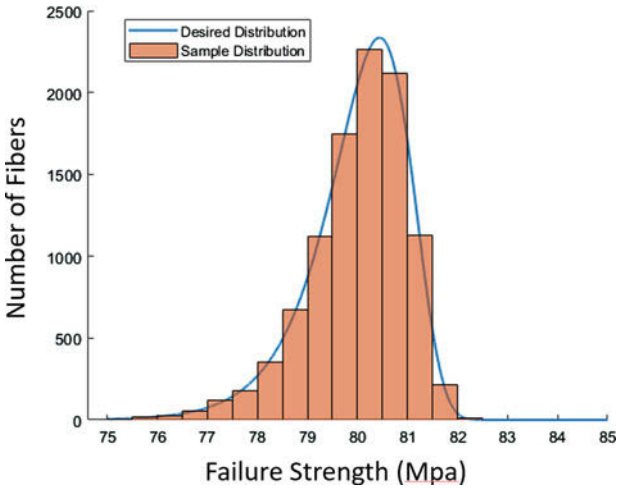

Fig. 7 Continuous and discrete distributions of interface strength values corresponding to an average of 80 MPa and a variance of approximately 3 MPa

3 Fiber-Pair Stress Concentration

As indicated earlier, postmortem fracture analyses of the composite laminate have shown that interfacial failure accounts for most of the transverse crack path. In this simplified model, we assume that crack initiation also takes place at fiber-matrix interfaces, when the stress concentration associated with a pair of adjacent fibers, which is a function of the distance between these fibers and of their orientation with respect to the loading direction, reaches the debonding strength of the weaker of the two interfaces. We also assume that, once a crack is initiated, it propagates instantaneously and vertically across the 90° ply.

To estimate the dependence of the stress concentration on the distance d between adjacent fibers and the angle β with the loading direction, we perform a parametric study using the interface-enriched generalized finite element method (IGFEM) of the problem described schematically in Fig. 8. In this model, the two fibers are assumed to have the same diameter, the interface to be perfect, and the fibers and the matrix to behave as linearly elastic solids. Figure 8 also illustrates the loading conditions, including the applied far-field transverse load σ_∞ that defines the loading direction. The domain is chosen large enough to avoid the influence of the boundary conditions on the stress field in the vicinity of the two fibers.

To capture accurately the geometry of the two fibers, we adopt the IGFEM formulation based on Non-Uniform Rational Basis Splines (NURBS). This approach allows for solving the problem with finite element meshes that do not conform to the material interfaces by introducing in the elements traversed by a fiber/matrix interface enrichments based on the NURBS representation of that interface [10].

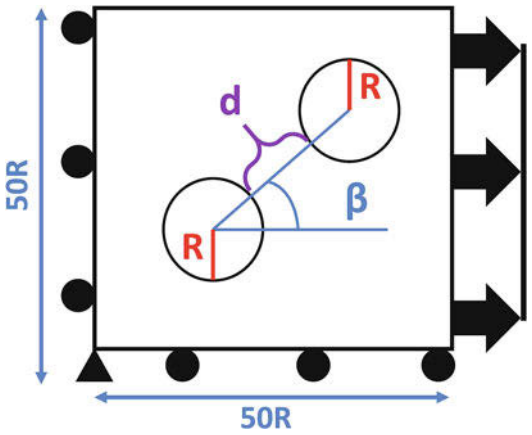

Fig. 8 Extraction of the stress concentration associated with two adjacent fibers of radius R

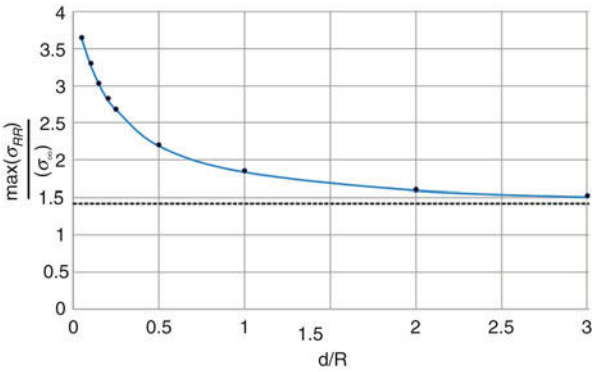

Fig. 9 Dependence of the stress concentration factor on the separation d between two fibers of radius R aligned with the loading direction (β= 0). The dotted horizontal line represents the stress concentration factor for a single fiber [11]

The parametric study is conducted for $-90° \leq \beta \leq 90°$ and $0.05 \leq d/R \leq 3$, and, for each case, the maximum radial stress along the two fiber/matrix interfaces is computed.

Figure 9 presents the dependence of the stress concentration factor (defined as the ratio between the maximum radial stress along the fiber/matrix interfaces and the applied far-field transverse load σ_∞) on the distance d separating the two fibers for the case where the fibers are aligned with the loading direction ($\beta = 0$). As expected, the stress concentration increases as the fiber-to-fiber distance decreases and tends to the single fiber value given by Goodier [11] when the fiber-to-fiber separation exceeds three times the radius.

Figure 10 shows the β-dependence of the stress concentration factor for nine values of d. As apparent in that figure, a stress concentration is obtained for $-45° \leq \beta \leq 45°$, with the highest stress concentration obtained for fiber pairs aligned with the loading direction. The β and d-dependence of the stress concentration is summarized in the 3-D plot shown in Fig. 11.

The results of this study are used to determine the stress concentration factor, labeled γ_g hereafter, that amplifies the applied stress (σ_t) acting on the transverse

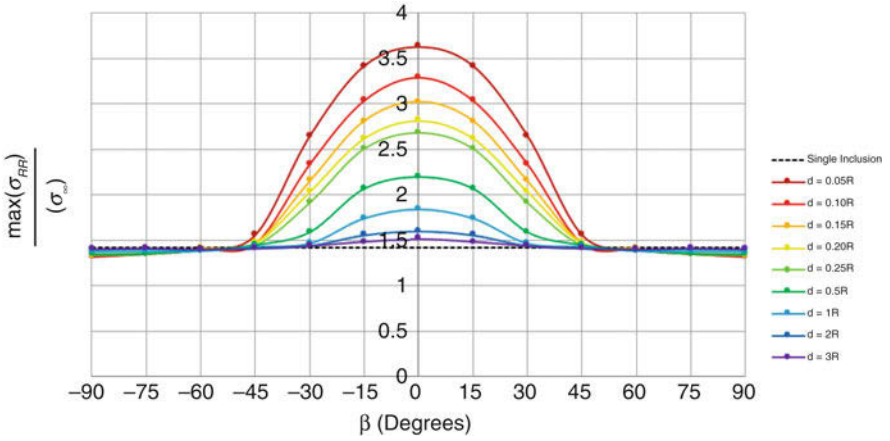

Fig. 10 Angular variation of the stress concentration factor obtained for different values of the fiber separation distance d

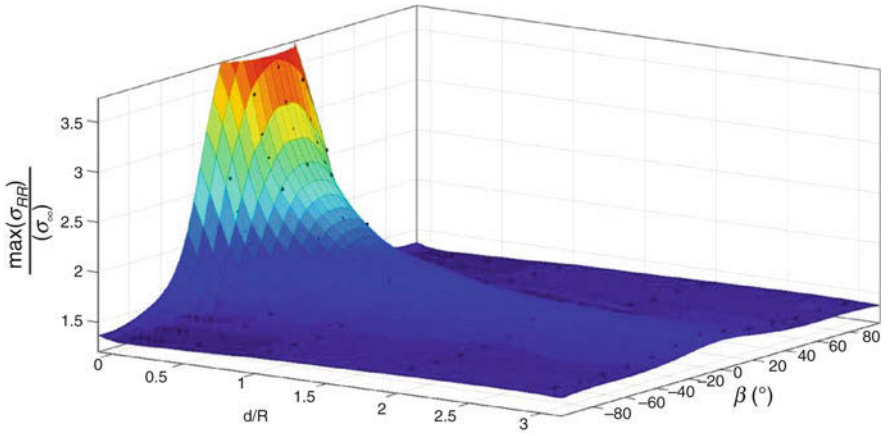

Fig. 11 3-D representation of the dependence of the interface stress concentration factor on the fiber-to-fiber separation distance d and orientation angle β

ply. The resultant interface radial stress is then compared to the interface strength value σ_c assigned to the weaker of two fiber interfaces to initiate a transverse crack. The condition for crack initiation thus reads

$$\sigma_c = \gamma_g \, \sigma_t = \gamma_g \, \frac{E_t}{E_c} \, \sigma_a, \tag{5}$$

where σ_a is the transverse stress applied on the composite laminate and E_t and E_c, respectively, denote the Young's modulus (in the direction of the loading direction) of the transverse ply and composite laminate.

4 Stress Shielding from Transverse Cracks

Equation (5) provides the load amplitude and location of the first transverse crack. The introduction of subsequent cracks, however, requires to account for the shielding effect of the previously introduced cracks on the stress field in the transverse layer. As a transverse crack is introduced across the 90° ply, the magnitude of the transverse stress in the transverse ply becomes zero in the plane of the crack and is reduced in the vicinity of that crack, thereby decreasing the probability of another crack in the adjacent region. The size of this shielding zone can be estimated using the shear lag approach described by Garret and Bailey [6]. The drop $\Delta\sigma_0$ in the axial stress due to the (assumed vertical) transverse crack is given by

$$\Delta\sigma_0 = \sigma_a \frac{d}{b} \frac{E_t}{E_c}, \tag{6}$$

where b and $2d$ represent the width of the 0° plies and of the 90° ply, respectively. This stress drop is transferred to the adjacent 0° plies through a spatially varying shear stress along the ply interfaces. The axial force $F(x)$ in the transverse ply, where x denotes the distance to the plane of the transverse crack, is related to the shear stress $\tau(x)$ acting along the ply interface by [6]

$$\frac{dF(x)}{dx} = 2c\tau(x), \tag{7}$$

where c denotes the out-of-plane dimension of the laminate, and

$$\tau(x) = b\Delta\sigma_0 \phi^{\frac{1}{2}} e^{-\phi^{\frac{1}{2}}x}. \tag{8}$$

In (8), ϕ is a material parameter given by

$$\phi = \frac{E_c G_t}{E_l E_t} \frac{(b+d)}{bd^2}, \tag{9}$$

where G_t is the shear modulus of the transverse ply in the horizontal direction, and E_l is the Young's modulus of the 0° plies. The stress $\sigma_t(x)$ in the transverse ply can readily be found by integrating (7) and dividing by the cross-sectional area $(2cd)$ of the transverse ply. The constant of integration is found by imposing $\sigma_t(0) = 0$ at the crack plane. The shielding coefficient, denoted hereafter by γ_s and defined by

$$\sigma_t(x) = \gamma_s(x)\, \sigma_a, \tag{10}$$

can be expressed as

$$\gamma_s(x) = \frac{E_t}{E_c}(1 - e^{-\phi^{\frac{1}{2}}x}). \tag{11}$$

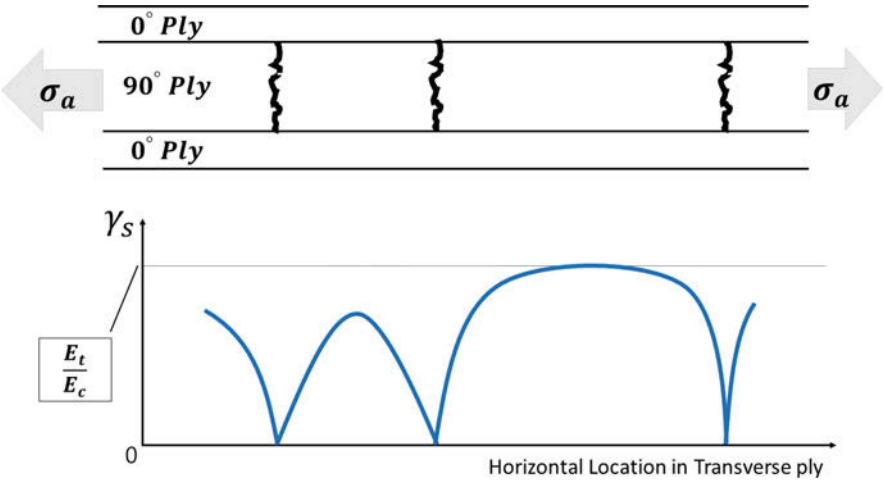

Fig. 12 Schematic illustration of the shielding effect of transverse cracks: spatial variation of the shielding coefficient γ_s in the presence of three transverse cracks

In the presence of crack shielding, the criterion for crack initiation (5) is thus rewritten as

$$\sigma_c = \gamma_g \gamma_s \sigma_a. \tag{12}$$

This formulation can be extended to the case of multiple cracks to define the stress distribution for the region between any pair of cracks with a spacing t. In this instance, the constant of integration is found by imposing $\sigma_t(0) = \sigma_t(t) = 0$. The shielding term can be shown to be

$$\gamma_s(x,t) = \frac{E_t}{E_c}(1 + e^{-\phi\frac{1}{2}t} - e^{-\phi\frac{1}{2}x} - e^{-\phi\frac{1}{2}t}e^{\phi\frac{1}{2}x}). \tag{13}$$

Equations (11) and (13) can now be combined to create a piecewise definition for the shielding factor in the transverse ply at any location, as illustrated schematically in Fig. 12 for the case of three cracks. As expected, $\gamma_s = 0$ at the location of the cracks and approaches the value E_t/E_c when there is sufficient distance between two neighboring cracks.

5 Model Testing and Calibration

Since the geometric model captures the interaction between cracks through the shear-lag-based shielding model described in the previous section, one would expect that adopting a small specimen size would rapidly lead to a "saturation," which

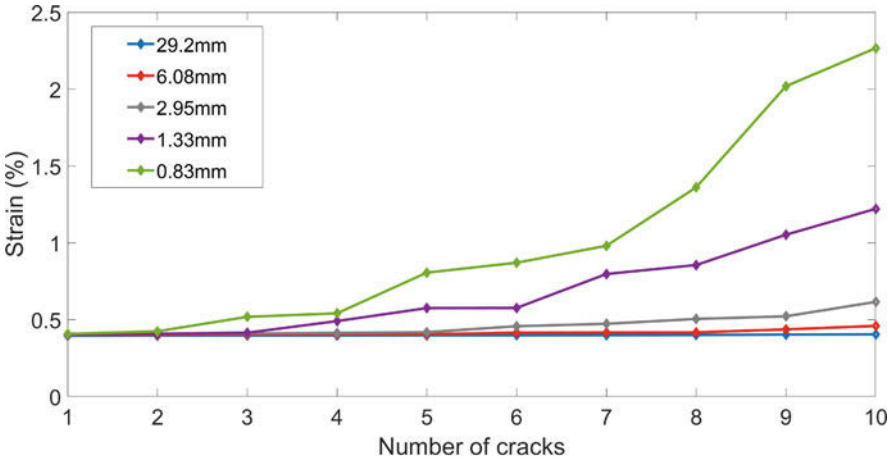

Fig. 13 Transverse strains associated with the appearance of the first ten transverse cracks in five virtual specimens with varying lengths, showing the shielding effect on the shorter specimens

would lead to a rapid increase in the predicted failure strain. Based on (9), the length scale associated with crack shielding is given by $\phi^{-1/2}$.

The largest sample for which an optical image is available is about 29 mm long and counts about 50,000 fibers in the 90° ply. While the model is able to capture transverse cracking in plies with tens of thousands of fibers, performing statistical studies such as those described in the next section will be substantially speeded up by using smaller domains. To that effect, we investigate the effect of the specimen size on the prediction of the transverse strain associated with the appearance of the first ten transverse cracks.

The results from that study are shown in Fig. 13. The smaller specimens correspond to sections of the large 29 mm-long specimen with similar fiber volume fractions. As apparent in that figure, the solution for shorter specimens deviates from that of the "reference" specimen due to the aforementioned saturation effect. Based on this study, 6.08 mm-long virtual specimens are selected for the calibration study described later on in this section.

Although the emphasis of the proposed geometric model is to incorporate the randomness inherent in the composite microstructure in the evolution of transverse cracking, the model can also be used in the special case where the transverse ply is homogenized, as was done in [7]. In this approach, there is no preferred microstructure-driven location for crack initiation, and, due to the symmetry of the axial stress field with respect to existing cracks, the new cracks are predicted to appear halfway between previously introduced cracks. In other words, if we adopt a normalized axial $\tilde{x}$ coordinate along the specimen running from 0 to 1, the first crack appears at location $\tilde{x} = 0.5$, the next two cracks appear simultaneously at locations $\tilde{x} = 0.25$ and $\tilde{x} = 0.75$, the next four at locations $\tilde{x} = 0.125, 0.375, 0.625$, and

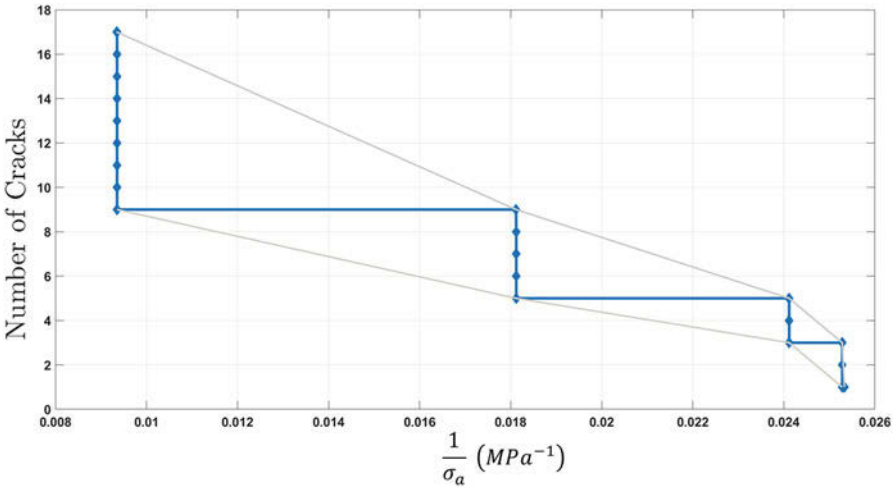

Fig. 14 Homogenized geometric model: Relation between the inverse of the applied stress σ_a and number of cracks, showing the step-like response described in [7]

0.875, etc. This predicted evolution of the transverse cracking, displayed, as was done in [7], as the number of cracks versus the inverse of the applied stress, is shown in Fig. 14.

As expected, we recover the step-like response described in [7], where the number of cracks at step $i + 1$ is related to that at the previous step i through

$$N_{i+1} = 2N_i - 1. \tag{14}$$

This result is quite different from the proposed model that incorporates the random nature of the geometry and material properties of the transverse ply microstructure.

In the final part of this section, we calibrate the model through a comparison with experimental measurements of the transverse cracking process. The key parameter to be calibrated is the failure strength σ_c of the fiber/matrix interfaces (assumed uniform for all fibers in this calibration study), which directly impacts the strain at which transverse cracking is initiated, as shown in Fig. 15. As expected, the higher the value of σ_c, the higher the critical strains associated with the onset of transverse cracking.

Based on these results, we adopt the value of 80 MPa for the average strength of the fiber/matrix interfaces, as it appears to capture the measured failure strains, especially for the first five transverse cracks. This value is used in the statistical study presented next.

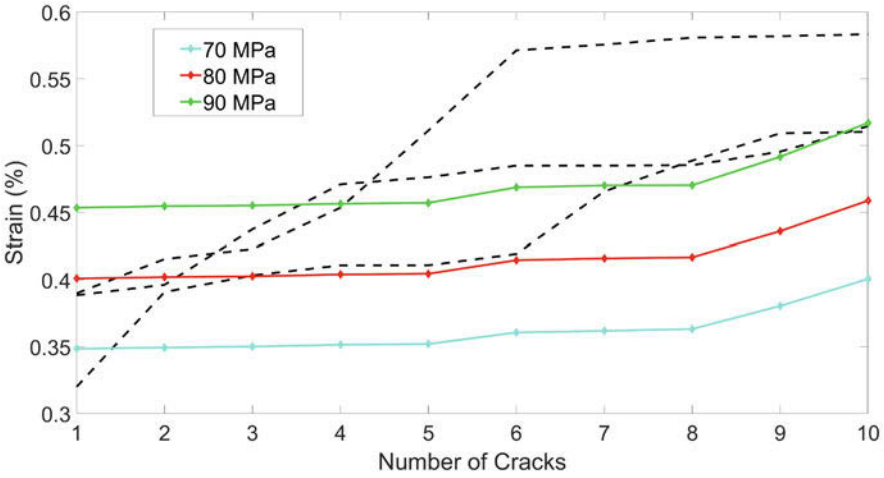

Fig. 15 Calibration of geometric model: effect of the interface strength on the strains associated with the appearance of the first ten transverse cracks. The black dashed curves correspond to the experimental measurements extracted from three separate tests, showing the variability of the experimental results

6 Statistical Analysis of the Impact of the Interface Strength Distribution

As indicated earlier, multiple microstructural parameters contribute to the statistical nature of the transverse failure response of the laminate. These include geometrical parameters, such as fiber placement and size, and material parameters such as the constitutive response of the fibers and the matrix and the failure response of the fiber/matrix interfaces. Taking advantage of the efficiency of the geometric model, we investigate in this section the impact of the variability of the interface strength σ_c modeled in the form of the Weibull distribution described by (1). Of particular interest is the quantification of the effect of the variance (4) of the failure strength distribution.

To that effect, five values of the variance σ ranging from 0 to 20 MPa are selected to generate five Weibull distributions for interface strength. For each value of the variance, 100 instantiations of the distribution are created and assigned to the approximately 10,000 fibers present in the microstructure of the 6.08 mm-long samples. To isolate the effect of the interfacial strength distribution, the geometry of the virtual specimen is kept constant.

The average values of the critical applied axial stress associated with the first 10 transverse cracks extracted from these 100 instantiations are presented for these five variance values in Fig. 16. As apparent there, the stress level corresponding to the appearance of the first transverse crack drops by about 7 MPa when a small

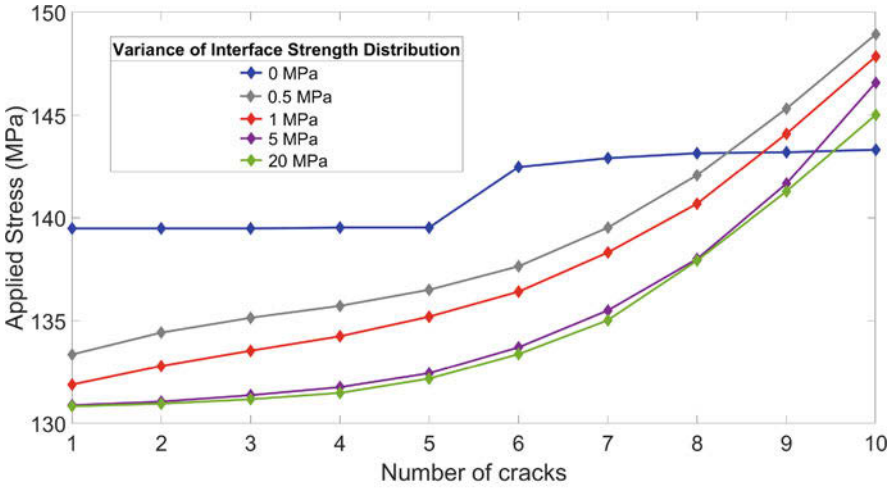

Fig. 16 Effect of the variance in fiber/matrix interface strength on the average failure load extracted over 100 instantiations (based on the same microstructure) for an average interface strength of 80 MPa

variability (0.5 MPa) is introduced. This drop increases for higher values of the variance, although it tends to stabilize when $\sigma \geq 5$ MPa. We also note that adding variability in the interface strength assigned to the fibers leads to a decrease of the predicted failure axial stress compared to the uniform strength case for the first 8 or 9 transverse cracks, beyond which it exceeds the solution obtained with $\sigma = 0$. It should also be noted how the introduction of a variability in the interface strength substantially changes the evolution of the failure stress with the number of cracks, leading to a steadily and smoothly increasing trend to be contrasted with the quasi-constant solution for $\sigma = 0$.

The value of the variance σ also affects the variability (i.e., the error bars) in the predicted failure transverse stress, as shown in Fig. 17.

Again, the error bars on the predicted failure stress increase with the number of cracks, following a similar trend for all four values of the variance σ, except for the first few cracks, where higher values of the variance (5 and 20 MPa) lead to substantially reduced error bars in the predicted failure stress values. This is to be expected: higher values of the variance in the interfacial strength distribution lead to the creation of weak interfaces for which the variability of the interface strength dominates that associated with the geometry. This effect yields consistent solutions with little variation.

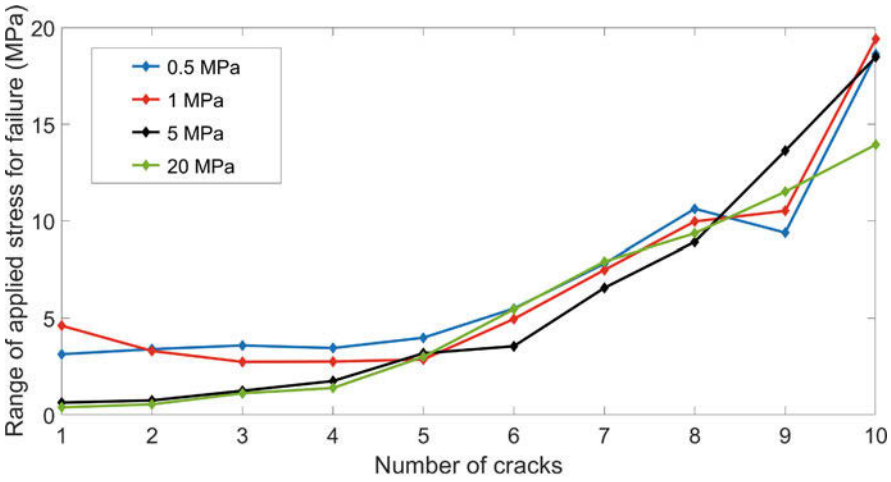

Fig. 17 Variability of the critical stress values associated with the appearance of the first ten cracks for the four non-zero values of the interfacial strength variance used in Fig. 16

7 Conclusion

This manuscript has presented a simplified geometric model used to predict the impact on the transverse failure of a composite laminate of the statistical nature of the material and geometrical parameters that define the microstructure of the transverse ply. The model is based on three key components: (i) realistic virtual models of the microstructure (fiber placement and size distribution) of the transverse ply, (ii) a simplified crack initiation model based on a critical value of the interface stress concentration associated with the separation distance and orientation of adjacent fibers, and (iii) a shear lag approximation of the stress shielding effect created in the transverse ply by transverse cracks. One of the key advantages of the geometric model is its computational efficiency, which enables the simulation of multiple transverse cracks in realistic virtual models of the laminate with tens of thousands of fibers and/or allows for the analysis of a large number of instantiations of the statistical parameters.

The geometric model has been calibrated through comparison with measured values of the critical transverse strains corresponding to the appearance of the first ten transverse cracks in a hybrid glass/carbon/epoxy laminate. The model was then used to perform a statistical analysis of the impact on the predicted failure response of the variability of the strength values assigned to the thousands of fiber/matrix interfaces present in the virtual specimen. The statistical analysis has shown that a small variability of the interfacial strength distribution leads to a reduction in the failure load associated with the appearance of the first transverse cracks. Further expansions of the model include accounting for the residual stresses associated with the property mismatch between plies and along the fiber/matrix interfaces.

Acknowledgements This work has been supported through a grant No. FA9550-12-1-0445 to the Center of Excellence on Integrated Materials Modeling (CEIMM) at Johns Hopkins University (partners JHU, UIUC, UCSB), awarded by the AFOSR/RSL (Computational Mathematics Program, Manager Dr. A. Sayir) and AFRL/RX (Monitors Dr. C. Woodward and C. Przybyla).

References

1. P.K. Mallick, *Fiber Reinforced Composites: Materials, Manufacturing, and Design*, 3rd edn. (CRC Press, Boca Raton, FL, 2007)
2. C. Montgomery, Multiscale characterization of carbon fiber-reinforced epoxy composites. Ph.D. thesis, Department of Materials Science and Engineering, University of Illinois at Urbana-Champaign (2018)
3. S. Zacek, D. Brandyberry, A. Klepacki, C. Montgomery, M. Shakiba, M. Rossol, A. Najafi, X. Zhang, N. Sottos, P. Geubelle, C. Przybyla, G. Jefferson, Transverse failure of unidirectional composites: sensitivity to interfacial properties, in *Advancing Computational and Experimental Methods for Integrated Computational Materials Engineering (ICME)*, co-ed. by S. Ghosh, C. Przybyla, C. Woodward (Springer, New York, 2020)
4. M. Shakiba, D. Brandyberry, S. Zacek, P. Geubelle, Transverse failure of carbon fiber composites: analytical sensitivity to the distribution of fiber/matrix interface properties. Int. J. Numer. Methods Eng. **89**, 650–665 (2019)
5. X. Zhang, D. Brandyberry, P. Geubelle, Igfem-based shape sensitivity analysis of the transverse failure of a composite laminate. Comput. Mech. **64**(5), 1455–1472 (2019)
6. K. Garrett, J. Bailey, Multiple transverse fracture in 90° cross-ply laminates of a glass fibre-reinforced polyester. J. Mater. Sci. **12**, 157–168 (1977)
7. A. Parvizi, J. Bailey, On multiple transverse cracking in glass fibre epoxy cross-ply laminates. J. Mater. Sci. **13**(10), 2131–2136 (1978)
8. S. Kirkpatrick, C. Gelatt Jr, M.P. Vecchi, Optimization by simulated annealing. Science **220**(4598), 671–680 (1983)
9. S. Zacek, Exploring the link between microstructure statistics and transverse ply fracture in carbon/epoxy composites. Master's thesis, University of Illinois – Urbana-Champaign (2017)
10. M. Safdari, A.R. Najafi, N.R. Sottos, P.H. Geubelle, A nurbs-based interface-enriched generalized finite element method for problems with complex discontinuous gradient fields. Int. J. Numer. Methods Eng. **101**(12), 950–964 (2015)
11. J. Goodier, Concentration of stress around spherical and cylindrical inclusions and flaws. TASME **55**, 39 (1933)

Challenges in Understanding the Dynamic Behavior of Heterogeneous Materials

Manny Gonzales and Naresh N. Thadhani

1 Introduction

Extreme dynamic environments are ubiquitous in defense applications, industrial processing, and machining operations and in the study of celestial events such as micrometeorite impact or in the formation of planets. Often, the materials involved in these environments have microstructural and property heterogeneities which influence the bulk response to the dynamic event. For the purposes of this chapter, heterogeneous materials are reckoned as containing either inhomogeneities or inclusions as defined by Mura [56], i.e., anything that produces an eigenstrain in an otherwise continuously varying media. Multiphase materials such as dual-phase steels, precipitation-hardened materials, composite materials, and particulate or granular mixtures are naturally heterogeneous, and the heterogeneity may be observed at disparate length scales among the different material types.

The importance of loading rate on the dynamic response depends on the heterogeneity and degree of property contrasts in question [13, 24, 60]. For example, polycrystalline materials may be considered heterogeneous at the meso-scale under dynamic loading if there are significant property contrasts arising from orientation mismatch or texture, especially if this creates disparities in an otherwise isotropic wave propagation response. Highly deformed metals subjected to extreme dynamic events can respond quite differently to high strain rate loading than quasi-static loading due to metallurgical phenomena such as dynamic recovery and recrystalliza-

M. Gonzales (✉)
Materials and Manufacturing Directorate, Air Force Research Laboratory, WPAFB, Dayton, OH, USA
e-mail: manny.gonzales.1@us.af.mil

N. N. Thadhani
School of Materials Science and Engineering, Georgia Institute of Technology, Atlanta, GA, USA
e-mail: naresh.thadhani@gatech.edu

S. Ghosh et al. (eds.), *Integrated Computational Materials Engineering (ICME)*,
https://doi.org/10.1007/978-3-030-40562-5_14

tion, adiabatic shear localization, and other deformation modes becoming activated such as deformation twinning [54, 57–59]. Even if the quasi-static behavior of the material lends itself to a bulk isotropic formulation of its constitutive law, the meso-scale response at dynamic loading rates may be drastically different due to percolation effects [60]. The meso-scale response has implications on the measured bulk behavior in an experiment and cannot be ignored. The fascinating aspects of heterogeneous materials lie in the length scales, microstructural features, and property contrasts that impart the physical and mechanochemical properties that themselves make the materials suitable candidates for use in extreme dynamic environments.

1.1 The Challenge of Dynamic Property Measurements

Experimental methods to evaluate material response at dynamic loading rates involve generating stress waves in the material and evaluating the wave propagation response either via indirect or direct measurement or by inferring the response from computer simulation. The stress waves are generated by mechanical insult on a material to be tested, usually by striking the material with a projectile, via contact detonation with an explosive, or by the confined expansion of a plasma generated by a pulsed-power laser. Experimental methods in dynamic behavior can range in the strain rate regime of applicability, from quasi-static and slow-strain-rate testing using load frames to drop weight testing, split Hopkinson pressure bar (SHPB) testing, flyer plate testing, and contact detonation with explosives. The accessible strain rates depend on the materials tested as well as the size and shape of the testing articles. Figure 1 demonstrates the relative strain rate regimes achievable by common testing methods applied to metallic materials. The shock impedance and constitutive properties will determine the strain rates achievable. It should be noted that these strain rates are typical at meso-scales and that macro-scale strain rates may be up to an order of magnitude lower than those represented in this plot. The local strain rates at smaller scales may be much higher, as strain rate scales with the deformation length scale. Strain rates achievable in powder and particulate mixtures are a strong function of the packing density and local microstructure, as well as the topology of the void space and connectivity of phases. Furthermore, crush strength also affects the strain rate achievable and can disperse the insulting waves as they expend energy to compact the powder.

There are extensive descriptions in the monographs by Meyers [54], Field et al. [21], Ramesh [62], and Horie and Sawaoka [42] on dynamic testing, especially under shock compression conditions. Indirect measurements include the strain gage output from split Hopkinson pressure bars (SHPBs), postmortem measurements of the final bulk strain/deformation of recovered impacted specimens, or postmortem microstructural characterization. Direct measurement techniques include direct-contact stress gages, magnetic particle velocity gages, digital image correlation (DIC) measurements of speckle patterns, high-speed photography/videography, and

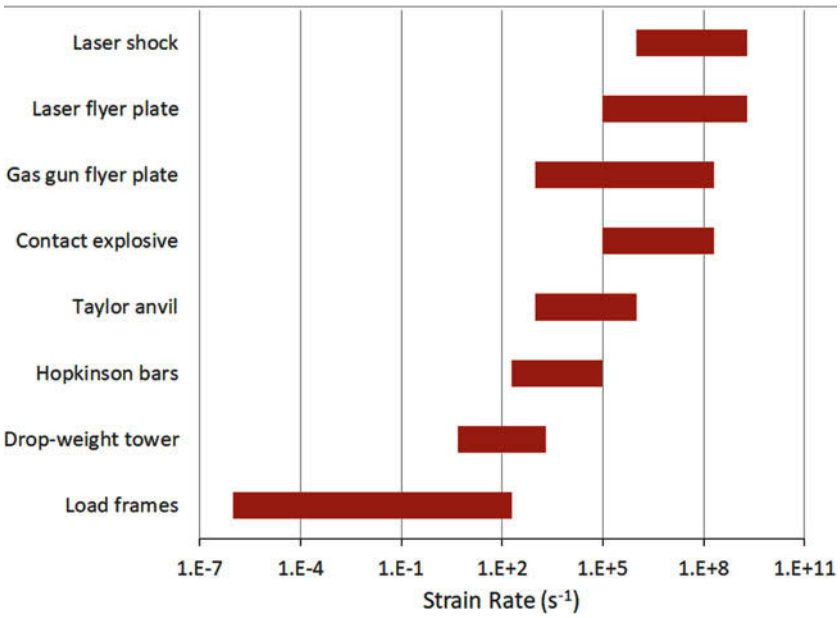

Fig. 1 Approximate strain rate regimes accessible by conventional dynamic testing. Custom configurations, specimen size and material, and local geometry all affect the accessible strain rates. Local strain rates at the meso- and microscales may be much higher due to size effects and inertia

velocimetry measurements on exposed moving surfaces. It can be argued that direct measurements only measure the modified propagated wave characteristics and are only valid if specific assumptions are met – namely, the Rankine-Hugoniot jump conditions for extremely high strain rates (i.e., where shock waves are generated). The structure and geometry of the microstructure affect the material response at high strain rates by changing the dynamics of wave propagation. The aforementioned measurement techniques have trade-offs in both spatial and temporal resolutions and may smear the meso-scale response due to these trade-offs.

The inherently destructive nature of an extreme dynamic event makes probing its behavior very challenging. Violent stress waves necessitate ultrafast measurement from devices that can withstand the onslaught for sufficient time to record the measurement. Due to the active area of the devices interacting with the material, the effects of microstructural features are averaged over the area of the sensor, which can artificially dampen the meso-scale response. Interactions between the probe (i.e., the gage in contact with the material) and the material itself can modify the response due to wave interaction/ringing and impedance-matching. Furthermore, the loading configuration can change the wave propagation event in ways that the gages or velocimetry probes cannot reckon (i.e., triaxial states of stress). The physical complexity of the dynamic event makes it difficult to glean valuable information from experimental measurements alone. Therefore, valuable information may be obtained via computer simulation in the Integrated Computational Materials Science

and Engineering (ICMSE) paradigm, where physics-based models on spatially resolved microstructures or meso-structures provide insight into the dynamic event that experimental measurements are unable to fully capture. Naturally, experimental validation guides highly resolved numerical simulations of impact processes, which can capture the microstructural complexity of the material if suitable constitutive models and equations of state exist.

1.2 ICMSE Approaches to Probing Dynamic Behavior of Materials

The advent of distributed memory and parallelized computing has enabled massively parallel numerical computations of physical phenomena. Complex numerical simulations using discretized forms of the conservation equations are now readily available and make multi-material dynamic simulations a possibility. The sophistication of constitutive models and equations of state is constantly evolving, rendering a predictive physics-based calculation tenable. However, there remain aspects of the phenomena where deterministic calculation fails to capture the true nature of the behavior, and stochastic methods become attractive. Meso-scale simulations of realistic microstructural configurations under extreme dynamic loads can provide a window into how these microstructures evolve and affect the bulk dynamic behavior of the system.

1.2.1 Molecular Dynamics and Coarse-Grained Methods

Molecular dynamics (MD) provides a simulation methodology whereby ensembles of atoms, treated as Newtonian bodies interacting in a field, [38] can provide bulk and continuum-level properties through statistical mechanics considerations. MD simulations relying on conventional thermo and barostats have been successfully used to study shock compression phenomena, cf. [43, 55]. Jarmakani et al. [43] studied shock propagation in both mono- and nanocrystalline Ni using the Mishin potentials through an embedded atom method (EAM). They observed stacking faults and partial dislocation formation consistent with experiments and found that the stress release process was responsible for the annihilation of partial dislocation loops formed after the shock wave traversed the crystal, which explained prior discrepancies between post-shock observations and MD predictions. Figure 2 shows a representative output of the deformed substructure in nanocrystalline Ni (Fig. 2a, b,) and Cu (Fig. 2c), which captures the richness in plastic deformation mechanisms, which includes stacking fault formation and twinning. Blue areas denote undeformed atomic configurations, green areas denote displacement by the Burgers vector of a Shockley partial, and red areas denote displacement by a full Burgers vector corresponding to a perfect dislocation. Perfect dislocations

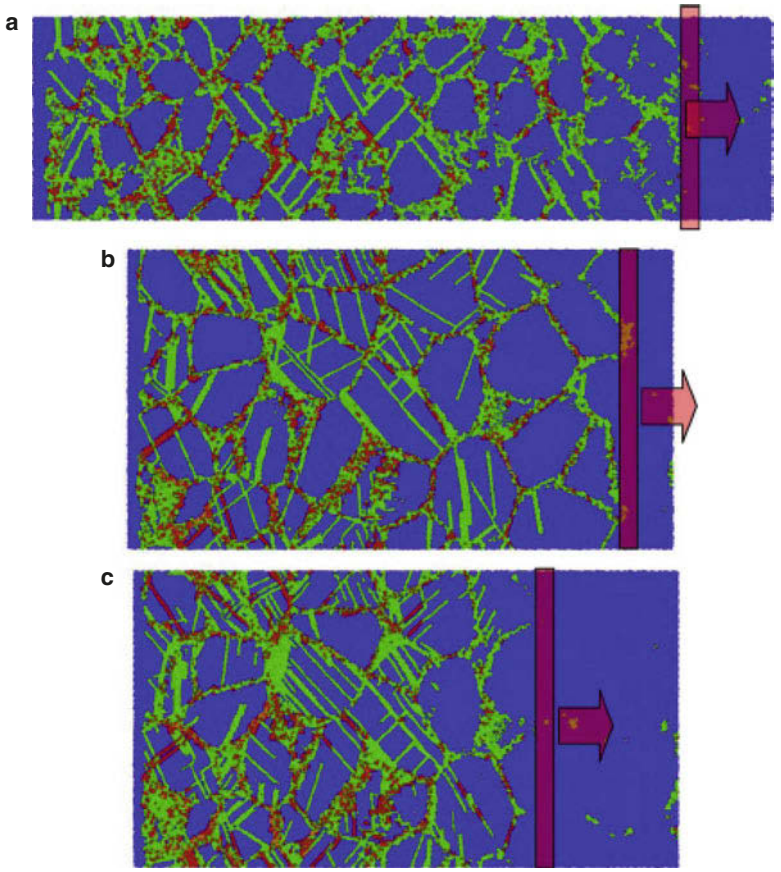

Fig. 2 MD simulations of the shock compression in polycrystalline Nickel. (Adapted from Jarmakani et al. [43])

concentrate at grain boundaries; the authors also concluded that grain boundary sliding accounts for an estimated 58–90% of the total shock-induced strain [43].

MD simulations have been successfully deployed to study the Ni+Al nanolaminate system to discern the mixing phenomena between the Ni+Al phases [83], which is driven by interfacial mixing and melting of the Al layers. The work also explored the effect of pressure on the chemical reaction rates (i.e., mixing propensity) and found that the rate of mixing decreased with increasing pressure. Specialized barostats (e.g., Holian and Ravelo's "Hugoniotstat" [49, 63]) and coarse-graining techniques for reactive and energetic materials as in Strachan, Antillon, and co-workers [3, 4, 71], which utilize "mesoparticles" with internal degrees of freedom and intramolecular potentials between phases, provide larger-scale information about the microscopic interactions between relevant constituents of reactive materials under dynamic loading. Density functional theory (DFT) can

also be invoked to construct interatomic potentials for use in MD simulations and has been successfully deployed to simulate shock compression, cf. [52, 53].

Further coarse-graining via dissipative particle dynamics (DPD) as described in the works by Español et al. [18–20] and Hoogerbrugge and Koelman [39] provides a truly mesoscopic simulation technique which links micro-level processes to meso-level processes via the fluctuation-dissipation theorem [34, 80]. The method combines lattice gas automata techniques and their time-stepping algorithms from Frisch et al. [23], which allowed a nonlinear system of particles to evolve microscopically and recover the Navier-Stokes equations, with MD to recover Galilean invariance and flow isotropy. The original method as employed by Hoogerbrugge and Koelman [39] involves N particles in a domain V, evolving the system by initializing positions $\mathbf{r}_i$ and momenta $\mathbf{p}_i$ and updating with discrete timesteps δt for the nth timestep via:

$$\mathbf{p}_i^{n+1} = \mathbf{p}_i^n + \sum_j \Omega_{ij}\mathbf{e}_{ij} \tag{1}$$

$$\mathbf{e}_{ij} = \frac{\mathbf{r}_i - \mathbf{r}_j}{\left|\mathbf{r}_i - \mathbf{r}_j\right|} \tag{2}$$

$$\mathbf{r}_i^{n+1} = \mathbf{r}_i + \frac{\delta t}{m_i}\mathbf{p}_i, \tag{3}$$

where m_i is the mass of particle i, $\mathbf{e}_{ij}$ is the unit vector pointing from particle i to particle j, and Ω_{ij}[1] represents the momentum transferred from particle j to particle i. The function Ω_{ij} must be suitably selected to ensure that a homogeneous equilibrium state is possible and that recovers Galilean invariance. The form selected by Hoogerbrugge and Koelman:

$$\Omega_{ij} = W\left(\left|\mathbf{r}_i - \mathbf{r}_j\right|\right)\left[\Pi_{ij} - \omega(\mathbf{p}_i - \mathbf{p}_j)\cdot\mathbf{e}_{ij}\right], \tag{4}$$

satisfies these conditions. The weight function $W(r)$ is dimensionless and non-negative $W(r) \in \mathscr{W}$, where the set $\mathscr{W}$ is defined by:

$$\mathscr{W} = \left\{ W(r) \;\middle|\; W(r) \in \mathbb{R},\ \frac{N}{V}\int W(r)d\mathbf{r} = 1,\ W(r \geq r_c) = 0 \right\}. \tag{5}$$

The general form of the DPD method is based on Newtonian mechanics [20], where spheres interact in a force field:

$$\mathbf{f}_i = m_i\ddot{\mathbf{r}}_i \tag{6}$$

[1] Ω_{ij} must be symmetric, i.e., $\Omega_{ij} = \Omega_{ji}$ to ensure conservation of momentum. Also, the authors restricted momentum transfer to a ball of radius r_c, $\Omega_{ij} = 0$ if $\left|\mathbf{r}_i - \mathbf{r}_j\right| > r_c$.

$$\mathbf{f}_i = \dot{\mathbf{p}}_i, \tag{7}$$

$$\mathbf{f}_{ij} = \sum_{j \neq i} (\mathbf{F}_{ij}^C + \mathbf{F}_{ij}^D + \mathbf{F}_{ij}^R), \tag{8}$$

where now the forces include a conservation term $\mathbf{F}^C$, a dissipative term $\mathbf{F}^D$, and a stochastic term $\mathbf{F}^R$ and consider the interaction of particle i with particle j. In a similar manner, Español and Warren [20] and Groot and Warren [34] defined the conservative force with a simple repulsion/decaying term:

$$\mathbf{F}_{ij}^C = \begin{cases} a_{ij}(1 - r_{ij})\hat{\mathbf{r}}_{ij} & (r_{ij} < 1) \\ 0 & (r_{ij} \geq 1) \end{cases}, \tag{9}$$

where the authors now define the particle relative displacement vectors, magnitudes, and unit vector directions appropriately:

$$\mathbf{r}_{ij} = \mathbf{r}_i - \mathbf{r}_j \tag{10}$$

$$r_{ij} = |\mathbf{r}_{ij}| \tag{11}$$

$$\hat{\mathbf{r}}_{ij} = \frac{\mathbf{r}_{ij}}{|\mathbf{r}_{ij}|}. \tag{12}$$

Defining the dissipative and random forces in a similar fashion to Hoogerbrugge and Koelman [39] gives force functions which include distance-dependent weight function expressions, $(w^D, w^R) \in \mathscr{W}$ [18, 20, 34]:

$$\mathbf{F}_{ij}^D = -\gamma w^D(r_{ij})(\hat{\mathbf{r}}_{ij} \cdot \dot{\mathbf{v}}_{ij})\hat{\mathbf{r}}_{ij}, \tag{13}$$

$$\mathbf{F}_{ij}^R = \sigma w^R(r_{ij})\theta_{ij}\hat{\mathbf{r}}_{ij}, \tag{14}$$

$$w^D(r) = [w^R(r)]^2, \tag{15}$$

$$\sigma^2 = 2\gamma k_B T. \tag{16}$$

where the term θ_{ij} is similar to the probabilistic function Π_{ij}, i.e., obtained from a Gaussian distribution $\mathcal{N}(\mu, s)$, and $\theta_{ij} \in \mathcal{T}$, where

$$\mathcal{T} = \left\{ \theta_{ij} \;\middle|\; \theta_{ij}(t) \sim \mathcal{N}(\mu, s),\ \langle \theta_{ij}(t) \rangle = 0,\ \langle \theta_{ij}(t)\theta_{kl}(t') \rangle = (\delta_{ik}\delta_{jl} + \delta_{il}\delta_{jk})\delta(t - t') \right\}. \tag{17}$$

The DPD method can be solved with Verlet or leapfrog updating schemes similar to MD methods but provides much faster relaxation to equilibrium states and incorporates both frictional and stochastic forces in addition to conservative forces [9]. The dissipative particle dynamics with energy conservation (DPD-E) extension provides for thermal gradient and heat transfer modeling [48, 65], as well as

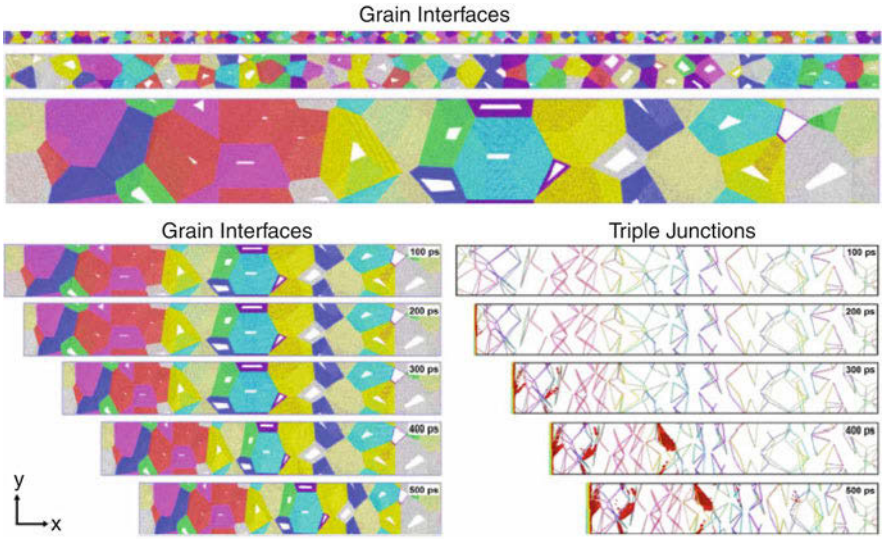

Fig. 3 Polycrystalline RDX samples simulated via coarse-graining techniques. (Adapted from Mattox et al. [51])

non-equilibrium and transient conditions. Further details on the implementation can be found in Mackie et al. [48] and Español et al. [19]. These methods have enabled the modeling of natural convection [1, 2] and energetic and reactive materials systems with success. Coarse-grained models of RDX have been generated to study the shock compression response and incorporate chemical reactivity in the DPD framework (the so-called DPD-RX extension) [14, 67]. Sood et al. [69] demonstrated an implementation of DPD-E for the modeling of shock compression of two RDX impactors using a Lennard-Jones potential and were able to capture the salient features of the shock, but were unable to capture the inelastic response upon release. Recent work by Mattox et al. [51] demonstrated the coarse-graining of MD methods via DPD-E techniques to model polycrystalline RDX samples under shock compression. Figure 3 shows the shock compression response of polycrystalline RDX employing coarse-grained DPD-E.

1.2.2 Meso-scale and Microstructure-Based Simulation at the Continuum Scale

Microstructure-based simulation presents an opportunity to link meso-scale response to bulk shock response in heterogeneous materials. By correctly capturing the deformation and relevant physics at the meso-scale and validating with suitable statistics and experiments, the problem of the dynamic behavior of heterogeneous materials can become tractable by linking relevant microstructural features to the response. This can help designers suitably select and tailor microstructures,

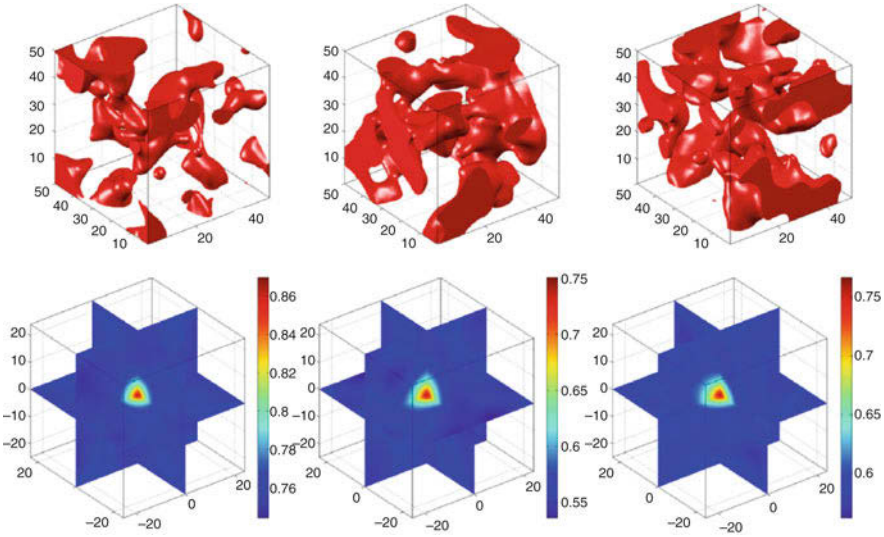

Fig. 4 Comparison of real (left) and synthetic (right) microstructures for Ti+B powder mixtures. The synthetic microstructures were generated using particle packing algorithms and particle libraries obtained from montage serial sectioning [35, 36]. There is good visual correspondence between the microstructures, and two-point correlation functions and lineal-path probability functions confirm this to a high degree [35]

providing optimization strategies for a desired performance outcome. However, the challenge remains to suitably describe the constitutive behavior of individual phases at meso-level length scales, correctly capture and model the nuanced behavior of the heterogeneity at relevant length scales, and describe interfacial phenomena and its effects on wave propagation and mechanochemistry. This is an active area of research, and contributions are still being made to develop suitable experiments and models and implement correct physics into hydrocodes for the simulation of strong dynamic events. Modeling strategies to correctly capture realistic and suitable microstructural statistics and behaviors are at the forefront of the problem.

Microstructural descriptions can be made by not only obtaining a snapshot of the microstructural configuration in time but also describing the distribution of microstructural features by probability functions. For example, a two-phase microstructure may be represented as a sampling of a stochastic process represented by the probability space $(\Omega, \mathcal{F}, \mathcal{P})$, where Ω represents a sample space of all possible microstructures, $\mathcal{F}$ represents all possible events or instantiations of sampling the space Ω, and $\mathcal{P}$ is the probability measure on $\mathcal{F}$ [45, 61, 78, 79]. Niezgoda et al. [61] define the methodology to stochastically represent microstructures and describe their spatial statistics with n-point correlation functions. The two-point correlation function of the microstructure measures the probability that a randomly placed vector will have its ends lie in specific phases of the microstructure (Fig. 4).

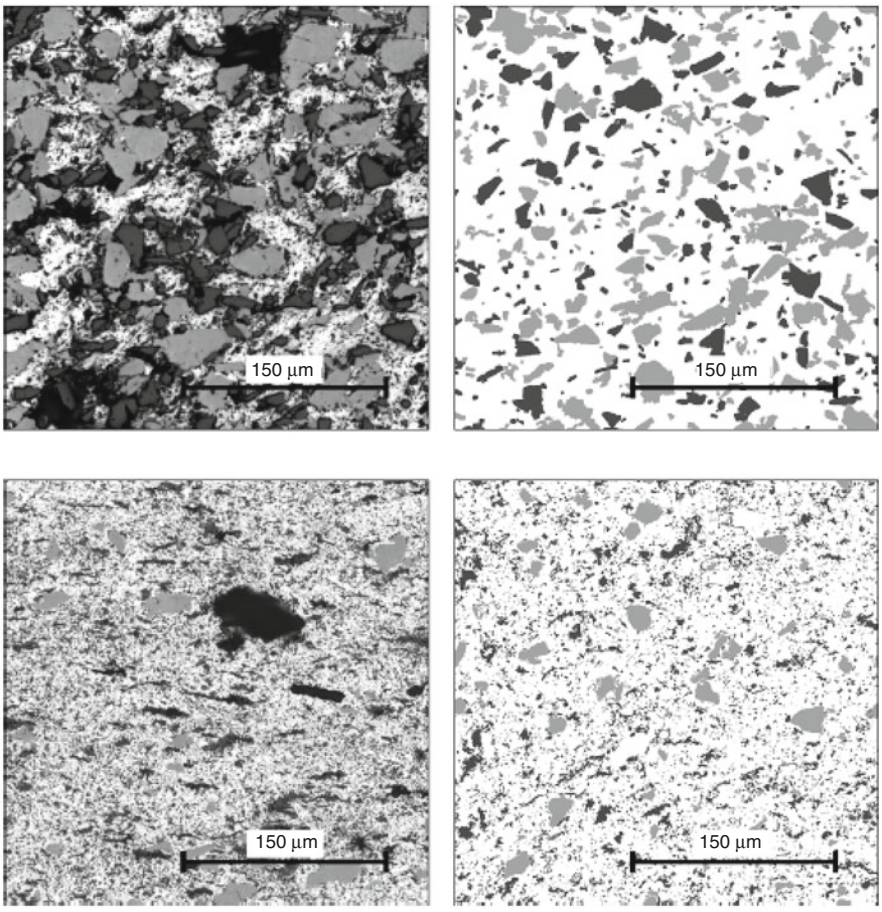

Fig. 5 Comparison of real (left) and synthetic (right) microstructures for Ti+B powder mixtures. The synthetic microstructures were generated using particle packing algorithms and particle libraries obtained from montage serial sectioning [35, 36]. There is good visual correspondence between the microstructures, and two-point correlation functions and lineal-path probability functions confirm this to a high degree [35]

Particle packing algorithms and simulation methodologies using vendor-based particle libraries [27, 36] have also been used to successfully build synthetic microstructures for direct numerical simulation. Figure 5 shows real and synthetic microstructures that can be built via particle packing and montage serial sectioning. These microstructural representations were validated by comparing the two-point correlation functions for the real and synthetic structures to ensure the microstructural features being simulated matched reality. Improved and automated ways of building synthetic microstructures present a new opportunity to explore possible effects that a microstructural configuration can have on the bulk dynamic response of a system.

Lastly, the authors would be remiss if crystal plasticity and viscoplastic self-consistent (VPSC) methods were omitted from this brief listing of ICMSE techniques to probe meso-scale heterogeneity. Specifically, Lebensohn and Tomé developed the VPSC method [46] as an extension of the Eshelby formulation for inclusions and inhomogeneities in a self-consistent continuum field. These codes have been successful at modeling texture evolution under rolling conditions [47]. However, these techniques are currently limited to quasi-static boundary conditions, although strides are being made to extend these techniques to model dynamic behavior. The many works by Lebensohn should be referenced for further discussion on these methods.

1.3 Outline of Chapter

The remainder of this chapter is devoted to outlining the challenges involved in the investigation of dynamic behavior of heterogeneous materials, namely, understanding the shock compression response of these materials and the inherent difficulties in experimentally assessing the equation of state of the aggregate material and defining the local and global properties. A case study will be provided from the author's work investigating the intermetallic-forming Ti+B reactive powder mixture under shock compression and high strain rate loading conditions. The importance of using ICMSE methodologies to understand bulk dynamic behavior of reactive powder mixtures will be presented. These methodologies provide insight into the physical phenomena that can only be indirectly inferred from experimental measurements.

This chapter is divided into three subsequent sections. Section 2 provides a brief background of shock compression science, focusing on the dynamic behavior of powder mixtures, granular media, and energetic/reactive materials. Section 3 provides an introduction to reactive materials, which take the form of heterogeneous powder mixtures. The case study on Ti+B reactive mixtures is presented and demonstrates how ICMSE has been employed to investigate the shock compression and dynamic behavior of this system. Section 4 provides a summary and concluding remarks on how the ICMSE framework can provide useful information on the response of heterogeneous materials to dynamic loading.

2 Background on Shock Compression Science

Dynamic behavior in heterogeneous materials has been studied in earnest since the founding of shock compression as a science at the end of World War II. Materials of interest included precipitation-hardened alloys, particulate mixtures, plastic-bonded explosives (PBX), geological materials such as rock, and sand. Powder and particulate mixtures in particular are of interest due to the spatial arrangements of the microconstituents and the behavior this imparts. Reactive and

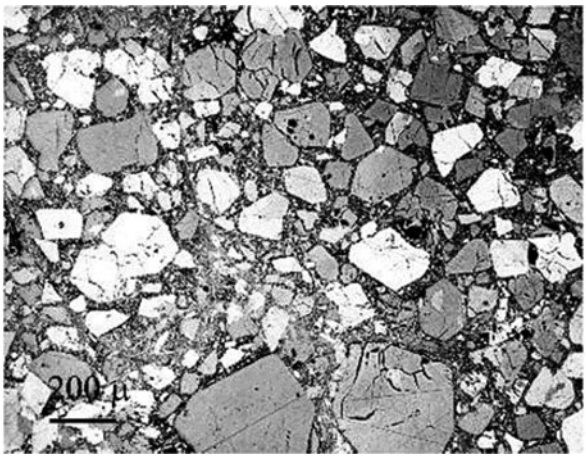

Fig. 6 Microstructure of pressed PBX9501, demonstrating a complex size, shape, and crystallographic distribution of the energetic particles in the estane binder, similar to a granular concrete mixture. (Adapted from [68])

energetic materials became particularly interesting due to defense applications, and these materials were naturally heterogeneous. Consider the case of PBXs, which involve the distribution of molecular explosive crystals in a plastic binder. One need only recall the classic picture by Skidmore et al. [68] of hot-pressed PBX 9501 (95% HMX, 2.5% estane 5703, 2.5% BDNPA/F) to note the level of complexity and heterogeneity in the microstructure. Clearly there are a multitude of size, morphology, and nearest-neighbor distributions of the HMX crystals, and the pressing/compaction process leads to cracking of the particles due to the limited accommodation of plastic deformation in the crystals and binder. This classic picture demonstrates the complexity and degree of heterogeneity of a PBX mixture. Reactive materials, granular solids, composite materials, and even some polycrystalline materials exhibit similar features (Fig. 6).

2.1 Shock Compression Science and Theory

This section will develop the conservation relations and implement them for the special case of a shock wave. Shock waves are defined as a near-discontinuous change in thermodynamic state variables brought on by a mechanical insult, and they are a special case of the axiomatic conservation relations for a moving discontinuity. Consider a one-dimensional body Ω that has been stressed such that the rapid application of the load caused a moving discontinuity to form in the body. Any applied stress will travel throughout the body in the form of a characteristic due to the form of the conservation of momentum. If the stress applied to the body is rapid and high enough, a shock wave may form where the material behind the traveling wave will be at a higher stress, velocity, density, etc. relative to the material ahead of the way. This variation is nearly discontinuous, as is shown in Fig. 7.

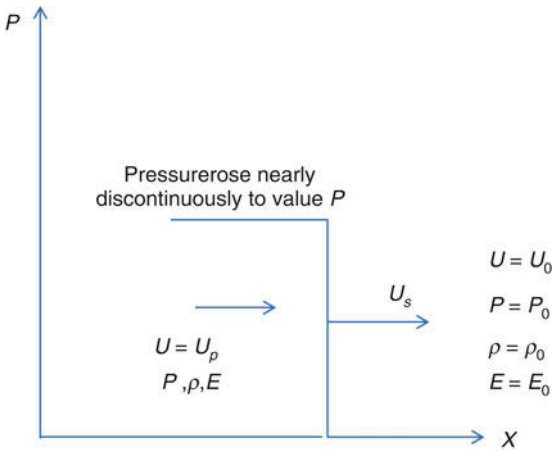

Fig. 7 Consider the stress amplitude plotted over the distance through a continuous medium. After a sufficiently large and rapid application of load on a material, a shock wave will develop which is a traveling discontinuity in thermodynamic state variables. The state variables behind the shock wave depend on the conservation relations and an equation of state. (Adapted from [25])

2.2 *Conservation Relations for a Shock Wave*

The conservation of mass, momentum, and energy can be derived by considering infinitesimal elements and matter/momentum/energy exchange therein, to formulate the strong form of the equations. For the conservation of mass, influx and efflux of matter in an infinitesimal volume lead to:

$$\int_{\Omega} \left[\rho(\mathbf{x}, t) + \nabla \cdot (\rho \mathbf{v})\right] d\Omega = 0 \qquad \forall d\Omega. \tag{18}$$

This expression is valid for all possible integration volumes and can thus only be true if the integrand is exactly zero, i.e.,

$$\frac{\partial \rho}{\partial t} + \nabla \cdot (\rho \mathbf{v}) = 0, \tag{19}$$

or in indicial notation:

$$\frac{\partial \rho}{\partial t} + \frac{\partial (\rho v_i)}{\partial x_i} = 0, \tag{20}$$

where the density of the material ρ is a continuous function of space and time – $\rho = \rho(x, y, z, t)$ – and v is the spatial velocity of the medium.[2]

In the case of a discontinuous change in state variables, the continuity equation (19) must take into account a moving discontinuity at velocity U_s relative to the disturbed material moving at a different material velocity U_p which propagates

[2]More details on the difference between material and spatial coordinates can be found in Malvern's excellent text [50] on continuum mechanics.

into a medium moving at a velocity U_0. Considering the shock wave front as the moving reference frame, the mass of material exiting the wave (to the left of the shock front in Fig. 7) will have a new density ρ and will be moving at a velocity $U_s - U_p$ relative to the shock front. Considering the mass conservation through the shock wave as the moving reference frame, the general expression becomes (after canceling the cross-sectional area and δt terms which are the same across the shock front) [22, 54]:

$$\rho_0(U_s - U_0) = \rho(U_s - U_p). \tag{21}$$

This equation is completely general and valid for any infinitely sharp discontinuity in thermodynamic state. It is used as an approximation to the highly dispersed compressed states observed in this work in the context of distended powder mixtures.

The conservation of momentum relates the momentum change of a body to an applied impulse. This equation can be cast in differential form relating incremental stresses applied to a body and a variety of forces. Derivations of this equation may be found in Gonzales [25], and it is expressed below for brevity:

$$\rho(U_s - U_p)U_p - \rho_0(U_s - U_0)U_0 = (P - P_0). \tag{22}$$

This equation is commonly combined with the conservation of mass to obtain the typical form of the conservation of momentum by noting that $\rho_0 U_s = \rho(U_s - U_p)$:

$$\rho_0 U_s U_p - \rho_0(U_s - U_0)U_0 = (P - P_0). \tag{23}$$

If the initial momentum is zero (stationary body impacted by a shock wave), the equation becomes:

$$P - P_0 = \rho_0 U_s U_p. \tag{24}$$

This is the form of the conservation of momentum that will be used to analyze the compressed state of the powder in this work.

The conservation of energy considers the work done by all external forces balancing the internal energy and the kinetic and potential energies:

$$\Delta E = \Delta KE + \Delta PE + \sum \Delta W, \tag{25}$$

where ΔE represents the change in internal energy of the system, KE and PE are the kinetic and potential energies of the system, and $\sum \Delta W$ is the sum of all sources of work done on to/by the system. This is similar to the classic definition of the First Law of Thermodynamics:

$$dE = \delta Q - \delta W, \tag{26}$$

where the differential δ denotes path dependence, i.e., the total differential of internal energy E, path independent by definition of a total differential (Pfaffian form), can be composed of path-dependent changes in heat Q and work W. The work done by the passage of the shock wave is composed of the force term (PA) and displacement ($U\delta t$). Using intensive quantities, each term becomes [22, 54]:

$$\Delta KE = KE_2 - KE_1 = \frac{1}{2}[\rho A(U_s - U_p)\delta t]U_p^2 - \frac{1}{2}[\rho_0 A(U_s - U_0)\delta t]U_0^2, \tag{27}$$

$$PU_p = \frac{1}{2}\rho(U_s - U_p)U_p^2 + E\rho(U_s - U_p) - E_0\rho_0 U_s. \tag{28}$$

The common form of the conservation of energy in a shock wave is obtained by modifying this general form noting that the conservation of mass must also apply:

$$PU_p = \frac{1}{2}\rho_0 U_s U_p^2 + \rho_0 U_s(E - E_0). \tag{29}$$

Rearranging the equation by dividing through by $\rho_0 U_s$ to isolate the energy term gives:

$$E - E_0 = \frac{PU_p}{\rho_0 U_s} - \frac{1}{2}\rho_0 \frac{U_s U_p^2}{\rho_0 U_s}. \tag{30}$$

Invoking the conservation of momentum, Eq. (24) for the U_p term gives, after rearranging (cf. Gonzales [25] for the full derivation):

$$E - E_0 = \frac{P(P - P_0)}{(P - P_0)} \cdot (V_0 - V) - \frac{1}{2}\frac{(P - P_0)^2}{P - P_0} \cdot (V_0 - V) \tag{31}$$

$$\therefore \quad E - E_0 = \frac{1}{2}(P + P_0)(V_0 - V), \tag{32}$$

which is the commonly used form of the conservation of energy. Equation (32) is integral to this work, as it is the partition of energy between the compaction of the loose powder and the shock compression that leads to the complex behavior of powder mixtures (i.e., the long rise times and dispersed wave fronts) under shock compression. The conservation equations are completely general, and there are five variables [54]: pressure P, material (particle) velocity U_p, shock velocity U_s, specific volume V, and energy E. Thus, a fourth equation is necessary for closure. This equation is in the form of a thermodynamic equation of state (EOS) which relates state variables, usually $U_s - U_p$ or some other equation.

The equations presented in this section are completely general and satisfied if a strictly one-dimensional uniaxial strain loading configuration is maintained during shock compression. This will allow the bulk compressibility of the material to stiffen the shock response and increase the pressure to yield the discontinuous

shock front embodied by the Rankine-Hugoniot jump conditions (Eqs. 21, 24, and 32). Three-dimensional forms of the equations can be found in Meyers [54] and Forbes [22]. The tensorial forms of the equations are required for simulation of the shock compression process in hydrocodes and are essential when considering local material heterogeneity, as the uniaxial strain condition will not be rigorously satisfied at the meso-scale.

2.2.1 Theoretical Equations of State for Reactive Powders

Mixture theories can predict the possible inert and reacted equation of state (EOS) or Hugoniot for a material. "Mixing" the $0K$ isotherms via mass fractions and using the Mie-Grüneisen EOS leads to:

$$\left(\frac{\partial P}{\partial V}\right)_H + \frac{P_H}{2V_0/\Gamma_0 + V - V_0} = \frac{(2V_0/\Gamma_0)(\partial P/\partial V)_{0K} + 2P_{0K}}{2V_0/\Gamma_0 + V - V_0}. \tag{33}$$

For a distended powder, the Hugoniot can be expressed as [25, 42]:

$$P = \frac{[2V - \Gamma(V_0 - V)]C^2(V_0 - V)}{[2V - \Gamma(V_{00} - V)][V_0 - S(V_0 - V)]^2}. \tag{34}$$

However, this EOS mixture form is multivalued in volume [42, 64, 84], which prompted Wu and Jing [84] to consider an isobaric process with enthalpy as the relevant energy term, which gives the Hugoniot volume for both a solid and porous mixture as:

$$\begin{aligned} V'_H =& \frac{1 - (R/2)}{1 - (R/2)[1 - (P_e/P)]} V_H \\ &+ \frac{(R/2)}{1 - (R/2)[1 - (P_e/P)]} \left((V_e - V_0) + \frac{P_e}{P} V_{00} + \frac{1 - R}{(R/2)} (V'_C - V_C) \right). \end{aligned} \tag{35}$$

Using the Wu Jing EOS or McQueen mixture theory EOS as possible solutions to the Hugoniot, a reaction-product Hugoniot may be determined from the Ballotechnic assumption [10, 42, 54], which is reproduced below:

$$V = \frac{V_S^* \left[(V/\Gamma)^*(K_S/V_S)^* - P_S^*\right] + P_S^* V_{00}/2 + \int_{V_0^*}^{V_S^*} P_S^* dV_S^* - (E_0^* - E_0)}{(V/\Gamma)^*(K_S/V_S)^* - P_S^*/2}. \tag{36}$$

Further details may be obtained from the respective citations.

2.3 Reactive Powder Mixtures and Explosives

Microstructurally sensitive and physics-based constitutive models [5–8, 12, 15, 76] provide greater resolution of the physical phenomena by incorporating fine-scale detail through direct numerical simulation on the microstructure or by suitable homogenization procedures to account for the microstructural effect on the material behavior. They depend on meso-scale information, equations of state, and material characteristics and properties that can be obtained from structural characterization. Many of the original simulations have involved idealized microstructures using simple shapes and packing routines, which do not wholly capture the nuances of real microstructures. Recent work by Gonzales et al. [25, 27–29, 37] has attempted to use real microstructures and synthetic representations which were validated via two-point correlation functions [27, 29, 37] to help generate valid synthetic microstructures. Prior work investigating energetic and reactive materials has involved flyer-plate gas gun experiments and explosively driven flyers.

Elemental powder precursors can undergo chemical reactions under shock compression through mechanisms that are fundamentally different from first-order physical and chemical changes [16]. The turbulent state within the shock wave, facilitated by the local heterogeneity within the powder, leads to extreme deformation of particles and enhanced material mixing, which can cleanse oxidized surfaces and lead to conditions favorable to chemical reactions [74, 75]. The natural porosity in powder compacts (of green strength or higher) provides sites for mixing and thermal buildup due to pore collapse during the densification process. Horie et al. [40, 41] were the first to study intermetallic-forming powder mixtures of Ni/Al and Ti/Al under shock compression. They observed an ordered phase of Ni_3Al in the high-temperature zones of the post-impact recovered material and various other stoichiometries interdispersed within the low-temperature zones [40], as shown in Fig. 8. The high-temperature regions were found near the periphery of the samples due to wave interactions at the edges of these regions. They also observed a region of a nearly homogeneous distribution of the Ni_3Al product dispersed alongside inhomogeneous, irregularly shaped Ni, which was partly attributed to localized inhomogeneous distributions of starting particles. Finally, regions of NiAl and $NiAl_3$ grains were also observed. The $NiAl_3$ phase was postulated to have formed by precipitation from the liquid state, as the structure had the classic eutectic form [40].

Horie's original works stimulated further research into intermetallic-forming systems. Thadhani et al. [72–74, 77] explored a number of materials systems under shock compression to investigate their reactivities and equations of state. Novel manufacturing strategies to develop ordered topologies have also been explored by Weihs and his group with Ni+Al laminates [70, 81, 82] to promote more intimate mixing and control the seemingly random nature of conventional powder mixtures. Meso-scale simulations provide a way to probe the structure property relations between these topologies and the bulk shock response of intermetallic-forming powder mixtures. The next section details a case study from the authors' own work on Ti+B mixtures.

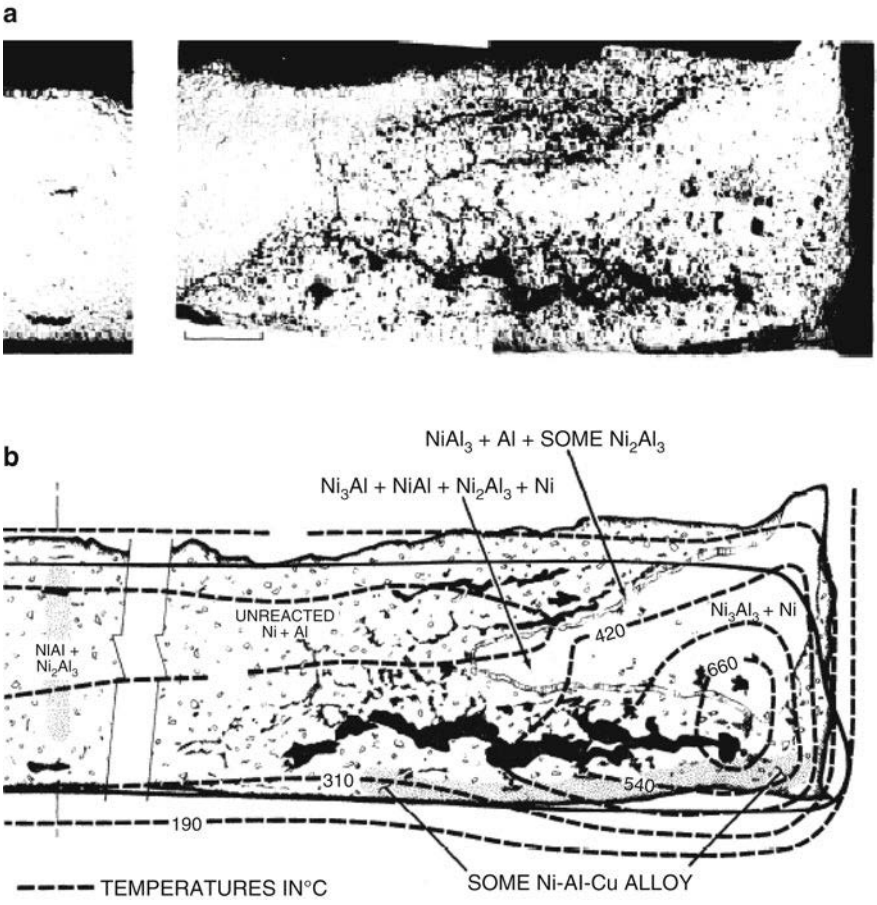

Fig. 8 (**a**) Recovered shock-compressed Ni/Al powder compact specimen (**b**) Calculated temperature isotherms superimposed on a schematic image of the recovered specimen. The crack was caused by spallation. (Adapted from Horie et al. [40])

3 Case Study: Dynamic Behavior of Reactive Powder Mixtures

Section 2.3 provides an abridged survey of the dynamic behavior of reactive powder mixtures and energetic materials. Conventional energetics take the form of plastic-bonded explosives (PBXs) as well as packed propellants. Reactive materials are typically composed of intermetallic-forming powder mixtures that are highly exothermic and can be combined with a typical metallic fuel such as aluminum powder.

This section presents a case study from the authors' work on the dynamic response of Ti+B+Al reactive powder mixtures. These mixtures form complex

microstructures when isostatically compacted and are both heterogeneous and topologically complex. Different load configurations, namely, uniaxial stress and uniaxial strain loading configurations, were studied to discern their effects on the reaction response and the local mechanical response leading to a reaction event. The compacts showed an optimum stoichiometric configuration in the uniaxial stress case whereby reaction thresholds were minimized. However, the uniaxial strain loading condition complicated the reaction response due to the limiting effects from the high crush strength of the boron constituents.

3.1 Impact-Induced Chemical Reactions

Impact- and strain-induced chemical reactions in Ti+B reactive powder mixtures will be discussed in this subsection. Uniaxial stress configurations were chosen to discern the effects of loading configuration on the local stress/strain states produced in the reactive compacts, and high-speed photography using an IMACON framing camera provided in situ imaging of the impact process. The procedure for discerning reactivity from light emission is detailed, and the implications of exogenous sources of light emission are discussed. The experiments show an optimal stoichiometry for enhanced reactivity under these impact loading conditions. Meso-scale simulations are employed to investigate the possible reason behind this optimal stoichiometry. The simulations reveal that boron agglomeration likely inhibits reactivity of pure Ti+2B but that adding aluminum (to a degree) lessens this effect by promoting a uniform distribution of the boron particles. The aluminum likely participates in the reaction as well, but the reaction pathway cannot be deciphered.

Uniaxial stress loading experiments were conducted using the setup described by Gonzales [25]. Reactive pellets were pressed and mounted onto a copper rod and shot at different velocities from a 7.62 mm helium-driven gas gun, and the reaction event was captured by the framing and video cameras. Figure 9 shows a time series of snapshots from a pellet-mounted rod-on-anvil Taylor test in the uniaxial stress configuration. The emitted light is taken as evidence of a chemical reaction event.

Plotting the observed reaction events based on a go/no-go criterion as a function of total kinetic energy of impact shows an interesting trend. Compacts were manufactured by controlling the volume fraction of Al but maintaining a stoichiometric ratio of Ti+B in a 1:2 molar ratio. Figure 10 demonstrates that for a similar %TMD (theoretical maximum density) of 75% for the given mixture stoichiometries,[3] there exists an optimal stoichiometry that reduces the threshold input energy required for impact-induced reactivity.

The enhanced reactivity may be due to a potential liquid-phase mechanism resulting from the plastic heating of the softer Al phase enhancing the kinetics of any

[3]This final density was selected because it was the maximum density achievable the cold isostatic pressing setup used in our lab for the pure Ti+B mixtures.

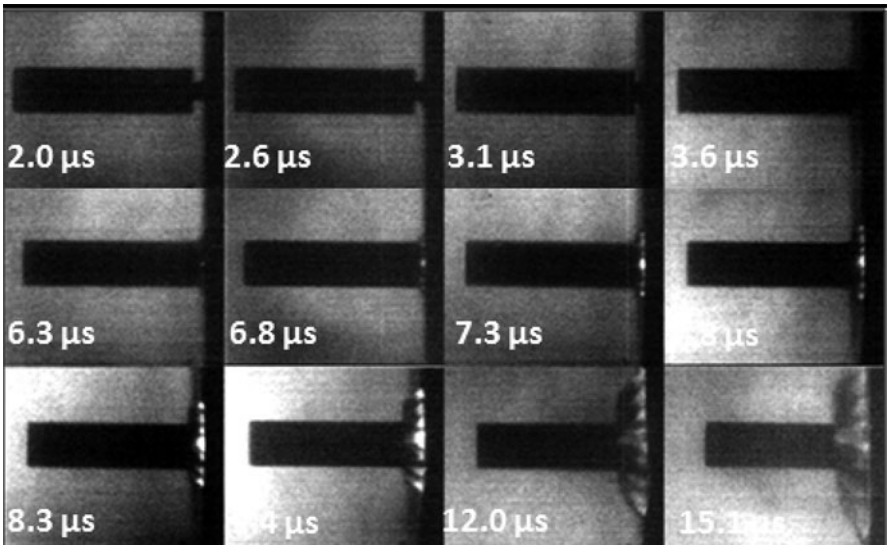

Fig. 9 Impact-induced chemical reaction from a pellet-mounted rod-on-anvil Taylor test. A heterogeneous reactive compacted powder mixture is mounted on the rod to simulate the one-dimensional bulk uniaxial stress configuration. However, the local state of stress at the meso-scale can be triaxial depending on the local microstructure

Ti/B reaction [26] for the 50% Al stoichiometry. This was investigated via ICMSE techniques, whereby actual microstructures were imaged and simulated in the multi-material Eulerian Hydrocode CTH (Version 9.0, Sandia National Laboratory). The reactive pellet was simulated using a particle packing algorithm and real particles for Ti obtained from a particle library built through montage serial sectioning. Further details of the method can be found in [25, 26, 29, 35–37].

Figure 11 shows two impacts from a Ti+B+Al simulated powder mixture. Microstructure-based simulations provide an in-depth look at the interaction between phases which can cause an observed bulk response. The enhanced reactivity of the 50% Al mixture is an astonishing discovery as it hints at potential optimal microstructural configurations that can enhance the reactivity of this mixture. This also indicates that topology (i.e., the microstructural spatial arrangement of microconstituents) may play a role in driving both local and global chemical reactivity. Ti+2B alone is suspected to be highly reactive, but did not exceed the reactive potential that the 50% Al mixture demonstrated. This points to a potential synergy beyond what is possible with Ti+2B alone at the densities considered, from bulk thermodynamic considerations alone. Thus, microstructure-based simulations can provide useful phenomenological explanations of observed bulk phenomena.

Comparing both the Ti+2B and Ti+2B+50%Al stoichiometries at the same snapshots reveals another startling observation – the boron particle boundaries coalesce and lead to the formation of the dark black regions, and zooming into these features reveals a highly comminuted region. This can be further appreciated

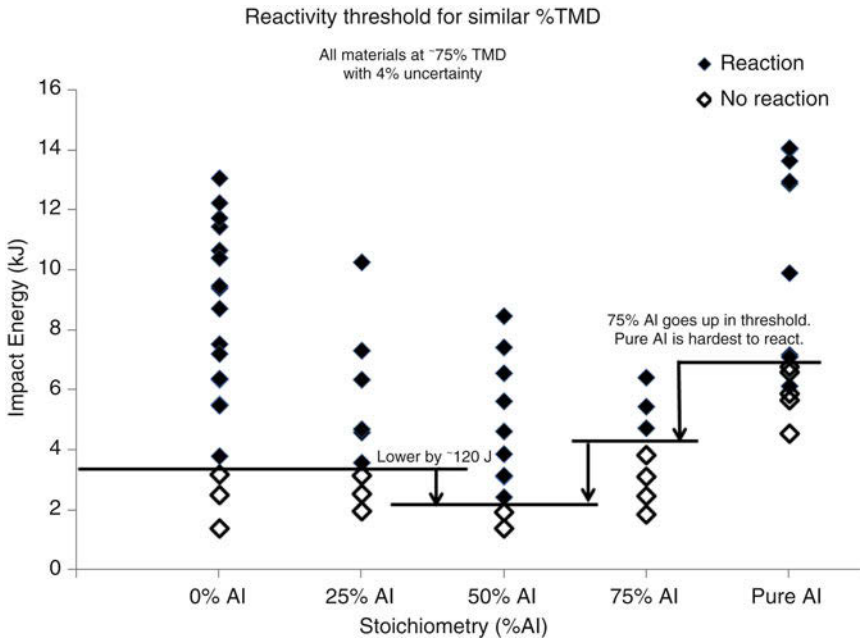

Fig. 10 Impact-induced reactivity threshold plot, demonstrating the threshold energy (for go/no-go chemical reactions) for Ti+B+Al mixtures. The %TMD of the mixtures was kept constant, and the Al content was systematically varied maintaining a 1:2 molar ratio of Ti:B. The plot demonstrates an optimal stoichiometry for reduced threshold for reactivity

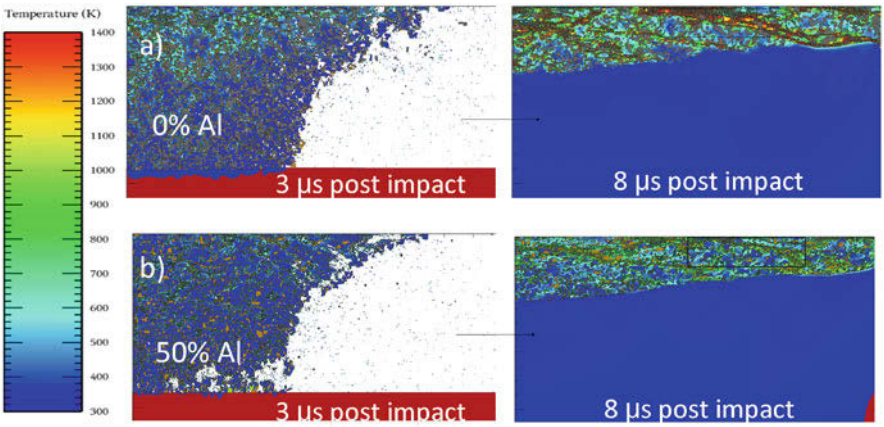

Fig. 11 Half-view of the rod-on-anvil impact simulations at 200 m/s impact velocity. The temperature distribution shows that the majority of the heat localizes in bands coincident with the agglomerated boron. This is in stark contrast with the fully dense structure simulations where the majority of the heating was at the interface between the copper and powder

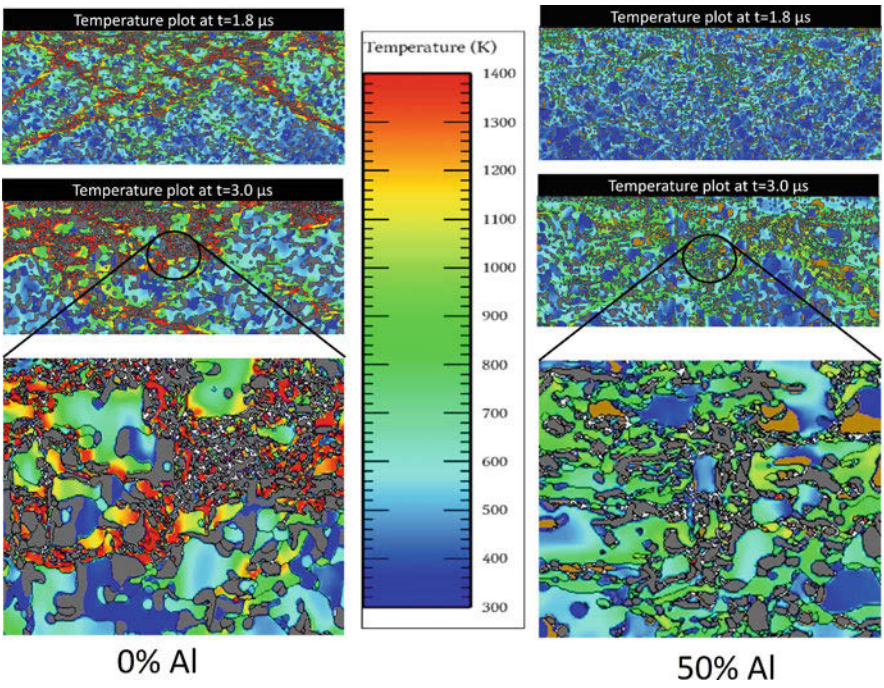

Fig. 12 Zoomed-in view comparing the 0% Al and 50% Al microstructures at two different times for an impact velocity of 200 m/s. There are much more agglomerates in the 0% Al structure, and their shape is more equiaxed since they pulverize and rotate in empty pores during crush-up. Temperatures are also much greater for the 0% Al structure but shows lower bulk heating of the Ti particles, which may account for the discrepancy in the threshold condition observed in Fig. 10

in Fig. 12 which shows a zoomed-in view of a shear band region. This was noted to be due to the natural particle rearrangement due to size and property contrasts between the Ti and B particles and also because of local elevated tensile stresses creating smaller fractured powders which comingle under the influence of complex material jetting and flow instabilities inherent in these processes.

The observations from the uniaxial stress loading configuration show that critical levels of strain and mixing are essential ingredients to drive chemical reactivity in these powder mixtures. The transformation of impact (i.e., kinetic) energy to local states of deformation, mixing, and ultimately high local temperatures satisfies the ingredients of the phenomenological Graham's CONMAH model [31, 32]. **CON**figurational changes in the microstructure are generated via deformation of a mixed microstructure, and optimizing the starting structure to enhance these configurational changes along with the **M**ixing of the constituents, enhanced **A**ctivation of the ingredients, and ultimately the local and global **H**eating shows the potential area that emergent ICMSE methods can address. The CONMAH model is a useful construct to consider the role of dissipative processes such as void collapse, crack nucleation and propagation, and interparticle friction and sliding during the

shock compression process. These processes are discussed in detail in Meyers [54] and Horie and Sawaoka [42] and remain of critical importance in understanding the response of explosives and reactive materials.

3.2 Shock-Induced Chemical Reactions

The uniaxial strain configuration sets up a much different loading state than the uniaxial stress configuration. Due to the lateral confinement of the powders, a shock wave develops in the material which ramps up the pressure within the particles and compacts the powder, setting up local deformation fields limited by the bulk compressibility of both the individual constituents and the bulk surrounding powder. Of note is the ability of a flyer-plate gas gun experiment to measure the thermodynamic shock-compressed state of the powder. If the measured shock response deviates from the predicted thermodynamic state of an inert compacted powder, it can be inferred that some event occurred which caused the deviation, namely, a shock-induced chemical reaction. The Ballotechnic model [11, 17, 27, 30, 33] can be used to infer the shock-induced chemistry event. The crush-up to full density of a distended powder mixture can greatly influence the chemical reactivity of the mixture due to local hot spot generation and particle friction, which needs to be accounted for in the reaction product equation of state.

Shock compression experiments on Ti+2B compacts at 50% TMD were performed to assess the equation of state and shock compression response of the mixture to assess the baseline performance of the mixture. The Hugoniot was measured from the equations of state and Rankine-Hugoniot jump conditions. Figure 13 casts the shock compression response of the Ti+2B powder mixture in P-V space, along with predicted equations of state. The Ballotechnic curve (Eq. 36) is also included, and it can be observed that a number of experiments fall within the Ballotechnic, which indicates a potential shock-induced chemical reaction.

Meso-scale simulations were performed to identify the possible precursor mechanisms for the observed chemical reaction. Synthetic microstructures were generated using the same methods as the uniaxial stress simulations, and shock compression simulations were performed as 1:4 scale models of the actual experiment. Individual stress traces at the backer "simulated gage" are plotted in Fig. 14 which show a distinct distribution in possible rise times and peak pressures, owing to the adjacency of B or Ti particles relative to where the measurement was taken. This manifests as a dispersed two-wave structure, reminiscent of the wave-splitting that occurs within elastic-plastic shock wave propagation.

This distinct heterogeneity influences how both the EOS and wave profiles are interpreted. It is also unique to heterogeneous materials and demonstrates how the probe smears the actual local response of the shock-breakout event. Gonzales [29] provides an assessment of measurement uncertainty in light of this heterogeneity. Of note is the observation that the bulk temperatures remain comparatively low, as shown in Fig. 15 [25]. However, the intimate mixing of the reactants and large

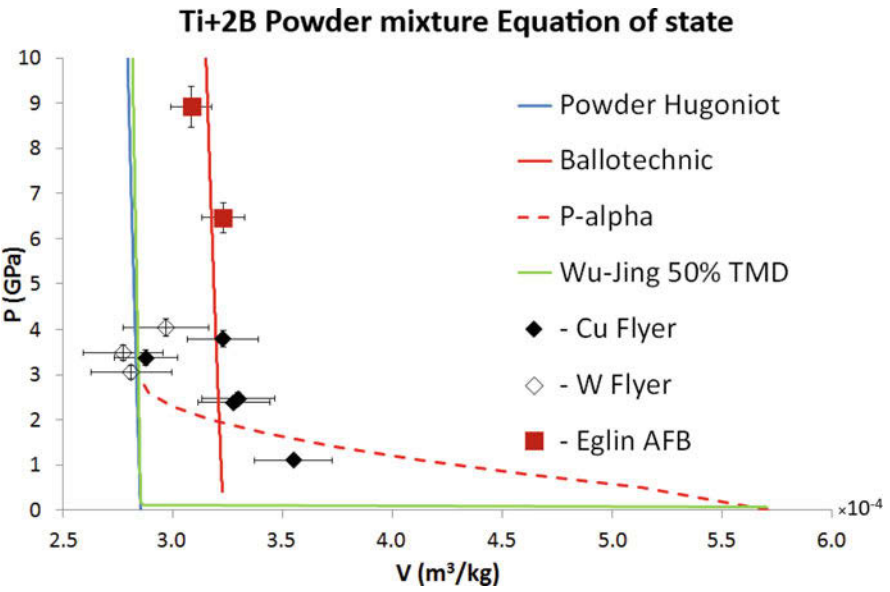

Fig. 13 The P-V Hugoniot for Ti/Al/B with the P-α prediction and Ballotechnic. The Wu-Jing EOS approaches the Mie-Grüneisen porous Hugoniot. Many data points lie along the Ballotechnic, hinting at a potential shock-induced chemical reaction

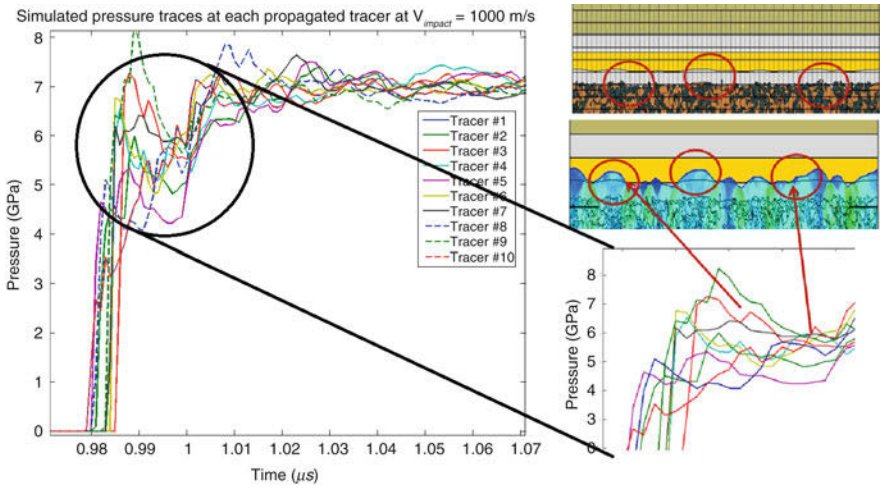

Fig. 14 The simulated stresses measured at each individual tracer point show a wide variability in both arrival-time signature and stress level. Averaging the stresses naturally leads to the observed characteristic "hump," which was reproduced by simulations. This is captured due to the inhomogeneous loading of the PVDF gage

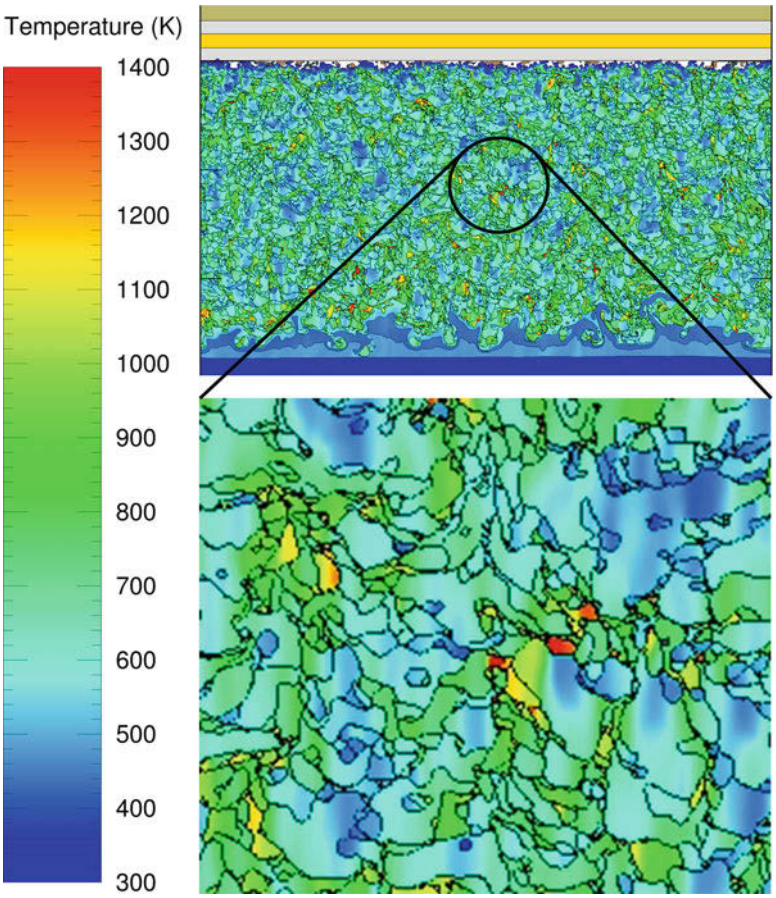

Fig. 15 Temperature distribution in a 50% TMD microstructure of Ti+2B shock compressed with a Cu flyer impact at 1000 m/s. A random distribution of highly strained regions and high-temperature hotspots are observed, along with highly deformed particles. Confined boron particles heat up more due to greater plastic deformation and friction

amounts of deformation seem to contribute to the enhanced reactivity observed in Fig. 13. The simulations were validated by comparing averaged wave profiles with PVDF stress gage measurements, and the salient features were correctly captured as shown in Fig. 14. Further work with reactive flow models is needed to substantiate the elevated pressures obtained from the experiments with the numerical simulations.

The challenge in discerning meso-scale response from macro-scale measurements remains ever-present, as macro-level measurements are poor surrogates for the local response. Indeed, the anomalous wave profiles obtained during the shock compression of Ti+2B reactive powder mixtures reveal a two-stage process, whereby the equation of state can be affected by the time of arrival (TOA)

of the breakout shock wave. Interferometry or stress gage-based measurement techniques average the response over the probe area as well as the temporal resolution of the sensor. Recent work by Kang et al. [44] attempts to address these limitations by introducing CdTe quantum dots directly into the microstructure of the heterogeneous material.

In situ sensing is a challenge because local interaction between the sensor material and the local microstructure can change the character of the shock wave and bias the true nature of the interaction. However, these sensors are small enough that this interference is minimized. Furthermore, these sensors provide a pressure-induced blueshift which can be normalized. Laser-driven flyer impact experiments on CdTe quantum dots embedded in glass show a well-defined blueshift in the photoluminescent emission spectra [44]. These blueshifts correspond strongly with the peak shock pressure and are indicators of the peak stress, up to a maximum at around 6 GPa. Optical microcavity structures [66] also show promise as in-situ pressure sensors taking advantage of the pressure-sensitive spectral shift in Al_2O_3 optical microcavity lamellar composites. This is a truly exciting work which merits further consideration, as in situ pressure and TOA data would be invaluable to validating and informing meso-scale shock compression simulations of heterogeneous materials.

4 Summary and Conclusions: Where Can ICMSE Continue to Provide Value in Understanding Dynamic Behavior of Heterogeneous Materials?

This chapter discussed some of the challenges in understanding the dynamic behavior of heterogeneous materials. The difficulties stem from the multiple length and time scales involved in the processes and how the microstructural effects interplay with the bulk response. Experimental challenges exist in probing the ultrafast response of heterogeneous and particulate materials under shock compression, and isolating the effects of individual phenomena at every length scale is a challenge that has yet to be conquered. Experiments probing the response tend to smear the meso-scale effects, but strides are continually being made to address this by the community.

With the continued refinement of experimental techniques, ultrafast imaging, synchrotron radiation sources, laser shock technologies, and improvements in ultrafast diagnostics, the method developers will have a wealth of information to refine their models and simulation capabilities. Numerical simulation remains a powerful tool to help assess the nature of the complex shock compression event.

In this regard, ICMSE has proven to be an invaluable tool in helping to explore the sources of chemical reactivity in intermetallic-forming powder mixtures. Microstructure-based simulations provided a possible explanation for the interesting observations of both optimal stoichiometries leading to enhanced chemical reactivity, as well as the dispersed wave mechanics inherent to the reactive powder mixture.

Probing the microstructure and quantifying the behavior for all possible instantiations is a difficult task and ongoing research. Better microstructural descriptions and statistical analysis are required to define structure-property linkages between the microstructure and the bulk shock response. In addition, microstructure-sensitive constitutive models and microstructurally aware experiments using time-resolved and highly spatially resolved measurement capabilities will continue to provide important data to help define these structure-property linkages. ICMSE toolsets sensitive to the complexities of high strain rate events can provide closure to some of the important questions of microstructural tailorability for performance of powder mixtures.

References

1. E. Abu-Nada, Natural convection heat transfer simulation using energy conservative dissipative particle dynamics. Phys. Rev. E **81**(5) (2010). https://doi.org/10.1103/physreve.81.056704
2. E. Abu-Nada, Application of dissipative particle dynamics to natural convection in differentially heated enclosures. Mol. Simul. **37**(2), 135–152 (2011). https://doi.org/10.1080/08927022.2010.533272
3. E. Antillon, K. Banlusan, A. Strachan, Coarse grain model for coupled thermo-mechano-chemical processes and its application to pressure-induced endothermic chemical reactions. Model. Simul. Mater. Sci. Eng. **22**(2), 025027 (2014). https://doi.org/10.1088/0965-0393/22/2/025027
4. E. Antillon, A. Strachan, Mesoscale simulations of shockwave energy dissipation via chemical reactions. J. Chem. Phys. **142**(8), 084108 (2015). https://doi.org/10.1063/1.4908309
5. R.A. Austin, D.L. McDowell, A dislocation-based constitutive model for viscoplastic deformation of FCC metals at very high strain rates. Int. J. Plast. **27**(1), 1–24 (2011). https://doi.org/10.1016/j.ijplas.2010.03.002
6. R.A. Austin, D.L. McDowell, Parameterization of a rate-dependent model of shock-induced plasticity for copper, nickel, and aluminum. Int. J. Plast. **32–33**, 134–154 (2012). https://doi.org/10.1016/j.ijplas.2011.11.002
7. R.A. Austin, D.L. McDowell, D.J. Benson, Numerical simulation of shock wave propagation in spatially-resolved particle systems. Model. Simul. Mater. Sci. Eng. **14**(4), 537–561 (2006). https://doi.org/10.1088/0965-0393/14/4/001
8. R.A. Austin, D.L. McDowell, D.J. Benson, Mesoscale simulation of shock wave propagation in discrete Ni/Al powder mixtures. J. Appl. Phys. **111**, 123511 (2012). https://doi.org/10.1063/1.4729304
9. J.B. Avalos, A.D. Mackie, Dissipative particle dynamics with energy conservation. Europhys. Lett. (EPL) **40**(2), 141–146 (1997). https://doi.org/10.1209/epl/i1997-00436-6
10. L.S. Bennett, Y. Horie, Shock-induced inorganic reactions and condensed phase detonations. Shock Waves **4**, 127 (1994)
11. L.S. Bennett, F.Y. Sorrell, I.K. Simonsen, Y. Horie, K. Iyer, Ultrafast chemical reactions between nickel and aluminum powders during shock loading. Appl. Phys. Lett. **61**(5), 520–521 (1992)
12. D. Benson, I. Do, M. Meyers, Computational modeling of the shock compression of powders, in *Shock Compression of Condensed Matter – 2001*, ed. by M. Furnish, N. Thadhani, Y. Horie (American Institute of Physics, Melville, 2002), pp. 1087–1092
13. D. Benson, V. Nesterenko, F. Jonsdottir, Micromechanics of shock deformation of granular materials, in *Shock Compression of Condensed Matter 1995*, ed. by S. Schmidt, W. Tao (American Institute of Physics, Woodbury/New York, 1996), pp. 603–606

14. J.K. Brennan, M. Lísal, J.D. Moore, S. Izvekov, I.V. Schweigert, J.P. Larentzos, Coarse-grain model simulations of nonequilibrium dynamics in heterogeneous materials. J. Phys. Chem. Lett. **5**(12), 2144–2149 (2014). https://doi.org/10.1021/jz500756s
15. H.J. Choi, R. Austin, J.K. Allen, D.L. McDowell, F. Mistree, D.J. Benson, An approach for robust design of reactive power metal mixtures based on non-deterministic micro-scale shock simulation. J. Comput.-Aided Mater. Des. **12**(1), 57–85 (2005). https://doi.org/10.1007/s10820-005-1056-1
16. G.E. Duvall, R.A. Graham, Phase transitions under shock-wave loading. Rev. Mod. Phys. **49**(3), 523 (1977)
17. D.E. Eakins, N.N. Thadhani, Shock compression of reactive powder mixtures. Int. Mater. Rev. **54**(4), 181 (2009)
18. P. Español, Hydrodynamics from dissipative particle dynamics. Phys. Rev. E **52**(2), 1734–1742 (1995). https://doi.org/10.1103/physreve.52.1734
19. P. Español, Dissipative particle dynamics with energy conservation. Europhys. Lett. (EPL) **40**(6), 631–636 (1997). https://doi.org/10.1209/epl/i1997-00515-8
20. P. Español, P. Warren, Statistical mechanics of dissipative particle dynamics. Europhys. Lett. (EPL) **30**(4), 191–196 (1995). https://doi.org/10.1209/0295-5075/30/4/001
21. J. Field, S. Walley, W. Proud, H. Goldrein, C. Siviour, Review of experimental techniques for high rate deformation and shock studies. Int. J. Impact Eng. **30**(7), 725–775 (2004). https://doi.org/10.1016/j.ijimpeng.2004.03.005
22. J.W. Forbes, *Shock Wave Compression of Condensed Matter – A Primer* (Springer, 2012)
23. U. Frisch, B. Hasslacher, Y. Pomeau, Lattice-gas automata for the navier-stokes equation. Phys. Rev. Lett. **56**(14), 1505–1508 (1986). https://doi.org/10.1103/physrevlett.56.1505
24. D.T. Fullwood, B.L. Adams, S.R. Kalidindi, A strong contrast homogenization formulation for multi-phase anisotropic materials. J. Mech. Phys. Solids **56**(6), 2287–2297 (2008). https://doi.org/10.1016/j.jmps.2008.01.003
25. M. Gonzales, The mechanochemistry in heterogeneous reactive powder mixtures under high-strain-rate loading and shock compression. Ph.D. thesis (2015)
26. M. Gonzales, A. Gurumurthy, G.B. Kennedy, A.M. Gokhale, N.N. Thadhani, Microstructure-based simulations of the high-strain-rate response of heterogeneous Ti/Al/B reactive powder mixtures, in *Proceedings of the Fall 2012 Meeting of the Materials Research Society* (MRS, Boston, 2012)
27. M. Gonzales, A. Gurumurthy, G.B. Kennedy, A.M. Gokhale, N.N. Thadhani, Shock compression response of Ti+B reactive powder mixtures. J. Phys. Conf. Ser. **500**, 052013 (2014)
28. M. Gonzales, A. Gurumurthy, G.B. Kennedy, A.M. Gokhale, N.N. Thadhani, Heterogeneity and microstructural topology effects on the shock response of Ti+B+Al reactive powder mixtures. In preparation (2015)
29. M. Gonzales, A. Gurumurthy, G.B. Kennedy, A.M. Gokhale, N.N. Thadhani, Meso-scale heterogeneity effects on the bulk shock response of Ti+Al+B reactive powder mixtures, in *AIP Conference Proceedings*, vol. 1793 (2017), p. 080007
30. R.A. Graham, Sandia Laboratories Report SAND88-1055. Technical report, Sandia National Laboratory (1988)
31. R.A. Graham, Issues in shock-induced solid state chemistry, in *3rd International Symposium High Dynamic Pressures*, Paris, ed. by R. Cheret, 1989, pp. 175–180
32. R.A. Graham, *Solids Under High-Pressure Shock Compression* (Springer, 1993)
33. R.A. Graham, M.U. Anderson, Y. Horie, S.K. You, G.T. Holman, Pressure measurements in chemically reacting powder mixtures with the Bauer piezoelectric polymer gauge. Shock Waves **3**, 79–82 (1993)
34. R.D. Groot, P.B. Warren, Dissipative particle dynamics: bridging the gap between atomistic and mesoscopic simulation. J. Chem. Phys. **107**(11), 4423–4435 (1997). https://doi.org/10.1063/1.474784
35. A. Gurumurthy, Simulation Methodologies for Multiphase Three-Dimensional Microstructures. Ph.D. thesis, Georgia Institute of Technology (2014)

36. A. Gurumurthy, A.M. Gokhale, A. Godha, M. Gonzales, Montage serial sectioning: some finer aspects of practice. Metallogr. Microstruct. Anal. **2**, 364–371 (2013)
37. A. Gurumurthy, M. Gonzales, A.M. Gokhale, N.N. Thadhani, Bulk orientational anisotropy without spatial anisotropy due to powder compaction in Al-Ti-B compacts. Scr. Mater. **86**, 28–31 (2014)
38. J.M. Haile, *Molecular Dynamics Simulation – Elementary Methods*, professional paperback ed. edn. (John-Wiley, 1997)
39. P.J. Hoogerbrugge, J.M.V.A. Koelman, Simulating microscopic hydrodynamic phenomena with dissipative particle dynamics. Europhys. Lett. (EPL) **19**(3), 155–160 (1992). https://doi.org/10.1209/0295-5075/19/3/001
40. Y. Horie, R. Graham, I. Simonsen, Synthesis of nickel aluminides under high-pressure shock loading. Mater. Lett. **3**(9–10), 354–359 (1985). https://doi.org/10.1016/0167-577X(85)90075-8. http://www.sciencedirect.com/science/article/pii/0167577X85900758
41. Y. Horie, R.A. Graham, I.K. Simonsen, in *Metallurgical Applications of Shock-Wave and High-Strain-Rate Phenomena*, ed. by L.E. Murr, K.P. Staudhammer, M.A. Meyers (Mercel Dekker, Inc., 1986), p. 1023
42. Y. Horie, A.B. Sawaoka, *Shock Compression Chemistry of Materials* (KTK, Tokyo, 1993)
43. H. Jarmakani, E. Bringa, P. Erhart, B. Remington, Y. Wang, N. Vo, M. Meyers, Molecular dynamics simulations of shock compression of nickel: from monocrystals to nanocrystals. Acta Mater. **56**(19), 5584–5604 (2008). https://doi.org/10.1016/j.actamat.2008.07.052
44. Z. Kang, A.A. Banishev, G. Lee, D.A. Scripka, J. Breidenich, P. Xiao, J. Christensen, M. Zhou, C.J. Summers, D.D. Dlott, N.N. Thadhani, Exploration of CdTe quantum dots as mesoscale pressure sensors via time-resolved shock-compression photoluminescent emission spectroscopy. J. Appl. Phys. **120**(4), 043107 (2016). https://doi.org/10.1063/1.4959257
45. M.I. Latypov, L.S. Toth, S.R. Kalidindi, Materials knowledge system for nonlinear composites. Comput. Methods Appl. Mech. Eng. **346**, 180–196 (2019). https://doi.org/10.1016/j.cma.2018.11.034
46. R. Lebensohn, C. Tomé, A self-consistent anisotropic approach for the simulation of plastic deformation and texture development of polycrystals: application to zirconium alloys. Acta Metallurgica et Materialia **41**(9), 2611–2624 (1993). https://doi.org/10.1016/0956-7151(93)90130-k
47. R. Lebensohn, C. Tomé, A self-consistent viscoplastic model: prediction of rolling textures of anisotropic polycrystals. Mater. Sci. Eng. A **175**(1–2), 71–82 (1994). https://doi.org/10.1016/0921-5093(94)91047-2
48. A.D. Mackie, J.B. Avalos, V. Navas, Dissipative particle dynamics with energy conservation: modelling of heat flow. Phys. Chem. Chem. Phys. **1**(9), 2039–2049 (1999). https://doi.org/10.1039/a809502g
49. J.B. Maillet, M. Mareschal, L. Soulard, R. Ravelo, P.S. Lomdahl, T.C. Germann, B.L. Holian, Uniaxial hugoniostat: a method for atomistic simulations of shocked materials. Phys. Rev. E **63**(1) (2000). https://doi.org/10.1103/physreve.63.016121
50. L.E. Malvern, *Introduction to the Mechanics of a Continuous Medium* (Prentice-Hall Inc., 1969)
51. T.I. Mattox, J.P. Larentzos, S.G. Moore, C.P. Stone, D.A. Ibanez, A.P. Thompson, M. Lísal, J.K. Brennan, S.J. Plimpton, Highly scalable discrete-particle simulations with novel coarse-graining: accessing the microscale. Mol. Phys. **116**(15–16), 2061–2069 (2018). https://doi.org/10.1080/00268976.2018.1471532
52. A.E. Mattsson, P.A. Schultz, M.P. Desjarlais, T.R. Mattsson, K. Leung, Designing meaningful density functional theory calculations in materials science—a primer. Model. Simul. Mater. Sci. Eng. **13**(1), R1–R31 (2004). https://doi.org/10.1088/0965-0393/13/1/r01
53. T. Mattsson, L. Shulenburger, S. Root, K. Cochrane, Density functional theory (DFT) simulations of co2 under shock compression and design of liquid co2 experiments on z (2011)
54. M.A. Meyers, *Dynamic Behavior of Materials* (John Wiley, 1994)
55. M.A. Meyers, H. Jarmakani, E.M. Bringa, B.A. Remington, Dislocations in shock compression and release, in *Dislocations in Solids*, chap. 89, ed. by J.P. Hirth, L. Kubin (Elsevier B. V., 2009)

56. T. Mura, *Micromechanics of Defects in Solids* (Kluwer Academic Publishers, 1991)
57. L. Murr, Examination of microstructural development by shock waves in condensed matter: theoretical and practical consequences, in *Shock Waves in Condensed Matter – 1987*, ed. by S. Schmidt, N. Holmes (Elsevier, Amsterdam, 1988), pp. 315–320
58. L. Murr, M. Pradhan-Advani, C. Niou, L. Schoenlein, Correlating critical process parameters and microstructures in explosively fabricated ceramic/metal matrix superconductors, in *Shock Compression of Condensed Matter – 1989*, ed. by S. Schmidt, J. Johnson, L. Davison (Elsevier, Amsterdam, 1990), pp. 587–590
59. L.E. Murr, K.P. Staudhammer, Shock wave sensitization, shock-induced reactivity, and new materials fabrication, in *Shock Waves for Industrial Applications*, chap. 12, ed. by L.E. Murr (Noyes Publications, 1988), pp. 441–472
60. V. Nesterenko, *Dynamics of Heterogeneous Materials* (Springer, 2001)
61. S.R. Niezgoda, Y.C. Yabansu, S.R. Kalidindi, Understanding and visualizing microstructure and microstructure variance as a stochastic process. Acta Mater. **59**(16), 6387–6400 (2011). https://doi.org/10.1016/j.actamat.2011.06.051
62. K.T. Ramesh, High rates and impact experiments, in *Springer Handbook of Experimental Solid Mechanics* (Springer, 2008), pp. 929–960. https://doi.org/10.1007/978-0-387-30877-7_33
63. R. Ravelo, B. Holian, T. Germann, P. Lomdahl, Constant-stress hugoniostat method for following the dynamical evolution of shocked matter. Phys. Rev. B **70**(1) (2004). https://doi.org/10.1103/physrevb.70.014103
64. M. Rice, J. Walsh, Dynamic compression of liquids from measurements on strong shock waves. J. Chem. Phys. **26**, 824 (1957)
65. M. Ripoll, P. Español, M.H. Ernst, Dissipative particle dynamics with energy conservation: heat conduction. Int. J. Mod. Phys. C **09**(08), 1329–1338 (1998). https://doi.org/10.1142/s0129183198001205
66. D.A. Scripka, G. Lee, Z. Kang, C.J. Summers, N.N. Thadhani, Time-resolved spectral response of asymmetrical optical microcavity structures under laser-driven shock compression. AIP Adv. **8**(1), 015021 (2018). https://doi.org/10.1063/1.5000376
67. M.S. Sellers, M. Lísal, I. Schweigert, J.P. Larentzos, J.K. Brennan, Shock simulations of a single-site coarse-grain RDX model using the dissipative particle dynamics method with reactivity. Author(s) (2017). https://doi.org/10.1063/1.4971502
68. C.B. Skidmore, D.S. Phillips, P.M. Howe, J.T. Mang, J.A. Romero, The evolution of microstructural changes in pressed HMX explosives, in *Proceedings of the Eleventh International Detonation symposium* (1998)
69. P. Sood, S. Dwivedi, J. Brennan, N. Thadhani, Y. Horie, DPDE-based mesoscale simulations of shock response of HE composites. J. Phys. Conf. Ser. **500**(17), 172002 (2014). https://doi.org/10.1088/1742-6596/500/17/172002
70. A.K. Stover, N.M. Krywopusk, J.D. Gibbins, T.P. Weihs, Mechanical fabrication of reactive metal laminate powders. J. Mater. Sci. **49**(17), 5821–5830 (2014). https://doi.org/10.1007/s10853-014-8187-2
71. A. Strachan, B.L. Holian, Energy exchange between mesoparticles and their internal degrees of freedom. Phys. Rev. Lett. **94**(1) (2005). https://doi.org/10.1103/physrevlett.94.014301
72. N. Thadhani, Shock induced chemical synthesis of intermetallic compounds, in *Shock Compression of Condensed Matter – 1989*, ed. by S. Schmidt, J. Johnson, L. Davison (Elsevier, Amsterdam, 1990), pp. 503–510
73. N. Thadhani, E. Dunbar, R. Graham, Characteristics of shock-compressed configuration of Ti and Si powder mixtures, in *High Pressure Science and Technology 1993*, ed. by S. Schmidt, J. Shaner, G. Samara, M. Ross (American Institute of Physics, New York, 1994), pp. 1307–1310
74. N.N. Thadhani, Shock-induced chemical reactions and synthesis of materials. Prog. Mater. Sci. **37**, 117–226 (1993)
75. N.N. Thadhani, Shock-induced and shock-assisted solid-state chemical reactions in powder mixtures. J. Appl. Phys. **76**(4), 2129–2138 (1994)

76. N.N. Thadhani, A. Gokhale, J. Quenneville, Meso-scale experimental and numerical studies for predicting macro-scale performance of advanced reactive materials. DTRA Proposal BRBAA08-Per3-E-2-0040 (2010)
77. N.N. Thadhani, R.A. Graham, T. Royal, E. Dunbar, M.U. Anderson, G.T. Holman, J. Appl. Phys. **82**(3), 1113 (1997)
78. S. Torquato, Random heterogeneous media: microstructure and improved bounds on effective properties. Appl. Mech. Rev. **44**(2), 37 (1991). https://doi.org/10.1115/1.3119494
79. S. Torquato, *Random Heterogeneous Materials* (Springer, New York, 2002). https://doi.org/10.1007/978-1-4757-6355-3
80. P.B. Warren, Dissipative particle dynamics. Curr. Opin. Colloid Interface Sci. **3**(6), 620–624 (1998). https://doi.org/10.1016/s1359-0294(98)80089-7
81. C. Wei, B. Maddox, A. Stover, T. Weihs, V. Nesterenko, M. Meyers, Reaction in ni–al laminates by laser-shock compression and spalling. Acta Mater. **59**(13), 5276–5287 (2011). https://doi.org/10.1016/j.actamat.2011.05.004
82. C. Wei, V. Nesterenko, T. Weihs, B. Remington, H.S. Park, M. Meyers, Response of Ni/Al laminates to laser-driven compression. Acta Mater. **60**(9), 3929–3942 (2012). https://doi.org/10.1016/j.actamat.2012.03.028
83. N.S. Weingarten, W.D. Mattson, A.D. Yau, T.P. Weihs, B.M. Rice, A molecular dynamics study of the role of pressure on the response of reactive materials to thermal initiation. J. Appl. Phys. **107**(9), 093517 (2010). https://doi.org/10.1063/1.3340965
84. Q. Wu, F. Jing, Thermodynamic equation of state and application to Hugoniot predictions for porous materials. J. Appl. Phys. **80**, 4343 (1996)

Correction to: Transverse Failure of Unidirectional Composites: Sensitivity to Interfacial Properties

Scott Zacek, David Brandyberry, Anthony Klepacki, Chris Montgomery, Maryam Shakiba, Michael Rossol, Ahmad Najafi, Nancy Sottos, Philippe Geubelle, Craig Przybyla, George Jefferson, and Xiang Zhang

Correction to:
Chapter 12 in: S. Ghosh et al. (eds.),
***Integrated Computational Materials Engineering (ICME)*,**
https://doi.org/10.1007/978-3-030-40562-5_12

The published version of the book has missed to include one of the co-author "Xiang Zhang" in chapter 12.

This error has been corrected, and the text has been updated in the book.

The updated online version of this chapter can be found at
https://doi.org/10.1007/978-3-030-40562-5_12

S. Ghosh et al. (eds.), *Integrated Computational Materials Engineering (ICME)*,
https://doi.org/10.1007/978-3-030-40562-5_15

Index

S. Ghosh et al. (eds.), *Integrated Computational Materials Engineering (ICME)*,
https://doi.org/10.1007/978-3-030-40562-5